THE
PHYSICAL REVIEW

A journal of experimental and theoretical physics established by E. L. Nichols in 1893

SECOND SERIES, VOL. 97, NO. 3 FEBRUARY 1, 1955

Thermodynamic Properties of He^3 and He^4 Solutions

V. S. NANDA*
Department of Physics and Astronomy, Ohio State University, Columbus, Ohio
(Received July 16, 1954)

In the present paper the thermodynamics of mixing of He^3 and He^4 solutions has been investigated on the basis of the existing theories. De Boer and Gorter's theory is modified to take account of the non-ideal character of the solution above the λ temperature. The theoretical vapor pressure results are compared with Sommers' measurements at the dew point. It is found that certain features can be explained only on the de Boer-Gorter-Taconis approach. However, the incompatibility of any theory based on Taconis' hypothesis with Sommers' extensive vapor pressure measurements at fixed liquid concentrations prevents us at present from drawing any definite conclusions. Valuable information about the proper choice of the model for He^3 and He^4 solutions might, however, be obtained by an experimental study of the variation of heat of mixing and specific heat of mixing with temperature and concentration.

I. INTRODUCTION

AN interpretation of the behavior of He^3 and He^4 solutions is at present difficult because of lack of reliable experimental data. For example, the results of various investigators[1–4] for vapor pressure below the λ temperature are not in mutual agreement and hence it is difficult to decide which of the existing theories represents a correct approximation to the problem. Among the theories which have been proposed to explain the variation of λ temperature with He^3 concentration, only those of de Boer and Gorter[5] and Heer and Daunt[6] have been applied in the explanation of vapor pressure results. Recently, Sommers has put forward the view that the λ transition does not have an appreciable effect on vapor pressure results and that a purely classical approach is adequate, at least as a first approximation. In fact, his extensive measurements, quite unlike the earlier results of Taconis,[1] gave little support to the theory of de Boer and Gorter. This cast doubt on Taconis' hypothesis, according to which He^3 dissolves only in the normal fluid. Taconis,[7] however, has very recently reported new measurements which are in line with his previous data and which he states are in substantial agreement with de Boer and Gorter's theory. Since the vapor pressure measurements did not seem to provide a unique answer to the necessity of Taconis' hypothesis, an alternative test was suggested by the author[8] in a recent paper. It was shown that the existing theories predict remarkably different behavior for the heat of mixing; in particular, de Boer and Gorter's theory gives rather high values for this quantity. Experimental determination of the heat of mixing should, therefore, give a clue to the correct model.

In the present paper we have carried out a detailed study of the thermodynamic functions of mixing. This appeared necessary not only because of its intrinsic interest but also because of its immediate importance. Extensive measurements on the heat of mixing might be hampered due to the nonavailability of pure He^3 in substantial quantities. On the other hand, experiments on the specific heat of mixing do not seem to involve this difficulty and may throw some light on this elusive problem. As it is now known definitely that even above the λ temperature of pure helium the solution exhibits

* Present address: Physics Department, Delhi University, Delhi, India.

[1] Taconis, Beenaker, Nier, and Aldrich, Physica 15, 733 (1949).
[2] J. G. Daunt and C. V. Heer, Phys. Rev. 79, 46 (1950).
[3] B. N. Eselsen and B. G. Lazarev, J. Exptl. Theorel. Phys. (U.S.S.R.) 20, 1055 (1950).
[4] H. S. Sommers, Jr., Phys. Rev. 88, 113 (1952).
[5] J. de Boer and C. G. Gorter, Physica 16, 225 (1950).
[6] C. V. Heer and J. G. Daunt, Phys. Rev. 81, 447 (1951).
[7] K. W. Taconis, Abstracts of the Third International Conference on Low Temperature Physics and Chemistry, Rice Institute, 1953 (unpublished).
[8] V. S. Nanda, Phys. Rev. 94, 241 (1954).

a non-ideal behavior, it therefore appears necessary here to discuss a suitable variant of de Boer and Gorter's theory which takes account of this departure from ideality. Lastly, we have compared the theoretical results with Sommers[4] vapor pressure data at the dew point. It was thought that these values should not be seriously affected by heat fluxes which are present in the customary methods of measurements.

II. A MODIFICATION OF DE BOER AND GORTER'S THEORY

De Boer and Gorter write the Gibbs free energy of the solution in the form

$$G=(1-X_L)G_4(T,x)+X_LG_3 +RT\frac{X_L}{X_e}\{X_e\ln X_e+(1-X_e)\ln(1-X_e)\}, \quad (1)$$

where the suffixes 3 and 4 refer to He^3 and He^4 components respectively, X_L denotes the actual concentration of He^3, while $X_e=X_L/\{X_L+x(1-X_L)\}$ is the effective concentration reckoned with respect to the normal fluid which contains a fraction x of the total number of He^4 atoms. Above T_λ, the λ temperature of pure helium (He^4), $G_4(T,x)$ has the same value in solution and in the pure form; also, because $X_e=X_L$, Eq. (1) reduces to expression for Gibbs free energy of an ideal solution. Thus, the partial pressures of the two components should be governed by Raoult's law for $T>T_\lambda$. Actually, the pressure above T_λ has been found by several workers[4,9–11] to be higher than the ideal value. As these results are not subject to any serious experimental errors which may be ascribed to measurements below the λ temperature, we should develop the theory of de Boer and Gorter in such a way that it takes proper account of non-ideality above T_λ. We have found a regular solution model adequate in this region. Thus, if the de Boer-Gorter-Taconis approach is correct, the Gibbs free energy of the solution should be written in the form

$$G=(1-X_L)G_4(T,x)+X_LG_3 +RT\frac{X_L}{X_e}\{(1-X_e)\ln(1-X_e)+X_e\ln X_e\} +X_L(1-X_e)W, \quad (2)$$

where $W=(l_{33}+l_{44}-2l_{34})$, the l's being a measure of the interaction energy between the like and unlike pairs. W is called the non-ideality parameter or the interchange energy.[12] Applying the condition of equilibrium, $(\partial G/\partial x)_{T,X}=0$, we get from Eq. (2) the relation

$$(\partial G_4/\partial x)_{T,X}+RT\ln(1-X_e)+WX_e^2=0. \quad (3)$$

For G_4, de Boer and Gorter adopt the expression,

$$G_4=-E_\lambda(1-x^{7/6})-xS_\lambda T, \quad (4)$$

which is suggested by the quasi-thermodynamic theory of Tisza, E_λ being a constant equal to $(6/7)T_\lambda S_\lambda$ and S_λ being the entropy of pure He^4 at T_λ. This choice is not a very happy one, as above T_λ this leads to temperature independent expression for entropy implying zero specific heat for helium I. Another expression for G_4, also used by de Boer,[13] involves a quadratic function for term in T. We have, in this case (see also Daunt[14]),

$$G_4=-E_\lambda(1-x^{7/6})-\frac{1}{2}\frac{S_\lambda}{T_\lambda}T^2x^{5/6}, \quad (5)$$

where $E_\lambda=(5/14)T_\lambda S_\lambda$. This expression gives an entropy for helium I which increases linearly with temperature, as observed experimentally, and hence it will be used here instead of (4).

We have yet to make a proper choice of the non-ideality parameter. This point has been discussed in some detail by Sommers[4] who finds Scatchard's expression,

$$W=(l_{33}^{\frac{1}{2}}-l_{44}^{\frac{1}{2}})^2, \quad (6)$$

unsuitable, as it leads to rather high positive deviations from the experimentally observed vapor pressure. He therefore adopts van Laars expression,

$$W=\left(\frac{a_{33}^{\frac{1}{2}}}{b_{33}}-\frac{a_{44}^{\frac{1}{2}}}{b_{44}}\right)^2, \quad (7)$$

obtained on the basis of van der Waals theory, the a's and b's being the usual constants. This expression is slightly better but still gives high values for the vapor pressure; also, since it has been obtained on the basis of van der Waal's model for the liquid, it is theoretically unsound. Actually, in the derivation of (6) and (7), it has been assumed that the interaction between the unlike pairs is the geometric mean of the interaction between the like pairs. Such an assumption has usually been found to be valid whenever the interaction forces are of the London dispersion-force type. There is, however, no special reason why this relation should always hold.[15] At least it does not appear to be justified

[9] Fairbank, Reynolds, Lane, McInteer, Aldrich, and Nier, Phys. Rev. 74, 345 (1948).
[10] Weinstock, Osborne, and Abraham, Phys. Rev. 77, 400 (1950).
[11] T. P. Tseng and J. G. Daunt (unpublished).
[12] This name is taken from Hildebrand and Scott, *Solubility of Non-electrolytes* (Reinhold Publishing Corporation, New York, 1950), p. 144.
[13] J. de Boer, Phys. Rev. 76, 852 (1949).
[14] J. G. Daunt, Phil. Mag. 1, 251 (1952).
[15] It might be pointed out here that, if the rule of the geometric mean were always true, only positive deviations from Raoult's law could be expected from a regular solution. Without this restriction the whole range of positive and negative deviations can be explained on this model. The condition of ideal behavior, instead of being $l_{AA}=l_{BB}$, takes the more general form $l_{AB}=\frac{1}{2}(l_{AA}+l_{BB})$ as proposed by Guggenheim [*Mixtures* (Clarendon Press, Oxford, 1952), p. 24].

in the case of the helium problem. Under these conditions we have no means of evaluating W theoretically. This is, however, not a serious difficulty, since for a regular solution W is constant and may be determined readily from the excess chemical potential. Morrow[16] has made such calculations for He^3-He^4 solutions from Sommers' experimental results. We find from his computations an average value for W of 1.81 calories per mole. This choice of W also gives a satisfactory explanation of the vapor pressure results of Tseng and Daunt[11] on four percent He^3 solution in the temperature region $T>T_\lambda$.

III. THERMODYNAMICS OF MIXING

Since the term involving W does not appear in the original theory of de Boer and Gorter, it would be of interest to study its effect on the variation of λ temperature with concentration. Using Eqs. (3) and (5) and putting $X_e=X_L$, we have

$$1-X_L=\exp\left\{-\frac{1}{3}\left(\left(\frac{T_\lambda}{T}\right)^{1/6}-\left(\frac{T}{T_\lambda}\right)^{1/6}+\frac{3WX_L^2}{RT}\right)\right\}, \quad (8)$$

where we have substituted the numerical value $S_\lambda=0.8R$. For given X_L the value of T satisfying (8) corresponds to $T_\lambda{}^S$, the λ temperature of the solution. In Fig. 1 we have plotted $T_\lambda{}^S/T$ against X_L for $W=0$, 1.1, 1.81 cal/mole. The effect of the introduction of the non-ideality term is small for low values of X_L but it improves the agreement with experiment. For $X_L>0.5$, only $W=1.1$ describes the observed variation adequately. It appears tempting to assume that this value is the best choice for W. However, the agreement between theory and experiment at low temperatures may be fortuitous, since in our expression for the Gibbs free energy we have not taken account of phonons which play an important role at low temperatures.

Subtracting the value of the Gibbs free energy of the pure components from (2), we get the mixing term:

$$G_{\rm mix}=(1-X_L)\{G_4(T,x)-G_4(T,x_0)\}+RT(X_L/X_e)\{X_e\ln X_e+(1-X_e)\ln(1-X_e)\}+X_L(1-X_e)W, \quad (9)$$

where x_0 denotes the fraction of the normal fluid in pure helium at temperature T. A study of the variation of $G_{\rm mix}$ with T and X_L is important in connection with the problem of stability against phase separation. However, we shall not pursue this point here as such a situation, according to the present theory, can arise only in the temperature region where our expression for the Gibbs free energy requires modification.

We can calculate other thermodynamic functions of

[16] J. G. Morrow, Phys. Rev. 89, 1034 (1953).

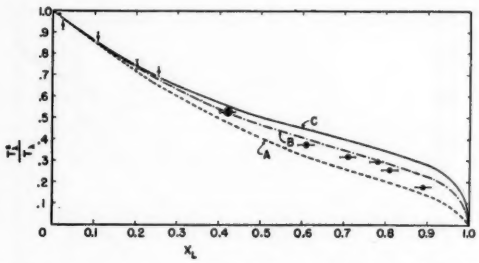

FIG. 1. The variation of $T_\lambda{}^s$ with X_L, the concentration of He^3. Curves A, B, and C correspond to $W=0$, 1.1 and 1.81 cal/mole respectively.

interest from Eq. (9). The entropy of mixing is

$$S_{\rm mix}=-\partial G_{\rm mix}/\partial T=(1-X_L)\{S_4(T,x)-S_4(T,x_0)\}-R\frac{X_L}{X_e}\{X_e\ln X_e+(1-X_e)\ln(1-X_e)\}. \quad (10)$$

Since $S_4(T,x)>S_4(T,x_0)$ for $T<T_\lambda$, the terms in the first braces give a positive contribution to the entropy of mixing. Above $T_\lambda{}^S$ the terms in the second braces have a constant value equal to the ideal entropy of mixing, but their value decreases continuously below this temperature. Therefore, in the temperature region $T_\lambda>T>T'$, $S_{\rm mix}$ has a value greater than the ideal value, where T' is some temperature lower than T.

In what follows we shall not distinguish between internal energy and enthalpy, as is usual for liquids not subject to high pressures. From Eqs. (5) and (9) we obtain the heat of mixing,

$$U_{\rm mix}=-T^2\frac{\partial}{\partial T}\left(\frac{G_{\rm mix}}{T}\right)=S_\lambda T_\lambda(1-X_L)\left\{\frac{5}{14}(x^{7/6}-x_0{}^{7/6})+\frac{1}{2}\left(\frac{T}{T_\lambda}\right)^2(x^{5/6}-x_0{}^{5/6})\right\}+X_L(1-X_e)W. \quad (11a)$$

Above the λ temperature of pure helium, $x=x_0=1$, and therefore the heat of mixing is given by the classical value $X_L(1-X_L)W$. For $T<T_\lambda$, x_0 is obtained from the relation $x_0=(T/T_\lambda)^6$, while x can be calculated from the equation

$$\left(\frac{T_\lambda}{T}\right)x^{1/6}-\left(\frac{T}{T_\lambda}\right)x^{-1/6}+3\ln(1-X_e)+\frac{3WX_e^2}{RT}=0, \quad (12)$$

obtained from (3) and (5). Since the term involving W is quadratic in X_e, the x values are not significantly affected by it so long as the condition $X_e\ll1$ is satisfied. In Fig. 2 we have plotted $\Delta U_{\rm molar}(=U_{\rm mix}/X_L)$, the

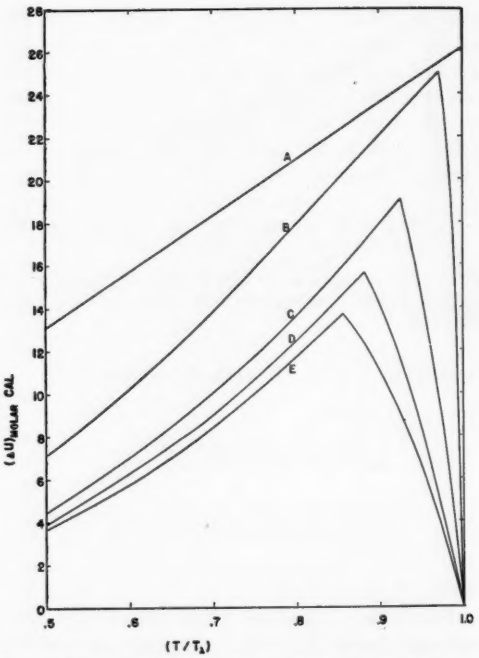

FIG. 2. The variation of ΔU_{molar}, the heat of mixing for a mole of He^3 in solution, with temperature according to de Boer and Gorter theory with a quadratic model for G_4. Curves A, B, C, D, and E correspond respectively to $X_e \to 0$, $X_L = 0.01$, 0.05, 0.08, and 0.10.

heat of mixing for a mole of He^3 in solution, for different concentrations. The values of ΔU_{molar} for $W = 1.81$, to a first approximation, can be obtained from Fig. 2 by adding the contribution $(1-X_e)W$. In Table I these contributions have been tabulated for different concentrations.

In the case of infinite dilution, characterized by $X_e \to 0$, Eq. (11a) reduces to a rather simple form. Assuming $x = x_0 + \alpha$ and substituting in (12), we find $\alpha = 9X_L$, provided terms quadratic in X_e are ignored. Equation (11a) can then be written in the form

$$U_{\text{mix}} = X(6RT + W). \tag{11b}$$

The expression for the specific heat of mixing may be obtained from Eq. (11a). Taking $S_\lambda = 0.8R$ and $x_0 = (T/T_\lambda)^6$, we have

$$C_{\text{mix}} = dU_{\text{mix}}/dT = 0.8(1-X_L)\left\{\frac{5}{6}T\frac{dx}{dT}\left[\frac{T_\lambda}{T}x^{1/6} + \frac{T}{T_\lambda}x^{-1/6} + \frac{3}{2}X_e^2\frac{W}{RT}\right] + 2\left(\frac{T}{T_\lambda}\right)x^{5/6} - 12\left(\frac{T}{T_\lambda}\right)^6\right\}, \tag{13a}$$

where

$$T\frac{dx}{dT} = 18x\frac{\{\ln[1+X_L/x(1-X_L)] + \frac{2}{3}(T/T_\lambda)x^{-1/6}\}}{\{(T_\lambda/T)x^{1/6} + (T/T_\lambda)x^{-1/6} + 18X_e - 36WX_e^2(1-X_e)/RT\}}.$$

For infinite dilution,

$$C_{\text{mix}} = 6RX. \tag{13b}$$

In Fig. 3 we have plotted $\Delta C_{\text{molar}} = (C_{\text{mix}}/X_L)$ against temperature for different concentrations, taking $W = 0$. These values, to a first approximation, give the specific heat value also for nonzero values of W provided $X_e \ll 1$. It should be noticed that theory predicts rather high values for the specific heat of mixing, which jumps from a large negative value above T_λ^S to a large positive value below this temperature. To take a specific example, for a ten percent solution at 1.1°K the relative contributions of He^3, He^4, and the mixing term are roughly 1:1:8. Measurements of the specific heat of the solution should, thus, clearly show the large contribution of the mixing term. In this connection it is interesting to note that a regular solution model in the classical form involves zero specific heat of mixing. This result is intuitively unacceptable for the helium solution as it implies that the anomaly in the specific heat of the solution should occur at T_λ and not at T_λ^S.

On the basis of the theory of Heer and Daunt,[6] the expressions for the specific heat of mixing above and below the λ temperature can be obtained from Eqs. (2a) and (2b) for the heat of mixing given in our previous paper.[8] We have, for $T < T_\lambda^S$,

$$C_{\text{mix}} = \frac{15}{4}X_L R\frac{\zeta(5/2)}{\zeta(3/2)}\frac{v_3^0}{v_4^0}\left(\frac{T}{T_\lambda}\right)^{\frac{3}{2}}; \tag{14a}$$

and for $T > T_\lambda$, assuming X_L very small, we get

$$C_{\text{mix}} = -\frac{3}{2}X_L R\frac{v_3^0}{v_4^0}\left(\frac{T_\lambda^S}{T}\right)^{\frac{3}{2}}\left\{0.261 + 0.090\left(\frac{T_\lambda^S}{T}\right)^{\frac{3}{2}} + 0.0207\left(\frac{T_\lambda^S}{T}\right)^{5/2} + \cdots\right\}. \tag{14b}$$

In the case of an infinitely dilute solution, T_λ and T_λ^S coincide and an interesting conclusion follows. The

TABLE I. The contribution $(1-X_e)W$ in calories to be added to the ΔU_{molar} values plotted in Fig. 2 to allow for a finite value of W (taken equal to 1.81 calories per mole).

T/T_λ	X_e	$(1-X_e)W$	T/T_λ	X_e	$(1-X_e)W$
	(a) $X_L = 0.01$			(b) $X_L = 0.05$	
0.95	0.0121	1.79	0.926	0.0500	1.72
0.9	0.0162	1.78	0.9	0.0557	1.71
0.8	0.0285	1.76	0.8	0.0840	1.66
0.7	0.0513	1.72	0.7	0.1237	1.59
0.6	0.0878	1.65	0.6	0.1753	1.50
0.5	0.1345	1.57	0.5	0.2364	1.38
	(c) $X_L = 0.08$			(d) $X_L = 0.10$	
9	0 0800	1.67	9	0.1000	1.63
8	0.1072	1.62	8	0.1194	1.59
7	0.1494	1.54	7	0.1631	1.51
6	0.2013	1.45	6	0.2132	1.42
5	0.2692	1.32	5	0.3012	1.26

specific heat of mixing, which is negative above T_λ, jumps to a positive value below this temperature (see Fig. 4) even though the theoretical values of the specific heat of the pure components are always continuous. The discontinuity, however, is characteristic only of an infinitely dilute solution and changes to a smooth transition for finite concentrations. The magnitude of the mixing term also is smaller by an order of magnitude in comparison with the result obtained from Eq. (13).

IV. EXPRESSIONS FOR PARTIAL VAPOR PRESSURES

The formulas for partial vapor pressures can be deduced by equating the chemical potentials of the components in the vapor and the liquid phases. From Eq. (9), we have

$$\mu_{3L}-\mu_{3L}^0=kT\log X_e+(1-X_e)^2(W/N), \tag{15a}$$

$$\mu_{4L}-\mu_{4L}^0=kTx\log(1-X_e)+xX_e^2(W/N)+(1/N)\{G_4(T,x)-G_4(T,x_0)\}, \tag{16a}$$

where μ and μ^0 represent the chemical potentials in the mixed and pure states respectively. For the vapor, taking account of imperfections up to the second virial coefficient, we can write

$$\mu_{3v}-\mu_{3v}^0=kT\log(p_3/p_3^0)+(P-p_3^0)B_{33}+(1-X_v)^2P\gamma, \tag{15b}$$

and

$$\mu_{4v}-\mu_{4v}^0=kT\log(p_4/p_4^0)+(P-p_4^0)B_{44}+X_v^2P\gamma, \tag{16b}$$

where $\gamma=(2B_{34}-B_{33}-B_{44})$ and $P=p_3+p_4$, B's being the virial coefficients. The values of B_{33} and B_{44} have been calculated by van Kranendonk *et al.*,[17] but we have no knowledge of the cross virial coefficient B_{34}.

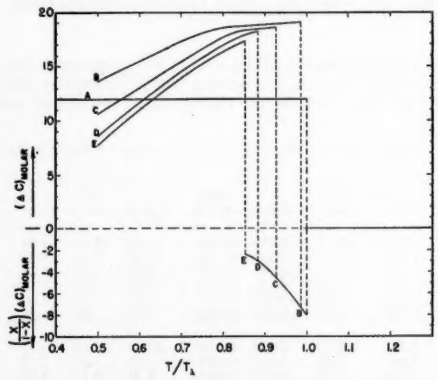

FIG. 3. The variation of ΔC_{molar} with temperature according to de Boer and Gorter theory with a quadratic model for G_4. The curves A, B, C, D, and E correspond respectively to $X_e\to 0$, $X_L=0.01$, 0.05, 0.08, 0.1. (The word "cal" should be added to the ordinate.)

[17] van Kranendonk, Compaan, and de Boer, Phys. Rev. **76**, 998 (1946).

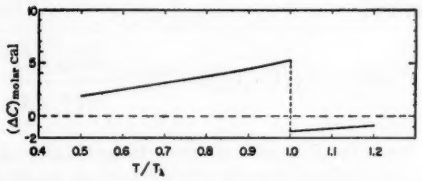

FIG. 4. The variation of ΔC_{molar} with temperature according to the theory of Heer and Daunt for $X_L\to 0$.

Kilpatrick,[18] in his computations, has made use of the simple assumption $B_{34}=(B_{33}+B_{44})/2$, whereas Morrow[15] has recourse to the Lorentz approximation (see also Beattie[19]), which gives $B_{34}=(B_{33}^{\frac{1}{3}}+B_{44}^{\frac{1}{3}})^3/8$. The difference between the two expressions, however, above 1.2°K is very small. Equating the chemical potentials in the liquid and the vapor phases, we have

$$p_3=p_3^0X_e\exp[\{(1-X_e)^2W-B_{33}(P-p_3^0)-\gamma(1-X_v)^2\}/RT], \tag{17a}$$

$$p_4=p_4^0(1-X_e)^x\exp[\{G_4(T,x)-G_4(T,x_0)-B_{44}(P-p_3^0)-\gamma X_v^2\}/RT]. \tag{17b}$$

The existence of discontinuities in the temperature derivatives of vapor pressure at the λ point of the solution is of interest both from the experimental and theoretical standpoints. Assuming a second order transition for the solution, de Boer and Gorter[20] have shown from purely thermodynamic considerations that dp_3/dT and dp_4/dT should have discontinuities at $T_\lambda{}^S$. Dropping the virial corrections for the sake of simplicity, we have

$$kT\log(p_3/p_3^0)=(\mu_{3L}-\mu_{3L}^0)=\frac{1-X_L}{N}\left(\frac{\partial G_{\text{mix}}}{\partial X_L}\right).$$

Since p_3, p_3^0, and dp_3^0/dT are continuous functions of T, we can write

$$\Delta\frac{\partial}{\partial T}\log p_3=-\frac{1-X_L}{RT^2}\Delta C_{\text{mix}}\frac{dT_\lambda{}^S}{dX_L}, \tag{18}$$

where $\Delta F=F_{\text{I}}-F_{\text{II}}$ is the change in the value of the function on crossing the transition temperature from phase I to phase II. Following the same procedure, the relation

$$\Delta\frac{\partial}{\partial T}\log p_4=\frac{X_L}{RT^2}\frac{dT_\lambda{}^S}{dX_L}\Delta C_{\text{mix}} \tag{19}$$

is obtained from Eq. (16b). Combining (18) and (19)

[18] J. E. Kilpatrick, Phys. Rev. **79**, 529 (1950).
[19] J. A. Beattie, Chem. Revs. **44**, 178 (1949).
[20] J. de Boer and C. G. Gorter, Physica **18**, 565 (1952).

we can write

$$\Delta\frac{\partial}{\partial T}(P-p_4^0)=-\{(1-X_L)p_3-X_Lp_4\}\frac{\Delta C_{\text{mix}}}{RT^2}\frac{dT_\lambda^S}{dX_L}. \quad (20)$$

The theoretical value of the discontinuity in the temperature derivative of $P-p_4^0$ can be easily determined, as the values of all the quantities involved are calculable from the formulas of this paper.

V. COMPARISON WITH EXPERIMENTAL DATA

It is generally believed that Sommers' measurements gave no evidence of discontinuities in the partial vapor pressures at the λ point. However, on plotting the observed values of $P-p_4^0$, given in Table IV of his paper, against temperature a discontinuous change in slope at T_λ^S is revealed as shown in Fig. 5. It should be noticed that on crossing the λ temperature from phase I to phase II the slope of the curve [i.e., $d(P-p_4^0)/dT$] increases contrary to what is expected from Eq. (20). This suggests that some other phenomenon appearing at the λ point causes a much larger discontinuity in the opposite direction. This effect might be caused by the inevitable heat fluxes which arise with the appearance of the superfluid and drive He^3 away from the surface.

Sommers has also measured the vapor pressure at the dew point when the vapor just begins to condense. These measurements should not be seriously affected by heat fluxes which come into play when the bulk liquid has been actually formed. Accordingly, we have analyzed his dew-point data in the following way: From $\Delta P/P$ values given in his Table I we have calculated p_3, which is used to determine X_L according to the regular solution model and Eq. (17a) of the present paper. Knowing X_L, p_4 can be calculated and compared with the experimental values. The results of such calculations are presented in Table II, where we have used only those ΔP values for which the experimental error is less than 2 percent. A strange feature of Sommers' dew-point measurements was that at low temperatures and high concentrations of He^3 in the vapor, partial pressures for He^4 higher than the pressure in the pure phase were observed. Such a behavior cannot be understood on the basis of the classical solution theory. Sommers, therefore, concludes that there must have been some hidden source of error in his measurements at low temperatures. The observed high values of p_4, however, receive a natural explanation on the basis of the de Boer-Gorter-Taconis approach. It will be seen from Eq. (16a) that at low temperatures when x is small $\mu_{4L}-\mu_{4L}^0$ will also be small even though X_v (which determines p_3 and hence X_v) is large. Thus, in Eq. (16b), we have a situation in which the left-hand side is very small, its sign of course being negative. The contribution arising from the virial correction terms on the right is also negative. This may become larger than the left-hand side if $P-p_4^0$, which is governed essentially by X_v, is large. Then the equation can be balanced only if the first term on the right makes a positive contribution, which implies $p_4>p_4^0$. It will be seen from Table II that the formulas of this paper actually give p_4 values greater than p_4^0 for large X_v and low temperatures, as observed experimentally.

The reverse calculation, i.e., using p_4 for calculating X_L and determining p_3 from it, brings out the difference between various theories more clearly as will be seen from Tables III and IV. In Table III we have used smoothed values for calculating X_L at 1.7°K for different X_v, while in Table IV unsmoothed data have

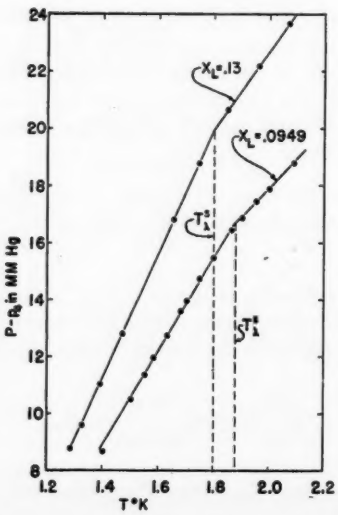

FIG. 5. A plot of $P-p_4^0$ against temperature, where the $P-p_4^0$ values are taken from Sommers' data (reference 4) at constant liquid concentration.

TABLE II. Calculation of X_L and p_4 from Sommers' dew-point data according to C.R.S. (classical regular solution) and dBG +R.S. (de Boer and Gorter theory based on regular solution model).

X_v	T°K	p_3 mm Hg	X_L C.R.S.	X_L dBG +R.S.	p_4 mm Hg C.R.S.	p_4 mm Hg dBG +R.S.	p_4 mm Hg Exp.	p_4^0 mm Hg
	2.142	85.91	0.418	0.418	23.45	23.47	24.09	34.32
	1.703	27.65	0.270	0.270	6.88	7.46	7.65	8.62
	1.702	26.71	0.257	0.257	6.99	7.58	7.49	8.60
0.781	1.688	25.26	0.254	0.254	6.56	7.15	7.19	8.10
	1.285	3.86	0.107	0.013	1.02	1.12	1.09	1.11
	1.268	3.57	0.080	0.0067	0.93	1.00	1.00	0.99
	1.978	28.13	0.154	0.154	19.48	19.80	20.37	21.97
	1.662	9.87	0.130	0.084	6.56	7.07	7.15	7.32
0.58	1.546	6.35	0.072	0.0096	4.20	4.43	4.60	4.44
	1.486	4.75	0.061	0.0011	3.20	3.40	3.45	3.38
	1.448	3.85	0.053	0.0008	2.67	2.79	2.79	2.79
	2.155	22.84	0.092	0.092	33.14	33.15	33.56	35.53
0.405	1.697	5.76	0.048	0.016	8.10	8.38	8.45	8.40
	1.695	5.72	0.048	0.016	8.04	8.32	8.41	8.34
	2.159	5.36	0.027	0.027	35.75	35.76	35.84	36.30
0.13	2.052	4.07	0.020	0.016	27.08	27.17	27.23	27.48
	1.918	2.76	0.015	0.008	18.36	18.46	18.44	18.57

TABLE III. Calculation of X_L and p_3 from Sommers' smoothed dew-point data according to H.D. (Heer and Daunt) theory, C.R.S., and dBG+R.S. at 1.7°K.

	P	p_4	X_L			p_3 mm Hg			
X_v	mm Hg	mm Hg	H.D.	C.R.S.	dBG +R.S.	H.D.	C.R.S.	dBG +R.S.	Exp.
0.781	34.49	7.55	0.178	0.172	0.245	23.55	19.13	25.26	26.94
0.58	19.58	8.22	0.054	0.053	0.091	8.63	6.90	14.42	11.33
0.405	14.38	8.55	0.0042	0.0042	0.0126	0.71	0.58	4.77	5.79

TABLE IV. Calculation of X_L and p_3 from Sommers' unsmoothed data on pressure at the dew point according to H.D., C.R.S., and dBG+R.S.

		p_4	X_L			p_3 mm Hg			
X_v	T°K	mm Hg	H.D.	C.R.S.	dBG +R.S.	H.D.	C.R.S.	dBG +R.S.	Exp.
0.781	2.142	24.09	0.447	0.398	0.398	91.56	82.63	82.63	85.91
	1.688	7.19	0.163	0.205	0.249	22.37	21.57	25.12	25.61
0.58	1.978	20.37	0.133	0.111	0.127	25.72	20.92	25.79	28.13
	1.662	7.15	0.035	0.034	0.059	3.73	2.93	8.52	9.87

been employed.[21] It will be seen that the deviations of the classical regular solution and the Heer-Daunt theory from the experimental values are more severe for low He^3 concentrations in the vapor; for higher concentrations they become pronounced only at lower temperatures. It appears that the deviations are large whenever the concentration of the normal fluid in the solution is small. The formulas of this paper, however, always yield results which are (considering the uncertainty in the measured values) in reasonable agreement with experiment.

VI. CONCLUSION

The general agreement of the theoretical results of this paper with Sommers' dew-point measurements seemingly provides some evidence in favor of Taconis' hypothesis. On the other hand, Sommers himself, on comparing with various theories his vapor pressure results for fixed liquid concentrations, noticed a considerable departure of his results from the original de Boer and Gorter's theory at low temperatures, the theoretical values being too high. Since we have introduced here an additional positive heat-of-mixing term, our vapor pressure results are still higher. Thus Sommers' two sets of data, obtained by different methods do not seem to be in mutual agreement. The wrong sign of the discontinuity in the temperature derivative of $P-p_4^0$ provides some ground for believing that the experimental results at a fixed liquid concentration might have been affected by heat fluxes which keep He^3 away from the surface. But the evidence is not quite conclusive. Since no definite conclusions can be drawn from vapor pressure results alone, the need of experimental investigation of other properties of the solution can hardly be overemphasized. The present paper shows that measurements on the heat of mixing and the specific heat of mixing may provide a clue to the correct model.

It is a pleasure to record my thanks to Professor J. G. Daunt for his continued interest in the above investigation and several valuable suggestions. I am also thankful to Dr. T. P. Tseng for friendly discussions and to the Institute of International Education for arranging the award of a U. S. Government fellowship.

[21] Only the data for high He^3 concentration in the vapor for $T>1.6$°K has been used for the calculation of X_L from p_4 because of the limited accuracy of the experimental results.

Compressibilities of Some Solidified Gases at Low Temperature

JOHN W. STEWART*
Jefferson Physical Laboratory, Harvard University, Cambridge, Massachusetts
(Received October 26, 1954)

The compressibilities of several solidified gases have been measured by applying a one-sided compression directly to a cylindrical sample, and observing the resulting volume change. Pressure was conveyed to the samples at low temperature by means of long stainless steel compression and tension members. Preliminary extrusion experiments with these solidified gases assured that the pressure applied to the samples was always at least approximately hydrostatic. Compressibility data have been obtained at pressures up to 10 000 kg/cm² for solid hydrogen and deuterium at 4°K, and to 4000 kg/cm² for solid neon at 4°, solid argon at 65° and 77°, and solid krypton at 77°. A single less accurate determination has also been made for solid nitrogen up to 3000 kg/cm².

I. INTRODUCTION

EXPERIMENTAL measurements of compressibilities by the piston displacement method have not previously been feasible at very low temperature because of technical problems involved in the simultaneous production of high hydrostatic pressure and low temperature. The only existing low-temperature compressibility measurements have made use of techniques other than the observation of piston displacement, and have necessarily been confined to relatively low pressures. The two main difficulties heretofore confronting the more direct approach have been (1) the excessive quantity of heat that would be transferred to a liquid helium cooling bath by conduction through the heavy steel parts of conventional high-pressure equipment, and (2) the absence at such temperatures of suitable fluid pressure-transmitting media.

In the present work, the cooling problem was overcome through the use of long cylindrical compression and tension members which were attached to a conventional hydraulic press at room temperature. These could apply compressive force to samples maintained at 4°K. They were made of an 18–8 austenitic stainless steel (Type 304), since these alloys combine unusually high mechanical strength and ductility at low temperature with low thermal conductivity. Forces up to a ton and a half could be applied at 4°K to samples $\frac{1}{4}$ inch in diameter. Once the apparatus had been cooled down, less than 100 cm³ of liquid helium per hour were lost by evaporation from the cryostat.

Even at low pressures there exist no liquids or gases at liquid helium temperatures. Helium itself solidifies at 4.2° at a pressure of only 140 atmospheres. Therefore the usual technique of embedding the samples under investigation in a pressure-transmitting liquid cannot be used. Instead, it is necessary to rely upon solid materials to transmit hydrostatic pressure. Bridgman[1] has encountered and solved this same problem at room temperature during his investigations at pressures of 100 000 kg/cm².

The force applied to the cylindrical samples was, in the present apparatus, always a one-sided compression. Under these conditions, meaningful compressibility data can be obtained only if the applied uniaxial stress system is effectively translated into a hydrostatic pressure within the solid sample. For this to be the case, the material under investigation must have a very low shear strength. It must be capable of flowing plastically under low applied force so that the shear components of stress within a confined sample are always small compared with the hydrostatic component. Only for such plastic substances can the compressibility be directly calculated from the displacement of the piston with which the one-sided compression is applied.

The most convenient measure of plastic flow strength turned out to be the applied pressure required to cause extrusion of the cylindrical samples through a smaller axial hole. The samples varied between $\frac{1}{4}$ inch and $\frac{1}{2}$ inch in length, while the diameter of the extrusion hole ranged from $\frac{1}{16}$ inch to $\frac{3}{16}$ inch. Extrusion pressures were measured for a number of different materials, sometimes at both liquid nitrogen and liquid helium temperatures. The sample holder used in these measurements is shown in Fig. 1. Several normally solid substances, including some of the alkali metals, were investigated as well as solidified gases.

In all cases, the extrusion pressures were taken to be those at which relatively rapid flow through the hole

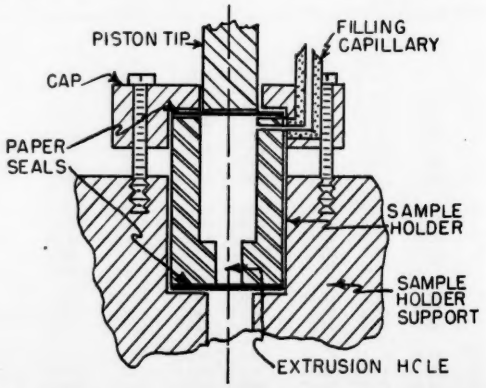

FIG. 1. The apparatus for solidified gas extrusion experiments.

* Now at the University of Virginia, Charlottesville, Virginia.
[1] P. W. Bridgman, Proc. Am. Acad. Arts Sci. 74, 425 (1942).

took place. These values were often considerably above the initial yield points. The best pressure transmitters are clearly those materials which extrude rapidly and smoothly at low pressure. Solid hydrogen and deuterium proved to be by far the most satisfactory, with the other solidified gases listed in Table I being somewhat inferior. The most plastic of the normally solid materials investigated at 4°K were the alkali metals, but all of these were poorer than the majority of the gases of Table I. A number of substances which are quite plastic at room temperature were found to harden up greatly at low temperature.

The quoted extrusion pressures, while reproducible to perhaps 10 percent, have little absolute significance. They depend upon several variables, including the sample length and the size of the extrusion hole. However, the relative magnitudes of these pressures, for fixed sample length and hole size, are meaningful as measures of the comparative ability of different substances to transmit hydrostatic pressure.

Compressibility data were taken for each of the solidified gases of Table I at each temperature listed. These were all felt to be sufficiently good pressure transmitters to justify the direct method of measurement, especially since there is evidence that this criterion of complete extrusion is a bit too stringent. The observed extrusion pressures were often higher than the initial yield points by an amount greater than could reasonably be expected from work hardening.

It is worth remarking that, while quite plastic at liquid nitrogen temperatures, the solid argon and krypton samples were shattered instead of being extruded by pressure at 4°K. Solid nitrogen at 4° was also somewhat brittle. All the gases were used directly from storage tanks without prepurification. The presence of a small amount of impurity might be expected to make the samples more brittle at low temperature while having only negligible effect upon their compressibilities.

II. EXPERIMENTAL TECHNIQUE

The stainless steel tension and compression members were hollow concentric cylinders approximately two feet long, the lower ends of which were immersed in the cooling bath of liquid helium or liquid nitrogen. Pressures up to 4000 kg/cm² could be exerted on the samples at low temperature by means of a piston tip $\frac{1}{4}$ inch in diameter. The piston tips and sample holders were made of hardened steel or beryllium copper. The highest pressures attainable were limited by buckling of the long slender compression member rather than by the ultimate strength of any part of the equipment, although, to reduce heat influxes, all designs were close to yield strength. The external diameter of the compression member was $\frac{3}{4}$ inch and its wall thickness 0.06 inch.

Force was applied to the upper end of the compression member (always at room temperature) by means of the piston of a hydraulic press, which was driven by oil under pressure. This pressure was generated with a hand pump, and was accurately measured by means

TABLE I. Pressures at which cylindrical solidified gas samples, $\frac{1}{4}$ inch in diameter and $\frac{1}{2}$ inch long, extrude through $\frac{1}{8}$-inch hole.

Substance	Temperature °K	Extrusion pressure (kg/cm² × 10⁻³)
Hydrogen	4	0.24
Deuterium	4	0.29
Neon	4	0.67
Argon	77	0.26
Argon	63	0.58
Krypton	77	0.34
Nitrogen	4	0.88

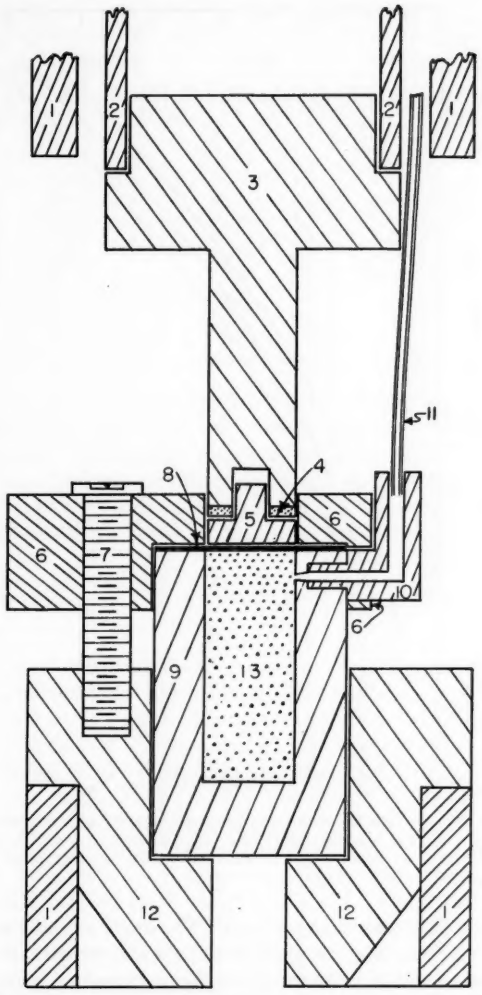

FIG. 2. The apparatus for compressibility measurements at low temperature. 1. Tension member. 2. Compression member. 3, 4, 5. Experimental piston tip with potassium packing washer. 8. Sealing paper. 9. Sample holder. 10, 11. Filling capillary. 12. Sample holder support. 13. Solidified gas sample.

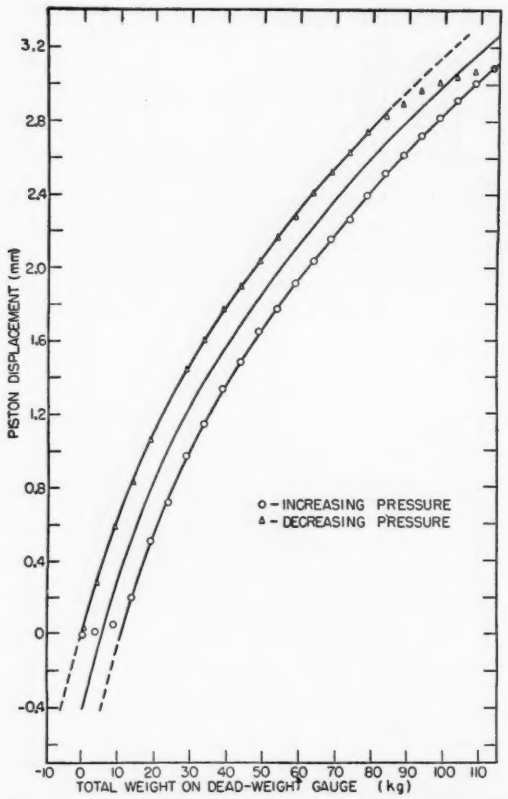

FIG. 3. Plot of piston displacement against sample pressure for a typical compressibility run (solid deuterium sample). (One kilogram on dead-weight gauge corresponds to pressure of 37.8 kg/cm².)

of a dead-weight piston gauge. The use of a dead-weight gauge also made it possible to hold the pressure on the sample at a constant value for a period of minutes. The maximum sample pressure of 4000 kg/cm² corresponded to an oil pressure of about 5000 lb/in.²

Values of the displacement under pressure of the experimental piston at 4° were deduced from observations of the position of a fine scratch machined near the top of the compression member. This scratch was visible through a window in the wall of the hydraulic press. Readings reproducible within a few thousandths of a millimeter could be made by means of a small traveling microscope.

The cryostat was of all-metal construction, based upon the original design of Henry and Dolecek.[2] The inner helium pot, of 1.5 liters capacity, was separated from the liquid nitrogen space by a vacuum jacket, while a second separate vacuum jacket insulated the liquid nitrogen from room temperature. The heat influxes were sufficiently small so that, at 4°K, runs lasting more than six hours could be made on one filling.

The sample holder rested on a support which was inserted in a slot milled near the bottom of the stainless steel tension member. The experimental piston tip was attached to the bottom of the compression member (Fig. 2).

The solidified gas samples were prepared by direct condensation into the sample holder through the capillary tube. This was connected with a supply of the appropriate gas at room temperature. The solidified samples as prepared in this manner were all $\frac{1}{4}$ inch in diameter and about $\frac{1}{2}$ inch long. During the condensation process, leakage of gas around the piston was prevented by the sealing paper (a Glassine envelope window). As soon as pressure was applied, the piston easily broke through the paper and pressed directly upon the solidified sample. During the filling care had to be exercised that the capillary did not become blocked with solid. This required holding the apparatus at precisely the correct level in the cryostat.

The same technique was used to prepare the gas samples for the extrusion experiments which have been described above. During the filling, the extrusion hole was also covered by a paper seal (Fig. 1). When extrusion started, the extruded plug readily punched a hole through the lower paper.

The actual compressibility measurements were made by a method due originally to Bridgman.[1] It was assumed, as indicated by the results of the extrusion measurements for these substances, that the applied uniaxial compression was translated into a purely hydrostatic pressure. After each gas had been condensed into the sample holder of Fig. 2, readings of piston displacement *versus* pressure were taken for increasing and decreasing pressure. In order to obtain reproducible results, however, one first had to raise the pressure rapidly to its maximum value. This irreversibly compacted the samples, which had always frozen loosely. Once this compaction had been completed, the piston displacement *versus* pressure curves became quite reproducible from run to run. The considerable friction in the apparatus always resulted in a "hysteresis loop" of piston displacement *versus* pressure, such as is shown in Fig. 3. Usually two or three complete cycles could be obtained with each sample. The size of the steps by which the sample pressure was changed between readings made no significant difference in the results. The increments varied between about 50 kg/cm² and 400 kg/cm².

"Blank" runs with no sample in the sample holder

TABLE II. Values of K_0 and ξ for solidified gases.

Substance	Temperature °K	K_0 kg/cm²×10⁻³	ξ
Hydrogen	4	2.1	−1.9±0.1
Deuterium	4	3.3	−1.6±0.1
Neon	4	10.7	−4.3±0.5
Argon	65	16.1	−4.7±0.3
Argon	77	11.5	−6.5±0.5
Krypton	77	18.2	−5.1±0.2

[2] W. Henry and R. Dolecek, Rev. Sci. Instr. 21, 496 (1950).

TABLE III. Pressure-volume relations and isothermal compressibilities (in $cm^3/kg \times 10^6$) for some solidified gases.

Pressure kg/cm²	Hydrogen 4°K $-\frac{\Delta V}{V_0}$	Hydrogen 4°K $-\frac{1}{V_0}\left(\frac{\partial V}{\partial P}\right)_T$	Deuterium 4°K $-\frac{\Delta V}{V_0}$	Deuterium 4°K $-\frac{1}{V_0}\left(\frac{\partial V}{\partial P}\right)_T$	Neon 4°K $-\frac{\Delta V}{V_0}$	Neon 4°K $-\frac{1}{V_0}\left(\frac{\partial V}{\partial P}\right)_T$	Argon 65°K $-\frac{\Delta V}{V_0}$	Argon 65°K $-\frac{1}{V_0}\left(\frac{\partial V}{\partial P}\right)_T$	Argon 77°K $-\frac{\Delta V}{V_0}$	Argon 77°K $-\frac{1}{V_0}\left(\frac{\partial V}{\partial P}\right)_T$	Krypton 77°K $-\frac{\Delta V}{V_0}$	Krypton 77°K $-\frac{1}{V_0}\left(\frac{\partial V}{\partial P}\right)_T$
0	0	48	0	30	0	9.4	0	6.2	0	8.7	0	5.5
200	0.075	28	0.055	20	0.016	8.0	0.011	5.5	0.017	7.0	0.010	4.9
400	0.120	19	0.091	16	0.031	6.9	0.021	5.0	0.030	5.9	0.019	4.4
600	0.156	15	0.118	13	0.044	6.1	0.030	4.5	0.041	5.2	0.028	4.0
1000	0.206	10.7	0.162	10.0	0.064	5.0	0.047	3.8	0.059	4.2	0.042	3.4
2000	0.287	5.8	0.237	5.5	0.107	3.4	0.080	2.8	0.093	3.0	0.072	2.5
3000	0.337	4.0	0.284	4.0	0.136	2.6	0.105	2.2	0.119	2.3	0.095	2.0
4000	0.370	3.0	0.318	3.0	0.158	2.2	0.124	1.9	0.140	1.9	0.113	1.7
6000	0.418	2.0	0.368	2.0								
8000	0.451	1.5	0.402	1.5								
10 000	0.477	1.2	0.426	1.2								

had to be made in order to obtain the distortion under pressure of the apparatus itself. Correction for friction was made by averaging (horizontally) between the curves for increasing and decreasing pressure. This gave rise to the central curve of Fig. 3. The length of the sample under zero pressure (after initial compaction) could be determined quite accurately from a comparison of piston positions during the actual run and the blank run. After the corrections had been applied, the relative change of volume $(-\Delta V/V_0)$ was calculated as a function of pressure with an estimated experimental error of less than 5 percent.

For neon, argon, krypton, and nitrogen, the measurements were carried up to about 4000 kg/cm², while, as has previously been described,[3] hydrogen and deuterium have been investigated to 10 000 kg/cm², using for some of the runs a larger similar apparatus constructed by Dr. C. A. Swenson at Massachusetts Institute of Technology.

III. RESULTS AND DISCUSSION

The relative volume changes and compressibilities for five solidified gases are given in Table III. The results for solid hydrogen and solid deuterium have previously been discussed.[3] The unstable extrusion of these two solids through the small annular space between the piston and the cylinder wall which, during the earlier measurements, often resulted in the complete loss of the samples was eliminated through the use of a Bridgman-type unsupported area packing made of metallic potassium[3] (Fig. 2). Potassium at 4° was found to be soft enough to flow and seal around the piston before the highly plastic H_2 or D_2 could start to extrude. Once such extrusion does start, it proceeds rapidly to completion because the heat released when a small amount of the solid escapes past the piston is considerably more than sufficient to warm up and melt the extruded H_2 or D_2. The solidified rare gases and solid nitrogen showed no such tendency to be extruded, and so did not require any packing.

As in the case of hydrogen and deuterium,[3] the pressure-volume relations for the solidified rare gases neon, argon, and krypton at the temperatures for which they were determined can conveniently be represented in terms of Murnaghan's theory of finite strain. Birch[4] has pointed out that Bridgman's data for a considerable number of solid substances can be treated in this manner. Birch develops the general expression

$$P=\tfrac{3}{2}K_0\left(\frac{V_0}{V}\right)^{5/3}\left\{\left(\frac{V_0}{V}\right)^{\frac{2}{3}}-1\right\}\left\{1-\xi\left[\left(\frac{V_0}{V}\right)^{\frac{2}{3}}-1\right]\right\}, \quad (1)$$

where P and V are the pressure and volume respectively, K_0 the reciprocal of the compressibility at zero pressure, and V_0 the volume at zero pressure. ξ is a constant, involving the higher-order elastic constants of the material, which is adjusted for best fit to the experimental data. It has been found that $\xi=0$ for many metals.[4] However, each of the solidified gases of the present investigation requires the use of nonzero values of ξ in order to represent the experimental results. Table II gives those values of K_0 and ξ which best fit the data. In all cases the fit turns out to be quite good.

The isothermal compressibilities, $-(1/V_0)(\partial V/\partial P)_T$, as functions of pressure may most readily be obtained by differentiation of Eq. (1), using the values of K_0 and ξ from Table II. Table III gives the relative volume changes and compressibilities at different pressures.

The compressibilities of solid hydrogen and deuterium are higher than those for any solid previously measured. The solidified rare gases have compressibilities of the same order of magnitude as those of the alkali metals, which are still large values for solids in general.

In Table IV is given the compressibility of solid nitrogen at 4°K as a function of pressure, as determined with the present apparatus. These results may be considerably less accurate than the others because of the observed brittleness of nitrogen.

The only previous experimental measurements of the compressibilities of solid hydrogen and deuterium are those of Miss Megaw[5] for pressures up to 100 kg/cm². The present results are in satisfactory agreement with

[3] J. W. Stewart and C. A. Swenson, Phys. Rev. 94, 1069 (1954).

[4] F. Birch, J. Geophys. Research 57, 227 (1952).

[5] H. D. Megaw, Phil. Mag. 28, 129 (1939).

TABLE IV. Isothermal compressibility of solid nitrogen at 4°K.

Pressure kg/cm²	$-\frac{1}{V_0}\left(\frac{\partial V}{\partial P}\right)_T$ cm²/kg×10⁶
0	5.2
1000	2.9
2000	2.2
3000	1.9

these over the limited range of pressures where comparison can be made. At zero pressure, her values for the compressibilities are: H_2, $(68\pm15)\times10^{-5}$ cm²/kg, and D_2, $(45\pm20)\times10^{-5}$ cm²/kg. At 100 kg/cm² pressure, she obtains for H_2, 32×10^{-5} cm²/kg, and for D_2, 21×10^{-5} cm²/kg.

Barker, Dobbs, and Jones[6] have determined the adiabatic compressibility of argon at zero pressure at 78°K and 60°K by measuring the velocity of ultrasonic longitudinal waves in the solid. Even allowing for a possible 20 percent difference between the adiabatic and isothermal compressibilities of solid argon, one still finds that the results of Barker *et al.* are nearly 50 percent lower than the current ones. The compressibilities as calculated from ultrasonic data are somewhat uncertain because a value for Poisson's ratio had to be estimated, there being no experimental value for solid argon.

It should be emphasized that Murnaghan's theory of finite strain, while a convenient means for representing compressibility data, is not a real "theory" in the stricter sense through which quantitative correlation with other properties of the solidified gases could be obtained.

A few theoretical calculations of the pressure-volume-temperature relations have been made for the solidified rare gases, particularly for argon. The most promising, that recently performed by Henkel,[7] which is based upon actual determination of the energy eigenvalues, appears to agree quite closely with the present experimental compressibilities below 1000 kg/cm². His calculations do not extend to higher pressure.

Two older theories, those of Kane[8] and Rice,[9] lead to calculated compressibilities which disagree rather badly with the experimental values. Kane's results for neon, argon, and krypton, which are obtained from an assumed interatomic potential function of the van der Waal type, tend to be higher than the experimental data, while the somewhat more empirical results of Rice for argon are considerably too low. The calculations of Kane, however, indicate that the variations with pressure and temperature of the compressibilities of neon, argon, and krypton should be in roughly the same proportions as were actually observed.

There exists no detailed theoretical calculation for the compressibilities of solid hydrogen and deuterium. These are more difficult cases than the solidified rare gases because they do not possess a closed-shell structure. It can be said that solid hydrogen has a greater initial compressibility than solid deuterium because of its larger zero-point energy. The very rapid decrease of compressibility with pressure for both hydrogen and deuterium is also a consequence of the high zero-point energies, which cause the volumes at zero pressure to be larger than they otherwise would be. As the pressure is raised, the energy of compression eventually become much greater than the zero-point energy of either H_2 or D_2. Thus the compressibilities at high pressures are more nearly alike. However, because of the quite appreciable difference between the initial molar volumes, it is fortuitous that the compressibilities as defined herein become exactly the same within the experimental range of pressures. At zero pressure,[5] solid H_2 at 4° has a molar volume of 22.65 cm³ per mole, and solid D_2, 19.56 cm³ per mole. From the data of Table III, it is found[3] that, at the highest observed pressures, the molar volume of hydrogen remains greater than that of deuterium.

In the cases of the solidified rare gases, the decrease of compressibility with increasing atomic weight is consistent with the greater ion core repulsion exhibited by the heavier atoms.

Further measurements of compressibilities of solidified gases at higher pressures are now in progress.

IV. ACKNOWLEDGMENTS

The author would like to thank particularly C. A. Swenson for inspiration and assistance in performing these experiments, as well as for the use of his apparatus for the measurements to 10 000 kg/cm² on solid hydrogen and deuterium. He would also like to express his gratitude to Harvey Brooks and to P. W. Bridgman for many helpful suggestions. Earl Wilkie, of the Jefferson Physical Laboratory machine shop, gave a great deal of invaluable technical assistance.

[6] Barker, Dobbs, and Jones, Phil. Mag. 44, 1182 (1953).
[7] J. Henkel (to be published).
[8] G. Kane, J. Chem. Phys. 7, 603 (1939).
[9] O. Rice, J. Chem. Phys. 12, 289 (1944).

Enhancement of Fluorescence in Solutions Under High-Energy Irradiation*

MILTON FURST AND HARTMUT KALLMANN
New York University, Physics Department, Washington Square, New York, New York
(Received August 23, 1954)

Organic solutions with poor high-energy-induced fluorescence can often be made much more efficient by introducing large concentrations of substances such as naphthalene and some related compounds. The naphthalene can be considered as an intermediate solvent; the energy originally mainly absorbed in the less effective solvent goes over to the naphthalene from which it then proceeds to the fluorescent solute. Naphthalene is considerably more effective as such an intermediate solvent than any other of the known efficient solvents, e.g., xylene. It is shown that the particular effectiveness of naphthalene stems from two causes: first, the energy transfer from the "poor" solvent to naphthalene is faster than to other substances; secondly, the excited naphthalene molecule is often quenched less than, e.g., xylene by quenching atoms present in the solution. These results are applied to the enhancement of the high-energy-induced fluorescence of solutions containing various elements even as heavy as bismuth.

IN recent work,[1] it was shown that the absence of considerable high-energy-induced fluorescence in some solutions is due to a lack of energy transfer from the solvent to the fluorescent molecule, most likely as a consequence of the very short lifetime of the excited solvent molecule. Another effect frequently impeding high-energy-induced fluorescence is that some molecules, especially those of a "poor" solvent, often have the property of quenching other excited molecules, both of the solvent and solute, thereby reducing the high-energy- (and light)-induced fluorescence. It was found that quenching of this latter type more often affects excited solvent molecules than those of the solute.

The purpose of this paper is to show that substances exist which, when put into poorly fluorescent solutions in sizeable amounts, enhance the fluorescence to a greater extent than does the introduction of the known most efficient solvents. Naphthalene and some related compounds can be employed in this manner and are considerably more effective than xylene.

The effectiveness of these substances as intermediate solvents may be due to two processes: First, a more efficient energy transfer occurs from the "poor" solvent to naphthalene than, for example, to xylene. Secondly, the excited naphthalene molecules undergo a smaller quenching (in many instances) by surrounding molecules than do the excited molecules of other substances. The quenching of the excited solvent molecule by the addition of special molecules is often more prominent than that of the solute molecule and is demonstrated by some examples as follows:

High-energy fluorescence is often strongly reduced by the presence of oxygen.[2,3] Thus if the fluorescence is determined as a function of the solute concentration (for example in solutions of xylene and terphenyl), the addition of oxygen is found to produce a shift in the maximum of the curve of fluorescence *vs* concentration toward larger solute concentrations, and similarly the removal of oxygen results in a shift of the maximum toward lower concentrations. The maximum light intensity, however, is changed comparatively little by the removal of oxygen, indicating that mainly the solvent rather than the solute molecule is quenched by oxygen.[4]

Another example is tetralin which, though a very "effective" solvent when pure, deteriorates (from the fluorescence point of view) upon standing in air. This deterioration decreases the high-energy-induced fluorescence tremendously but only comparatively slightly influences the light-induced fluorescence, for example, of 9,10-diphenylanthracene. This shows that the decrease of fluorescence in such tetralin solutions occurs because of quenching of the excited solvent molecules rather than those of the solute.[4]

A final illustration is presented by nitric acid molecules which produce strong quenching of the high-energy fluorescence of xylene or phenylcyclohexane solutions. It is again found that the quenching acts most strongly upon the excited solvent molecule, and the replacement of xylene by naphthalene results in a considerable improvement of the high-energy-induced fluorescence.

EXPERIMENTAL RESULTS

The experiments described below were performed with the same arrangement as that described in a previous paper by the authors[5] except that a nonreflecting beaker was used. Integrated intensity measurements were made, and the high-energy excitation source was 1 mC radium.

The particular effect of naphthalene is demonstrated in Figs. 1 to 4. *n*-butylphosphate was used as the basic solvent; it is very stable and little deterioration of the fluorescence of suitable solutes with time is found. Considerable quantities of many organic substances of

* This work was supported by the Signal Corps Engineering Laboratories, Evans Signal Laboratory, Belmar, New Jersey.
[1] M. Furst and H. Kallmann, Phys. Rev. (to be published).
[2] E. J. Bowen and A. Norton, Trans. Faraday Soc. 35, 44 (1939).
[3] Pringle, Black, Funt, and Sobering, Phys. Rev. 92, 1582 (1953).
[4] This will be discussed more fully in a forthcoming paper.
[5] H. Kallmann and M. Furst, Phys. Rev. 79, 857 (1950).

interest for high-energy fluorescence can be dissolved in it. This solvent by itself, however, displays only small high-energy fluorescence with most of the well-known fluorescent solutes in the usual moderate concentrations.

Figure 1 presents the gamma-ray-induced fluorescence of solutions in *n*-butylphosphate with two different concentrations of 2,5-diphenyloxazole as a function of additional xylene and naphthalene. It is seen that for both solute concentrations the naphthalene curve is above the xylene curve by a factor 1.5. This is interpreted as being due to a faster energy transfer from the *n*-butylphosphate to naphthalene than to xylene when equal masses of naphthalene and xylene are added, since there is no difference in energy transfer from naphthalene or xylene respectively to the solute as shown below. If the fluorescent intensities are compared when equal numbers of molecules are added to the original solvent (instead of equal masses), the difference is even more favorable for naphthalene. It is unfortunate that the naphthalene curve cannot be obtained for high concentrations; only about 23 percent of the solution can consist of naphthalene at room temperature. If the fluorescence of 2,5-diphenyloxazole in pure naphthalene could be determined, the intensity would probably be the same and not higher than that in pure xylene. This conclusion can be deduced from the result that the addition of naphthalene to xylene does not noticeably alter the fluorescence although it is known that with sufficient naphthalene the energy is first transferred from xylene to naphthalene and then finally to the solute.[6] If this conclusion is correct, the curves for xylene and naphthalene of Fig. 1 would merge for 100 percent xylene and naphthalene.

Figure 2 describes similar experiments, this time with a fixed concentration of 9,10-diphenylanthracene serving as the light emitting solute and various amounts of different additional "solvents." Again it can be seen that added naphthalene is more effective than xylene. Acenaphthene behaves very much the same as naphthalene; its own fluorescence is larger than that of naphthalene, but it is still small when compared to that produced by the 9,10-diphenylanthracene. α,α'-binaphthyl gives a much larger fluorescence than naphthalene; in this case the energy is transferred to diphenylanthracene by absorption of radiation as well as by collision, and this makes the fluorescence curve higher. The effect of absorption is noticeable because of the small concentration of diphenylanthracene, which is only slightly soluble. These measurements show that the energy transfer to naphthalene and to related compounds is very similar. The energy transfer to *m*-diethoxybenzene has also been measured in order to study the behavior of a substance which is a moderately effective solvent (as a pure solvent it is about half as effective as xylene). In *n*-butylphosphate it is again about half as good as xylene, indicating that the energy transfer from *n*-butylphosphate to this substance is of the same order as to xylene.

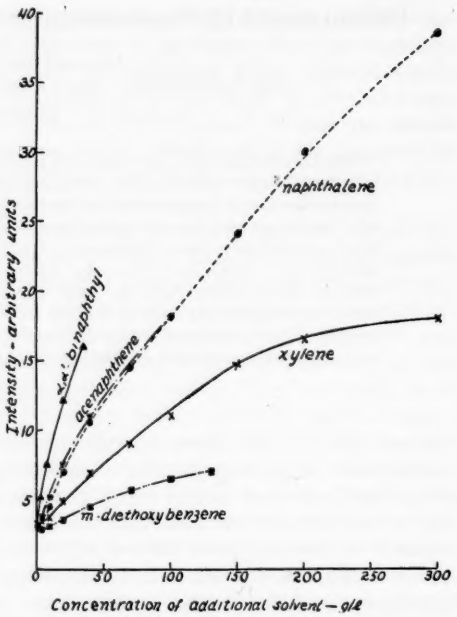

FIG. 2. Effects of additional "solvents" on *n*-butylphosphate +9,10-diphenylanthracene (0.5 g/l).

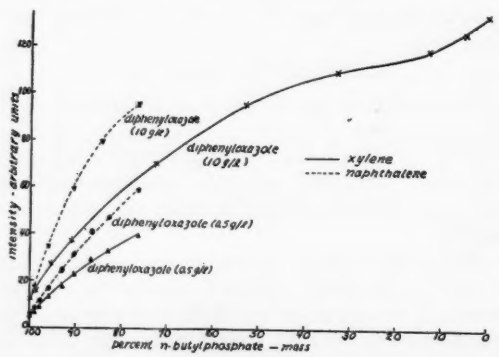

FIG. 1. Florescence of 2,5-diphenyloxazole in mixtures with *n*-butylphosphate.

Comparison of these results with those obtained from the addition of naphthalene to a solution of *p*-terphenyl in xylene[5] reveals that the lifetime of the excited solvent molecule is shorter in *n*-butylphosphate than it is in xylene; this is seen from the better energy transfer to naphthalene in solutions made with xylene than in those with *n*-butylphosphate. Thus when 10 g/l of naphthalene are added to a terphenyl-xylene solution a decrease in fluorescence by a factor of more than three is found.[6] In a solution of 2,5-diphenyloxazole in *n*-butylphosphate, however, the addition of 10 g/l of naphthalene produces only a small increase as can be seen

[6] M. Furst and H. Kallmann, Phys. Rev. **94**, 503 (1954).

in Fig. 1. In the terphenyl-xylene solutions most of the energy originally in the xylene proceeds to the naphthalene with only 10 g/l; but it cannot then go to the terphenyl because of the close proximity of the energy levels of naphthalene and terphenyl; thus the observed large decrease in light output occurs. In *n*-butylphosphate, however, with the same amount of naphthalene only a small fluorescence change occurs because of the poorer transfer of energy to the naphthalene due to the shorter lifetime of the excited butylphosphate molecule. Only when larger amounts of naphthalene are present can this effect of shorter lifetime be overcome. It is interesting to note that the fluorescence of the highest available naphthalene concentration is only about 25 percent below the maximum fluorescence in solutions with pure xylene. This shows that the energy transfer process from *n*-butylphosphate to naphthalene does not involve much loss of energy, which is in agreement with the contention made earlier.

Figure 3 presents the fluorescent light output as a function of the 2,5-diphenyloxazole concentration for various amounts of xylene and naphthalene in *n*-butylphosphate. For the maximum naphthalene concentration (~23 percent of solution by mass), the intensity is already 75 percent of that of a 100 percent xylene solution. Since 25 percent of the primary energy is directly absorbed in the naphthalene, it is calculated from the preceding result that about 70 percent of the energy directly absorbed in *n*-butylphosphate is transferred to the naphthalene at these concentrations whereas with xylene only about 50 percent is transferred. This conclusion is drawn since measurements with light-induced fluorescence have shown that the addition of naphthalene or xylene does not change the light output and thus the internal quenching of such a solute, and since the curves of fluorescence *vs* concentration for naphthalene and xylene respectively in *n*-butylphosphate have the same forms. These curves display shifts of the optimum concentration toward higher

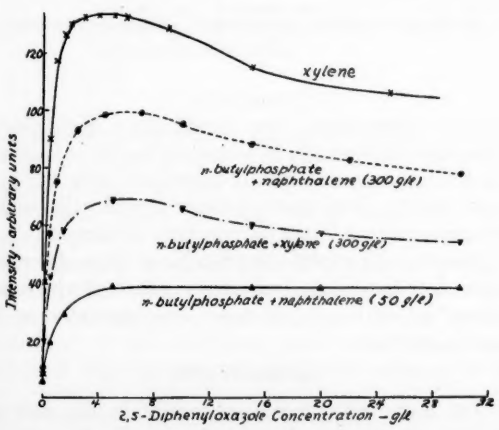
xylene
n-butylphosphate + naphthalene (300 g/l)
n-butylphosphate + xylene (300 g/l)
n-butylphosphate + naphthalene (50 g/l)
Intensity - arbitrary units
2,5-Diphenyloxazole Concentration - g/l

FIG. 3. Gamma-ray-induced fluorescence of 2,5-diphenyloxazole solutions.

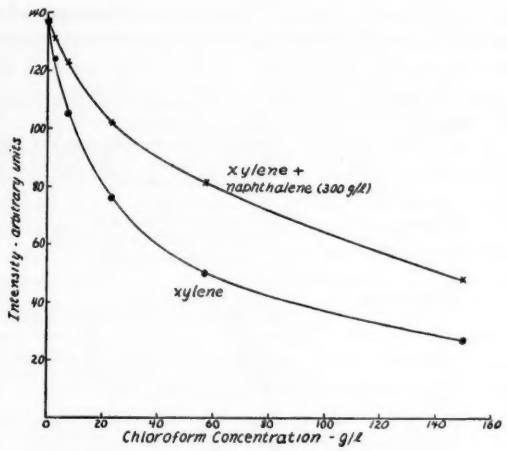

FIG. 4. Effect of chloroform on solutions with 2,5-diphenyloxazole (5 g/l).

concentrations when compared to the curve of 2,5-diphenyloxazole in xylene. This can be interpreted as stemming from a shorter lifetime (due to a stronger quenching) of the excited naphthalene or xylene molecules by surrounding *n*-butylphosphate molecules than without this substance being present. Such an increase of quenching reduces the true lifetimes of these excited molecules thereby decreasing the energy transfer probability to the solute; the result of the shortening of lifetime is a shift in the maximum of the fluorescence *vs* concentration curve. Such stronger quenching by the addition of *n*-butylphosphate to xylene can also be seen from the xylene curve of Fig. 1. There the drop in fluorescence occurring when small amounts of *n*-butylphosphate are added to xylene is probably due to this quenching. One must also consider that some energy transfer still takes place directly from *n*-butylphosphate to the solute; this increases with greater 2,5-diphenyloxazole concentration. Its contribution, however, is still too small in the case of 300 g/l of naphthalene or xylene to account for the observed shift in the curve; with only 50 g/l of naphthalene present this process does become important and partially accounts for the different shape of the corresponding curve. The forms of the 300 g/l naphthalene curve and that of the respective xylene curve, however, are so similar to each other that no difference in lifetime between the excited xylene and excited naphthalene molecules (i.e., in energy transfer from these molecules to the solute) is indicated under these conditions where the *n*-butylphosphate quenching is relatively small.

Such a difference is, however, indicated in other cases in which strong quenching by the surrounding molecules occurs and becomes quite evident from the experiments described in Fig. 4. Here the quenching influence of chloroform on γ-ray-induced fluorescence is studied in solutions of 2,5-diphenyloxazole in pure xylene and in xylene plus 300 g/l naphthalene; in the latter case the

TABLE I. γ-ray fluorescence of solutions containing various elements.

Elements	Solution "Solvent"[a]	Fluorescent solute	Percent of intensity of the same solute in xylene
Boron	Trimethylborate	2,5-diphenyloxazole (3 g/l)	5
	Trimethylborate 50%+xylene 50%	2,5-diphenyloxazole (3 g/l)	79
	Trimethylborate 47%+xylene 31% +naphthalene 22%	2,5-diphenyloxazole (3 g/l)	95
Silicon	Tetraethylorthosilicate	α-naphthylphenyloxazole (3 g/l)	5
	Tetraethylorthosilicate 75% +naphthalene 25%	α-naphthylphenyloxazole (3 g/l)	74
Phosphorous	*n*-Butylphosphate	2,5-diphenyloxazole (10 g/l)	9
	n-Butylphosphate 70%+naphthalene 30%	2,5-diphenyloxazole (10 g/l)	72
Sulfur	Phenylcyclohexane 47%+thiophene 53%	9,10-diphenylanthracene (20 g/l)	28[b]
	Phenylcyclohexane 43%+thiophene 48% +naphthalene 9%	9,10-diphenylanthracene (20 g/l)	61[b]
Chlorine	Chloroform 15%+xylene 85%	2,5-diphenyloxazole (4.5 g/l)	20
	Chloroform 14%+xylene 64% +naphthalene 22%	2,5-diphenyloxazole (4.5 g/l)	35
Arsenic	Xylene 96%+triphenylarsine 4%	9,10-diphenylanthracene (10 g/l)	42
	Xylene 86.5%+triphenylarsine 3.5% +naphthalene 10%	9,10-diphenylanthracene (10 g/l)	83
	Xylene 81%+triphenylarsine 9.5% +naphthalene 9.5%	9,10-diphenylanthracene (10 g/l)	58
Antimony	Xylene+triphenylstibine 1%	9,10-diphenylanthracene (2 g/l)	34
	Xylene 87%+naphthalene 12% +triphenylstibine 1%	9,10-diphenylanthracene (2 g/l)	81
	Xylene 81%+naphthalene 16% +triphenylstibine 3%	9,10-diphenylanthracene (2 g/l)	57
Mercury	Xylene 90%+di-*n*-butylmercury 10%	α-naphthylphenyloxazole (5 g/l)	9
	Xylene 69%+di-*n*-butylmercury 10% +di-*n*-butylmercury 7%	α-naphthylphenyloxazole (5 g/l)	18
	Xylene 66%+naphthalene 23% +di-*n*-butylmercury 11%	α-naphthylphenyloxazole (5 g/l)	15
Lead	Tetraethyllead 10%+xylene 90%	9,10-diphenylanthracene (10 g/l)	24
	Tetraethyllead 9%+xylene 81.5% +naphthalene 9.5%	9,10-diphenylanthracene (10 g/l)	39
	Tetraethyllead 42.5%+xylene 42.5% +naphthalene 15%	9,10-diphenylanthracene (10 g/l)	15
Bismuth	Xylene+triphenylbismuthene 2.5%	α-naphthylphenyloxazole (3 g/l)	25
	Xylene 73%+naphthalene 25% +triphenylbismuthene 2%	α-naphthylphenyloxazole (3 g/l)	54
	Xylene 70%+naphthalene 24% +triphenylbismuthene 6%	α-naphthylphenyloxazole (3 g/l)	21

[a] The percentages indicated are of mass.
[b] In phenylcyclohexane rather than xylene.

energy transfer to the fluorescent solute takes place from the naphthalene molecules. The influence of chloroform on the diphenyloxazole molecule does not differ in the two solutions. Now it is seen that the quenching in the xylene plus naphthalene solution is smaller than in the solution with xylene alone throughout the entire range of chloroform concentrations including small concentrations. Energy transfer from the "poor" solvent (chloroform), especially at low chloroform concentrations, produces little interference and therefore does not conceal the actual quenching process. The difference between the two "solvents" is due to the difference in quenching of the excited molecules of xylene and naphthalene respectively; the naphthalene molecule is therefore considered to be quenched less by chloroform than the xylene molecule in agreement with the previous results. These results provide a verification of the statements made in the introductory paragraphs.

Results with naphthalene similar to those described above in *n*-butylphosphate are also obtained with other "poor" solvents and quenchers; some examples can be seen in Table I.

APPLICATIONS

For many experiments, especially in the field of nuclear physics, it is desirable for specific elements (or more complicated substances) to be present in a scintil-

lating material. Frequently, however, the substance by itself has only poor fluorescent properties under high-energy radiation, and when it is put into an efficient fluorescent solution a considerable decrease in light output results because of quenching. Such behavior is often found when materials contain elements of medium or heavy atomic weights. By applying the results obtained with added naphthalene, solutions which exhibit considerable fluorescence have been made with such quenching molecules present.

A list of substances containing different elements is presented in Table I with which at least moderate high-energy fluorescence efficiencies can be obtained in organic liquid solutions. (The common elements in organic substances such as hydrogen, carbon, nitrogen, and oxygen are not included.) In most cases, as can be seen from the table, the addition of large amounts of naphthalene produces sizeable enhancement of the light output although considerable amounts of the quenching material may be present in the solution. The various fluorescent solutes shown in the table give comparable results, and in many cases α,α'-binaphthyl may also be used. p-terphenyl cannot be utilized because of the insufficient energy transfer found with naphthalene.[6] The heaviest element that has been successfully used to the present has been bismuth. The list which is presented represents the results of a preliminary search for successful substances. Finding substances with desirable properties presents certain problems. One of the major difficulties is the lack of solubility in suitable organic solvents. Once a soluble material is found, it must generally be such that it does not quench the solution too strongly. The naphthalene, as discussed above, acts as a "solvent" in which less quenching occurs and provides a medium to and from which more energy is transferred.

The investigation presented in this paper opens up the possibility of studying the influence of various atoms and molecules on other excited molecules not normally present in work with fluorescence.

PHYSICAL REVIEW VOLUME 97, NUMBER 3 FEBRUARY 1, 1955

Energy Levels of a Disordered Alloy

R. H. PARMENTER
RCA Laboratories, Radio Corporation of America, Princeton, New Jersey
(Received October 1, 1954)

A study is made of the one-electron energy levels of a disordered alloy by means of perturbation theory, extending the results of Nordheim and Muto. To the accuracy of first-order perturbation theory, a disordered alloy is equivalent to a particular perfect crystal, the "virtual crystal," as was shown by Muto. For a certain rather general model, the effects of second-, third-, and fourth-order perturbation theory upon this "virtual-crystal" approximation are analyzed. The question of convergence of the perturbation approach is studied. A certain basic limitation of the perturbation approach is discussed, namely, the limitation to nonlocalized states. Accurate results obtained by Landauer and Helland for a hypothetical one-dimensional alloy are compared with results obtained by perturbation theory. It is pointed out that the same approach can be used with equal validity in discussing not only disordered alloys but also other types of imperfect crystals; e.g., imperfections resulting from dislocations. The most striking prediction of perturbation theory, i.e., the "tailing-off" of the density-of-states curve into a forbidden band, appears to have some experimental verification.

I. INTRODUCTION

IN this paper we will discuss the one-electron energy levels of a completely disordered alloy. For hypothetical one-dimensional alloys, this problem has recently been solved with the aid of computing machines.[1,2] For the three-dimensional problem, however, there seems to be little hope of a reasonably exact solution. The great difficulty, over and above the problem of a perfect crystal, lies in the lack of spacial periodicity of the disordered alloy even though the atoms of the alloy may reasonably be assumed to lie on periodic lattice sites. For this reason, we will attempt to solve the problem by perturbation theory. Such an approach was used by Muto[3] in an attempt to justify Nordheim's "virtual-crystal" approximation.[4] This approximation consists of replacing the correct one-electron potential (appropriate to a given configuration of atoms of the alloy) by its average (the average to be taken over all possible random configurations). In order to gain some physical insight into the accuracy of the approximation, we will now rephrase Muto's discussion in terms of electron scattering in the alloy.

[1] H. M. James and A. S. Ginzbarg, J. Phys. Chem. **57**, 840 (1953).
[2] R. Landauer and J. C. Helland, J. Chem. Phys. **22**, 1655 (1954).
[3] T. Muto, Sci. Papers Inst. Phys. Chem. Research (Tokyo) **34**, 377 (1938).
[4] L. Nordheim, Ann. Physik **9**, 607 and 641 (1931).

II. VIRTUAL-CRYSTAL APPROXIMATION

The straightforward way to obtain physical information about an alloy in the one-electron approximation would be to solve the one-electron Schrödinger equation appropriate to some particular configuration of atoms of the alloy. Results obtained for each configuration are then averaged over all possible configurations, weighting each configuration according to its probability of occurrence. In particular, the average of the wave function over all possible configurations, namely $\langle\Psi\rangle$, is known as the coherent-wave amplitude, and $\langle\Psi^*\rangle\langle\Psi\rangle$ as the coherent-wave intensity, while $\langle\Psi^*\Psi\rangle - \langle\Psi^*\rangle\langle\Psi\rangle$ is known as the incoherent-wave intensity. Thus $\langle\Psi^*\Psi\rangle$, the total intensity, is the sum of two parts, the coherent part and the incoherent part.

In atomic units, the one-electron Schrödinger equation for a particular configuration of atoms may be written

$$[-\nabla^2+\mathbf{V}(\mathbf{r},\mathbf{r}_n)]\Psi_q(\mathbf{r},t,\mathbf{r}_n)=E_q(\mathbf{r}_n)\Psi_q(\mathbf{r},t,\mathbf{r}_n),$$

where $\mathbf{r}$ is the electronic coordinate, while the N different $\mathbf{r}_n$, denoting the positions of the N atoms of the alloy for a given configuration, appear in $\mathbf{V}$, Ψ, and E parametrically. q is an index enumerating the solutions of the equation. Define

$$\mathbf{V}'(\mathbf{r},\mathbf{r}_n)=\mathbf{V}(\mathbf{r},\mathbf{r}_n)-\mathbf{V}_0(\mathbf{r}).$$

$\mathbf{V}_0(\mathbf{r})$, as yet unspecified, is independent of the $\mathbf{r}_n$ although it does depend upon the lattice structure of the alloy. Using the time-dependent Schrödinger equation, we may write

$$[-\nabla^2+\mathbf{V}_0(\mathbf{r})+\mathbf{V}'(\mathbf{r},\mathbf{r}_n)]\Psi_q(\mathbf{r},t,\mathbf{r}_n)=2i\frac{\partial}{\partial t}\Psi_q(\mathbf{r},t,\mathbf{r}_n).$$

Specify that at time $t=0$, Ψ be a particular solution to

$$[-\nabla^2+\mathbf{V}_0(\mathbf{r})]\Psi_q{}^0(\mathbf{r},t)=2i\frac{\partial}{\partial t}\Psi_q{}^0(\mathbf{r},t)$$
$$=E_{0q}\Psi_q{}^0(\mathbf{r},t).$$

Since $\mathbf{V}_0$ is independent of the $\mathbf{r}_n$, so also are $\Psi_q{}^0$ and E_{0q}. The development of Ψ with time can be determined by means of time-dependent perturbation theory. Thus we expand Ψ in terms of the Ψ^0's.

$$\Psi_q(\mathbf{r},t,\mathbf{r}_n)=\sum_p a_{qp}(t,\mathbf{r}_n)\Psi_p{}^0(\mathbf{r},t),\quad a_{qp}(0,\mathbf{r}_n)=\delta_{qp}.$$

The time-dependent coefficients a depend upon the matrix elements of $\mathbf{V}'$ with respect to the unperturbed wave functions Ψ^0. Thus $\mathbf{V}'$ causes scattering of the electron. $a_{qq}\Psi_q{}^0$ represents the unscattered portion of the electron wave while $\Psi_q-a_{qq}\Psi_q{}^0$ represents the scattered portion.

Thus far we have not defined $\mathbf{V}_0$. We now choose $\mathbf{V}_0$ such that the scattered wave is completely *incoherent*. In the approximation of *first-order* time-dependent perturbation theory, this requirement can always be met by choosing $\mathbf{V}_0$ such that

$$\left\langle\int_\infty \Psi_p{}^{0*}(\mathbf{r},t)\mathbf{V}'(\mathbf{r},\mathbf{r}_n)\Psi_q{}^0(\mathbf{r},t)d\tau\right\rangle_{\mathbf{r}_n}=0.$$

The above integration is over all of the space occupied by the alloy, and the averaging is over all possible configurations of the atoms. Let us now place the array of atoms in a box and impose periodic boundary conditions on the electronic wave function. The wave functions $\Psi_q{}^0$ may therefore be expanded in terms of the complete set of plane waves satisfying the boundary conditions and *vice versa*. It follows that the above equation is equivalent to

$$\left\langle\int_\infty \mathbf{V}'(\mathbf{r},\mathbf{r}_n)e^{i\mathbf{k}\cdot\mathbf{r}}d\tau\right\rangle_{\mathbf{r}_n}=0,$$

where $\mathbf{k}$ is any of the set of k-vectors allowed by the periodic boundary conditions. It should be pointed out that this equation, in conjunction with the original definition of $\mathbf{V}_0$, serves to determine $\mathbf{V}_0$ uniquely.

Following Nordheim,[4] we assume that the crystal potential can be written as a spacial sum of atomic-like potentials; i.e.,

$$\mathbf{V}(\mathbf{r})=\sum_n V_{s_n}(\mathbf{r}-\mathbf{R}_n),\qquad(1)$$

where $\mathbf{R}_n$ denotes the position of the nth lattice site and the index s denotes the type of atom on the nth lattice site. $V_s(\mathbf{r})$ is an atomic-like potential associated with an atom of type s. Let f_s be the fraction of lattice sites occupied by atoms of type s.

$$\sum_s f_s=1.\qquad(2)$$

We have

$$\int_\infty \mathbf{V}(\mathbf{r})e^{i\mathbf{k}\cdot\mathbf{r}}d\tau=\sum_n e^{i\mathbf{k}\cdot\mathbf{R}_n}\int_\infty V_{s_n}(\mathbf{r})e^{i\mathbf{k}\cdot\mathbf{r}}d\tau.$$

Thus

$$\left\langle\int_\infty \mathbf{V}(\mathbf{r})e^{i\mathbf{k}\cdot\mathbf{r}}d\tau\right\rangle=\sum_s f_s\int_\infty V_s(\mathbf{r})e^{i\mathbf{k}\cdot\mathbf{r}}d\tau\sum_n e^{i\mathbf{k}\cdot\mathbf{R}_n}.$$

We now see that only by picking

$$\mathbf{V}_0(\mathbf{r})=\sum_n V_0(\mathbf{r}-\mathbf{R}_n),\qquad(3)$$

where

$$V_0(\mathbf{r})=\sum_s f_s V_s(\mathbf{r}),\qquad(4)$$

can we satisfy the requirement that

$$\left\langle\int_\infty \mathbf{V}'(\mathbf{r})e^{i\mathbf{k}\cdot\mathbf{r}}d\tau\right\rangle=0,$$

so that $\mathbf{V}_0(\mathbf{r})$ is a potential having the periodicity of the lattice associated with the alloy. This periodicity results from the fact that the positions of the atoms in a disordered alloy are not completely random but must coincide with the lattice sites of the crystal. In an

ideal liquid, on the other hand, where the positions of the atoms are random, $\mathbf{V}_0$ is a constant. The band gap observed experimentally[5] in a disordered alloy is a manifestation of the band structure resulting from the periodic nature of $\mathbf{V}_0$. The effect of $\mathbf{V}'$ is to scatter the electrons of the alloy incoherently. A disordered alloy is analogous to a perfect crystal at a finite temperature, where lattice vibrations have destroyed the perfect periodicity of the crystal potential. For this latter case also, the crystal potential can be written as a periodic $\mathbf{V}_0$ and a $\mathbf{V}'$ resulting from lattice vibrations which gives rise to incoherent scattering.

Why did we choose $\mathbf{V}_0$ such that $\mathbf{V}'$ would give rise only to incoherent scattering (in the approximation of first-order perturbation theory)? We wish to pick our initial wave function $\Psi_q{}^0(\mathbf{r},t)$ such that, aside from the phase factor, $\exp(-\frac{1}{2}iE_{0q}t)$, the change in Ψ_q with time is a minimum when averaged over all possible configurations of atoms. In other words, we wish to minimize the time-dependence of the "spacial part" of the wave function, since it is the perturbing potential $\mathbf{V}'$ which is giving rise to this time dependence of the "spacial part" of the wave function, and the success of any perturbation scheme depends upon the weakness of the perturbation. Mathematically, we wish to minimize

$$\left|\left\langle\frac{\partial}{\partial t}\Psi_q(\mathbf{r},t,\mathbf{r}_n)e^{\frac{1}{2}iE_{0q}t}\right\rangle_{\mathbf{r}_n}\right|;$$

but by picking $\mathbf{V}_0$, and thus $\Psi_q{}^0$, such that only incoherent scattering occurs, we insure that the above quantity vanishes (to the accuracy of first-order perturbation theory).

The problem of a disordered alloy has been resolved into two parts: (1) The determination of the wave functions and energy levels of an electron in the periodic potential $\mathbf{V}_0$. (2) The determination of the amount of incoherent scattering of the electron by $\mathbf{V}'$, this scattering giving rise to the "residual resistance" of a metallic alloy. The theory of the "residual resistance" has been worked out[4] and will not be discussed here.

In the following sections we will study the corrections, resulting from second- and higher-order perturbation theory, to the wave functions and energy levels associated with the periodic potential $\mathbf{V}_0$.

III. EFFECT OF SECOND-ORDER PERTURBATION THEORY

The effect of second-order perturbation theory on the unperturbed energy E_{0q} is to correct it by an amount

$$E_{2q}=\sum_p{}'|\mathbf{V}_{qp}'|^2(E_{0q}-E_{0p})^{-1}, \tag{5}$$

where

$$\mathbf{V}_{qp}'=\int_\infty \Psi_q{}^{0*}\mathbf{V}'\Psi_p{}^0 d\tau. \tag{6}$$

The prime on the summation sign denotes that the term for $p=q$ is not included. As was pointed out by Muto,[3] when E_{0q} lies in the middle of an energy band there will be roughly equal positive and negative contributions to the above sum so that E_{2q} might be expected to be small. When E_{0q} is near the bottom or the top of a band, however, the leading terms in the sum will be negative or positive, respectively. Thus the effect of E_{2q} will be to "smear" band edges out into the band gaps. Muto implied that E_{2q} vanishes in the limit as N, the number of atoms in the alloy, becomes infinite. Such is not the case. As will be shown presently, E_{2q} approaches a finite limit as N approaches infinity.

In order to study E_{2q} in detail, it will be convenient to restrict ourselves to a very specific model; namely the case where $\mathbf{V}_0$ is a constant. We refer to this as the "empty-lattice virtual-crystal" model. The practical advantage of working with this model lies in the fact that the unperturbed wave functions are particularly simple; namely plane waves. Without further loss of generality we can redefine the zero of energy such that $\mathbf{V}_0$ vanishes identically and only energies greater than zero are allowed to the accuracy of first-order perturbation theory. We now assume that the energy region in the neighborhood of zero corresponds qualitatively to the energy region in the neighborhood of the minimum of an allowed band associated with a more realistic, nonvanishing $\mathbf{V}_0$. The justification for this assumption lies in the well-known effective-mass approximation,[6] which states that in the energy region in the neighborhood of a minimum or a maximum of a nondegenerate allowed band, the equations of motion of an electron in a periodic potential are equivalent, for qualitative purposes, to the equations of motion of a free particle with a certain reciprocal effective-mass tensor. A positive mass corresponds to an electron in the bottom of a band while a negative mass corresponds to an electron in the top of a band. The empty-lattice virtual-crystal model is a specialization to the case where the effective mass equals the free-electron mass, but the generalization to arbitrary effective mass is trivial.

The Hamiltonian for the empty-lattice virtual-crystal model can be written

$$H=H_0+\mathbf{V}'(\mathbf{r}), \tag{7}$$

where

$$H_0=-\nabla^2, \tag{8}$$

$$\mathbf{V}'(\mathbf{r})=\sum_n V_s{}'(\mathbf{r}-\mathbf{R}_n). \tag{9}$$

To conform with the results of the previous section, we must take

$$V_s{}'(\mathbf{r})=V_s(\mathbf{r})-\sum_t f_t V_t(\mathbf{r}), \tag{10}$$

where the various $V_s{}'$ must satisfy the relation

$$\sum_s f_s V_s{}'(\mathbf{r})=0 \tag{11}$$

[5] E. R. Johnson and S. M. Christian, Phys. Rev. **95**, 560 (1954). See also Levitas, Wang, and Alexander, Phys. Rev. **95**, 846 (1954).

[6] J. C. Slater, Phys. Rev. **76**, 1592 (1949).

for all values of $\mathbf{r}$. The solution to the unperturbed Schrödinger equation

$$H_0\psi_0(\mathbf{k},\mathbf{r})=E_0(\mathbf{k})\psi_0(\mathbf{k},\mathbf{r})$$

is given by

$$\psi_0(\mathbf{k},\mathbf{r})=(N\Omega)^{-\frac{1}{2}}e^{i\mathbf{k}\cdot\mathbf{r}}, \tag{12}$$

$$E_0(\mathbf{k})=k^2. \tag{13}$$

Here Ω is the volume per lattice site in the alloy, and N, as before, is the number of atoms in the alloy. The propagation vector $\mathbf{k}$ is any member of the set of k-vectors satisfying the periodic boundary conditions. As is shown in the Appendix, Eq. (5) becomes

$$E_2(\mathbf{k}_i)=\sum_j{}'|\mathbf{V}'(\mathbf{k}_j)|^2(2\mathbf{k}_i\cdot\mathbf{k}_j-k_j^2)^{-1}, \tag{14}$$

where

$$\mathbf{V}'(\mathbf{k}_j)\equiv\mathbf{V}_{0j}'. \tag{15}$$

Now

$$\langle|\mathbf{V}'(\mathbf{k})|^2\rangle=(N\Omega)^{-2}\left\langle\left|\int_\infty e^{i\mathbf{k}\cdot\mathbf{r}}\mathbf{V}'(\mathbf{r})d\tau\right|^2\right\rangle$$

$$=(N\Omega)^{-2}\left\langle\sum_{n,p}e^{i\mathbf{k}\cdot(\mathbf{R}_n-\mathbf{R}_p)}\int_\infty V_{sn}'(\mathbf{r})e^{i\mathbf{k}\cdot\mathbf{r}}d\tau\times\int_\infty V_{sp}'(\mathbf{r})e^{-i\mathbf{k}\cdot\mathbf{r}}d\tau\right\rangle$$

$$=(N\Omega)^{-2}\left\langle\sum_n\left|\int_\infty V_{sn}'(\mathbf{r})e^{i\mathbf{k}\cdot\mathbf{r}}d\tau\right|^2\right\rangle$$

$$=N^{-1}\Omega^{-2}\sum_s f_s|\mathcal{U}_s'(\mathbf{k})|^2, \tag{16}$$

where

$$\mathcal{U}_s'(\mathbf{k})=\int_\infty V_s'(\mathbf{r})e^{i\mathbf{k}\cdot\mathbf{r}}d\tau. \tag{17}$$

Since there are N allowed states of a given spin in the first Brillouin zone, whose volume is $\Omega_k=(2\pi)^3/\Omega$, then the volume of k-space per allowed state of a given spin is given by

$$\Omega_k/N=(2\pi)^3/N\Omega.$$

In the limit as N becomes infinite, a summation over the allowed states of a given spin may be replaced by the corresponding integral over k-space, when the latter is divided by the volume of k-space per state, i.e.,

$$\sum_{\mathbf{k}}=N\Omega(2\pi)^{-3}\int d\tau_k. \tag{18}$$

Substituting (16) and (18) in (14), we find that E_2, suitably averaged over all possible configurations, is given by

$$E_2(\mathbf{k})=(2\pi)^{-3}\Omega^{-1}\sum_s f_s\int_\infty|\mathcal{U}_s'(\boldsymbol{\sigma})|^2(2\mathbf{k}\cdot\boldsymbol{\sigma}-\sigma^2)^{-1}d\tau_\sigma. \tag{19}$$

If we assume that $V_s'(\mathbf{r})$ is independent of the orientation of $\mathbf{r}$ then $\mathcal{U}_s'(\boldsymbol{\sigma})$ will be independent of the orientation of $\boldsymbol{\sigma}$ and the angular integrations in the above integral can be performed immediately.

$$E_2(\mathbf{k})=(2\pi)^{-2}\Omega^{-1}\sum_s f_s\int_0^\infty d\sigma\sigma^2|\mathcal{U}_s'(\sigma)|^2\times\int_0^\pi d\theta\sin\theta(2k\sigma\cos\theta-\sigma^2)^{-1}$$

$$=(8\pi^2\Omega k)^{-1}\sum_s f_s\int_0^\infty|\mathcal{U}_s'(\sigma)|^2\times\ln[(\sigma-2k)/(\sigma+2k)]\sigma d\sigma.$$

We may define $\mathcal{U}_s'(\sigma)$ to be a real even function of σ, so that the complete integrand will be an even function of σ, and we may write

$$E_2(\mathbf{k})=(4\pi)^{-2}(\Omega k)^{-1}\sum_s f_s\int_{-\infty}^\infty[\mathcal{U}_s'(\sigma)]^2\times\ln[(\sigma-2k)/(\sigma+2k)]\sigma d\sigma. \tag{20}$$

Letting σ range over the entire complex plane, we will finally assume that $\mathcal{U}_s'(\sigma)$ is analytic except at a finite number of singular points. We assume that none of these singular points lie on the real axis and that $\mathcal{U}_s'(\sigma)$ approaches zero at least as fast as σ^{-1} as σ approaches infinity in the complex plane. It is now possible to evaluate the above integral by integration around the contour illustrated in Fig. 1. Define

$$F_s(\sigma)=[\mathcal{U}_s'(\sigma)]^2\sigma\ln[(\sigma-2k)/(\sigma+2k)]. \tag{21}$$

$F_s(\sigma)$ has branch points at $\sigma=\pm2k$ with branch lines extending to infinity is the lower half plane. Denote by R_1 the radius of the semicircular contours about the branch points, and denote by R_2 the radius of the large semicircular contour about the origin. The integral of $F_s(\sigma)$ over the latter contour, in the limit as $R_2\to\infty$, is

$$8kR_2[\mathcal{U}_s'(R_2)]^2=0.$$

The integral of $F_s(\sigma)$ over the contour at $\sigma=+2k$, in the limit as $R_1\to0$, is

$$4k[\mathcal{U}_s'(2k)]^2R_1\ln R_1=0.$$

Similarly, the integral of $F_s(\sigma)$ over the contour at $\sigma=-2k$ vanishes in the limit as $R_1\to0$. By the residue

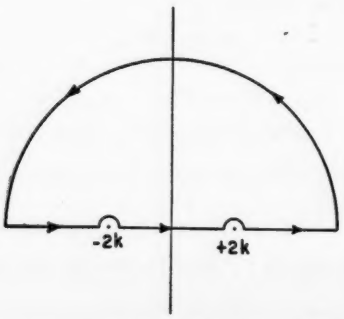

FIG. 1. Contour of integration in the σ-plane.

theorem, we now have

$$\int_{-\infty}^{\infty} F_s(\sigma)d\sigma = 2\pi i \sum' \mathrm{Res} F_s(\sigma); \tag{22}$$

i.e., the integral equals $2\pi i$ times the sum of the residues of $F_s(\sigma)$ in the *upper* half plane (excluding the real axis). The fact that the integrand diverges at $\sigma=\pm 2k$ results from the fact that second-order perturbation theory is invalid in the neighborhoods of these two points. Since, however, the total contribution to the integral in Eq. (22) comes from the residues of poles none of which lie in the neighborhoods of the points $\sigma=\pm 2k$, and since we may assume that perturbation theory correctly predicts the integrand in the neighborhood of these poles, then there appears to be some justification for using perturbation theory as we have done here.

We now take the specific example where

$$V_s'(\mathbf{r}) = r^{-1}A_s e^{-ar}. \tag{23}$$

From Eq. (11) it follows that

$$\sum_s f_s A_s = 0. \tag{24}$$

$\mathcal{V}_s'(\boldsymbol{\sigma})$ is given by

$$\begin{aligned}\mathcal{V}_s'(\boldsymbol{\sigma}) &= \int_{\infty} V_s'(\mathbf{r}) \exp(i\boldsymbol{\sigma}\cdot\mathbf{r})d\tau \\ &= 4\pi A_s \sigma^{-1}\int_0^{\infty} \sin(\sigma r)e^{-ar}dr \\ &= 4\pi A_s(a^2+\sigma^2)^{-1}.\end{aligned} \tag{25}$$

Note that $\mathcal{V}_s'(\sigma)$ has all the properties previously assumed in evaluating the integral. $F_s(\sigma)$ will have second-order poles at $\sigma=\pm ia$. We are interested in the pole at $\sigma=+ia$. The residue at this pole is

$$\mathrm{Res} F_s(ia) = (4\pi A_s)^2 ika^{-1}(a^2+4k^2)^{-1},$$

so that

$$E_2(k) = -(2\pi/a\Omega)(\textstyle\sum_s f_s A_s^2)(a^2+4k^2)^{-1}. \tag{26}$$

Taking

$$E(k) = E_0(k)+E_2(k), \tag{27}$$

and solving for k in terms of E, we get

$$\begin{aligned}2k^2 &= [E-(\tfrac{1}{2}a)^2] \\ &\quad +\{[E+(\tfrac{1}{2}a)^2]^2+(2\pi/a\Omega)\textstyle\sum_s f_s A_s^2\}^{\frac{1}{2}}.\end{aligned} \tag{28}$$

Define n as the total number of states (of a given spin) per unit volume of the crystal having an energy less than $E(k)$.

$$\begin{aligned}n &= (1/N\Omega)(4\pi k^3/3\Omega_k)N = (k^3/6\pi^2), \\ dn/dE &= (dn/dk)(dk/dE) \\ &= 2^{\frac{1}{2}}(4\pi)^{-2}\{[E-(\tfrac{1}{2}a)^2]+([E+(\tfrac{1}{2}a)^2]^2 \\ &\quad +(2\pi/a\Omega)\textstyle\sum_s f_s A_s^2\}^{\frac{1}{2}} \\ &\quad \times\{1+[E+(\tfrac{1}{2}a)^2]([E+(\tfrac{1}{2}a)^2]^2 \\ &\quad +(2\pi/a\Omega)\textstyle\sum_s f_s A_s^2)^{-\frac{1}{2}}\}.\end{aligned} \tag{29}$$

In order to study the shape of the density-of-states curve, we introduce the following variables.

$$\left.\begin{aligned}\epsilon(k) &= (2/a)^2 E(k), \\ \epsilon_0 &= (8\pi/a^5\Omega)\textstyle\sum_s f_s A_s^2, \\ \eta &= (2\pi)^2(2/a)^3 n.\end{aligned}\right\} \tag{30}$$

Thus

$$\epsilon(k) = (2k/a)^2 - \epsilon_0[1+(2k/a)^2]^{-1}, \tag{31}$$

so that

$$\epsilon(0) = -\epsilon_0. \tag{32}$$

Also

$$\begin{aligned}d\eta/d\epsilon &= \tfrac{1}{4}\sqrt{2}\{1+(\epsilon+1)[(\epsilon+1)^2+4\epsilon_0]^{-\frac{1}{2}}\} \\ &\quad \times\{(\epsilon-1)+[(\epsilon+1)^2+4\epsilon_0]^{\frac{1}{2}}\}^{\frac{1}{2}}.\end{aligned} \tag{33}$$

As $\epsilon\to\infty$,

$$d\eta/d\epsilon \to \sqrt{\epsilon}.$$

Also, for $\epsilon_0=0$,

$$d\eta/d\epsilon = \sqrt{\epsilon}.$$

As can be seen from Fig. 2, the shape of the $d\eta/d\epsilon$ curve depends upon ϵ_0. For large values of ϵ_0, the low-energy tail of the curve becomes very sharp. This represents that portion of the density-of-states curve which has penetrated into the forbidden band. Let us examine this tail in more detail. Consider the case where ϵ is negative and

$$2\sqrt{\epsilon_0} \lesssim |\epsilon+1| \lesssim \epsilon_0.$$

By picking $\epsilon_0 \gg 4$, we can insure that there will be a large range of values of ϵ for which the above conditions hold. To see this, we note that the ratio of the upper to the lower limit is given by

$$(\epsilon_0/2\sqrt{\epsilon_0}) = \tfrac{1}{2}\sqrt{\epsilon_0} \gg 1,$$

since $\epsilon_0 \gg 4$. Since

$$\begin{aligned}(\epsilon-1)+[(\epsilon+1)^2+4\epsilon_0]^{\frac{1}{2}} &\cong 2(\epsilon_0-|\epsilon|)|\epsilon|^{-1}, \\ 1+(\epsilon+1)[(\epsilon+1)^2+4\epsilon_0]^{-\frac{1}{2}} &\cong 2\epsilon_0|\epsilon|^{-2},\end{aligned}$$

then

$$d\eta/d\epsilon \cong \epsilon_0|\epsilon|^{-5/2}(\epsilon_0-|\epsilon|)^{\frac{1}{2}}, \tag{34}$$

for ϵ negative such that

$$2\sqrt{\epsilon_0} \lesssim |\epsilon| \lesssim \epsilon_0 \gg 4.$$

Equation (34) shows that for large ϵ_0 the density-of-states curve drops off very rapidly as it penetrates the forbidden band. For small ϵ_0, on the other hand, the shape of the curve is hardly affected, as can be seen in Fig. 2, the apparent band edge merely being shifted down in energy. The case of small ϵ_0 corresponds qualitatively to the effect of thermal vibrations on the energy levels of a perfect crystal.[7]

IV. CONDUCTIVITY

If

$$E = E_0 + E_2$$

represents the energy to the accuracy of second-order perturbation theory, and if

$$\mathbf{v} = \mathbf{v}_0 + \mathbf{v}_2$$

[7] H. Y. Fan, Phys. Rev. 82, 900 (1951).

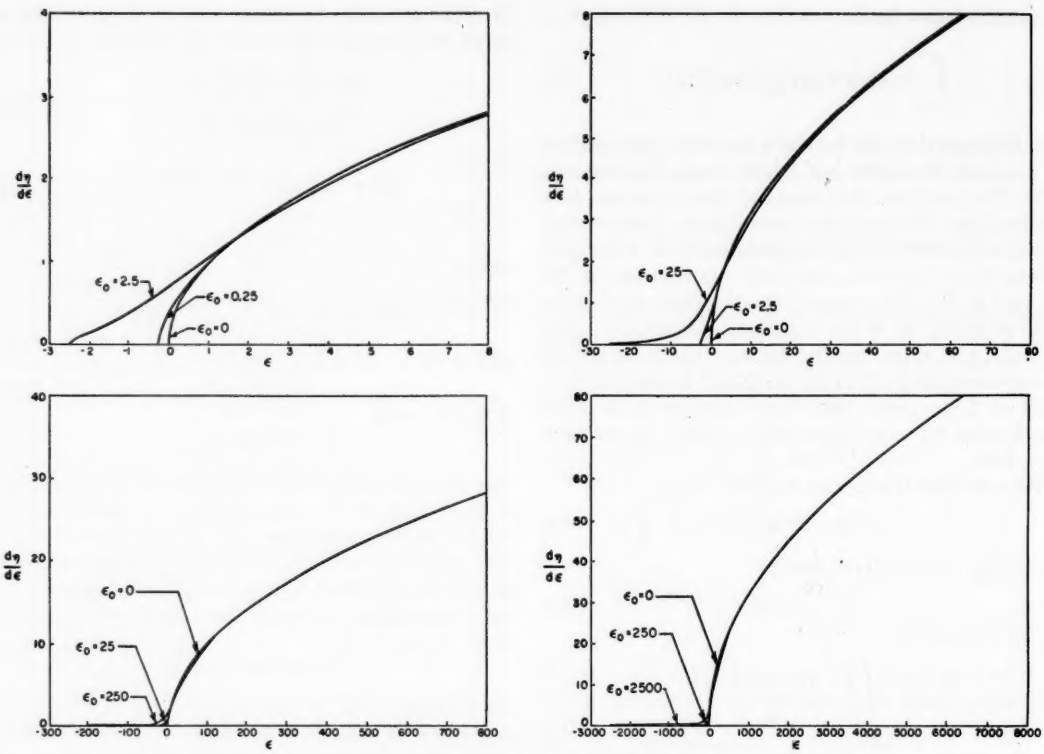

FIG. 2. $d\eta/d\epsilon$ *versus* ϵ for various values of ϵ_0.

represents the expectation value of velocity to the same approximation, then it can be shown (see Appendix) that for the empty-lattice virtual-crystal model

$$\mathbf{v}_n(\mathbf{k})=\tfrac{1}{2}\nabla_k E_n(\mathbf{k}), \quad n=0, 1, 2. \tag{35}$$

(It is also true for $n=3$ in the case of third-order perturbation theory.) Note that Eq. (35) is identical with the usual relationship between $\mathbf{v}$ and E in the conventional theory of energy bands. Define

$$A=\pi(2a\Omega)^{-1}\textstyle\sum_s f_s A_s^2. \tag{36}$$

Thus

$$\begin{aligned} E(\mathbf{k})&=k^2-A[(\tfrac{1}{2}a)^2+k^2]^{-1},\\ \mathbf{v}(\mathbf{k})&=\mathbf{k}\{1+A[(\tfrac{1}{2}a)^2+k^2]^{-2}\}. \end{aligned} \tag{37}$$

In particular,

$$E(0)\equiv -E_0=-(2/a)^2A. \tag{38}$$

If E_0 stays finite but a becomes very small, then there will be very large values of $\mathbf{v}$ (diverging as a^{-2}) in the low-energy tail. We wish to show that these very large values of $\mathbf{v}$ make a negligible contribution to the total electronic current in the allowed band in the limit as $a\to 0$ (E_0 remaining finite). This results from the vanishing of dn/dE in the same limit.

We assume that all electrons in the conduction band have a mean life τ between collisions. According to the elementary theory of electric conductivity, in the presence of an electric field $\mathfrak{E}$ the distribution of electrons in momentum space is shifted by an amount $\mathbf{K}$, where

$$\mathbf{K}=e\mathfrak{E}\tau. \tag{39}$$

We will assume that the Fermi level E_F lies far enough below $E(0)$ so that we may use Boltzmann statistics. In the presence of an electric field in the z-direction, we have

$$\langle v_z\rangle=\frac{\int_\infty v_z(\mathbf{k})e^{-[E(\mathbf{k}-\mathbf{K})-E_F]/\kappa T}d\tau_k}{\int_\infty e^{-[E(\mathbf{k}-\mathbf{K})-E_F]/\kappa T}d\tau_k},$$

$$n=2(2\pi)^{-3}\int_\infty e^{-[E(\mathbf{k}-\mathbf{K})-E_F]/\kappa T}d\tau_k,$$

$$J=n\langle v_z\rangle.$$

$\langle v_z\rangle$ is the mean value of velocity in the field direction, J is the electronic current density, κ is Boltzmann's constant, and n, in this section, refers to the number of electrons (of both spins) per unit volume. J and n may

be written in the forms

$$J=2(2\pi)^{-3}e^{E_F/\kappa T}\int_\infty v_s(\mathbf{k}+\mathbf{K})e^{-E(\mathbf{k})/\kappa T}d\tau_k, \quad (40)$$

$$n=2(2\pi)^{-3}e^{E_F/\kappa T}\int_\infty e^{-E(\mathbf{k})/\kappa T}d\tau_k. \quad (41)$$

For all reasonable values of $\mathfrak{E}$, $\mathbf{K}$ will be very small, so that

$$v_s(\mathbf{k}+\mathbf{K})\cong v_s(\mathbf{k})+K\frac{\partial}{\partial k_s}v_s(\mathbf{k})$$
$$=(k\mu+K)[1+A(\tfrac{1}{4}a^2+k^2)^{-2}]$$
$$-4Kk^2\mu^2A(\tfrac{1}{4}a^2+k^2)^{-3}$$

where μ is the cosine of the angle between $\mathbf{k}$ and $\mathbf{K}$. Thus

$$\int_\infty v_s(\mathbf{k}+\mathbf{K})e^{-E(\mathbf{k})/\kappa T}d\tau_k$$
$$=(4/3)\pi K\int_0^\infty k^2[3-A(\tfrac{1}{4}a^2+k^2)^{-2}$$
$$+a^2A(\tfrac{1}{4}a^2+k^2)^{-3}]e^{-E(k)/\kappa T}dk.$$

Define

$$t=A^{-\frac{1}{2}}(\tfrac{1}{4}a^2+k^2), \quad B=\tfrac{1}{4}aA^{-\frac{1}{2}}.$$

We now see that

$$E_0=(2B)^{-2},$$
$$E(k)=(a/4B)(t-t^{-1})-\tfrac{1}{4}a^2,$$
$$k^2dk=\tfrac{1}{2}(a/4B)^{\frac{1}{2}}(t-aB)^{\frac{1}{2}}dt.$$

Thus

$$J=(K/6\pi^2)(a/4B)^{\frac{1}{2}}\exp[(E_F+\tfrac{1}{4}a^2)/\kappa T]$$
$$\times\int_{aB}^\infty[3-t^{-2}+4aBt^{-3}](t-aB)^{\frac{1}{2}}$$
$$\times\exp[-(t-t^{-1})(a/4B\kappa T)]dt.$$

Define

$$w=\tfrac{1}{2}a(t-t^{-1}),$$

so that

$$at=w+(w^2+a^2)^{\frac{1}{2}}.$$

Thus

$$J=(K/6\pi^2)\exp[(E_F+\tfrac{1}{4}a^2)/\kappa T](4B)^{-\frac{1}{2}}$$
$$\times\int_{-(1-a^2B^2)(2B)^{-1}}^\infty\left[3-\frac{a^2}{[w+(w^2+a^2)^{\frac{1}{2}}]^2}\right.$$
$$\left.+\frac{4a^4B}{[w+(w^2+a^2)^{\frac{1}{2}}]^3}\right]\left[1+\frac{w}{(w^2+a^2)^{\frac{1}{2}}}\right]$$
$$\times[w-a^2B+(w^2+a^2)^{\frac{1}{2}}]^{\frac{1}{2}}e^{-(w/2B\kappa T)}dw.$$

In the limit as $a\to 0$,

$$J=K\pi^{-2}(4B)^{-\frac{1}{2}}e^{E_F/\kappa T}\int_0^\infty(2w)^{\frac{1}{2}}e^{-(w/2B\kappa T)}dw$$
$$=\tfrac{1}{4}K(\kappa T/\pi)^{\frac{1}{2}}e^{E_F/\kappa T}. \quad (42)$$

Also,

$$n=2(2\pi)^{-3}e^{E_F/\kappa T}\int_\infty e^{-E(\mathbf{k})/\kappa T}d\tau_k$$
$$=\pi^{-2}e^{E_F/\kappa T}\int_0^\infty k^2e^{-E(k)/\kappa T}dk$$
$$=\tfrac{1}{2}\pi^{-2}(a/4B)^{\frac{1}{2}}\exp[(E_F+\tfrac{1}{4}a^2)/\kappa T]$$
$$\times\int_{aB}^\infty(t-aB)^{\frac{1}{2}}\exp[-(t-t^{-1})(a/4B\kappa T)]dt$$
$$=\tfrac{1}{2}\pi^{-2}(4B)^{-\frac{1}{2}}\exp[(E_F+\tfrac{1}{4}a^2)/\kappa T]$$
$$\times\int_{-(1-a^2B^2)(2B)^{-1}}^\infty[1+w(w^2+a^2)^{-\frac{1}{2}}]$$
$$\times[w-a^2B+(w^2+a^2)^{\frac{1}{2}}]^{\frac{1}{2}}e^{-(w/2B\kappa T)}dw.$$

In the limit as $a\to 0$,

$$n=\pi^{-2}(4B)^{-\frac{1}{2}}e^{E_F/\kappa T}\int_0^\infty(2w)^{\frac{1}{2}}e^{-(w/2B\kappa T)}dw$$
$$=\tfrac{1}{4}(\kappa T/\pi)^{\frac{1}{2}}e^{E_F/\kappa T}. \quad (43)$$

We can show that Eqs. (42) and (43) are identical with the equations appropriate for J and n in the case where there is no low-energy tail (i.e., $A=0$). Applying the condition $A=0$ to the general equations obtained previously, we get

$$\int_\infty v_s(\mathbf{k}+\mathbf{K})e^{-E(\mathbf{k})/\kappa T}dT_k=4\pi K\int_0^\infty k^2e^{-E(k)/\kappa T}dk$$
$$=2\pi K(\kappa T)^{\frac{1}{2}}\int_0^\infty x^{\frac{1}{2}}e^{-x}dx=K(\pi\kappa T)^{\frac{1}{2}},$$

so that

$$J=2(2\pi)^{-3}e^{E_F/\kappa T}\int_\infty v_s(\mathbf{k}+\mathbf{K})e^{-E(\mathbf{k})/\kappa T}d\tau_k$$
$$=\tfrac{1}{4}K(\kappa T/\pi)^{\frac{1}{2}}e^{E_F/\kappa T}. \quad (44)$$

Likewise,

$$n=\pi^{-2}e^{E_F/\kappa T}\int_0^\infty k^2e^{-E(k)/\kappa T}dk$$
$$=\tfrac{1}{2}\pi^{-2}(\kappa T)^{\frac{1}{2}}e^{E_F/\kappa T}\int_0^\infty x^{\frac{1}{2}}e^{-x}dx$$
$$=\tfrac{1}{4}(\kappa T/\pi)^{\frac{1}{2}}e^{E_F/\kappa T}. \quad (45)$$

The significance of the above results lies in the fact that the vanishing of the density of states in the tail

overrides the divergence of the velocity. It should be pointed out, however, that for finite A and a there can be an appreciable contribution to the current from the electrons in the tail, in particular for temperatures low enough such that κT is much smaller than the width of the tail in energy.

V. EFFECT OF THIRD-ORDER PERTURBATION THEORY

As is shown in the Appendix, the third-order contribution to the energy for the empty-lattice virtual-crystal model is

$$E_3(\mathbf{k}_i)=\sum_{j,p}{}' \mathbf{V}'(-\mathbf{k}_j)\mathbf{V}'(\mathbf{k}_j-\mathbf{k}_p)\mathbf{V}'(\mathbf{k}_p) \times(2\mathbf{k}_i\cdot\mathbf{k}_j-k_j^2)^{-1}(2\mathbf{k}_i\cdot\mathbf{k}_p-k_p^2)^{-1}. \quad (46)$$

(Here we have made use of the fact that $\mathbf{V}'(\mathbf{k})$ vanishes for $\mathbf{k}=0$.) Now

$$\langle \mathbf{V}'(\mathbf{k}_1)\mathbf{V}'(\mathbf{k}_2)\mathbf{V}'(\mathbf{k}_3)\rangle = (N\Omega)^{-3}\Big\langle \sum_{n_1n_2n_3} \exp[i(\mathbf{k}_1\cdot\mathbf{R}_{n1}+\mathbf{k}_2\cdot\mathbf{R}_{n2} +\mathbf{k}_3\cdot\mathbf{R}_{n3})]\mathcal{U}_{sn1}'(\mathbf{k}_1)\mathcal{U}_{sn2}'(\mathbf{k}_2)\mathcal{U}_{sn3}'(\mathbf{k}_3)\Big\rangle,$$

where the averaging is to be taken over all possible configurations of atoms in the alloy. The total contribution to the average comes from the terms where

$$\mathbf{R}_{n1}=\mathbf{R}_{n2}=\mathbf{R}_{n3}.$$

We are interested only in the case

$$\mathbf{k}_1+\mathbf{k}_2+\mathbf{k}_3=0,$$

so that

$$\langle \mathbf{V}'(\mathbf{k}_1)V'(\mathbf{k}_2)V'(\mathbf{k}_3)\rangle = N^{-2}\Omega^{-3}\textstyle\sum_s f_s\mathcal{U}_s'(\mathbf{k}_1)\mathcal{U}_s'(\mathbf{k}_2)\mathcal{U}_s'(\mathbf{k}_3). \quad (47)$$

Applying Eq. (18), we have, in the limit as $N\to\infty$,

$$E_3(\mathbf{k})=\frac{1}{(2\pi)^6\Omega}\sum_s f_s \times\int_\infty\int_\infty \frac{\mathcal{U}_s'(-\kappa)\mathcal{U}_s'(\kappa-\sigma)\mathcal{U}_s'(\sigma)}{(2\mathbf{k}\cdot\kappa-\kappa^2)(2\mathbf{k}\cdot\sigma-\sigma^2)}d\tau_\kappa d\tau_\sigma, \quad (48)$$

where E_3 is understood to be suitably averaged over all configurations of atoms. Returning to the special case denoted by Eqs. (23) and (25), we get

$$E_3(\mathbf{k})=\pi^{-3}\Omega^{-1}\sum_s f_sA_s^3\int_\infty\int_\infty\{(a^2+\kappa^2)[a^2+(\kappa-\sigma)^2] \times(a^2+\sigma^2)(2\mathbf{k}\cdot\kappa-\kappa^2)(2\mathbf{k}\cdot\sigma-\sigma^2)\}^{-1}d\tau_\kappa d\tau_\sigma. \quad (49)$$

It does not appear that this integral can be evaluated exactly. Therefore we will make the following approximation:

$$[a^2+(\kappa-\sigma)^2]^{-1}\cong a^2(a^2+\kappa^2)^{-1}(a^2+\sigma^2)^{-1}. \quad (50)$$

To this approximation, we have

$$E_3(\mathbf{k})=(a^2/\pi^3\Omega)\sum_s f_sA_s^3\left[\int_\infty(a^2+\sigma^2)^{-2}(2\mathbf{k}\cdot\sigma-\sigma^2)^{-1}d\tau_\sigma\right]^2.$$

The above integral is identical with that evaluated in Sec. III, so that finally

$$E_3(k)=(\pi/\Omega)(\textstyle\sum_s f_sA_s^3)(a^2+4k^2)^{-2}. \quad (51)$$

As a check on the approximation used in evaluating E_3, we will find the exact value for $k=0$ where

$$E_3(0)=(\pi^3\Omega)^{-1}\sum_s f_sA_s^3\int_\infty\int_\infty\{\kappa^2(a^2+\kappa^2)\sigma^2(a^2+\sigma^2) \times[a^2+(\kappa-\sigma)^2]\}^{-1}d\tau_\kappa d\tau_\sigma.$$

Now if

$$g(\mathbf{r})=(4\pi r)^{-1}e^{-ar},$$

then

$$G(\mathbf{k})\equiv\int_\infty e^{i\mathbf{k}\cdot\mathbf{r}}g(\mathbf{r})d\tau=(a^2+k^2)^{-1}.$$

Similarly if

$$h(\mathbf{r})=(4\pi a^2r)^{-1}[1-e^{-ar}],$$

then it follows that

$$H(\mathbf{k})=a^{-2}[k^{-2}-(a^2+k^2)^{-1}]=[k^2(a^2+k^2)]^{-1}.$$

We may write

$$E_3(0)=(\pi^3\Omega)^{-1}\sum_s f_sA_s^3\int_\infty\int_\infty H^*(\kappa)G(\kappa-\sigma)H(\sigma)d\tau_\kappa d\tau_\sigma.$$

From the following form of Parseval's theorem,[8]

$$\int_\infty f^*(\mathbf{r})g^*(\mathbf{r})h(\mathbf{r})d\tau = (2\pi)^{-6}\int_\infty\int_\infty F^*(\kappa)G(\kappa-\sigma)H(\sigma)d\tau_\kappa d\tau_\sigma,$$

it follows that

$$E_3(0)=(4\pi)^3\Omega^{-1}\sum_s f_sA_s^3\int_\infty h^*(\mathbf{r})g^*(\mathbf{r})h(\mathbf{r})d\tau = (4\pi/a^4\Omega)\sum_s f_sA_s^3\int_0^\infty(1-e^{-ar})^2e^{-ar}r^{-1}dr.$$

The above integral can be evaluated by the following trick.

$$\int_0^\infty(1-e^{-ar})^2e^{-ar}r^{-1}dr = \int_a^\infty db\int_0^\infty(1-e^{-ar})^2e^{-br}dr=\ln(4/3).$$

[8] See, for example, I. N. Sneddon, *Fourier Transforms* (McGraw-Hill Book Company, Inc., New York, 1951), p. 26.

Thus the exact value of $E_3(0)$ is

$$(\pi/a^4\Omega)(\sum_s f_s A_s^3)[4\ln(4/3)],$$

while the previously obtained approximate value was

$$(\pi/a^4\Omega)(\sum_s f_s A_s^3).$$

Since $4\ln(4/3)\cong 1.151$, we see that the exact value is about 15 percent larger than the approximate value.

A rough measure of the rapidity of convergence of perturbation theory is the smallness of the ratio

$$E_3(0)/E_2(0)=2a^{-1}\ln(4/3)(\sum_s f_s A_s^3)/(\sum_s f_s A_s^2). \quad (52)$$

In many cases, a single term in each sum over s predominates so that

$$E_3(0)/E_2(0)\cong 4\ln(4/3)(A_{s\,\max}/2a). \quad (53)$$

Equation (53) shows that for perturbation theory to be valid the maximum value of A_s must be smaller than $2a$.

The effect of third-order perturbation theory is similar to second-order in that only energies near the bottom or the top of a band are shifted appreciably; however, third-order differs from second-order in that the former shifts both ends of an allowed band in the same direction, this direction depending upon whether the perturbative potential is predominantly attractive or repulsive.

VI. EFFECT OF FOURTH-ORDER PERTURBATION THEORY

As is shown in the Appendix, the fourth-order contribution to the energy for the empty-lattice virtual-crystal model is

$$E_4(\mathbf{k}_i)=\sum_{j,p,q}{}' \frac{\mathbf{V}'(-\mathbf{k}_j)\mathbf{V}'(\mathbf{k}_j-\mathbf{k}_p)\mathbf{V}'(\mathbf{k}_p-\mathbf{k}_q)\mathbf{V}'(\mathbf{k}_q)}{(2\mathbf{k}_i\cdot\mathbf{k}_j-k_j^2)(2\mathbf{k}_i\cdot\mathbf{k}_p-k_p^2)(2\mathbf{k}_i\cdot\mathbf{k}_q-k_q^2)}$$
$$-\left[\sum_j{}'\frac{|\mathbf{V}'(\mathbf{k}_j)|^2}{(2\mathbf{k}_i\cdot\mathbf{k}_j-k_j^2)}\right]\left[\sum_j{}'\frac{|\mathbf{V}'(\mathbf{k}_j)|^2}{(2\mathbf{k}_i\cdot\mathbf{k}_j-k_j^2)^2}\right]. \quad (54)$$

(Here we have made use of the fact that $\mathbf{V}'(\mathbf{k})$ vanishes for $\mathbf{k}=0$.) Now

$$\langle\mathbf{V}'(\mathbf{k}_1)\mathbf{V}'(\mathbf{k}_2)\mathbf{V}'(\mathbf{k}_3)\mathbf{V}'(\mathbf{k}_4)\rangle$$
$$=(N\Omega)^{-4}\langle\sum_{n_1n_2n_3n_4}\exp[i(\mathbf{k}_1\cdot\mathbf{R}_{n_1}+\mathbf{k}_2\cdot\mathbf{R}_{n_2}$$
$$+\mathbf{k}_3\cdot\mathbf{R}_{n_3}+\mathbf{k}_4\cdot\mathbf{R}_{n_4})]$$
$$\times\mathcal{V}_{sn_1}'(\mathbf{k}_1)\mathcal{V}_{sn_2}'(\mathbf{k}_2)\mathcal{V}_{sn_3}'(\mathbf{k}_3)\mathcal{V}_{sn_4}'(\mathbf{k}_4)\rangle, \quad (55)$$

The only nonvanishing terms occur if all four running indices in the quadruple sum coincide or if the running indices coincide in pairs; i.e.,

$$n_1=n_2=n_3=n_4,$$

or

$$n_i=n_j,\quad n_k=n_l,\quad i,j,k,l=1,2,3,4.$$

Furthermore, these terms fail to vanish only if the sum of the k-vectors associated with a set of coincident running indices is equal to a vector of the reciprocal lattice, $\mathbf{K}_i$. Since we are interested in the case where

$$\mathbf{k}_1+\mathbf{k}_2+\mathbf{k}_3+\mathbf{k}_4=0,$$

we have

$$\langle\mathbf{V}'(\mathbf{k}_1)\mathbf{V}'(\mathbf{k}_2)\mathbf{V}'(\mathbf{k}_3)\mathbf{V}'(\mathbf{k}_4)\rangle$$
$$=N^{-3}\Omega^{-4}\sum_s f_s\mathcal{V}_s'(\mathbf{k}_1)\mathcal{V}_s'(\mathbf{k}_2)\mathcal{V}_s'(\mathbf{k}_3)\mathcal{V}_s'(\mathbf{k}_4)$$
$$+N^{-2}\Omega^{-4}[\sum_s f_s\mathcal{V}_s'(\mathbf{k}_1)\mathcal{V}_s'(\mathbf{k}_2)]$$
$$\times[\sum_s f_s\mathcal{V}_s'(\mathbf{k}_3)\mathcal{V}_s'(\mathbf{k}_4)]$$
$$\times\delta(\mathbf{k}_1+\mathbf{k}_2,\mathbf{K}_i)\delta(\mathbf{k}_3+\mathbf{k}_4,-\mathbf{K}_i)$$
$$+N^{-2}\Omega^{-4}[\sum_s f_s\mathcal{V}_s'(\mathbf{k}_1)\mathcal{V}_s'(\mathbf{k}_3)]$$
$$\times[\sum_s f_s\mathcal{V}_s'(\mathbf{k}_2)\mathcal{V}_s'(\mathbf{k}_4)]$$
$$\times\delta(\mathbf{k}_1+\mathbf{k}_3,\mathbf{K}_i)\delta(\mathbf{k}_2+\mathbf{k}_4,-\mathbf{K}_i)$$
$$+N^{-2}\Omega^{-4}[\sum_s f_s\mathcal{V}_s'(\mathbf{k}_1)\mathcal{V}_s'(\mathbf{k}_4)]$$
$$\times[\sum_s f_s\mathcal{V}_s'(\mathbf{k}_2)\mathcal{V}_s'(\mathbf{k}_3)]$$
$$\times\delta(\mathbf{k}_1+\mathbf{k}_4,\mathbf{K}_i)\delta(\mathbf{k}_2+\mathbf{k}_3,-\mathbf{K}_i).$$

Since

$$\sum_{\mathbf{k}}\to N\Omega(2\pi)^{-3}\int d\tau_k,$$

we have for the fourth-order contribution to the energy $E_4(\mathbf{k})$, in the limit as $N\to\infty$, a large number of terms, including terms of the following type:

$$(2\pi)^{-6}\Omega^{-2}\sum_i(2\mathbf{k}\cdot\mathbf{K}_i-K_i^2)^{-1}\left|\sum_s f_s\int_\infty\mathcal{V}_s'(\mathbf{K}_i-\boldsymbol{\sigma})\right.$$
$$\left.\times\mathcal{V}_s'(\boldsymbol{\sigma})[2\mathbf{k}\cdot\boldsymbol{\sigma}-\sigma^2]^{-1}d\tau_\sigma\right|^2. \quad (56)$$

It is clear that, because of the factor $(2\mathbf{k}\cdot\mathbf{K}_i-K_i^2)^{-1}$, the above expression diverges as $\mathbf{k}$ approaches the face of a Brillouin zone. This behavior results from our use of *nondegenerate* perturbation theory. If we had used degenerate perturbation theory however, there would be no divergences, but energy discontinuities would be introduced at the faces of the Brillouin zones. It is interesting that in the case of the empty-lattice virtual-crystal model, the presence of lattice periodicity asserts itself in fourth-order perturbation theory. Of course, in a more realistic model where the average potential does not vanish, then the presence of the lattice is felt in all orders of perturbation theory.

VII. ONE-DIMENSIONAL ALLOYS

It is instructive to apply the perturbation approach to the hypothetical one-dimensional alloys[1,2] for which reasonably exact solutions are available. In particular, we consider the problem solved by Landauer and Helland,[2] which consists of two types of square-well potentials occurring with equal probability on a one-dimensional lattice of lattice-constant 2π. Each well is centered on its lattice-site and has a width of π. The top of each well is at the zero of energy. One type of

well has a depth of 2.5, the other a depth of 4. (These numbers are expressed in atomic units.) In the virtual-crystal approximation, each well would be replaced by a well of depth 3.25. The band edges appropriate to this virtual-crystal problem can be obtained immediately by reading numbers off a graph in a paper by Allen.[9] The "effective band edges" obtained by Landauer and Helland in their accurate solution to the true problem are shown in Fig. 3(a) and should be compared with the band edges given by the virtual-crystal approximation which are shown in Fig. 3(b). For energies greater than $+1$, there is a one-to-one correspondence between the two sets of band gaps. The gaps given by the virtual-crystal approximation occur at about the right mean energy but are too wide. This discrepancy would probably be removed by second-order perturbation theory, since, as we have already seen, the effect of second-order perturbation theory is to push band edges out into the forbidden bands, thus effectively narrowing the latter. This probably also explains the fact that Landauer and Helland see no band gap at 0.9 whereas the virtual-crystal approximation gives a very narrow one. Thus for positive energies the perturbation approach appears to be satisfactory. For negative energies, however, this is certainly not the case. The negative energy levels are associated with wave functions localized in a given well, so that these levels are characteristic of the separate constituents composing the alloy. Obviously the virtual-crystal approximation is unsatisfactory here. These negative energy levels correspond to the localized ion-core states in a real alloy. Another type of localized state are the impurity levels of a semiconductor. As James and Ginzbarg[1] have emphasized, it would be impossible to obtain these levels from the virtual-crystal approximation. This points up the major limitation of the perturbation approach; namely that it cannot predict the localized states which may occur in a given problem. This limitation, however, does not negate the method's usefulness in studying nonlocalized states, in particular those lying near a "band edge."

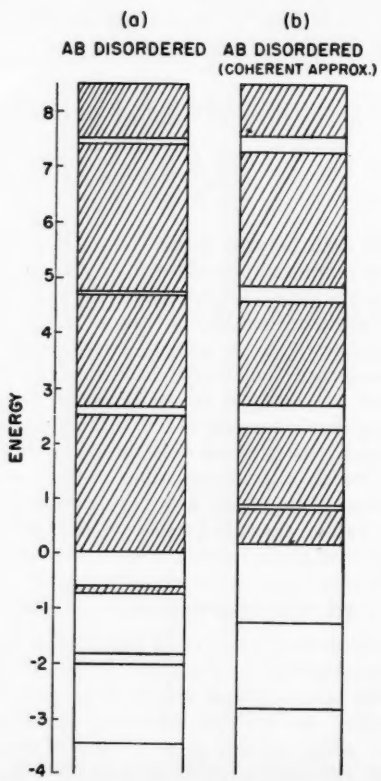

FIG. 3. "Allowed bands" of a one-dimensional alloy (a) exact, (b) virtual-crystal approximation.

[9] G. Allen, Phys. Rev. **91**, 531 (1953).

VIII. DISCUSSION

Although this paper is concerned primarily with disordered alloys, it is clear that the perturbation approach may be used with equal validity in determining energy levels in a number of other problems concerned with imperfections in crystals. The conventional treatment of thermal vibrations in a crystal follows this approach. The problem already mentioned of a semiconductor doped with impurities is really the alloy problem. The problem of vacancies in a crystal is a special case of a binary alloy where one of the constituents is a missing atom. Likewise, other types of dislocations in crystals will probably give rise to qualitatively similar changes in the energy-band structure appropriate to the associated perfect crystal. The most striking aspect of these changes, namely the "tailing-off" of the density-of-states curve into a forbidden band, appears to have some experimental verification. One example is the low-energy tail appearing in the soft x-ray emission spectra of metals,[10] an experimental effect which has never been satisfactorily explained. Experimental results on a variety of photoconductors also suggest a tailing-off of the density-of-states curve into a forbidden band.[11] The fact that a rather large electronic velocity (see Sec. IV) may be associated with the states in this tail could explain the unexpectedly large "dark currents" sometimes seen in photoconductors.

The writer is indebted to D. O. North, F. Herman, and L. P. Smith for many stimulating discussions. The writer is also indebted to Rolf Landauer for a copy of his paper prior to publication.

APPENDIX

We wish to obtain expressions for the expectation values of the energy and of the velocity by means of

[10] See, for example, F. Seitz, *Modern Theory of Solids* (McGraw-Hill Book Company, Inc., New York, 1940), p. 436.

[11] A. Rose, R.C.A. Rev. **12**, 362 (1951).

time-independent nondegenerate perturbation theory. The Hamiltonian is

$$H=H_0+\lambda H'. \tag{1a}$$

The wave function and the expectation values will be written as power series in λ. Thus

$$\psi_i=\psi_{0i}+\sum_{n=1}^{\infty}\lambda^n\psi_{ni}, \tag{2a}$$

where

$$\psi_{ni}=\sum_p{}'\,{}_na_{ip}\psi_{0p};\quad n\geqslant 1, \tag{3a}$$

the prime denoting that $p\neq i$ in the sum.

$$E_i=E_{0i}+\sum_{n=1}^{\infty}\lambda^nE_{ni}. \tag{4a}$$

Substituting these expressions into Schrödinger's equation, we get

$$\begin{aligned}
&H\psi_i-E\psi_i=0\\
&=H_0\psi_i+\lambda H'\psi_i-E_i\psi_i\\
&=E_{0i}\psi_{0i}+\sum_{n=1}^{\infty}\lambda^n\sum_p{}'\,{}_na_{ip}E_{0p}\psi_{0p}+\lambda H'\psi_{0i}\\
&\quad+\sum_{n=1}^{\infty}\lambda^{n+1}\sum_p{}'\,{}_na_{ip}H'\psi_{0p}\\
&\quad-\left(E_{0i}+\sum_{n=1}^{\infty}\lambda^nE_{ni}\right)\left(\psi_{0i}+\sum_{n=1}^{\infty}\lambda^n\sum_p{}'\,{}_na_{ip}\psi_{0p}\right)\\
&=\lambda\Big[\sum_p{}'\,{}_1a_{ip}(E_{0p}-E_{0i})\psi_{0p}+(H'-E_{1i})\psi_{0i}\Big]\\
&\quad+\sum_{n=2}^{\infty}\lambda^n\Bigg[\sum_p{}'\,{}_na_{ip}(E_{0p}-E_{0i})\psi_{0p}+\sum_p{}'\,{}_{n-1}a_{ip}H'\psi_{0p}\\
&\qquad-E_{ni}\psi_{0i}-\sum_{n'=1}^{n-1}\sum_p{}'\,{}_{n'}a_{ip}E_{n-n',i}\psi_{0p}\Bigg].
\end{aligned}$$

Here we have taken

$$(H_0-E_{0i})\psi_{0i}=0. \tag{5a}$$

Multiplying on the left by ψ_{0j}^* and integrating, we get

$$\begin{aligned}
&\lambda\big[(E_{0j}-E_{0i})\,{}_1a_{ij}+H_{ji}'-E_{1i}\delta_{ij}\big]\\
&\quad+\sum_{n=2}^{\infty}\lambda^n\Bigg[(E_{0j}-E_{0i})\,{}_na_{ij}+\sum_p{}'\,{}_{n-1}a_{ip}H_{jp}'\\
&\qquad-E_{ni}\delta_{ij}-\sum_{n'=1}^{n-1}{}_{n'}a_{ij}E_{n-n',i}(1-\delta_{ij})\Bigg]=0,
\end{aligned}$$

where

$$H_{ji}'\equiv\int_\infty\psi_{0j}^*H'\psi_{0i}d\tau. \tag{6a}$$

Equating to zero the coefficients of each power of λ, we get for $n=1$

$$E_{1i}=H_{ii}', \tag{7a}$$

$${}_1a_{ij}=H_{ji}'(E_{0i}-E_{0j})^{-1},\quad i\neq j, \tag{8a}$$

while for $n\geqslant 2$

$$E_{ni}=\sum_j{}'\,{}_{n-1}a_{ij}H_{ij}', \tag{9a}$$

$${}_na_{ij}=(E_{0i}-E_{0j})^{-1}\Bigg[\sum_p{}'\,{}_{n-1}a_{ip}H_{jp}'-\sum_{n'=1}^{n-1}{}_{n'}a_{ij}E_{n-n',i}\Bigg]. \tag{10a}$$

Thus

$$\begin{aligned}
{}_2a_{ij}&=(E_{0i}-E_{0j})^{-1}\sum_p{}'\,H_{jp}'H_{pi}'(E_{0i}-E_{0p})^{-1}\\
&\quad-H_{ii}'H_{ji}'(E_{0i}-E_{0j})^{-2},\\
{}_3a_{ij}&=(E_{0i}-E_{0j})^{-1}\Big[\sum_{p,q}{}'\,H_{jp}'H_{pq}'H_{qi}'(E_{0i}-E_{0p})^{-1}\\
&\quad\times(E_{0i}-E_{0q})^{-1}-{}_1a_{ij}E_{2i}-{}_2a_{ij}E_{1i}\Big],
\end{aligned}$$

$$E_{2i}=\sum_j{}'|H_{ij}'|^2(E_{0i}-E_{0j})^{-1}, \tag{11a}$$

$$\begin{aligned}
E_{3i}&=\sum_{i,p}{}'\,H_{ij}'H_{jp}'H_{pi}'(E_{0i}-E_{0j})^{-1}(E_{0i}-E_{0p})^{-1}\\
&\quad-H_{ii}'\sum_j{}'|H_{ij}'|^2(E_{0i}-E_{0j})^{-2},
\end{aligned} \tag{12a}$$

$$\begin{aligned}
E_{4i}&=\sum_{i,p,q}{}'\,H_{ij}'H_{jp}'H_{pq}'H_{qi}'(E_{0i}-E_{0j})^{-1}\\
&\quad\times(E_{0i}-E_{0p})^{-1}(E_{0i}-E_{0q})^{-1}\\
&\quad-\Big[\sum_j{}'|H_{ij}'|^2(E_{0i}-E_{0j})^{-1}\Big]\\
&\quad\times\Big[\sum_j{}'|H_{ij}'|^2(E_{0i}-E_{0j})^{-2}\Big]\\
&\quad-H_{ii}'\sum_{i,p}{}'\,H_{ij}'H_{jp}'H_{pi}'\\
&\quad\times(E_{0i}-E_{0j})^{-2}(E_{0i}-E_{0p})^{-1}.
\end{aligned} \tag{13a}$$

The expectation value of velocity is given by

$$\begin{aligned}
\mathbf{v}_i&=\int_\infty\psi_i^*(-i\nabla)\psi_i d\tau\Big/\int_\infty\psi_i^*\psi_i d\tau\\
&=\mathbf{v}_{0i}+\sum_{n=1}^{\infty}\lambda^n\mathbf{v}_{ni},
\end{aligned} \tag{14a}$$

where

$$\mathbf{v}_{0i}=\int_\infty\psi_{0i}^*(-i\nabla)\psi_{0i}d\tau. \tag{15a}$$

We will assume that

$$\int_\infty\psi_{0j}^*(-i\nabla)\psi_{0i}d\tau=0,\quad i\neq j. \tag{16a}$$

This assumption is true for the case studied in detail in this paper where the unperturbed wave functions are plane waves. For the more general energy-band problem it is true for two different wave functions belonging to the same energy band. We now obtain

$$\mathbf{v}_i\int_\infty \psi_i^*\psi_i d\tau-\int_\infty \psi_i^*(-i\nabla)\psi_i d\tau=0$$

$$=\lambda\mathbf{v}_{1i}+\lambda^2[\mathbf{v}_{2i}+\sum_p{}' {}_1a_{ip}^*\,{}_1a_{ip}\,(\mathbf{v}_{0i}-\mathbf{v}_{0p})]$$

$$+\sum_{n=3}^{\infty}\lambda^n\Bigg[\mathbf{v}_{ni}+\sum_{n'=1}^{n-1}\sum_p{}' {}_{n-n'}a_{ip}^*\,{}_{n'}a_{ip}\,(\mathbf{v}_{0i}-\mathbf{v}_{0p})$$

$$+\sum_{n''=2}^{n-1}\sum_{n'=1}^{n''-1}\sum_p{}' {}_{n''-n'}a_{ip}^*\,{}_{n'}a_{ip}\,\mathbf{v}_{n-n'',i}\Bigg].$$

Equating to zero the coefficients of each power of λ, we get for $n=1$,

$$\mathbf{v}_{1i}=0, \tag{17a}$$

for $n=2$

$$\mathbf{v}_{2i}=\sum_j{}'|H_{ij}'|^2(E_{0i}-E_{0j})^{-2}(\mathbf{v}_{0j}-\mathbf{v}_{0i}), \tag{18a}$$

while for $n\geqslant 3$

$$\mathbf{v}_{ni}=\sum_{n'=1}^{n-1}\sum_p{}' {}_{n-n'}a_{ip}^*\,{}_{n'}a_{ip}\,(\mathbf{v}_{0p}-\mathbf{v}_{0i})$$

$$-\sum_{n''=2}^{n-1}\sum_{n'=1}^{n''-1}\sum_p{}' {}_{n''-n'}a_{ip}^*\,{}_{n'}a_{ip}\,\mathbf{v}_{n-n'',i}. \tag{19a}$$

Thus

$$\mathbf{v}_{3i}=\sum_{i,p}{}'\frac{H_{ij}'H_{jp}'H_{pi}'}{(E_{0i}-E_{0j})(E_{0i}-E_{0p})}$$

$$\times\left\{\left(\frac{\mathbf{v}_{0j}-\mathbf{v}_{0i}}{E_{0i}-E_{0j}}\right)+\left(\frac{\mathbf{v}_{0p}-\mathbf{v}_{0i}}{E_{0i}-E_{0p}}\right)\right\}$$

$$-2H_{ii}'\sum_j{}'|H_{ij}'|^2(E_{0i}-E_{0j})^{-3}(\mathbf{v}_{0j}-\mathbf{v}_{0i}). \tag{20a}$$

We now consider the special case where

$$\psi_{0i}=(N\Omega)^{-\frac{1}{2}}e^{i\mathbf{k}_i\cdot\mathbf{r}}, \tag{21a}$$

the plane wave being normalized over the volume $N\Omega$, and the propagation vector $\mathbf{k}_i$ satisfying the periodic boundary conditions associated with this volume. We write

$$H_{ji}'\equiv H'(\mathbf{k}_i-\mathbf{k}_j). \tag{22a}$$

We have

$$E_{0i}=k_i^2, \qquad \mathbf{v}_{0i}=\mathbf{k}_i,$$
$$E_{1i}=H'(0), \quad \mathbf{v}_{1i}=0, \tag{23a}$$

so that

$$E_{2i}=\sum_j{}'|H'(\mathbf{k}_j)|^2(2\mathbf{k}_i\cdot\mathbf{k}_j-k_j^2)^{-1}, \tag{24a}$$

$$\mathbf{v}_{2i}=-\sum_j{}'|H'(\mathbf{k}_j)|^2\mathbf{k}_j(2\mathbf{k}_i\cdot\mathbf{k}_j-k_j^2)^{-2}. \tag{25a}$$

In obtaining the last two equations, we have replaced $\mathbf{k}_j$ by $(\mathbf{k}_i-\mathbf{k}_j)$ as a dummy index. The primes on the summation signs now mean that $\mathbf{k}_j\neq 0$. In a similar fashion we get

$$E_{3i}=\sum_{i,p}{}' H'(-\mathbf{k}_j)H'(\mathbf{k}_j-\mathbf{k}_p)H'(\mathbf{k}_p)$$

$$\times[2\mathbf{k}_i\cdot\mathbf{k}_j-k_j^2]^{-1}[2\mathbf{k}_i\cdot\mathbf{k}_p-k_p^2]^{-1}$$

$$-H'(0)\sum_j{}'|H'(\mathbf{k}_j)|^2(2\mathbf{k}_i\cdot\mathbf{k}_j-k_j^2)^{-2}, \tag{26a}$$

$$\mathbf{v}_{3i}=-\sum_{i,p}{}'\frac{H'(-\mathbf{k}_j)H'(\mathbf{k}_j-\mathbf{k}_p)H'(\mathbf{k}_p)}{(2\mathbf{k}_i\cdot\mathbf{k}_j-k_j^2)(2\mathbf{k}_i\cdot\mathbf{k}_p-k_p^2)}$$

$$\times\left\{\frac{\mathbf{k}_j}{2\mathbf{k}_i\cdot\mathbf{k}_j-k_j^2}+\frac{\mathbf{k}_p}{2\mathbf{k}_i\cdot\mathbf{k}_p-k_p^2}\right\}$$

$$+2H'(0)\sum_i{}'\frac{|H'(\mathbf{k}_j)|^2\mathbf{k}_j}{(2\mathbf{k}_i\cdot\mathbf{k}_j-k_j^2)^3}. \tag{27a}$$

It is now seen that

$$\mathbf{v}_{ni}=\tfrac{1}{2}\nabla_{ki}E_{ni}, \quad n=0,\,1,\,2,\,3, \tag{28a}$$

so that, through third-order perturbation theory at least, the standard energy-band relation holds between $\mathbf{v}$ and E for the special case denoted by Eq. (21a). It can be seen that Eq. (28a) follows as a result of the fact that the matrix elements of H' can be written in the form given in Eq. (22a). The expression for E_{4i} is given by

$$E_{4i}=\sum_{i,p,q}{}'\frac{H'(-\mathbf{k}_j)H'(\mathbf{k}_j-\mathbf{k}_p)H'(\mathbf{k}_p-\mathbf{k}_q)H'(\mathbf{k}_q)}{(2\mathbf{k}_i\cdot\mathbf{k}_j-k_j^2)(2\mathbf{k}_i\cdot\mathbf{k}_p-k_p^2)(2\mathbf{k}_i\cdot\mathbf{k}_q-k_q^2)}$$

$$-\left[\sum_i{}'\frac{|H'(\mathbf{k}_j)|^2}{(2\mathbf{k}_i\cdot\mathbf{k}_j-k_j^2)}\right]\left[\sum_i{}'\frac{|H'(\mathbf{k}_j)|^2}{(2\mathbf{k}_i\cdot\mathbf{k}_j-k_j^2)^2}\right]$$

$$-H'(0)\sum_{i,p}{}'\frac{H'(-\mathbf{k}_j)H'(\mathbf{k}_j-\mathbf{k}_p)H'(\mathbf{k}_p)}{(2\mathbf{k}_i\cdot\mathbf{k}_j-k_j^2)^2(2\mathbf{k}_i\cdot\mathbf{k}_p-k_p^2)}. \tag{29a}$$

Irradiation Effects in Cu, Ag, and Au Near 10°K*

H. G. Cooper,† J. S. Koehler, and J. W. Marx‡
Department of Physics, University of Illinois, Urbana, Illinois
(Received August 3, 1954)

Electrical resistivity increases produced by 12-Mev deuteron irradiation were measured as a function of integrated deuteron flux in Cu, Ag, and Au. The bombardment temperature was near 10°K and no thermal recovery of the irradiation effects was observed; however, evidence that appreciable radiation annealing occurred during the bombardment was found. The resistivity increases near 10°K were much larger than those previously obtained in these metals for equal irradiations made near liquid nitrogen temperature. The observed Z-dependence of the irradiation effects agreed closely with that predicted by Seitz's theory.

Warmups made following the bombardments revealed that 40 to 50 percent of the total resistivity increase in Cu recovers near 43°K and from 13 to 24 percent of that in Ag anneals near 30°K; the rapid recovery in each case indicates that a unique process may be involved, and the associated activation energy is estimated to be 0.1 ev for both. It is suggested that volume diffusion of interstitial atoms or annihilation of very close interstitial atom-vacancy pairs are two possible processes responsible for the low temperature recovery. In addition, for all three metals, a gradual annealing rate was observed in the intermediate temperature range 50°K–220°K, and then a more rapid rate took place in the range 220°–280°K.

I. INTRODUCTION

FAST particle irradiation of metals introduces lattice defects which are believed to be largely equal concentrations of interstitial atoms and vacancies.[1] Although many physical properties of the metals are altered by the presence of such imperfections, electrical resistivity changes have extensively been used for their study since this property is both sensitive to small defect concentrations and easily measured experimentally. Previous work[2–4] on Cu, Ag, and Au, irradiated near liquid nitrogen temperature, has shown that most of the resulting increases in resistivity anneal out below room temperature and that considerable thermal recovery still occurs at temperatures as low as −180°C. For these basic studies it would be highly desirable that all of the imperfections created by the bombardment be "frozen in," since it is possible that new types may be observed, and in addition, it should then be possible to unambiguously decide whether radiation annealing, due to collisions of the fast particles with the lattice, is important. When thermal and radiation recovery simultaneously occur during the bombardment, it is difficult to separate the two types of annealing since they both cause a decrease in resistivity. All of the above experiments were performed near liquid nitrogen temperature, hence it is evident that bombardments using liquid hydrogen or helium as a coolant are necessary for further reduction or total exclusion of the thermally activated processes.

In the present investigation,[5] pure wires of Cu, Ag, and Au were mounted on a liquid helium cryostat and irradiated by 12-Mev deuterons from the University of Illinois cyclotron. The choice of these three metals was made for the following reasons: the results of previous theoretical work and the above mentioned experimental studies on them were available, high purity specimens of each could readily be obtained, and their similar electronic structure permitted Z-dependence estimates of the irradiation effects. Changes in resistivity were measured during the bombardment and the recovery was followed as the cryostat subsequently warmed to room temperature.

II. SAMPLE DESIGN AND MOUNTING

Samples in the form of 5-mil diameter Cu and Ag and 4-mil diameter Au wires were used. Wires were selected, rather than foils, in order to reduce the specimen area exposed to the beam and thus lower the liquid helium consumption. The sizes were chosen such that the diameter of each was about 60 percent of the 12-Mev deuteron range in that material. In this region the rate of deuteron energy loss $(dE/dx)_{\text{displ}}$, due to the displacement of atoms, is essentially constant;[1] and hence a desirable homogeneity of defects throughout the irradiated portion of the metal wires is approximately produced.

Special design of the specimens and their holder was necessary since a Wheatstone bridge circuit, similar to one previously used in this laboratory by Overhauser,[3] was employed for the resistivity measurements. This method permitted the thermal part of the irradiated specimen's resistance to be cancelled out by placing, in an opposite leg of the bridge, an equal but unbombarded specimen of the same metal. This circuit is shown in Fig. 3 and will be discussed further in the next section.

The required two identical samples were made by

* This research was supported by the U. S. Atomic Energy Commission.

† Present address: Bell Telephone Laboratories, Inc., Murray Hill, New Jersey. Submitted in partial fulfillment of the requirements for the degree of Doctor of Philosophy.

‡ Present address: Phillips Petroleum Company, Bartlesville, Oklahoma.

[1] F. Seitz, Discussions Faraday Soc. 5, 271 (1949).
[2] Marx, Cooper, and Henderson, Phys. Rev. 88, 106 (1952).
[3] A. W. Overhauser, Phys. Rev. 90, 393 (1953).
[4] R. R. Eggleston, Acta Metallurgica 1, 679 (1953).

[5] Preliminary results of this experiment were reported in Phys. Rev. 94, 496 (1954).

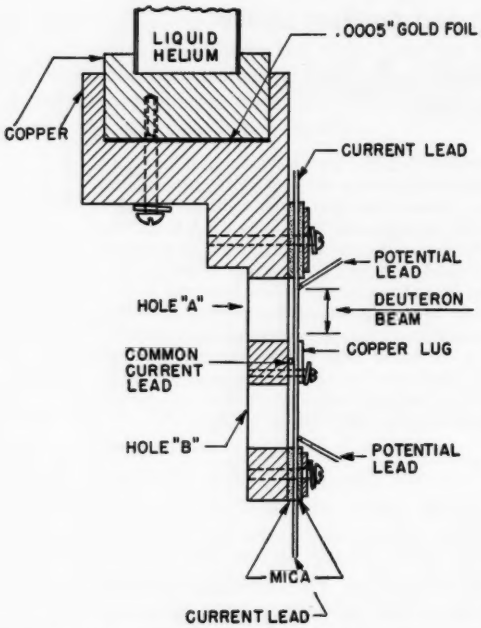

FIG. 1. Target block and specimen mounting.

accurately spot welding three copper leads, equally spaced $\frac{7}{16}$ inch apart, at right angles to a four inch length of pure specimen wire. The center welded contact, which was a 10-mil copper wire, served as a common current lead to the two equal sections of the sample; and the other two, consisting of 3-mil copper wire, were utilized as potential leads. With the aid of a Lucite jig for the spot welding operation, the two halves of each specimen were balanced to within one percent of the single section resistance.

The problem of mounting the specimens such that they are properly cooled, and at the same time insulated for resistance measurements, has been among the more difficult ones that arise in an experiment of this nature. Immersion of the specimens in the coolant was precluded by the short range of the 12-Mev deuterons (8 mils in Cu). A rather satisfactory solution was obtained by mounting the balanced specimens, as shown in Fig. 1, on a copper target block which was in contact with liquid helium. The 10-mil common current lead was fastened directly against the block with a copper lug, thus insuring good thermal contact to the specimens. The two ends of the specimen were clamped between mica sheets of 0.5-mil thickness with copper bars. The thin mica provided electrical insulation necessary for resistance measurements, and in addition it permitted a moderate thermal connection between the copper block and the ends of the samples. The 3-mil potential wires were similarly insulated and clamped on either side of the target block for the twofold purpose of preventing excessive strains at the spot weld joints and reducing heat conduction to the specimens through these leads.

Since it would be very wasteful of liquid helium if the energy of the entire deuteron beam were dissipated on the target block, the hole "*A*" was cut so that all of the beam could pass through the block. Hence only the small portion of beam energy lost in traversing the thin wire specimens was expended to liquid helium and the remainder was absorbed at a liquid nitrogen cooled radiation shield. For subsequent annealing studies, identical mounting of the matched specimens was desired, thus hole "*B*" was placed adjacent to the unbombarded sections and was made the same size as hole "*A*."

III. EXPERIMENTAL PROCEDURE

The polycrystalline specimens, which had a purity of 99.97 ± 0.02 percent, were mounted as described above and the complete assembly was then annealed for three hours at 400°C in a 10^{-5} mm of Hg vacuum. With a 0.5-mil gold foil at the interface for good thermal contact, the target block was bolted to the base of a spherical liquid helium flask in a metal cryostat especially designed for irradiation studies.[6] The lower section of the cryostat and beam tube arrangement are shown in Fig. 2. A copper cylinder, cooled by liquid nitrogen, shielded the target block from thermal radiation and also served as a Faraday cage for collection of the charged deuterons and secondary electrons. The grounded collimator No. 1 defined the area of the beam entering the Faraday cage; this beam was then further reduced in cross section by collimator No. 2, which accurately aligned it to hole "*A*" in the target block. A 0.5-mil copper foil, placed over the No. 2 aperature, prevented admission of thermal radiation. Electrical leads for resistivity and temperature measurements were brought in the top of the cryostat through Kovar seals. A P.I.G. gauge mounted on the outer cryostat wall indicated that the vacuum inside the cryostat was maintained near 10^{-5} mm of Hg during the bombardments. The liquid helium evaporation rate,

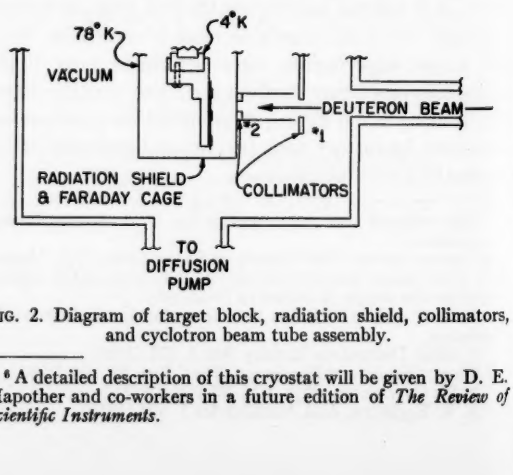

FIG. 2. Diagram of target block, radiation shield, collimators, and cyclotron beam tube assembly.

[6] A detailed description of this cryostat will be given by D. E. Mapother and co-workers in a future edition of *The Review of Scientific Instruments*.

which varied between 2.5 and 4.0 liters per day, was monitored by a gas flow meter connected in series with the helium flask exhaust tube.

The deuteron flux was recorded by insulating the entire inner part of the cryostat from the cyclotron ground, with a Teflon gasket, and then passing the charge collected on the Faraday cage through an electronic current integrator. The homogeneity of the beam distribution was determined from five copper monitor wires placed in the beam near the specimens. The radioactive Zn^{65} induced in these wires was counted and found to be constant, within 10 percent, over the beam area $\frac{3}{4}$ inch wide by $\frac{1}{4}$ inch high that was used.

Two experiments were performed, denoted as Run I and Run II, with the duration of the bombardments being seven and five days, respectively. Throughout these periods the specimens were maintained at 10°K ±2°K for Run I and 12°K±2°K for Run II, as determined from a copper-constantan thermocouple on the target block and correlation of the unbombarded specimen's resistance values to the Gruneisen function. The deuteron beam intensity had to be kept below 0.05 microampere per cm^2 at all times to avert excessive heating of the specimens.

At various intervals during the irradiations the beam was turned off, and resistance measurements were made with the circuit shown in Fig. 3. When switch S_1 was in position 2, as drawn, the two initially balanced halves of the sample, labeled R_b for the bombarded half and R_d for the dummy part, were incorporated as two legs of a bridge. The other two sections each consisted of 50 ohm precision resistors and maintained essentially equal currents in the two parallel branches at all times during the irradiation, since R_b never exceeded 3×10^{-3} ohm and R_d was about 10^{-4} ohm for all specimens. The single branch current was determined from the emf across a standard 1-ohm resistor, which was read

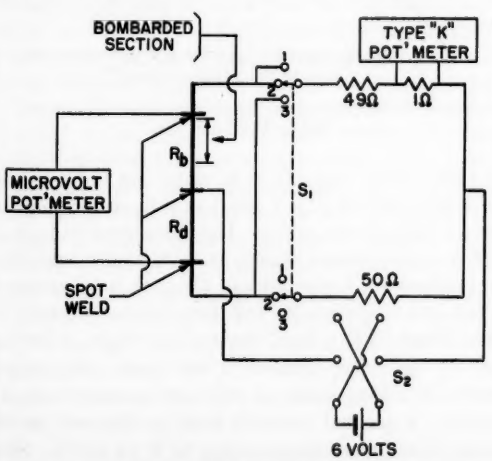

FIG. 3. Schematic diagram of circuit used for the resistance measurements. The matched bombarded and dummy specimens are R_b and R_d respectively.

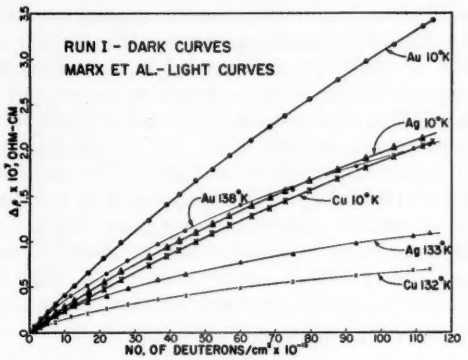

FIG. 4. Resistivity increase as a function of integrated deuteron flux—Run I and, for comparison, previous data obtained near 135°K by Marx *et al.* (See reference 2.)

on a Leeds and Northrup type K potentiometer. The off-balance voltage between the two potential leads was measured by a Rubicon Cat. No. 2766 thermofree microvolt potentiometer to an accuracy of $\pm5\times10^{-8}$ volt. Errors due to stray thermal voltages in the potential leads were eliminated by reversing the current through the bridge, with switch S_2, and taking the average of the readings for the two current directions. Simultaneous current and bridge voltage measurements made in this fashion yielded the resistance difference between R_b and R_d to a precision of 1×10^{-6} ohm, which was about 0.1 percent of the maximum difference. By switching S_1 to position 1, current was passed through the bombarded specimen only and R_b was measured directly using the standard potentiometric technique. Resistance changes obtained by this method were identical to the bridge values, within the experimental accuracy, and thus established confidence in the bridge method. The geometric conversion factor from resistance to resistivity, A/L, was determined from the ratio ρ_0/R_0 for the three metals, where ρ_0 is the handbook resistivity value at 0°C and R_0 is the measured specimen resistance at 0°C prior to irradiation.

After termination of the bombardments, the annealing of the defects was studied as the coolants ran out and the target block slowly warmed to room temperature. The warmup rate was usually in the range 15°K–30°K per hour. The bridge technique previously described was specifically designed for these studies, since it allowed the troublesome thermal resistance changes of the irradiated specimens to be balanced out. Simultaneous readings of the current, bridge voltage, and target block temperature were made for the specimens at frequent intervals during the warmup from 10°K to 300°K. Since it was not possible to match the bombarded and dummy specimens exactly, corrections for small resistance and temperature differences were determined from a similar warmup made before the irradiation and another following the annealing warmup. The average corrections from the latter two warmups

were taken, and subtracted from the appropriate measured values of the annealing warmup; thus yielding the desired net resistivity increase left in the bombarded specimen as a function of the annealing temperature.

In addition, at temperature intervals of about 10°K, resistance measurements of R_d for all samples were made potentiometrically by switching S_2 to position 3 in the circuit of Fig. 3. The temperature of the specimens at each of these points was then obtained by fitting these resistance values to the Gruneisen function. Substantial agreement, usually within 1°K, with the copper-constantan thermocouple attached to the target block was found.

IV. EXPERIMENTAL RESULTS

The plots of resistivity increase *versus* deuteron flux for Cu, Ag, and Au, that were obtained during Run I, are given by the dark curves of Fig. 4. These are to be compared with previous results of Marx *et al.*,[2] shown by the light curves on this figure, where the bombardment temperature was near that of liquid nitrogen. The initial slope of the 10°K curves are about a factor of two larger, for all three metals, than those of the liquid nitrogen curves; indicating that a considerable number of defects recover immediately in the latter case. The annealing curves that are shown later will shed some light on the nature of these recoveries.

A second experiment, Run II, was made for the purpose of checking the results of Run I and, in addition, to improve the annealing data. In this case the specimen temperatures were about 2°K higher than those of Run I, as a result of poorer thermal contact between the block and helium flask. The bombardment curves obtained from this run are shown in Fig. 5. Although the temperature difference between the two runs was small, the points on the Run II curves lie slightly below those of Run I for all metals and the percentage deviation becomes larger at higher deuteron fluxes. Figure 6 shows a comparison of the two curves for Cu, which is typical for the three metals. These differences would seem to indicate that thermal annealing was occurring at these low temperatures. However, after the end of the bombardments the specimens were held at or below (as much as 4°K) the irradiation temperature for 40 hours in Run I and 6 hours in Run II; with the result that no thermal recovery was observed, within the experimental accuracy of 0.1 percent. It then appears that this annealing must be due to collisions of the fast deuterons with the lattice; possibly in the form of thermal spikes, as originally suggested by Billington and Siegel.[7] The slightly higher ambient temperature of Run II would allow a higher absolute temperature to be reached in the vicinity of collisions, and hence result in more recovery for the second run. Table I contains a summary of the bombardment data for both runs.

The annealing curves obtained during Run I, as the specimens warmed to room temperature, are shown in Fig. 7. Unfortunately, a copious amount of deuterium had condensed on the liquid helium flask and created a gas burst in the cryostat during the very first part of the warmup. In turn, the ensuing pressure rise in the vacuum chamber produced a temperature pulse in the target block, the effects of which are indicated by the dashed lines on Fig. 7, because of increased thermal contact to the surroundings. The block went as high as 70°K and reached equilibrium at 27°K, as the deuterium was pumped out. Consequently, the data is not accurate at very low temperatures, but some conclusions may be made. Near 40°K a sharp drop of $\Delta\rho$ occurs in the Cu sample, indicating that a rather large and unique process is taking place at this low temperature. In addition, a gradual recovery rate is observed for all metals in the temperature range 50°K to 220°K. Near 220°K more rapid annealing processes take over until

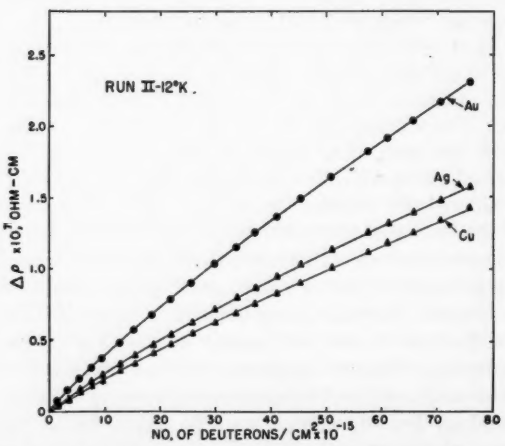

FIG. 5. Resistivity increase as a function of integrated deuteron flux—Run II.

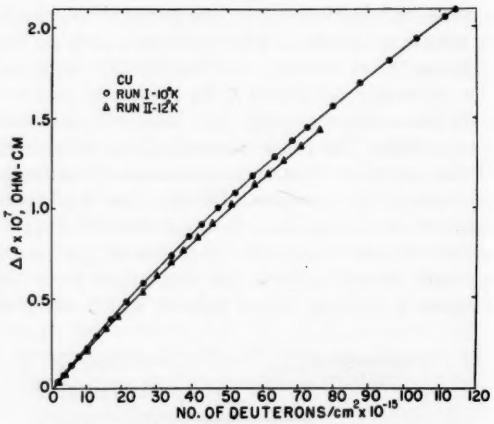

FIG. 6. Comparison of the resistivity increase produced in Cu during Run I and Run II.

[7] D. S. Billington and S. Siegel, Metal Progr. 58, 847 (1950).

temperatures of 250°K–280°K are reached, where recovery then proceeds at extremely slow rates.

In order to reduce the gas burst effects in Run II, the cryostat vacuum chamber was connected to the large cyclotron diffusion pumps and, as a result, the thermal pulse in the specimens persisted for less than a minute with a maximum temperature of about 30°K. The annealing curves observed in Run II are shown in Fig. 8. The percentages of $\Delta\rho_{max}$ that recovered during this pulse, shown by dashed lines near 15°K on the figure, were 5, 10, and 2 for Cu, Ag, and Au respectively, as compared to 28, 23, and 4 percent

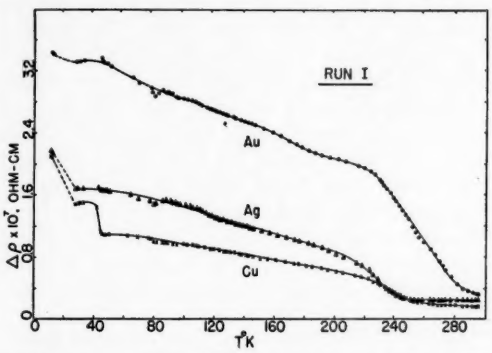

FIG. 7. Thermal recovery during warmup from 10°K to 300°K —Run I. The resistivity increase remaining at temperature T is plotted *versus* T.

respectively for the larger effect in Run I. In the temperature range 35°K–45°K on Fig. 8, 40 percent of $\Delta\rho_{max}$ annealed in Cu, which clearly indicates that the large recovery observed in Cu during the gas burst of Run I would have occurred near 40°K if a gradual warmup had been made. In addition the improved technique made it possible to resolve an analogous drop in Ag near 30°K, where 13 percent of $\Delta\rho_{max}$ recovered between 27°K and 33°K. From the difference in the results on Cu between Run I and Run II, it appears that the ten percent of $\Delta\rho_{max}$ which disappeared in Ag during the thermal pulse would normally recover near 30°K also. No similar abrupt low temperature drop was observed in Au, and since all three metals have f.c.c. lattice structure, this seems rather surprising. Possible explanations are that this annealing process occurs below 10°K in Au or that the drop is too small to be resolved in this type of measurement. Because of the radiation shield at liquid nitrogen temperature, which surrounded the target block, the warmup rate became very slow in the temperature range 75°K–85°K during both runs and caused the anomalous dips in the annealing curves. The relative amounts of $\Delta\rho$ that remain at various annealing temperatures are tabulated for the two runs in Table II.

V. DISCUSSION

The theory of Seitz[1] predicts that the fractional concentration of interstitial atom and vacancy pairs, here-

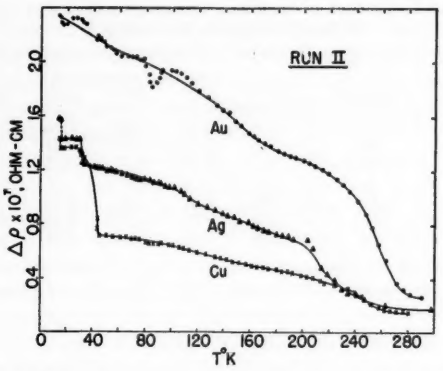

FIG. 8. Thermal recovery during warmup from 10°K to 300°K —Run II. The resistivity increase remaining at temperature T is plotted *versus* T.

after called I-V pairs, produced by an irradiation of 10^{17} deuterons/cm² is the order of 10^{-3} in Cu, Ag, and Au. When similar quantities of impurity atoms are added, *e.g.*, Ni in Cu, the resistivity increase is linear with the impurity concentration;[8] hence it seems reasonable that the same linear dependence should hold for the small quantities of defects which were induced in this experiment. The deviation from linearity observed in all of the $\Delta\rho$ *vs* n curves, shown in Figs. 4 and 5, should then be direct evidence that annealing of some nature does occur at irradiation temperatures as low as 10°K. It has previously[2] been pointed out that if there is no recovery during the bombardment other than radiation annealing, then the differential production of lattice defects could be described by the relation

$$dN=\alpha dn-\beta N dn, \tag{1}$$

where N is the number of I-V pairs per unit volume, n is the number of incident particles per unit area, α is the number of I-V pairs produced per particle in a unit distance, and β is the probability that one existing pair per unit volume would be annihilated through the action of one fast particle per unit area. The integration of this equation and the assumption that $\Delta\rho$ is proportional to N result in the following theoretical ex-

TABLE I. Summary of bombardment data obtained near 10°K.

Run	Sample	$10^{-17}\times$flux d/cm²	$10^7\times\Delta\rho_{max}$ Ω-cm	$\Delta\rho_{max}/\rho_0$ [a]
I	Cu	1.1	2.1	0.13
I	Ag	1.1	2.2	0.15
I	Au	1.1	3.4	0.15
II	Cu	0.8	1.4	0.09
II	Ag	0.8	1.6	0.11
II	Au	0.8	2.3	0.10

[a] ρ_0 = resistivity at 0°C.

[8] D. K. C. MacDonald and W. B. Pearson, Phys. Rev. 88, 149 (1952).

TABLE II. Fraction of the initial resistivity increase that remains at various annealing temperatures.

Run	Sample	$\Delta\rho/\Delta\rho_{max}$ remaining at 35°K[a]	45°K	77°K	220°K	300°K
I	Cu	···	0.53	0.48	0.26	0.07
I	Ag	···	0.76	0.70	0.31	0.10
I	Au	···	0.97	0.87	0.57	0.10
II	Cu	0.89	0.49	0.41	0.25	0.08
II	Ag	0.77	0.76	0.69	0.27	0.10
II	Au	0.98	0.93	0.86	0.51	0.10

[a] Annealing data at 35°K for Run I was invalidated by a gas burst.

pression for the bombardment curves:

$$\Delta\rho = A(1-e^{-\beta n}). \quad (2)$$

This equation predicts a saturation value of $\Delta\rho_s = A$ for large fluxes, when the rate of radiation annealing becomes equal to the rate of I-V pair production.

It was found that Eq. (2) would not satisfactorily describe the $\Delta\rho$ *vs* n curves obtained for Cu, Ag, and Au near liquid nitrogen temperature;[2] and it then appeared that this discrepancy was due to the accumulation of secondary defects, possibly in the form of defect clusters. However, when this expression was fitted to the irradiation data of the present investigation, close agreement was achieved for all metals. The fact that the nonlinearity in all of the curves can be accounted for by Eq. (2) forms rather strong evidence that the primary source of recovery during the liquid helium bombardments is radiation annealing. The values of A, β, the maximum deviation from the measured points, and the initial slopes for the best theoretical curves are given in Table III. This information serves as a more accurate definition of the data plotted in Figs. 4 and 5. It is interesting to note that the annihilation probability of I-V pairs, β, is about the same for all three metals, which tends to confirm that the internal structure of Cu, Ag, and Au is quite similar. The Ag specimens had the highest β value; this indicates that more thermal recovery may have occurred for this metal, since there is a sizeable annealing process near 30°K, as shown in Fig. 8.

As mentioned above, the similar electronic structure of Cu, Ag, and Au should allow at least qualitative conclusions to be made from the $\Delta\rho$ data in regard to the Z-dependence of the irradiation effects. It is seen from Fig. 4 that, for the bombardments made near liquid nitrogen temperature, the $\Delta\rho$ values are larger as the atomic number Z increases; and that this same relation still exists for the data obtained near 10°K. The theoretical Z-dependence, calculated by Seitz,[1] is given to a good approximation by the relation

$$(dE/dx)_{c,d} \propto Z^2 N_0/M, \quad (3)$$

where $(dE/dx)_{c,d}$ is the rate at which deuteron energy is lost to those collisions which result in I-V pair displacements, N_0 is the number of metal atoms per unit volume, and M is their atomic mass. The minimum energy required for the production of an I-V pair is expected to be about the same for all three metals;[1] thus the proportionality factor between $(dE/dx)_{c,d}$ and defect concentration should be nearly equal for Cu, Ag, and Au, and would cancel out when ratios relative to Cu are taken. The initial slopes of the $\Delta\rho$ *versus* n curves presumably would represent the results for the ideal case where all of the induced I-V pairs are retained in the metal, i.e., no radiation or thermal annealing, and hence this particular irradiation data should be the best for use in a check with theory. Table IV contains a comparison, relative to Cu, between the theoretical and observed Z-dependence of the irradiation effects. The theoretical ratios are calculated from Eq. (3) and the experimental ones are obtained from the initial slopes of the $\Delta\rho$ *vs* n curves, that are tabulated in the last column of Table III. The rather good agreement with theory, in view of the approximations involved, indicates that the Z-dependence calculated by Seitz is quite accurate.

TABLE III. Results from fitting Eq. (2) to the experimental irradiation data.

Run	Sample	A $\mu\Omega$-cm	$10^{17}\times\beta$ cm²/d	Maximum deviation in percent of $\Delta\rho_{max}$	Initial slope[a] ($=A\beta$)
I	Cu	0.519	0.450	0.3	0.234
I	Ag	0.396	0.690	0.6	0.273
I	Au	0.749	0.530	0.7	0.397
II	Cu	0.513	0.430	0.3	0.221
II	Ag	0.398	0.660	0.4	0.263
II	Au	0.612	0.620	0.6	0.379

[a] Initial slope is given in units of $\mu\Omega$-cm per 10^{17} d/cm².

TABLE IV. Z-dependence comparison of irradiation effects in Ag and Au relative to Cu.

	Ratio of observed initial $\Delta\rho$ *versus* n slopes Run I	Run II	Theoretical ratio from Eq. (3)
Ag/Cu	1.16	1.19	1.07
Au/Cu	1.70	1.71	1.67

The determination of the absolute I-V pair concentrations from the $\Delta\rho$ data is complicated by uncertainties in the contribution of a single pair to the conduction electron scattering. Jongenburger[9] has calculated that one percent of vacancies in Cu, Ag, and Au would increase their resistivity by 1.3, 1.5, and 1.5 μohm-cm respectively. Unfortunately, similar work has not been carried out for interstitial atoms; however, if it is assumed that the interstitial and vacancy make equal contributions to $\Delta\rho$, his calculations in conjunction with the initial $\Delta\rho$ *versus* n slope data from Table III yield the results that 10^{17} deuterons/cm² would produce 0.09, 0.09, and 0.13 percent of I-V pairs in

[9] P. Jongenburger, Appl. Sci. Research B3, 237 (1953).

Cu, Ag, and Au respectively. The corresponding values obtained from the Seitz theory are 0.2, 0.3, and 0.6 percent. Overhauser[10] has made calorimetric measurements on the energy released when I-V pairs recombine in Cu. He observes that an energy of 1.7 cal/g is liberated when 1 μohm-cm of resistivity is recovered. If it is assumed that the energy from a single pair is 5 ev, then one may conclude from his data that one percent of I-V pairs in Cu would increase ρ by 11 μohm-cm; this would imply, from Jongenburger's value for vacancies, that the interstitital contribution to $\Delta\rho$ is about seven times greater than that from vacancies. When the 11 μohm-cm factor is applied to the initial slope data, one finds that the amount of I-V pairs created by 10^{17} deuterons/cm^2 is 0.02 percent in Cu, which is about one-tenth of the theoretical value. It seems highly unlikely that the interstitial electron scattering is more than a factor of ten greater than that from a vacancy; so it should be safe to conclude that, on the basis of Jongenburger's calculations, agreement between experiment and theory for the absolute magnitude of the defect concentrations induced in Cu, Ag, and Au is obtained to within an order of magnitude.

An estimate of the total number of metal atoms, denoted as Q, that are heated above the annealing temperature when one I-V pair is produced may be made if the values of α and β are known. Since α is the total number of pairs produced in a unit distance by one deuteron and β is the annihilation probability for one I-V pair per unit volume per incident deuteron, Q is given by the quantity $\beta N_0/\alpha$, where N_0 is the number of metal atoms per unit volume. Now if K is denoted as the resistivity increase due to one I-V pair per unit volume, then α may be expressed by the equation $\alpha = A\beta/K$, where A is defined in Eq. (2). Upon assuming that one percent of I-V pairs in Cu increases the resistivity by 2.6 μohm-cm, one obtains from the values of A and β in Table III that $\alpha = 740$ I-V pairs/cm for each 12-Mev deuteron incident on Cu. From this value for α and the relation given above for Q, one may then conclude that Q is 500 atoms per I-V pair created in Cu. If the shape of the "anneal zone" is taken as spherical, the radius associated with the above Q value is less than four lattice parameters. Corresponding figures for Ag and Au may be obtained and will be similar to those of Cu, providing that comparable values for K are assumed.

The general behavior of the annealing phenomena, occurring during the warmups from 10°K to room temperature, may be grouped into three temperature ranges: 1. Low, below 50°K; 2. Intermediate, 50°K–220°K; and 3. High, 220°K–280°K. Previous[2–4] isothermal studies on Cu, Ag, and Au have been made in the intermediate and high regions, with most of this work confined to Cu. A wide spread of activation energies for migration, which were substantially proportional to the absolute temperature of the isothermal anneal, were found for the processes recovering in the intermediate region in Cu; while only a single activation energy, of 0.68 ev for Cu, was observed in the high range. It appears[3] that the process in the latter case is of second order, i.e., $dN/dt \propto N^2$, and may therefore be ascribed to the volume diffusion of either interstitial atoms or vacancies. At the present time, there does not seem to be sufficient evidence for an unambiguous choice between the two possibilities. Although this high temperature recovery has not previously been studied in detail for Ag and Au, the annealing curves of Figs. 7 and 8 indicate that the process occurs at about the same temperature for all three metals and presumably it is due to the same mechanism in all cases. However, as seen from Table II, a considerably larger percentage of $\Delta\rho_{max}$ is recovered in Au than in Cu or Ag during the anneal from 220°K–280°K; it is very probable that this difference is related to the apparent absence of a low temperature process in Au.

Recently T. H. Blewitt (as yet unpublished work) has discovered that no recovery occurs in the intermediate range for neutron irradiated Cu single crystals, where the total induced I-V concentration is small and about equivalent to that from 10^{15} deuterons/cm^2. A possible reason for this result is the absence of grain boundaries; another is the relatively dilute amount of I-V pairs, since the $\Delta\rho$ *versus* n curves for the present experiment were essentially linear up to a flux of 10^{16} deuterons/cm^2. It has previously[2,3] been suggested that the intermediate annealing may be due to pairs in which the interstitial and vacancy are very close to each other and the energy barrier between them is lowered by the interactions. A spectrum of activation energies could then be obtained from the various spacings that exist within the region of appreciable mutual influence; however, Seitz[11] has pointed out that the frequency factors observed for these processes are several orders of magnitude below the expected value of around 10^{12} sec^{-1}. In view of this fact it now appears that some other mechanism, *e.g.*, defect clusters such as divacancies; or defect traps in the form of impurity atoms, grain boundaries, or dislocations, is responsible for the intermediate processes.

The present experiment reveals that in addition to these previously observed recoveries, a very unique process takes place in both Cu and Ag below 50°K which is denoted as the low temperature process in this discussion. During Run II, these phenomena were manifest through the disappearance of 40 and 13 percent of $\Delta\rho_{max}$, for Cu and Ag respectively, in corresponding temperature intervals of 35°K–45°K and 27°K–33°K. Under ideal experimental conditions it is estimated that the above values would be about 50 percent for Cu and 25 percent for Ag; it is also possible that a somewhat smaller effect, certainly less than 10 percent of $\Delta\rho_{max}$, may be resolved in Au if very precise

[10] A. W. Overhauser, Phys. Rev. 94, 1551 (1954).

[11] F. Seitz (private communication).

annealing techniques are used. The time rate of the low temperature recovery in Cu was maximum at 43°K and, if an extrapolation is performed on activation energy data obtained by Overhauser[3] in the range 90°K–270°K, this recovery temperature would correspond to a process with an activation energy for motion of 0.1 ev. The analogous maximum occurred at 30°K in Ag and, since the activation energies observed in Cu and Ag at −165°C are the same,[2] it is expected that the low temperature activation energy for Ag is near 0.1 ev also.

Huntington[12] has recently calculated the energy for migration of interstitial Cu atoms in Cu and obtained results of 0.07 and 0.24 ev, for the two types of interaction potentials that were considered. Previous theoretical computations[13,14] of the activation energy for the motion of vacancies in Cu yielded values of around 1 ev. These theoretical results would then indicate that the low temperature (0.1 ev) process in Cu should be assigned to interstitial motion and the high temperature (0.68 ev) process to vacancy motion. These assignments would imply that both the 0.1 and 0.68 ev processes be approximately second order; I-V pair annihilation would result precisely in a bimolecular reaction, however, if some of the migrating defects are trapped slight deviations from second order may be expected. This has been observed for the 0.68 ev process, but it appears that additional work such as the formidable task of isothermal annealing at 40°K is necessary for definite establishment of the low temperature kinetics. The question of how vacancies can be annihilated in a second order fashion, when they begin to diffuse rapidly, arises. This could be accomplished by the coagulation of two vacancies into a divacancy, for Bartlett and Dienes[15] have calculated that the activation energy for migration of the latter is lower than that of vacancies; hence the divacancies could move to traps, such as dislocations or the surface, within a very short time and their formation should then be equivalent to vacancy annihilation. In addition, the presence of interstitial traps or clusters, which have activation energies for motion of 1 ev or more, could account for this phenomena, although it is questionable at the present time whether such aggregations do exist.

It is also possible that the low temperature process may be due to close I-V pairs. This was previously discounted as the source of intermediate recovery, because of discrepancies in the frequency factor; however, if the interactions between the interstitial and vacancy are very short range, there is the potentiality that only stable I-V pairs with the very smallest separations have their activation energies altered and hence their annihilation would result in a unique process. A sizable fraction of the defects could possess this configuration since many of the secondary and tertiary knock-on atoms do not have appreciable energy above that of the displacement threshold.[1] Such correlated pairs would result in a first order process and hence a determination of the kinetics should decide between the possibilities of close pairs and a second order recovery, such as interstitial motion, for the low-temperature process.

From Table II it is seen that about ten percent of the initial resistivity increase still remains in all metals at 300°K. Recent studies of recoveries in electrical resistivity[4] and critical resolved shear stress,[16] made in the region above room temperature, reveal that an annealing process with an activation energy of about 2 ev, which is nearly the same value as that observed for self-diffusion in Cu, proceeds at an appreciable rate near 300°C in irradiated Cu. The source of this process is likely to be associated with dislocations, since a relatively large proportion of the radiation-induced resolved shear stress increase anneals in this very high temperature range.

VI. SUMMARY

1. Near 10°K the initial rate of resistivity increase with the integrated deuteron flux is 0.23, 0.27, and 0.36 μohm-cm per 10^{17} deuterons/cm^2 respectively for Cu, Ag, and Au.

2. The Z-dependence of the resistivity increase induced in Cu, Ag, and Au by the radiation varies essentially as Z^2N_0/M, as predicted by the theory of Seitz.

3. No thermal recovery occurs when the deuteron beam is turned off and the specimens are held near the bombarding temperature.

4. The $\Delta\rho$ *versus* n curves deviate from linearity at high deuteron fluxes and this "bending over" may be accounted for by radiation annealing.

5. A very rapid low temperature recovery is observed in Cu near 43°K and in Ag near 30°K. Between 40 and 50 percent of the initial resistivity increase in Cu and from 13 to 24 percent of the initial increase in Ag anneals within a temperature interval of ten degrees absolute for these processes.

6. In the temperature range 50°K–220°K, a gradual recovery occurs for all three metals during which about 24, 47, and 41 percent of $\Delta\rho_{\max}$ disappear in Cu, Ag, and Au, respectively.

7. Near 220°K the recovery rate becomes more rapid in all metals, which persists until temperatures of 250°–280°K are reached, where it then proceeds at an extremely slow rate. It was previously established that a second order process took place in this region for Cu and this investigation indicates that it also occurs in Ag and Au at nearly the same temperature. This process accounts for 18, 19, and 44 percent of $\Delta\rho_{\max}$ in Cu, Ag, and Au, respectively.

8. The percentages of the initial resistivity increase

[12] H. B. Huntington, Phys. Rev. **91**, 1092 (1953).
[13] H. B. Huntington and F. Seitz, Phys. Rev. **61**, 315 (1942).
[14] H. B. Huntington, Phys. Rev. **61**, 325 (1942).
[15] J. H. Bartlett and G. J. Dienes, Phys. Rev. **89**, 848 (1953).
[16] Redman, Coltman, and Blewitt, Phys. Rev. **91**, 448 (1953).

remaining at 300°K are 8, 10, and 10 for Cu, Ag, and Au, respectively.

VII. ACKNOWLEDGMENT

The authors are indebted to Mr. J. W. Henderson, Mr. J. E. Mercereau, Professor F. Seitz, and Professor C. A. Wert of the Radiation Damage Group for many discussions and assistance with the experimental measurements; to the Cryogenics Group under the direction of Professor D. E. Mapother for liberal quantities of liquid helium; to Professor D. E. Mapother and Mr. F. E. L. Witt for the design and construction of the cryostat; to the cyclotron crew under the supervision of Professor W. K. Jentschke for the deuteron bombardments; and to Dr. A. W. Overhauser for suggesting the bridge method used in the annealing measurements.

PHYSICAL REVIEW VOLUME 97, NUMBER 3 FEBRUARY 1, 1955

Measurements of Electrical Conductivity and Magnetoresistance of Gray Tin Filaments*

A. W. EWALD AND E. E. KOHNKE
Department of Physics, Northwestern University, Evanston, Illinois
(Received September 17, 1954)

A method for the preparation of gray tin filaments suitable for electrical measurements is described. Results of measurements of the temperature dependence of the electrical conductivity and of the magnetoresistance on pure gray tin and on alloys containing various amounts of Sb, As, In, Al, and Zn are reported. For 99.998 percent pure tin the activation energy is 0.082 ev and the conductivity at 0°C is 2090 ohm^{-1} cm^{-1}. Addition of impurities results in an increase in the "intrinsic" activation energy and a decrease in the absolute value of the conductivity in the "intrinsic" range. Samples doped with *n*-type impurities exhibit a positive temperature coefficient of resistance at low temperatures whereas the low-temperature conductivity of *p*-type samples becomes temperature-independent at high impurity concentrations. The three *p*-type impurities In, Zn, and Al show marked differences in their effectiveness in producing *p*-type conductivity, In being 40 times more effective than Al. The magnetoresistance coefficient in the lattice-scattering region shows a stronger temperature dependence than is predicted by the simple theory. Impurity scattering appears to be relatively more important in *p*-type than in *n*-type material.

I. INTRODUCTION

IN 1950 Busch, Wieland, and Zoller[1] found that gray tin is a semiconductor similar to the other Group IV elements, carbon (in the form of diamond), silicon, and germanium. The subsequent investigations by Busch and his collaborators[2–4] and by Kendall[5,6] have revealed many of the semiconducting properties of gray tin. The measured values of some of the most important quantities have remained uncertain, however, because of the difficulty of preparing suitable specimens. The only method of obtaining gray tin is through the well known phase transition from the metallic phase. More direct methods, such as evaporation onto a cold substrate or electrolytic deposition at reduced temperatures, though tried by several investigators, have not proved successful. Using the phase transition method one generally obtains gray tin as a powder because of the large volume expansion associated with the white-to-gray transformation. Using such powder samples, Busch and his co-workers have measured the Hall coefficient, the magnetoresistance coefficient, the temperature dependence of the conductivity and the magnetic susceptibility. They conclude however that neither high-frequency loss measurements nor direct conductivity measurements made on powder are suited to an exact determination of the absolute value of the conductivity. Kendall has used two types of samples, lumps selected from a large quantity of powder and rods of compressed powder. Only an approximate value of the conductivity could be determined using the first type because of the difficulty in measuring the cross section and electrode areas. While this difficulty was eliminated through the use of compressed-powder rods, measurements on these samples yielded an unusually low value of the activation energy and therefore the value of the specific conductivity obtained using them is also open to question. In view of these difficulties, need for an improved method of preparing gray tin samples has been recognized. More suitable specimens were needed both to establish precise and reliable values of previously measured quantities, especially the value of the specific conductivity, and to extend the investigation to include phenomena such as the thermoelectric effect and photoelectric effect.

In searching for an improved method of preparation one of us[7a] found that fine wires of metallic tin would transform to the gray phase without the usual crumbling

* Parts of this material were reported at the North Carolina and Michigan meetings of the American Physical Society [Phys. Rev. 91, 244 (1953); Phys. Rev. 94, 1428 (1954)].

[1] Busch, Wieland, and Zoller, Helv. Phys. Acta 23, 528 (1950).
[2] Busch, Wieland, and Zoller, Helv. Phys. Acta 24, 49 (1951).
[3] G. Busch and E. Mooser, Helv. Phys. Acta 26, 611 (1953).
[4] G. Busch and J. Wieland, Helv. Phys. Acta 26, 697 (1953).
[5] J. T. Kendall, Proc. Phys. Soc. (London) B63, 821 (1950).
[6] J. T. Kendall, Phil. Mag. 45, 141 (1954).

[7a] A. W. Ewald, Phys. Rev. 91, 244 (1953).

to a powder. Filaments of gray tin approximately 0.1 mm in diameter and up to several centimeters in length are readily obtained.[7b] These filaments are free of cracks and other gross imperfections and are mechanically strong. X-ray Laue patterns show well defined spots indicating that the filaments are probably single crystals. Because of their relative dimensions, these specimens have proved to be well suited to measurements of the electrical conductivity, its change in a magnetic field, and the thermoelectric power. It is anticipated that under the proper conditions of purity and low-temperature photoelectric effects should also be observable.

II. PREPARATION OF GRAY TIN FILAMENTS

Filaments of metallic tin are first prepared by a modified form of the Taylor technique.[8] A glass capillary of approximately 0.5-mm inside diameter is drawn from the center portion of a 10-mm diameter glass tube one end of which has been closed. Approximately one gram of tin is inserted in the open end and rests at the upper end of the capillary portion when the tube is mounted vertically and attached to a vacuum line. After pumping out (rough vacuum), the tin pellet is melted by heating with a flame and the molten tin is forced down the capillary by collapsing the evacuated tube just above it. Having the closed segment of 10-mm tubing at the lower end of the capillary prevents any appreciable increase in pressure on the advancing side of the tin column as the tin is forced downward. This bulb is removed by sealing off the capillary after the latter has been filled. The filled capillary is then drawn out to reduce the core diameter to about 0.1 mm by heating short segments ($\sim$1 cm) and pulling. Some care is necessary to prevent fracture of the glass due to expansion of the metal upon melting. Cracking can be avoided by softening the glass at the lower seal-off point first and then working upward step by step keeping the tin in the lower end of the undrawn capillary molten. The result of the drawing operation is a chain of small-diameter segments, 10 to 20 cm in length, separated by nodules having the original capillary diameter. The segments are broken apart keeping a nodule at one end of each, and a hook is formed at the other end. The glass is conveniently removed by hanging the segments in a wax-lined test tube containing hydrofluoric acid. The filaments are then dipped in distilled water, in sulfuric acid, and in distilled water again. The nodules serve as sinkers to prevent doubling up of the filaments as they are lowered into the baths.

The metallic tin filaments are buried in gray tin powder and stored in a cold chest at -30°C to transform them to gray tin. In the earlier work the transformation was stopped when segments a few millimeters long had converted to the gray phase so that the remaining metallic portions could be used as electrical leads, contact to them being made through spring-loaded clamps. Later, when tin of higher purity was obtained, this method was abandoned because during measurements on the samples the transformation of the metallic portions would proceed at an appreciable rate when the temperature was in the vicinity of -30°C. The current procedure is to allow the transformation to go to completion and to solder the samples to the holder with a low melting-point solder. The time required for complete transformation varies depending upon the purity, but is of the order of one day for the samples of highest purity.

III. APPARATUS AND PROCEDURE

The apparatus was designed to permit simultaneous measurement of the conductivity and its change in a magnetic field as well as determination of the sign of the thermal emf in the temperature range from 77 to 273°K. The sample holder consisted of two brass blocks which when insulated from each other and fastened together formed a block measuring $1\times1\times2\frac{1}{2}$ cm. To reduce strains set up by the differential thermal contraction of the sample and brass, the sample was connected to the two insulated blocks through flexible strips of silver foil. The connection of the sample to these strips was made using solder composed of one part indium to four parts gallium which is liquid at room temperature and solid at the measurement temperatures. The sample diameter and the distance between soldered contacts were measured after the sample was mounted using a microscope equipped with a filar eyepiece. The effective length, approximately fixed by the dimensions of the sample holder, was about 3 mm for all samples. A $\frac{1}{2}$-watt carbon resistor imbedded in one of the brass blocks served as a heater for the thermal emf determinations. The sample temperature was varied by means of a liquid nitrogen bath and a heating coil wound on a copper tube surrounding the sample holder. To prevent excessive heat loss to the nitrogen bath this tube was surrounded by another constructed of lead, both tubes being closed at the lower ends.

A dc, constant current method was used for the conductivity measurements. The sample current, which ranged from 0.25 to 10 ma depending upon sample diameter, was monitored by a microammeter. The sample voltage as well as the voltages generated in two thermocouples imbedded in the two blocks of the sample holder were measured potentiometrically through suitable switching arrangements which also allowed for

[7b] *Note added in proof.*—Groen and Burgers have recently reported the formation of large compact pieces of gray tin of the order of 1 mm thick by 25 mm^2 in area. [L. J. Groen and W. G. Burgers, Proc. Koninkl. Ned. Akad. Wetenschap. (Amsterdam) **B57**, 79 (1954)]. However, subsequent investigations [L. J. Groen, Nature **174**, 836 (1954)] indicated the presence of mercury in the tin and that at least 0.2 atomic percent mercury was necessary for the formation of the large compact pieces. Our starting material was free of mercury and there was no possibility of contamination during preparation since only oil pumps were used in the vacuum system.

[8] G. F. Taylor, Phys. Rev. **23**, 655 (1924).

reversal of sample current direction so that thermal emf effects could be cancelled out of the conductivity measurements. Separate current and potential leads were connected between the sample holder and the external measuring circuit. Because of the small sample dimensions it was not convenient in routine work to make separate connections to the sample itself. A check measurement made with a third potential lead soldered directly to the midpoint of the sample established that the different methods of connection gave the same value for the conductivity.

Conductivity measurements with and without a magnetic field were made in a single temperature run. The sample was positioned approximately perpendicular to the magnetic field and then adjusted for maximum magnetic resistance change. To stay within the square-law range of the magnetoresistance effect the field intensity was readjusted at each temperature to the minimum value that would produce an accurately measurable effect. The determination of the magnetic resistance change $\Delta\rho/\rho_0$ was accomplished graphically since it was in general impossible to get readings of the sample resistance with and without the magnetic field at exactly the same temperatures.

TABLE I. Analyses of two lots of tin used. Values given in percent by weight.

Impurity	Lot I	Lot II
Lead	0.0012%	0.0001%
Antimony	0.001	...
Iron	0.00027	0.001
Arsenic	0.0002	...
Sulfur	0.00003	...
Copper	0.0002	0.0003
Bismuth	0.00012	0.0001
Tin (by difference)	99.997	99.998

The present investigation was started in 1952 using 99.997 percent pure tin from Johnson, Matthey & Company, Ltd. The analysis supplied by the manufacturer is given in Table I under the heading Lot I. In 1953 a second supply of tin, Lot II, was obtained from the same supplier but from a new manufacturer's lot. The absence of antimony and arsenic and the reduction in concentration of lead in Lot II as compared to Lot I is noteworthy since these elements are active impurities in gray tin. Thus, although the total impurity content of the two lots is about the same, the second is more pure in the sense that it contains less of the known active impurities.

IV. RESULTS

A. Conductivity of Pure Gray Tin

Figure 1 shows a typical curve of the temperature dependence of the conductivity of filaments prepared from tin of Lot I.[9] Measurements on five samples yielded the values 2250 ohm^{-1} cm^{-1} for the conductivity at 0°C and 0.088 ev for the activation energy determined in the usual manner. In Fig. 2, which shows the conductivity of a sample prepared from tin of Lot II, the effect of higher purity is quite apparent. In addition to a marked reduction of the conductivity at low temperatures and disappearance of the minimum there is a change in slope of the "intrinsic" line and in the high temperature conductivity. Tin of this lot yielded the values 0.082 ev for the activation energy and 2090 ohm^{-1} cm^{-1} for the conductivity at 0°C. The dependence of the conductivity at all temperatures upon purity suggested further work along two different lines: further purification and doping with various known amounts of different impurities. Attempts thus far at purification by recrystallization and zone refining have not produced a significant change in the shape of the conductivity curve. Work along this line is continuing, however.[10] The effects of alloying are described in the next section.

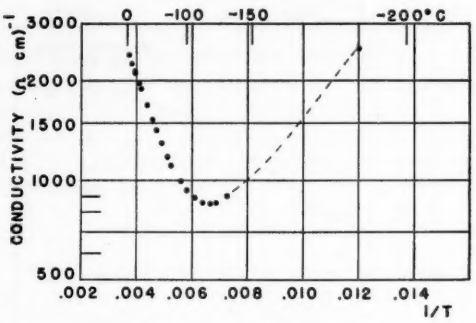

FIG. 1. Conductivity of pure gray tin prepared from Lot I.

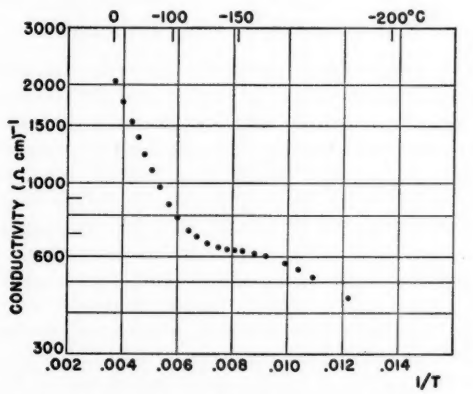

FIG. 2. Conductivity of pure gray tin of Lot II.

[9] These early measurements, made with a cryostat different from that described above, did not include the temperature range immediately above liquid nitrogen temperature.

[10] Tanenbaum, Goss, and Pfann have recently reported the reduction in concentration of certain impurities in metallic tin by an order of magnitude through extensive zone refining. [J. Metals 6, 762 (1954).]

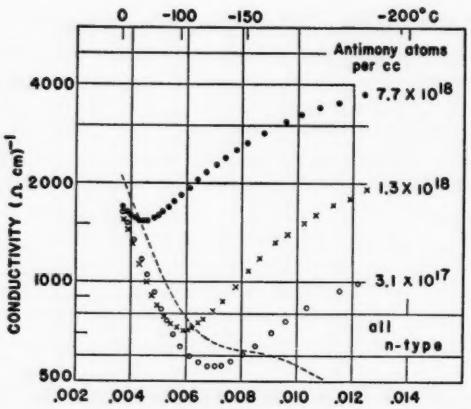

FIG. 3. Conductivity of Sb-Sn alloys. Impurity concentrations were calculated from amount of impurity added to melt. Pure tin curve (broken line) reproduced from Fig. 2 for comparison. Letters p and n designate conductivity types. Arrows indicate approximate temperatures at which conductivity changes type.

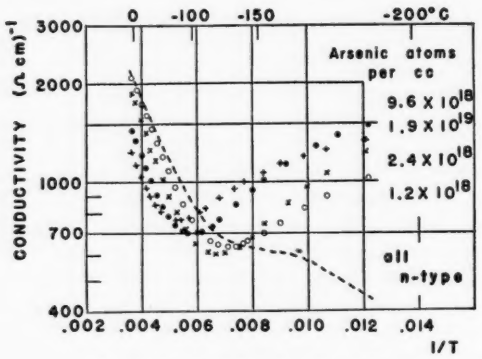

FIG. 4. Conductivity of As-Sn alloys.

B. Conductivity of Gray Tin Alloys

The conductivity curves for gray tin containing various amounts of Sb, As, In, Al, and Zn are shown in Figs. 3 to 7. Impurity concentrations specified in the figures were calculated from the amount of impurity added to the melt taking into account the larger specific volume of the gray phase. All specimens were prepared using tin of Lot II and the corresponding curve (of Fig. 2) is reproduced in each figure for comparison. The conductivity types as determined by thermal emf measurements are designated on the curves by the letters p and n, and the approximate cross-over points from one type to the other are indicated by arrows. It will be noted that Sb and As leave the material n-type whereas In, Al, and Zn in sufficiently high concentrations produce excess hole conduction.

The series of curves shown in these figures all exhibit, in varying degree, two new features. Addition of increasing amounts of any impurity results in (1) an increase in slope in the "intrinsic" temperature range and (2) a decrease in absolute value of the conductivity within this temperature range. Values of the activation energy determined from the slopes wherever possible together with conductivity values at $T=-50°C$ are given in Table II. In the cases of the highest impurity concentrations showing a straight-line behavior, e.g., 1.9×10^{19} As atoms/cc or 2.6×10^{18} In atoms/cc, the activation energies must be considered only lower limit values as it is impossible to ascertain in the limited temperature range available whether these curves have attained their steepest slope. There seems no question, however, that the pure sample slopes have reached a constant value since pure filaments stabilized by the addition of germanium to prevent the gray-to-white transformation at the normal temperature maintained the same slope to the limit of measurement at $+60°C$.[11]

At low temperatures doped samples of n-type show a positive temperature coefficient of resistance whereas the conductivity of p-type samples become temperature independent with increasing impurity content. For samples doped with n-type impurities the conductivity in this temperature range increases with increasing impurity content. For those doped with p-type impurities it decreases with the addition of small amounts of impurity (due to the neutralization by the added acceptors of the donors originally present) and then increases with further increase in impurity concentration. The three p-type impurity elements show striking differences in their effectiveness in producing excess hole conduction. The concentrations required to bring the material to the neutral condition are approximately 1.2×10^{19} atoms/cc of Al, 1.4×10^{18} atoms/cc of Zn and 2.9×10^{17} atoms/cc of In. Thus

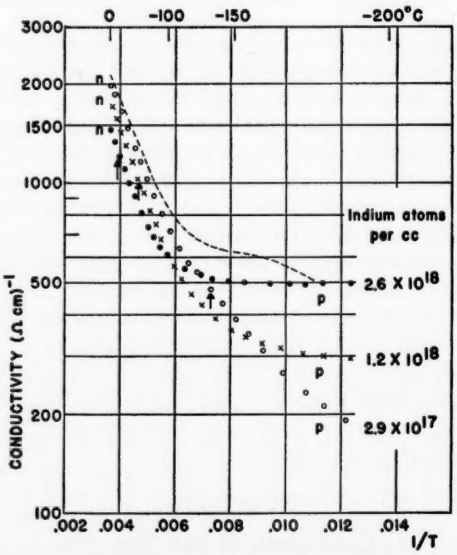

FIG. 5. Conductivity of In-Sn alloys.

[11] A. W. Ewald, J. Appl. Phys. (to be published).

In is 40 times more effective than Al for these concentrations. At higher concentrations this ratio is considerably reduced because of the remarkable increase in conductivity (a factor of 10) of the Al-doped samples as the concentration is increased from 1.2×10^{19} to 1.8×10^{19} atoms/cc.

C. Magnetoresistance

The magnetoresistance coefficient, $B(T)$, was calculated using the relation

$$\Delta\rho/\rho_0=3.8\times10^{-17}B(T)H^2,$$

where H is in gauss and $B(T)$ in cm⁴/(volt sec)². The values obtained for several typical specimens are plotted in Figs. 8, 9, and 10. Pure samples show the largest coefficient throughout the temperature range as is to be expected. Doping with the n-type impurities Sb and As reduces somewhat the magnetoresistance effect at low temperatures. Curves obtained for the three Sb-Sn alloys (two of which are shown) are essentially the same and agree with the values for the lowest concentration of As. Higher concentrations of As reduce the effect still further but not as much as even the lowest concentrations of p-type impurities such as Zn. With high concentration of p-type impurities the magnetoresistance change becomes too small for accurate measurement. For example, the maximum value of $B(T)$ for the sample containing 5.7×10^{18} Zn atoms/cc was 10^6 cm⁴/(volt sec)². Results for the In-Sn alloys were very similar to those of the Zn-doped samples and therefore are not included in the figures. The irregular variation of conductivity with impurity content of Al-Sn alloys was reflected in the magnetoresistance effect. For the lowest concentration (6.6×10^{18} Al atoms/cc) the plot of $B(T)$ was practically identical to that for the pure material, whereas for a concentration of 2.4×10^{19} atoms/cc, $B(T)$ was less than 5×10^5 cm⁴/(volt sec)² throughout the temperature range.

V. DISCUSSION

It is of interest to compare the above values of the conductivity and activation energy for pure material

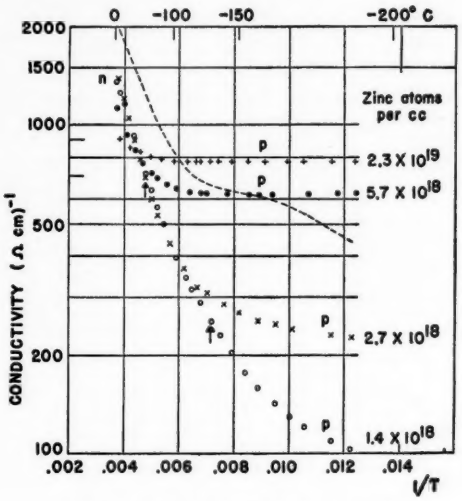

FIG. 7. Conductivity of Zn-Sn alloys.

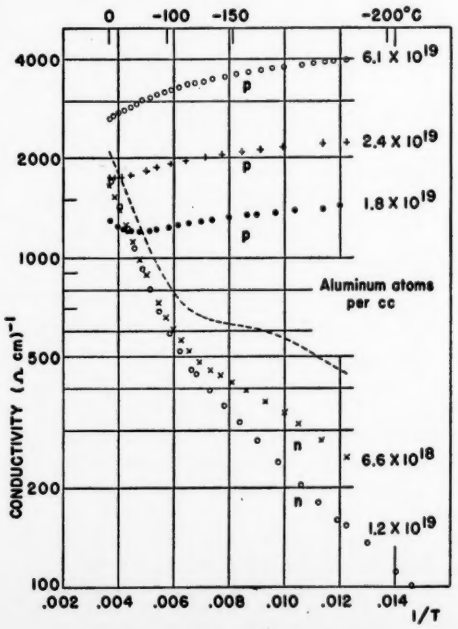

FIG. 6. Conductivity of Al-Sn alloys.

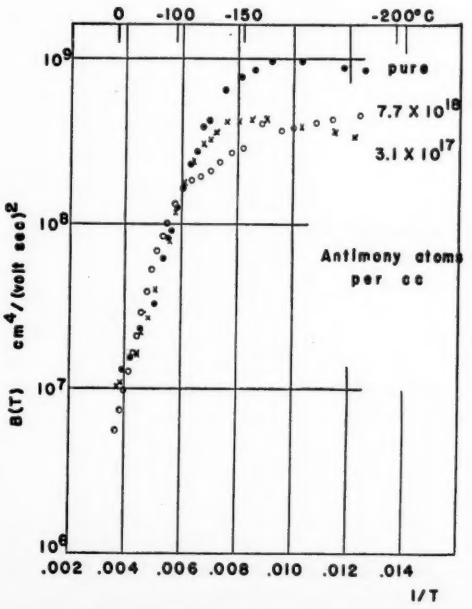

FIG. 8. Magnetoresistance coefficient of pure gray tin of Lot II and of alloys with Sb.

TABLE II. Variation of conductivity and activation energy with impurity content.

Impurity	Impurity atoms added per cc	ΔE(ev)	σ at −50°C (ohm^{-1} cm^{-1})
Pure	...	0.0820	1405
Aluminum	6.6×10^{18}	0.0844	1116
	1.2×10^{19}	0.0936	1124
Zinc	1.4×10^{18}	0.1010	850
	2.7×10^{18}	0.1203	810
Antimony	3.1×10^{17}	0.0862	1102
	1.3×10^{18}	0.0941	1018
Indium	2.9×10^{17}	0.0881	1317
	1.2×10^{18}	0.0944	1125
	2.6×10^{18}	0.1032	899[a]
Arsenic	1.2×10^{18}	0.0912	1349
	2.4×10^{18}	0.0983	1160
	9.6×10^{18}	0.0969	910[a]
	1.9×10^{19}	0.0908	766[a]

[a] Values extrapolated from straight line portion of conductivity curve.

with those found by other investigators. Since our Lot I tin was identical in purity to that used by Kendall,[6] differences in results are probably due to different methods of preparing specimens. Kendall found 0.064 ev for the activation energy which is remarkably low in comparison with all other results, and 4100 ohm^{-1} cm^{-1} for the conductivity at 0°C which is almost twice our value for tin of the same purity. After extensive measurements on gray tin powder obtained from three different lots, Busch and Wieland[4] conclude that the activation energy is (0.08 ±0.008) ev in good agreement with our values, especially with that for tin of Lot II. As mentioned in the introduction these authors conclude that measurements on powder do not yield a reliable value for the absolute magnitude of the conductivity. Through the assumption of a particular model they have calculated the value 2700 ohm^{-1} cm^{-1} for the conductivity at the transition temperature (13.2°C). When reduced to 0°C this value is about 20 percent higher than our value for tin of Lot II.

The variation with impurity content of the temperature dependence and the absolute value of the conductivity in the "intrinsic" range noted in Sec. IVB has not, to the authors' knowledge, been observed previously in gray tin. Kendall[6] has noted slightly different values of σ_0 (in the relation $\sigma=\sigma_0\exp[-\Delta E/2kT]$) for different alloys but the smallest value was found

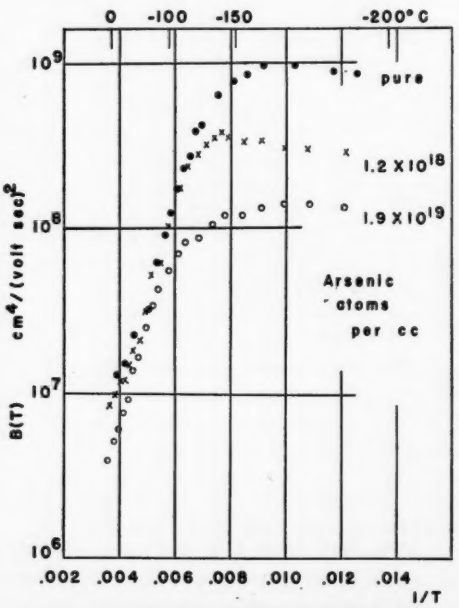

FIG. 9. Magnetoresistance coefficient of As-Sn alloys.

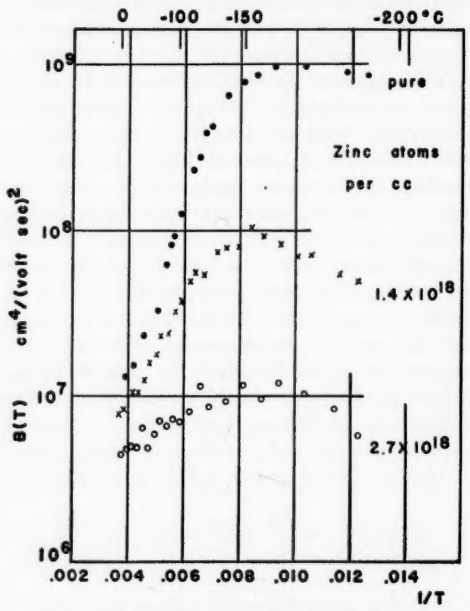

FIG. 10. Magnetoresistance coefficient of Zn-Sn alloys.

for the purest material which is the reverse of the effect noted above. An increase in the optical energy gap of InSb with increasing impurity content has been observed by Tanenbaum and Briggs[12] and attributed by Burstein[13] to the degeneracy of the material at relatively low charge-carrier densities. Whether or not this is also the explanation of the anomalous behavior of gray tin can best be decided after suitable optical measurements have been made. According to the present work the conductivity decreases as the slope increases suggesting that this decrease might be due entirely to the decrease in carrier concentration associated with the increased activation energy. That a decrease in carrier concentration does occur is also indicated by the Hall data of Busch and Wieland[4] and of Kendall[6] which, at high temperatures, show an increasing Hall coefficient with increasing impurity

[12] M. Tanenbaum and H. B. Briggs, Phys. Rev. 91, 1561 (1953).
[13] E. Burstein, Phys. Rev. 93, 632 (1954).

content. To investigate quantitatively the relationship between increased activation energy and decreased conductivity two quantities were calculated for various impurity concentrations and are compared in Fig. 11: (1) δE_c, the increase in activation energy required to account for the decrease in conductivity (at $-50°C$) observed between the pure sample and the doped sample in question and (2) δE_s, the observed increase in activation energy determined from the slopes of the corresponding conductivity curves. The displacement of some points from the 45-degree line is considerably larger than the experimental uncertainty, indicating that the added impurities influence the charge-carrier mobility as well as the activation energy. It should be mentioned that the measurements on germanium-stabilized gray tin referred to above gave the same slope as for pure material but a conductivity only 72 percent as large. The addition of an inactive impurity such as Ge apparently influences only the mobility.

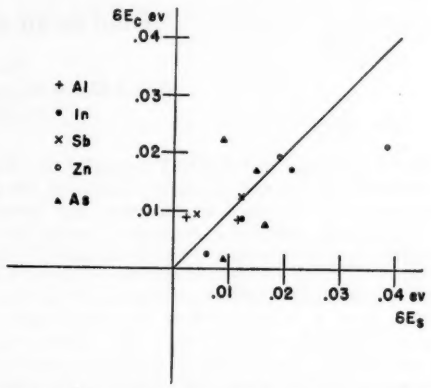

FIG. 11. Relationship of decrease in conductivity upon addition of impurities to the corresponding increase in activation energy observed. δE_c is the calculated increase in activation energy required to account for the observed decrease in conductivity at $-50°C$. δE_s is the increase in activation energy determined from slopes of the conductivity curves. Individual points correspond to different amounts of the added impurities shown in the legend.

There is considerable evidence that the pronounced minima displayed in Figs. 3 and 4 are characteristic of doped n-type material. In addition to the present data on Sb and As alloys, Busch and Wieland[4] have found this behavior in a Bi-doped specimen. This hypothesis would account for the minimum of Fig. 1 as well as that found by Busch, Wieland, and Zoller[2] in earlier work. In both cases the material contained 0.001 weight percent Sb in addition to smaller amounts of As and Bi. Since Sb is a very active impurity the minima in these cases are probably due primarily to it. If so, one would expect that the activation energy determined using tin of Lot I should compare favorably with that for the bottom curve of Fig. 3 and this is seen to be true. There is, however, a difference in conductivity which remains unexplained.

The temperature dependence of the magnetoresistance coefficient has been of considerable interest. According to usual theory based upon a number of simplifying assumptions,[14] the transverse magnetoresistance coefficient $B(T)$, defined in Sec. IVC, should be equal to the square of the charge-carrier mobility where carriers of only one sign are present. In the more complex situation involving the presence of carriers of both signs which we must consider in the high-temperature region of measurement for our samples, $[B(T)]^{\frac{1}{2}}$ should give the temperature dependence of the mobilities although more information is required to obtain absolute values.

For relatively pure material in this high-temperature range Busch and Wieland[4] have found a dependence of the form

$$[B(T)]^{\frac{1}{2}}=AT^{-x},$$

with values of x between 3 and 3.5. This has led them to conclude that in particular the simplifying assumption of spherical energy surfaces in momentum space made in the theory is not justified since a $T^{-1.5}$ dependence is predicted for the mobility due to the scattering of the charge carriers by lattice vibrations. Our curves for pure tin as well as for alloys with Sb and As confirm their results and thus also their conclusion. However, comparison of absolute values for pure material shows that those of Fig. 8 are higher (by almost an order of magnitude) than those given by the above authors.

The rapid decrease of the magnetoresistance coefficient with increasing impurity content shown in Fig. 10 and the similar behavior of In-Sn and Al-Sn alloys was previously observed in Al-Sn alloys[2] and now appears to be characteristic of p-type gray tin. The reasons for the distinctly different behavior of p-type and n-type material are not entirely clear but the indications are that the addition of p-type impurity causes a greater tendency toward degeneracy and an increased importance of impurity scattering.

More quantitative analysis and interpretation of the conductivity and magnetoresistance data await the completion of Hall measurements now in progress. A method of mounting filaments to allow Hall coefficient determination has recently been devised, but only preliminary measurements have been completed.

The assistance of Mr. J. B. Singletary with the early conductivity measurements is gratefully acknowledged.

[14] An up-to-date summary of the standard theory and assumptions involved is given by C. Goldberg, Westinghouse Research Reports R-94416-3-0, 1953; and R-94416-3-P, 1953 (unpublished).

Gold as an Acceptor in Germanium

W. C. DUNLAP, JR.*
General Electric Research Laboratory, Schenectady, New York
(Received October 28, 1954)

Results are presented and discussed concerning the effects of gold in germanium, measured by means of Hall effect, resistivity, photoconductivity, diffusion, heat treatment, and other techniques. It is shown that gold is an acceptor having high-lying states unlike those of the ordinary impurity elements. Evidence is presented to show that each gold atom produces two such levels, one at 0.15 ev above the valence band, the other 0.2 ev below the conduction band. It is assumed that these are brought about through the formation of Au^- and Au^{--}. The implications of this model are discussed. Depending upon the relative proportions of gold atoms and other donors and acceptors, the gold-doped samples may be either high- or low-resistance, *p*- or *n*-type at 77°K. The resistivity may be as high as 10^8 ohm-cm at this temperature. The segregation coefficient, measured from the electrical properties, was about 1.5×10^{-5}. The solubility of gold in germanium is about 10^{16} atoms/cm³. Photoconductivity studies confirm several features of the model proposed. In particular, gold-doped germanium has been shown to be an infrared photoconductor with response out to about 8 micron. A number of interesting trapping phenomena have been observed with gold-doped germanium. The diffusion coefficient of gold into germanium was measured. It is about 4×10^{-9} cm²/sec at 900°C, with activation energy of about 2.5 ev, the same as found for other elements. Gold-doped germanium has been studied as a function of heat-treatment (copper diffusion). Several anomalous results are discussed. Gold-doped germanium has also been studied at low temperatures, for the purpose of detecting scattering by doubly charged impurity ions. The results were inconclusive in deciding whether or not doubly charged Au^{--} ions were present. Also results on the scattering of neutral gold atoms were obtained. The Fermi statistics for gold-doped germanium are considered, and theoretical curves have been obtained for the temperature variation of the Fermi level, and of the Hall coefficient, under various conditions of gold-doping. Agreement of experimental and theoretical results was found to be fair. A discussion is also given of the applications of gold-doped germanium to research on other problems.

INTRODUCTION

IT has been known for a number of years that germanium is sensitive in its electrical properties to small traces of impurities.[1] The third column elements, boron, aluminum, and gallium, produce *p*-type (hole-conducting) germanium; whereas phosphorus, arsenic, and antimony produce *n*-type (electron-conducting) germanium. All these elements produce centers in the germanium that require about 0.01 ev for ionization of the carrier at 0°K. The impurity action of these elements is fairly well accounted for by the Bethe "hydrogen-like" model of the impurity center. According to this theory, the ionization energy is just the ionization energy of hydrogen, 13.6 ev, divided by the square of the dielectric constant, which in germanium is 16. In addition, the ionization must be lowered by the ratio of the effective mass of the carrier to the mass of the electron.[1] Since the effective mass from other measurements is of the order $0.2m$, the theoretical result, 0.01–0.02 ev, is in reasonable agreement with the experimental value, in the neighborhood of 0.008–0.01 ev.

Zinc, copper, and platinum[2] also produce acceptor centers in germanium, with energy at about 0.04 ev. These are indicated, along with the energy for the ordinary impurities in Fig. 1.[3] The ionization energy of the zinc-type impurities has not been adequately accounted for, although a "helium-like" model may be partially the answer. In this model, because of the difference of 2 in the valence of the impurity and of germanium, the carriers are assumed to move in the field of a double charge; thus they should be more tightly bound.

The present paper deals with gold,[4] which, as seen in Fig. 1 appears to produce acceptor states high up in the forbidden energy region.† The procedure in the present paper has been to add gold to a germanium melt during the growth of a single crystal, and to study properties of wafers cut from such ingots. The properties have been studied mostly with Hall effect and resistivity measurements.

Following a discussion of the techniques of experimental measurement, the results of Hall and resistivity data are presented. Next some of the time-dependent trapping phenomena that have been discovered are discussed. A theoretical analysis of the electrical properties is given, and a general discussion of the proposed model of the gold center in germanium is given. Application of gold-doping to a number of important research problems is given.

* Present address: Electronics Laboratory, General Electric Co., Syracuse, New York.

[1] See for example, W. Shockley, *Electrons and Holes in Semiconductors* (D. Van Nostrand Company, Inc., New York, 1950).

[2] W. C. Dunlap, Jr., Phys. Rev. **96**, 40 (1954).

[3] Results on iron, nickel, and cobalt were obtained by Tyler, Woodbury, and Newman, Phys. Rev. **94**, 1419 (1954). Copper and nickel were investigated by Burton, Hull, Morin, and Severiens, J. Phys. Chem. **57**, 853 (1954); and copper by J. F. Battey and R. M. Baum, Phys. Rev. **94**, 1393 (1954).

[4] It has been pointed out by W. Kaiser and H. Y. Fan, Phys. Rev. **93**, 977 (1954), that germanium ingots containing gold have been made and studied at Purdue University. Previous publications by the author are Phys. Rev. **90**, 208 (1953); and Phys. Rev. **91**, 1282 (1953).

† *Note added in proof.*—Recently, evidence has been obtained that gold also produces a donor level about 0.05 ev above the valence bond. This evidence and its effect upon observed properties are to be discussed in a forthcoming paper. The validity of the data and interpretations of the present paper are not affected by this discovery, except in the case of "strongly *p*-type" gold-doped specimens.

EXPERIMENTAL

Crystal Growing

The crystals described in the present report were made in a Czochralski furnace of rather conventional design. The melt was contained in a quartz crucible surrounded by a graphite liner, all inside a long quartz envelope. The graphite liner served to equalize inhomogeneities in the thermal flow pattern about the axis of growth. The crystal was withdrawn from the melt by a seed held in a molybdenum chuck, suspended from a drawing head that raised the seed and rotated independently of the raising motion. The heater was a nichrome winding surrounding the envelope, controlled by "Variac" and "Sola" transformers.

Doping was done during the growth of the crystal by adding the impurity, either as the metal, or as an alloy with germanium. The ingot was usually lifted from the melt during doping to allow complete mixing of the impurity.

Most of the crystals studied were grown with the (111) axis along the direction of crystal growth. X-ray examination of a few crystals was made. They were found to be good single crystals, with little evidence of local distortion and inhomogeneity, provided the gold content was well below the solubility limit ($\sim 10^{15}$ atoms/cm^3).

Approximately seventy-five single crystals of gold-doped germanium have been produced. Included were a wide range of relative proportions of the ordinary and gold impurity centers. In many of these crystals, the crystal was doped, either with gold, or gold plus some impurity such as arsenic, five to eight times during growth.

Purity of the Additions

The question of the purity of the additions is a crucial one in such a study as the present one. In addition, the purity of the germanium used as starting material, and the contamination arising in the furnace during growth are important.

Germanium for these studies was generally purified to the intrinsic range by several pre-melts, each of which leads to purification through the normal segregation process. The ultimate resistivity, or rather the ultimate impurity density, is determined by the rate at which impurities enter the melt during the growth process from the furnace. In a few cases, the material had only 5×10^{12} impurities/cm^3, although it cannot be said definitely that this was not the result of compensation.

The gold used came from three sources, and all three varieties of gold led to equivalent results, as far as could be determined. They were (a) cp gold wire from Baker; no chemical analysis was available on this material, (b) gold wire from Handy and Harmon, stated to be 99.96 percent pure; (c) gold ingot procured from Sigmund Cohn, and assayed spectroscopically in the General Electric Research Laboratory. The purity was found to be 99.99 percent or better.

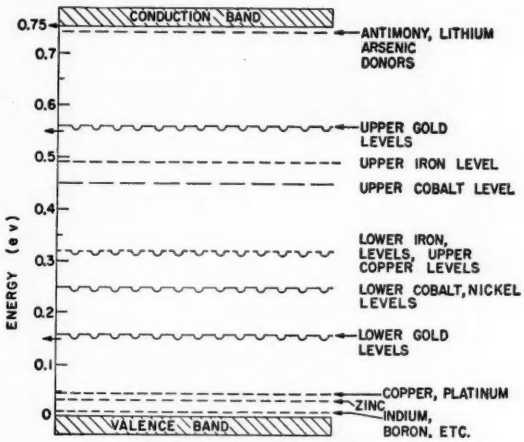

FIG. 1. Energy level diagram for gold and other impurity atoms in germanium.

It was not found to be easy to produce gold-doped germanium to desired specifications in any given run. This would mean specifying both the gold content and the donor (or acceptor) content to perhaps a few percent. The normal segregation process and the possibility of contamination of the furnace both complicate the problem of getting the various types of impurity in their desired proportions. This is found to be especially true for producing high-resistivity n-type germanium, for in this case the donor density must be between n_{Au} and $2n_{Au}$, where n_{Au} is the gold density in atoms/cm^3. If more donors than this are present, the material stays low resistance at 77°K, and if less than this amount is present, the material is p-type.

Measurements

Most of the data of the present paper were obtained from Hall and resistivity measurements on rectangular plates cut from ingots prepared in the above manner. Mobility was determined from the ratio (R/ρ), in cm^2/volt sec.

The measuring equipment consisted of a low-impedance Rubicon potentiometer, and suitable current supplies, standard resistances, etc. It was found that satisfactory measurements could be made at impedance levels as high as 1–2 megohm in many cases. For higher impedance measurements, a Leeds and Northrup Electronic Amplifier, Model 7673, was used as an impedance transformer. Pickup of stray signals became a severe problem at impedance levels above 20 megohm, and relatively little work was done at higher impedances.

Temperatures ranged from 77°K to 400°K for most of the measurements, although some measurements of scattering were made at temperatures as low as 15°K in a cryostat described in another paper.[2] Most of the measurements were made by cementing the sample to a

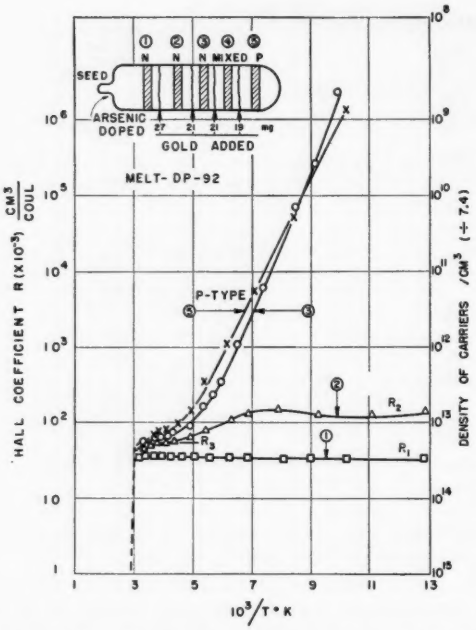

FIG. 2. Hall coefficient and carrier density of *n*-type gold-doped samples made by adding gold in steps to germanium already slightly doped with arsenic.

stainless steel holder mounted in a heavy copper block, in turn mounted in a large Dewar flask. A thermocouple was mounted near the sample. Thermal leakage through the lead wires was minimized since they passed through fine slots in the copper housing. With this equipment temperatures could be kept constant to ±0.1°C during the course of a measurement.

Indium-soldered contacts were used for all samples. For *n*-type samples, the indium was alloyed with small amounts of arsenic to prevent formation of rectifying contacts.

Since some of the samples were extremely photosensitive, precautions had to be taken to keep them in the dark for all measurements.

HALL EFFECT AND CONDUCTIVITY STUDIES OF GOLD-DOPED GERMANIUM

Addition of Gold to *n*-Type Germanium

Figure 2 shows the Hall coefficient and density of carriers of several plates of germanium cut from ingot DP-92. The doping sequence is also shown. To a melt already slightly *n*-type because of the addition of arsenic, gold was added four times, about 25 mg each time. Curve (1) shows the normal variation of the Hall coefficient of a sample of germanium. There is no deionization of these carriers until the temperature is well below 77°K. After addition of 27 mg of pure gold, two effects occur: (1) the room temperature resistivity increases, showing the acceptor effect of the gold, but the sample remains *n*-type; and (2) there is a slope to the Hall curve between 77°K and room temperature. This is a sign of a high-energy donor being present.

With further addition of gold, it is seen that from Curve (3) there are still electrons present, but in still smaller numbers. Here the large activation energy of the "donors" is clear. From the slope of the Hall curve we estimate 0.18 ev for the ionization energy. On further addition of gold, we see that *p*-type germanium is formed, again with a high ionization energy, about 0.15 ev. Sample 4 was not measured because it was mixed *n*- and *p*-type.

Figure 3 shows the resistivities of these samples, and Fig. 4 the mobilities. The room temperature mobilities of gold-doped samples are often low, and so also is the slope of the $\log\mu$ *vs* $\log T$ curve, compared to that for pure undoped samples. However, the mobilities were high enough at the lower temperatures to assure us that few or no barriers were present in the samples.

Addition of Gold to *p*-type Germanium

Figure 5 shows the Hall curves for a series of samples prepared by adding gold to an ingot originally slightly doped with gallium. Now the crystals start out *p*-type, and with each addition of gold the resistivity drops. Here the picture is complicated by the apparent tendency of the furnace to contribute *n*-type contamination, so that the drop in resistivity is not always appropriate to the amount of gold added. Also, the presence of the trace of gallium in the ingot has dis-

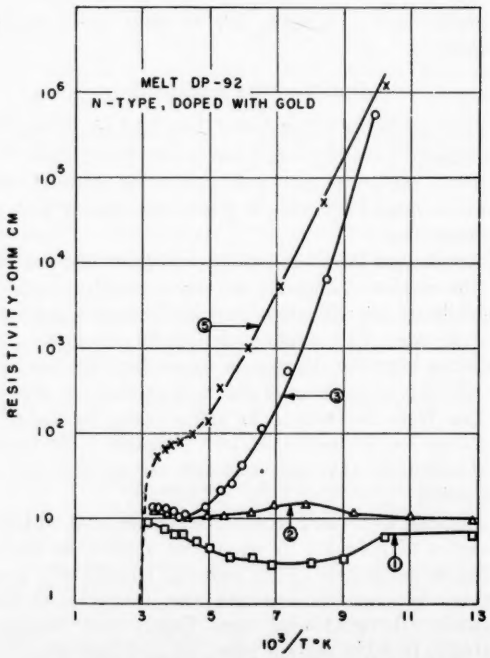

FIG. 3. Resistivities of the samples of Fig. 2.

appeared after the second doping, again presumably because of the effects of contamination by donors. The high-energy gold acceptors now become clearly evident in the high slopes of the Hall and resistivity curves. Figures 6 and 7 show the resistivities and mobilities of these same samples.

Energy Level Scheme for Gold in Germanium

Based upon evidence of the type just discussed, the energy level scheme of Fig. 1 is proposed for gold. The following features of the model are important.

(1) Gold produces two acceptor levels in germanium. However, because the upper acceptor state is so close to the conduction band, the material may act as an *n*-type semiconductor, through excitation of the trapped electrons into the conduction band.

(2) The observed properties are determined by the extent to which the gold states are filled by electrons from donors present. Thus the germanium may be high- or low-resistance, *p*- or *n*-type, depending on the ratio of gold states to the normal impurity states. A further discussion of the theory is given below where the Fermi statistics is discussed.

(3) Because one state is above, the other below the middle of the forbidden band, it is not possible to see ionization from both states in the same Hall or resistivity curve. The ionization of the upper level can only be seen with *n*-type material, and the ionization of the lower state is seen only with *p*-type material.

(4) For reasons to be outlined below, it is suggested that both states are different ionization states of the gold atom, and hence that, when electrons are added to germanium containing neutral gold, the gold first becomes Au^- and then Au^{--}. A corollary of this statement is that the two states cannot properly be listed on the same diagram, in the sense that the upper state when filled destroys the lower state.

(5) Although the values 0.15 ev and 0.20 ev have been quoted, actually there is some variation in ionization energy as determined from the slopes of the Hall curves. This may partly be due to the effect of compensating donors, and partly to short-circuiting influences such as surface conductivity, dislocation conductivity, etc. Also, the degree of occupation of the levels affects the slope, as discussed below under "Fermi statistics."

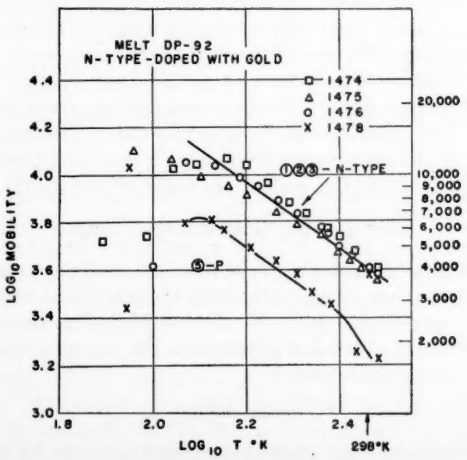

FIG. 4. Mobilities (R/ρ) of the samples of Fig. 2.

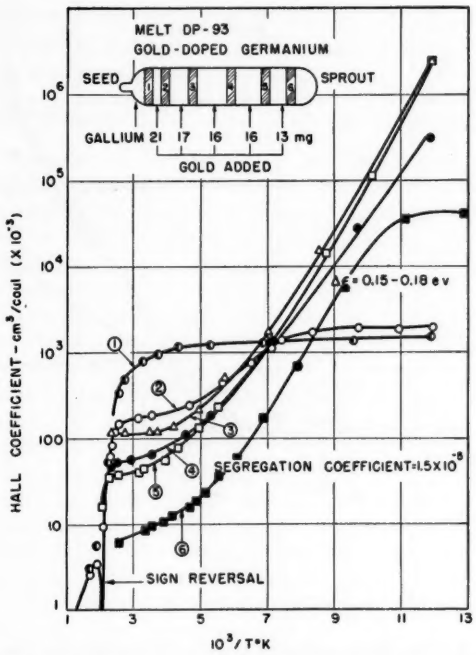

FIG. 5. Hall coefficient *vs* $1/T$ for a series of samples prepared by adding gold to a melt already doped with gallium.

Relative Density of Upper and Lower States

The nature of the model depends on whether we can answer the question as to the equality of the number of upper and lower states introduced. One method for doing this is the following: When gold is added to the crystal, the increase in resistivity after adding gold should tell us the total number of electrons removed from the crystal by the gold atoms. The excitation curve such as that of (1) in Fig. 2 should tell us the number of electrons in upper gold states, which should be half the total. Calculations on this basis show, for DP-92, that this prediction is borne out, to better than 25 percent.

Referring to Fig. 2, we take the Hall coefficients R_1, R_2, and R_3.

(1) R_1 should give the total number of electrons available from arsenic donors.

(2) R_2 gives the number of arsenic electrons remaining, at 77°K.

(3) R_3 gives the number of electrons excited from the upper gold states.

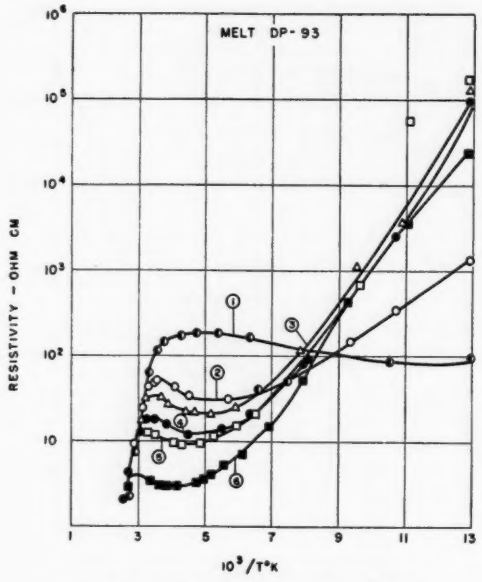

FIG. 6. Resistivities of the samples of Fig. 5.

If N^L is the number of lower gold levels, N^U that of the upper, and if $n_1=7.4\times10^{18}/R_1$, namely the number of carriers at R_1, then

$$N^U=n_3-n_2,$$
$$N^L+N^U=n_1-n_2.$$

Using the appropriate values of the Hall coefficients, we find

$$n_1=20\times10^{13}/\text{cm}^3,$$
$$n_2=6.1\times10^{13},$$
$$n_3=14.8\times10^{13},$$

whence $N^U=8.7\times10^{13}/\text{cm}^3$ and $N^L=6\times10^{13}/\text{cm}^3$, and we conclude that these two numbers are equal to within the experimental error.

This result also depends upon the following assumptions: (a) the samples (1) and (2) were sufficiently close together that normal segregation did not significantly change the arsenic concentration; this assumption is a good one, since the wafers were only a few mm apart and far from the sprout end of the crystal. Also, (b) no additional donors were added along with the gold. This assumption is more difficult to justify.

Other experiments have been done tending to verify the above conclusion. However, the agreement has not always been as good as in this case, and the numbers N^U and N^L have varied as much as a factor 2.

Segregation Coefficient and Solubility

Studies of segregation of gold have been made using radioactive gold 198. However, errors are introduced in this method because of precipitation of tiny droplets of gold, and it is thought that changes in electrical properties are the most reliable method of estimating segregation coefficient.

The segregation coefficient is determined by the ratio of gold concentration in the solid to that in the liquid at equilibrium. From melt DP-92, it was found that 8.2×10^{18} atoms of gold were added to each cm³ of melt. The density of gold atoms in the solid was $8\times10^{13}/\text{cm}^3$, assuming that each gold atom furnished *two* acceptors. The result, 1.5×10^{-5}, was identical with that obtained from the change in carrier density in p-type germanium, assuming *one* acceptor per gold atom in that case. While the degree of agreement is almost certainly fortuitous, it does appear to lend additional weight to the hypothesis that each gold atom furnishes two acceptor states in germanium.

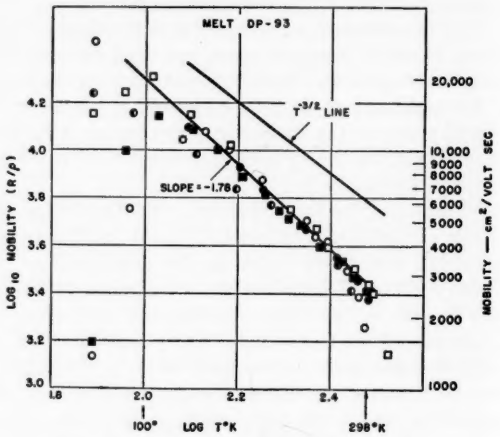

FIG. 7. Mobilities of the samples of Fig. 5.

The lowest resistivity observed in any of the p-type ingots was about 1 ohm-cm. It is concluded that the solubility of gold in germanium is about 10^{15} atoms/cm³ at the melting point. Metallographic examination has been made of some of the gold-doped ingots. It is found that close to the point where the gold content is approaching 10^{15}, the single-crystal character tends to deteriorate—first indications of "lineage," in the form of numerous fine lines in the etched surface appear, and, in a fairly narrow belt, the crystal becomes polycrystalline. Close examination shows a large number of pockets containing metallic gold in this region of the crystal.

Model of the Gold Acceptor States

Figure 8 shows the model assumed to apply to gold in germanium. Gold, on the basis of the previous results, and the diffusion data to be discussed below, is assumed to be substitutional in germanium. The electronic structure of the gold atom is

$$5s^25p^65d^{10}6s^1.$$

Thus, gold is a transition element with the $5f$ shell completely empty in the free atom, and with one

valence electron in the 6*s* shell. In its chemical compounds, gold may have a valence of either 1 or 3.

The properties of gold in germanium are best accounted for if gold is assumed to have a valence of two. This would require promotion of one of the 5*d* electrons to form a $6s^2$ structure.

There is at present no reliable evidence regarding the electronic state of gold in germanium. Such information might be obtained by (1) paramagnetic resonance experiments, (2) magnetic susceptibility measurements, (3) measurement of ionic mobility of the gold ion (although measurement at high temperature may be misleading if the electronic state changes with temperature).

Pending determination of this information, it is assumed that gold takes up two electrons, and becomes Au^{--}. It should be remembered that the lower acceptor level is defined by placing an electron upon a neutral gold atom, the upper level by placing an electron upon a singly charged (Au^-) ion. It is further assumed that in this state it has acquired four electrons, and matches the germanium bond structure, as do the 3–5 column impurities. However, it is possible that gold goes in with only the one 6*s* electron, takes up two electrons, and has three electron pair bonds with the germanium.

Figure 8 shows a possible atomic arrangement in the gold center as compared to the similar center containing indium. The first electron is seen being bound to the gold from a germanium lattice atom, whereas the second is made only by trapping electrons from other impurities, since too much energy is required to break a second germanium bond.

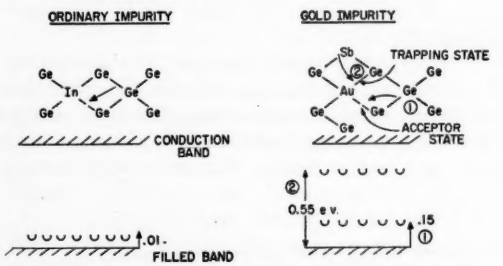

FIG. 8. Model of the gold impurity center in germanium.

Figure 9 shows a possible curve for the potential energy *vs* distance for an electron approaching (a) the neutral gold atom, and (b) the singly charged Au^- ion. The forces of attraction are relatively weak in (a) until the electron is within an atomic spacing or so, at which distances the exchange forces become quite strong. In (b) we see the repulsion at long range arising from the Coulomb forces, and the strong attractive effect if the electron is able, in spite of the Coulomb repulsion, to come within an atomic distance of the ion. The height of the Coulomb barrier was calculated to be of the order 0.1 ev, with a reasonable form for the exchange energy function. However, the nature of the electronic structure about the gold center is sufficiently uncertain that the Fig. 9 should not be considered to have more than semiquantitative validity.

PHOTOCONDUCTIVITY AND TRAPPING PHENOMENA

Soon after the preparation of both the *p*-type and the *n*-type gold-doped germanium, a number of unusual time-dependent effects were discovered, apparently related to the deep-lying levels previously discussed in this paper.

Most prominent of these involve photoconductivity. Gold-doped germanium samples are good photoconductors: (a) the high resistivity at 78°K makes it easy to detect small photocurrents, and (b) because of the relatively small ionization energy, photoconductivity is observed at wavelengths much longer than those of fundamental photoconductivity: out to 8–10 micron.

The photoconductivity of a number of the specimens used in the conductivity studies has been measured by Newman.[5] These studies are of interest particularly because they give a means of checking the location of the energy levels as determined from the Hall and conductivity data. Newman studied both *p*- and *n*-type samples of high-resistivity, and his values for the threshold energy for photoconduction agreed almost identically with those obtained here, namely, 0.15 ev for *p*-type, 0.20 ev for *n*-type samples.

Besides the threshold conductivity effect, Newman noticed a "quench" effect in gold-doped samples. In this effect, the application of infrared radiation in certain narrow bands of wavelength, particularly at 0.66 ev (~2 micron), led to a *decrease* of current flowing through the sample rather than an increase. Since the dark current consists of electrons, it may be presumed that there were trapped holes which permitted passage of these electrons. If the quenching radiation were to excite electrons into the hole traps, the latter would be destroyed, and the dark current would be correspondingly reduced.

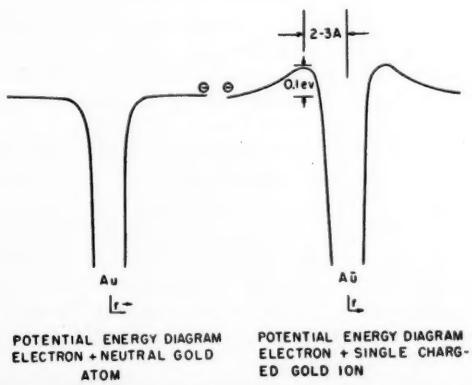

FIG. 9. Potential energy diagrams for electrons in the Au^- and Au^{--} centers in gold-doped germanium.

[5] R. Newman, Phys. Rev. 94, 278 (1954).

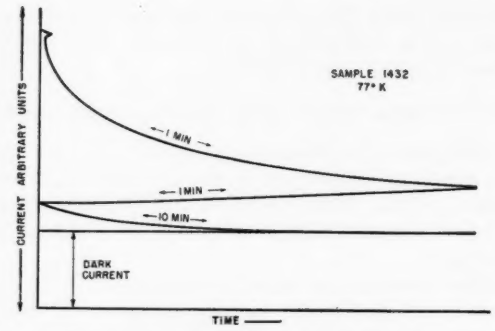

FIG. 10. Time dependence of photoconductivity of gold-doped specimens of germanium.

The existence of the narrow wavelength band is, up to this point, a mystery. It points, in all likelihood, to an internal transition in the gold center as an essential part of the quench process.

The quench effect is found only in *n*-type samples, but it has been found in both high-resistivity and low-resistivity samples. There seems to be a dependence upon gold concentration.

Time Delay of Photoconductivity

Along with the large photoconductivity there is a large time delay that often appears when the sample is illuminated by white and infrared light while at 78°K. Such a recovery curve is shown in Fig. 10. The time constant for the recovery is of the order of 1 minute. As in the quench effect, these slow recoveries were seen only with *n*-type gold-doped germanium.

Pulsing Effects

A number of interesting effects were found when the voltage applied to a sample of *n*-type high-resistivity gold-doped germanium was changed to a new value or reversed. A typical result is that of Fig. 11, which is a copy of a chart made with an *x-y* recorder, plotting the current through the sample at constant applied measuring voltage as a function of time. Just prior to the measurement, the sample had been pulsed with a 100-volt pulse of the sign opposite to that of the measuring voltage, and about 2 sec in duration.

Study of this pulsing effect has indicated that there exist in gold-doped samples regions of space-charge, and that under certain conditions the sample will exhibit polarization voltages of appreciable magnitude, capable, for example, of driving current in the reverse direction through batteries of voltage as high as 1 volt.

Similar effects were observed whenever current was changed—again these effects were found only for *n*-type, high-resistivity samples.

The effect has been found to vary considerably from sample to sample—in some samples, the current after pulsing will start out in the same direction as the pulsing current, then rapidly reverse to the sign of the measuring voltage. In others, it remains of the sign of the measuring voltage throughout. In addition, the effect depends to a considerable extent upon the contacts, and replacement of the contact by a similar but not identical one will usually change the shape, although not the nature of the response. This dependence upon contact has led to the assumption that the effects observed may be the result of current injection of minority carriers into the gold samples, and the effects of the trapping states upon these carriers.

Further work needs to be done on the nature of the polarization effects in gold-doped germanium.

Effect on Recombination Lifetime

A relatively small amount of work has been done on the effect of gold-doping on the lifetime of germanium specimens. Tests have generally been made using the decay of the reverse characteristic of a fused-contact rectifier made on the surface of the specimen. With gold content of the order 10^{14} atoms/cm^3, lifetimes of the order 1 microsecond were generally observed.[6] No quantative estimates of cross sections have been made.

HEAT TREATMENT STUDIES

In the previously described studies on gold-doped germanium, evidence for two sets of levels has been obtained on different samples containing relatively different proportions of gold and ordinary impurities such as arsenic or gallium. Similar evidence can be obtained on a single specimen by heat treatment, that is, by maintaining a uniform gold content and by varying the content of an acceptor such as copper, which diffuses rapidly, and which can be easily spread through the crystal.

A typical study was carried out with Sample 1531. It was first soaked for a few minutes in copper nitrate solution, in order to coat it with a thin layer of copper. Then the sample was heated to 800°C in argon for two hours and cooled rapidly to room temperature. The

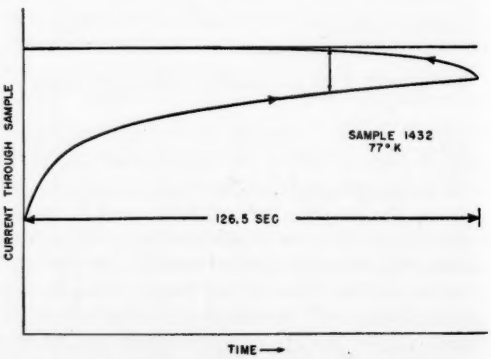

FIG. 11. Pulsing effect in gold-doped germanium. The trace shown was obtained by applying a 100-volt pulse for ~2 sec in the opposite direction to that of the small measuring voltage.

[6] E. M. Pell (private communication, to be published).

sample was thus converted from high-resistance *n*-type to low-resistance *p*-type. The temperature curve of the Hall effect and resistivity was taken at various times of annealing at 450°C, until the sample had been restored almost identically to its original condition.

Results of the Hall curves are shown in Fig. 12. The most surprising thing about the results is that after the quench there is no evidence for the 0.15 ev lower gold states, which should show up as a slope of the Hall curve between 200° and 300°K. This behavior has been checked with similar samples, and the same results have been found in almost all cases. It is possible that there is an interaction between the gold and copper centers, which changes the electronic structure of the impurity centers. This would be plausible if the copper tended to diffuse preferentially to locations near the gold atoms, and it is also possible that both the gold and copper atoms occur preferentially near imperfections in the lattice.

On annealing, the slope of the Hall curve increases, until the value is of the order 0.13 ev, comparable to that obtained with the doped crystals.

On further annealing, the properties return to the original ones; namely, *n*-type germanium, with the high ionization energy, 0.20 ev, characteristic of *n*-type gold-doped material.

Repetitions of this series of tests have been carried out on six or seven samples, not always with uniform results. In several cases the *p*-type states have been visible in the Hall curve after quenching, while in others there has been only the same flat portion seen in Fig. 12.

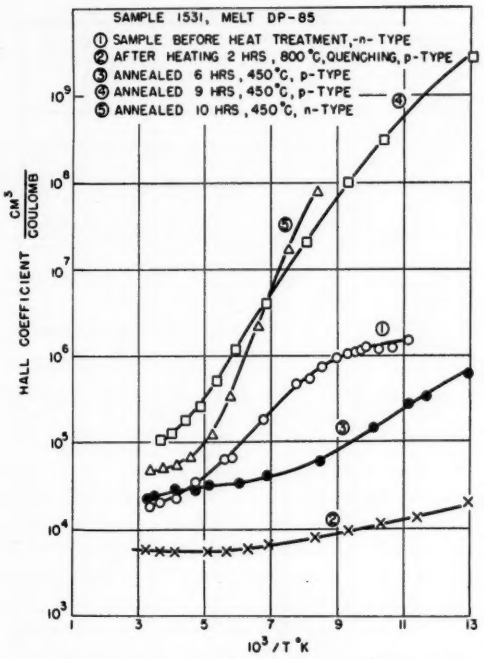
SAMPLE 1531, MELT DP-85
① SAMPLE BEFORE HEAT TREATMENT,-n- TYPE
② AFTER HEATING 2 HRS, 800 °C, QUENCHING, p-TYPE
③ ANNEALED 6 HRS, 450°C, p-TYPE
④ ANNEALED 9 HRS, 450°C, p-TYPE
⑤ ANNEALED 10 HRS, 450°C, n-TYPE
HALL COEFFICIENT CM³/COULOMB
10³/T °K

FIG. 12. Hall curves on gold-doped specimens quenched from 800°C and annealed various times at 400°C.

DIFFUSION OF GOLD IN GERMANIUM

Study of diffusion has been found to be quite helpful in the evaluation of new materials as doping agents in germanium and silicon. In particular, the order of magnitude of the diffusion is useful in determining the nature of the impurity—whether it is interstitial or substitutional in germanium.

Diffusion coefficients have been measured both by the *p-n* junction technique,[7] and the radioactive tracer method.[7] In the *p-n* junction method, the sample is coated with the unknown, and heated. The penetration of the impurity converts the material from one type to the other, and the boundary is determined by a thermoelectric or a rectification probe.

The diffusion coefficient of gold was determined using *n*-type samples of 5–10 ohm-cm resistivity, and coated with gold by immersing the sample for about 5 sec in 1 percent $AuCl_3$ solution. The samples were then sealed in quartz tubes, in an atmosphere containing 15 cm Hg of pure dry argon. Heating was accomplished in accurately controlled ovens.

In order to prevent heat treatment effects from interfering with results, all samples were annealed 4–8 hours at 575°C following the diffusion heating. This guaranteed that the base germanium returned to its level at 5–10 ohm-cm *n*-type.

Because of the limited solubility of gold in germanium (assumed 3×10^{15} for all temperatures), the constant-source solution previously used is no longer valid. Instead the "step-function" solution is used; this leads to higher values of diffusion coefficient than the other method of calculation.

Results on diffusion of gold are shown in Fig. 13. Also shown are previously published results on antimony. It is at first noteworthy that gold diffuses more rapidly than antimony, the most rapidly diffusing of the donor elements. All the ordinary acceptors such as indium and gallium diffuse much more slowly than antimony. On the other hand, gold, though diffusing more rapidly than antimony, is much less rapidly diffusing than copper[8] or lithium.[9]

The activation energy for diffusion of gold is almost identical with that for antimony; namely, 2.5 ev, or 57000 cal./mol. This similarity makes it appear that both these elements diffuse by the same mechanism, and thus that they are both substitutional in germanium. The rapid diffusion of gold is inconsistent with the previous picture that gold acquires two electrons to become Au^{--} in the lattice. It is probable that at

[7] See for example, W. C. Dunlap, Jr., Phys. Rev. **94**, 1531 (1954).

[8] Fuller, Struthers, Ditzenberger, and Wolfstirn, Phys. Rev. **93**, 1182 (1954).

[9] C. S. Fuller and J. A. Ditzenberger, Phys. Rev. **92**, 846 (1953); J. C. Severiens and C. S. Fuller, Phys. Rev. **92**, 1322 (1953).

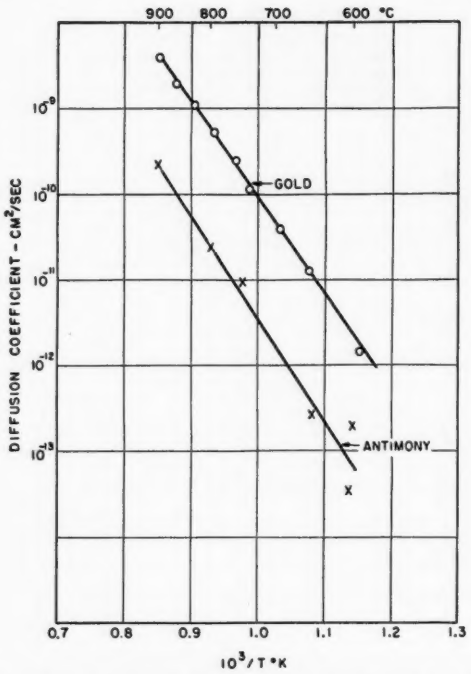

FIG. 13. Diffusion coefficient of gold in germanium, determined by the depth of penetration of the p-n junction. Also shown for comparison is the diffusion curve for antimony.

elevated temperatures both electrons are lost, and that the gold actually diffuses as a neutral atom, or even as a positive ion. This conclusion is similar to that recently arrived at in the case of copper.[10]

IMPURITY SCATTERING IN GOLD-DOPED GERMANIUM

Gold-doped germanium containing various relative proportions of gold and arsenic-type impurities offers the means for obtaining new information on impurity scattering. It also makes possible an independent check on the hypothesis previously made, that gold can acquire two electrons to become Au^{--}. By proper control of the concentration of ordinary donors and acceptors, it should be possible to study the scattering by doubly charged ions, singly charged ions, and by neutral impurities. Data have been taken in the temperature range 15°–300°K for all these cases, but the results have not been conclusive.

The difficulties stem from several sources:

(1) The solubility of gold is limited to about 3×10^{15} atoms/cm³, and this density is not sufficient to make impurity scattering easily observable except at the very lowest temperatures, say below about 50°K.

(2) The experimental accuracy of the method is such that it is difficult to distinguish between the scattering between doubly-charged and singly-charged impurity ions. Although an examination of the theory shows that doubly-charged ions should scatter 4 times as strongly as singly-charged ones, still only half as many would be present, so that the scattering would be only 2 times as great, and this difference is not great enough for easy detection since there are natural differences between samples arising from differences in crystal structure, impurity distributions, etc.

The most suitable procedure for producing doubly-charged ions in samples for scattering measurements is to add gold, and also sufficient arsenic to just fill all the gold levels. This requires, on the basis of the present model, an arsenic concentration that is equal to twice the gold concentration. Thus the added impurity scattering produced by the arsenic must also be taken into account.

Scattering by neutral ions is studied after adding gold to pure germanium containing no other impurities. On going to low temperatures, one should find scattering due only to neutral impurities.

Figure 14 shows mobility data on various samples of germanium, both with and without gold, in the temperature range between 15° and 300°K. Several comparison specimens are included of both n- and p-type. It is found that in general the mobility of gold-doped specimens is considerably lower than that for specimens

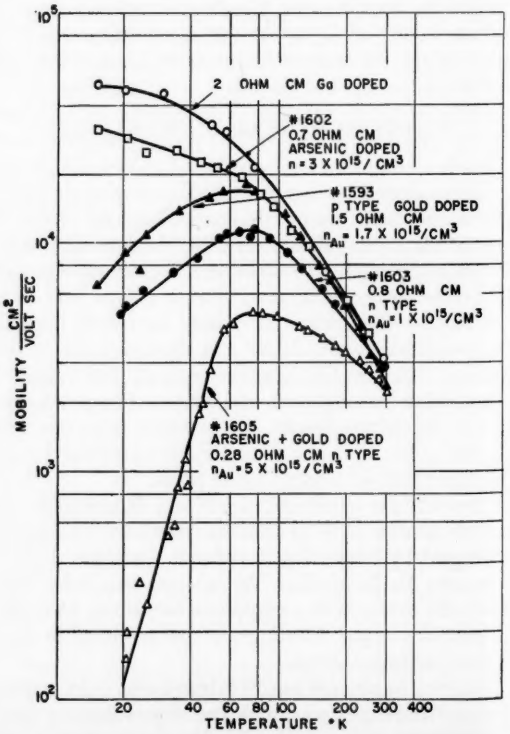

FIG. 14. Mobility of various samples of gold-doped germanium at low temperatures, in the impurity scattering range.

[10] See reference 8, and J. C. Severiens and C. S. Fuller, Phys. Rev. 94, 750 (1954).

containing the equivalent charge density of arsenic or other ions. It is not possible, however, to conclude that evidence is found for the existence of the doubly charged Au^{--} ion. In particular, the possibility that the gold introduces structure defects or space charge barriers with temperature sensitivity similar to that for impurity scattering cannot be overlooked.

FERMI STATISTICS FOR GOLD-DOPED GERMANIUM

General

In this section we discuss the determination of the theoretical Hall curves for gold-doped germanium containing different amounts of both gold and normal-type donors and acceptors. Although both the gold states are acceptors, we adopt here a viewpoint toward these levels that is somewhat broader than usually used.[11,12]

It is possible to set up the statistics of trapping levels on a fairly general basis, based upon the calculation of the partition function. However, in the present discussion, no attempt at a formalism that covers all cases is made. Instead, we shall examine several particular cases, and show how the Fermi level is determined in each case.

A general analysis is complicated by the fact, previously mentioned, that the upper state is the energy level for an electron in the field of the Au^- ion, and when an electron is in this state, the lower state no longer exists. Here again, we can avoid the difficulty by dealing with situations in which we need regard only one of the two levels at a time.

A major simplification is attained in the present analysis because the ionization energy of the gold is large in comparison both to kT and to the ionization energy of the ordinary donors and acceptors. In the first instance, we can use Boltzmann statistics in practically every case of interest. In the second, we can neglect the statistical effect of the ordinary impurity states and regard them as part of the conduction or valence bands. In carrying out the calculations, a partly graphical method has been employed. From the calculated Fermi level as a function of temperature, the Hall coefficient curves have been derived.

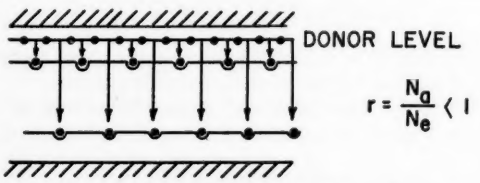

FIG. 15. Energy diagram showing the filling of states in "strongly n-type gold-doped germanium."

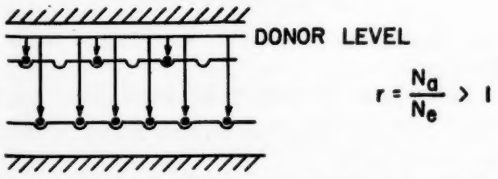

FIG. 16. Energy level diagram for weakly n-type (high resistivity) n-type gold-doped germanium.

[11] See reference 1, Chap. 11.

[12] Several of the results quoted here were taken from a report by J. K. Bragg and M. H. Hebb, General Electric Research Laboratory Report RL-468, December, 1950 (unpublished).

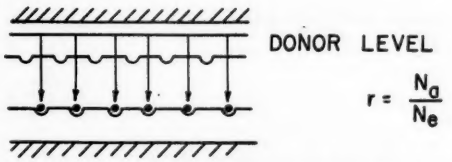

FIG. 17. Energy level diagram for intrinsic gold-doped germanium.

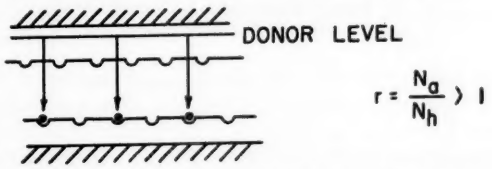

FIG. 18. Energy level diagram for weakly p-type (high-resistivity) gold-doped germanium.

The relative concentration of gold and other impurities is defined here by the "trapping ratio." This quantity, r, is defined as the ratio of the number of acceptor (gold) states to the number of electrons available (in the upper gold states, the donor levels, and the conduction band).

We discuss next five important situations ranging from strongly n-type through intrinsic to strongly p-type.

In Fig. 15 we see the situation at 0°K for a strongly n-type sample, for which $r \sim 0$. Here there are many more donor atoms than gold atoms, all the gold states are filled, and the material is low-resistivity at all temperatures. However, the presence of the upper gold state will still be seen in the ionization of electrons from the upper gold level, at a temperature somewhere between 77° and 300°K. The smaller the trapping ratio, the higher the temperature at which this ionization becomes appreciable, since the greater is the tendency of the conduction electrons to refill the gold state.

In Fig. 16 we see the situation where there are not enough electrons to completely fill all gold states at 77°K, with the result that the material is of n-type, but high-resistivity at 77°K. The trapping ratio is greater than 1. This is the case of rapidly varying resistivity, since all the electrons will be emptied from the upper gold levels at room temperature.

In Fig. 17 we see the intrinsic situation where $r \to \infty$, since there are just as many electrons as lower gold states, and the number of available electrons is ~ 0.

Figure 18 shows the case of weakly (high-resistivity) p-type material, where the number of electrons is only sufficient partly to fill the lower gold states. At 77°K there will be no appreciable number of holes excited to

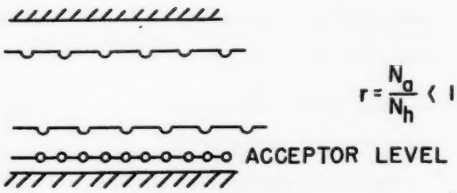

FIG. 19. Energy level diagram for strongly p-type gold-doped germanium.

the gold states from the valence band because of the high ionization energy. The trapping ratio r is defined now by $r=N_a/N_h$, where N_h is the number of available holes (those in the lower gold level, any additional normal acceptor level, and the valence band). In this situation the trapping level is greater than 1.

In Fig. 19 we see the case of strong p-type material.§ Where there are additional acceptor levels of the usual kind, there are carriers present at lower temperatures, and thus the material is of low resistivity. The trapping ratio is less than unity.

In all the above cases, there can be mixtures of ordinary donor and acceptor levels in many proportions. To a first approximation, however, the results are determined only by the number of gold states and by the trapping ratio. This follows from our neglect of the statistical effect of the normal impurity levels, which are much closer to the conduction bands than to the gold level or to the Fermi level, under most conditions.

It is seen that there is a high degree of symmetry between the situations for n- and for p-type material. Ignoring the difference in mass between holes and electrons, and in the ionization energies of the upper and lower states, there is almost complete symmetry.

Examination of all the practical cases shows that in none of them do we have to deal with both levels in the same problem. The upper level is important only for n-type material (Fermi level in the upper half); and the lower for p-type (Fermi level in the lower half).

Normalization Process in Fermi Statistics

The Fermi distribution f has the form

$$f=\frac{1}{1+\exp[(E-\zeta)/kT]}, \tag{1}$$

where E is the energy of any particular energy state, and ζ is the Fermi level. The downward direction is assumed negative, and the zero is taken at the bottom of the conduction band. Similarly the distribution function for holes is f_h:

$$f_h=1-f=1-\frac{1}{1+\exp[(E-\zeta)/kT]}=\frac{1}{1+\exp(\zeta-E/kT)}. \tag{2}$$

If we transform coordinates so that $E'=-E-E_g$, $\xi=-\zeta-E_g$, then

$$f_h=\frac{1}{1+\exp[(E'-\xi)/kT]}, \tag{3}$$

where E_g is the energy gap between the conduction and valence bands, and ξ may be considered the Fermi energy for holes in the new energy coordinate system.

The density of energy states is assumed to be

$$N_e=4\pi(2m/h^2)^{\frac{3}{2}}E^{\frac{1}{2}}, \tag{4}$$

where we take the effective electron mass to be the electron mass. Consequently, the number of electrons in the conduction band is

$$n_c=\int_0^\infty \frac{N_e}{1+\exp[(E-\zeta)/kT]}dE$$
$$=4\pi\left(\frac{2m}{h^2}\right)^{\frac{3}{2}}\int_0^\infty \frac{E^{\frac{1}{2}}dE}{1+\exp[(E-\zeta)/kT]}. \tag{5}$$

Because the upper gold level, and thus also the Fermi level, is in units of kT, far away from the conduction band, the Boltzmann approximation to the Fermi statistics is justified and Eq. (5) becomes

$$n_c=4\pi\left(\frac{2m}{h^2}\right)^{\frac{3}{2}}\int E^{\frac{1}{2}}\exp[-(E-\zeta)/kT]dE$$
$$=2\left(\frac{2\pi mkT}{h^2}\right)^{\frac{3}{2}}e^{\zeta/kT}. \tag{6}$$

Also, if N_a is the number of acceptor states in the upper acceptor level, then the density of electrons in this level is given by

$$n_1=N_a/\{1+\exp[-(\Delta E_1+\zeta)/kT]\}, \tag{7}$$

where ΔE_1 is the energy gap between the upper acceptor level and the bottom of the conduction band.

Similarly, the density of states at the top of the valence band is taken to be:

$$N_v=4\pi(2m/h^2)^{\frac{3}{2}}E'^{\frac{1}{2}}, \tag{8}$$

and the hole concentration is found to be

$$n_v=2(2\pi mkT/h^2)^{\frac{3}{2}}e^{\xi/kT}. \tag{9}$$

Also, the density of holes in the acceptor levels is given by

$$n_2=N_a/\{1+\exp[-(\Delta E_2+\xi)/kT]\}, \tag{10}$$

where ΔE_2 is the energy gap between the gold level and the valence band.

Let us now take up the normalization for electrons in n-type samples. The basic condition for electrical neutrality is:

$$N_e=n_c+n_1,$$

which states that the total number of excess electrons

§ *Note added in proof.*—Recent evidence indicating a donor state 0.05 ev above the valence bond may require revising the point of view toward the statistics of strongly p-type gold-doped germanium. This point will be discussed in a forthcoming paper.

(above that number required to fill acceptor levels) is equal to the number in the conduction band and in the donor levels. Now, in the case of gold-doped germanium, we consider the upper acceptor level as a donor level, for statistical purposes. However, we ignore the lower acceptor level in this calculation, since it cannot furnish electrons to the conduction band, being below the middle of the band.

Then

$$N_e=2\left(\frac{2\pi mkT}{h^2}\right)^{\frac{3}{2}}e^{\zeta/kT}+\frac{N_a}{1+\exp[-(\Delta E_1+\zeta)/kT]}. \quad (11)$$

Letting $\eta=\zeta/kT$, Eq. (11) can be solved for e^η, yielding:[12]

$$e^\eta=\frac{N_e}{2B}\left[-\frac{B}{N_e}e^{-x_1}-r+1 + \left(\frac{B^2}{N_e^2}e^{-2x_1}+\frac{2B}{N_e}(r+1)e^{-x_1}+(r-1)^2\right)^{\frac{1}{2}}\right], \quad (12)$$

where we have $B=2(2\pi mkT/h^2)^{\frac{3}{2}}$, $x_1=\Delta E_1/kT$. Again, r is the trapping ratio N_a/N_e. Evaluation of e^η for different T yields the Fermi level in the ionization region of n-type gold-doped germanium. This we shall do graphically in the next section.

In the region of intrinsic conduction, the normalization condition is:

$$N_e=n_c-n_v. \quad (13)$$

This expression leads to the following equation for e^η in the approach to intrinsic conduction:

$$e^\eta=\frac{N_e}{2B}\left[1+\left(1+\frac{4B^2}{N_e^2}e^{-K_0}\right)^{\frac{1}{2}}\right], \quad (14)$$

where $K_0=E_g/kT$. The final region of consideration is the saturation region, which, fortunately in the case of gold in germanium, is reached well before the intrinsic range is reached. Thus the n_1 term becomes negligible before the n_v term assumes any importance. That this is so is best seen by making a few sample calculations.

The identical calculations are made for p-type samples: the normalization condition for the ionization region is:

$$N_h=n_v+n_2,$$

where again N_h is the number of "active" holes in the system (those in the valence band and in additional acceptor levels plus those in the lower acceptor level). This normalization leads to the formula:

$$e^\gamma=\frac{N_h}{2B}\left[-\frac{B}{N_h}e^{-x_2}-r+1 + \left(\frac{B^2}{N_h^2}e^{-2x_2}+\frac{2B}{N_h}(r+1)e^{-x_2}+(r-1)^2\right)^{\frac{1}{2}}\right], \quad (15)$$

where $\gamma=\xi/kT$ and $x_2=\Delta E_2/kT$. Again the trapping ratio is $r=N_a/N_h$.

Determination of the Fermi Levels *vs* Temperature

Although Eqs. (12) and (15) can be used directly for the calculation of the Fermi level for particular cases, graphical solutions are required for most Fermi level calculations. We write the normalization expression in the form:

$$e^\eta=\frac{N_e}{B}\left[1-\frac{r}{1+e^{x-\eta}}\right]. \quad (16)$$

The graphical method involves plotting the right and the left hand sides separately as functions of η, and determining the η value of the point of intersection. For depicting the course of the results, all plots are made on semilog paper, and a coordinate transformation is made so that calculations for a variety of temperatures can be shown on the same sheet of paper.

Figures 20 and 21 show the results for both n- and p-type samples containing 10^{14} atoms gold/cm^3, and for various temperatures and trapping ratios r. The straight lines are, essentially, simply the function e^η, but shifted to the left by the amount the curves would normally have been shifted to the right for the various T's.

For very low temperatures, the Fermi level is located at the value

$$\eta=\zeta/kT=-\ln(r-1)+(\Delta E_1/kT), \quad (\text{for } r>1). \quad (17)$$

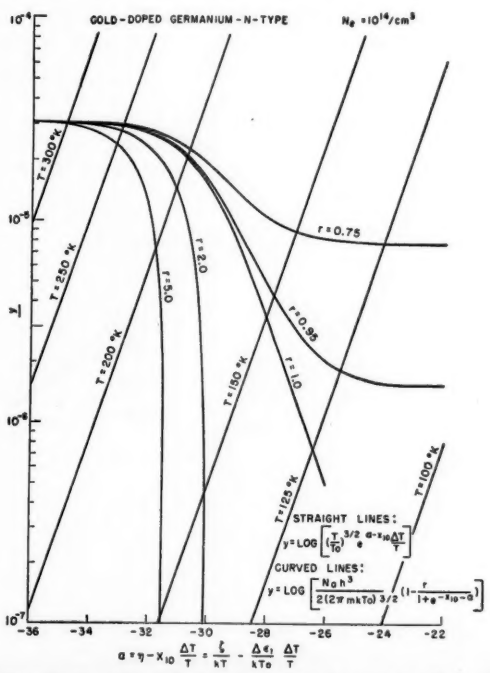

FIG. 20. Graphical solution for the Fermi level of gold-doped, n-type germanium containing 10^{14} gold atoms/cm^3 and various concentrations of donors, determined by the trapping ratio r.

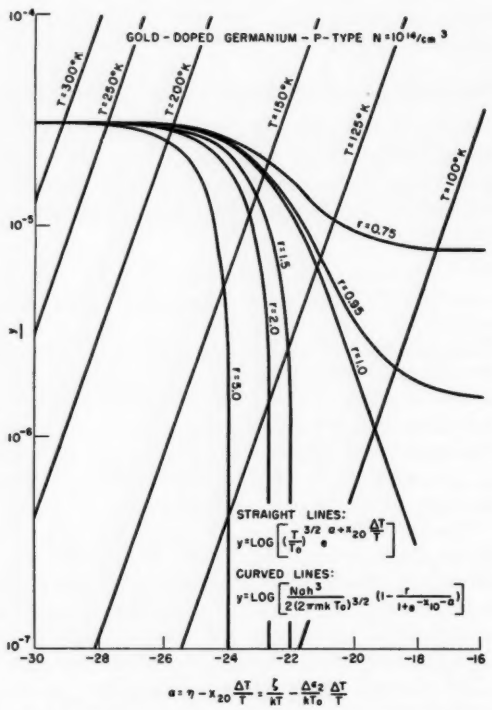

FIG. 21. Graphical solution for the Fermi level for p-type gold-doped germanium.

As the temperature rises, for large r, the Fermi level remains nearly constant until the saturation region is approached, at which state the point of intersection begins to move around the corner at A. For higher temperatures, the intersection gives constant values of η, which means that the Fermi level is increasing (negatively), and moving back down toward the middle of the forbidden energy gap.

As is expected, for low r, $r<1$, the Fermi level remains closer to the conduction band for all temperatures than for the larger r.

Figures 22 and 23 show the course of the Fermi level itself plotted *vs* temperature. Indicated also are the gold level and the middle of the forbidden energy band. As the temperature rises, the Fermi level moves to the middle of the band neglecting the term of the order kT arising from the different effective masses of holes and electrons.

Comparison of Theoretical and Experimental Hall Curves

The Hall coefficient is easily determined from the Fermi level, and thus it is easy to compare predicted shapes of the Hall curve for various trapping ratios with those actually observed.

The density of conduction electrons (for the n-type case) is given by

$$n_c = 2(2\pi mkT/h^2)^{\frac{3}{2}} e^{\zeta/kT}, \tag{18}$$

and since the Hall coefficient is given by

$$R = (3\pi/8e)(1/n_c), \tag{19}$$

then we have the Hall coefficient for n-type material:

$$R = (3\pi/8eB)e^{-\zeta/kT}, \tag{20}$$

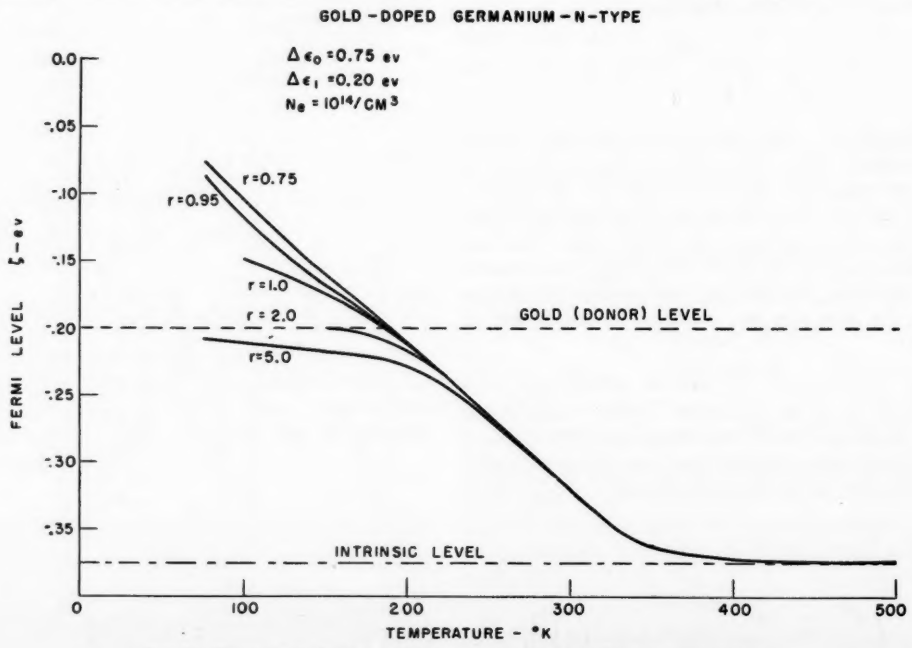

FIG. 22. Fermi level of n-type gold-doped germanium, plotted *vs* temperature.

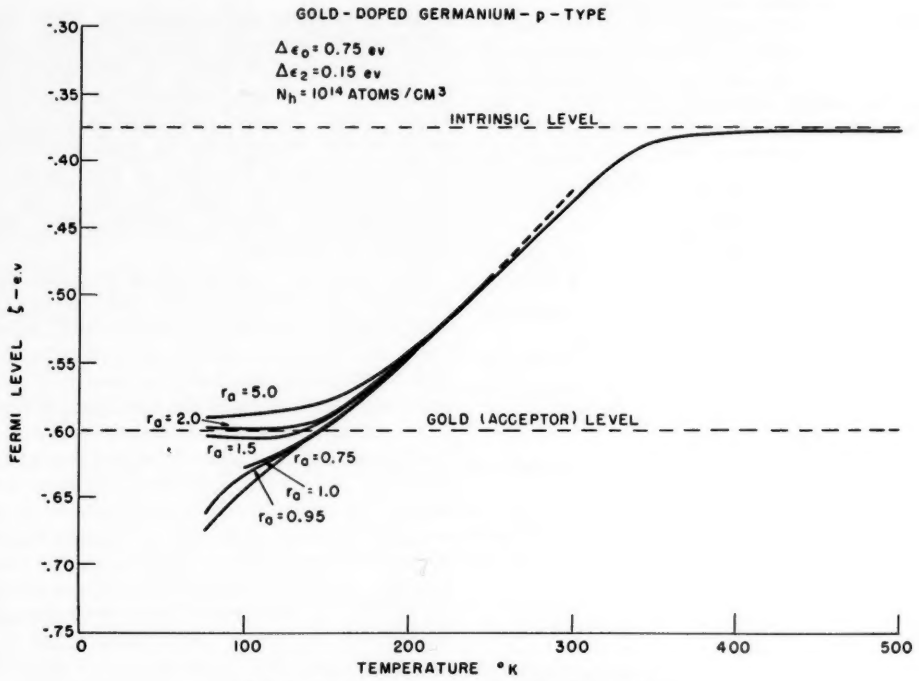

FIG. 23. Fermi level of p-type gold-doped germanium.

and for p-type material:

$$R = (3\pi/8eB)e^{-\xi/kT}. \quad (21)$$

Figures 24 and 25 show theoretical Hall curves for p- and n-type material respectively. Results are plotted for various trapping ratios. Of particular interest is the fact that for $r \sim 1$, linear curves are obtained which could lead to erroneous values of ionization energy if not correctly interpreted.

Included in Fig. 25 are experimental points for two n-type samples of various trapping ratios. The experimental points apply for samples with nearly, but not exactly 10^{14} gold states. The trapping ratio of the measured samples is not known exactly, because of the presence of a small number of donors arising from contamination in the furnace. The trapping ratio can probably be estimated reasonably well from these plots. The agreement between the experimental and theoretical curves appears to be quite good. This agreement appears to lend additional weight to the validity of the present model.

APPLICATIONS OF GOLD-DOPED GERMANIUM

We have shown that gold-doped specimens having a wide range of properties can be produced. In the present discussion, we shall deal with applications of these special properties that have been made, or which may be made, in various research fields. These applications are based upon the following special characteristics: (1) high resistivity, (2) high ionization energy, (3) effects characteristic of gold, (4) studies of trapping phenomena.

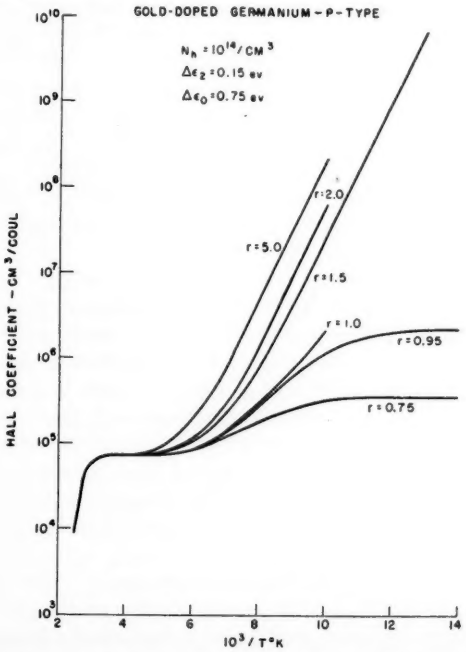

FIG. 24. Plot of Hall coefficient of p-type gold-doped germanium, for various values of trapping ratio, as determined theoretically.

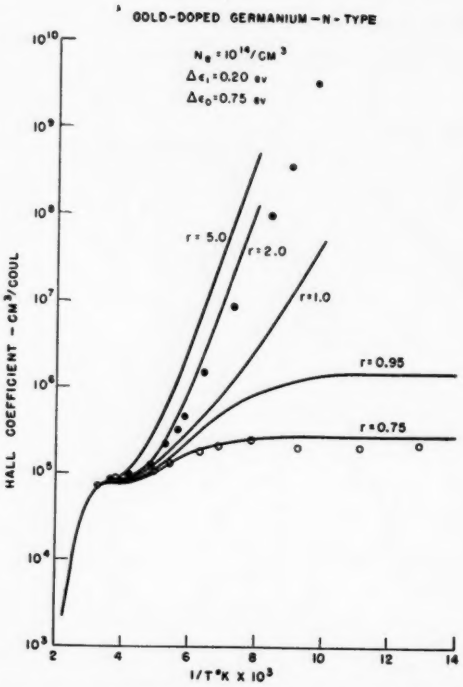

FIG. 25. Plot of Hall coefficient of n-type gold-doped germanium for various r. Also shown are experimental results on two samples.

(1) Studies made possible by the high-resistivity of gold-doped germanium. As indicated previously, the high ionization energy of gold in germanium makes possible the doing of experiments that were difficult in the past with the available material, which would have required the use of liquid helium, or liquid hydrogen. Since it is possible to obtain resistivities of the order 10^8 ohm-cm at liquid nitrogen temperatures, with gold-doped, and even higher with copper and iron-doped material, many such experiments can be more easily done. Among these are:

(a) Measurement of the dielectric constant and studies of dielectric properties of germanium in general. Availability of gold-doped germanium made possible the first direct measurements of the dielectric constant of germanium.[13] Previous measurements had been done at infrared and microwave frequencies only. The average value for K obtained with the gold-doped germanium, namely 15.8, was in good agreement with the value 16.0 found for example, by Briggs from infrared measurements, and by Benedict and Shockley from microwave studies.

(b) Studies on optical absorption are simplified by the use of gold-doped germanium. Kaiser and Fan,[4] for example, have used gold-doped germanium for investigating absorption under conditions where the free-carrier absorption would not have to be corrected for.

(c) Gold-doping is useful in eliminating the conductivity from certain regions of the sample. For example, Tweet[14] has used gold-doped germanium for the study of the conductivity in grain boundaries. By making gold-doped bicrystals of germanium, he was able to freeze out the bulk conductivity and measure the conductivity along the grain boundary for various angles of the bicrystal.

This technique is useful for other similar purposes, where the other source of conductivity has an activation energy smaller than that of the gold itself. Attempts to study the surface conduction of germanium by using gold-doped germanium have not been very successful, apparently because under the conditions of the experiment, the surface conduction layers had an activation energy comparable to that of the gold, and at low temperatures, not enough differences could be seen with various surface treatments to make valid measurements.

(d) Similarly, the gold-doping has been found useful in determining possible acceptor action of some very insoluble elements in germanium, such as silver. Since the carrier concentration of gold-doped germanium is only about $10^7/cm^3$ at 78°K, if an element with a solubility of only 10^{10} atoms/cm^3 were dissolved, and if the ionization energy of the acceptors formed was considerably less than 0.15, then a great difference in conductivity would show up at 78°K; whereas the change would be negligible if attempted with ordinary germanium containing perhaps 10^{13} carriers/cm^3.

Similar applications have been made in the study of effects of particle bombardment[15] and mechanical deformation.[16] In these cases the same situation applies, namely that lower energy acceptors are produced by the action say of electrons, or of mechanical bending, than of the gold, so that large changes of conductivity are produced when the material is studied at liquid nitrogen temperature.

(2) The use of gold is of advantage in the study of the ionization region of semiconductors, again because the temperatures of study are removed from the inconvenient helium-hydrogen range, to that of liquid nitrogen to room temperature. Such problems as those of the comparison of the statistics with experimental results of Hall measurements already discussed are of interest.

(3) Of particular importance are the many problems involving the nature of the gold states and the interaction of the gold atom with the lattice. These studies may be approached by measurements of photoconductivity and Hall coefficient, the optical properties, magnetic susceptibility, the dependence of the resistivity upon pressure, and by other techniques. It is to

[13] W. C. Dunlap, Jr., and R. L. Watters, Phys. Rev. **92**, 1396 (1953).

[14] A. G. Tweet, Phys. Rev. **96**, 828 (1954).

[15] Pepper, Klontz, Lark-Horovitz, and MacKay, Phys. Rev. **94**, 1410A (1954).

[16] C. J. Gallagher and A. G. Tweet, Phys. Rev. **96**, 834 (1954).

be hoped that results from such investigations may answer many of the questions raised in the present work.

(4) The use of gold permits the introduction in reasonably large quantities ($>10^{15}/cm^3$), of electron traps located at a definite level. These have already been shown to be involved, in all probability, in various trapping phenomena. Further studies should add considerably to knowledge of secondary photoconduction and other phenomena but poorly understood up to the present time.

(5) Gold-doped germanium has particular promise as a photoconductor for the long-wavelength infrared region because of its response out to about 8 microns. In this respect it is much superior to both lead telluride and lead selenide, whose long wavelength response dies out at about 6 and 4 microns respectively. Of course, gold-doped germanium has to be cooled sufficiently that deionization of the carriers can take place, and that sensitivity be increased and dark current reduced.

ACKNOWLEDGMENT

I should like to acknowledge the contribution of William Bernard, who carried out many of the computations reported in this paper.

PHYSICAL REVIEW VOLUME 97, NUMBER 3 FEBRUARY 1, 1955

Molecular Field in the Spherical Model*

MELVIN LAX
Physics Department, Syracuse University, Syracuse, New York
(Received August 30, 1954)

The Heisenberg model of ferromagnetism is replaced by a classical model in which the interaction between a pair of neighboring atoms is $-2JS(S+1)\boldsymbol{\varepsilon}_i\cdot\boldsymbol{\varepsilon}_j$, where S is the spin of any atom, J is the exchange integral, and the $\boldsymbol{\varepsilon}_i$ are classical unit vectors. The spherical model is then used to evaluate the molecular field acting on any atom i. This effective field is found to have the generalized Weiss form, $H+W(T)M+W'(T)M'\gamma_i^\pi$, where H is the magnetic field, M the magnetization, and M' the antiferromagnetic order (in units of magnetization). The coefficient γ_i^π changes sign from one sublattice to another. The "Weiss" coefficients $W(T)$ and $W'(T)$ are slowly temperature-dependent and obey $dW/dT>0$; $dW'/dT>0$.

A phase transition is found in three dimensions, but not in one or two dimensions. For spin ½ lattices of simple cubic, body-centered cubic, and face-centered cubic type, the ferromagnetic transition temperature T_c in units kT_c/J is found to be 1.98, 2.87, and 4.45, respectively. Corresponding values for the simple cubic case due to P. R. Weiss and V. Zehler are 1.85 and 1.93 respectively. The susceptibility and the paramagnetic temperature θ are found for the three lattices. The ratio θ/T_c is found to be independent of spin with the values 1.52, 1.39, and 1.34 for the s.c.c., b.c., and f.c.c. lattices respectively. Corresponding results for the transition temperatures, susceptibility, etc., are obtained for the antiferromagnetic cubic lattices.

1. INTRODUCTION

THE treatment of dielectric and magnetic phenomena has often been facilitated by the use of appropriate effective fields. Some typical examples are the Lorentz electric field in nonpolar cubic crystals, the Weiss molecular field treatment of ferromagnetism, and the Van Vleck[1] sub-lattice treatment of antiferromagnetism.

The effective field method usually asserts that the behavior of a single member of an assembly of interacting particles can be treated as if it stood alone in a modified field. The modified or effective field differs from the applied field (if any) because it includes the average effects of all other members of the assembly (computed holding the particle in question fixed).[2]

These remarks may be made more definite by considering a classical system[3] described by the (vector) parameters $\boldsymbol{\varepsilon}_1, \boldsymbol{\varepsilon}_2, \cdots \boldsymbol{\varepsilon}_N$, the energy $U=U(\boldsymbol{\varepsilon}_1,\cdots\boldsymbol{\varepsilon}_N)$ and the partition function,

$$Q=\int \exp(-U/kT)d\boldsymbol{\varepsilon}_1\cdots d\boldsymbol{\varepsilon}_N. \qquad (1.1)$$

The distribution function $Q(\boldsymbol{\varepsilon}_j)$ for the single particle can be obtained by integrating (i.e., averaging) over all other particles:

$$Q(\boldsymbol{\varepsilon}_j)=\int \exp(-U/kT)d\boldsymbol{\varepsilon}_1\cdots d\boldsymbol{\varepsilon}_N/d\boldsymbol{\varepsilon}_j. \qquad (1.2)$$

There is, of course, no guarantee that the distribution function of a single particle in an effective field has the same form as $Q(\boldsymbol{\varepsilon}_j)$ but the two can usually be made to coincide by permitting the effective field to be a sufficiently complicated function of temperature and $\boldsymbol{\varepsilon}_j$.

In practice, the effective field is often estimated by intuitive procedures (as, in the Bragg-Williams treat-

* Supported in part by the U. S. Office of Naval Research, and in part by the Office of Scientific Research of the U. S. Air Force. A summary of the work included in this paper, with results for the simple cubic case, was presented to the U. S. Office of Naval Research Conference on Magnetism, September 1952; see Revs. Modern Phys. 25, 160, 337 (1953). The results for body-centered cubic and face-centered cubic lattices were presented to the American Physical Society in January, 1953; see Phys. Rev. 90, 374 (A) (1953).

[1] J. H. Van Vleck, J. Chem. Phys. 9, 85 (1941).

[2] Compare with the definition that arises naturally in M. Lax, Phys. Rev. 85, 621 (1952).

[3] The succeeding remarks can be translated into quantum mechanics by replacing integrations of the Boltzmann factor over phase space by traces of the corresponding Boltzmann operator.

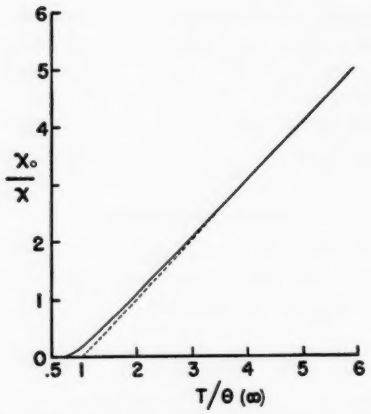

FIG. 1. The inverse susceptibility for a face-centered cubic lattice *versus* absolute temperature, with the asymptotic Curie-Weiss line drawn in for comparison. The curve is universal as plotted: χ_0/χ *versus* $T/\theta(\infty)$, where $\chi_0=n(g\beta)^2/(2ZJ)$, and $\theta(\infty)=2ZS(S+1)J/(3k)$ is the paramagnetic temperature. The results for simple cubic and body-centered cubic lattices are so close to those of a face-centered cubic lattice when plotted in these units, that they would be difficult to distinguish on the scale used. Calculated values for all three lattices are based on Eqs. (7.17) and (B2).

ment of the Ising model problem)[4] because of the difficulty involved in evaluating the integrals (1.1) and (1.2). Part of the difficulty involved in evaluating (1.2) lies in the assymmetry of integrating over all but one variable. This difficulty may be eliminated by rewriting (1.2) in the form

$$Q(\varepsilon_j^0)=\int \exp(-U/kT)\delta(\varepsilon_j-\varepsilon_j^0)d\varepsilon_1\cdots d\varepsilon_N, \quad (1.3)$$

and using the customary exponential, integral representation for the Dirac delta function:

$$\delta(\varepsilon_j-\varepsilon_j^0)=(2\pi)^{-3}\int \exp[i\mathbf{n}\cdot(\varepsilon_j-\varepsilon_j^0)]d\mathbf{n}. \quad (1.4)$$

The remainder of the difficulty in evaluating (1.2) is common to the difficulty in evaluating the partition function (1.1) itself. Since the spherical model[5] has made possible an approximate evaluation of the partition function for a class of problems, we consider here the evaluation of the effective field in the spherical approximation. For the sake of definiteness, the methods will be applied to the problem of a lattice of magnetic dipoles. The partition function for this problem has been evaluated previously by the author in the spherical approximation,[6] and it will be possible to follow the notation of reference 6.

[4] W. L. Bragg and E. J. Williams, Proc. Roy. Soc. (London) **A145**, 699 (1934).
[5] E. W. Montroll, Nuovo cimento **6**, Suppl. 2, 265 (1949); T. H. Berlin and M. Kac, Phys. Rev. **86**, 821 (1952).
[6] M. Lax, J. Chem. Phys. **20**, 1351 (1952), hereafter referred to as I.

A comparison will be made between the results of this paper and the molecular field treatment of ferromagnetism and antiferromagnetism. The principal conclusion of this paper is that the molecular field in the ferromagnetic case has the form $H+W(T)M$, where the Weiss molecular field coefficient $W(T)$ is a (slowly varying) function of temperature above the Curie temperature and a constant below the Curie temperature. As a consequence the Curie-Weiss law for the susceptibility $\chi=C/(T-\theta)$ is only asymptotically valid for large temperatures. (See Fig. 1 for the face-centered cubic case.) Furthermore the so-called paramagnetic temperature θ is found to be larger than the actual ferromagnetic transition temperature T_c. (See Table II for the ratio of θ/T_c for several lattice structures.) The transition temperatures T_c for the various cubic lattices, listed in Table I are found to be in excellent agreement with results obtained by Weiss[7] using the Bethe-Peierls method[8,9] and by Zehler[10] using the Opechowski[11] method.

For the antiferromagnetic case, it is demonstrated that the molecular field contains a term (proportional to the antiferromagnetic order) that changes in sign from one sublattice to the next. Thus the molecular field has the same form as in the Van Vleck phenomenological theory[1] (with a modified coefficient) and his analysis of the susceptibility below the transition temperature can be carried over using our molecular field, with no significant changes. Above the Curie temperature, however, there are deviations from the Curie-Weiss susceptibility and a ratio of θ/T_c differing from unity (without requiring interactions beyond nearest neighbors).[12,13]

To summarize, the molecular fields calculated in this paper have the advantage of simplicity: they can be incorporated directly into the widely applied phenomenological theory. And the temperature dependence of the Weiss coefficients is in such a direction as to decrease the principal discrepancies between the usual theory (with $W=$constant) and experiment. Furthermore the spherical model treatment indicates that phase transitions occur in three but not in one or two dimensions whereas the usual theory always predicts a phase transition.

TABLE I. The critical temperature in units kT_c/J for ferromagnetic cubic lattices with isotropic exchange interaction. Unless otherwise specified the spin is $\frac{1}{2}$.

Lattice/method	Spherical	P. R. Weiss	V. Zehler
Simple cubic	1.98	1.85	1.93
Body-centered cubic	2.87	2.90	···
Face-centered cubic	4.45	···	4.25
Body-centered cubic, spin 1	7.65	6.65	···

[7] P. R. Weiss, Phys. Rev. **74**, 1493 (1948).
[8] H. Bethe, Proc. Roy. Soc. (London) **150**, 552 (1935).
[9] R. Peierls, Proc. Roy. Soc. (London) **154**, 207 (1936).
[10] V. Zehler, Z. Naturforsch. **5**, 344 (1950).
[11] W. Opechowski, Physica **4**, 181, 715 (1937); **6**, 112 (1938).
[12] P. W. Anderson, Phys. Rev. **79**, 705 (1950).
[13] J. S. Smart, Phys. Rev. **86**, 968 (1952).

2. THE SPHERICAL MODEL

The energy U of a set of dipoles $\mathfrak{y}_j=\mu\mathfrak{e}_j$ situated at the lattice points $\mathbf{r}_j$ can be written in the form[6]

$$-U=\tfrac{1}{2}n\mu^2\sum_{i,j}(\mathfrak{e}_i\cdot\mathbf{G}_{ij})\cdot\mathfrak{e}_j+\mu\sum_j\mathfrak{e}_j\cdot\mathbf{H}_0, \quad (2.1)$$

where $\mathbf{H}_0$ is the applied magnetic field external to the sample, μ is the dipole moment, the $\mathfrak{e}_j$ are unit vectors, and n is the number of dipoles per unit volume. The interaction dyadic $\mathbf{G}_{ij}$ contains an exchange term[14] and a dipole-dipole term:

$$\mathbf{G}_{ij}=2\mathbf{J}_{ij}S(S+1)/n\mu^2+r_{ij}^{-5}[3\mathbf{r}_{ij}\mathbf{r}_{ij}-r_{ij}^2\mathbf{1}]. \quad (2.2)$$

The vector distance between dipoles, r_{ij}, is measured in units of $n^{-\frac{1}{3}}$. The exchange dyadic $\mathbf{J}_{ij}$, in the absence of anisotropy, can be written $J_{ij}\mathbf{1}$. If only nearest neighbor interactions are assumed, then $J_{ij}=J$ for nearest neighbors and zero otherwise, where J is the usual exchange integral. (These remarks are made for definiteness but the method used in this paper does not require any restrictive assumptions.) If $\mathbf{s}$ is the spin operator of the dipole in units of $\hbar$, then $S(S+1)$ is the eigenvalue of s^2 and

$$\mathfrak{y}=\mu\mathfrak{e}=g\beta\mathbf{s}; \quad \mu^2=(g\beta)^2S(S+1), \quad (2.3)$$

where $\beta=(e\hbar/2mc)$ is the Bohr magneton, and g is the dimensionless gyromagnetic ratio.

The spherical model consists in replacing the N restrictions $\epsilon_j^2=1$, by the simple restriction

$$\sum\epsilon_j^2=N. \quad (2.4)$$

This restriction on the integrals (1.1) to (1.3) can be applied by inserting under the integral sign the delta function:

$$\delta(N-\sum\epsilon_j^2)=(K/2\pi i)\times\int_{c-i\infty}^{c+i\infty}\exp[Kt(N-\sum\epsilon_j^2)]dt, \quad (2.5)$$

where

$$K=n\mu^2/(2kT).$$

With the help of the integration formula,[15]

$$\int_{-\infty}^{+\infty}\cdots\int\exp[-\sum a_{ij}x_ix_j\pm 2\sum b_jx_j]dx_1\cdots dx_n=(\pi)^{n/2}[\det(a_{ij})]^{-\frac{1}{2}}\exp[\sum b_i(a^{-1})_{ij}b_j], \quad (2.6)$$

all of the integrations in (1.1) and (1.3) may be performed, except for the integration over t. [The term $(a^{-1})_{ij}$ is the ij element of the matrix reciprocal to a_{ij}.] The partition function (1.1), together with (2.5) and (2.6), takes the form:[6]

$$Q=\int\exp[NKt+N\ln Z(t)]dt, \quad (2.7)$$

$$\ln Z(t)=-\tfrac{3}{2}\ln K+[\mathbf{H}_0\cdot(\mathbf{t}-\boldsymbol{\lambda}_0)]^{-1}\cdot\mathbf{H}_0/(2nkT)-\tfrac{3}{2}f(t), \quad (2.8)$$

$$f(t)=(3N)^{-1}\sum_{a=1}^{3}\sum_{p=1}^{N}\ln[t-\lambda_a(\mathbf{p})], \quad (2.9)$$

$$\boldsymbol{\lambda}(\mathbf{p})=\sum_j\mathbf{G}_{ij}\exp[i\mathbf{p}\cdot\mathbf{r}_{ji}]. \quad (2.10)$$

The $\boldsymbol{\lambda}(\mathbf{p})$ are the dyadic eigenvalues of the dyadic matrix $\mathbf{G}_{ij}$. The $\lambda_a(\mathbf{p})$ $(a=1, 2, 3)$ are the three eigenvalues of the dyadic $\boldsymbol{\lambda}(\mathbf{p})$. We abbreviate $\boldsymbol{\lambda}(0)$ by $\boldsymbol{\lambda}_0$ and represent $t\mathbf{1}$ (t times the unit dyadic) by $\mathbf{t}$.

The integration formula (2.6) assumes that the matrix a_{ij} is positive definite. In our case, this requires that $\mathbf{t}-\mathbf{G}_{ij}$ be positive definite, or that $t>\lambda_m$, where λ_m is the largest of the eigenvalues $\lambda_a(\mathbf{p})$. The path of integration for t in (2.7) and (2.5) must therefore be so chosen that it passes to the right of the branch point at $t=\lambda_m$.

Because of the large value of N, the major contribution to (2.7) comes from a saddle point t_s:

$$Q\simeq\exp[NKt_s+N\ln Z(t_s)], \quad (2.11)$$

where t_s is determined by the usual saddle condition,

$$(d/dt)[Kt+\ln Z(t)]=0,$$

or

$$[n\mu^2/(3kT)][1-(H_s/n\mu l_s)^2]=f'(t_s), \quad (2.12)$$

where

$$\mathbf{H}_s=t_s(t_s-\boldsymbol{\lambda}_0)^{-1}\cdot\mathbf{H}_0. \quad (2.13)$$

It is of interest to note that the results (2.11) and (2.12) could also have been obtained by disregarding the micro-canonical condition (2.4) and replacing it by the less restrictive "canonical" condition,[16]

$$\langle\sum\epsilon_j^2-N\rangle=0. \quad (2.14)$$

The canonical treatment consists in inserting a factor $\exp[-Kt\sum\epsilon_j^2]$ into (1.1) and determining t so that (2.14) is satisfied. No integration over t is then required, one simply replaces t by t_s.

For values of t such that $N(t-\lambda_m)\gg 1$, $f'(t)$ may be replaced by its limiting value as $N\to\infty$:

$$\lim_{N\to\infty}(3N)^{-1}\sum_{a=1}^{3}\sum_{p=1}^{N}[t-\lambda_a(p)]^{-1}=\langle(t-\lambda)^{-1}\rangle=\tfrac{1}{3}\sum_{a=1}^{3}\int[t-\lambda_a(\mathbf{p})]^{-1}d\mathbf{p}\Big/\int d\mathbf{p}, \quad (2.15)$$

where the integration is over one cell of the reciprocal

[14] The exchange term agrees with the usual quantum-mechanical energy, $-2J\mathbf{s}_i\cdot\mathbf{s}_j$, between the pair of spins s_i and s_j.

[15] H. Cramer, *Mathematical Methods of Statistics* (Princeton University Press, Princeton, 1946).

[16] H. W. Lewis and G. H. Wannier, Phys. Rev. 88, 682 (1952). There are, however, circumstances in which the "canonical" procedure can lead to erroneous results. See M. Lax, Phys. Rev. (to be published).

lattice space. (For a simple cubic lattice the three components of $\mathbf{p}$ have the range 0 to 2π in our units.) At high temperatures, $t_s \simeq 3kT/n\mu^2$. As T decreases t_s decreases monotonically. But t_s cannot decrease below the value λ_m. Thus a critical temperature is reached at which

$$(n\mu^2/3kT_c)[1-(H_e/n\mu\lambda_m)^2]=\langle(\lambda_m-\lambda)^{-1}\rangle, \quad (2.16)$$

or in the absence of a field,

$$(n\mu^2/3kT_c)=\langle(\lambda_m-\lambda)^{-1}\rangle. \quad (2.17)$$

Of course if the integral (2.15) for $\langle(\lambda_m-\lambda)^{-1}\rangle$ diverges, as it does in the one- and two-dimensional cases, no transition occurs since t need never assume the value λ_m. In the three-dimensional case $\langle(t-\lambda)^{-1}\rangle$ is continuous and approaches its maximum value as t becomes equal to λ_m.

For temperatures below the critical temperature, we cannot assume that $N(t-\lambda_m)\gg 1$, but we can approximate $f'(t)$ by

$$f'(t)\simeq(b/3N)(t-\lambda_m)^{-1}+\langle(\lambda_m-\lambda)^{-1}\rangle, \quad (2.18)$$

since the saddle value t_s will differ from λ_m by terms of order $1/N$ and with sufficient accuracy $\langle(t_s-\lambda)^{-1}\rangle$ can be replaced by $\langle(\lambda_m-\lambda)^{-1}\rangle$. Here b is the degeneracy of the states of energy λ_m. To summarize, below the critical temperature, t_s may be replaced by λ_m in all continuous functions, but it differs from λ_m by an amount of order $1/N$ determined by combining (2.12), (2.17), and (2.18):

$$(n\mu^2/3kT_c)[1-(H_e/n\mu\lambda_m)^2-T/T_c] = (b/3N)(t_s-\lambda_m)^{-1}. \quad (2.19)$$

Equation (2.18) expresses the fact that the system has partially condensed into the state λ_m of lowest energy and Eq. (2.19) yields a measure of the order achieved [reference 6, Eq. (7.7)].

If the calculations discussed in this section are repeated in the presence of a fixed magnetization,

$$(\sum \epsilon_j)/N=(\mathbf{M}/n\mu). \quad (2.20)$$

The results are unchanged except that $(H_e/n\mu t_s)$ is everywhere replaced by $(M/n\mu)$. Thus the saddle point condition (2.12) becomes

$$(n\mu^2/3kT)[1-(M/n\mu)^2]=\langle(t_s-\lambda)^{-1}\rangle. \quad (2.21)$$

3. THE MOLECULAR FIELD

Any straightforward evaluation of the mean moment $\mu\langle\epsilon_j\rangle$ of a dipole in the absence of an external field will yield zero because ϵ_j is odd and U is even on a reversal of the direction of all spins. This seems to imply that spontaneous magnetization cannot exist. However, there is a degeneracy between states of opposite magnetization, and it is not correct to average over such pairs of states since an infinitesimal applied field will split this degeneracy and favor the direction of the field by an enormous factor (below the Curie temperature). The customary classical treatment of this problem is (1) to assume that a given order or magnetization exists in a specified direction (2) to calculate the effective or molecular field in the presence of this order (3) to investigate whether the molecular field is sufficiently strong to sustain this order.

Because of the above use to which the molecular field is put, we must evaluate the molecular field regarding $\mathbf{H}_0$ and $\mathbf{M}$ as independent variables. In other words, we must evaluate the partition sum (1.3) in an applied field, holding the magnetization fixed through (2.20). Unfortunately, however, $\mathbf{M}$ and $\mathbf{H}_0$ represent corresponding extensive and intensive variables and it is not consistent to specify them simultaneously (at a given temperature). Furthermore, we may anticipate that the correct effective field will take the form:

$$\mathbf{H}_{eff}=\mathbf{H}+W\mathbf{M}=\mathbf{H}_0-4\pi\mathbf{L}\cdot\mathbf{M}+W\mathbf{M}, \quad (3.1)$$

with unity as the coefficient of $\mathbf{H}_0$. ($\mathbf{L}$ is the demagnetization tensor and $\mathbf{H}$ is the field within the specimen.) The only way to satisfy these two requirements simultaneously is not to specify the magnetic moment of the entire lattice—but rather the magnetic moment of the *remainder* of the lattice excluding the dipole on which the molecular field acts.

In the antiferromagnetic case, it is convenient to introduce an order parameter $\mathbf{M}'$ with the dimensions of magnetization defined by

$$\mathbf{M}'/n\mu=N^{-1}\sum y_j^{\pi}\epsilon_j, \quad (3.2)$$

where y_j^{π} is the normal coordinate associated with the ground state; for example, for a simple cubic lattice with negative exchange constant,

$$y_j^{\pi}=\cos(\pi\cdot\mathbf{r}_j)=\cos(\pi x_j+\pi y_j+\pi z_j) \quad (3.3)$$

takes on the values plus one on one sublattice and minus one on the other.[17] It is also convenient for the sake of symmetry to introduce a field $\mathbf{H}_1$, the intensive parameter conjugate to $\mathbf{M}'$. (If the ground state is degenerate, it is useful to introduce several order parameters and their conjugate intensive parameters.)

Since we shall be interested in the susceptibility or magnetization below the Curie temperature of an antiferromagnetic, it is necessary to hold $\mathbf{M}$ and $\mathbf{M}'$ fixed simultaneously. The one-particle partition function for dipole ϵ_s can then be written in the form:

$$\begin{aligned}Q(\epsilon_s^0)=\int d\epsilon_1\cdots d\epsilon_N \exp[&K\sum\epsilon_i\cdot\mathbf{G}_{ij}\cdot\epsilon_j \\ &+(\mu/kT)\sum(\mathbf{H}_0+\mathbf{H}_1y_j^{\pi})\cdot\epsilon_j] \\ &\times\delta(KN-K\sum\epsilon_j^2)\delta\left(-\frac{N\mathbf{M}}{nkT}+\frac{\mu}{kT}\sum{}'\epsilon_j\right) \\ &\times\delta\left(-\frac{N\mathbf{M}'}{nkT}+\frac{\mu}{kT}\sum{}'y_j^{\pi}\epsilon_j\right) \\ &\times\delta[(\epsilon_s-\epsilon_s^0)\mu/kT], \quad (3.4)\end{aligned}$$

[17] More generally y_j^{π} can be a tensor so that the magnetization direction on one sublattice can differ from that on another. The latter case arises however only for polyatomic lattices in the presence of certain kinds of anisotropic interactions.

where $K=n\mu^2/(2kT)$ and the primed sums indicate that the term ε_s is omitted, i.e., that the order is specified in the *remainder* of the lattice.

For all delta functions we shall use an integral representation of the form

$$\delta(x)=(2\pi i)^{-1}\int_{c-i\infty}^{c+i\infty}\exp(xt)dt, \tag{3.5}$$

with the variables t, $\mathbf{h}$, $\mathbf{h}'$, and $\mathbf{h}_s$ for the spherical condition, magnetization, antimagnetization, and ε_s respectively. By inserting these delta functions and omitting some factors of 2π, (3.4) can be written in the form

$$Q(\epsilon_s{}^0)=\int dt\int d\mathbf{h}_s\int\int d\mathbf{h}d\mathbf{h}'\exp[-(\mu/kT)\boldsymbol{\varepsilon}_s{}^0\cdot\mathbf{h}_s$$
$$-\mathbf{h}\cdot N\mathbf{M}/(nkT)-\mathbf{h}'\cdot N\mathbf{M}'/(nkT)]Q(H^i), \tag{3.6}$$

$$Q(H^i)=\exp(NKt)\int d\boldsymbol{\varepsilon}_1\cdots d\boldsymbol{\varepsilon}_N$$
$$\times\exp[-K\sum\boldsymbol{\varepsilon}_i(\mathbf{t}-\mathbf{G})_{ij}\boldsymbol{\varepsilon}_j$$
$$+(\mu/kT)\sum\boldsymbol{\varepsilon}_j\mathbf{H}^j], \tag{3.7}$$

$$Q(H^i)=\exp[NKt+N\ln Z(t)]$$
$$\times\exp[(2nkT)^{-1}\sum\mathbf{H}^i(\mathbf{t}-\mathbf{G})_{ij}{}^{-1}\mathbf{H}^j], \tag{3.8}$$

where

$$\mathbf{H}^j=\mathbf{H}_0+\mathbf{h}+(\mathbf{H}_1+\mathbf{h}')y_j{}^\pi+P_j(\mathbf{h}_j-\mathbf{h}-\mathbf{h}'y_j{}^\pi), \tag{3.9}$$

and

$$P_j=\delta_{js} \tag{3.10}$$

is a projection operator that selects dipole s. In Eq. (3.8), $\ln Z(t)$ is understood to be given by (2.8) in the limit as $N\to\infty$, with H_0 set equal to zero in the latter expression.

The expression (3.8) is a quadratic form in the variables $\mathbf{h}$, $\mathbf{h}'$, and $\mathbf{h}_s$ so that the integrations over these variables in (3.6) can be performed with the help of (2.6). One finally obtains, for the one-particle distribution function,

$$Q(\boldsymbol{\varepsilon}_s{}^0)=\int dt\exp N\{Kt-\tfrac{3}{2}\ln K-\tfrac{3}{2}\langle\ln(t-\lambda)\rangle$$
$$-(2nkT)^{-1}[\mathbf{M}\cdot(\mathbf{t}-\boldsymbol{\lambda}_0)\cdot\mathbf{M}+\mathbf{M}'\cdot(\mathbf{t}-\boldsymbol{\lambda}_\pi)$$
$$\cdot\mathbf{M}'-2\mathbf{M}\cdot\mathbf{H}_0-2\mathbf{M}'\cdot\mathbf{H}_1]\}$$
$$\times\exp[-(2nkT)^{-1}(\mathbf{A}_s-n\mu\boldsymbol{\varepsilon}_s{}^0)$$
$$\times\mathbf{D}_{ss}{}^{-1}(\mathbf{A}_s-n\mu\boldsymbol{\varepsilon}_s{}^0)], \tag{3.11}$$

where

$$\mathbf{A}_s=\mathbf{M}+\mathbf{M}'y_s{}^\pi+\mathbf{D}_{ss}\cdot\{\mathbf{H}_0-(\mathbf{t}-\boldsymbol{\lambda}_0)\cdot\mathbf{M}$$
$$+y_s{}^\pi[\mathbf{H}_1-(\mathbf{t}-\boldsymbol{\lambda}_\pi)\cdot\mathbf{M}']\}, \tag{3.12}$$

and

$$\mathbf{D}_{ss}=\lim_{N\to\infty}(1/N)\sum{}''(\mathbf{t}-\boldsymbol{\lambda}(\mathbf{p}))^{-1}=\langle(\mathbf{t}-\boldsymbol{\lambda})^{-1}\rangle, \tag{3.13}$$

where the double prime on the sum indicates that the terms in $t-\lambda_0$ and $t-\lambda_\pi$ have been *omitted* where λ_π is the eigenvalue associated with the antiferromagnetic mode. These terms *actually cancelled* out in the above calculation thus rendering D_{ss} a smooth function of t usable below as well as above the Curie temperature.

We may remark that the first exponential in (3.11) is the result that would be obtained if all ε_j were integrated over including ε_s. Since the second exponential factor (that arises because ε_s is held fixed) contains no terms of order N, the saddle condition is unaffected and remains

$$(n\mu^2/3kT)[1-(M/n\mu)^2-(M'/n\mu)^2]=\langle(t_s-\lambda)^{-1}\rangle, \tag{3.14}$$

with the transition temperature determined by setting t_s equal to the maximum eigenvalue λ_m, which for the cases of interest will be λ_0 or λ_π.

If t is replaced by t_s in the second exponential factor of (3.11), the latter is the unnormalized distribution function for $\boldsymbol{\varepsilon}_s{}^0$. If the dyadic $\mathbf{D}_{ss}$ is nondiagonal, $\boldsymbol{\varepsilon}_s{}^0$ experiences anisotropy forces in addition to an effective field. For cubic crystals, however, we may expect $\mathbf{D}_{ss}$ to be a scalar. The term in $(\boldsymbol{\varepsilon}_s{}^0)^2$ may now be omitted since it is constant, and the distribution function finally takes the form

$$Q(\boldsymbol{\varepsilon}_s{}^0)\propto\exp[(\mu/kT)\boldsymbol{\varepsilon}_s{}^0\cdot\mathbf{H}_{\text{eff}}{}^s], \tag{3.15}$$

where

$$\mathbf{H}_{\text{eff}}{}^s=\mathbf{A}_sD_{ss}{}^{-1}$$
$$=\mathbf{H}_0-(t_s-\boldsymbol{\lambda}_0)\cdot\mathbf{M}+[\mathbf{H}_1-(t_s-\boldsymbol{\lambda}_\pi)\cdot\mathbf{M}']y_s{}^\pi$$
$$+[\langle(t_s-\lambda)^{-1}\rangle]^{-1}(\mathbf{M}+\mathbf{M}'y_s{}^\pi), \tag{3.16}$$

or

$$\mathbf{H}_{\text{eff}}{}^s=\mathbf{H}+W\mathbf{M}+(\mathbf{H}_1+W'\mathbf{M}')y_s{}^\pi, \tag{3.17}$$

where

$$W(T)=[\langle(t_s-\lambda)^{-1}\rangle]^{-1}-(t_s-\lambda_0-4\pi L), \tag{3.18}$$

$$W'(T)=[\langle(t_s-\lambda)^{-1}\rangle]^{-1}-(t_s-\lambda_\pi). \tag{3.19}$$

The "Weiss" coefficients W and W' depend on temperature through the saddle point t_s above the Curie temperature. Since W and W' are both continuous functions at the maximum eigenvalue λ_m, t_s may be replaced by λ_m at or below the Curie temperature. Thus below the Curie temperature, the Weiss coefficients are constants independent of temperature (and magnetization). Above the Curie temperature W and W' depend slightly on the magnetization. (The dependence is only appreciable if M is near its saturation value, i.e., in a very large field.)

4. SUSCEPTIBILITY ABOVE THE CURIE TEMPERATURE

The susceptibility above the Curie temperature in both the antiferromagnetic and ferromagnetic cases can be computed using the effective field (3.17) with $\mathbf{H}_1$ and $\mathbf{M}'$ set equal to zero. The partition sum for the last dipole (3.15) is to be computed by replacing $\mu\boldsymbol{\varepsilon}$ by $g\beta\mathbf{s}$ and treating this dipole quantum mechanically. This leads to the usual Brillouin function for the mag-

netization:

$$(M/ng\beta S)=B_S(y)\mathbf{H}_{\rm eff}/H_{\rm eff}, \tag{4.1}$$

$$B_S(y)=\frac{2S+1}{2S}\coth\left(\frac{2S+1}{2S}y\right) -\frac{1}{2S}\coth\left(\frac{y}{2S}\right), \tag{4.2}$$

$$y=g\beta SH_{\rm eff}/kT, \tag{4.3}$$

$$\mathbf{H}_{\rm eff}=\mathbf{H}+W\mathbf{M}. \tag{4.4}$$

For small fields, the Taylor expansion of the Brillouin function,

$$B_S(y)\simeq(S+1)y/(3S), \tag{4.5}$$

can be used to obtain the susceptibility:

$$\chi=M/H=(n\mu^2/3k)[T-\theta(T)]^{-1}, \tag{4.6}$$

$$\theta(T)=(n\mu^2/3k)W(T). \tag{4.7}$$

If Eqs. (3.18) and (3.14) with $M=M'=0$ are combined, one may verify that the susceptibility may also be written in the form

$$\chi=(l_s-\boldsymbol{\lambda}_0-4\pi\mathbf{L})^{-1}, \tag{4.8}$$

identical to that found in the usual spherical model treatment. See I, Eq. (4.11).

Equation (4.6) reduces to the Curie-Weiss form only at sufficiently high temperatures that $\theta(T)$ can be replaced by the limiting "paramagnetic" temperature,

$$\theta=\theta(\infty)=(n\mu^2/3k)W(\infty). \tag{4.9}$$

Taking (3.18) in the limit as T (and hence l) approaches infinity, and using $\langle\lambda\rangle=0$, we get

$$W(\infty)=\lambda_0+4\pi L, \tag{4.10}$$

$$W(\infty)=4\pi L'+(2S(S+1)/n\mu^2)\textstyle\sum_j J_{ij}, \tag{4.11}$$

where (2.10) and (2.2) have been used to evaluate λ_0. The term $4\pi L'$ is the usual Lorentz factor ($4\pi/3$ for cubic lattices) that arises from the dipole-dipole terms. See I (4.11)ff. Since $J/n\mu^2\gg1$ for most materials, we shall henceforth, for simplicity, omit the dipole-dipole contributions. Then,

$$W(\infty)\simeq 2ZJ/[n(g\beta)^2], \tag{4.12}$$

where $Z=J^{-1}\sum_j J_{ij}$ can for nearest neighbor interactions (only) be interpreted as the coordination number.

At finite temperatures above the critical temperature the Weiss coefficient (3.18) can be rewritten in the form

$$W(T)=W(\infty)+(3kT/n\mu^2)-t_s. \tag{4.13}$$

Using the general expansion[6] of l_s in inverse powers of T Eq. I (8.13) and specializing the results to isotropic exchange forces, we find

$$W(T)/W(\infty)\simeq 1-b\langle(\lambda/\lambda_0)^2\rangle-b^2\langle(\lambda/\lambda_0)^3\rangle -b^3[\langle(\lambda/\lambda_0)^4\rangle-2\langle(\lambda/\lambda_0)^2\rangle^2]+\cdots, \tag{4.14}$$

$$b=\theta(\infty)/T;\quad \theta(\infty)=2ZS(S+1)J/(3k), \tag{4.15}$$

$$\lambda/\lambda_0=(ZJ)^{-1}\textstyle\sum_j J_{ij}\exp[i\mathbf{p}\cdot\mathbf{r}_{ji}]. \tag{4.16}$$

Using (4.6) and (4.14), we can write the inverse susceptibility χ in the general form:

$$n\mu^2/(3kT\chi)\simeq 1-b+b^2\langle(\lambda/\lambda_0)^2\rangle+b^3\langle(\lambda/\lambda_0)^3\rangle +b^4[\langle(\lambda/\lambda_0)^4\rangle-2|\langle(\lambda/\lambda_0)^2\rangle|^2]+\cdots. \tag{4.17}$$

Comparing with Eqs. I (8.11) and I (8.12), we see that

$$\langle(\lambda/\lambda_0)^2\rangle=(ZJ)^{-2}\textstyle\sum_j J_{ij}J_{ji}, \tag{4.18}$$

$$\langle(\lambda/\lambda_0)^3\rangle=(ZJ)^{-3}\textstyle\sum_{jk} J_{ij}J_{jk}J_{ki}, \tag{4.19}$$

$$\langle(\lambda/\lambda_0)^4\rangle=(ZJ)^{-4}\textstyle\sum_{jkl} J_{ij}J_{jk}J_{kl}J_{li}. \tag{4.20}$$

For the case of nearest neighbor interactions only, the number of terms in the cluster sums (4.18)–(4.20) have a simple interpretation: the number of two step, three step, or four step paths, respectively, that return to the origin. For a simple cubic lattice, for example, there are 6 two step paths, no three step paths and 90 four step paths. Using $Z=6$, we have $\langle(\lambda/\lambda_0)^2\rangle=1/Z=\frac{1}{6}$ and $\langle(\lambda/\lambda_0)^4\rangle=90/(6)^4=5/72$, for a simple cubic lattice.

The first two terms in (4.17) yield the Curie-Weiss law, and the remaining terms represent deviations. For temperatures that are not sufficiently high for the power expansion in b to converge rapidly, it is more expedient to use the exact formulas (4.6), (4.7), (4.13) in conjunction with (3.14). A more detailed discussion of the susceptibility for the cubic lattices will be presented in Sec. 7.

5. SPONTANEOUS FERROMAGNETISM

Spontaneous ferromagnetism exists if Eq. (4.1) possess a solution $M\neq0$ where there is no external field: $H_0=0$. We should however, neglect the distinction between H_0 and H due to depolarization produced by the dipole-dipole interactions since the latter causes a break-up into domains.[18] Equation (4.1) can now be rewritten in the form

$$\left(\frac{M}{ng\beta S}\right)=B_S\left(\frac{3S}{S+1}\frac{\theta(T)}{T}\frac{M}{ng\beta S}\right). \tag{5.1}$$

A nonvanishing solution exists if the slope of the right-hand side with respect to the variable $(M/ng\beta S)$ is greater than unity. According to (4.5) this will occur when $\theta(T)\geq T$, so that the critical temperature satisfies

$$\theta(T_c)=T_c. \tag{5.2}$$

[18] If dipole-dipole forces are included, the largest eigenvalue will not be λ_0 since λ_0 contains $-4\pi L$, but rather $\lambda(\hat{p})$ for small p which approaches $\lambda_0+4\pi L$ as $p\to0$ i.e., the lowest energy state possesses some oscillations of magnetization, or domains, so chosen as to reduce the depolarization energy.

However the condition $\theta(T)\geq T$ or $W(T)\geq(3kT/n\mu^2)$ cannot be satisfied in view of (3.14) with $M=M'=0$ and (3.18) with $L=0$ unless $t_s=\lambda_0$. However $t_s\geq\lambda_m$, where λ_m is the maximum eigenvalue. Therefore a necessary condition for the existence of a ferromagnetic transition is that λ_0 be the maximum eigenvalue (i.e., the ferromagnetic state be lowest in energy). In addition, however, t_s must assume the value $\lambda_m=\lambda_0$ at a finite temperature (not absolute zero). And this will occur in view of (3.14) only if $\langle(\lambda_m-\lambda)^{-1}\rangle$ is a convergent integral. These two conditions were previously obtained in Sec. 2, and in reference 6 were used to explain the existence of a transition in three dimensions but not in one or two.

We may note that the temperature dependence of the Weiss coefficient $W(T)$ is essential to an understanding of the existence or nonexistence of a phase transition. Constant W always implies the existence of a phase transition. Conversely $W(T)$ must approach zero as T approaches zero to avoid a phase transition.

In the spherical model t_s sticks at the value $\lambda_0=\lambda_m$ for all $T<T_c$. Thus $W(T)$ remains constant at the value $W(T_c)$ for all $T<T_c$ with

$$W(T_c)=\langle(\lambda_0-\lambda)^{-1}\rangle^{-1}=3kT_c/n\mu^2. \tag{5.3}$$

The ratio of the paramagnetic temperature to the ferromagnetic or Curie temperature can then be written

$$\frac{\theta}{T_c}=\frac{\theta(\infty)}{\theta(T_c)}=\frac{W(\infty)}{W(T_c)}=\frac{\lambda_0}{\langle(\lambda_0-\lambda)^{-1}\rangle^{-1}}$$

$$=\left\langle\left(1-\frac{\lambda}{\lambda_0}\right)^{-1}\right\rangle. \tag{5.4}$$

Ratios θ/T_c for several lattice types are listed in Table II. They are all greater than unity. From (3.18) and (3.14) we learn that

$$dW/dt_s>0, \quad dT/dt_s\geq(n\mu^2/3k), \tag{5.5}$$

so that

$$dW/dT>0 \quad \text{and} \quad d\theta(T)/dT>0. \tag{5.6}$$

Thus we arrive at the conclusion that $\theta>T_c$ for *ferromagnetic* lattices is general (in the spherical model) and does not depend on the range or strength of the interaction.

6. ANTIFERROMAGNETIC LATTICES

The effective field, $\mathbf{H}_{\text{eff}}{}^s=\mathbf{H}+W\mathbf{M}+W'\mathbf{M}'y_s{}^\tau$, may be used to investigate susceptibility and antiferromagnetic order in an antiferromagnetic material, i.e., a material whose largest eigenvalue λ_τ (lowest energy) corresponds to an antiferromagnetic state.[19] The normal coordinate[6] vector $\mathbf{y}_\tau$, one or more of whose components has the eigenvalue λ_τ, can be expanded in the form

$$\mathbf{y}_\tau=N^{-\frac{1}{2}}\sum\mathbf{y}_s{}^\tau\cdot\boldsymbol{\varepsilon}_s. \tag{6.1}$$

Comparison with (3.2) indicates that

$$\mathbf{M}'/n\mu=N^{-\frac{1}{2}}\mathbf{y}_\tau, \tag{6.2}$$

i.e., the order parameter is proportional to the normal coordinate associated with the largest eigenvalue (lowest energy) of the system. The coefficients $y_s{}^\tau$ usually take the value plus one on one sublattice and minus one on the other sublattice.[20] If M_+ and M_- are the magnetizations of the two sublattices, so that

$$\mathbf{M}=\tfrac{1}{2}(\mathbf{M}_++\mathbf{M}_-),$$
$$\mathbf{M}'=\tfrac{1}{2}(\mathbf{M}_+-\mathbf{M}_-), \tag{6.3}$$

the corresponding molecular fields are

$$\mathbf{H}_{\text{eff}}{}^\pm=\mathbf{H}+W\mathbf{M}\pm W'\mathbf{M}'. \tag{6.4}$$

Thus, from (4.1),

$$(\mathbf{M}_\pm/ng\beta S)=B_S(y_\pm)\mathbf{H}_{\text{eff}}{}^\pm/H_{\text{eff}}{}^\pm,$$
$$y_\pm=g\beta S|H_{\text{eff}}{}^\pm|/kT$$
$$=g\beta S/kT|\mathbf{H}+W\mathbf{M}\pm W'\mathbf{M}'|. \tag{6.5}$$

Following Van Vleck,[1] we investigate spontaneous order by setting $H=M=0$. The effective field then changes sign from one sublattice to the next. Therefore $-\mathbf{M}_-=\mathbf{M}_+=\mathbf{M}'$ (thus verifying that $\mathbf{M}=0$). The order parameter therefore obeys

$$(M'/ng\beta S)=B_S\left(\frac{3S}{S+1}\frac{\theta'(T)}{T}\frac{M'}{ng\beta S}\right), \tag{6.6}$$

where

$$\theta'(T)=n\mu^2W'(T)/(3k). \tag{6.7}$$

As in the ferromagnetic case, spontaneous order occurs only if $\theta'(T)\geq T$ so that the transition temperature obeys

$$\theta'(T_c)=T_c. \tag{6.8}$$

Furthermore, by arguments analogous to those of the previous section, such a transition exists only (1) if λ_τ is the largest eigenvalue (2) $\langle(\lambda_\tau-\lambda)^{-1}\rangle$ is finite, the usual conditions of the spherical model. For $T\leq T_c$, $\theta'(T)$ takes the value $\theta'(T_c)=T_c$ in (6.6).

Above the Curie temperature no spontaneous order

TABLE II. The ratio $\theta(\infty)/T_c$ of the paramagnetic temperature $\theta(\infty)$ to the Curie temperature T_c for the cubic lattices for positive and negative exchange integrals.

	Simple cubic	Body-centered cubic	Face-centered cubic
$J>0$	1.51538	1.39320	1.34466
$J<0$	−1.51538	−1.39320	···

[19] For isotropic exchange forces, the largest eigenvalue will be triply degenerate to account for the fact that all orientations of antiferromagnetic order possess the same energy. The order parameter, $\mathbf{M}'/n\mu$, is, in fact, a vector because of this triple degeneracy. If further degeneracy were present, additional order parameters would have to be used in the entire analysis. For simplicity of exposition, we neglect the possibility of additional degeneracy.

[20] More complicated results (see reference 17) are possible. In particular, if the lowest energy state is degenerate, four or more sublattices may be needed in a sublattice treatment.

$\mathbf{M}'$ exists and the Eqs. (6.5) for the magnetization reduce to (4.1). The susceptibility above the Curie temperature then obeys the results obtained in Sec. 4. One need only remember that with a negative exchange integral $\theta(T)$ will be negative. The ratio of paramagnetic to Curie temperatures is given by

$$\frac{\theta}{T_c}=\frac{\theta(\infty)}{\theta'(T_c)}=\frac{W(\infty)}{W'(T_c)}=\lambda_0\langle(\lambda_\pi-\lambda)^{-1}\rangle. \tag{6.9}$$

In contrast to the ferromagnetic case $|\theta|/T_c$ may be less than as well as greater than unity depending on the relative magnitudes of λ_0 and λ_π. This result differs from the elementary molecular field theory approach[1] in which $|\theta|/T_c$ is always unity, when only nearest neighbor interactions are assumed.

The susceptibility below the Curie temperature can be obtained from (6.5) and (6.3) in the manner of Van Vleck.[1] Only if H is either parallel or perpendicular to M' will M be parallel to the applied H. For small applied fields $|H+WM|\ll W'M'$. Thus if $H\|M'$, H_{eff}^{+} is parallel to H and H_{eff}^{-} is antiparallel to H. Also

$$y_{-}^{+}=y_0\pm(g\beta S/kT)(H+WM), \tag{6.10}$$

where

$$y_0=(g\beta S/kT)W'M'.$$

By expanding (6.5) around y_0, the parallel susceptibility is found to be

$$\chi_{\|}(T)=\frac{n\mu^2S}{k(S+1)}\frac{B_S'(y_0)}{T-3S(S+1)^{-1}B_S'(y_0)\theta(T_c)}. \tag{6.11}$$

For $\mathbf{H}\perp\mathbf{M}'$, $y^{\pm}\simeq y_0$ and

$$\cos(H_{\text{eff}}^{\pm},H)\simeq|H+WM|/W'M', \tag{6.12}$$

where M_+ and M_- are to be combined vectorially by using (6.5). Eliminating $B_S(y_0)$ with the help of (6.6), we find

$$\chi_\perp(T)=\frac{n\mu^2}{3k}\frac{1}{T_c-\theta(T_c)}, \tag{6.13}$$

i.e., $\chi_\perp(T)$ is independent of temperature and is equal to the total susceptibility just above the Curie temperature, Eq. (4.6) with $T=T_c$. We furthermore verify the usual relation,

$$\chi_{\|}(T_c)=\chi_\perp(T_c)=\chi(T_c). \tag{6.14}$$

The usual molecular field susceptibility[1,13] $\chi_\perp(T)$ differs from (6.13) in that $\theta(T_c)$ is replaced by θ. However, according to (5.6) $\theta(\infty)>\theta(T_c)$, an algebraic inequality that remains true even though θ and $\theta(T_c)$ are both negative. Our result (6.13), therefore yields a lower susceptibility at the Curie temperature, a change that generally improves agreement with experiment.[13]

If $\mathbf{H}$ is neither perpendicular nor parallel to $\mathbf{M}'$, we find[1] by decomposing in these two directions that

$$\begin{aligned}&\mathbf{M}\cdot\mathbf{H}/H^2=\chi_{\|}\cos^2(\mathbf{H},\mathbf{M}')+\chi_\perp\sin^2(\mathbf{H},\mathbf{M}'),\\&|\mathbf{M}\times\mathbf{H}|/H^2=\sin(\mathbf{H},\mathbf{M}')\cos(\mathbf{H},\mathbf{M}')[\chi_\perp-\chi_{\|}].\end{aligned} \tag{6.15}$$

For isotropic powder sample, we may average over orientations to obtain the usual results,

$$\begin{aligned}&\chi(T)=\tfrac{1}{3}\chi_{\|}(T)+\tfrac{2}{3}\chi_\perp(T),\\&\chi(0)=\tfrac{2}{3}\chi(T_c),\end{aligned} \tag{6.16}$$

where, in the last relation, we have used (6.13), (6.14), and $\chi_{\|}(0)=0$. Note that the above pair of equations will not be valid in crystals requiring the use of more than one order parameter.

7. THE CUBIC LATTICES

In this section we shall indicate the application of the general results previously obtained to the simple cubic (s.c.), body-centered cubic (b.c.c.) and face-centered cubic (f.c.c.) lattices. We shall assume isotropic exchange forces with $J_{ij}=J$ for i and j nearest neighbors and $J_{ij}=rJ$ for second nearest neighbors. The eigenvalues (2.10) can then be rewritten using (2.2) in the form:

$$\begin{aligned}\text{s.c.:}\quad\lambda(\mathbf{p})/A=&(\cos p_1+\cos p_2+\cos p_3)\\&+2r(\cos p_1\cos p_2+\cos p_2\cos p_3\\&+\cos p_3\cos p_1),\end{aligned} \tag{7.1}$$

$$\begin{aligned}\text{b.c.c.:}\,\lambda(\mathbf{p})/A=&\cos p_3+\cos(p_3-p_2)+\cos(p_3-p_1)\\&+\cos(p_1+p_2-p_3)+r[\cos p_1\\&+\cos p_2+\cos(p_1+p_2-2p_3)],\end{aligned} \tag{7.2}$$

$$\begin{aligned}\text{f.c.c.:}\,\lambda(\mathbf{p})/A=&\cos p_1+\cos p_2+\cos p_3+\cos(p_2-p_3)\\&+\cos(p_3-p_1)+\cos(p_1-p_2)\\&+r[\cos(p_2+p_3-p_1)+\cos(p_3+p_1-p_2)\\&+\cos(p_1+p_2-p_3)],\end{aligned} \tag{7.3}$$

where

$$A=4JS(S+1)/(n\mu^2)=4J/[n(g\beta)^2]. \tag{7.4}$$

In (7.2) and (7.3) the b.c.c. and f.c.c. lattices were treated in terms of their primitive translations, i.e., as monatomic lattices. In terms of the cube, the basic vectors used for the b.c.c. case were

$$a_1=(1,0,0),\quad a_2=(0,1,0),\quad a_3=(\tfrac{1}{2},\tfrac{1}{2},\tfrac{1}{2}),$$

whereas for the f.c.c. lattice they were

$$a_1=(0,\tfrac{1}{2},\tfrac{1}{2}),\quad a_2=(\tfrac{1}{2},0,\tfrac{1}{2}),\quad a_3=(\tfrac{1}{2},\tfrac{1}{2},0).$$

The sum (2.10), or more simply $\sum_j J_{0j}\cos(\mathbf{p}\cdot\mathbf{r}_j)$, was evaluated by expressing $\mathbf{r}_j$ in terms of the primitive translations and $\mathbf{p}$ in terms of the corresponding reciprocal vectors:

$$\mathbf{r}_j=j_1\mathbf{a}_1+j_2\mathbf{a}_2+j_3\mathbf{a}_3, \tag{7.5}$$

$$\mathbf{p}=p_1\mathbf{b}_1+p_2\mathbf{b}_2+p_3\mathbf{b}_3, \tag{7.6}$$

$$\mathbf{a}_i\cdot\mathbf{b}_j=\delta_{ij}.$$

Because of the periodic boundary conditions there are exactly N discrete eigenvalues uniformly spaced over

the volume

$$0\leq p_1\leq 2\pi, \quad 0\leq p_2\leq 2\pi, \quad 0\leq p_3\leq 2\pi, \tag{7.7}$$

i.e., over one cell of the reciprocal lattice space.

Luttinger[21] has obtained a related set of eigenvalues by treating the b.c.c. lattice as a cubic lattice with two atoms per cell and the f.c.c. lattices as a cubic lattice with four atoms per cell. If $\mathbf{p}$ is expressed in terms of the unit vectors of the cubic reciprocal lattice, the new components $\kappa_1, \kappa_2, \kappa_3$, of $\mathbf{p}$ are related to those of (7.6) by

$$\text{b.c.c.:}\quad \kappa_1=p_1, \quad \kappa_2=p_2, \quad \kappa_3=2p_3-p_1-p_2, \tag{7.8}$$

$$\text{f.c.c.:}\quad \kappa_1=-p_1+p_2+p_3, \tag{7.9}$$
$$\kappa_2=p_1-p_2+p_3,$$
$$\kappa_3=p_1+p_2-p_3,$$

and the eigenvalues reduce to Luttinger's form:

$$\text{b.c.c.:}\lambda(\boldsymbol{\kappa})/A=4\cos\tfrac{1}{2}\kappa_1\cos\tfrac{1}{2}\kappa_2\cos\tfrac{1}{2}\kappa_3 +r[\cos\kappa_1+\cos\kappa_2+\cos\kappa_3], \tag{7.10}$$

$$\text{f.c.c.:}\quad \lambda(\boldsymbol{\kappa})A=2[\cos\tfrac{1}{2}\kappa_2\cos\tfrac{1}{2}\kappa_3+\cos\tfrac{1}{2}\kappa_3\cos\tfrac{1}{2}\kappa_1 +\cos\tfrac{1}{2}\kappa_1\cos\tfrac{1}{2}\kappa_2] +r[\cos\kappa_1+\cos\kappa_2+\cos\kappa_3]. \tag{7.11}$$

The saddle conditions may be obtained directly from (3.14), (7.1), (7.10), and (7.11). To illustrate the results with equations of moderate length we shall introduce the dimensionless variables

$$z=t/\lambda_0, \quad b=\theta(\infty)/T, \tag{7.12}$$

and assume nearest neighbor interactions only. Then the relation between t and T or z and b is given by

$$F(z)=\langle[z-(\lambda/\lambda_0)]^{-1}\rangle=b, \tag{7.13}$$

where the function $F(z)$ for the three cubic lattices may be written explicitly,

$$F_{\text{s.c.}}(z)=\frac{1}{\pi^3}\int_0^\pi\int\int\frac{dudvdw}{z-\frac{1}{3}(\cos u+\cos v+\cos w)}, \tag{7.14}$$

$$F_{\text{b.c.c.}}(z)=\frac{1}{\pi^3}\int_0^\pi\int\int\frac{dudvdw}{z-\cos u\cos v\cos w}, \tag{7.15}$$

$$F_{\text{f.c.c.}}(z)=\frac{1}{\pi^3}\int_0^\pi\int\int\times\frac{dudvdw}{z-\frac{1}{3}(\cos u\cos v+\cos v\cos w+\cos w\cos u)}. \tag{7.16}$$

In terms of these dimensionless units, the susceptibility χ, (4.6) with (4.13) can be rewritten in the simple form,

$$(2ZJ\chi)/[n(g\beta)^2]=(z-1)^{-1}, \tag{7.17}$$

where z is determined as a function of temperature through the saddle condition (7.13). A plot of the susceptibilities for the cubic lattices is given in Fig. 1. $F_{\text{b.c.c.}}(z)$ is plotted in Fig. 2.

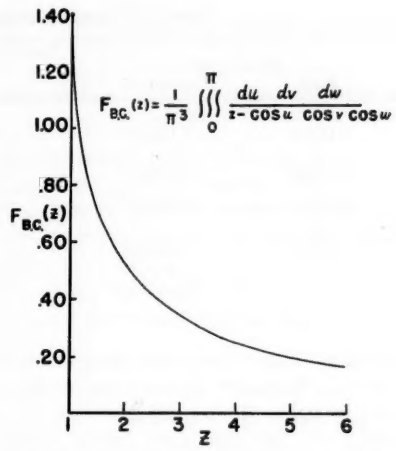

FIG. 2. The function $F(z)$ that enters the saddle condition equation is plotted for the body-centered cubic case. Results for simple cubic and face-centered cubic lattices were so close that plotting on the scale used would have been impractical. Accurate values for these functions are easily obtained from Eq. (B2).

The high-temperature susceptibility has already been discussed in detail in Sec. 4 [see (4.17)] and evaluated in terms of the moments $\langle(\lambda/\lambda_0)^n\rangle$. The first few moments for the cubic lattices are listed in Table III. In Appendix A, it will be shown that these moments have the asymptotic form,

$$\langle(\lambda/\lambda_0)^n\rangle\sim A(n+\alpha)^{-\frac{1}{2}}, \tag{7.18}$$

at least for even n.

The susceptibility near the Curie point depends on the asymptotic form (7.18), or on the behavior of $F(z)$ near $z=1$. For three-dimensional lattices we shall show in Appendix B that

$$F(z)\simeq F(1)-C(z-1)^{\frac{1}{2}}, \tag{7.19}$$

so that the susceptibility near the Curie temperature is given by

$$2ZJ\chi/[n(g\beta)^2]\simeq C^2T_c^4\theta^{-2}(\infty)(T-T_c)^{-2}. \tag{7.20}$$

Values of C for the three cubic lattices are discussed in Appendix B.

For ferromagnetic lattices, J and z are both positive, and a transition occurs when $z=t/\lambda_0=1$, i.e., at the same temperature as the divergence in the susceptibility. The Curie temperatures using (7.13) are then given by

$$\theta(\infty)/T_c=F(1), \tag{7.21}$$

which also yields the ratio of the paramagnetic temperature $\theta=\theta(\infty)$ to the ferromagnetic temperature T_c. The

[21] J. Luttinger, Phys. Rev. **81**, 1015 (1951).

TABLE III. Moments of the eigenvalue spectrum for the cubic lattices.

	Simple cubic		Body-centered cubic		Face-centered cubic	
n	Exact	Asymptotic	Exact	Asymptotic	Exact	Asymptotic
1	0		0		0	
2	0.16666	0.16693	0.12500	0.12850	0.083333	0.059018
3	0		0		0.027778	0.035628
4	0.06944	0.06912	0.05273	0.05321	0.026042	0.024439
5	0		0		0.017361	0.018086
6	0.03987	0.03982	0.03052	0.03065	0.014146	0.014078
7	0		0		0.011253	0.011358
8	0.026631	0.026626	0.02044	0.02050	0.009392	0.009414
n		$\frac{(6/\pi)^{\frac{1}{2}}}{4(n+0.5)^{\frac{1}{2}}}$	$\left[\frac{\Gamma[\frac{1}{2}(n+1)]}{\pi^{\frac{1}{2}}\Gamma(\frac{1}{4}n+1)}\right]^3$	$\frac{(2/\pi)^{\frac{1}{2}}}{(n+0.5)^{\frac{1}{2}}}$		$\frac{(3/\pi)^{\frac{1}{2}}}{4(n+0.5)^{\frac{1}{2}}}$

three integrals (7.14)–(7.16) have been evaluated exactly at $z=1$ by Watson.[22] The resulting values of θ/T_c are quoted in Table II. A comparison of the critical temperatures T_c for the three lattice types with corresponding values computed by Weiss[7] and Zehler[10] is given in Table I. The excellent agreement between the spherical model and the Weiss, Zehler methods is partly fortuitous, and will be discussed in Sec. 8.

It may be of interest to note that θ/T_c in the spherical model depends on the lattice type but not on the spin, whereas T_c is also sensitive to spin.

For the antiferromagnetic case, the exchange integral J is negative. Thus z and b are both negative. Equations (7.12) to (7.17) remain formally correct providing we remember b and z are negative. Thus (7.17) now shows that the susceptibility is finite at all temperatures.

Since $F_{s.c.}(z)$ and $F_{b.c.c.}(z)$ are odd functions of z, it follows from (7.13) that the dependence of $|z|$ on $|b|$ is the same as for a ferromagnetic lattice of the same $|J|$. Furthermore, for the s.c. and b.c.c. lattices $\lambda_\pi=-\lambda_0=|\lambda_0|$ so that the antiferromagnetic transition temperatures in units $kT_c/|J|$ are identical to those quoted in Table I for the corresponding ferromagnetic lattice.

For face-centered cubic lattices, $F_{f.c.c.}(z)$ is not odd. Furthermore for $J<0$, the maximum eigenvalue occurs when

$$\tfrac{1}{2}\kappa_1=u=0, \quad \tfrac{1}{2}\kappa_2=v=\pi, \quad \tfrac{1}{2}\kappa_3=w=\pi,$$

so that $\lambda_\pi/\lambda_0=-\frac{1}{3}$. Thus the antiferromagnetic transition temperature may be obtained from (7.13) by setting $z=-\frac{1}{3}$:

$$\theta(\infty)/T_c=F_{f.c.c.}(\lambda_\pi/\lambda_0)=F_{f.c.c.}(-\tfrac{1}{3}), \qquad (7.22)$$

or

$$\frac{|\theta(\infty)|}{T_c}=\frac{3}{\pi^3}\int_0^\pi\int\int \times\frac{dudvdw}{1+\cos u\cos v+\cos v\cos w+\cos w\cos u}=\infty, \qquad (7.23)$$

because the integral diverges at the point $u=0$, $v=\pi$, $w=\pi$.

It may be of interest to explain why $F(z)$ is odd for s.c. and b.c.c. lattices while the f.c.c. lattice is not. The reason is that $\langle\lambda^n(p)\rangle$ for odd n vanishes in the first two cases, and not in the third, i.e., by using (4.18) ff, it is not possible in a s.c. or b.c.c. lattice to return to the origin in an odd number of steps, whereas in the f.c.c. lattice it is possible to do so.

8. CONCLUSIONS

The predictions made by the spherical model for the transition temperatures in the cubic lattices are in surprisingly good agreement with corresponding values calculated by Weiss[7] and Zehler[10] as Table I shows. Zehler's results are based on Opechowski's procedure[11] for expanding the reciprocal susceptibility $1/\chi$ in inverse powers of the temperature. He then estimates T_c from the temperature at which $1/\chi$ vanishes, using a two term expansion, then a three term, then a four term expansion. Since this procedure converges, and he used exact expansion coefficients, Zehler's results can be regarded as within a few percent of the (unknown) exact transition temperature.

The unusual agreement with Zehler's results achieved by the spherical model must be regarded as at least partly fortuitous. Perhaps the explanation is as follows: we have really made two approximations (a) we have replaced the quantum-mechanical lattice by a classical lattice—thus neglecting quantum fluctuations (b) we have then replaced the classical lattice by a spherical lattice—thus introducing some nonphysical fluctuations. It seems possible that the errors involved in using the two approximations at least partly cancel.

Although we do not feel at this point, that the spherical model need be taken seriously from the quantitative point of view many of the qualitative conclusions arrived at in this paper may turn out to have a more general validity. For example, the statement that the effective field is of the form $\mathbf{H}+W(T)\mathbf{M}+W'(T)\mathbf{M}'y_s^\pi$ with the temperature-dependent Weiss coefficient $W(T)$, and a corresponding term $W'(T)$ which changes sign from one sublattice to another, is likely to remain true. Indeed, the more specific statements $dW/dT>0$, $dW'/dT>0$ are also likely to remain true. Furthermore, since the actual transition temperature T_c depends on $W(T_c)$ rather than the usual molecu-

[22] G. N. Watson, Quart. J. Math. **10**, 266 (1939).

lar field $W(\infty)$, the latter procedure overestimates W and hence underestimates T_c.

A corollary of the above conclusion is that in the ferromagnetic case $\theta/T_c>1$ and in the antiferromagnetic case $|\theta|/T_c$ can be greater or less than unity. These conclusions do not, as in the usual molecular field case[13] require interactions beyond nearest neighbors but, in the spherical model are true in general.

As a general conclusion, we may state that the dependence of $W(T)$, and $W'(T)$ on temperature is such as to reduce the principal discrepancies between the usual molecular field theory and experiment.[1,13]

To improve the quantitative accuracy of the coefficients $W(T)$ and $W'(T)$ the spherical model must be modified in a more fundamental way than we have done in this paper. Here, we have treated in spherical model all dipoles but one. The last dipole is then treated exactly. A natural generalization of this procedure is to treat exactly a cluster of dipoles with the remainder of the lattice treated in spherical model. As in (1.2), one must integrate the Boltzmann exponential over all dipoles but those in the cluster. The result is a distribution function for the cluster:[23]

$$Q(\boldsymbol{\varepsilon}_s)=\exp[-K\sum \boldsymbol{\varepsilon}_r\cdot(\mathbf{D}^{-1})_{rs}\cdot\boldsymbol{\varepsilon}_s+(\mu/kT)\sum \boldsymbol{\varepsilon}_r\cdot\mathbf{H}_{\mathrm{eff}}{}^r],$$

where

$$K=\tfrac{1}{2}n\mu^2/kT,$$

$$\mathbf{D}_{rs}=\langle[(t-G)^{-1}]_{rs}\rangle_{\mathrm{Av}}$$

$$=\frac{1}{N}\sum_{\mathbf{p}}{}''[\mathbf{t}-\boldsymbol{\lambda}(\mathbf{p})]^{-1}\exp(i\mathbf{p}\cdot\mathbf{r}_{ji}),$$

$$\mathbf{H}_{\mathrm{eff}}{}^r=\mathbf{H}_0+\mathbf{W}_r(T)\cdot\mathbf{M}+\mathbf{W}_r'(T)\cdot\mathbf{M}'y_r{}^\pi,$$

$$\mathbf{W}_r(T)=\textstyle\sum_s \mathbf{D}_{rs}{}^{-1}-(\mathbf{t}-\boldsymbol{\lambda}_0),$$

$$\mathbf{W}_r'(T)=\textstyle\sum_s(y_r{}^\pi)^{-1}\mathbf{D}_{rs}{}^{-1}y_s{}^\pi.$$

The sum in the exponential is over the variables of the cluster. The double prime over the sum in the definition of D_{rs} implies that the terms in λ_0 and λ_π are to be omitted. Although D_{rs} is an $N\times N$ matrix, we restrict r and s to the variables of the cluster. The reciprocal of this truncated matrix is then denoted $(D^{-1})_{rs}$. The integration variable t is to be replaced by its saddle value obtained from the usual spherical approximation.

The Bethe-Peierls type consistency requirement that all dipoles in the cluster have the same mean value is an overdetermining condition since the molecular fields $H_{\mathrm{eff}}{}^r$ are known. One possible procedure is to allow the interactions *in the remainder of the lattice* to be modified by an unknown temperature-dependent factor whose value is then determined by the self-consistency requirement. This procedure has been applied by Levitas[23,24] to the Ising model problem in two and three dimensions.

[23] A. Levitas and M. Lax, Phys. Rev. 90, 374 (A) (1953).

APPENDIX A. ASYMPTOTIC FORM OF THE MOMENTS

If the eigenvalue $\lambda(\mathbf{p})$ or $\lambda(u,v,w)$ has a maximum value λ_m at some point $\mathbf{p}_m$, then the value of the moment $\langle(\lambda(\mathbf{p})/\lambda_m)^n\rangle$ for large n is determined almost entirely by the behavior of $\lambda(\mathbf{p})$ near p_m. In that neighborhood, we can write

$$\lambda(p)/\lambda_m\simeq 1-ar^2+br^4$$
$$\simeq\exp[-ar^2+(b-\tfrac{1}{2}a)r^4], \qquad \text{(A1)}$$

where $r^2=(\mathbf{p}-\mathbf{p}_m)^2$ and a and b can be functions of the angles. Thus

$$\langle(\lambda(p)/\lambda_m)^n\rangle$$

$$\simeq(2\pi)^{-3}\int d\Omega\int_0^\infty \exp\{-n[ar^2-(b-\tfrac{1}{2}a)r^4]\}r^2dr \qquad \text{(A2)}$$

$$\simeq\tfrac{1}{8}\pi^{-\frac{1}{2}}\langle a^{-\frac{1}{2}}\rangle(n+\alpha)^{-\frac{1}{2}}, \qquad \text{(A3)}$$

where

$$\alpha=(5/4)-(5/2)\langle ba^{-7/2}\rangle/\langle a^{-\frac{1}{2}}\rangle, \qquad \text{(A4)}$$

and $\langle\ \rangle\equiv(4\pi)^{-1}\int d\Omega$.

Equation (A2) has been written assuming that the integration around $\mathbf{p}_m$ can be extended to infinity in all directions. In general, the point $\mathbf{p}_m$ will be at one of the boundary points of the unit cell so that only $\frac{1}{2}$, $\frac{1}{4}$, or $\frac{1}{8}$ of the region will be available. There will, however, be several equivalent points $\mathbf{p}_m$. The product of these two factors yields a multiplicity or weight factor $w(\lambda_m)$. In addition, for the s.c. and b.c.c. lattices, the eigenvalue $-\lambda_m$ occurs with equal weight: $w(-\lambda_m)=w(\lambda_m)$ and yields the same contribution to the integral. Thus the coefficient A of the asymptotic moment (7.18) is

$$A=\langle a^{-\frac{1}{2}}\rangle[w(\lambda_m)+w(-\lambda_m)]/(8\pi^{\frac{3}{2}}). \qquad \text{(A5)}$$

For the f.c.c. lattice the eigenvalue $(-\lambda_m)$ does not occur and (A5) is valid providing we regard $w(-\lambda_m)=0$ for the f.c.c. lattice.

Table IV lists the values of a (which happen to be independent of angle), b, $\langle b\rangle$, $w(\lambda_m)$, and A for the cubic lattices.

TABLE IV. Data needed for the asymptotic form of the moments, where I has the form $(u^4+v^4+w^4)/(u^2+v^2+w^2)^2$ and $\langle I\rangle=\frac{3}{5}$.

Lattice type	s.c.	b.c.c.	f.c.c.
a	1/6	1/2	1/3
b	$I/72$	$1/8-(1/12)I$	$1/24-(1/72)I$
$\langle b\rangle$	1/120	3/40	1/30
$w(\lambda_m)$	1	4	1
A	$(6/\pi)^{\frac{1}{2}}/4$	$(2/\pi)^{\frac{1}{2}}$	$(3/\pi)^{\frac{1}{2}}/4$
α	1/2	1/2	1/2
C	$6^{\frac{1}{2}}/(4\pi)$	$2^{\frac{1}{2}}/\pi$	$3^{\frac{1}{2}}/(2\pi)$

[24] A. Levitas, Ph.D. dissertation, Syracuse University, 1955 (unpublished).

A comparison between the exact and asymptotic values of the first eight moments is shown in Table III. The agreement is more than satisfactory for the s.c. and b.c.c. cases. For the f.c.c. case, we have neglected an eigenvalue $-(\lambda_m/3)$. The contribution of the latter eigenvalue is of the asymptotic form $(-\frac{1}{3})^n n^{-1}\ln n$ and eventually becomes negligible compared to the dominant term $n^{-\frac{1}{2}}$. The comparison between exact and asymptotic moments indeed exhibits poor agreement for the first few moments and good agreement for $n=8$, by which time this secondary contribution is negligible.

APPENDIX B. EVALUATION OF THE SADDLE CONDITION FUNCTIONS $F(z)$

The functions $F(z)$ of (7.13) possess the expansion

$$F(z)=z^{-1}\sum z^{-n}\langle(\lambda/\lambda_0)^n\rangle, \tag{B1}$$

where λ_0 coincides with λ_m for the cubic lattices. Adequate numerical values for $F(z)$ may be obtained by using the exact values of the first few moments, and asymptotic values of the remaining moments. The asymptotic terms can then be summed approximately with the help of the comparison functions $(1-1/z)^{\frac{1}{2}}$ and $(1-1/z)^{\frac{3}{2}}$ whose asymptotic terms are of the form $z^{-n}/n^{\frac{1}{2}}$ and $z^{-n}/n^{5/2}$, respectively. In this way, we obtain the useful results:

$$F(z)=[\sum_{n=0}^{8} z^{-n}\langle(\lambda/\lambda_0)^n\rangle+R(z)]/z,$$

$$R(z)\simeq A\sum_9^\infty z^{-n}/(n+0.5)^{\frac{1}{2}},$$

$$A_{s.c.}=(6/\pi)^{\frac{1}{2}}/4,\quad A_{b.c.c.}=(2/\pi)^{\frac{1}{2}},$$

$$A_{f.c.c.}=(3/\pi)^{\frac{1}{2}}/4,$$

$$R_{b.c.c.}(z)\simeq(2\pi)^{-1}\{2z^2+1-(2/z)[(z^2-1)^{\frac{1}{2}}+2(z^2-1)^{\frac{1}{2}}]-(5/4)z^{-2}-(3/8)z^{-4}-(13/64)z^{-6}-(17/128)z^{-8}\}, \tag{B2}$$

$$R_{s.c.}(z)\simeq[3\sqrt{3}/4]R_{b.c.c.}(z),$$

$$R_{f.c.c.}(z)\simeq[3\sqrt{3}/(8\pi)]\{z^{-\frac{1}{2}}[3z^{\frac{1}{2}}-3(z-1)^{\frac{1}{2}}-4(z-1)^{\frac{3}{2}}]-(1/2)-(7/8)z^{-1}-(5/16)z^{-2}-(23/128)z^{-3}-(31/256)z^{-4}-(91/1024)z^{-5}-(141/2048)z^{-6}-(1815/32\,768)z^{-7}-(2703/65\,536)z^{-8}\}.$$

For s.c. and b.c.c. lattices, only even-n terms are included in $R(z)$ and $F(z)$.

The accuracy of these expressions may be tested by evaluating them at the worst point $z=1$ and comparing with Watson's exact values of $F(1)$:

	$F_{s.c.}(1)$	$F_{b.c.c.}(1)$	$F_{f.c.c.}(1)$	
Approximate	1.51743	1.39407	1.34581	(B3)
Exact	1.51638	1.39320	1.34466.	

The approximate expressions (B2) indicate that $F(z)$ has the singular form at $z=1$ suggested in (7.19). An alternative proof can be given in the form:

$$F(1)-F(z)=(z-1)\langle[1-(\lambda/\lambda_m)]^{-1}[z-(\lambda/\lambda_m)]^{-1}\rangle$$

$$=w(\lambda_m)\frac{(z-1)}{(2\pi)^3}4\pi\int d\Omega/4\pi \times\int_0^\infty \frac{r^2dr}{(ar^2)(z-1+ar^2)}. \tag{B4}$$

so that

$$F(1)-F(z)=C(z-1)^{\frac{1}{2}}, \tag{B5}$$

with

$$C=w(\lambda_m)\langle a^{-\frac{1}{2}}\rangle/4\pi. \tag{B6}$$

Values of C are given in Table IV.

Effective Carrier Mobility in Surface-Space Charge Layers*

J. R. SCHRIEFFER
Physics Department, University of Illinois, Urbana, Illinois
(Received August 16, 1954)

Carriers held to a region near the surface by the potential well of a space charge layer may have their mobility reduced by surface scattering, if the width of the well is of the order of a mean free path. An effective mobility, which may differ from the bulk mobility by as much as a factor of ten, has been obtained from a solution of the Boltzmann equation. Solutions have been carried out for two types of potential functions: (*a*) a linear potential corresponding to a constant space-charge field, and (*b*) a solution of Poisson's equation including an external bias applied normal to the surface. The results have been used to calculate changes in surface conductance of germanium with changes in surface potential and predict the "field effect" and "channel effect" mobilities.

I. INTRODUCTION

THE surface of a semiconductor is the seat of a space-charge double layer produced by a surface charge distribution which is counterbalanced by a space-charge region consisting of holes, electrons, and impurity ions.[1,2]

The surface charge distribution arises from the trapping of holes or electrons at the surface of the material. There are three obvious types of surface traps. First, by adjusting the mathematics of the energy band solution for an ideal infinite crystal to take the surface into account, one may find allowed levels which correspond to states localized near the surface, and which lie in the forbidden gap of the energy level diagram. A second type of surface trap arises from the impurity ions found in increased quantity near the surface. A third type is that arising from chemisorbed material on the semiconductor surface. The chemisorption process in general requires a charge transfer from the body to the surface of the semiconductor. The chemisorption traps are often separated from the bulk material by an oxide layer. By changing the gaseous ambient surrounding the sample, one can change the density of chemisorption traps and therefore alter the magnitude of the space-charge double layer.

Morrison[3] has used this technique on a free germanium surface to displace the energy bands near the surface relative to the Fermi level. The conductance of the sample is changed by such a displacement because the carrier concentrations in the space-charge region are different from the bulk concentrations. Figure 1(a) shows a *p*-type semiconductor with a large positive charge on the surface causing an *n*-type surface layer, or "inversion layer," to be formed. Similarly, a large negative surface charge would cause the bands to rise and a strongly *p*-type layer would exist at the surface. The intermediate case is obtained when a small positive charge exists on the surface which is counterbalanced primarily by a space-charge of impurity ions, termed an "exhaustion layer." Since the hole concentration is reduced under such conditions while the electron concentration is still relatively small, the conductivity in an exhaustion layer will be smaller than that of the bulk semiconductor.

If an alternating field is applied normal to the surface, by arranging the semiconductor to be one plate of a condenser, an effective mobility of the carriers introduced by this field can be determined from the change in conductance of the sample. This type of effective mobility will be called the "field effect" mobility. Unlike the bulk carrier mobilities, the field effect mobility can change its sign, the positive value corresponding to electrons. Morrison finds in general that the sign of the field effect mobility changes when the ambient causes the conductance to go through a minimum value.[4]

Brown[5] and Kingston[6] have measured the conductance of a "channel" or *n*-type surface layer on a normally *p*-type base region of an *n–p–n* junction transistor, as a function of applied reverse bias. By fitting theoretical curves to experimental data, Brown estimates the mobility of electrons in the channel to be one-fifth to one-tenth the bulk mobility. Kingston carried out measurements in a water vapor atmosphere for several values of vapor pressure. The water vapor tends to form a positive surface charge distribution on the *p*-type base and creates an *n*-type inversion layer as described above. Kingston finds the surface conductance appears to vary inversely with applied bias, and has proposed a theory to explain this effect by taking into account the reduction in mobility of the channel electrons.

To estimate the change in conductance of a semiconductor due to a space-charge layer existing at the surface, one must consider at least two effects. The first is simply the change in the number of holes and electrons in the space-charge region. The second is the

* This work was supported by a grant from Motorola, Inc.
[1] J. Bardeen, Phys. Rev. **71**, 717 (1947).
[2] W. H. Brattain and J. Bardeen, Bell System Tech. J. **32**, 1 (1953).
[3] S. R. Morrison, Tech. Report No. 2, Electrical Engineering Research Laboratory, University of Illinois, and private communication.
[4] W. Shockley and G. L. Pearson, Phys. Rev. **74**, 232 (1948).
[5] W. L. Brown, Phys. Rev. **91**, 518 (1953).
[6] R. H. Kingston, Phys. Rev. **93**, 346 (1954).

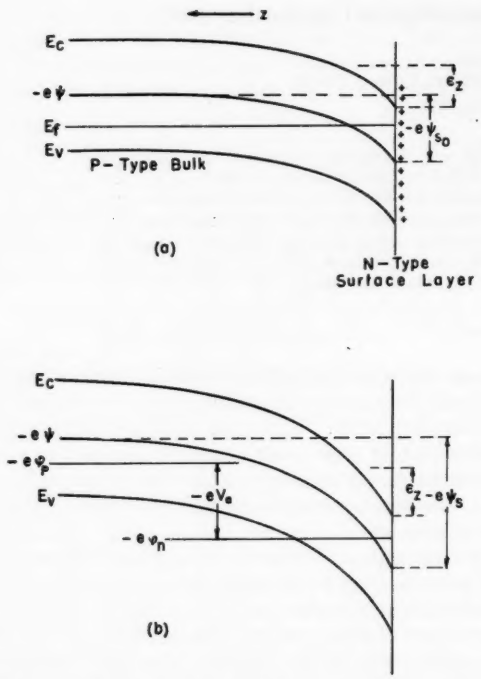

FIG. 1. (a) Energy level diagram of an n-type inversion layer existing at the free surface of a p-type material. (b) A voltage V_a applied across the surface shown in (a).

reduction of the carrier mobility by surface scattering if the width of the space-charge potential well is comparable to a mean free path or less. For example, if electrons in an n-type inversion layer are held near the surface by the potential well, the surface may scatter the electrons more frequently than the conventional bulk scattering mechanism, therefore reducing the electronic mobility appreciably. This reduction may be quite important in the channel effect where widths of the order of several hundred angstroms are attained. If a large dipole exists at the free surface of a semiconductor, surface scattering will play a role in determining both the total change in conductance due to ambient and the results of the field effect measurement. The considerations presented here primarily deal with the influence of surface scattering on such measurements.

The increase in resistance of thin metallic films from a decrease in electronic mobility, in the absence of a magnetic field, has been discussed by Fuchs[7] and a generalization of the problem to include magnetic effects was carried out by Sondheimer.[8] The theory presented here in general follows these analyses, the essential difference arising from the spatial dependence of the unperturbed carrier distribution function due to the space-charge potential. The general solution for the surface conductance is given in Part II for diffuse surface scattering and applied to (*a*) a linear space-charge potential corresponding to a constant electric field, and (*b*) a solution of Poisson's equation including an externally applied potential, V_a, across the surface. The change in the number of holes and electrons in the space-charge layer as a function of ψ_{s0} (see Fig. 1), has been computed for impurity densities from intrinsic up to $10^{18}/\text{cm}^3$.[9] These results are combined with the carrier mobility obtained from the surface scattering considerations to discuss Morrison's work and predict the carrier mobility in the channel effect.

II. GENERAL THEORY

We consider a volume extending inward from a unit surface area of a semiconductor, subjected to an electric field E_x, parallel to the surface, and a field E_z along the inward normal to the surface, due to the space-charge layer. The carriers are regarded as free in the sense that the energy depends upon the absolute square of the wave vector only. Under steady state conditions, the distribution function for the holes or electrons is determined by the Boltzmann equation,[10]

$$\mathbf{v}\cdot\text{grad}_r f+\mathbf{a}\cdot\text{grad}_v f=-(f-f_0)/\tau, \tag{1}$$

where $\mathbf{v}$ and $\mathbf{a}$ are the velocity and acceleration of a carrier, τ the relaxation time, and $f=f_0+f_1(v,z)$, f_0 being taken as the Maxwell-Boltzmann distribution function and f_1 a small perturbing function. Thus,

$$f_0=C\exp[-(mv^2/2+q\psi)/kT], \tag{2}$$

where ψ is the potential associated with E_z, m the effective mass and q the charge of the carrier. When products of f_1 and E_x are neglected in (1), f_1 is found to satisfy the equation:

$$v_z\frac{\partial f_1}{\partial z}+\frac{qE_z}{m}\frac{\partial f_1}{\partial v_z}+\frac{f_1}{\tau}=\frac{qv_xE_xf_0}{kT}. \tag{3}$$

By introducing an energy parameter,

$$\epsilon_s=\tfrac{1}{2}mv_s^2+q(\psi-\psi_s), \tag{4}$$

where ψ_s is the value of the potential at the surface, Eq. (3) is reduced to

$$\frac{qE_z}{m}\frac{\partial f_1}{\partial v_z}+\frac{f_1}{\tau}=\frac{qv_xE_xf_0}{kT}. \tag{5}$$

If the boundary condition of random scattering at the surface is imposed by making f_1 vanish at $v_z=v_{zs}$, where v_{zs} is the positive z component of velocity asso-

[7] K. Fuchs, Proc. Cambridge Phil. Soc. **34**, 100 (1938).
[8] E. H. Sondheimer, Phys. Rev. **80**, 401 (1950).

[9] This calculation has been carried out independently by R. H. Kingston (private communication). A somewhat similar calculation has been carried out by C. G. B. Garrett.
[10] See A. H. Wilson, *The Theory of Metals* (Cambridge University Press, London, 1953), Chap. VIII.

ciated with a carrier at the surface with energy parameter ϵ_z, Eq. (5) has the solution,

$$f_1=\frac{mv_xE_xf_0}{kT}\exp[-K(v_z,\epsilon_z)]\int_{v_z}^{v_{zs}}\frac{\exp[K(v_z',\epsilon_z)]}{E_z(v_z',\epsilon_z)}dv_z', \tag{6}$$

and where

$$K(v_z',\epsilon_z)=\frac{m}{q}\int_0^{v_z'}\frac{dv_z''}{\tau E_z(v_z'',\epsilon_z)}. \tag{7}$$

The current density can now be calculated as

$$i_x=q\int dv_xdv_ydv_zv_xf_1. \tag{8}$$

Introducing the distribution function, Eq. (6), performing the v_x and v_y integrations and integrating the current density over z to obtain the total current in the potential well for a unit surface area, we find

$$I_x=\frac{2\pi qE_xCkT}{m}\int_{-\infty}^{\infty}dv_z\int_0^{\infty}dz \times\exp\left\{\left[-\left(\frac{mv_z^2}{2}+q\psi\right)\Big/kT\right]-K\right\} \times\int_{v_z}^{v_{zs}}\frac{\exp(K')}{E_z'}dv_z'. \tag{9}$$

The z integration has been carried to infinity assuming the form of ψ insures a negligible contribution from the region beneath the space charge layer. Since

$$\partial K/\partial v_z=m/q\tau E_z,$$

Eq. (9) reduces to

$$I_x=2\pi q^2\frac{E_xCkT\tau^2}{m^3}\exp[-q\psi_s/kT]\int_0^{\infty}d\epsilon_z \times\exp[-\epsilon_z/kT][\exp 2K(\epsilon_z)-2K(\epsilon_z)-1]=DA, \tag{10}$$

where $K(\epsilon_z)$ is evaluated from Eq. (7), the upper limit being $(2\epsilon_z/m)^{\frac{1}{2}}=v_{zs}$, and D the group of constants appearing before the integral. To evaluate the current explicitly, some form of the space-charge potential must be assumed.

(*a*) The first case considered is $E_z=E_{zs}$, a constant. The relaxation time is assumed constant and the surface scattering random. By introducing Eq. (7) into Eq. (10) and defining

$$\alpha=(qE_{zs}\tau)^{-1}(2mkT)^{\frac{1}{2}}, \tag{11}$$

one obtains

$$I_x=\pi^{\frac{1}{2}}D\alpha kT[1-\exp(\alpha^2)(1-\operatorname{erf}\alpha)],$$

$$\operatorname{erf}\alpha\equiv\frac{2}{\pi^{\frac{1}{2}}}\int_0^{\alpha}\exp(-x^2)dx. \tag{12}$$

The reduction in the conductivity of the carriers in the well due to surface scattering can be taken into account by defining an effective mobility such that

$$I_x=Nq\mu_{\text{eff}}E_x, \tag{13}$$

where N is the total number of either holes or electrons in the well, depending upon whether a p-type or n-type surface is under consideration. If the zero of potential is taken at the surface, N is given by

$$N=C\int dv_xdv_ydv_zdz\exp\left[-\left(\frac{mv^2}{2}+q\psi\right)\Big/kT\right] =C\left(\frac{2\pi kT}{m}\right)^{\frac{1}{2}}\frac{kT}{qE_{zs}}. \tag{14}$$

By combining Eqs. (12), (13), and (14) and writing $\mu_{\text{bulk}}=q\tau/m$, one obtains

$$\mu_{\text{eff}}/\mu_{\text{bulk}}=1-\exp(\alpha^2)(1-\operatorname{erf}\alpha). \tag{15}$$

Figure 2 shows this ratio plotted as a function of α. For the limit of large E_{zs}, the expression reduces to

$$\mu_{\text{eff}}/\mu_{\text{bulk}}\cong 2\alpha/\pi^{\frac{1}{2}}. \tag{16}$$

Thus the effective mobility is inversely proportional to the space charge field for large constants fields. For small fields, the effective mobility reduces to the bulk value as expected.

(*b*) The second case considered is that in which E_z is obtained from a solution of Poisson's equation for the space-charge layer. For definiteness, the problem will be solved for a p-type material with an n-type inversion layer existing at the surface and an external bias, V_a, applied in the z direction such that the energy bands are depressed further at the surface as shown in Fig. 1(b). The results are valid for an n-type material with a p-type inversion layer with an appropriate change in the definition of quantities involved.

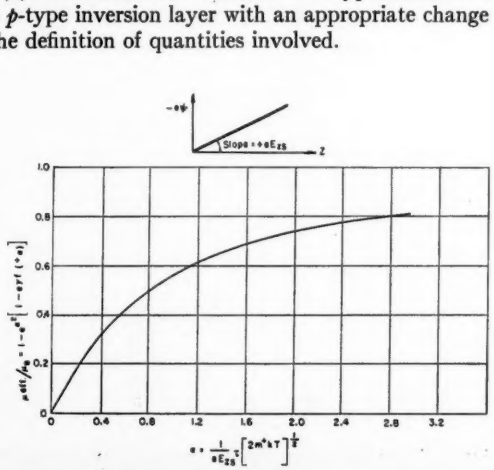

FIG. 2. The effective mobility for the constant field case, as a function of the parameter α.

We define ψ to be the mid-gap potential relative to the mid-gap potential deep within the sample. φ_n and φ_p are the quasi Fermi potentials and assumed constant over the region of interest. From Fig. 1(b), we note

$$\varphi_n=\varphi_p+V_a.$$

The charge density is taken as

$$\rho=e[-N_a+p_0\exp(-e\psi/kT)-n_0\exp(e\psi/kT)], \quad (17)$$

where

$n_s=n_0\exp[e\psi_s/kT]$=electron density at the surface,

$n_0=n_i\exp[(\Delta E_F-eV_a)/kT]$,

$p_0=n_i\exp[-\Delta E_F/kT]$, (18)

$\Delta E_F=E_{F(\text{sample})}-E_{F(\text{intrinsic})}$,

n_i is the intrinsic carrier density, N_a the acceptor density, and κ the dielectric constant.

Poisson's equation becomes

$$\frac{d^2\psi}{dz^2}=-\frac{4\pi e}{\kappa}[-N_a+p_0\exp(-e\psi/kT)-n_0\exp(e\psi/kT)]. \quad (19)$$

Let $d\psi/dz=\psi=0$ at some point within the sample as an origin for integration. Multiplying Eq. (19) by $d\psi/dz$ and integrating over z, we obtain the electric field as a function of the potential.

$$E_z^2=\frac{8\pi eN_a}{\kappa}\left[\psi+\frac{kT}{e}\left\{\left(\frac{p_0}{N_a}\right)(\exp[-e\psi/kT]-1)+\left(\frac{n_0}{N_a}\right)(\exp[e\psi/kT]-1)\right\}\right]. \quad (20)$$

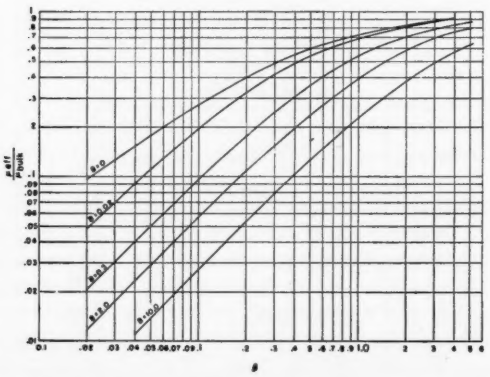

FIG. 3. The effective mobility corresponding to the potential obtained from a solution of Poisson's equation for the space charge layer, plotted as a function of the parameter β for several values of the parameter B.

However, to evaluate K, Eq. (7), E_z must be expressed as a function of v_z and ϵ_z by using the defining relationship for ϵ_z, Eq. (4). The expression for K becomes

$$K=-\frac{m}{e\tau}\left(\frac{\kappa}{8\pi N_a kT}\right)^{\frac{1}{2}}\int_0^{v_z}dv_z\Big/\left\{\frac{e\psi_s}{kT}+\frac{n_0}{N_a}\exp(e\psi/kT)+\left[-\frac{(p_0+n_0)}{N_a}-\left(\epsilon_z-\frac{mv_z^2}{2}\right)\Big/kT+\frac{p_0}{N_a}\exp(-e\psi/kT)\right]\right\}^{\frac{1}{2}}, \quad (21)$$

where

$$e\psi=e\psi_s+\tfrac{1}{2}mv_z^2-\epsilon_z.$$

We now make the approximation that the bracketed portion in the denominator of Eq. (21) is negligible compared to the terms retained, over the region of major contribution to the current integral. This approximation is equivalent to setting the field due to the impurity ions equal to a constant value, given by its value at the surface, and neglecting the contribution of holes to the space charge. If $e\psi_s$ is greater than several kT, the population of states in the region where $\epsilon_z-\frac{1}{2}mv_z^2$ is comparable to $e\psi_s$, is very small compared to the population at the bottom of the well. The bracketed expression also indicates that the maximum possible hole contribution to the denominator corresponds to a decrease of $e\psi_s$ by kT. Thus for most problems of interest, the above approximation appears valid and K reduces to

$$K=-(2/\pi)^{\frac{1}{2}}\beta\int_0^{\sqrt{(\epsilon_z/kT)}}\frac{dy}{B+\exp[-(\epsilon_z/kT)+y^2]}, \quad (22)$$

where

$$\beta=\frac{1}{e\tau}\left[\frac{m\kappa}{8n_0}\exp(-e\psi_s/kT)\right]^{\frac{1}{2}}=\frac{1}{e\tau}\left[\frac{m\kappa}{8n_s}\right]^{\frac{1}{2}} \quad (23a)$$

$$B=\frac{N_a}{n_0}\frac{e\psi_s}{kT}\exp(-e\psi_s/kT)=\frac{N_a}{n_s}\frac{e\psi_s}{kT}. \quad (23b)$$

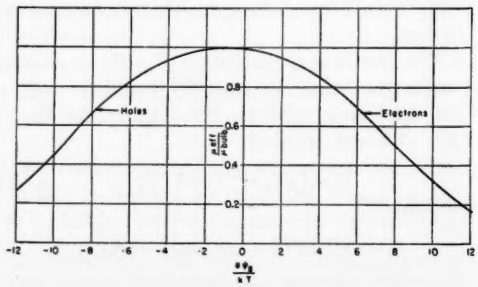

FIG. 4. The effective mobility plotted as a function of the depression of the energy bands at the surface.

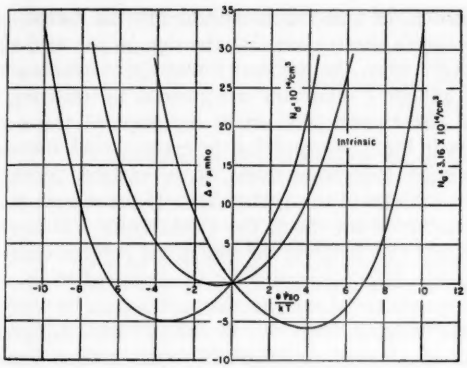

FIG. 5. The change in surface conductivity as a function of the depression of the energy bands at the surface.

The current is given by substituting Eq. (22) into Eq. (10) and after some calculation gives

$$I_x = DkT\left\{2\sqrt{2}\beta[(B+1)^{\frac{1}{2}}-B^{\frac{1}{2}}] + \int_0^\infty \exp\left[-x-2(2/\pi)^{\frac{1}{2}}\beta \times \int_0^{\sqrt{x}} [B+\exp(-x+y^2)]^{-\frac{1}{2}}dy\right]dx-1\right\}. \quad (24)$$

An effective mobility is again defined by Eq. (13) and proceeding exactly as in the constant field case we obtain the expression,

$$\frac{\mu_{\text{eff}}}{\mu_{\text{bulk}}} = 1+\frac{1}{2\sqrt{2}\beta[(B+1)^{\frac{1}{2}}-B^{\frac{1}{2}}]} \times\left\{\int_0^\infty \exp\left[-x-2(2/\pi)^{\frac{1}{2}}\beta \times \int_0^{\sqrt{x}} (B+\exp(-x+y^2))^{-\frac{1}{2}}dy\right]dx-1\right\}. \quad (25)$$

This ratio is plotted in Fig. 3 as a function of β for several values of B. Figure 4 shows $\mu_{\text{eff}}/\mu_{\text{bulk}}$ for intrinsic germanium.

III. APPLICATIONS

The results of Sec. II may be applied to the problem of determining the position of the energy bands at the free surface of a semiconductor if the conductance of the sample is known relative to the conductance at a definite band position. The conductance due to the space-charge layer is given by

$$\Delta\sigma = e[\mu_{(n)\text{eff}}\Delta n+\mu_{(p)\text{eff}}\Delta p], \quad (26)$$

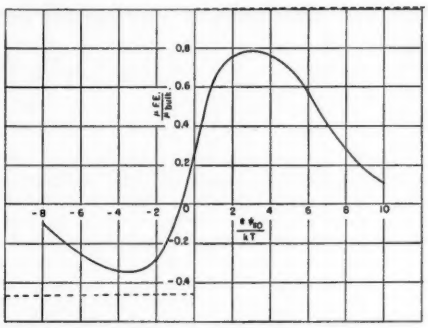

FIG. 6. The "field effect" mobility as a function of the depression of the energy bands at the surface, assuming the charge associated with surface traps is independent of the applied field.

where

$$\Delta n = n_0\int_0^{\psi_{s0}}\left[\frac{\exp(e\psi/kT)-1}{d\psi/dz}\right]d\psi, \quad (27a)$$

$$\Delta p = p_0\int_0^{\psi_{s0}}\left[\frac{\exp(-e\psi/kT)-1}{d\psi/dz}\right]d\psi, \quad (27b)$$

and n_0 and p_0 are defined as in Eqs. (18) by setting $V_a=0$. The effective mobility is to be considered different from the bulk mobility when the carrier is constrained to conduct in the potential well, thus neglecting the small correction due to some carriers of opposite sign scattering from the potential barrier rather than the surface. Since all quantities in Eq. (26) are expressible as functions of ψ_{s0}, this relationship and the sign of the field effect give the band position. There is some question as to what values to assume for the effective mass and relaxation time for both holes and electrons. Assuming $m_n=m_p=0.25m_e$, we have plotted $\Delta\sigma$ in Fig. 5 for intrinsic, n-type and p-type germanium. The relaxation times have been determined from the relationship $\mu_{\text{bulk}}=e\tau/m$. It should be noted that the conductance decreases and goes through a minimum as the surface conductance tends to become inverted. For the p-type material this is due to the hole density near the surface decreasing to a small value before the electron density has increased appreciably. The conductance minimum can be used to establish the definite band position needed above. Changes in conductance may be interpreted as moving along this conductance curve and the energy band position is read directly once the minimum has been established.

The magnitude of the field effect can be estimated if one assumes the charge associated with surface traps is unchanged when the field is applied. Since there can exist no net field deep within the semiconductor, Gauss's law applied to the free surface gives the total charge, Q, in the space charge region by the value of the field just inside the surface, Eq. (20). Defining a

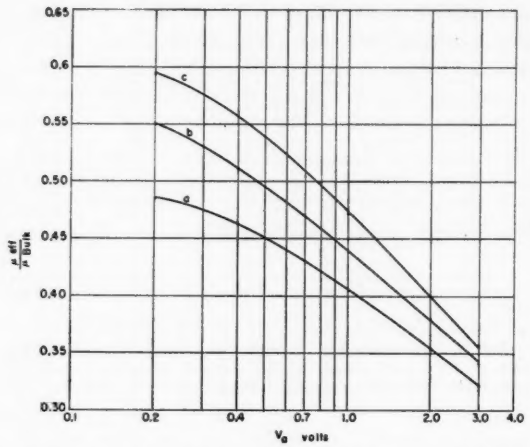

FIG. 7. The theoretical effective mobility corresponding to Kingston's data on the channel effect, for ambient water vapor pressure (*a*) 19.8 mm of Hg, (*b*) 14.5 mm, and (*c*) 4.6 mm.

field-effect mobility, $\mu_{F.E.}$, one finds

$$\mu_{F.E.} \equiv d\Delta\sigma/dQ$$

$$= \Big\{ \mu_{(n)\text{eff}} n_0 [\exp(e\psi_s/kT) - 1]$$

$$+ \mu_{(p)\text{eff}} p_0 [\exp(-e\psi_s/kT) - 1]$$

$$+ \left(\frac{d\psi}{dz}\right)\Big|_{\psi_s} \left[\Delta n \frac{\partial \mu_{(n)\text{eff}}}{\partial \psi_s} + \Delta p \frac{\partial \mu_{(p)\text{eff}}}{\partial \psi_s} \right] \Big\} \Big/$$

$$[N_a + n_0 \exp(e\psi_s/kT) - p_0 \exp(-e\psi_s/kT)], \quad (28)$$

where $(d\psi/dz)_{\psi_s}$ is given in Eq. (20), the derivatives of the effective mobility are obtained from Eq. (25), and Δn and Δp as defined above have been tabulated as functions of $e\psi_s/kT$. The first two terms in the numerator of Eq. (28) are due to the number of electrons and holes in the space-charge layer changing, while the last terms arise from the fact that the effective mobility of the carriers already present in the space charge layer changes. In general both types of terms must be considered. The field-effect mobility is shown in Fig. 6 for intrinsic germanium. If surface scattering were not included, the mobility for a large surface dipole would approach the bulk values indicated by the dotted lines. Morrison's observation that the sign on the field effect changes when the ambient forces the conductance to go through a minimum is explained by realizing the field effect essentially senses the slope of the *n*-type curve in Fig. 5. By applying the external field, the bands are either lowered or raised at the surface, depending upon the sign of the applied field. If the sample is at a conductance minimum, the conductance will increase in either case however the sign of the induced charge is opposite, thus accounting for the observed effect.

An estimate of the effective mobility to be expected in the channel effect can be derived from Kingston's data of channel conductance *versus* reverse bias on *n-p-n* junction transistors by extrapolating his conductance curves to zero bias. Since Kingston's data give directly the conductance due to the existence of the channel, the depression of the bands at zero bias is given by the value of ψ_{s0} corresponding to the intercept. The values obtained in this way for several values of ambient water vapor pressure are

	Vapor pressure	$\Delta\sigma(V_a=0)$	ψ_{s0}
a	19.8 mm of Hg	26 micromhos	0.25 volt
b	14.5 mm of Hg	10 micromhos	0.22 volt
	8.6 mm of Hg	6.6 micromhos	0.21 volt
c	4.6 mm of Hg	4.0 micromhos	0.20 volt

If one assumes the Fermi level at the surface is stabilized relative to the energy bands, as Kingston has proposed,[11] the effective mobility is then given by Eq. (25), where β assumes a fixed value for each value of ψ_{s0} and B depends linearly upon V_a. Figure 7 indicates the mobility is reduced to about one third the bulk mobility for a reverse bias of several volts.

ACKNOWLEDGMENTS

The author wishes to express his sincere appreciation to Professor John Bardeen who suggested the problem and made many valuable suggestions during the course of the work. I am indebted to Dr. S. R. Morrison and Professor Harry Letaw, Jr. for several informative discussions and their critical reading of the manuscript. Thanks are also due to Mr. Walter Helly for carrying out the numerical integrations on the Illiac.

[11] R. H. Kingston, Phys. Rev. 94, 1416 (1954).

Band Model for Hall Effect, Magnetization, and Resistivity of Magnetic Metals*

EMERSON M. PUGH
Carnegie Institute of Technology, Pittsburgh, Pennsylvania
(Received October 11, 1954)

The ordinary Hall coefficients for Cu, Ni, Co, and the binary alloys of these elements agree to within a factor of two with predictions based upon the usual band model in which the number of conduction electrons per atom is postulated to be the number, $n_s=0.6$, of 4*s* electrons required to explain the saturation magnetization in these materials. The factor of two, however, created a dilemma, since both the magnetization data and the Hall data were accurately determined. The Hall results appeared to require that $n_s<0.3$ whereas the magnetization data requires that $n_s>0.54$. It will be shown that this dilemma disappears when the 4*s* band is considered divided into two parts in which the electrons with spins parallel to the spontaneous magnetization have much greater mobility than those with spins antiparallel. According to Mott, the antiparallel electrons have low mobility, because they can be scattered into the partially empty 3*d* band, whereas the parallel electrons cannot.

It will be shown that the ordinary Hall data, the saturation magnetization data, and the resistivity data for these transition elements and their alloys, can be made understandable by employing a four-band model, consisting of two 4*s* bands and two bands from the 3*d* shell.

I. INTRODUCTION

HALL effect measurements,[1,2] on Ni, Co, Fe, and on the binary alloys of Cu-Ni and Ni-Co, have yielded the two different coefficients R_0 and R_1 in the expression[3] for the Hall emf,

$$E_H=(R_0H+R_1M)I/t,$$

where H is the magnetizing field, M is the intensity of magnetization in the sample, I is the current in the sample, and t is the thickness of the sample.

The ordinary coefficient R_0 is positive in Fe[2], indicating hole conduction, but is negative in all of the rest of these materials. Except in Fe, these ordinary coefficients are in agreement, within a factor of two,[4] with the predictions of a simple one-band model in which the 4*s* electrons (0.6 per atom) are the carriers. For this one-band model the ordinary coefficients are given by

$$R_0=-1/Nn_sec, \qquad (1)$$

where N is the number of atoms per cc, e is the absolute value of the electronic charge, and c is the velocity of light. The number of conduction electrons per atom, $n_s\cong 0.6$, is obtained from the saturation magnetization of these materials at low temperatures. Within this factor of two, there are systematic variations in R_0 with electronic concentration, which show that the Hall effect must be complex in these materials.

The fact that the ordinary coefficient in Fe is positive[5] suggests that the Hall effect in the other materials may be affected by conduction in the 3*d* band as well as in the 4*s* band. An attempt to correlate the data, using the Jones-Zener equation[6] for the Hall coefficient, with two-band conduction showed that the data could not be explained with $n_s=0.6$. In fact, if one assumes that the mobility of the 4*s* electrons is greater[7] than the mobility of either the electrons or holes in the 3*d* band, the data can be explained only by taking $n_s<0.3$.

To show this, values of the Hall coefficient for a two-band model are calculated from the Jones-Zener equation and are plotted in Fig. 1 as functions of $\delta(=\mu_d/\mu_s)$, the ratio of the mobility in the 3*d* band to the mobility in the 4*s* band. In making these calculations the number of 4*s* electrons per atom has been kept constant, while the number of 3*d* holes or of 3*d* electrons per atom have been varied over the complete range of possible values. In this figure, dashed lines are used for the hole conduction and solid lines for the electronic conduction in the 3*d* band. Each curve is labeled with a ratio representing the number of 3*d* carriers/atom, used in calculating the curve, divided by 0.56, the assumed number of 4*s* electrons/atom. The sign of this ratio is taken as positive when the 3*d* carriers are electrons and negative when they are holes. The number $n_s=0.56$ is chosen because new measurements on the *g* factor[8] show that n_s lies between 0.57 and 0.54 electrons/atom. If as assumed, the 4*s* band mobility is greater than the 3*d* band mobility ($\delta=\mu_d/\mu_s<1$), only those parts of the curves extending from $\delta=0$ to $\delta=1$ are of interest. It is obvious that this equation cannot account for values of R_0 below -13×10^{-13} ohm-cm/oersted, with $n_s\geq 0.54$, although values below -20×10^{-13} ohm-cm/oersted are observed in both Ni-Cu and Ni-Co alloys. A value of $n_s<0.3$ is required to account for the R_0

* This research was supported in part by the Office of Naval Research.
[1] A. I. Schindler and E. M. Pugh, Phys. Rev. **89**, 295 (1953).
[2] Simon Foner and Emerson M. Pugh, Phys. Rev. **91**, 20 (1953).
[3] Emerson M. Pugh, Phys. Rev. **36**, 1503 (1930).
[4] Emerson M. Pugh and Norman Rostoker, Revs. Modern Phys. **25**, 151 (1953), and also references 1 and 2.
[5] The Hall coefficient is also positive in Mn, Cr, V, and Ti.
[6] H. Jones and C. Zener, Proc. Roy. Soc. (London) **A145**, 269 (1934), Eq. (4).
[7] While this assumption is most reasonable, the same conclusions are reached with a much less restrictive assumption; namely, that the mobility in the 3*d* band is not more than 4 or 5 times as great as the mobility in the 4*s* band.
[8] C. Kittel, *Introduction to Solid State Physics* (J. Wiley and Sons, New York, 1953), p. 171; and also *Ferromagnelism* by R. M Bozorth (D. Van Nostrand Company, New York, 1951), p. 809.

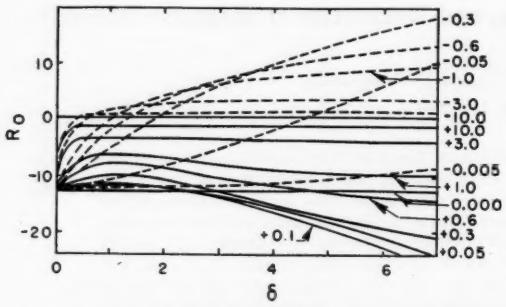

FIG. 1. Calculations of the ordinary Hall constant, R_0, for two-band models in which the first band always contains 0.56 electron/atom, while the second band contains different numbers of either holes or electrons. The R_0's are plotted against δ, the relative mobility in the second band compared to the first. The different curves are designated by the ratio obtained by dividing the number of carriers/atom in the second band by 0.56, the ratio being positive (solid lines) for electrons and negative (dotted lines) for holes. The $|R_0|$'s are not as great as that for the first band alone until δ considerably exceeds unity. This is a general conclusion for two-band models.

values. Thus the two-band model can account for the Hall data only with $n_s<0.3$, while it can account for the saturation magnetization of these alloys only with $n_s>0.54$.

At a conference[9] last summer the author proposed that this dilemma could be solved by separating the 4*s* band into two equal parts according to the spins of the electrons. Those 4*s* electrons with spins parallel to the spontaneous magnetization, according to Mott[10] have mobilities much greater than the electrons with spins antiparallel, since the latter can be scattered into the partly empty 3*d* band. Since the parallel 3*d* band is full at low temperatures the parallel electrons cannot be scattered into it. A. Bloembergen[9] pointed out that if the above were the correct explanation of the data, then R_0 in these materials should vary with temperature from a value corresponding to $n_s\cong 0.28$ at low temperatures to a value corresponding to $n_s\cong 0.56$ above the Curie temperature. Philip Cohen in this laboratory has completed measurements[11] from 4°K to room temperature on the Cu-Ni alloys, which verify this predicted temperature dependence for the magnetic alloys and the expected lack of temperature dependence for the nonmagnetic alloys. Furthermore the absolute values of R_0 are within 15 percent of the values predicted by such a model for all but the pure copper. In copper the measured Hall coefficient is only $\frac{2}{3}$ of the predicted value. There are at least two reasons for expecting the measured Hall coefficient in copper to be smaller than predicted by this simple model; first, the value would be reduced markedly if there is a small amount of conduction in the 4*p* band, second, the value might be reduced by the inaccuracies in the approximations of Eq. (1). This equation is a good approximation only when the band is not too full. A similar approximation holds when the band is nearly full. As a band is filled up the value of R_0 for that band passes through zero and becomes positive. The behavior of R_0 *versus* n for a single conduction band in a simple cubic crystal as calculated by Rostoker on the basis of the tight-binding approximation,[12] is shown in Fig. 2. When n is small as in a nearly empty band Eq. (1) is an excellent approximation. When n is nearly equal to n_f, the number of electrons required to fill the band, the equation

$$R_0=1/Nec(n_f-n) \qquad (2)$$

is an excellent approximation. For crystals other than the simple cubic, very good approximations for R_0 are obtained from Eq. (1) for a single conduction band that is not too full and from Eq. (2) when the band is nearly full. Between the two extremes the calculations are difficult and the results are more uncertain. For real crystals R_0 goes through zero at some point above $n=n_f/2$ as suggested by the dotted line in Fig. 2. From Fig. 2 it is not too surprising that most of the metals with half-filled *s* bands, like Cu, Ag, and Au, show absolute values of R_0 that are less[13] than those given by Eq. (1). Fortunately, in the region where the uncertainty in Eq. (1) is greatest the values of R_0 are small. This fact is of great importance when multiple band models are being analyzed.

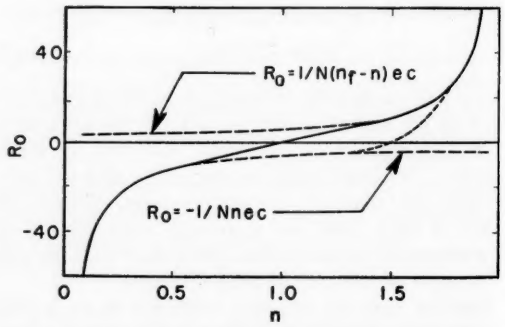

FIG. 2. Calculations of the ordinary Hall constant, R_0, for single-band conduction in a simple cubic crystal as a function of the number of electrons in the band. Near the bottom of the band $R_0=-1/Nnec$, while near the top of the band $R_0=1/N(n_f-n)ec$. In between, the curve changes sign by going through zero. The dotted line indicates qualitatively the behavior of real crystals.

[9] Gordon Conference, New Hampton, New Hampshire, July 1953 (unpublished). The author is indebted to several of the scientists who participated in this conference for many stimulating discussions. The verbal suggestion by A. Bloembergen concerning temperature dependence proved to be especially fruitful.

[10] N. F. Mott, Proc. Roy. Soc. (London) **A153**, 699 (1936).

[11] Philip Cohen, thesis, Carnegie Institute of Technology, June 1955 (unpublished).

[12] N. Rostoker (private communication).

[13] Lithium appears to be an exception, for the reported absolute values of R_0 are larger than expected from Eq. (1). It should be worth investigating whether or not some common impurity in Li could be responsible for this result.

The Hall effect in Cu, Ni, and some Cu-Ni alloys has been measured at room temperatures[14] and at low temperatures.[11] Their combined results for R_0 *versus* composition are plotted in Fig. 3. The values at liquid helium temperatures are now understandable. As the percent Ni in Cu increases from zero to 40 percent the number of 4*s* electrons per atom, n_s, decreases from ~1.0 to ~0.6. At the same time $|R_0|$ increases from $5.95\pm0.08\times10^{-13}$ volt cm/amp oersted for pure Cu to $13.1\pm0.1\times10^{-13}$ volt cm/amp oersted for the 40 percent Ni alloy. The latter figure corresponds to an $n^*=1/|R_0|Nec$ of 0.56 ± 0.05. As the Ni content is increased beyond 40 percent the antiparallel half of the 3*d* band begins to empty. This reduces the mobility of the antiparallel 4*s* electrons, because they can now be scattered into the 3*d* band. The mobility of the parallel 4*s* electrons remains high since they cannot be so scattered. Thus with increasing Ni content beyond 40 percent, R_0 gradually becomes more negative and reaches the value -23.7×10^{-13} volt cm/amp oersted which corresponds to an n^* of 0.29, when the Ni content reaches 80 percent. Apparently in this alloy the ordinary effect is due almost entirely to those 4*s* electrons that have parallel spins. The mobility of the other carriers can be ignored. As the Ni content of these alloys is increased from 40 percent to 80 percent, the change of n^* from 0.56 to 0.29 takes place gradually, since at first the number of scattering centers in the antiparallel 3*d* band is small, so that the influence of the antiparallel 4*s* electrons disappears slowly. As the Ni content is increased beyond 80 percent, hole conduction in the antiparallel 3*d* band becomes increasingly important and reduces the absolute value of R_0. This should be expected from the calculations plotted in Fig. 1. A more complete discussion of behavior of pure Ni will be given in a later paragraph.

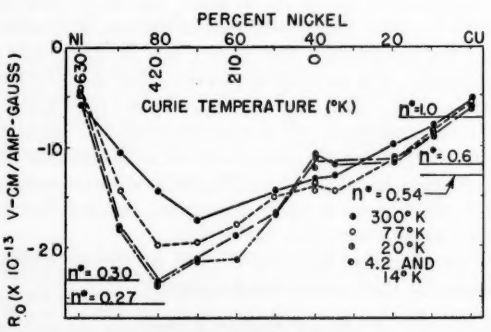

FIG. 3. Ordinary Hall coefficients for Ni-Cu alloys measured at various temperatures by Schindler and Cohen. Lines are drawn to show the values of R_0 corresponding to certain n^*'s, where $n^*=-1/R_0Nec$.

[14] A. I. Schindler and E. M. Pugh, Phys. Rev. **89**, 295 (1953). Some very accurate thickness measurements were made on the samples after this paper was published. The corrected values for all measurements are given in Fig. 3.

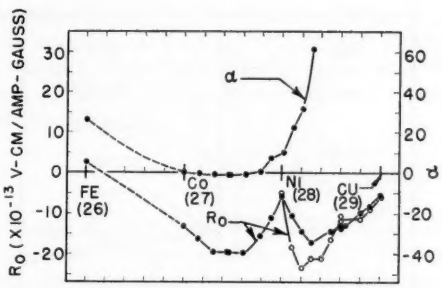

FIG. 4. Ordinary Hall coefficients for Fe, Co-Ni alloys and Cu-Ni alloys plotted against electron concentrations. Open circles were obtained at 4°K and solid circles were obtained at room temperature. The field parameters, α's, were obtained at room temperature.

It is seen that the large negative values of R_0 for the Cu-Ni alloys, whose compositions lie between 50 and 90 percent Ni, are due to 4*s* electrons with parallel spins having greater mobilities than those with antiparallel spins. This is true only at temperatures far below the Curie points. As temperatures approach the Curie temperatures, the two mobilities should approach each other and produce smaller ordinary Hall coefficients corresponding to conduction by all the 4*s* band electrons with n^* between 0.54 and 0.60. Thus in these alloys $|R_0|$ decreases with temperature up to the Curie point.

The electron concentration per atom can be reduced below that in pure Ni by adding Co ($Z=27$) to the Ni ($Z=28$). The Ni-Co alloys have been measured[2] at room temperatures. Since these alloys have fairly high Curie temperatures, room temperatures can be considered as relatively low. The available data on Cu-Ni and Ni-Co alloys at liquid helium and room temperatures are plotted in Fig. 4. The fact that R_0 again approaches -20×10^{-13} ohm-cm/oersted corresponding to $n^*\cong0.35$ as Co is added to Ni, suggests that the 3*d* contribution to the conduction which is so prominent in Ni, passes through zero[15] somewhere between 25 and 50 percent Co in Ni and becomes negative with increasing Co content thereafter. The Jones-Zener equation plotted in Fig. 1 shows that when there is either electronic or hole conduction in the 3*d* band, it tends to reduce the absolute magnitude of R_0. As can be seen from the solid lines in Fig. 1, 3*d* electrons having a given mobility are less effective in reducing $|R_0|$ than are 3*d* holes having the same mobility. This may account for the fact, shown in Fig. 4, that the absolute value of R_0 reduces very slowly with composition as pure Co is approached.

[15] It is significant that the extraordinary coefficient R_1 also changes sign in this same neighborhood. Robert Karplus and J. M. Luttinger, Phys. Rev. **95**, 1154 (1954), have shown that scattering within the 3*d* band is primarily responsible for the values of R_1. Apparently R_1 becomes zero at approximately the electronic concentration where the contribution of the 3*d* band to R_0 becomes zero. This point where the ordinary Hall coefficient for the top 3*d* sub-band passes through zero should be near the maximum of the density of states curve.

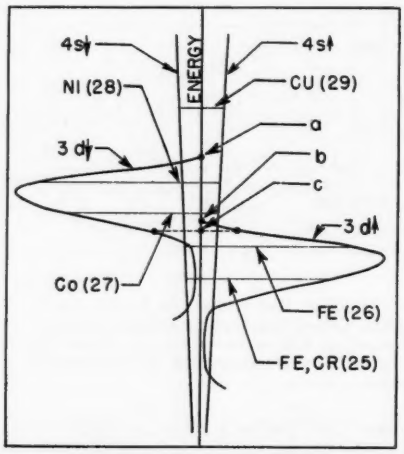

FIG. 5. Assumed density of states *versus* energy curves for the two 4*s* and the two 3*d* bands used in analyzing the data. The bands with spins parallel to the field are plotted to the right while those with antiparallel spins are plotted to the left of the energy axis.

In the foregoing analysis it has been assumed tacitly that in ferromagnetic metals the electrical conduction can be described by four independent groups of carriers, each having its own characteristic mobility and its own characteristic Hall constants. The need for four instead of two groups of carriers lies in the fact that antiparallel electrons may have mobilities different from those of the parallel electrons in both the 3*d* and the 4*s* bands. The assumption that the conduction carriers can be separated into groups is a commonly used device for analyzing data that is too complex for a more sophisticated treatment. Some justification for assigning separate Hall constants and separate mobilities to each of these groups is found in the fact that this treatment for two bands leads to the same equation as that obtained by Jones and Zener.

For the purpose of this analysis the density of states *versus* energy curves for the 3*d* and 4*s* bands of these transition metals may be divided into four curves somewhat as shown in Fig. 5. The density of those states with spins parallel to the spontaneous magnetization are plotted to the right of the vertical axis, while those with spins antiparallel are plotted to the left. Because there is no net spin in the 4*s* band the two 4*s* band curves are symmetrical about the energy axis. Presumably the 3*d* curves are also symmetrical in shape though the parallel curve is displaced to lower energies because of exchange interactions. The Hall data can be explained more simply if the two 3*d* bands which contribute to the conduction process are sub-bands,[16] each containing between 2 and 3 electronic states/atom.

[16] J. C. Slater and G. F. Koster have pointed out [Massachusetts Institute of Technology Quarterly Progress Report No. 12 (unpublished)], that a simplified tight-binding approximation for the body-centered cubic structure predicts a minimum in the middle of the density of states *versus* energy curve for the 3*d* band. When applied to Cr the minimum becomes an energy gap.

It can be seen that such a model readily explains the existing ordinary Hall effect data. It also provides the usual collective electron interpretation of the fact that the saturation magnetization at low temperatures in Cu-Ni and Ni-Co alloys is a linear function of the electron concentration. In addition the model provides a simple qualitative explanation of that part of the Slater-Pauling curve which shows decreasing saturation magnetization toward the lower values of electron concentration.

As the electron concentration is reduced from 29 per atom at Cu to 28.6, the number of 4*s* electrons/atom is reduced from 1.0 to 0.6 at which point the Fermi level reaches point *a* in Fig. 5. As the Fermi level descends from *a* to *b* the antiparallel 3*d* shell begins to empty leaving a net parallel spin. Thus the saturation magnetization increases linearly. From *b* to *c* the net spin increases more and more slowly because electrons are being removed with increasing rapidity from the parallel 3*d* band with decreasing rapidity from the antiparallel. The maximum net spin occurs at *c* where the rates of removal of electrons from the two bands become equal. When the top sub-band of the antiparallel *d* shell becomes empty near Fe, the top sub-band of the parallel *d* shell empties more rapidly. The reduction in saturation magnetization should be linear except for the few antiparallel electrons that may still be removed from the antiparallel band.

II. FOUR-BAND MODEL

Because of the different mobilities in the two halves of the 4*s* band and because of the different numbers of carriers and their different mobilities in the top two 3*d* sub-bands, a four band model is required. It is assumed that ordinary coefficients R_{01}, R_{02}, R_{03}, and R_{04} can be defined for the four bands, each of which behave like the R_0 in Fig. 2. The subscripts 1, 2, 3, and 4 refer to the parallel half of the 4*s* band, the antiparallel half of the 4*s* band, the parallel half of the top 3*d* sub-band, and the antiparallel half of the top 3*d* sub-band, respectively. The number of electrons per atom in these bands, when filled, are $n_{f1}=n_{f2}=1$ and $n_{f3}=n_{f4}\cong 2.5$. For completeness it will also be assumed that associated with each of these bands, there are extraordinary Hall coefficients R_{11}, R_{12}, R_{13}, and R_{14}. Whenever the ordinary Hall effect alone is being considered, this last assumption has no effect upon the results.

The measured Hall emf divided by the distance between the Hall probes can be written

$$E_y=R_0H\sigma E_x+R_1M\sigma E_x, \tag{3}$$

where E_x is the electric field applied in the x-direction. The conductivity of the sample is given by

$$\sigma=\sigma_1+\sigma_2+\sigma_3+\sigma_4, \tag{4}$$

where σ_1, σ_2, etc., are the individual conductivities, which may be expressed in terms of the effective number

of carriers per atom and their corresponding mobilities, μ_1, μ_2, μ_3, or μ_4.

$$\sigma_1=e\nu_1\mu_1, \quad \sigma_2=e\nu_2\mu_2, \quad \sigma_3=e\nu_3\mu_3, \quad \sigma_4=e\nu_4\mu_4. \tag{5}$$

In Eqs. (5), $\nu_1=\nu_2=n_a/2$ while ν_3 and ν_4 depend upon how the 3*d* band is split into sub-bands and upon how these sub-bands are filled in the particular element or alloy.

It is convenient to introduce a convention for the signs of the carriers and their mobilities. This convention states that, whenever the Hall effect due to the *i*th band is *n*-type, ν_i will be a positive number representing the effective number of electronic carriers/atom in this band and μ_i will be a positive number representing their mobility. When, however, the Hall effect due to the *i*th band is *p*-type, ν_i will be a negative number representing the number of holes/atom in the band and μ_i will be a negative number representing the mobility of these holes. This convention eliminates the confusion caused by carrying the plus-or-minus sign in the multiple band equations for the Hall constants. Obviously the product $\mu_i\nu_i$ must have the plus sign for either holes or electrons, since the conductivity is always positive.

Now the measured Hall emf is given by

$$E_y=E_{y1}+E_{y2}+E_{y3}+E_{y4}, \tag{6}$$

and the method of measuring this emf with a potentiometer guarantees that the net current in the *y*-direction is zero. Hence

$$\sigma_1E_{y1}+\sigma_2E_{y2}+\sigma_3E_{y3}+\sigma_4E_{y4}-\sigma E_y=0. \tag{7}$$

The individual Hall emf's are given from Eq. (3) by

$$\begin{aligned} E_{y1}&=R_{01}H\sigma_1E_x+R_{11}M\sigma_1E_x, \\ E_{y2}&=R_{02}H\sigma_2E_x+R_{12}M\sigma_2E_x, \text{ etc.} \end{aligned} \tag{8}$$

Multiplying each equation in (8) by its corresponding σ and substituting in Eq. (7), the following equation is obtained:

$$\sigma E_y=HE_x\textstyle\sum_j\sigma_j^2R_{0j}+ME_x\sum_j\sigma_j^2R_{1j}. \tag{9}$$

Experimentally, at least in ferromagnetic materials,[17] the Hall effect proportional to M can be separated from that proportional to H. Hence, Eq. (9) can be combined with Eq. (3) and separated into two equations,

$$\sigma^2R_0=\textstyle\sum_j\sigma_j^2R_{0j}, \tag{10}$$

$$\sigma^2R_1=\textstyle\sum_j\sigma_j^2R_{1j}.[18] \tag{11}$$

Equation (10) for two bands is identical to the Jones-Zener equation, if $R_{0j}=-1/(N\nu_jec)$ and j takes the two values 1 and 2. Thus, if the bands are either nearly empty or nearly filled so that $R_{0j}=-1/(N\nu_jec)$ is a good approximation,

$$R_0Nec=-\sum_j\left(\frac{\sigma_j}{\sigma}\right)^2\frac{1}{\nu_j}. \tag{10'}$$

Actually, Eq. (10') is generally a good approximation for Eq. (10) whenever any one of the bands is either nearly empty or nearly full. If the R_0 for each band behaves like the R_0 shown in Fig. 2, significant contributions to the summation must come only from those bands that are nearly full or nearly empty. Thus the bands in which the approximation is valid make large contributions while those in which the approximation is invalid make only small contributions.

In ferromagnetic materials in which the 3*d* conduction can be neglected; e.g., in the alloys 80 Ni-20 Cu and 62 Ni-38 Co (in atomic percent), Eq. (10) gives $R_0Nec=-1/\nu_1=-2/n_a$ at low temperatures where $\mu_1\gg\mu_2$ and $R_0Nec=-1/2\nu_1=-1/n_a$ above the Curie temperature where $\mu_1=\mu_2$. Intermediate values are obtained at intermediate temperatures which accounts for the temperature dependence observed in R_0 for the Cu-Ni alloys lying between 50 and 90 atomic percent Ni. The measured values of R_0 for these alloys which are shown in Fig. 3 agree with the qualitative predictions of Eq. (10) using only $j=1$ and 2. The Ni-Co alloys have been measured only at room temperatures, but these may be considered as low temperatures since their Curie temperatures are high.

It is desirable to determine whether or not Eq. (10) can account for the low values of R_0 found in the Ni-rich alloys with reasonable values of μ_3 and μ_4. If the mobilities needed to explain the ordinary Hall data are reasonable they should be able to account for the observed resistivities at the various temperatures. Since pure Ni has the smallest Hall constant of the Ni-rich group it will be treated in most detail.

III. FOUR BANDS OF NICKEL

Fortunately values of ρ in Ni are relatively simple to calculate from the Hall coefficients since above the Curie temperature, $\nu_3=\nu_4=-n_a/2$. Furthermore, below the Curie temperature, these numbers are determined rather simply from $m=M_a/M_0$, the ratio of the saturation magnetization at the given temperature to that at absolute zero. That is,

$$\begin{aligned} \nu_3&=-(1-m)n_a/2, \\ \nu_4&=-(1+m)n_a/2, \\ \nu_1&=\nu_2=n_a/2, \end{aligned} \tag{12}$$

at all temperatures.

[17] Kevane, Legvold, and Spedding, Phys. Rev. **91**, 6, 1372 (1953) separate these two effects in gadolinium by means of their different temperature dependence.

[18] J. M. Luttinger and Robert Karplus have calculated R_1 from spin-orbit coupling and their equation provides the right order of magnitude and the observed temperature dependence, neither of which have been obtained before. It does not appear to provide the observed dependence on alloy composition. Their equation does not come out in the form of Eq. (11). To put Eq. (11) in the form given by Luttinger and Karplus, one should assume $R_{11}\cong R_{12}\cong R_{14}\cong 0$ and $R_{13}\cong A/\sigma_3^2$. However, if it is assumed instead that $R_{13}=AR_{03}/\sigma_3^2$, Eq. (11) will provide the observed dependence on both alloy composition and temperature. Some modification of this sort is needed to account for the experimental fact that the extraordinary coefficient R_1 changes sign by passing through zero at nearly the Co-Ni alloy composition where the ordinary coefficient R_{03} changes sign by passing through zero.

To calculate R_0 it is necessary to know the relative mobilities in the four bands. According to Mott,[10] 4*s* electrons with a given spin can be scattered only by holes in that half of the 3*d* band that has the same spin. Hence the ratio $\beta=\mu_2/\mu_1$ should depend upon ν_4/ν_3. Assume Mott's[10] relation $\beta=(\nu_4/\nu_3)^{\frac{1}{2}}$. The ratio μ_4/μ_3 is less certain, but $\mu_4/\mu_3\cong\beta$ may be a reasonable assumption. Fortunately, the results obtained are not at all critically dependent upon this last assumption. Finally the ratio $\delta=-\mu_3/\mu_1$ must be considered as an unknown which can be determined from the Hall data. The experimental values of δ can then be used to calculate resistivity as a function of temperature, from

$$\sigma=\sum_j \sigma_j=e\sum_j \nu_j\mu_j.$$

Thus, with the foregoing assumptions,

$$\sigma=\sigma_1\{1+\beta+(1-m)\delta+(1+m)\beta\delta\}, \tag{13}$$

and from Eqs. (10′) and (12),

$$\sigma^2R_0=\sigma_1^2R_{01}\{1+\beta^2-(1-m)\delta^2-(1+m)\beta^2\delta^2\}, \tag{14}$$

which can be written as

$$\sigma=\sigma_1\{1+\beta+\alpha\delta\}, \tag{13′}$$

$$\{1+\beta+\alpha\delta\}^2=r\{1+\beta^2-\gamma\delta^2\}, \tag{14′}$$

where $r=R_{01}/R_0$, $\alpha=(1-m)+(1+m)\beta$, and $\gamma=(1-m)+(1+m)\beta^2$. Solving (14′) for δ yields

$$\delta=\frac{\{r(\alpha^2+r\gamma)(1+\beta^2)-r\gamma(1+\beta)^2\}^{\frac{1}{2}}-\alpha(1+\beta)}{\alpha^2+r\gamma}. \tag{15}$$

The values for r at different temperatures are obtained from the Hall data. Figure 3 shows that, for the purest Ni measured $R_0\cong-5.9\times10^{-13}$ ohm-cm/oersted at low temperatures and changes very little with temperature up to room temperature.[19] Data on pure Ni is not available above room temperature, but the old data of Smith[20] suggests[21] that the ordinary Hall coefficient for Ni remains essentially constant through the Curie temperature. The values of $\delta=\mu_3/\mu_1$ needed to produce the observed Hall effect in Ni can be obtained from Eq. (15) by setting $r=4.3$ as obtained from the Cohen data.[19]

At the Curie temperature this mobility ratio δ is 0.365. Since in Ni the number of 3*d* holes equals the number of 4*s* electrons, this indicates that at and above the Curie temperature, 27 percent of its conductivity is due to the holes. Below the Curie temperature δ increases with decreasing temperature, slowly at first and more rapidly as the absolute zero is approached.

This increase in δ toward absolute zero suggests that as the parallel 3*d* band is filled, the few remaining holes acquire a high mobility. However, the antiparallel 3*d* band does not fill up and the holes in it should not acquire this high mobility, so that it should have little effect on the Hall constant at low temperatures. This indicates that one of our assumptions cannot be valid at very low temperatures; that is, while the ratio, μ_4/μ_1, is probably equal to $\beta\delta$ at the Curie temperature as has been assumed it is probably more nearly equal to a constant times β at low temperatures. Since at the Curie temperature $\delta=0.365$, the fourth term in the brackets of Eq. (13) should be written as $0.365(1+m)\beta$ and the fourth term in the brackets of Eq. (14) should be written $-(0.365)^2(1+m)\beta^2=-0.133(1+m)\beta^2$. In any case, these terms are both too small to affect the results very much.

The modified Eqs. (13′) and (14′),

$$\sigma=\sigma_1\{1+\beta+(1-m)\delta+0.365(1+m)\beta\}, \tag{13″}$$

$$\sigma^2R_0=\sigma_1^2R_{01}\{1+\beta^2-(1-m)\delta^2-0.133(1+m)\beta^2\}, \tag{14″}$$

can now be combined and solved for δ. In Fig. 6 the new values of δ are plotted *versus* $|\nu_3|$, the number of holes in the parallel 3*d* band. Values of δ are quite high for small values of $|\nu_3|$, but as $|\nu_3|$ increases δ approaches the constant value of 0.365. Probably the large hole mobilities in the parallel 3*d* band ($\mu_3=\delta\mu_1>\mu_1$) are to be found only in relatively pure Ni which is well annealed. Probably, too, the values of δ at low temperatures are quite sensitive to the nature of the impurities and to the state of anneal. This may account for the different R_0's reported for Ni by other observers.[19]

If the assumptions employed in accounting for the Hall effect data are reasonable, they must be capable of accounting for the resistivities. In particular one wonders whether or not the large values of μ_3 required to account for the low temperature Hall data on Ni

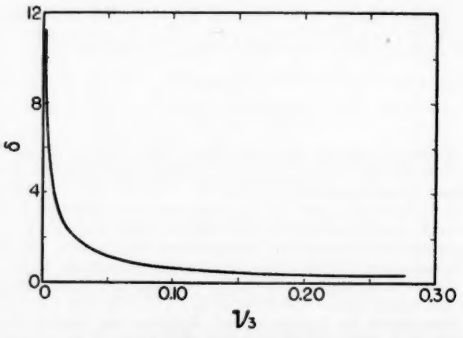

FIG. 6. Plot of δ, the relative mobility of the holes in the parallel 3*d* band compared to the mobility of the electrons in the parallel half of the 4*s* band, against ν_3, the holes/atom in this 3*d* band.

[19] This statement is based upon measurements in this laboratory by Philip Cohen on two different samples of Ni; one being 99.9 percent pure and the other 99.99 percent pure by weight. Both were carefully annealed in an He atmosphere. J. P. Jan and H. M. Gijsman, Physica **18**, 5, 277 (1952) report R_0's for their Ni sample from -5.5×10^{-13} at room temperature to -3.0×10^{-13} at liquid hydrogen temperatures. J. Smit and J. Volger, Phys. Rev. **92**, 6, 1577 (1953) report R_0's (A_H in their symbols) for four different samples of Ni at 20°K, 77°K, and 290°K that vary from -3.6×10^{-13} to -13.3×10^{-13}. One of their samples varies only slightly with temperature.

[20] A. W. Smith, Phys. Rev. **30**, 1 (1910).

[21] Pugh, Rostoker, and Schindler, Phys. Rev. **80**, 688 (1950).

are consistent with the observed variation in resistivity with temperature.

IV. RESISTIVITY OF NICKEL

The resistivity of Ni could be calculated directly from Eq. (13′) if σ_1 were known as a function of temperature. However, even if σ_1 were known exactly one should not expect perfect agreement with experiment. While the assumptions used in Eq. (13′) are consistent with modern band models, they are nevertheless somewhat arbitrary. For example, the assumption, due to Mott, that $\mu_2/\mu_1=(\nu_4/\nu_3)^{\frac{1}{2}}$, is based upon spherical symmetry and cannot be considered exact. Nevertheless, with these assumptions the Hall data on Ni yields numerical constants which are consistent with the observed resistivities of Ni.

Considering 4*s* band conduction only, one can see that the resistivity of Ni, Co, and Fe around −180°C qualitatively bear the expected relation to the resistivity of Cu at this temperature. If Ni and Co have 0.28 highly mobile 4*s* electrons/atom while Cu has 1.0, the resistivities of Ni and Co should be near 1.0/0.28 or 3.6 times that of Cu, which is close to that observed. In Fe there are holes in both the parallel and antiparallel 3*d* bands so that none of its 4*s* electrons should have high mobility. As should be expected its resistivity is greater than the others, being about 5.5 times that of Cu.

Now σ_1 is that part of the conductivity that can be ascribed to the 4*s* electrons with parallel spins. The corresponding resistivity, $\rho_1=1/\sigma_1$ can be divided into three parts due to (1) scattering by lattice vibrations, (2) scattering by holes in the 3*d* band, and (3) scattering by impurities. Assuming negligible impurities in the nickel the last can be ignored. The first can be calculated from the resistivity of Cu and the second can be calculated from the resistivity of Ni above the Curie temperature. Mott[10] has pointed out that the temperature dependence of ρ is the same for Ni above its Curie point as it is for Pd in the same temperature region. He concludes that the two should have the same temperature dependence at all temperatures if Ni remained paramagnetic at low temperatures. This similarity stems from the two having such similar band structures, with approximately 0.6 electron/atom in the *s* shell and approximately 0.6 hole/atom in the *d* shell.

That part of ρ_1 that is due to lattice vibrations should be given by $\rho_{1e}=(\theta_{Cu}/\theta_{Ni})^2(1.0/0.28)\rho_{Cu}$, where θ_{Cu} and θ_{Ni} are the Debye temperatures for these elements. This is

$$\rho_{1e}=2.57\rho_{Cu}.$$

Calculating the part of ρ_1 due to scattering by holes is more difficult. Above the Curie temperature there is a constant ratio between ρ_1 and ρ, given by either Eq. (13) or (13′); namely

$$\rho_1=2.73\rho, \text{ since } m=0 \text{ and } \beta=1.$$

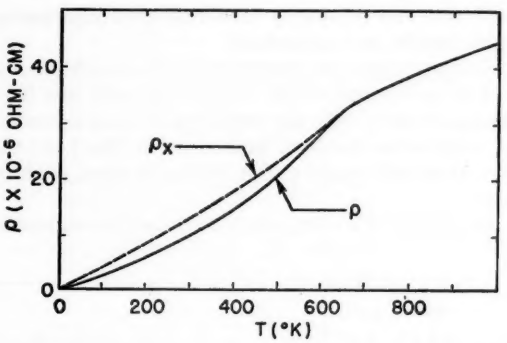

FIG. 7. Plot showing the observed resistivity of Ni, ρ, compared to the resistivity, ρ_x, that Ni should have if it remained paramagnetic to low temperatures. The ρ_x is calculated from Hall effect data.

Above the Curie point then, the part of ρ_1 due to scattering by holes is $\rho_{1h}=2.73\rho-2.57\rho_{Cu}$. If we call ρ_x the resistivity Ni would have if it remained paramagnetic to low temperatures, then the value of ρ_{1h} under these same conditions would be $2.73\rho_x-2.57\rho_{Cu}$. However, the number of holes/atom into which the parallel *s* electrons can scatter is given by $(1-m)0.28$ and

$$\rho_{1h}=(1-m)^{\frac{1}{2}}(2.73\rho_x-2.57\rho_{Cu}),$$
$$\rho_1=2.57\rho_{Cu}+(1-m)^{\frac{1}{2}}(2.73\rho_x-2.57\rho_{Cu});$$

but from Eq. (13′),

$$\rho_1=\rho\{1+\beta+(1-m)\delta+0.365(1+m)\beta\}.$$

Combining these last two equations, ρ, the resistivity of Ni, can be calculated provided ρ_x is known. This can be obtained by using the resistivity *versus* temperature curve of Pd to extrapolate the high temperature Ni data to low temperatures.

It is simpler, however, to use the observed ρ *versus* T data on Ni to calculate ρ_x to compare with the Pd curve. In Fig. 7 the observed Ni data (ρ *versus* T) and the calculated "paramagnetic" nickel curve (ρ_x *versus* T) are plotted. This latter curve is much like the Pd curve though it still changes direction a little too rapidly around the Curie temperature. Actually the shape of this curve is quite sensitive to the value of the exponent b in the relation $\beta=\mu_2/\mu_1=(\nu_4/\nu_3)^b$ which is $\frac{1}{3}$ for spherical symmetry. Only a small increase in b above $\frac{1}{3}$ is required to eliminate the rapid change in direction of the ρ_x curve at the Curie point. Thus the resistivity data on Ni is consistent with this simple band model.

V. CONCLUSIONS

The ordinary Hall constants for Co, Ni, Cu, and their binary alloys, measured at different temperatures, can be understood on the basis of a simple four-band model. The four bands consist of the two halves of the 4*s* band with spin parallel and antiparallel to the magnetic

field and two sub-bands of the 3*d* shell also having spins parallel and antiparallel.

It appears that the resistivities of these materials also can be understood on the basis of the same four-band model. Actually only the resistivity of Ni as a function of temperature has been worked out in detail but this had appeared, at the outset, to be the most doubtful case.

Since all of the calculations have used the saturation magnetization data to determine the number of carriers in each band, the saturation magnetization data is also consistent with this model.

The author desires to thank the many colleagues who have contributed by discussions and constructive criticism. He is especially indebted to Dr. Norman Rostoker, Professor Walter Kohn, Professor J. E. Goldman, of this institution and to Professor Harry Jones of Imperial College.

PHYSICAL REVIEW VOLUME 97, NUMBER 3 FEBRUARY 1, 1955

Elastic Spectrum of Copper from Temperature-Diffuse Scattering of X-Rays*

E. H. JACOBSEN
Massachusetts Institute of Technology, Cambridge, Massachusetts

(Received September 27, 1954)

Measurements have been made of the temperature-diffuse scattering of x-rays from a single crystal of copper at 300°K by using crystal monochromated Cu $K\alpha$ radiation. The measurements were analyzed by the method of Laval and James to give dispersion curves of frequency *vs* wave vector for longitudinal and transverse waves in the 100, 110, and 111 directions. These results were then expressed in terms of the generalized force constants of the Born theory of lattice dynamics.

By considering the interaction of first, second, and third neighbors, nine force constants are involved, and these have been evaluated from the dispersion curves. These force constants appear in the secular equation of frequency *vs* wave vector and constitute the necessary data for computing a complete vibrational frequency spectrum.

Such a spectrum has been calculated from the secular equation, by machine computation, for 3417 wave vectors. From this spectrum a specific heat curve was calculated and compared with experiment in the range of 15°K to 100°K.

I. INTRODUCTION

THE interaction of radiation with a thermally vibrating crystal lattice is equivalent to the case of radiation scattered from a vibrating molecule. In the case of a molecule, the levels manifest themselves as absorption-emission lines in the infrared spectrum and as lines of modified frequency in the visible spectrum, the frequency shift being of the order of 10^{12} out of 10^{14} cps. The latter phenomenon is known as the Raman effect and is of interest here by way of giving a unified picture.

It is possible to study the lattice dynamics of a crystal from the standpoint of the Raman effect. The crystal may be thought of as a giant molecule, the vibrational levels comprising the vast vibration spectrum of the lattice. Experimental and theoretical work has been carried out along this line, notably by Krishnan,[1] Bhagavantam,[2] Placzek,[3] Born,[4] and Smith.[5] However, the use of visible light is generally not permitted since most crystals are opaque to optical frequencies. Furthermore, even for transparent crystals, the interpretation of the experimental data is rather difficult.

One may study crystal lattice dynamics more conveniently with x-rays. In this case a Raman shift does indeed still occur but it is generally below the level of observation, being about 10^{12} out of 10^{18} cps. Fortunately, it is unnecessary to detect this shift in the case of x-ray investigations. Born[4] has shown that the general mechanical treatment of Placzek reduces to the relatively simple and direct interpretation of Laval[6] and James.[7] Their formulation quantitatively relates the diffuse scattering of x-rays to the frequency and wavelength of traveling elastic waves in the crystal. The thermal motion of the lattice is described by a linear superposition of these waves. By measuring the diffuse intensity along directions in reciprocal space of high symmetry, such as the 100, 110, and 111 in the case of cubic crystals, it is a simple matter to obtain dispersion curves of frequency and velocity *vs* wave vector for waves propagating along these axes. It is

* Assisted at different times by the Armco Foundation Fellowship and the National Science Foundation.

[1] K. S. Krishnan, Proc. Indian. Acad. Sci. **19**, 216 (1944).
[2] S. Bhagavantam, Proc. Indian. Acad. Sci. **11**, 62 (1940).
[3] G. Placzek, *Handbuch Der Radiologie* (Verlag Julius Springer, Berlin, 1934), Vol. 6, Part 2, p. 205.
[4] M. Born, Repts. Progr. Phys. **9**, 356 (1942–2).
[5] H. M. J. Smith, Trans. Roy. Soc. (London) **A241**, 105 (1948).
[6] J. Laval, Bull. soc. franc. mineral. **64**, 1 (1941).
[7] R. W. James, *The Optical Principles of the Diffraction of X-Rays* (G. Bell and Sons, London, 1948), Chap. V.

usually not possible to obtain directly dispersion curves for waves of arbitrary direction because such waves do not possess a pure longitudinal and transverse vibrational character. A number of investigators[8–11] have employed the Laval-James relation to obtain dispersion curves for waves propagating along the symmetry axes of a crystal, from which approximate vibrational frequency spectra and specific heats were calculated.

It is possible to extend the meaning of the Laval-James analysis by relating the dispersion curves to the Born theory of lattice dynamics. This approach allows one to calculate a number of interatomic tensor force constants which are the fundamental quantities governing the vibrational behavior of the lattice. Curien[10] has by this method obtained a set of force constants for α iron (b.c.c.) and Joynson[12] has by a similar method obtained force constants for the hexagonal lattice of zinc.[13] Having experimentally obtained the values of the force constants, one may then obtain a complete frequency spectrum by solving a secular determinant. The secular equation relates frequency to wave vector, and must be solved for a large number of wave vectors distributed throughout an appropriate section of the first Brillouin zone of reciprocal space. From the frequency spectrum, the partition function and specific heat may be calculated. Also, a relation between the elastic constants and the atomic constants may be obtained by considering the long wave limit of the secular determinant. These topics are discussed briefly in the following section. For a more detailed account, the reader should consult the work of Laval[6] and James[7] concerning temperature-diffuse x-ray scattering and the work of Born,[4] Born and Begbie,[14] and Smith[5] concerning lattice dynamics.

II. SECULAR EQUATION AND DIFFUSE X-RAY SCATTERING

Symmetry considerations show that, for a monatomic face-centered cubic lattice, a total of 9 atomic force constants are required to describe general interactions between an origin atom and all neighbor groups out to and including the third. The secular equation for this case is the 3×3 determinant represented by

$$|D(q)-\omega^2 I|=0, \tag{1}$$

composed of the elements

$$D_{ii}(q)=\frac{4}{m}\{\alpha_1''-\alpha_1'C_{jk}-\beta_1'(C_{ij}+C_{ki})+S_i^2(\alpha_2+4\alpha_3C_{jk}) +S_j^2(\beta_2+4\beta_3C_{ki})+S_k^2(\beta_2+4\beta_3C_{ij})\},$$

$$D_{ij}(q)=\frac{4}{m}\{S_iS_j\gamma_1'-4\gamma_3S_k^2+4\epsilon_3(C_{ki}+C_{jk})\},$$

$$\alpha_1'=\alpha_1+2\alpha_3, \quad \beta_1'=\beta_1+2\beta_3,$$
$$\alpha_1''=\alpha_1'+2\beta_1', \quad \gamma_1'=\gamma_1+2\gamma_3,$$
$$C_{ij}=\cos(2\pi aq_i)\cos(2\pi aq_j), \quad S_i=\sin(2\pi aq_i).$$

ω is the angular frequency of a traveling elastic wave with wave vector $\mathbf{q}=\mathbf{i}q_1+\mathbf{j}q_2+\mathbf{k}q_3$, $|\mathbf{q}|=1/\lambda$, where λ is the wavelength, I is the identity matrix, and $2a$ is the lattice constant. The additional elements of $D(q)$ are obtained by cyclic permutation of the indices i, j, k. The atomic force constants α_1, β_1, and γ_1 describe interactions between an origin atom and its first neighbor group. Similar meaning applies to the other constants, the subscripts denoting the particular neighbor group. The atomic force constants are clearly defined by Cribier.[15] These constants are proportional to the second derivatives in the expansion of the total potential energy. Higher order terms are neglected here but may be treated by perturbation theory. For the special case of central forces, $\alpha_1=\beta_2=0$, $\beta_1=\gamma_1$, and $\epsilon_3=2\gamma_3=2\beta_3=\frac{1}{2}\alpha_3$.

A comparison of the long-wave limit of Eq. (1) with the elastic matrix for a cubic crystal yields the following relations between elastic and atomic force constants:

$$\begin{aligned} ac_{11}&=2\beta_1+2\alpha_2+8\alpha_3+4\beta_3,\\ ac_{44}&=\alpha_1+\beta_1+2\beta_2+2\alpha_3+10\beta_3,\\ a(c_{12}+c_{44})&=2\gamma_1+4\gamma_3+16\epsilon_3. \end{aligned} \tag{2}$$

The elastic constants of Eqs. (2) are understood to be those obtainable from the dynamic (ultrasonic pulse) method.

For a monatomic cubic crystal, connection between the atomic constants of Eq. (1) and the x-ray data is achieved through the relation [Eq. (3)] of Laval and James. Equation (3) gives the first order diffuse scattering, in electron units per atom, in terms of the elastic waves of thermal vibration.

$$I_1=\frac{1}{m}[f^2e^{-2M}]\left|\frac{S}{\Lambda}\right|^2\sum_{j=1}^{3}\frac{E_{qj}}{\nu_{qj}^2}\cos^2(S,f)\cos^2(S,j), \tag{3}$$

$$E_{qj}=\left[\frac{1}{\exp(h\nu_{qj}/kT)-1}+\frac{1}{2}\right]h\nu_{qj}. \tag{4}$$

The quantity $[f^2e^{-2M}]$ is the square of the atomic scattering factor modified by the debye factor e^{-2M} and is obtainable from a separate experiment. For copper,

[8] Ph. Olmer, Acta Cryst. **1**, 57 (1948); Bull soc. franc. mineral. **71**, 144 (1948).
[9] H. Cole and B. E. Warren, J. Appl. Phys. **23**, 335 (1952).
[10] H. Curien, Acta Cryst. **5**, 392 (1952).
[11] H. Cole, J. Appl. Phys. **24**, 472 (1953).
[12] R. E. Joynson, Phys. Rev. **94**, 851 (1954).
[13] Joynson employed Born's formulation of x-ray scattering instead of that of Laval and James. The Born formulation relates diffuse scattering directly to the atomic constants and so bypasses the aspect of elastic waves.
[14] M. Born and G. H. Begbie, Proc. Roy. Soc. **A188**, 179 (1947).
[15] D. Cribier, Acta Cryst. **6**, 293 (1953).

the values of Brindley[16] were used: m is the atomic mass, and $(\mathbf{S}/\Lambda)$ is the diffraction vector, i.e., the difference in wave vector between the incident and reflected x-ray beam. The sum extends over the three directions of vibration j for a given elastic wave vector q, where q is the vector from the nearest Bragg reflection to the terminus of the diffraction vector $(\mathbf{S}/\Lambda)$. ν_{qj} is the frequency of the elastic wave. (S,j) is the angle between the diffraction vector and direction of vibration. E_{qj} is the quantum energy of an elastic wave, and it approaches kT for high temperatures. The value of E_{qj} can be most conveniently obtained by an iterative procedure: assume $E=kT$ and solve for ν_j by Eq. (3). Substitute ν_j in Eq. (4) and so obtain a new value of E which is to be inserted in Eq. (3) and ν_j solved for again. The cycle is repeated until successive values of ν_j agree. This procedure is generally necessary.

In addition to the first order term [Eq. (3)], the total intensity at points in reciprocal space away from Bragg reflections is composed of Compton scattering and higher order temperature diffuse terms. These contributions must be calculated and subtracted from the total intensity before using Eq. (3) to compute dispersion curves of frequency ν *vs* wave vector q. The Compton scattering was taken from Compton and Allison[17] for copper. The second order diffuse term

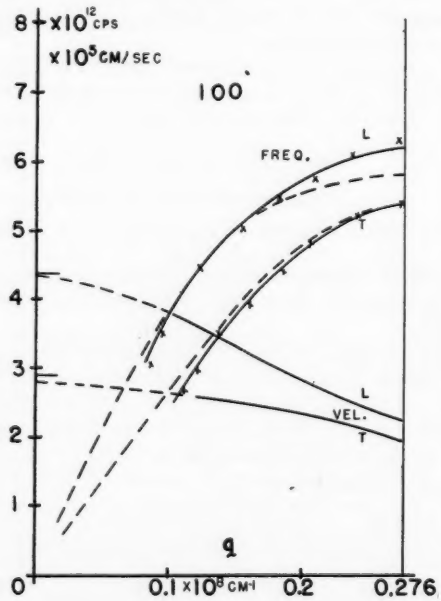

FIG. 1. Frequency and velocity *vs* wave vector for longitudinal and transverse elastic waves propagating in the 100 direction in copper. The solid lines are drawn through the experimental points. The dotted lines are the best fit obtainable and were calculated from the secular equation (1) with the constants of Table I.

[16] G. W. Brindley, Phil. Mag. **21**, 786 (1936).
[17] A. H. Compton and S. K. Allison, *X-Rays in Theory and Experiment* (D. Van Nostrand Company, Inc., New York, 1935).

(scattering from two waves) is given by Eq. (5),

$$I_2=\frac{f^2e^{-2M}v}{2m^2}\left|\frac{\mathbf{S}}{\Lambda}\right|^4\sum_Z\int\int\int\sum_i^3\sum_j^3 \times\frac{E_{\alpha i}\cos^2(S,i)E_{\beta j}\cos^2(S,j)}{\nu_{\alpha i}^2\nu_{\beta j}^2}dq_1dq_2dq_3, \quad (5)$$

where v is the volume of the primitive cell. The sum over Z refers to the number of zones intersecting an imaginary zone centered on the terminus of $(\mathbf{S}/\Lambda)$. The integration is performed over the regious of overlap between this imaginary zone and neighboring zones. By replacing the zones with spheres of the same volume and assuming an average velocity for all waves in the crystal, the second order term can be simplified and evaluated numerically.

In a similar manner the third order contribution can be calculated. For details concerning the method of calculation for higher order terms, the reader should consult reference 8. The maximum contribution of the second and third order terms to the total temperature diffuse scattering is 20 percent and 3 percent respectively. Higher order terms are negligible for copper.

The pure longitudinal and transverse character of waves propagating along the symmetry axes simplifies the first order term [Eq. (3)] for x-ray data taken along these special directions. For example, for $(\mathbf{S}/\Lambda)$ along a symmetry axis, Eq. (3) becomes

$$I_1=\frac{1}{m}[f^2e^{-2M}]\left|\frac{S}{\Lambda}\right|^2\frac{E_{ql}}{\nu_{ql}^2},$$

and thereby yields dispersion curves for longitudinal waves. Transverse curves are obtained by measuring intensities along an appropriate line in reciprocal space at right angles to a symmetry axis. In this case $(\mathbf{S}/\Lambda)$ is at some angle ϕ relative to the original longitudinal direction and Eq. (3) becomes

$$I_1=\frac{1}{m}[f^2e^{-2M}]\left|\frac{S}{\Lambda}\right|^2\left\{\frac{E_{ql}\sin^2\phi}{\nu_{ql}^2}+\frac{E_{qt}\cos^2\phi}{\nu_{qt}^2}\right\}.$$

With the aid of the previously determined longitudinal dispersion curve, one may then obtain the corresponding transverse curve.

These dispersion curves provide the information necessary to determine the inter-atomic force constants through the secular determinant (1). For waves propagating along the symmetry axes, the determinant factors into simple terms. Ideally, by considering a few points along each symmetry axis, such as $q=1/4a$ and $q=1/2a$ for the 100 direction, one may determine all nine atomic constants through a set of simultaneous equations. That is, the frequency obtained from the x-ray data by Eq. (3) is equated to the frequency

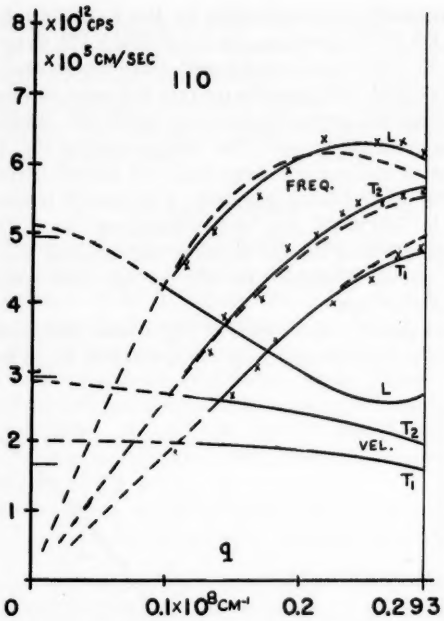

FIG. 2. Frequency and velocity *vs* wave vector for longitudinal and transverse elastic waves propagating in the 110 direction in copper. The solid lines are drawn through the experimental points. The dotted lines are the best fit obtainable and were calculated from the secular equation (1) with the constants of Table I.

appearing in the secular determinant Eq. (1) for the particular wave vector being considered. Actually it was necessary here to so choose the atomic force constants as to give the best over-all fit with the x-ray dispersion curves because not all the data were self-consistent.

III. EXPERIMENTAL PROCEDURE AND RESULTS

Three copper crystals were prepared from a single crystal of 99.99 percent purity for which we are indebted to Professor B. L. Averbach of the Department of Metallurgy. The three crystals were cut with faces parallel to the 100, 110, and 111 planes respectively. Each face was polished and then etched with ferric chloride. Laue photographs taken at several points on each face revealed sharp crystalline reflections.

All temperature diffuse measurements were made at about 300°K with Cu $K\alpha$ radiation from a full-wave rectified copper target tube operating at 35 kv and 21 ma. The radiation was monochromated by a bent lithium fluoride crystal and then passed through a balanced nickel-iron filter to cancel the half-wavelength component. The beam divergence was limited to $\pm 0.5°$ both vertically and horizontally. The scattered radiation was detected by a Geiger counter and was recorded at each angle setting for 20-minute intervals for both the nickel and iron positions of the balanced filter. The face of each copper crystal was so oriented as to maintain equal angles relative to the incident and diffracted beam in order to keep the absorption correction angularly independent. The air scattering was subtracted from the total recorded counts, the remainder being converted to electron units per atom by comparison with radiation scattered from a block of paraffin at large angles.

Intensity measurements taken along the 100 direction between 200 and 400 provided the longitudinal dispersion curve of Fig. 1 through Eq. (3). This curve together with data recorded along the line 400 to 410 produced the 100 transverse dispersion curve also shown in Fig. 1. In the same manner longitudinal and transverse curves for the 110 direction were obtained from intensity data along 5/4, 5/4, 0 to 11/4, 11/4, 0 (long.), 200 to 11/4, 5/4, 0 (trans. 1), and 400 to 4, 3/4, 3/4 (trans. 2). Similarily, the 111 dispersion curves were obtained from data along 3/2, 3/2, 3/2 to 5/2, 5/2, 5/2 (long.) and 222 to 311 (trans.). These results are shown in Figs. 2 and 3. It is to be understood that the dispersion curves are obtained from the average values of intensity measurements made in equivalent regions of a Brillouin zone. The solid lines are drawn through the experimental points. The dotted lines are the best over-all fit presently obtainable with the experimental curves and are derived from the secular determinant [Eq. (1)] with the choice of force constants given in Table I. Shown in Table II is the comparison with elastic constants through Eqs. (2).

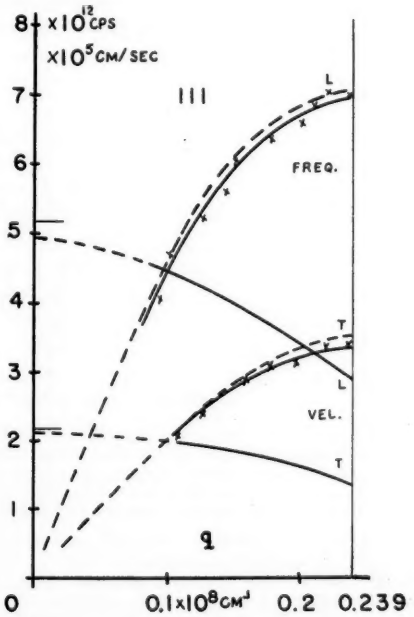

FIG. 3. Frequency and velocity *vs* wave vector for longitudinal and transverse elastic waves propagating in the 111 direction in copper. The solid lines are drawn through the experimental points. The dotted lines are the best fit obtainable and were calculated from the secular equation (1) with the constants of Table I.

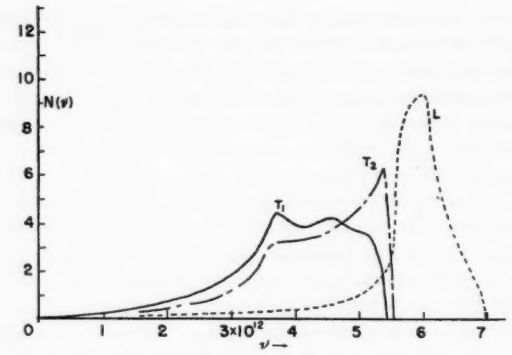

FIG. 4. Decomposition of the vibrational frequency spectrum of copper into "longitudinal" and "transverse" branches for 3417 wave-vector solutions of Eq. (1) employing the general force constants of Table I.

A vibrational spectrum has been calculated from the roots of the secular determinant [Eq. (1)] for 3417 wave vectors distributed uniformly throughout 1/48 of a Brillouin zone.[18] This calculation employed the general atomic force constants listed in Table I and will be referred to here as the general force spectrum. A decomposition of this spectrum into "longitudinal" and "transverse" branches is given in Fig. 4. The composite general force spectrum (solid line) is compared with the central force[19] (broken line) and Debye (dotted line) spectra in Fig. 5. The central force calculation utilized the constants given by Leighton[20] appropriate to copper at room temperature. This

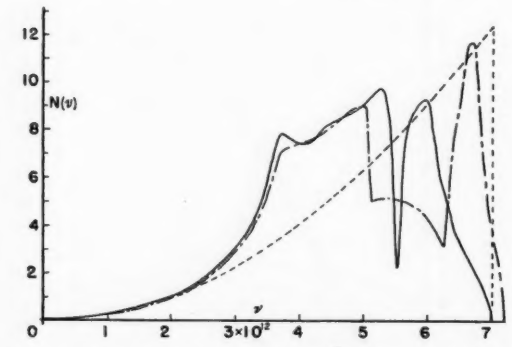

FIG. 5. Comparison of composite general force (solid line), central force (broken line), and Debye (dotted line) spectra for copper. The general force spectrum utilized the force constants of Table I. The central force spectrum utilized the force constants given by Leighton. Both spectra contain 3417 wave vector solutions.

[18] The method is outlined in reference 15.

[19] The term central force as applied to lattice dynamics has a very special meaning: i.e., forces between atoms exist only when a component of relative displacement occurs along the line of centers. No forces are exerted for a small displacement perpendicular to the line of centers. A physical central force, such as that produced by a coulomb field, does not satisfy the latter requirement of no force for small perpendicular displacements, as may be readily verified.

[20] R. B. Leighton, Revs. Modern Phys. 20, 166 (1948).

approximation is equivalent to the following: $\beta_1=\gamma_1=1.355\times10^4$ dynes/cm, $\alpha_2=-0.0244\times10^4$ dynes/cm and all other constants are zero. Both the general force and central force spectra contain the same number of solutions and were calculated on the M.I.T. Whirlwind I electronic computer.[21] The Debye curve of Fig. 5 was adjusted to have the same area and cut-off frequency as the general force spectrum. This cut-off frequency, ν_m, is 7.01×10^{12} cps and corresponds to a Debye temperature of $\theta=335°$K using the relation $h\nu_m=k\theta$. The cut-off frequency for the central force spectrum is 7.2×10^{12} cps.

The specific heat curves of Fig. 6 were calculated by numerical integration from the spectra of Fig. 5 by the

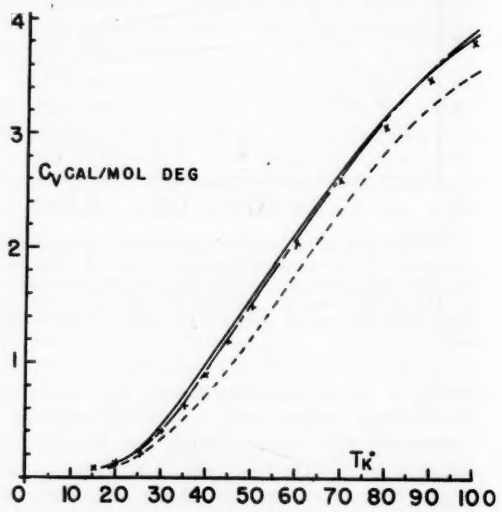

FIG. 6. Calculations of the specific heat, c_v, for copper from the spectra of Fig. 5. The solid, broken, and dotted lines correspond to the general force, central force, and Debye spectra respectively. The crosses are the experimental points of Giauque and Meads.

relation $c_v=k\int_0^{\nu_m}N(\nu)E(\nu,T)d\nu$, where

$$E(\nu,T)=(h\nu/kT)^2\exp(h\nu/kT)/[\exp(h\nu/kT)-1]^2.$$

The experimental specific heat values were taken from the work of Giauque and Meads.[22] Strictly speaking these specific heat calculations should have employed the low temperature atomic force constants. Such information is not yet available, although Gaffney and Overton[23] have recently experimentally determined that for copper the elastic constants c_{12}, c_{11}, and c_{44} increased by 2.8 percent, 4.8 percent, and 8.6 percent respectively near absolute zero. This suggests similar changes in the atomic constants which would consequently stretch the vibrational spectrum toward a higher cut-off fre-

[21] Availability of Digital Computer Laboratory time for this problem was made possible by the Office of Naval Research.

[22] W. F. Giauque and P. F. Meads, J. Am. Chem. Soc. 63, 1897 (1941).

[23] J. Gaffney and W. C. Overton, Phys. Rev. 95, 602(A) (1954).

quency and so reduce slightly the calculated specific heat at low temperatures. However, this calculation was omitted because such changes in the atomic force constants lie within the present degree of experimental uncertainty. For the same reason the more sensitive plot θ *vs* T was omitted.

IV. CONCLUSION

Interatomic force constants for the face-centered cubic lattice of copper have been determined from x-ray measurements at 300°K and are listed in Table I. These constants describe general interaction between an origin atom and its first, second, and third neighbor groups. From these constants a vibrational frequency spectrum (Figs. 4 and 5) and a specific heat curve (Fig. 6) have been calculated. A spectrum for the special case of central forces is compared with that of the general force model in Fig. 5.

Possible errors in the atomic force constants of Table I may be due to omission of anharmonic terms

TABLE I. Atomic force constants (in dynes/cm) derived from the experimental dispersion curves of Figs. 1, 2, and 3.

$\alpha_1=0.48\times10^4$	$\alpha_3=0.09\times10^4$
$\beta_1=0.87\times10^4$	$\beta_3=-0.022\times10^4$
$\gamma_1=1.25\times10^4$	$\gamma_3=-0.015\times10^4$
$\alpha_2=0.35\times10^4$	$\epsilon_3=0.06\times10^4$
$\beta_2=-0.072\times10^4$	

in the potential energy, omission of more distant neighbor effects, and use of a theoretical value for the Compton modified scattering. Of these, the latter may be very important and as such precludes investigation of the others until its behavior is more precisely established. Experimental determination of the Compton scattering is in general rather difficult but has been achieved by Laval in the cases of aluminum and KCl.[24] His measurements do show deviations to an extent which would modify the apparent diffuse scattering by several percent at a zone boundary. This possibility along with the temperature dependence of diffuse scattering are currently being investigated in this laboratory. Until this information has been acquired, it is not possible to set margins of error for the x-ray-determined force constants. The agreement between atomic and elastic constants for c_{11} and c_{12} via Eqs. (2) may thus be somewhat fortuitous at this stage.

It will be noted that the central force model produces

[24] J. Laval, Bull. soc. franc. mineral. **62**, 137 (1939).

TABLE II. Comparison of ultrasonic and x-ray values of elastic constants (in dynes/cm²).

Ultrasonic values[a]	x-ray values
$c_{11}=17.0\times10^{11}$	$c_{11}=17.0\times10^{11}$
$c_{12}=12.3\times10^{11}$	$c_{12}=12.4\times10^{11}$
$c_{44}=7.52\times10^{11}$	$c_{44}=6.45\times10^{11}$

[a] J. Gaffney and W. C. Overton, Phys. Rev. **95**, 602(A) (1954).

a vibrational spectrum in close agreement with that of the general force model over the first 5/7 of the frequency scale. Furthermore, the general force spectrum exhibits no character essentially different from that of the central force model. Thus the specific heats calculated from both models agree well with one another over the temperature range considered. They also agree quite well with the observed specific heat of copper, although it should be added that the choice of a lower characteristic temperature θ will produce a Debye specific heat which is also close to the observed values in this temperature range.

In connection with the x-ray dispersion curves, the central force model is not so consistant. While this model is in fair accord with most of the curves of Figs. 1, 2, and 3, there are discrepancies of over 20 percent for the 100 longitudinal and 110 (trans. 2) cases. Such discrepancies require consideration of a more general type of force between atoms when dealing with lattice vibrations in copper. This statement disagrees with the theoretical results of Fuchs.[25]

It is felt by this author that the future value of temperature diffuse scattering experiments lies mainly in the determination of interatomic forces in solids. Diffraction experiments, including those with electrons and neutrons, are the only direct means presently available for such determinations. Through the study of interatomic forces, it may be possible to acquire supplementary information about the electronic configuration in some solids, particularly metals, the character of which is necessarily reflected in the tensor force constants of Eq. (1). This topic is in fact being studied by a member of the Solid State and Molecular Theory Group at M.I.T. for copper.

The author is indebted to B. E. Warren for suggesting this problem, and for his continued interest and helpful advice on many occasions. He also wishes to thank F. J. Corbató for help in machine computational techniques, and R. E. Joynson and H. Cole for valuable discussion.

[25] K. Fuchs, Proc. Roy. Soc. (London) **A153**, 622 (1936).

Slow Electrons in a Polar Crystal

R. P. FEYNMAN
California Institute of Technology, Pasadena, California
(Received October 19, 1954)

A variational principle is developed for the lowest energy of a system described by a path integral. It is applied to the problem of the interaction of an electron with a polarizable lattice, as idealized by Fröhlich. The motion of the electron, after the phonons of the lattice field are eliminated, is described as a path integral. The variational method applied to this gives an energy for all values of the coupling constant. It is at least as accurate as previously known results. The effective mass of the electron is also calculated, but the accuracy here is difficult to judge.

AN electron in an ionic crystal polarizes the lattice in its neighborhood. This interaction changes the energy of the electron. Furthermore, when the electron moves the polarization state must move with it. An electron moving with its accompanying distortion of the lattice has sometimes been called a polaron. It has an effective mass higher than that of the electron. We wish to compute the energy and effective mass of such an electron. A summary giving the present state of this problem has been given by Fröhlich.[1] He makes simplifying assumptions, such that the crystal lattice acts much like a dielectric medium, and that all the important phonon waves have the same frequency. We will not discuss the validity of these assumptions here, but will consider the problem described by Fröhlich as simply a mathematical problem. Aside from its intrinsic interest, the problem is a much simplified analog of those which occur in the conventional meson theory when perturbation theory is inadequate. The method we shall use to solve the polaron problem is new, but the pseudoscalar symmetric meson field problems involve so many further complications that it cannot be directly applied there without further development.

We shall show how the variational technique which is so successful in ordinary quantum mechanics can be extended to integrals over trajectories.

STATEMENT OF THE PROBLEM

With Fröhlich's assumptions, the problem is reduced to that of finding the properties of the following Hamiltonian:

$$H=\tfrac{1}{2}\mathbf{P}^2+\sum_K a_K^+ a_K+i(\sqrt{2}\alpha/V)^{\frac{1}{2}}\sum_K \frac{1}{K}\times[a_K^+\exp(-i\mathbf{K}\cdot\mathbf{X})-a_K\exp(i\mathbf{K}\cdot\mathbf{X})]. \quad (1)$$

Here $\mathbf{X}$ is the vector position of the electron, $\mathbf{P}$ its conjugate momentum, a_K^+, a_K the creation and annihilation operators of a phonon (of momentum $\mathbf{K}$). The frequency of a phonon is taken to be independent of $\mathbf{K}$. Our units are such that $\hbar$, this frequency, and the electron mass are unity. The quantity α acts as a coupling constant, which may be large or small. In conventional units it is given by

$$\alpha=\frac{1}{2}\left(\frac{1}{\epsilon_\infty}-\frac{1}{\epsilon}\right)\frac{e^2}{\hbar\omega}\left(\frac{2m\omega}{\hbar}\right)^{\frac{1}{2}},$$

where ϵ, ϵ_∞ are the static and high frequency dielectric constant, respectively. In a typical case, such as NaCl, α may be about 5. The wave function of the system satisfies ($\hbar=1$)

$$i\partial\psi/\partial t=H\psi, \quad (2)$$

so that if φ_n and E_n are the eigenfunctions and eigenvalues of H,

$$H\varphi_n=E_n\varphi_n, \quad (3)$$

then any solution of (2) is of the form

$$\psi=\sum_n C_n\varphi_n e^{-iE_n t}.$$

Now we can cast (1) and (2) into the Lagrangian form of quantum mechanics and then eliminate the field oscillators (specializing to the case that all phonons are virtual). Doing this in exact analogy to quantum electrodynamics,[2] we find that we must study the sum over all trajectories $\mathbf{X}(t)$ of $\exp(iS')$, where

$$S'=\frac{1}{2}\int\left(\frac{d\mathbf{X}}{dt}\right)^2 dt+2^{-\frac{1}{2}}\alpha i\int\int|\mathbf{X}_t-\mathbf{X}_s|^{-1}e^{-i|t-s|}dtds. \quad (4)$$

This sum will depend on the initial and final conditions and on the time interval T. Since it is a solution of the Schrödinger Eq. (2), considered as a function of T it will contain frequencies E_n, the lowest of which we seek. It is difficult to isolate the lowest frequency, however.

For that reason, consider the mathematical problem of solving

$$\partial\psi/\partial t=-H\psi, \quad (5)$$

without question as to the meaning of t. This has the same eigenvalues and eigenfunctions as (3), but a

[1] H. Fröhlich, Advances in Physics 3, 325 (1954). References to other work is given here.

[2] R. P. Feynman, Phys. Rev. 80, 440 (1950).

solution will have the form

$$\psi=\sum_n C_n e^{-E_n t}\varphi_n.$$

For large t any solution therefore asymptotically dies out exponentially, the last exponent surviving being that of the lowest E, say E_0.

An equation such as (5) can be converted to a path integral just as easily as (2) is, and the integral over the oscillator coordinates can again be done in an analogous way. The Lagrangian form corresponding to (5) turns out to be

$$K=\int \exp S\mathfrak{D}\mathbf{X}(t), \tag{6}$$

with

$$S=-\frac{1}{2}\int\left(\frac{d\mathbf{X}}{dt}\right)^2 dt + 2^{-\frac{1}{2}}\alpha\int\int |\mathbf{X}_t-\mathbf{X}_s|^{-1}e^{-|t-s|}dtds. \tag{7}$$

This is just as one might expect from replacing t in (4) by $-it$. Now, since K is a solution of (5), its asymptotic form for a large t interval, 0 to T is

$$K\sim e^{-E_0 T} \tag{8}$$

as $T\to\infty$. Therefore, we must estimate the path integral (6) for large T.

VARIATIONAL PRINCIPLE

The method we shall use is a type of variational method. Choose any S_1 which is simple and purports to be some sort of approximation to S. Then write

$$\int \exp S\mathfrak{D}\mathbf{X}(t)=\int \exp(S-S_1)\exp S_1\mathfrak{D}\mathbf{X}(t). \tag{9}$$

Now this last expression can be looked upon as the average of $\exp(S-S_1)$, the average being taken with positive weight $\exp S_1$. But for any set of real quantities f the average of $\exp f$ exceeds the exponential of the average,

$$\langle\exp f\rangle\geq\exp\langle f\rangle. \tag{10}$$

Hence if in (9) we replace $S-S_1$ by its average,

$$\langle S-S_1\rangle = \int (S-S_1)\exp S_1\mathfrak{D}\mathbf{X}(t)\Big/\int \exp S_1\mathfrak{D}\mathbf{X}(t), \tag{11}$$

we will underestimate the value of (9). Therefore, if E is computed from

$$\int \exp(\langle S-S_1\rangle)\exp S_1\mathfrak{D}\mathbf{X}(t)\sim\exp -ET, \tag{12}$$

then we know that E exceeds the true E_0,

$$E\geq E_0. \tag{13}$$

If there are any free parameters in S_1 we can choose as the "best" values those which minimize E.

Since $\langle S-S_1\rangle$ defined in (11) is proportional to T, let us write

$$\langle S-S_1\rangle=sT. \tag{14}$$

Furthermore, the factor $\exp\langle S-S_1\rangle$ in (12) is constant, of course, and may be taken outside the integral. Finally, suppose the lowest energy E_1 for the action S_1 is known,

$$\int \exp S_1\mathfrak{D}\mathbf{X}(t)\sim\exp(-E_1T), \tag{15}$$

then we have

$$E=E_1-s \tag{16}$$

from (12), with s given by (11) and (14). (In the case that S and S_1 are both simple actions [of the form of (18) below] this can readily be shown to be equivalent to the usual variational principle.)

POSSIBLE TRIAL ACTIONS

Some of the methods which have been applied to this problem, so far, correspond to various choices for S_1. The perturbation method corresponds to $S_1=-\frac{1}{2}\int(d\mathbf{X}/dt)^2dt$ and gives

$$E=-\alpha. \tag{17}$$

We see immediately that the perturbation result is an upper limit to E_0, a result proven only with much greater effort by more usual methods, by Gurari[3] and Lee and Pines.[4] Another suggestion is

$$S_1=-\tfrac{1}{2}\int(d\mathbf{X}/dt)^2dt+\int V(\mathbf{X}_t)dt, \tag{18}$$

where V is a potential to be chosen. If a Coulomb potential is chosen, $V(R)=Z/R$, and the parameter Z varied, one finds

$$E=-(25/256)\alpha^2=-0.098\alpha^2$$

asymptotically for the case that α is very large. For large α this corresponds to Landau's method[1] with a trial function of the form $e^{-\beta r}$. If a harmonic potential $V(R)=kR^2$ is used (corresponding to a Gaussian trial function in Landau's method) the value is somewhat improved:

$$E=-(1/3\pi)\alpha^2=-0.106\alpha^2. \tag{19}$$

If α is not so large, the form (18) can still be used in (16). The evaluation of s requires knowledge of the eigenfunctions and eigenvalues for the potential V.

[3] M. Gurari, Phil. Mag. 44, 329 (1953).
[4] T. Lee and D. Pines, Phys. Rev. 88, 960 (1952). Lee, Low, and Pines, Phys. Rev. 90, 297 (1953).

The result is somewhat difficult to evaluate for the Coulomb potential, but fairly simple for the harmonic case [see (34) below]. However, it is readily shown that for any α less than about 6 no choice of V can improve the result (17) for $V=0$. Fröhlich has asked for a method which works uniformly over the entire range of α. He points out that the artificial binding to a special origin, which (18) implies, is a disadvantage. It is this which presumably makes any potential V give a poorer result than $V=0$ for small α.

To remedy this, I thought a good idea would be to use for S_1 the action for a particle bound by a potential $V(\mathbf{X}-\mathbf{Y})$ to another particle of coordinate $\mathbf{Y}$. This latter could have finite mass, so no permanent origin would be assumed. Of course the action for such a system would contain both $\mathbf{X}(t)$ and $\mathbf{Y}(t)$. But the variables $\mathbf{Y}(t)$ could be integrated out, at least in principle, leaving an effective S_1 depending only on $\mathbf{X}$. At first I tried a Coulomb interaction for $V(\mathbf{X}-\mathbf{Y})$ but it was rather complicated. The technique may be useful in more difficult problems. But here we have already seen that an harmonic binding should be as good, if not better. Further, an extra particle bound harmonically has its variables $\mathbf{Y}(t)$ appearing quadratically in the action. It may therefore be easily eliminated explicitly. The result we know from studies of similar problems in electrodynamics. We are, in this way, led to consider the choice

$$S_1=-\tfrac{1}{2}\int\left(\frac{d\mathbf{X}}{dt}\right)^2dt-\tfrac{1}{2}C\int\int[\mathbf{X}_t-\mathbf{X}_s]^2\times\exp(-w|t-s|)dtds, \quad (20)$$

where C and w are parameters, to be chosen later to minimize E.

EVALUATION OF THE ENERGY

Since S_1 contains $\mathbf{X}$ only quadratically, all the necessary path integrals are easily done.[5] Because the method may not be familiar we outline it briefly here. Define the symbol $\langle\ \rangle$ as

$$\langle F\rangle=\int F\exp S_1\mathfrak{D}\mathbf{X}(t)\Big/\int\exp S_1\mathfrak{D}\mathbf{X}(t).$$

Then comparison of S_1 and S shows that

$$s=\frac{1}{T}\langle S-S_1\rangle=2^{-\frac{1}{2}}\alpha\int\langle|\mathbf{X}_t-\mathbf{X}_s|^{-1}\rangle e^{-|t-s|}ds+\tfrac{1}{2}C\int\langle(\mathbf{X}_t-\mathbf{X}_s)^2\rangle e^{-w|t-s|}ds=A+B. \quad (21)$$

[5] R. P. Feynman, Phys. Rev. 84, 108 (1951), Appendix C.

We concentrate first on the first term A of (21). In it we may express $|\mathbf{X}_t-\mathbf{X}_s|^{-1}$ by a Fourier transform,

$$|\mathbf{X}_t-\mathbf{X}_s|^{-1}=\int d^3\mathbf{K}\exp[i\mathbf{K}\cdot(\mathbf{X}_t-\mathbf{X}_s)](2\pi^2K^2)^{-1}. \quad (23)$$

For this reason we need to study

$$\langle\exp[i\mathbf{K}\cdot(\mathbf{X}_\tau-\mathbf{X}_\sigma)]\rangle=\int\exp S_1\exp[i\mathbf{K}\cdot(\mathbf{X}_\tau-\mathbf{X}_\sigma)]\mathfrak{D}\mathbf{X}(t)\Big/\int\exp S_1\mathfrak{D}\mathbf{X}(t). \quad (23)$$

The integral in the numerator is of the form

$$I=\int\exp\left[-\tfrac{1}{2}\int\left(\frac{d\mathbf{X}}{dt}\right)^2dt-\tfrac{1}{2}C\int\int(\mathbf{X}_t-\mathbf{X}_s)^2\times e^{-w|t-s|}dtds+\int\mathbf{f}(t)\cdot\mathbf{X}(t)dt\right]\mathfrak{D}\mathbf{X}(t), \quad (24)$$

where specifically

$$\mathbf{f}(t)=i\mathbf{K}\delta(t-\tau)-i\mathbf{K}\delta(t-\sigma). \quad (25)$$

Now we shall find (24) insofar as it depends on $\mathbf{f}$ or $\mathbf{K}$ aside from a normalization factor which drops out in (23). Incidentally let us notice that the three rectangular components separate in (24) and we need only consider a scalar case. The method of integration is to substitute $X(t)=X'(t)+Y(t)$, where $X'(t)$ is that special function for which the exponent is maximum. The variable of integration is now $Y(t)$. Since the exponent is quadratic in $X(t)$ and X' renders it an extremum, it can contain $Y(t)$ only quadratically. Evidently Y then separates off as a factor not containing f, which may be integrated to give an unimportant constant (depends on T only). Therefore within such a constant

$$I=\exp\left[-\tfrac{1}{2}\int\dot{X}_t'^2dt-\tfrac{1}{2}C\int\int(X_t'-X_s')^2\times e^{-w|t-s|}dtds+\int f(t)X_t'dt\right], \quad (26)$$

where X' is that function which minimizes the expression [subject for convenience, to $X'(0)=X'(T)=0$ if the time interval is 0 to T]. The variation problem gives the integral equation

$$d^2X'(t)/dt^2=2C\int(X_t'-X_s')e^{-w|t-s|}ds-f(t). \quad (27)$$

Using (27), (26) can be simplified to

$$I=\exp\left[\tfrac{1}{2}\int f(t)X'(t)dt\right]. \quad (28)$$

We need merely solve (27) and substitute into (28). To do this we define

$$Z(t)=\frac{w}{2}\int e^{-w|t-s|}X_s'ds,$$

so that

$$d^2Z(t)/dt^2=w^2[Z(t)-X'(t)],$$

while (27) is

$$d^2X'(t)/dt^2=\frac{4C}{w}[X'(t)-Z(t)]-f(t).$$

The equations are readily separated and solved. The solution for $X'(t)$ substituted into (28) gives, for the case (25),

$$I=\langle\exp[i\mathbf{K}\cdot(\mathbf{X}_\tau-\mathbf{X}_\sigma)]\rangle$$
$$=\exp\left[-\frac{2CK^2}{v^3w}(1-e^{-v|\tau-\sigma|})-\frac{w^2}{2v^2}K^2|\tau-\sigma|\right], \quad (29)$$

where we have made the substitution

$$v^2=w^2+(4C/w). \quad (30)$$

The result is correctly normalized since it is valid for $\mathbf{K}=0$. The integral on K in (22) is a simple Gaussian, so that substitution into A gives

$$A=\pi^{-\frac{1}{2}}\alpha v\int_0^\infty\left[w^2\tau+\frac{v^2-w^2}{v}(1-e^{-v\tau})\right]^{-\frac{1}{2}}e^{-\tau}d\tau. \quad (31)$$

To find B we need $\langle(\mathbf{X}_t-\mathbf{X}_s)^2\rangle$. This can be obtained by expanding both sides of (29) with respect to $\mathbf{K}$ up to order K^2. Therefore

$$\tfrac{1}{3}\langle(\mathbf{X}_\tau-\mathbf{X}_\sigma)^2\rangle=\frac{4C}{v^3w}(1-e^{-|\tau-\sigma|})+\frac{w^2}{v^2}|\tau-\sigma|.$$

The integral in B is now easily performed and the expression simplifies to

$$B=3C/vw. \quad (32)$$

Finally we need E_1, the energy belonging to our action S_1. This is most easily obtained by differentiating both sides of (15) with respect to C. One finds immediately

$$CdE_1/dC=B,$$

so that, in view of (32) and (30), integration gives

$$E_1=\tfrac{3}{2}(v-w),$$

since $E_1=0$ for $C=0$. Since $E_1-B=(3/4v)(v-w)^2$ we obtain finally for our energy expression:

$$E=\frac{3}{4v}(v-w)^2-A, \quad (33)$$

with A given in (31). The quantities v, w can be considered as two parameters which may be varied separately to obtain a minimum.

The integral in A unfortunately cannot be performed in closed form, so that a complete determination of E requires numerical integration. It is, however, possible to obtain approximate expressions in various limiting cases. The case of large α corresponds to large v. The choice $w=0$ leads to an integral

$$A=\pi^{-\frac{1}{2}}\alpha v^{\frac{1}{2}}\int_0^\infty e^{-\tau}d\tau[1-e^{-v\tau}]^{-\frac{1}{2}}=\frac{\alpha\Gamma(1/v)}{v^{\frac{1}{2}}\Gamma(\frac{1}{2}+1/v)}, \quad (34)$$

and $E_1=3v/4$. It corresponds to the use of a fixed harmonic binding potential in (18). For large v, $e^{-v\tau}$ can be neglected, so that $A=\pi^{-\frac{1}{2}}\alpha v^{\frac{1}{2}}$. This corresponds to using a Gaussian trial function in Landau's method. For α less than 5.8 and $w=0$, (33) does not give a minimum unless $v=0$, so that the $w=0$ case does not give a single expression for all ranges of α. In spite of this disadvantage the result with (34) is relatively simple and fairly accurate. For $\alpha>6$, only fairly large v are important, and the asymptotic formula (good to 1 percent for $v>4$),

$$A=\alpha(v/\pi)^{\frac{1}{2}}[1+(2\ln 2)/v],$$

is convenient. Fröhlich, however, considers the discontinuity at $\alpha=6$ as a serious disadvantage, which it is the purpose of this paper to avoid. This we do by choosing w different from zero.

Let us study (33), just for small α, in case w is not zero. The minimum will occur for v near w. Therefore write $v=(1+\epsilon)w$, consider ϵ small, and expand the root in (31). This gives

$$A=\alpha(v/w)\left[1-\epsilon\int_0^\infty\tau^{-\frac{1}{2}}e^{-\tau}(1-e^{-w\tau})d\tau/w\pi^{\frac{1}{2}}+\cdots\right].$$

The integral is

$$2w^{-1}[(1+w)^{\frac{1}{2}}-1]=P. \quad (35)$$

The problem (33) then corresponds, in this order, to minimizing

$$E=\tfrac{3}{4}w\epsilon^2-\alpha-\alpha\epsilon(1-P).$$

That is,

$$\epsilon=2\alpha(1-P)/3w,$$

which is valid for small α only, as ϵ was assumed small. The resulting energy is

$$E=-\alpha-\alpha^2(1-P)^2/3w.$$

Our method therefore gives a correction even for small α. It is least for $w=3$, in which case it gives

$$E=-\alpha-\alpha^2/81=-\alpha-1.23(\alpha/10)^2. \quad (36)$$

It is not sensitive to the choice of w. For example, for $w=1$ the 1.23 falls only to 0.98. The method of Lee and Pines[6] gives exactly this result (36) to this order. The perturbation expansion has been carried to

[6] T. Lee and D. Pines, Phys. Rev. 92, 883 (1953).

second order by Haga[7] who shows that the exact coefficient of the $(\alpha/10)^2$ term should be 1.26, so that our variational method is remarkably accurate for small α.

The opposite extreme of large α corresponds to large v, and, as we shall see, w near 1. Since $v \gg w$ the integral (31) reduces in the first approximation to (34), which we can use in its asymptotic form. The next approximation in w can be obtained by expanding the radical in (31), considering $w/v \ll 1$. Furthermore, e^{-vr} is negligible. In this way we get

$$E=\frac{3}{4v}(v-w)^2-\alpha(v/\pi)^{\frac{1}{2}}\left(1+\frac{2\ln 2}{v}-\frac{w^2}{2v}\right). \quad (37)$$

This is minimum, within our approximation of large v, when $w=1$, and $v=(4\alpha^2/9\pi)-(4\ln 2-1)$:

$$E=-\alpha^2/3\pi-3\ln 2-\tfrac{3}{4}=-0.106\alpha^2-2.83. \quad (38)$$

The approximations do not keep E as an upper limit as, unfortunately, the further terms, of order $1/\alpha^2$ are probably positive.

For further numerical work it is probably sufficiently accurate to take $w=1$ for all α, rather than do the extra work needed to minimize this extra variable. This value of w means that the trial S_1 has the same time exponential in the interaction term as does S. For small α, that is, v near 1, the integral can be expanded in a power series in $(v-1)$. The resulting energy is $(w=1)$:

$$E=-\alpha-0.98(\alpha/10)^2-0.60(\alpha/10)^3 -0.14(\alpha/10)^4\cdots. \quad (39)$$

The two expressions (38), (39) fit fairly well near $\alpha=5$. For practical purposes it may suffice to use (39) below $\alpha=5$ and (38) above. If more accuracy than 3 percent is needed near $\alpha=5$ numerical integration of A must be performed. The value of v which gives (39) is

$$v=1+1.14(\alpha/10)+1.35(\alpha/10)^2+1.88(\alpha/10)^3.$$

This may help to choose an appropriate v. For $w=3$ the results are

$$E=-\alpha-1.23(\alpha/10)^2-0.64(\alpha/10)^3\cdots,$$
$$v=3+2.22(\alpha/10)+1.97(\alpha/10)^2\cdots.$$

EFFECTIVE MASS

Another quantity of interest is the effective mass. If the particle moves with a mean group velocity V, its energy should be greater. For small V the energy goes as V^2, and writing it as $mV^2/2$ we call m the effective mass. Since there is an operator analogous to the momentum which commutes with the Hamiltonian, it would be expected that there is a variational principle which minimizes the energy for each momentum. That is, we ought to be able to extend our method to yield an upper limit to the energy for each value of V, or better, of momentum Q. We have not found the expected extension.

If we limit ourselves just to finding the effective mass for low velocities, however, we may proceed in this manner: For a free particle of mass m whose initial coordinate is 0 and final coordinate is $\mathbf{X}_T$ the sum on trajectories is

$$\exp(-m\mathbf{X}_T^2/2T). \quad (40)$$

Hence we can study the effective mass for our system by studying the asymptotic form of (6) in the case $\mathbf{X}_T \neq 0$. The asymptotic form should vary for small $\mathbf{X}_T$ as $\exp(-E_0T-m\mathbf{X}_T^2/2T)$, its dependence on $\mathbf{X}_T$ determining m. This only requires that (27) be solved for the boundary conditions $\mathbf{X}'=0$ at $t=0$ and $\mathbf{X}'=\mathbf{X}_T$ at $t=T$. There are some confusing complications at the end points so it is easier to proceed as follows. We will put $\mathbf{X}_T=\mathbf{U}T$ so that the propagation (40) is $\exp(-\frac{1}{2}mU^2T)$. [Note that $\mathbf{U}$ is not a physical velocity because t is an artificial parameter in Eq. (5), and is not the time.] That is, we seek the total energy and equate it to $E_0+\frac{1}{2}mU^2$. But if we substitute $\mathbf{X}=\mathbf{X}''+\mathbf{U}t$ into (27), we see that it is a solution if $\mathbf{X}''$ is. This $\mathbf{X}''$ goes from 0 at $t=0$ to 0 at $t=T$, and is therefore our previous solution. Such a substitution into (26) means that the term involving $\mathbf{f}$ adds a term $\exp(\int t\mathbf{U}\cdot\mathbf{f}dt)$ so that this is the factor by which I is multiplied, aside from normalization. For the $\mathbf{f}$ given in (25) this is $\exp[i\mathbf{K}\cdot\mathbf{U}(\tau-\sigma)]$ so that we now have

$$\langle\exp[i\mathbf{K}\cdot(\mathbf{X}_\tau-\mathbf{X}_\sigma)]\rangle = \exp\left[-\frac{K^2}{2v^2}F(|\tau-\sigma|)+i\mathbf{K}\cdot\mathbf{U}(\tau-\sigma)\right], \quad (41)$$

where

$$F(\tau)=w^2\tau+\frac{v^2-w^2}{v}(1-e^{-v\tau}). \quad (42)$$

Substitution into (22) and (21) gives for A the value

$$A(\mathbf{U})=2^{-\frac{1}{2}}\alpha\int_0^\infty\int(2\pi^2K^2)^{-1}e^{-\tau} \times\exp\left[-\frac{K^2}{2v^2}F(\tau)+i\mathbf{K}\cdot\mathbf{U}\tau\right]d^3\mathbf{K}d\tau. \quad (43)$$

Second differentiation of (41) with respect to $\mathbf{K}$ shows that

$$\langle(\mathbf{X}_t-\mathbf{X}_s)^2\rangle=3F(t-s)v^{-2}+U^2(t-s)^2,$$

so that one obtains for B the value

$$B=\frac{3C}{vw}+\frac{2C}{w^3}U^2.$$

We again find E_1 from $dE_1/dC=B/C$ and $E_1=\frac{1}{2}U^2$ for $C=0$. Thus

$$E_1=\tfrac{3}{2}(v-w)+\tfrac{1}{2}U^2(1+4Cw^{-3}),$$

[7] E. Haga, Progr. Theoret. Phys. (Japan) 11, 449 (1954).

and our final expression is

$$E=\tfrac{1}{2}U^2+(3/4v)(v-w)^2-A(\mathbf{U}). \tag{44}$$

We next expand $A(\mathbf{U})$ to order U^2 and write the kinetic energy as $mU^2/2$ to find, finally,

$$m=1+\tfrac{1}{3}\pi^{-\frac{1}{2}}\alpha v^3\int_0^\infty [F(\tau)]^{-\frac{3}{2}}e^{-\tau}\tau^2 d\tau. \tag{45}$$

The values of the parameters to use in (45) are those which were previously found to minimize E when $\mathbf{U}=0$.

For small α this gives

$$m=1+\tfrac{1}{6}\alpha+0.025\alpha^2+\cdots \tag{46}$$

for $w=3$, while for $w=1$ the 0.025 becomes 0.023. For large α it becomes

$$m=16\alpha^4/81\pi^4=202(\alpha/10)^4. \tag{47}$$

Our energy values, coming from a minimum principle, are much more accurate than the mass values, whose precision, especially for large α, is hard to judge. Since (46) and (47) do not match well, intermediate values of α require numerical integration of (45).

Lee and Pines[6] have worked with a different type of variational principle. It seems to be nearly as good as ours for α less than about 5, but is poor for larger α (for example, at $\alpha=15$, Lee and Pines find $E_0<-17.6$, while we find $E_0<-26.8$). This appears to contradict their statement that their method is exact for large α. They are referring to a different problem, however, in which the upper momenta are cut off. This means that in S in (7) the function $|\mathbf{X}_t-\mathbf{X}_s|^{-1}$ is replaced by some other function $V(|\mathbf{X}_t-\mathbf{X}_s|)$ which differs for small $|\mathbf{X}_t-\mathbf{X}_s|$. It is evident, for large α, that the best trajectory will be the one that wanders only slightly and the energy will be $2^{-\frac{1}{2}}\alpha V(0)$ in the limit. Their method gives this result in the limit, as ours would also. For the case where V is singular, so $V(0)$ does not exist their method is not exact, and it is inaccurate for for intermediate values of α even if $V(0)$ exists, if V has steep walls.

The method is readily extended to cases in which the photon frequencies are not constant, and the coupling is not just proportional to K^{-1}. The same trial action S_1 can be used, but the integral for A becomes more complicated. For the Hamiltonian

$$H=\tfrac{1}{2}P^2+\textstyle\sum_K\omega_K a_K^+a_K+V^{-\frac{1}{2}}\sum_K[C_K^*a_K^+\exp(-i\mathbf{K}\cdot\mathbf{X})+C_Ka_K\exp(+i\mathbf{K}\cdot\mathbf{X})],$$

Eq. (33) still holds; the only change is that the integral for A becomes

$$A=\int\int_0^\infty \exp\left[-\omega_K\tau-\frac{K^2}{2v^2}F(\tau)\right]|C_K|^2 d\tau d^3\mathbf{K}(2\pi)^{-3},$$

where $F(\tau)$ is given in (42).

An attempt has been made to apply this method to meson problems. The case of scalar nucleons interacting by scalar mesons seems tractable, but the greater complexity of the more realistic problems shows the need for further development.

We are limited in our choice of S_1 to quadratic functionals, for those are the only ones we can evaluate directly as path integrals. It would be desirable to find out how this method may be expressed in conventional notation, for a wider class of trial functionals might thereby become available.

I am indebted to H. Fröhlich for bringing the problem to my attention, and for his comments on it, and to G. Speisman for emphasizing the importance of the general inequality (10).

Note added in proof.—Professor Frölich and Professor Pines have kindly informed me that S. I. Pekar [Zhur. Eksptl. i Teort. Fiz. **19**, 796 (1949)] has calculated the limiting values of energy and mass for large α, by an adiabatic approximation. The energy is $-0.1088\alpha^2$ and the mass is $232(\alpha/10)^4$. Therefore our variational method gives an error of only 3 percent in the energy and 15 percent in the mass for large α, and presumably smaller errors for smaller α.

Resistance and Thermoelectric Measurements of Cold-Worked Copper and the Resistance Minimum at Low Temperatures

W. B. PEARSON
Division of Physics, National Research Council, Ottawa, Canada
(Received October 18, 1954)

Measurements of the change of residual resistance ratio of copper as a function of the percentage reduction in cross-sectional area by cold-working in liquid helium, liquid nitrogen or at room temperature and subsequent ageing treatments show (1) the relative change of the ratio during recovery between 77°K and room temperature to that accompanying recovery and recrystallization at higher temperatures; (2) that there appears to be no recovery process taking place below 77°K; (3) that specimens cold-worked in liquid helium or nitrogen and aged at room temperature have a higher residual resistance ratio than specimens both cold-worked and aged at room temperature.

We find that the thermoelectric force, E, of copper specimens cold-worked at room temperature or liquid helium is positive relative to annealed copper in the range 4°–40°K (taking 4°K as zero). The measurements are discussed in relation to the origin of the electrical resistance minimum which is found in copper at 10°–14°K.

THE effect of lattice defects on the electrical resistivity of metals has recently been reviewed by Broom.[1] Recovery and recrystallization of cold-worked metals at room temperature and above have long been investigated, but it is only recently through the work of Molenaar and Aarts[2] that attention has been drawn to recovery processes between 90°K and room temperature. Druyvesteyn and Manintveld[3] and Manintveld[4,5] have identified two recovery processes in copper in this temperature range. As a result of this and other work, it now seems probable that the recovery of copper following cold work, involves three stages; the first at 120° to 200°K, is of uncertain origin, but may well involve the elimination of interstitial atoms; the second at 230° to 310°K is almost certainly concerned with elimination of vacancies; and the final process involves movement of dislocations and ends with recrystallization.

Preliminary to investigating the recovery processes of sodium at low temperatures, we have carried out some experiments on the electrical resistivity and thermoelectric force of cold-worked copper. As these provide new information, it seemed worthwhile publishing the data, especially as the thermoelectric measurements throw further light on the relation of lattice imperfections to the origin of the resistance minimum in copper at low temperatures.

RESISTANCE EXPERIMENTS

(1) Measurements of the electrical resistance of copper wires extended by tensile deformation in liquid helium (6 percent and 10 percent reduction in cross-sectional area[6]) and subsequently aged in liquid nitrogen for 43 hours showed that there were no recovery processes which occurred below 77°K.

(2) The increase of residual resistivity of specimens extended by tension in liquid helium, or cold-rolled in liquid nitrogen has been measured as a function of percentage reduction in cross-sectional area (Curve A, Fig. 1). After measurement the specimens were then aged several days at room temperature and the residual resistivity was again determined (Curve B, Fig. 1). These measurements show the decrease of residual resistivity which accompanies the low-temperature recovery processes relative to that accompanying recovery and recrystallization above room temperature. The effects of the low-temperature recovery processes are several times larger than the high-temperature process which is accompanied by recrystallization. This proportion is increasing up to the limit of measurement at a reduction of ~57 percent in cross-sectional area.

Curve C, Fig. 1, shows the variation of residual resistivity with percentage reduction of cross-sectional area of specimens cold-worked at room temperature by tensile extension or rolling and then aged for several hours to complete the first two, low energy, recovery processes. (The scatter of the points is due mainly to an uncertainty of some ±5 percent in the determination of the cross-sectional area of the rolled specimens.) Specimens cold-worked in liquid helium or liquid nitrogen on subsequent ageing at room temperature for several days (Curve B), do not return to the same residual resistivity as specimens cold-worked to the same extent at room temperature and aged for a few hours (Curve C). Some additional lattice distortion appears therefore to be locked in on cold-working at low temperatures.

[1] T. Broom, Advances in Physics **3**, 26 (1954).
[2] J. Molenaar, and W. H. Aarts, Nature **166**, 690 (1950).
[3] M. J. Druyvesteyn, and J. A. Manintveld, Nature **168**, 868 (1951).
[4] J. A. Manintveld, Nature **169**, 623 (1952).
[5] J. A. Manintveld, *Change of the Resistivity of Some Face Centered Cubic Metals After Cold-Working at Liquid Air Temperature* (Delft Technische, Hageschool, 1954).

[6] Percentage reduction in cross-sectional area is taken as $100(A_{\text{initial}}-A_{\text{final}})/A_{\text{initial}}$.

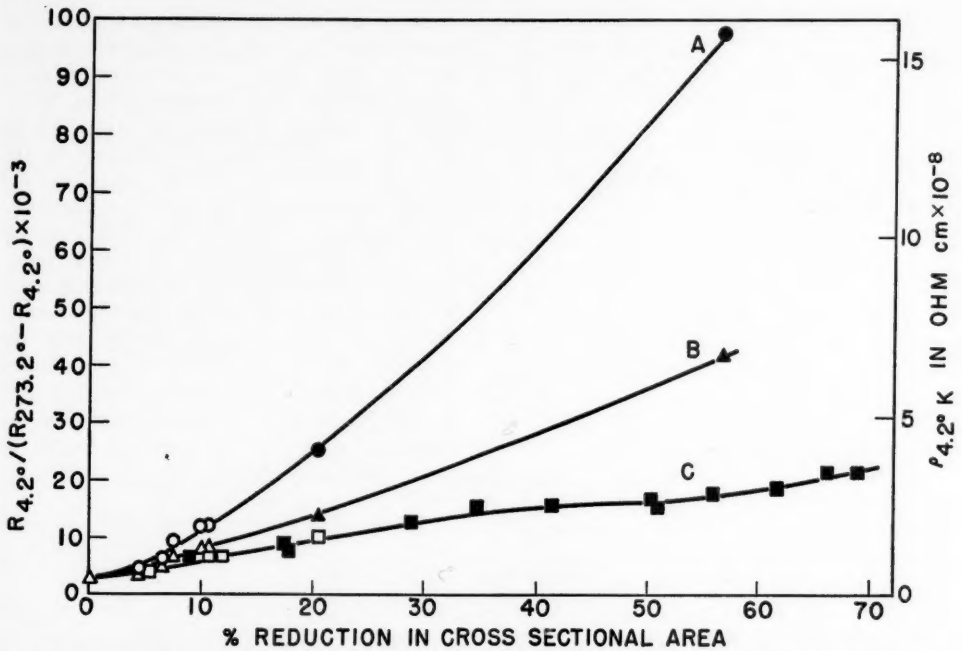

FIG. 1. Variation of residual resistance ratio with percentage reduction in cross-sectional area, for cold-worked copper specimens. The scale of residual resistivity $\rho_{4.2°K}$ has been calculated using the value 1.724 ohm cm×10⁻⁶ as the resistance of annealed copper at 293.2°K. ○ Specimen cold-worked by tensile deformation in liquid helium. △ The same specimens after ageing several days at room temperature. ● Specimens cold-worked by rolling in liquid nitrogen. ▲ The same specimens after ageing several days at room temperature. □ Specimens both extended by tensile deformation and aged at room temperature. ■ Specimens both cold-rolled and aged at room temperature.

THERMOELECTRIC FORCE

Following our earlier work on the influence of small amounts of chemical impurities on the thermoelectric force, E, of copper at low temperatures,[7,8] we have now investigated the effects of cold-work on thermoelectric force both for a number of specimens cold-worked at room temperature and aged for several hours before measurement, and also for a specimen deformed by tension in liquid helium. It was of considerable interest to find that in all cases the thermoelectric force of cold-worked specimens was *positive* relative to annealed copper in the range 4°–40°K, since we have always found that small additions of chemical impurities lead to a *negative* thermoelectric force relative to pure copper. In addition, the effects even of severe cold-work are relatively small compared to the remarkable effects of adding small amounts of heterovalent chemical impurities. For example, at 15°K the change of thermoelectric power (dE/dT) relative to pure annealed copper due to an 80 percent reduction in cross-sectional area by cold-work at room temperature is only about 1/150 of, and in the opposite sense to, that produced by the presence of ~0.055 wt percent of iron in solid solution in copper.

In Fig. 2 we show a few typical curves for the temperature variation of the absolute thermoelectric force at low temperatures of copper specimens cold-worked at room temperature, together with an annealed copper specimen from the same source. The measurements between 4.2° and 20°K have been made directly against annealed copper, or together with annealed copper against lead,[9] and the sign of dE/dT is undoubtedly positive relative to annealed copper.

The absolute thermoelectric power at 15°K as a function of the degree of cold-work is shown in Fig. 3. These measurements must be regarded as preliminary. The best procedure for accurate determination of thermoelectric force against annealed copper would be to use a galvanometer amplifier[10] in conjunction with a reversing-switch *operating in liquid helium*. Only in this way can the small spurious potentials, which may develop in the copper leads passing through the steep thermal gradient existing above the liquid helium, be eliminated. These potentials may, in extreme cases, be of the same order as those being measured *at the lowest temperatures*. However, under the conditions in which the present measurements have been made, it

[7] D. K. C. MacDonald, and W. B. Pearson, Proc. Roy. Soc. (London) **A219**, 373 (1953).
[8] D. K. C. MacDonald and W. B. Pearson (to be published).
[9] For the methods employed in this Laboratory, see D. K. C. MacDonald, and W. B. Pearson, Proc. Roy. Soc. (London) **A221**, 534 (1954).
[10] D. K. C. MacDonald, J. Sci. Instr. **24**, 9 (1947).

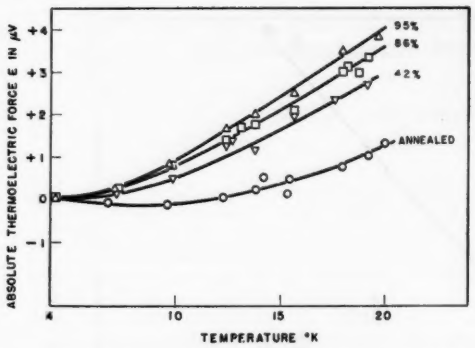

FIG. 2. Temperature variation of absolute thermoelectric force, E, of cold-worked and annealed copper specimens in μv. The measurements are referred to 4.2°K as zero. The figures on the curves refer to the percentage reduction in cross-sectional area by rolling the specimens at room temperature.

is not expected that this factor will greatly influence the derived thermoelectric power. We are at present trying to develop a suitable reversing switch to operate in liquid helium for work of this kind and related investigations.

Earlier work on the thermoelectric force of cold-worked copper has been discussed by Brindley,[11] and more recently measurements have been made by Druyvesteyn and van Laer.[12] As, however, all previous measurements have been made at 78°K or higher, they will not be further discussed here, except to say that we find an 'S' shaped curve for variations of thermoelectric force with percentage reduction in cross-sectional area, say at 20°K, similar to that found by Brindley[13] at room temperature.

THERMOELECTRIC FORCE OF COLD-WORKED COPPER AND THE RESISTANCE MINIMUM AT LOW TEMPERATURES

We have stressed elsewhere the importance of the presence of chemical impurities in dilute copper alloys

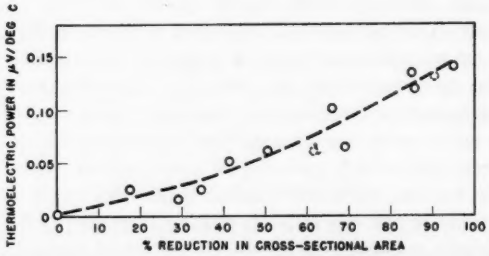

FIG. 3. Thermoelectric power (dE/dT) in μv/°C at 15°K of copper specimens cold-worked at room temperature relative to annealed copper, as a function of the percentage reduction in cross-sectional area.

[11] G. W. Brindley, *Report on a Conference on Strengths of Solids, Bristol* (Physical Society of London, London, 1948), p. 95.
[12] M. J. Druyvesteyn and K. J. R. van Laer, Nature **173**, 591 (1954).
[13] G. W. Brindley, Proc. Leeds Phil. Lit. Soc. Sci. Sect. **4**, Part 1, 1 (1941).

which show a minimum in electrical resistance at low temperature[14] (see also MacDonald[15]), while the relationship between the resistance minimum and thermoelectric behavior at low temperatures of dilute copper alloys containing specific added impurities has been discussed by MacDonald and Pearson.[16] In Fig. 4, for instance, we show for copper-indium alloys, the linear variation of the size of the resistance minimum, taken as $(R_{4.2°}-R_{Tm})/R_{Tm}\times 10^{-3}$ [17] with the absolute thermoelectric power, S, at 15°K (at which temperature thermal scattering is generally small compared to the residual impurity scattering, and the thermoelectric force varies approximately linearly with the temperature). An alternative origin for the resistance minimum has been proposed by Blewitt, Coltman and Redman[18] (see also Koehler.[19] This point of view emphasizes the importance of grain boundaries alone as the origin of the resistance minimum in copper.

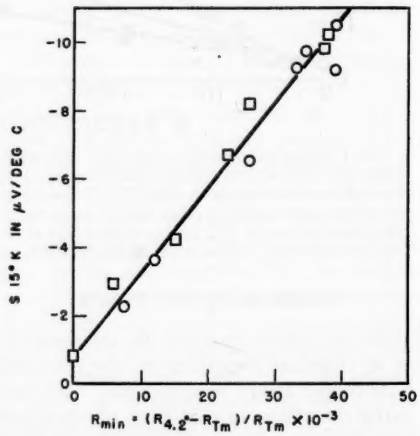

FIG. 4. Absolute thermoelectric power of very dilute copper-indium alloys at 15°K, as a function of the size of the resistance minimum shown by the same alloys at low temperatures. For discussion of R_{min} see references 17 and 8. ○ Alloys melted in reducing conditions under hydrogen. □ Vacuum-melted alloys.

In the case of the aforementioned cold-worked polycrystalline copper specimens, the positive deviation of thermoelectric force relative to pure copper at low temperatures is a strong indication that the presence of lattice imperfections such as interstitial atoms, vacancies, and dislocations *in themselves* is in no way connected with the origin of the resistance minimum. This is in agreement with the findings of Blewitt,

[14] W. B. Pearson, Phil. Mag. **45**, 1087 (1954).
[15] D. K. C. MacDonald, Phys. Rev. **88**, 148 (1952).
[16] D. K. C. MacDonald, and W. B. Pearson, Phil. Mag. **45**, 991 (1954).
[17] R_{Tm} is the resistance of the specimen at the temperature at which the minimum occurs, while $R_{4.2°}$ is the resistance of the specimen at 4.2°K (for further discussion of this ratio see MacDonald and Pearson[8]).
[18] Blewitt, Coltman, and Redman, Phys. Rev. **93**, 891 (1954).
[19] J. S. Koehler, Phys. Rev. **94**, 1071 (1954).

Coltman, and Redman[18] that cold-worked single-crystal copper does not show a resistance minimum. Insofar as grain boundaries are a further type of lattice imperfection, and low angle grain boundaries may perhaps be regarded as an array of dislocations, it is difficult to understand how grain boundaries, *per se*, can be the origin of the resistance minimum in pure copper. On the other hand, we have suggested how grain boundaries may be of importance *in the presence of certain impurity atoms*.[14] Alternatively, the presence of certain heterovalent and transition metals as impurities may *alone* be sufficient to give rise to a resistance minimum, and we have now observed a resistance minimum in *single-crystal* copper containing iron and tin as impurities.

The author wishes to thank Dr. D. K. C. MacDonald and Dr. J. S. Dugdale for valuable discussions on this subject.

PHYSICAL REVIEW VOLUME 97, NUMBER 3 FEBRUARY 1, 1955

Properties of Germanium Doped with Cobalt

W. W. TYLER, R. NEWMAN, AND H. H. WOODBURY
General Electric Research Laboratory, Schenectady, New York

(Received September 16, 1954)

Measurements of the temperature dependence of electrical resistivity in *n*- and *p*-type cobalt-doped germanium crystals indicate that cobalt introduces acceptor levels in germanium at 0.31 ± 0.01 ev from the conduction band and 0.25 ± 0.01 ev from the valence band. Ionization energies deduced from infrared photoconductivity studies at 77°K are in good agreement with the values obtained from resistivity measurements. *N*-type samples show higher intrinsic photosensitivity than *p*-type samples and demonstrate quenching effects.

I. INTRODUCTION

THIS paper presents information concerning the properties of germanium single crystals doped with cobalt. A preliminary account of this work has been given.[1] The properties of iron-doped germanium, which are in many respects similar to those of cobalt-doped germanium, are described in detail elsewhere.[2,3] A brief review of the literature relating to deep impurity levels in germanium is given in reference 2.

II. PREPARATION OF SAMPLES

The method of crystal growth and doping was similar to that described for iron-doping.[2] The concentration of cobalt in the melt just after doping was between 0.05 and 0.1 atomic percent. Lineage developed on the crystals at about the same concentration of impurity in the melt (0.3 percent) observed in the case of iron-doping. Samples used for experimental work were approximately 2 mm×3 mm×9 mm, cut from transverse sections of the crystals above the regions of observable lineage. After heavy etching in 80 percent HNO_3, 20 percent HF, contacts were fused to the samples in a hydrogen atmosphere. For *n*-type samples, contacts were of tin or tin, 1 percent arsenic; for *p*-type samples, contacts were of indium. Heavy etching after fusing on contacts was necessary, particularly for *p*-type samples.

The cobalt used for most of the doping experiments was cut from a second generation cobalt single crystal[4] grown from high purity sponge cobalt obtained from the Johnson Matthey Company. Later doping experiments were made using Johnson Matthey Company electrolytic cobalt. As in the case of iron-doping, the effective distribution coefficient of cobalt in germanium is low and the presence of high distribution coefficient impurities in the cobalt would be serious. Spectroscopic analysis[5] failed to detect the presence of boron in either source of cobalt. Traces of arsenic and antimony were observed in each source at about the same concentration. Aluminum and gallium were detected in the electrolytic cobalt but not in the single crystal cobalt. The concentration of each of these impurities detected is probably a few parts per million or less. The doping experiments indicate that both sources of cobalt behave similarly and are sufficiently pure that results are probably not dominated by impurities in the cobalt.

III. EXPERIMENTAL RESULTS

A. Resistivity, Mobility, and Lifetime Measurements

Both *n*- and *p*-type cobalt-doped crystals which show high resistivity at 77°K have been prepared. Doping pure germanium with cobalt from either source yields high resistivity *p*-type samples. Because there is no

[1] Tyler, Woodbury, and Newman, Phys. Rev. 94, 1419 (1954).
[2] W. W. Tyler and H. H. Woodbury, Phys. Rev. 96, 874 (1954).
[3] R. Newman and W. W. Tyler, Phys. Rev. 96, 882 (1954).

[4] We are indebted to Eric Asp of the General Electric Research Laboratory for providing us with the single crystal cobalt.
[5] We are indebted to L. B. Bronk of the General Electric Research Laboratory for spectroscopic analyses.

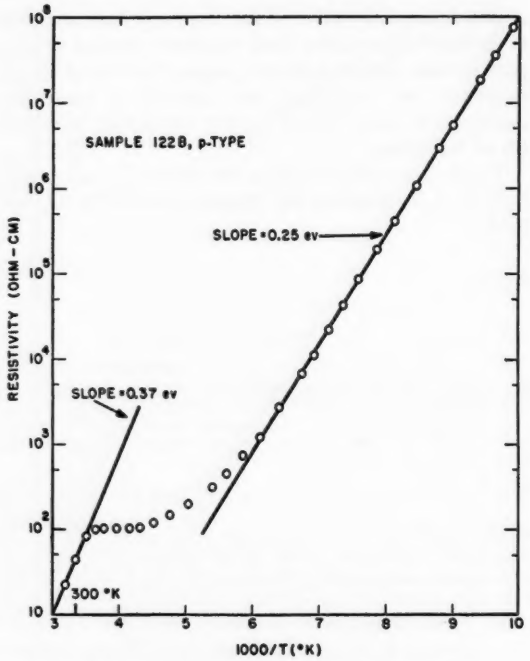

FIG. 1. Resistivity *vs* reciprocal temperature for a *p*-type, Co-doped Ge crystal (sample 122B).

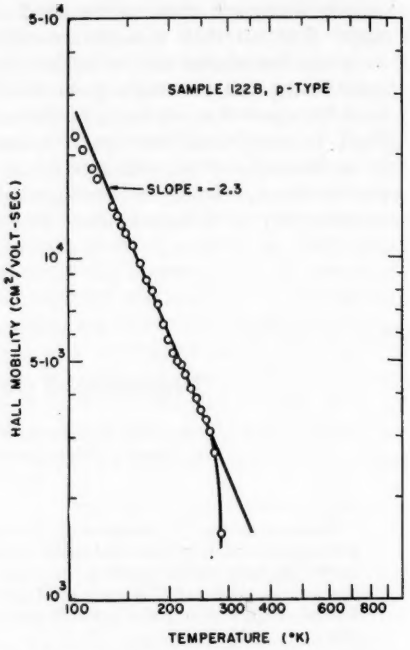

FIG. 2. Hall mobility *vs* temperature for a *p*-type, Co-doped Ge crystal (sample 122B).

evidence for impurities in the cobalt sources which might contribute acceptor states in the crystals comparable in concentration to the cobalt, it is assumed that cobalt acts as an acceptor in germanium. By careful doping of the melt with small amounts of antimony in addition to the cobalt, *n*-type samples have been obtained which show high resistivity when cooled, indicating that cobalt must contribute at least two acceptor states, one below and one above the center of the band. The effective distribution coefficient of cobalt in germanium, estimated from the resistivity measurements is about 10^{-6} in agreement with the value reported by Burton *et al.*[6] obtained from radioactive tracer measurements. As in the case of iron-doping, there is evidence that the amount of cobalt in the crystal is not exactly proportional to the amount in the melt.

Measurements of resistivity *vs* temperature for cobalt-doped samples which go to high resistivity when cooled to nitrogen temperature, indicate ionization energies of 0.25 ± 0.01 ev for *p*-type samples and 0.31 ± 0.01 ev for *n*-type samples. These ionization energies are obtained directly from the slopes of $\ln\rho$ *vs* $1/T$ plots without correction for the difference in the temperature dependence of the mobility for *n*- and *p*-type samples. The 0.01 ev uncertainity quoted represents internal consistency of the data. Measurements were made on *p*-type samples from four crystals, two doped with the single-crystal cobalt and two with the electrolytic cobalt. Three high resistivity *n*-type crystals were studied, two doped with single-crystal cobalt and one with the electrolytic cobalt. Figure 1 shows the dependence of resistivity on temperature for a typical *p*-type cobalt-doped sample. Figure 2 shows the dependence of mobility on temperature for the same sample. Figures 3 and 4 show similar curves for an *n*-type cobalt-doped sample. General features of these curves are similar to those reported for iron-doped crystals. Plots of $\ln\mu$ *vs* $\ln T$ give approximately linear regions with slopes from -2.1 to -2.3 for *p*-type samples and from -1.5 to -1.6 for *n*-type samples. The mobility for *p*-type samples show an H field dependence similar to that reported by Harman *et al.*[7] whereas the mobility for *n*-type samples is considerably less dependent on H field up to 4000 gauss. All mobility data reported were measured using a field of 4000 gauss.

Measurements of carrier lifetime at 300°K were made on the cobalt-doped crystals. Lifetime values fell from somewhere in the range 200 to 400 μsec before doping to values from 10 to 20 μsec after doping. Lifetime values for samples before doping are decreased to some extent by diffusion of cobalt up the crystal and are in general lower than values obtained in undoped crystals. For the cobalt-doped samples as well as iron-doped samples studied previously,[2] resistivities are intrinsic or

[6] Burton, Kolb, Slichter, and Struthers, J. Chem. Phys. **21**, 1991 (1953).

[7] Harman, Williamson, and Beer, Phys. Rev. **94**, 1065 (1954).

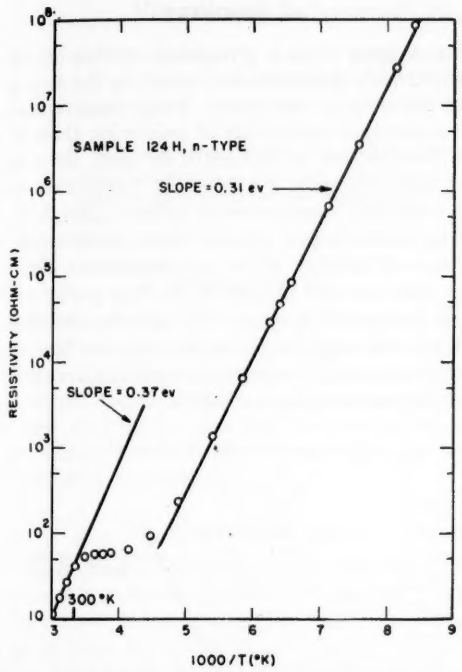

FIG. 3. Resistivity *vs* reciprocal temperature for an *n*-type, Co-doped Ge crystal (sample 124H).

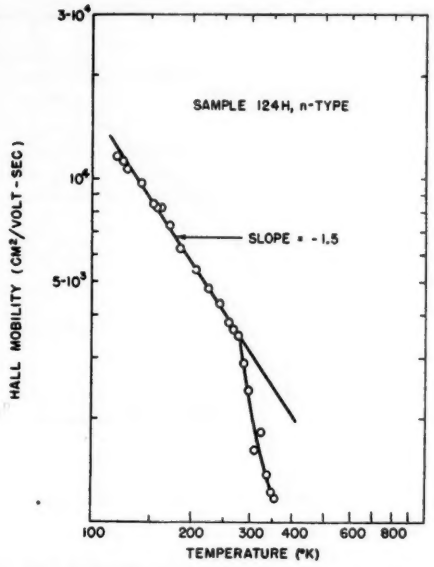

FIG. 4. Hall mobility *vs* temperature for an *n*-type, Co-doped Ge crystal (sample 124H).

near intrinsic at 300°K. No attempt has been made to determine limiting values of τ_{n0} and τ_{p0} for cobalt in germanium as have been reported by Burton *et al.*[8] for nickel and copper in germanium.

Photoconductivity decay measurements were made on several *n*- and *p*-type high-resistivity cobalt-doped samples at 77°K. Recovery times in most cases were less than several milliseconds and could not be measured accurately due to the decay time of the light source used.[2] One *n*-type cobalt-doped sample showed slow photoconductivity decay and high photosensitivity comparable to *n*-type iron-doped samples.[2] However, this sample showed anomalous mobility behavior, injection effects and nonlinearity and is not considered representative of *n*-type cobalt-doped crystals. The possibility exists that well behaved, *n*-type cobalt-doped crystals showing higher photosensitivity and long decay times might be obtained by properly controlling trapping ratios.[2,3*]

B. Photoconductivity

Figures 5 and 6 show spectral response of impurity photoconductivity in *p*- and *n*-type cobalt-doped samples at 77°K. Intrinsic photoconductivity begins to dominate at about 0.7 ev. The measurements were made with equipment described elsewhere.[3,9] The sample was exposed to unmodulated light from the

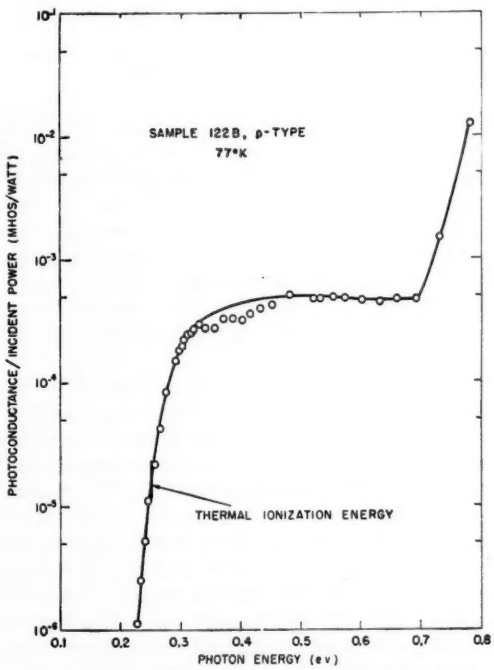

FIG. 5. Photoconductive spectrum of a *p*-type, Co-doped Ge crystal at 77°K (sample 122B).

[8] Burton, Hull, Morin, and Severiens, J. Phys. Chem. **57**, 853 (1953).

[*] *Note added in proof.*—Recent studies of time decay of photoconductivity in high-resistivity *n*-type Fe-doped crystals, using filtered light, indicate that the long decay times reported (see reference 2) may in part be due to surface effects. Studies of photoconductivity decay in high resistivity Ge crystal sdoped with Fe, Co, and Ni are in progress.

[9] R. Newman, Phys. Rev. **94**, 278 (1954).

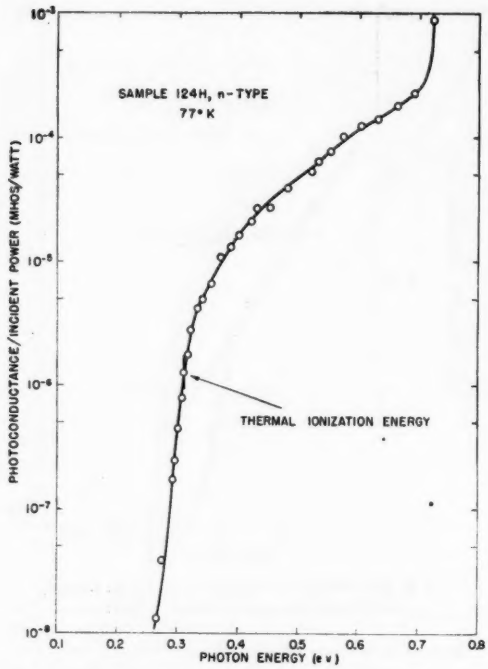

FIG. 6. Photoconductive spectrum of an *n*-type, Co-doped Ge crystal at 77°K (sample 124H).

Perkin-Elmer spectrometer. Photocurrents of the order of 10^{-10} ampere were measured in a series circuit consisting of sample, six-volt battery, and load resistor. Spectral response curves shown are typical of results for *p*-type samples from 5 different crystals and *n*-type samples from 3 different crystals. *P*-type samples give a flatter spectral response and sharper cut-off than do *n*-type samples. Optical threshold energies are in reasonable agreement with thermal ionization energies obtained from resistivity data.

In two of the *n*-type samples, quenching effects were observed. Quenching had been observed previously in *n*-type gold-doped[9] and iron-doped[3] germanium crystals. Figure 7 shows a quench spectrum for an *n*-type cobalt-doped sample. The technique used for this measurement has been described.[9,3] In neither of the cobalt-doped crystals in which the effect was obtained was the quenching as pronounced as for gold- and iron-doped crystals and it was not easy to separate the effects of normal intrinsic photoconduction and quenching. Quenching effects seem to maximize at a photon energy of about 0.32 ev.

IV. SUMMARY

Two acceptor levels in germanium crystals have been identified with the presence of cobalt in the melt from which the crystals were grown. From measurements of the temperature dependence of resistivity, these levels have been located at 0.25±0.01 ev from the valence band and 0.31±0.01 ev from the conduction band. Hall coefficient measurements indicate that high resistivity cobalt-doped crystals show temperature dependence of mobility which is in agreement with previous measurements of mobility in high purity *n*- and *p*-type germanium crystals. The effective distribution coefficient for cobalt in germanium is about 10^{-6}. Deep states introduced by cobalt in germanium are effective as recombination centers at 300°K.

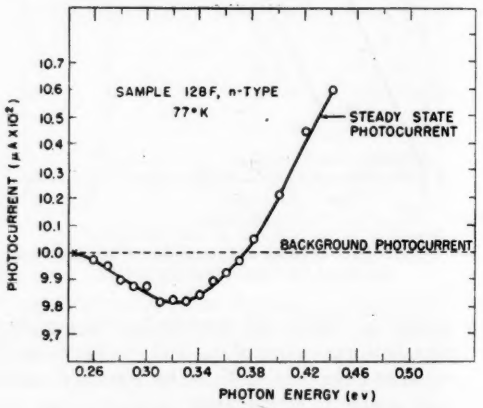

FIG. 7. Quench spectrum of an *n*-type, Co-doped Ge crystal at 77°K (sample 128F).

Impurity photoconductivity studies in *n*- and *p*-type cobalt-doped germanium crystals yield optical threshold energies which are consistent with thermal ionization energies. In agreement with results of gold- and iron-doped crystals, *n*-type cobalt-doped crystals have higher intrinsic photosensitivity than *p*-type samples and show quenching effects. Both of these observations suggest the presence of hole traps and are in accord with the model[2,3] that doubly charged negative impurities sites act as hole traps in germanium.

ACKNOWLEDGMENT

The authors are indebted to T. J. Soltys and J. H. Racette for help in growing crystals, preparing samples and taking data.

Vibrational Anharmonicity and Lattice Thermal Properties. II

D. K. C. MacDonald and S. K. Roy*
Division of Physics, National Research Council, Ottawa, Canada
(Received August 25, 1954)

Following an earlier paper based on the Morse potential, the analysis of the thermal properties of a linear chain is now extended to cover an interatomic potential of arbitrary form. The Lennard-Jones potential is taken as an example and the results for the thermal expansion coefficient are compared with experimental data.

1. INTRODUCTION

IN a previous paper[1] which we shall refer to as (I), an analysis was made of the statistical thermodynamics of a linear assembly of atoms interacting with nearest neighbors through a Morse potential. We now show that the analysis may be extended to cover an interatomic potential of arbitrary form, and apply the Lennard-Jones potential.

2. ANALYSIS

As in (I), we consider a linear chain of $N+1$ identical particles of mass m which at 0°K and under zero tension have a uniform separation A_0 (Fig. 1); let the potential energy between two particles, at arbitrary distance r, be $\Phi(r)$. We now assume that $\Phi(r)$ has the general form of Fig. 2 such that

$$\text{(i)}\quad \Phi'(A_0)=0;\quad \Phi(A_0)=-D,$$

$$\text{(ii)}\quad (a)\ \lim_{r\to\infty}\Phi(r)=0,$$

$$(b)\ \lim_{r\to\infty}\{r\Phi'(r)\}=0, \qquad (1)$$

$$\text{such that: } \int^{\infty} r\Phi'(r)dr \text{ exists}$$

$$\text{(iii)}\quad \lim_{r\to-\infty}\{\Phi(r)/-r\}=\infty.$$

The potential energy of the whole system with arbitrary displacements, y_n, is

$$V=\sum_{n=1}^{N}\Phi(A_0+y_n-y_{n-1})\equiv\sum_{n=1}^{N}\Phi(A_0+x_n),$$

$$=\sum_{n=1}^{N}D(\psi(ax_n)-1),$$

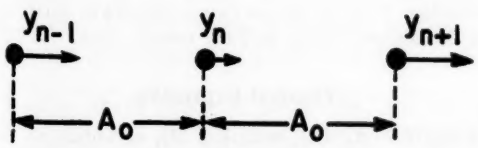

FIG. 1. Section of linear chain.

where

$$\psi(ax_n)=(ax_n)^2+\lambda_3(ax_n)^3+\cdots+\lambda_s(ax_n)^s+\cdots,^2$$

so that

$$a=(\Phi''(A_0)/2D)^{\frac{1}{2}},\quad \lambda_s=\{2^{s/2}D^{(s-2)/2}\Phi^{(s)}(A_0)\}/s!(\Phi'')^{s/2}, \qquad (2)$$

and (writing $z=ax$)

$$\psi(z)=1 \quad \text{for} \quad \begin{cases} z\to\infty \\ z=-z_0 \end{cases} \quad \text{(see Fig. 3).}$$

We now proceed essentially as in (I) to set up the partition function $Z_G(P,N,T)$, which may then be written

$$Z_G(P,N,T)=(2\pi mkT)^{N/2}\exp\left(-\frac{NPA_0-ND}{kT}\right)a^{-N}I^N,$$

$$\equiv KI^N;$$

where

$$I=\int_{-\infty}^{+\infty}\exp\left\{-\left(\frac{Pz}{akT}+\frac{D}{kT}\psi(z)\right)\right\}dz$$

$$=-\frac{akT}{P}\left[\exp\left\{-\left(\frac{Pz}{akT}+\frac{D}{kT}\psi(z)\right)\right\}\right]_{-\infty}^{\infty}$$

$$-\frac{aD}{P}\left\{\int_{-\infty}^{-z_0}+\int_{-z_0}^{\infty}\exp\left\{-\left(\frac{Pz}{akT}+\frac{D}{kT}\psi(z)\right)\right\}\right.$$

$$\left.\times\psi'(z)dz\right\}.$$

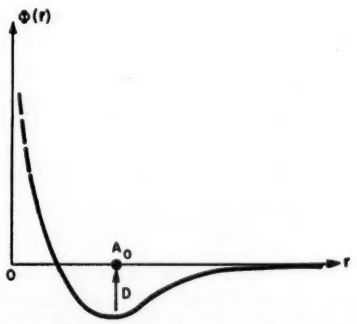

FIG. 2. General form of interatomic potential.

* National Research Laboratories Postdoctorate Fellow.
[1] J. S. Dugdale and D. K. C. MacDonald, Phys. Rev. **96**, 57 (1954).

[2] It follows readily that the one-dimensional Grüneisen parameter, $\gamma\equiv-d\log\nu/d\log L$ is given by $\gamma=-\frac{1}{2}\lambda_3 aA_0$ (ν: characteristic frequency; L: length of chain).

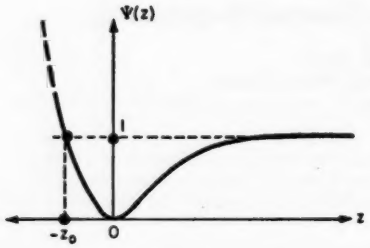

FIG. 3. General form of normalized interatomic potential.

The first term then vanishes identically for all $P>0$, using 1(iii). In the curly brackets, the first term becomes significant as $P\to 0$, assuming the form $(akT/P)\times\exp(-D/kT)$, and corresponds exactly as in (I) to the gas-like state at sufficiently low "pressures." The remaining term, say J, which is dominant for all normal values of P, determines the properties of the condensed state and we shall now evaluate it.

3. CONDENSED STATE

Writing $\chi(z)=\psi(z)-z^2=\lambda_3 z^3+\lambda_4 z^4+\cdots$,

$$J=-\frac{aD}{P}\sum_{s=0}^{\infty}\left(-\frac{P}{akT}\right)^s\frac{1}{s!}\int_{-z_0}^{\infty}\exp\left\{-\frac{D}{kT}z^2\right\}z^s \times\exp\left\{-\frac{D}{kT}\chi(z)\right\}\psi'(z)dz.$$

Assuming $D/kT\gg 1$, we may now extend the lower limit of integration to $-\infty$, and evaluate the integrals by expansion of the *second* exponential factor.

Hence:

$$Z_G=K(\pi kT/D)^{N/2}\{1+A_1(kT/D)+A_2(kT/D)^2+\cdots +B_1(P/aD)+B_2(P/aD)(kT/D)+\cdots +C_1(P/aD)^2(kT/D)^{-1}+C_2(P/aD)^2+\cdots\},$$

where

$$A_1=\tfrac{3}{16}(5\lambda_3^2-4\lambda_4),$$

$$A_2=-(15/8)[\lambda_6-(7/4)\lambda_4^2+(7/2)\lambda_3\lambda_5 +(63/8)\lambda_4\lambda_3^2-(231/64)\lambda_3^4],$$

$$B_1=\tfrac{3}{4}\lambda_3,\quad B_2=\tfrac{3}{8}[5\lambda_5-(35/2)\lambda_3\lambda_4+(105/8)\lambda_3^3],$$

$$C_1=\tfrac{1}{4},\quad C_2=\tfrac{1}{8}[-(15/2)\lambda_4+(105/8)\lambda_3^2].$$

TABLE I. Table of values of $(m+n+3)/mn$.

$n\backslash m$	1	2	3	4
6	1.67	0.92	0.67	0.54
9	1.44	0.78	0.56	0.44
12	1.33	0.71	0.50	0.40

Thus,

$$G=-kT\ln Z_G =-NkT\ln(2\pi^2mk^2/a^2D)^{\frac{1}{2}}-NkT\ln T+PNA_0 -ND-ND\{A_1(kT/D)^2+D_2(kT/D)^3+\cdots +B_1(P/aD)(kT/D)+E_2(P/aD)(kT/D)^2+\cdots +C_1(P/aD)^2+\cdots\}, \quad (3)$$

where

$$D_2=A_2-\tfrac{1}{2}A_1^2=(15/8)(-\lambda_6+\tfrac{3}{5}\lambda_4^2+(7/2)\lambda_3\lambda_5 -(15/2)\lambda_3^2\lambda_4+(27/8)\lambda_3^4),$$

$$E_2=B_2-A_1B_1=(15/8)(\lambda_5-(16/5)\lambda_3\lambda_4+(9/4)\lambda_3^3),$$

$$F_2=C_2-\tfrac{1}{2}B_1^2-A_1C_1=\tfrac{3}{4}(-\lambda_4+\tfrac{3}{2}\lambda_3^2).$$

4. SPECIFIC INTERATOMIC POTENTIALS

If we now introduce the values of the λ's [Eq. (2)] to generate the Morse potential (i.e., $\lambda_3=-1$, $\lambda_4=7/12$, $\lambda_5=-1/4$, $\lambda_6=31/360$, etc.), we find complete agreement with the direct analysis given in (I). Let us consider also the well-known Lennard-Jones potential:

$$\Phi(r)=\frac{A}{r^n}-\frac{B}{r^m}\quad(n>m>0),$$

which satisfies the conditions of (1) above. Then from (2):

$$\lambda_3=-(2/mn)^{\frac{1}{2}}(m+n+3)/3,$$

$$\lambda_4=(1/6nm)(n^2+nm+m^2+6n+6m+11),$$

$$\lambda_s=\{(-)^s2^{s/2}/s!\}[(n+1)(n+2)\cdots(n+s-1) -(m+1)(m+2)\cdots(m+s-1)/(n-m)(nm)^{\frac{1}{2}s-1}]. \quad (4)$$

Following (I) let us discuss two properties in particular, the thermal expansion and the specific heat.

Thermal Expansion

Using $L=(dG/dP)_T$ with Eq. (3), we obtain

$$\frac{1}{L_0}\left(\frac{dL}{dT}\right)_P=-\frac{k}{aA_0D}\{B_1+2E_2(kT/D)+\cdots +2F_2(P/aD)+\cdots\},$$

TABLE II. Alkali metals (Structure: b.c.c.).

Element	D(cal/mole)[a]	α_{exp}(deg^{-1})	aD
Li	36 000	5.6×10^{-5}	2.02
Na	26 200	7.2×10^{-5}	1.89
K	21 900	8.3×10^{-5}	1.82
Rb	20 600	9.0×10^{-5}	1.85
Cs	18 700	9.7×10^{-5}	1.81

[a] D is interpreted as the latent heat of vaporization at absolute zero.

which, for $(kT/D)\ll 1$ and $(P/aD)\ll 1$ gives:

$$\frac{1}{L_0}\left(\frac{dL}{dT}\right)_{P\simeq 0} \equiv \alpha = \frac{3}{4}\frac{k\lambda_3}{aA_0D} = \frac{k}{2}\left(\frac{m+n+3}{mnD}\right).^3 \quad (5)$$

Noting also that now

$$\gamma = (m+n+3)/2,$$

we may write

$$\alpha = k\gamma/Dmn.$$

This may be compared with the relationship deduced by Grüneisen[4]:

$$\bar{\alpha} = C_v\bar{\gamma}/\Lambda_0\bar{m}\bar{n}.$$

$\bar{\alpha}, \bar{\gamma}, \bar{m}, \bar{n}$ are the appropriate analogs in three-dimensions, and Λ_0 is the sublimation energy at absolute zero. To compare with experiment, Grüneisen then evaluated approximately the factor $\bar{\gamma}/\bar{m}\bar{n}$; however, we can proceed more directly from Eq. (5). If then we risk a comparison with the experimental data on metals, one might expect that for a reasonable approximation

TABLE III. Noble metals (Structure: f.c.c.).

Element	D(cal/mole)[a]	α_{exp}(deg^{-1})[b]	αD
Cu	81.7×10^3	16.4×10^{-6}	1.34
Ag	69.4×10^3	19.0×10^{-6}	1.31
Au	90.7×10^3	14.4×10^{-6}	1.31

[a] Extracted from Landolt-Börnstein Tables.
[b] Extracted from *Smithell's Metals Reference Book* (Butterworth's Publications, London, 1949).

to the physical potential m would lie between the extreme values 1 and 4 and n between 6 and 12. Table I then shows that the factor $(m+n+3)/mn$ lies between the extreme values 1.67 and 0.40. Taking therefore unity as a mean value for this factor, we find from Eq. (5) that $\alpha\approx 0.5k/D$, which we may compare with Grüneisen's result: $\bar{\alpha}\approx 0.6C_v/\Lambda_0$.

Using the data collected in (I) (Table II), we have the results of Table II, while in Table III similar calculations have been made for the noble metals (Cu, Ag, Au) (see also Grüneisen[5]).

The relative constancy of the last column in Tables II and III suggests that within the limits of the model the values of m and n may be considered as constant within each of these monovalent metal groups, i.e., that a law of corresponding states is valid within each group.

Turning to the Group II metals (Be, Mg; Ca, Sr, Ba; Zn, Cd, Hg) the experimental data conflict in a

[3] It then follows that the one-dimensional Grüneisen relationship $\gamma = \alpha L/\beta C_L$, where $\beta = (1/L)(dL/dP)_T$, holds true to the first approximation.
[4] E. Grüneisen, Ann. Physik. **39**, 289 (1912).
[5] E. Grüneisen, Verhandl. deut. physik. Ges. **10**, 322 (1912).

TABLE IV. Group II metals.

Element	D(cal/mole)[a]	α_{exp}(deg^{-1})[b]	αD	Structure
Be	55×10^3	$18.7^c\times10^{-6}$	1.03	hex.
Mg	36.6×10^3	26×10^{-6}	0.95	hex.
Ca	42.9×10^3	22×10^{-6}	0.94	f.c.c.
Zn	31.4×10^3	31.2×10^{-6}	0.98	hex.
Sr	40×10^3	...	...	f.c.c.
Cd	27.0×10^3	29×10^{-6}	0.79	hex.
Ba	40.9×10^3	$(18?)\times10^{-6}$	0.74	b.c.c.
Hg	15.5×10^3	...	...	rhomb.

[a] Extracted from Landolt-Börnstein Tables.
[b] Extracted from *Smithell's Reference Book* (Butterworth's Publications, London, 1949).
[c] The value of α at room temperature is 12×10^{-6}/°C and this has been multiplied by the ratio $3R/C_v$ (θ for Be~1000 °K). All the other metals considered are essentially classical at room temperature.

number of cases, but Table IV shows that, even in this very diverse group of metals, αD is still sufficiently constant to lead us to suggest that the as yet unknown expansion coefficient of Sr should be close to 23×10^{-6}, and that the uncertain value for Ba taken from Smithell's Handbook is possibly low.

Considering now solids such as the frozen inert gases where the binding forces are of the van der Waals' type, we should expect that here the requirements of central forces and nearest-neighbor interaction [implicit in the model—see (I)] would be best satisfied. Using data deduced from gas-kinetic studies, we may estimate values for the linear thermal expansion coefficient, α. In Table V data are collected for the heavier inert gases (Xe, Kr, A).

For these solids $m=6$ semitheoretically and, as is common, n is taken as 12. Thus

$$\alpha = 21k/144D.$$

Although α_{exp} for argon is only approximate, the agreement with theory is sufficiently good to suggest that the at present unknown values for Kr and Xe must be close to those predicted.

Since the Lennard-Jones and Morse potentials give results which appear physically quite reasonable, it might be thought that any hypothetical interatomic potential which satisfies the elementary requirements of a large repulsive energy for $r=0$, a finite value at $r=+\infty$ and a single intervening minimum would suffice. However, one may readily choose an artificial potential (e.g., see Fig. 4) which satisfies *these* require-

TABLE V. The heavier inert gases.

Element	D(cal/mole)	$\alpha_{theor.}$	α_{exp}
Xe	448[a]	6.5×10^{-4}	...
Kr	344[b]	8.4×10^{-4}	...
A	237[c]	1.21×10^{-3}	1×10^{-3} [d]

[a] Beattie, Barriault, and Brierley, J. Chem. Phys. **19**, 1223 (1951).
[b] Beattie, Brierley, and Barriault, J. Chem. Phys. **20**, 1613 (1952).
[c] R. L. Fowler and E. A. Guggenheim, *Statistical Thermodynamics* (Cambridge University Press, Cambridge, 1949).
[d] F. E. Simon and F. Kippert, Z. physik. Chem. **135**, 113 (1928).

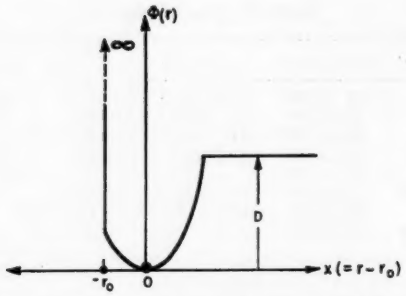

FIG. 4. Hypothetical form of interatomic potential.

ments but which predicts physically quite unrealistic behavior for the thermal expansion.

Specific Heat

Using $C_P=-T(\partial^2 G/\partial T^2)_P$ with Eq. (3), we find

$$C_P=Nk\{1+\tfrac{3}{8}(5\lambda_3^2-4\lambda_4)kT/D+\cdots\},$$

and thus, using $C_P-C_L=T(\partial L/\partial T)_P(\partial P/\partial T)_L$,

$$C_{L;P\simeq 0}=Nk\{1+\tfrac{3}{4}(\lambda_3^2-2\lambda_4)kT/D+\cdots\}.$$

Introducing now the Lennard-Jones potential [see Eq. (4)], we obtain

$$C_{P;P\simeq 0}=Nk\{1+(1/12mn)(2m^3+2n^3+7mn+12m+12n+27)kT/D+\cdots\},$$

$$C_{L;P\simeq 0}=Nk\{1-(1/12mn)[(n-m)^2+nm+6m+6n+15]kT/D-\cdots\}.$$

Thus, for *all* $m,n>0$, $C_{P;P\simeq 0}$ is predicted to increase with T, whereas $C_{L;P\simeq 0}$ is predicted to diminish with T as found also in (I) for the Morse potential.

The general condition that the term in C_L linear with temperature should be negative may be written (see also Damköhler[6])

$$[\Phi'''(A_0)]^2>\tfrac{3}{2}\Phi''(A_0)\Phi^{iv}(A_0).$$

This inequality is satisfied by both the Morse and Lennard-Jones potentials (whatever the values of n and m). We may therefore conclude, as foreseen in (I), that it is extremely unlikely that any physically plausible potential would give rise to a C_L increasing with temperature, in agreement with Damköhler's conclusions.

We are most grateful to Dr. J. S. Dugdale for many helpful discussions in the preparation of this paper.

[6] G. Damköhler, Ann. Physik. 24, 1 (1935).

PHYSICAL REVIEW VOLUME 97, NUMBER 3 FEBRUARY 1, 1955

Physical Defects in Silver Halides*

CHESTER R. BERRY
Research Laboratories, Eastman Kodak Company, Rochester, New York
(Received September 27, 1954)

The concentrations of imperfections in silver halides grown from the melt were investigated by comparing the measured densities with the ideal densities computed from the lattice dimensions. The density defect of the most perfect specimen of silver bromide was $\Delta\rho/\rho=-0.8\times10^{-4}$. The greatest amount of imperfection was $\Delta\rho/\rho=-18\times10^{-4}$ in a specimen of silver bromide containing about 4 mole percent silver iodide. Considering the effects of various configurations of voids, it seems reasonable to attribute most of the density defect in the best crystals to immobile aggregates of vacancies and to dislocations associated with small-angle mosaic structure. The contributions of large-angle grain boundaries and Schottky defects are negligible.

INTRODUCTION

THE concentration of imperfections in a crystal is of importance in determining many of its properties. In the silver halides considered here, the number of imperfections is undoubtedly closely associated with photographic behavior and with such related properties as optical absorption and electron- and hole-trapping.[1]

A direct method of obtaining information on the soundness of a crystal is to compare the measured density with an ideal density computed from the weight and volume of material in the unit cell. Straumanis[2] has recently reconsidered this type of measurement, and has determined the best values of atomic constants to use in the computations, assuming calcite to be a perfectly sound crystal.

The present investigation is a study of the defects at room temperature in pure specimens, prepared from the melt, of silver bromide, silver chloride, and solid solutions of a few mole percent silver iodide in silver bromide. Measurements reported by Keith and Mitchell[3]

* Communication No. 1690 from the Kodak Research Laboratories.

[1] F. Seitz, Revs. Modern Phys. 23, 328 (1951).

[2] M. E. Straumanis, Phys. Rev. 92, 1155 (1953).

[3] H. D. Keith and J. W. Mitchell, Phil. Mag. 7, 42, 1331 (1951).

were interpreted as indicating a possible lack of soundness in silver bromide but hardly a significant amount compared with the experimental uncertainties. It seems likely that the concentration of impurities and imperfections in precipitates and emulsion grains will be somewhat greater than in the specimens crystallized slowly from the melt.

EXPERIMENTAL

Measurements of density were obtained from pieces of clear crystal containing only a few large-angle grain boundaries, but no cracks or bubbles. The specimens were prepared in various ways. One of the silver chloride crystals was drawn from the melt in air, and the other was obtained from the Harshaw Chemical Company. The silver bromide specimens were produced in different atmospheres by filtering the molten material through a Pyrex capillary and solidifying it in quartz. One of the silver bromoiodide specimens was formed after dripping part of the molten mixture through a capillary, and the other specimen was prepared by mixing and melting the material in a Pyrex beaker.

A representative silver bromide specimen and the two silver chloride specimens were examined for metallic impurities by spectroscopic analysis. In the silver bromide, silicon was the major impurity, and amounted to about one part per million. Slightly smaller amounts of calcium, magnesium, and lead were found, and only a few parts in ten million of iron, aluminum, cadmium, copper, and zinc were detected. Studies of the effects of silver oxide on the surface tension of molten silver bromide indicate that a few parts per million of silver oxide are probably present in those specimens which were not melted in the presence of HBr.[4] The level of impurities in the silver chloride was somewhat higher than in silver bromide, there being a few parts per million of aluminum, calcium, iron, silicon, and zinc. The main difference between the silver chloride grown here and that obtained from the Harshaw Chemical Company was the presence of lead in the Harshaw specimen to the extent of about 20 parts per million.

All of the specimens examined under crossed polarizers were slightly birefringent except one silver bromide crystal, which was carefully annealed.

Measurements of lattice parameter of silver bromide and silver chloride were made on powdered specimens with a General Electric Geiger Counter Diffractometer XRD-3. Each determination of lattice parameter was corrected for a variety of possible errors by using the extrapolation procedure of Nelson and Riley.[5] A correction for the refraction of the x-rays was applied.[6] The values of lattice parameter were obtained from the same material whose density was measured, except in the case of silver bromide. The value for silver bromide is the average of a large number of determinations made with specimens of various origins. There appear to be no differences of significance for the computations which follow in the values for photographic grains, gelatin-free precipitates, and annealed precipitates. The value for silver bromide at 25.00°C is 5.77475±0.00005 A.[7] The value for silver chloride is 5.55023±0.00005 A.

TABLE I. Lattice parameter and ideal density at 25.00°C.

AgBr	5.77475±0.00005 A	6.4753 g/cm³±0.0002
AgCl	5.55023±0.00005 A	5.5667 g/cm³±0.0002
AgBr-I 4.6%	5.7908 ±0.0005 A	6.4965 g/cm³±0.0020
AgBr-I 4.0%	5.7884 ±0.0005 A	6.4931 g/cm³±0.0020

A Straumanis-type powder camera was used for determining the lattice parameters of the silver bromoiodide specimens, since only a small quantity of powder was available for measurement. The values were not nearly so accurate as those obtained from the pure bromide and chloride, partly because of strains in the lattice which gave somewhat broadened diffraction lines.

The values of lattice parameter and of ideal density for all the specimens are given in Table I. The computations of the values of density of the mixed silver bromoiodide crystals depend on the compositions of the specimens. The fraction of silver iodide present was estimated from the known amounts of silver bromide and silver iodide added to the melts, and was checked by comparing the lattice parameters with values determined by Griffith and Berntson[8] relating composition to lattice parameter for coprecipitates of silver bromoiodide. The specimen mixed and fused in the beaker contained 4.0 mole percent iodide based on known weights of material in the melt, and on the lattice parameter. The other specimen contained 4.6 mole percent iodide according to the lattice dimensions, although 5.5 percent iodide was in the melt. This discrepancy may be caused by the tendency of the iodide to decompose rapidly when maintained at too high a temperature. The value, 4.6 mole percent, was assumed to be correct since it was obtained from filings of that portion of the solid actually used in the density measurements.

Measurements of density were made with a pycnometer having a volume of about 11 cm³. Distilled water at 25.00°C was the displacement liquid. Flotation methods of density measurement do not appear to be

[4] G. W. Luckey (private communication from the Kodak Research Laboratories).

[5] J. B. Nelson and D. P. Riley, Proc. Phys. Soc. (London) 57, 160 (1945).

[6] A. J. C. Wilson, Proc. Cambridge Phil. Soc. 36, 485 (1940).

[7] Values of lattice parameter of silver bromide at 25.0°C given in the literature recently, when compared on the basis of the copper $K\alpha$ wavelength of 1.54050 A, are: 5.7743—C. R. Berry, Phys. Rev. 82, 422 (1951); 5.7743—H. E. Swanson and R. K. Fuyat, National Bureau of Standards Report 2508, 1953 (unpublished); 5.7748—J. Teltow, Z. physik. Chem. 195, 213 (1950); 5.7749—H. D. Keith and J. W. Mitchell, Phil. Mag. 42, 1331 (1951).

[8] R. L. Griffith and C. M. Berntson, Kodak Research Laboratories, have recorded in an unpublished report that the change in lattice parameter per mole percent iodide is $\Delta a = 0.00346$ A.

TABLE II. Density measurements and departure from the ideal values.

Specimen		Density, g/cm³	Density defect, $\Delta\rho/\rho$
AgBr	X-ray value	6.4753	
AgBr	N_2 atmosphere	6.4746±0.0004	$(-\ 1.1\pm0.9)\times10^{-4}$
AgBr	N_2 atmosphere	6.4741±0.0005	$(-\ 1.9\pm1.1)\times10^{-4}$
AgBr	N_2, cold worked	6.4719±0.0005	$(-\ 5.3\pm1.1)\times10^{-4}$
AgBr	HBr and Br_2 atmosphere while above mp	6.4748±0.0002	$(-\ 0.8\pm0.6)\times10^{-4}$
AgBr	HBr and Br_2 above mp, N_2 annealed at 393°C, 64 hr, cooled to room temp. 40 hr	6.4736±0.0002	$(-\ 2.6\pm0.6)\times10^{-4}$
AgBr-I 4.6%	X-ray value	6.4965	
AgBr-I 4.6%	N_2 atmosphere	6.4880±0.0024	$(-13\ \pm7)\times10^{-4}$
AgBr-I 4.0%	X-ray value	6.4931	
AgBr-I 4.0%	N_2 atmosphere	6.4814±0.0007	$(-18\ \pm4)\times10^{-4}$
AgCl	X-ray value	5.5667	
AgCl	Drawn in air	5.5655±0.0005	$(-\ 2.2\pm1.3)\times10^{-4}$
AgCl	Harshaw	5.5645±0.0002	$(-\ 4.0\pm0.7)\times10^{-4}$

feasible for the silver halides because of the lack of appropriate liquids having high density.

The measurements of density and the extent of the defects, which may be characterized by the relative change in density, $\Delta\rho/\rho$, are recorded in Table II. Each of the density values is the average of about ten individual determinations. The errors recorded are the probable errors of the mean. The rather large error in density in one case was caused by the small amount of specimen available. The few cases where the probable error was only ±0.0002 g/cm³ were the last measurements, where improved experimental procedures were used. For comparison, Keith and Mitchell[9] gave the density of their specimen of silver bromide as 6.4752 g/cm³.

In every case there is a density defect which is beyond the limits of experimental error. The smallest defect is $\Delta\rho/\rho=-0.8\times10^{-4}$, for the silver bromide kept in an HBr and Br_2 atmosphere when it was above the melting point. It is surprising that a similar annealed specimen has a greater concentration of defects. Straumanis[9] found that the departure from perfection of sublimed NaCl exceeded the experimental errors, and the imperfection expressed as a density defect was $\Delta\rho/\rho=-4.1\times10^{-4}$.

Although cold-working increased the density defect, the addition of silver iodide had a considerably greater effect. Even so, the imperfection is much less than the value of about $\Delta\rho/\rho=-1.3\times10^{-2}$ produced by adding 10 percent KBr to KCl.[10] Back-reflection Laue photographs were obtained with a beam having a diameter of 125 microns and a divergence of about 0.21 degree. Reflected beams from unannealed silver bromide and silver chloride were observed to contain fine structures and breadths, indicating mosaic misalignments of about 0.5° within the area covered by the beam. The breadths of the spots from the annealed specimen were somewhat smaller and not significantly greater than the divergence of the x-ray beam.

[9] M. E. Straumanis, Am. Mineralogist **38**, 662 (1953).
[10] W. E. Wallace and R. A. Flinn, Nature **172**, 681 (1953).

DISCUSSION

The concentration of impurities present does not appear to be sufficient to have a direct effect on the measured density. Reasonable configurations which could conceivably account for the observed lack of soundness of the crystals are isolated vacancies, groups of vacancies in arrays such as large-angle grain boundaries or collapsed disks, single-edge dislocations, and arrays of edge dislocations associated with small-angle grain boundaries. In the observed specimens, there is undoubtedly a certain amount of each of these configurations. The effect of each of these defects on the decrease in density will now be estimated.

If the decrease in density were attributed solely to Schottky defects, their concentration in pure silver bromide would have to be $-\Delta\rho/\rho=0.8\times10^{-4}$. It may be shown that this is far too high to agree with estimates of the concentration of mobile Schottky defects in silver bromide at room temperature. Extrapolation to room temperature of the ionic conductivity results of Koch and Wagner[11] indicates a silver vacancy concentration of about 1.2×10^{-6}, and these vacancies are not Schottky defects, but predominantly Frenkel defects,[12] which should have no differential effect on the ideal and measured densities. Thus, essentially none of the density defect in silver bromide may be attributed to Schottky defects.

In considering the nature of the vacancies in silver bromide, the bubble models of metal structures described by Bragg[13–16] and his collaborators are very helpful, although their description of the silver bromide structure is only approximate.

The models indicate that large-angle grain boundaries have associated with them a void region varying from one atom diameter at the points of greatest mis-

[11] E. Koch and C. Wagner, Z. physik. Chem. **B38**, 295 (1937).
[12] C. R. Berry, Phys. Rev. **82**, 422 (1951).
[13] W. L. Bragg and J. F. Nye, Proc. Roy. Soc. (London) **A190** 474 (1947).
[14] W. L. Bragg and W. M. Lomer, Proc. Roy. Soc. (London) **A196**, 171 (1949).
[15] W. M. Lomer, Proc. Roy. Soc. (London) **A196**, 182 (1949).
[16] W. M. Lomer and J. F. Nye, Proc. Roy. Soc. (London) **A212**, 576 (1952).

match to zero at the points of good fit. Since this void volume is associated equally with the grains on the two sides of the boundary, we may consider that each grain is surrounded by a void sheath which has an average thickness of not more than one-fourth atom diameter. Considering cube-shaped grains with N atoms per edge, the change in density associated with the grain structure is

$$\Delta\rho/\rho = -\Delta V/V = -6(\tfrac{1}{4}N^2)/N^3 = -3/2N.$$

With grain sizes of a few millimeters or more in the specimens observed, N is about 10^7. So we can say with assurance that the effects of large-angle grain boundaries on the measured density defects in fused silver halides is negligible.

There may be an appreciable void volume associated with small-angle grain boundaries, however. The existence of mosaic structure has been indicated by studies of the width and intensity of x-ray reflection lines.[17] Although some mosaic structure exists in calcite from which Straumanis calculated the constants used in this paper, most crystals appear to have a more imperfect structure than calcite in this respect. Since small-angle grain boundaries appear to be composed of arrays of regularly spaced edge dislocations,[16] it is desirable to consider now the void volume associated with single edge dislocations.

Expansion at an edge dislocation is associated with the increased separation of planes of atoms which bound the slip plane. At the position of maximum distortion, the centers of the atoms have a separation equal to their diameter, D (assuming hard spheres), whereas their separation in the close-packed crystal is $(\sqrt{3}/2)D$. The difference is $0.13D$. The area associated with this separation of the planes depends on the length of the dislocation. If the lack of registry exists over a length of n atoms, the area increase will be $0.065nD^2$. Lomer[15] discusses the length of dislocations for metals, and he concludes that the value for copper is about five atoms. The dislocation length, according to Lomer's definition (the number of spaces where corresponding atoms or bubbles have lost contact), appears to be only about half the value required to describe the distance for the atoms to come into good register again. Then the value $\Delta A = 0.65D^2$ will be used as the increase in area at a dislocation.

The effect on the external volume of a crystal caused by an increase in volume at a singularity which causes a radial distortion has been discussed by Seitz[18] and Eshelby.[19] They find that the over-all expansion of the crystal is somewhat greater (1.5 to 1.8 times) than the increase in volume at the singularity. For a two-dimensional expansion, as with an edge dislocation, the two values of volume increase should be roughly equal.

Although the pattern of dislocations in silver bromide may be one in which the Burgers vector is in a [110] direction and the (111) plane is the slip plane, it is simpler, for rough computations, to picture the array of dislocations as forming cubic mosaics. Consider, then, a 1-cm cube having a concentration, C, of dislocations in each face. The change in density is then $\Delta\rho/\rho = -3C\Delta A = -2.0CD^2$.

The concentration of dislocation lines may be related to the size and misalignment of the mosaic elements in the following way: For square mosaic blocks which contain N atoms per side and an angle α between blocks, the number of dislocations along each edge of the block will be $N\alpha$. Since the total number of dislocations associated with each block is $2N\alpha$, the concentration will be $C = 2N\alpha/(ND)^2 = 2\alpha/ND^2$. The change in density associated with this concentration is $\Delta\rho/\rho = -2.0CD^2 = -4.0\alpha/N$. If the misalignment of the blocks is taken as $\alpha = 1/200$ radian, then, for the most perfect silver bromide specimen, N is 250 and the size of the mosaics is 1000 A (using for D the distance of closest approach of bromide ions). The mosaic size is not in good agreement with more common estimates of about 10 000 A, but it is interesting to note the mosaic sphere diameter of 2300 A for natural rock salt which was deduced from light-scattering measurements.[20] Although the present estimate of mosaic size is doubtless too small, it indicates that mosaic structure may be one of the more important configurations contributing to the density defect in silver bromide.

The failure of any of the configurations of voids which have been considered to account properly for the density defect leads to the supposition that most of the defect must be associated with immobile groups of vacancies. The number and size of such groups cannot be determined independently from density measurements, but might very well be determined from light-scattering.

ACKNOWLEDGMENT

It is a pleasure to acknowledge the cooperation of P. E. Goddard and F. Urbach, who provided the silver bromide and silver bromoiodide crystals, and of J. Moore and R. E. Beach, who made the spectroscopic analyses.

[17] A. H. Compton and S. K. Allison, *X-Rays in Theory and Experiment* (D. van Nostrand Company, Inc., New York, 1943), pp. 399–405.

[18] F. Seitz, Revs. Modern Phys. **18**, 384 (1946).

[19] J. D. Eshelby, J. Appl. Phys. **25**, 255 (1954).

[20] R. Fürth and S. P. F. Humphreys-Owen, Nature **167**, 715 (1951).

Millimeter Wave Spectra of SbH_3 and SbD_3†

ALBERT W. JACHE, GILBERT S. BLEVINS, AND WALTER GORDY
Department of Physics, Duke University, Durham, North Carolina

(Received October 25, 1954)

The $J=0\rightarrow1$ rotational transitions of normal and deuterated stibine have been measured in the shorter millimeter wave region. The B_0 values obtained are, in Mc/sec: 88 031.9 for $Sb^{121}H_3$, 88 015.5 for $Sb^{123}H_3$, $Sb^{123}H_3$, 44 693.3 for $Sb^{121}D_3$, and 44 677.1 for $Sb^{123}D_3$. The observed Sb nuclear quadrupole couplings, eQq, differ for the normal and deuterated forms of stibine and are, in Mc/sec: for Sb^{121}, 458.7±0.8 in SbH_3, and 465.4±0.8 in SbD_3; for Sb^{123}, 586.0±0.8 in SbH_3, and 592.8±0.8 in SbD_3. These couplings lead to the ratio $Q^{123}/Q^{121}=1.275\pm0.003$. The Sb nuclear quadrupole moments are estimated to be: $Q^{121}=-0.8\times10^{-24}$ cm², $Q^{123}=-1.0\times10^{-24}$ cm². Significant Sb nuclear magnetic coupling was observed for the normal stibine. In SbH_3 the magnetic coupling constant is found to be 0.33 Mc/sec for Sb^{121} and 0.18 Mc/sec for Sb^{123}. The ratio of these, $C^{121}/C^{123}=1.84$, is in good agreement with the known ratio of the nuclear g factors, $g^{121}/g^{123}=1.8465$. Slightly different values of the interatomic distances were observed for the normal and deuterated forms. In SbH_3 the Sb-H distance is 1.707 A and the H-Sb-H angle 91°18′. In SbD_3 the Sb-D distance is 1.702 A and the D-Sb-D angle 90°56′.

INTRODUCTION

BOTH SbH_3 and SbD_3 have been previously investigated in the near infrared region,[1] and the asymmetric species SbH_2D has been studied in the microwave region.[2] Because of their small moments of inertia the symmetric-top forms SbH_3 and SbD_3 could not be investigated with microwave methods until the recent development of the shorter millimeter region.[3] Precise microwave measurements have now been made on the symmetric-top forms. Both nuclear and molecular information has been obtained to supplement that known from the other studies. The results are reported here.

EXPERIMENTAL METHOD

The methods of generating and detecting the millimeter wave energy are those described by King and Gordy.[3] The deuterated stibines were observed with the third harmonic of the driving klystron, whereas the normal stibines were observed with the seventh harmonic. The frequencies were measured at the fundamental of the klystron with the usual secondary frequency standard[4] monitored by Station WWV. Because of the small dipole moment of stibine, 0.11 debye units, its rotational lines are weak, $\alpha_{peak}=\sim10^{-6}$ cm^{-1}. They could not be readily detected with the video spectrometer, but were easily measured with the automatic recording techniques[4] employing a phase-lock-in detector with repeller modulation of the klystron at the lock-in frequency.

The SbH_3 was prepared by reacting a Zn−Sb alloy with phosphoric acid. The alloy was prepared by heating a mixture of Zn_3Sb until fusion occurred. Sb was in slight excess of that needed to give a mixture corresponding to Zn_3Sb. The SbD_3 was prepared in a similar fashion using a completely deuterated phosphoric acid prepared from P_2O_5 and D_2O. In both of these preparations a large amount of a gas (presumably H_2 or D_2) not condensable in liquid air was formed. All reactions were carried out in a previously evacuated system. Fluorinated stop-cock grease was employed with the SbD_3 to prevent exchange of D with H.

EXPERIMENTAL RESULTS

Figure 1 shows a recorder tracing of the $J=0\rightarrow1$ transition of SbH_3. There are six component lines, three for each Sb isotope. The relative spacing and intensities are not faithfully reproduced by the recorder, primarily because of the nonuniform rate of sweep of the klystron.

Table I gives the observed frequencies and the calculated relative intensities. No effort was made to

TABLE I. Observed frequencies with calculated relative intensities.

Molecule	Transition $J=0\rightarrow1$ $F\rightarrow F$	Observed frequency in Mc/sec	Relative intensity (theoretical)
$Sb^{121}H_3$	5/2→5/2	176 142.92±0.5	75
	5/2→7/2	176 047.74	100
	5/2→3/2	176 004.64	50
$Sb^{123}H_3$	7/2→7/2	176 120.60±0.5	80
	7/2→9/2	176 008.39	100
	7/2→5/2	175 973.49	60
$Sb^{121}D_3$	5/2→5/2	89 462.46±0.3	75
	5/2→7/2	89 365.05	100
	5/2→3/2	89 322.65	50
$Sb^{123}D_3$	7/2→7/2	89 440.38±0.3	80
	7/2→9/2	89 326.39	100
	7/2→5/2	89 291.93	60

† This research was supported by the United States Air Force through the Office of Scientific Research of the Air Research and Development Command.

[1] W. H. Haynie and H. H. Nielsen, J. Chem. Phys. **21**, 1839 (1953); R. C. Smith, J. Chem. Phys. **19**, 384 (1951).

[2] C. C. Loomis and M. W. P. Strandberg, Phys. Rev. **81**, 798 (1951).

[3] W. C. King and W. Gordy, Phys. Rev. **90**, 319 (1953); **93**, 407 (1954).

[4] Gordy, Smith, and Trambarulo, *Microwave Spectroscopy* (John Wiley and Sons, Inc., New York, 1953).

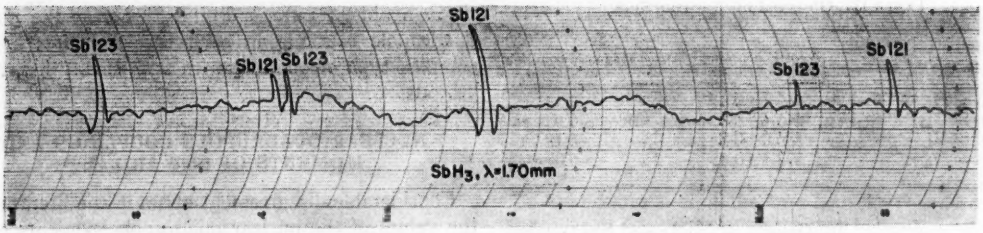

FIG. 1. Recorder tracing of the $J=0\rightarrow1$ transitions of $Sb^{121}H_3$ and $Sb^{123}H_3$ in the region of 176 kMc/sec.

measure the line intensities to an accuracy beyond that needed for identification of the different components.

The frequency of the $J=0\rightarrow1$ transition of a symmetric-top molecule in the ground vibrational state, if nuclear interaction is neglected, is

$$\nu_0=2B_0-4D_J, \tag{1}$$

where $B_0=h/8\pi^2I_b$ and I_b is the moment of inertia about any axis perpendicular to the symmetry axis, and D_J is a small stretching constant. Since only one transition was observed in the present work, D_J could not be obtained. From a comparison with arsine (see the following paper) it is estimated to be of the order of 1.5 Mc/sec for SbH_3 and 0.4 Mc/sec for SbD_3. It, therefore, can be neglected entirely in the structural determinations.

Regardless of the nuclear spin values, the hyperfine structure of a $J=0\rightarrow1$ transition consists of only three lines for a single coupling nucleus. The relative level spacing in terms of the nuclear quadrupole coupling constant, eQq, as well as the relative intensities are readily obtained from the numerical tables in the appendix of reference 4.

Because of the large values of B as compared with eQq, the second order terms in the quadrupole coupling are smaller than the experimental error. Nevertheless, it was found that the observed line spacing did not fit, within the experimental error, the spacing calculated with first order quadrupole coupling theory. The nuclear magnetic interaction term,

$$E=\tfrac{1}{2}A[F(F+1)-J(J+1)-I(I+1)], \tag{2}$$

superimposed upon the quadrupole coupling did account completely for the results. See Table II. The extremely good agreement in the last column is partly fortuitous because there are in each case two adjustable parameters to fit only three observed frequencies.

The magnetic coupling constant A for $Sb^{121}H_3$ is large. The fact that it is appreciably larger than that for $Sb^{121}D_3$ suggests that the magnetic field which gives rise to the interaction is generated by the molecular rotation. The magnetic coupling constants of $Sb^{121}H_3$ and $Sb^{123}H_3$ have the ratio 1.84, in good agreement with ratios of the nuclear g factors, $g(Sb^{121})/g(Sb^{123})=1.8465$. The ratios for the corresponding deuterides do not agree so well with the g-factor ratios because the smaller A's for the deuterides could not be measured with as good accuracy.

The Sb nuclear quadrupole couplings, eQq, and magnetic coupling constants for the different isotopic forms are given in Table III. The B_0 values and moments of inertia, I_B, obtained from the ν_0 values ($J=0\rightarrow1$ frequencies corrected for nuclear perturbations) are listed in Table IV.

MOLECULAR STRUCTURES

Since only one principal moment of inertia per isotopic species is obtained and since there are two independent molecular parameters, we must employ data from two different isotopic species for calculation of the molecular structure. In so doing, we make the assumption that the effective molecular dimensions are the same for both species. Because the zero-point vibrational energies are only slightly altered by exchange of the two heavy antimony isotopes, the assumption of equivalent dimensions in $Sb^{121}H_3$ and $Sb^{123}H_3$ or in $Sb^{121}D_3$ and $Sb^{123}D_3$ is justified. The error in the molecular dimensions caused by our inability to measure accurately the small differences, about 33 Mc/sec, of the $0\rightarrow1$ frequencies for the two Sb isotopes is believed to be the limiting factor in the accuracy and is of the order of 0.2 percent. In contrast, the differences in vibrational energies of the normal and deuterated forms of stibine are so great that significant differences in the

TABLE II. Values of nuclear quadrupole coupling of Sb from the three different hyperfine spacings.

Molecules	With magnetic coupling neglected (Mc/sec)	With correction for magnetic coupling (Mc/sec)
$Sb^{121}H_3$	460.93	458.74
	453.24	458.72
	478.89	458.69
$Sb^{121}D_3$	466.04	465.42
	463.85	465.35
	471.13	465.57
$Sb^{123}H_3$	588.44	585.96
	581.85	585.99
	610.75	585.99
$Sb^{123}D_3$	593.79	592.77
	591.10	592.80
	602.99	592.78

TABLE III. Observed nuclear couplings.

Nucleus	Electric coupling eQq in Mc/sec	Magnetic coupling A in Mc/sec
Sb^{121} in SbH_3	458.7±0.8	0.33
Sb^{121} in SbD_3	465.4±0.8	~0.9
Sb^{123} in SbH_3	586.0±0.8	0.18
Sb^{123} in SbD_3	592.8±0.8	~0.07

effective molecular dimensions of SbH_3 and SbD_3 exist. For this reason we do not combine the normal and deuterated species in the solutions although the wide separations of their rotational frequencies allow a highly accurate evaluation of the differences in their moments of inertia.

Table V gives the molecular dimensions of SbH_3 and SbD_3 as obtained from the two Sb isotopic species of each. Note that in agreement with its smaller zero point vibrational energy, the bond length and bond angle in SbD_3 are smaller than those of SbH_3. A comparably smaller size is found for the deuterated forms of arsine (see next paper) and of phosphine.[5]

In the work of Loomis and Strandberg[2] on SbH_3D it was necessary to assume the equivalence of the Sb-H

TABLE IV. Rotational constants.

Molecule	$\nu_0(J=0\rightarrow1)$ in Mc/sec[a]	B_0 in Mc/sec[b]	I_B in 10^{-40} g cm²
$Sb^{121}H_3$	176 069.85	88 031.92	9.529_{82}
$Sb^{123}H_3$	176 037.07	88 015.54	9.531_{40}
$Sb^{121}D_3$	89 388.08	44 693.29	18.77_{04}
$Sb^{123}D_3$	89 355.77	44 677.13	18.77_{72}

[a] Rotational frequency corrected for nuclear perturbations.
[b] Obtained from ν_0 with $D_J=1.5$ Mc/sec for SbH_3 and 0.4 Mc/sec for SbD_3, both estimated from the known stretching constants of arsine.

and Sb-D lengths and H-Sb-H and H-Sb-D angles to obtain a structural evaluation. For this reason their values of the bond angle (91.5°) and bond length (1.712 A) are not directly comparable with our results. It would seem that the mean values for the hybrid species should lie between the values for SbH_3 and SbD_3 whereas the Loomis-Strandberg values are larger than those we find for SbH_3. The discrepancy is not great, however, and is probably well within the range of errors in the two experiments.

The most surprising feature of the structure is the fact that the bond angle is so nearly a right angle, considering the large nuclear quadrupole coupling which exists. As in AsH_3 (see following paper), the almost normal bond angle implies bonding to the heavier atom through almost pure p orbitals, whereas the nuclear quadrupole coupling in each case indicates a more complex type of bonding with appreciably hybridized orbitals.

TABLE V. Molecular structures.

Molecule	Bond length	Bond angle
SbH_3	1.7073±0.0025 A	91°18′±20′
SbD_3	1.7021±0.0025 A	90°56′±20′

[5] Burrus, Jache, and Gordy, Phys. Rev. 95, 706 (1954).

NUCLEAR QUADRUPOLE COUPLINGS AND MOMENTS OF Sb^{121} AND Sb^{123}

Considerable disagreement exists in the literature on the values of the nuclear quadrupole moments of the antimony isotopes. From hyperfine structure in optical spectra. Murakawa[6] recently deduced the values $Q^{121}=-(0.52\pm0.1)\times10^{-24}$ cm² and $Q^{123}=-(0.67\pm0.1)\times10^{-24}$ cm², while concurrently Sprague and Tomboulian,[7] also from optical hyperfine structure, obtained the values $Q^{121}=-1.3\times10^{-24}$ cm² and $Q^{123}=-1.7\times10^{-24}$ cm². The work of Murakawa is based upon a more completely resolved spectra obtained by concentrated isotopic samples. Both sets of values are outside the range of limits $Q^{121}=(-0.35$ to $-0.50)\times10^{-24}$ cm² and $Q^{123}=(-0.45$ to $-0.62)\times10^{-24}$ cm² estimated by Loomis and Strandberg[2] from their microwave measurements. Although the principle applied by Loomis and Strandberg seems sound to the approximation they expected, their limits are badly off, primarily because the nuclear quadrupole moment of I^{127} and the I^{127} coupling per unbalanced p electron which they employed in the estimation are now known to be incorrect.

Loomis and Strandberg estimated $q\equiv\partial^2V/\partial z^2$ per unbalanced p electron in Sb in terms of the q for I by applying a correction for the difference in nuclear change of the two atoms. The q's should be in the approximate ratios of the fourth powers of their effective nuclear charges,

$$q(\mathrm{Sb})/q(\mathrm{I})\approx(Z_{\mathrm{Sb}}-4)^4/(Z_{\mathrm{I}}-4)^4=0.85. \quad (3)$$

For I, q can now be accurately obtained from the atomic beam results[8] and is

$$q_{m=0}=13.8\times10^{-12}\frac{eQq\ (\mathrm{Mc/sec})}{Q\ (\mathrm{cm}^2)}\ \mathrm{esu}. \quad (4)$$

$$q(\mathrm{I})_{m=0}\ (\text{per } p \text{ electron})=13.8\times10^{-12}\frac{(0.2296)}{0.819\times10^{-24}}=3.86\times10^{16}\ \mathrm{esu}.$$

Hence,

$$q(\mathrm{Sb})_{m=0}\ (\text{per } p \text{ electron})=3.3\times10^{16}\ \mathrm{esu}.$$

We now express the nuclear quadrupole moments in terms of the unbalanced p electrons in SbH_3,

$$Q(\mathrm{cm}^2)=\frac{13.8\times10^{-12}eQq\ (\mathrm{Mc/sec})}{U_pq_{m=0}\ (\text{per } p \text{ electron})}, \quad (5)$$

[6] K. Murakawa, Phys. Rev. 93, 1233 (1954).
[7] G. Sprague and D. H. Tomboulian, Phys. Rev. 92, 105 (1953).
[8] Jaccarino, King, Satten, and Stroke, Phys. Rev. 94, 1798 (1954).

where U_p represents the fractional number of unbalanced p electrons in SbH_3.

From the measured couplings in SbH_3 and the estimated q one obtains:

$$Q^{121}=0.192\times10^{-24}\ \text{cm}^2/(U_p \text{ in } SbH_3),$$
$$Q^{123}=0.245\times10^{-24}\ \text{cm}^2/(U_p \text{ in } SbH_3),$$

where the sign of U_p is taken to be negative for an excess concentration of p electronic charge along the symmetry axis as in stibine. Now U_p for AsH_3 can be obtained from the known coupling and $Q(As)$; it is -0.27. Because of the smaller bond angle in SbH_3 over that in AsH_3 and because of the greater ionic character (of the form $Sb^-H_3^+$) expected for stibine, we are inclined to agree with Loomis and Strandberg that U_p SbH_3 will not be greater in magnitude than that in AsH_3. This assumption yields, with the new values:

$$Q^{121}>|-0.71\times10^{-24}\ \text{cm}^2|,$$
$$Q^{123}>|-0.91\times10^{-24}\ \text{cm}^2|.$$

These limits are above the upper error limits of the values given by Murakawa[6] but are appreciably lower than the values given by Sprague and Tomboulian.[7] If, as is assumed by Loomis and Strandberg, the unbalanced p electronic charge can at most decrease in proportion to the decrease in the angle toward 90°, then U_p for Sb must be at least one-half the magnitude of that for As. This assumption, with Eq. (5), leads to the upper limits:

$$Q^{121}>|-1.4\times10^{-24}\ \text{cm}^2|,$$
$$Q^{123}>|-1.8\times10^{-24}\ \text{cm}^2|.$$

Thus the values -1.3×10^{-24} and -1.7×10^{-24} cm² of Sprague and Tomboulian lie within the maximum and minimum values estimated here and near the upper limits. We are inclined to believe the actual values lie much nearer to the lower than to the upper limits here given, since it does not seem reasonable that a change of only one degree in the bond angle from AsH_3 to SbD_3 would correspond to the large change in bond hybridization required to change U_p by 0.14. A more reasonable assumption is that the approximately equal bond angles in AsH_3 and SbH_3 indicate essentially equivalent bonding orbitals of Sb and As. Certainly there is no close correlation of bond angle with hybridization for these elements where both d and s contributions to the bonding orbitals are possible.

We select the values of Q listed in Table VI as the most probable estimates from present information. These values are somewhat nearer to the lower than to the upper limits estimated above from microwave data. They are the approximate means of the two sets of values obtained from optical hyperfine structure. We have not applied directly the Sternheimer[9] correction for the polarization of the core because this correction is indirectly applied through the I^{127} moment employed. The sign and order of magnitude of the Sb quadrupole moments are those expected from the correlation with the shell model.[10] Although the absolute values of the Sb quadrupole moments are still only roughly evaluated, accurate values of the ratios Q^{121}/Q^{123} are known with good accuracy. The ratios obtained here are in good agreement with the ratio obtained with pure quadrupole resonance by Dehmelt and Kruger.[11]

A measurable difference has been found in the coupling constants of normal and completely deuterated stibine (see Table III). A similar difference was found for arsine (see the following paper). In each instance the coupling is larger for the deuterated compound. If one considers the difference in bond angles alone, the opposite variation would be predicted since presumably the s hybridization and hence the coupling would be expected to decrease with decreasing angle. Nevertheless, the s hybridization should be greater the shorter the bond length, and a comparison of bond lengths suggests a larger coupling for the deuterides, as is observed.

TABLE VI. Nuclear moments.

Nucleus	Spin	Quadrupole moment Q in 10^{-24} cm²	Ratio $Q(Sb^{123})/Q(Sb^{121})$
Sb^{121}	5/2	−0.8	1.275±0.003
Sb^{123}	7/2	−1.0	

We are now attempting, in collaboration with the Oak Ridge National Laboratory, to use the same transitions of stibine observed here to measure the nuclear moments of radioactive Sb^{125}.

[9] R. Sternheimer, Phys. Rev. **80**, 102 (1950); **84**, 244 (1951).
[10] W. Gordy, Phys. Rev. **76**, 139 (1949).
[11] H. G. Dehmelt and H. Kruger, Z. Physik **130**, 385 (1951).

Millimeter Wave Spectra of AsH_3 and AsD_3*

GILBERT S. BLEVINS, ALBERT W. JACHE, AND WALTER GORDY
Department of Physics, Duke University, Durham, North Carolina

(Received October 25, 1954)

The $J=0\rightarrow1$ rotational transitions of AsH_3 and of AsD_3 have been measured in the one to three millimeter wave region. The B_0 values obtained are, in Mc/sec: 112 468.46 for $As^{75}H_3$ and 57 477.15 for $As^{75}D_3$. The observed nuclear quadrupole coupling, eQq, of As^{75} differs for the two species and is -160.1 ± 0.4 Mc/sec for $As^{75}H_3$ and -165.9 ± 0.4 Mc/sec for $As^{75}D_3$. Detectable As^{75} nuclear magnetic interaction was found with the magnetic coupling constant $A=0.33$ Mc/sec for AsH_3 and $A=\sim0.07$ Mc/sec for AsD_3. From a consideration of previous microwave work on AsH_2D and a consideration of the differences in the bond angles in normal and deuterated stibine, the bond angle in AsH_3 is assumed to be 91°50′ and that in AsD_3 to be 91°31′. These angles with the observed moments of inertia yield the value 1.5192 A for the As-H length and 1.5145 A for the As-D length.

INTRODUCTION

PURE rotational transitions of both AsH_3 and AsD_3 have been previously measured in the far infrared region at wavelengths of 0.2 mm and shorter by Stroup, Oetjen, and Bell.[1] In the present work are reported measurements of lower J rotational transitions of the same molecules in the region above one-millimeter wavelength. The rotation vibration spectra of arsine have been investigated in the near infrared region by McConaghie and Nielsen,[2] and the asymmetric hybrid AsH_2D has been studied with microwave methods in the centimeter wave region by Loomis and Strandberg.[3] No previous microwave measurements of AsH_3 nor AsD_3 have been made because the pure rotational spectra of these symmetric forms originate in the shorter millimeter wave region where sensitive measuring techniques have only recently been developed.[4] The present work reveals observable differences in the molecular dimensions and nuclear couplings of the normal and the deuterated forms.

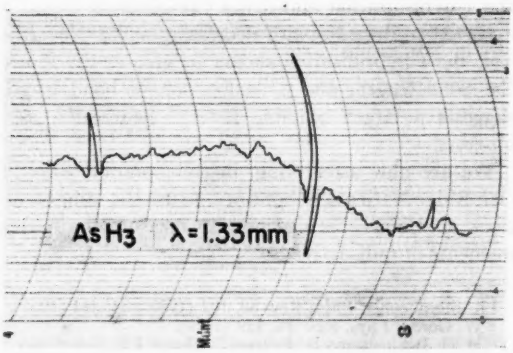

FIG. 1. Recorder tracing of the $J=0\rightarrow1$ transition of $As^{75}H_3$ in the region of 225 kMc/sec.

EXPERIMENTAL METHOD

The spectrometer employed was the same as that referred to in the previous paper on stibine. The fourth harmonic of the klystron power was employed for the AsD_3 measurements and the ninth harmonic for AsH_3.

Arsine was prepared by the action of H_2O on Na_3As. The deuterated arsine was prepared in a similar manner with D_2O being substituted for H_2O. The Na_3As was prepared by heating the elements until reaction occurred. All operations were carried out in a previously evacuated system.

EXPERIMENTAL RESULTS

The As^{75} nucleus has a spin of 3/2 and a sizeable electric quadrupole moment. The $0\rightarrow1$ transition is split into three components with intensity ratios 1, 3, and 2. Figure 1 shows a recorder tracing of the $0\rightarrow1$ transition of AsH_3 at 1.33 mm. The lines were also observed on the cathode-ray oscilloscope with the usual video spectrometer but with difficulty. The $0\rightarrow1$ lines of AsD_3 which fall at 2.60 mm were easily observed and measured with the video spectrometer.

Table I gives the observed frequencies and the calculated relative intensities of the lines. Table II lists the B_0 values and moments of inertia, and Table III the nuclear quadrupole couplings derived from the data. As in the Sb coupling for stibine, the nuclear quad-

TABLE I. Observed frequencies with calculated relative intensities.

Molecule	Transition $J=0\rightarrow1$ $F\rightarrow F'$	Observed frequency in Mc/sec	Relative intensity (theoretical)
$As^{75}H_3$	3/2→1/2	224 967.56±0.5	33
	3/2→5/2	224 936.78	100
	3/2→3/2	224 895.91	67
$As^{75}D_3$	3/2→1/2	114 993.50±0.3	33
	3/2→5/2	114 960.57	100
	3/2→3/2	114 918.94	67

* This research was supported by the United States Air Force through the Office of Scientific Research of the Air Research and Development Command.

[1] Stroup, Oetjen, and Bell, J. Opt. Soc. Am. 43, 1096 (1953).
[2] V. M. McConaghie and H. H. Nielsen, Phys. Rev. 75, 663 (1949).
[3] C. C. Loomis and M. W. P. Strandberg, Phys. Rev. 81, 778 (1951).
[4] W. C. King and W. Gordy, Phys. Rev. 90, 319 (1953); 93, 407 (1954).

TABLE II. Rotational constants.

Molecule	$\nu_0(J=0\rightarrow1)$ in Mc/sec[a]	B_0 in Mc/sec	I_B in 10^{-40} g cm^2
$As^{75}H_3$	224 928.22	112 468.46[b]	7.459_{08}
$As^{75}D_3$	114 952.20	57 477.15[b]	14.595_{56}

[a] The $J=0\rightarrow1$ rotational frequency corrected for nuclear perturbations.
[b] Obtained from ν_0 measured in the present work with $D_J=2.2$ Mc/sec for AsH_3 and $D_J=0.5$ Mc/sec for AsD_3 as taken from infrared data by Stroup, Oetjen, and Bell [J. Opt. Soc. Am. 43, 1096 (1953)].

rupole coupling of As^{75} is about 5 Mc/sec higher in the deuterated than in the normal arsine. The value obtained by Loomis and Strandberg for AsH_2D, -165 Mc/sec, falls between that which we obtained for AsH_3 and AsD_3.

It was found necessary to add to the nuclear quadrupole energy a small nuclear magnetic interaction term of the form given in Eq. (2) of the previous paper. The magnetic coupling constant A of $As^{75}H_3$, 0.33 Mc/sec, is roughly four times that observed for AsD_3. The latter is too small to be measured with accuracy.

MOLECULAR STRUCTURE

There is only one stable As isotope, and hence we cannot use the method of isotopic substitution to solve separately for the structures of AsH_3 and AsD_3. We can of course combine the normal and deuterated forms for the solution, but this will not lead to accurate values because of the effectively different sizes of these two isotopic forms. A more instructive treatment is obtained by making certain reasonable assumptions regarding the bond angles.

From near-infrared data Nielsen[5] has obtained the value 91°35′ for H-As-H angle in AsH_3. From microwave measurements Loomis and Strandberg[3] obtained the value 92° for the bond angle in the hybrid species AsH_2D. The latter value represents, presumably, a mean of the angles H-As-H and H-As-D. It should, therefore, be somewhat closer to the angle H-As-H than to the angle D-As-D. We assume for the H-As-H angle a value of 91°50′ which is consistent with the previous microwave and infrared work. From a consideration of the smaller angle (about 20′ smaller) of the deuterated over the normal forms in phosphine and stibine (see Table V), we assume the angle in AsD_3 to be 91°30′, or 20′ smaller than that in AsH_3. With these assumptions the As-H and As-D distances were calculated. The results are given in Table IV. It is seen that the effective As-D distance is about 0.005 A shorter than the As-H distance, in good agreement with the phosphine and stibine results. The values are compared in Table V.

TABLE III. Observed nuclear couplings.

Nucleus	Electric coupling eQq in Mc/sec	Magnetic coupling A in Mc/sec
As^{75} in AsH_3	-160.1 ± 0.4	0.33
As^{75} in AsD_3	-165.9 ± 0.4	0.07

[5] H. H. Nielsen, J. Chem. Phys. 20, 759 (1952); 20, 1955 (1952).

TABLE IV. Molecular structures.

Molecule	Bond angle	Bond length
AsH_3	91°50′±20′ (assumed)	1.5192±0.002 A
AsD_3	91°31′±20′ (assumed)	1.5145±0.002 A

NUCLEAR COUPLINGS

The nuclear quadrupole coupling per unbalanced p electron in atomic As^{75} has been measured from optical atomic hyperfine structure.[6] This result allows a simple calculation of the number of unbalanced p electrons in AsH_3 as

$$U_p=eQq(AsH_3)/(eQq)_{U_p=1}=-160/600=-0.27.$$

If the bonds were formed with pure p orbitals, there would be electrical symmetry about the As nucleus, the unbalanced p electron charge U_p would be zero, and no quadrupole coupling would be observed. If we assume that the unbalanced p charge indicated by the coupling arises from s hybridization alone with three equivalent directed-valence-bonds, the s hybridization required[7] for each bond orbital is approximately eight percent. With this type bonding the three equivalent hybridized orbitals would be directed at angles of 97° approximately, whereas the observed bond angle is only 91°50′. Evidently the bond orbitals cannot be nearly pure p as indicated by the bond angles alone, nor directed s-p hybrids as is suggested by the coupling alone. If the orbitals are the usual directed valence bond orbitals, the As bonding orbitals must have significant d as well as s character. A similar situation[8] exists in H_2S where a large asymmetry in the S^{33} coupling is found with a bond angle close to 90°.

It may also be possible to reconcile the bond angles and nuclear couplings in arsine with the nonlocalized molecular orbital treatment.[8] The 1s orbitals of the hydrogens would be combined to form a symmetric

TABLE V. Comparison of structures of phosphine, arsine, and stibine.

Molecule	Bond angle	Bond length
PH_3[a]	93°47′	1.4206 A
PD_3[a]	93°10′	1.4166 A
AsH_3[b]	91°50′	1.5192 A
AsD_3[b]	91°30′	1.5145 A
SbH_3[c]	91°18′	1.7073 A
SbD_3[c]	90°56′	1.7021 A

[a] From Burrus, Jache, and Gordy, Phys. Rev. 95, 706 (1954).
[b] Present work.
[c] Jache, Blevins, and Gordy (see preceding paper in this issue).

[6] H. Schuler and M. Marketu, Z. Physik 102, 703 (1936).
[7] For methods of evaluation see: Gordy, Smith, and Trambarulo, *Microwave Spectroscopy* (John Wiley and Sons, Inc., New York, 1953), Chap. 7.
[8] C. A. Burrus and W. Gordy, Phys. Rev. 92, 274 (1953).

and two antisymmetric functions with respect to the figure axis of the molecule. Two pure p orbitals of the As would then be combined with the antisymmetric H functions to form two π molecular orbitals, whereas the third bonding orbital, a σ molecular orbital, would be formed by combination of the symmetric H orbital with a hybridized atomic orbital of the As. This description will be elaborated elsewhere.

The magnetic coupling constant of $As^{75}H_3$, 0.33 Mc/sec, is the same as that of $Sb^{121}H_3$ while the nuclear g factor of As^{75}, 0.96, is less than that of Sb^{121}, 1.34. This result shows that the molecular magnetic field of AsH_3 at the As nucleus is larger than that of the Sb nucleus in SbH_3 by a factor of 1.40. If the molecular field is generated purely by rotation of the molecule, one might expect this factor to be approximately equal to the ratio of the two B_0 values, or about 1.3. The magnetic coupling constants of deuterated arsine and stibine are too small to be measured with accuracy. They are several times lower than those of the normal species and appear to be reduced by approximately the square of the B_0 ratios from the hydride values.

We wish to thank C. A. Burrus for assistance with the millimeter wave components.

PHYSICAL REVIEW VOLUME 97, NUMBER 3 FEBRUARY 1, 1955

Polarization Energy for $3d$ and $4p$ Electrons

R. E. TREES
National Bureau of Standards, Washington, D. C.
(Received September 23, 1954)

Meshkov has demonstrated the presence of an appreciable polarization energy associated with the combination of a $3d$ and a $4p$ electron in the $3d^2\,4p$ configuration of Ti II. He has shown that the mean deviation between theory and experiment is reduced from ± 332 K to ± 249 K when this energy is considered. It is here noted that by use of a modified form of Meshkov's approximation a further reduction to ± 180 K is produced. This modification requires only three adjustable parameters, as compared with the five required in Meshkov's original method. It is suggested that the agreement could be made even better if a breakdown of LS-coupling due to the closeness of three terms in this spectrum were considered.

I. INTRODUCTION AND RESULTS

In a recent paper, Meshkov has demonstrated the existence of an appreciable polarization energy associated with the combination of a $3d$ and a $4p$ electron in the $3d^2\,4p$ configuration of Ti II.[1] His method evaluates the d-p and d-d polarization energy of Ti II by utilizing the experimental data for Ti III in Bacher and Goudsmit's first approximation formula.[2,3] The parameters of Slater's formulas (more accurately, the differences in value of these parameters in Ti II and Ti III) were evaluated by least squares to get best agreement with the experimental data. His results are reproduced in columns A of Table I; the final mean deviation, obtained with five arbitrarily adjustable parameters, is ± 249 K.

Racah also has calculated term values for this configuration, by using a method that accounts for the d-d polarization energy only.[4,5] He assumes that the total d^2 energy is proportional to the energy of the d^2 parent term in Ti III. The parameters of Slater's formulas that refer to dp energy, together with the proportionality factor for the d^2 energy, were evaluated by least squares. His results are reproduced in columns B of Table I; the final mean deviation, obtained with four adjustable parameters, is ± 332 K. Since this calculation omits d-p polarization energy entirely, the smaller mean deviation obtained in Meshkov's calculation would be due primarily to its inclusion, though his use of an additional adjustable parameter also would help a little.[6]

Meshkov's method accounts for polarization by utilizing experimental data with Bacher and Goudsmit's first approximation, but only a part of the Slater energy is accounted for at the same time. Its main advantage, compared to using Slater's formulas together with the $L(L+1)$ correction,[3,7] is that it requires fewer adjustable parameters, so that the chance of getting accidental

[1] S. Meshkov, Phys. Rev. **91**, 871 (1953).
[2] R. F. Bacher and S. Goudsmit, Phys. Rev. **46**, 948 (1934).
[3] R. E. Trees, J. Research Nat. Bur. Standards **53**, 35 (1954), Research Paper 2515. Section 2.2 of this paper discusses the use of a linear approximation [such as Bacher and Goudsmit's first approximation, or the $L(L+1)$ correction] for the polarization energy, and lists other references on this subject. Referred to as A.
[4] G. Racah, Phys. Rev. **62**, 438 (1942).
[5] T. Yamanouchi [Proc. Phys.-Math. Soc. Japan **22**, 841 (1940)] has analyzed this configuration by using still another method which would account for the d-d polarization energy. He regards the energies of the parent term in d^2 as adjustable parameters, so that the number of parameters needed is six. His results are not given in numerical form.
[6] Racah's calculation A in Table I of reference 4 shows that the mean deviation is ± 430 K if neither d-d nor d-p polarization energy is included. Five parameters are used in this calculation.
[7] In a term $d^n(\beta SL)pS'L'$ the correction would be generalized to the form $(\alpha_d-\alpha_p)L(L+1)+\alpha_p L'(L'+1)$ to include both d-d and d-p polarization effects, so that two additional parameters would be needed. Rigorously, corrections proportional to $S(S+1)$ and $S'(S'+1)$ should be included also, but these seem to have a small effect. However, it should be noted that formula (2) does include these latter corrections.

agreement is decreased. Indirectly, the method checks the theory in the spectra in which the polarization is evaluated (i.e., in Ti III as well as Ti II) and the number of experimental values that determine the parameters is effectively increased. The disadvantages are that approximations are involved in the procedure and the errors are likely to be greater than those obtained by using Slater's formulas and the $L(L+1)$ correction; also the results are obtained in a form that is not as easy to interpret.

In this paper Meshkov's method is modified to a form which requires only three adjustable parameters instead of five. This modification evaluates both the polarization energy and the Slater energy with experimental data taken from Ti III and Sc II. The final mean deviation obtained with this method is ± 180 K as given in calculation C of Table I. Meshkov's calculation is based on the assumption that the d-p polarization energy in the d^2p configuration of Ti II is equal to that in the dp configuration of Ti III. The improved agreement obtained in the present paper may be attributed to the fact that this energy is more nearly equal to the larger effect present in the dp configuration of Sc II, which is approximately the assumption made.

II. EXPLANATION OF PROCEDURE

The energy of a term in the d^4p configuration of Ti I can be calculated from observed energies in Ti II and Ti III without introducing any arbitrary parameters by use of Bacher and Goudsmit's second approximation. For this approximation to lead to correct results, one requirement is that the parameters in any one spectrum (i.e., Ti I, Ti II, or Ti III) have the same ratios with respect to each other as the parameters in either of the other two spectra.[8] If this were the case, then it would be much easier to calculate the energies by using the simpler formulas for Bacher and Goudsmit's first approximation and introduce a single arbitrary parameter as a scale factor. In the notation of A this procedure is defined by the following formula:

$$W_{\text{Ti II}}(d^2p) = e[\bar{W}_{\text{Ti III}}(d^2p; d^2) + 2\bar{W}_{\text{Ti III}}(d^2p; dp)]. \quad (1)$$

In this formula, $\bar{W}_{\text{Ti III}}(d^2p; dp)$ is the average energy of the combination of a $3d$ and a $4p$ electron in some term (assumed specified) of the $3d^24p$ configuration approximated from experimental data in the $3d4p$ configuration of Ti III.[9] The factor 2 occurs because the p electron can be combined with either of the two d electrons. A similar interpretation holds for $\bar{W}_{\text{Ti III}}(d^2p; d^2)$.

[8] Section 7 of A. Racah has noted that even if this condition is satisfied the second approximation would fail to account fully for the first-order energy and he has modified the Bacher and Goudsmit theory to overcome this defect; these points are covered in Secs. 4 and 5 of A. This defect of the theory would not invalidate formula (1) of the present paper. Formula (2) was suggested in part by Racah's modification.

[9] The necessary formulas are given explicitly in Table IV of reference 1. A general procedure for setting up these formulas is given in reference 1, and a different procedure is given in Sec. 3 of A.

TABLE I. Calculated and observed term values in $3d^2\,4p$ of Ti II.[a]

Term	Obs	A Calc	A Diff	B Calc	B Diff	C Calc	C Diff
z $(^3F)^4G$	29 936	30 001	65	29 823	−113	30 113	177
z $(^3F)^4F$	31 108	31 123	15	31 125	17	31 061	−47
z $(^3F)^2F$	31 369	31 387	18	31 471	102	31 394	25
z $(^3F)^2D$	31 918	32 003	85	32 251	333	31 794	−124
z $(^3F)^4D$	32 690	32 711	21	32 890	+200	32 452	−238
z $(^3F)^2G$	34 657	34 175	−482	34 109	−548	34 673	16
z $(^3P)^2S$	37 431	37 413	−18	37 628	197	37 516	85
y $(^1D)^2D$	39 380	39 928	548	40 000	620	39 848	468
z $(^1D)^2P$	39 627	39 321	−306	39 496	−131	39 300	−327
y $(^1D)^2F$	40 011	39 662	−349	39 507	−504	39 936	−75
z $(^3P)^4S$	40 027	40 260	233	40 237	210	40 239	212
y $(^3P)^4D$	40 612	40 506	−106	40 441	−171	40 615	3
z $(^3P)^4P$	42 127	42 018	−109	42 100	−27	41 965	−162
y $(^1G)^2G$	43 763	43 721	−42	43 675	−88	43 760	−3
x $(^3P)^2D$	44 907	44 897	−10	44 737	−170	45 083	176
y $(^3P)^2P$	45 524	45 814	+290	45 673	149	45 587	63
z $(^1G)^2H$	45 802	45 459	−343	45 184	−618	45 676	−126
x $(^1G)^2F$	47 535	47 801	266	48 078	543	47 411	−124
$(^1S)^2P$		(66 060)		(64 465)		(64 053)	
	Mean deviation		±249		±332		±180

[a] The symbols A, B, and C refer to the following calculations: A: S. Meshkov, Phys. Rev. 91, 871 (1953), Table VI. B: G. Racah, Phys. Rev. 62, 438 (1942), Table I, Calculation B. C: Formula 2, this paper.

The adjustable parameter "e" is introduced as a scaling factor.

The approximation (1) gives poor results because the parameter ratios do not behave as required. This can be seen from inspection of the parameters for Ti II, Ti III and Sc II which are listed in Table II. The parameters B and C defined by the two $3d$-electrons do have approximately the same ratio in all three spectra ($B/C = 0.29 \pm 0.03$). However, the parameters defined by a $3d$ and a $4p$ electron (i.e., F_2, G_1, and G_3) have mutual ratios, and ratios with respect to B and C, that differ in all three spectra. In particular, the ratio G_1/F_2 has the values 1.4, 1.2, and 1.0 in Sc II, Ti II and Ti III, respectively. Roughly speaking, the d^2 parameters in Ti II are nearly equal to the ones in Ti III, but the dp parameters are more nearly equal to those in Sc II. This is understandable from shielding considerations.

The preceding discussion shows that there will be a point intermediate between Sc II and Ti III where B and C will have the same values as in Ti II; this point is defined by "e_1," which is our first adjustable parameter. There will be also a point where the ratio G_1/F_2 will be equal to the value of this ratio in Ti II. The ratio

TABLE II. Radial parameters in spectra with $3d$ and $4p$ electrons.[a]

Parameter	Sc II (1)	Sc II (2)	Ti III (1)	Ti III (2)	Ti II (3)	Ti II (4)	Ti II (5)	Ti II (6)
B	481	502	695	718	669	681	682	684
C	1789	1535	2911	2629	2563	2493	2481	2459
F_2	242	259	444	450	290	288	291	281
G_1	380	360	435	441	332	337	357	346
G_3	8	7	46	46	18	20	22	16
α_d		31		35		33	35	34
α_p		100		35			35	75
Deviation					±430	±332	±249	±180

[a] The column numbers refer to the following calculations: (1) W. M. Cady, Phys. Rev. 43, 322 (1933). (2) R. E. Trees (unpublished). (3) G. Racah, Phys. Rev. 62, 438 (1942), Calculation A of Table I. (4) G. Racah, Phys. Rev. 62, 438 (1942), Calculation B of Table I combined with calculation (2) for Ti III given above. (5) S. Meshkov, Phys. Rev. 91, 871 (1953). Calculation of Table V combined with calculation (2) for Ti III given above. (6) Results of this paper.

of the other two adjustable parameters "e_3" and "e_2" defined this point. The scaling factor needed to make the values of F_2 and G_1 themselves the same as in Ti II is the second parameter "e_2." The complete formula is expressed as follows:

$$W_{\text{Ti II}}(d^2p) = \bar{W}_{\text{Sc II}}(d^2p; d^2) + e_1[\bar{W}_{\text{Ti III}}(d^2p; d^2) - \bar{W}_{\text{Sc II}}(d^2p; d^2)] + 2e_2\bar{W}_{\text{Sc II}}(d^2p; dp) + 2e_3[\bar{W}_{\text{Ti III}}(d^2p; dp) - \bar{W}_{\text{Sc II}}(d^2p; dp)]. \quad (2)$$

The average energies evaluated from experimental data in Sc II and Ti III are listed in Table III. The parameters were adjusted by least squares to give the best fit with the experimental data in Ti II, and were found to have the following values:

$$(A = 26423.8),\ e_1 = 0.84492,\ e_2 = 0.90551,\ e_3 = 0.24163.$$

The calculated values are given in column C of Table I; the mean deviation between theory and experiment is ± 180 K.

The values of e_1, e_2, and e_3 obtained above were used to interpolate between the values of the parameters in Sc II and Ti III (given in columns (2) of Table II) to obtain the parameters of the linear theory which would give the same results as formula (2); the results are given in column (6) of Table II. This correspondence is not exact, since the parameters used for Sc II and Ti III do not fit the experimental data in these spectra exactly. A check in the rational roots indicates that these parameters would lead to values that differ from those of calculation C by about 100 K, which is within the over-all accuracy of the original calculation. It will be noted that the parameter for the dp-polarization energy (i.e., α_p) is greater than the one for the d^2 energy (i.e., α_d), and that the value of this parameter depends strongly on the degree of ionization.

Two parameter formulas were considered also. A formula the same as (2) except that $e_2 = 1$, lead to a mean deviation of ± 293 K with the parameter values $e_1 = 0.8418$ and $e_3 = 0.2942$. This mean deviation could probably be reduced to about ± 280 K by fuller use of least squares in evaluating e_1 and e_3. A simpler two-parameter relation of the form

$$W_{\text{Ti II}}(d^2p) = e_1 W_{\text{Ti III}}(d^2p; d^2) + 2e_2 W_{\text{Ti III}}(d^2p; dp) \quad (3)$$

was not tried, as it was clear from the start that this was not as good an approximation as the one used by Meshkov.

TABLE III. Average energies.

SL	$S'L'$	Sc II $\bar{W}(d^2(SL)pS'L'; d^2)$	Ti III $\bar{W}(d^2(SL)pS'L'; d^2)$
^3P		12 128	10 661
^3F		4909	242
^1G		14 261	14 398
^1S		26 324	34 020
^1D		10 944	8473
		$2\bar{W}(d^2(SL)pS'L'; dp)$	
		−53 000	−151 000
^3P	^2S	154	422
^3P	^4S	3132	3506
^3P	^4P	4308	7419
^3F	^4F	3581	5355
^3F	^4G	2467	4494
^1G	^2H	4676	7328
^3P	^4D	2995	4842
^3F	^4D	5028	7734
$^3P, ^3F$	^4D	944	1854
^3F	^2G	7824	10 569
^1G	^2G	2562	3286
$^3F, ^1G$	^2G	−2153	−2365
^1S	^2P	4313	6721
^3P	^2P	8033	12 749
^1D	^2P	4041	6266
$^1S, ^3P$	^2P	−1912	−1697
$^1S, ^1D$	^2P	1757	3474
$^3P, ^1D$	^2P	17	553
^3P	^2D	6025	8570
^1D	^2D	4886	7882
^3F	^2D	4982	9177
$^3P, ^1D$	^2D	−2270	−2255
$^3P, ^3F$	^2D	3165	5137
$^1D, ^3F$	^2D	425	1063
^1D	^2F	4020	6086
^3F	^2F	4508	7028
^1G	^2F	5994	10 184
$^1D, ^3F$	^2F	−2422	−2559
$^1D, ^1G$	^2F	986	1950
$^3F, ^1G$	^2F	647	1240

[a] Calculated values.

III. ERRORS OF THE PROCEDURE

Because so few adjustable parameters were used in calculation C of Table I the inclusion or exclusion of any particular term has little effect on the resultant errors of other terms. The error in $y\,^2D$ is anomalously large since it exceeds twice the mean deviation. The mean deviation of the terms in calculation C, excluding the $y\,^2D$ in ± 146 K. If this term is omitted from the least squares calculation, the mean deviation of the other terms is reduced to ± 136 K,[10] which is only slightly less, so that including or excluding $y\,^2D$ does not make much difference in the over-all agreement. Comparison of the individual errors in calculation C with those of the least squares calculation with $y\,^2D$ omitted shows very little change; in particular, the $z\,^2P$ error is still the largest remaining error, though reduced slightly to -310 K in the latter calculation. When many adjustable parameters are used, there is more chance that terms with large errors will cause other terms in the calculation to have large errors and it is not easy to pick out the terms that are responsible for disagreements between theory and experiment.[11]

Unfortunately there are many sources of error in this

[10] We are indebted to Dr. P. Rabinowitz of the Computation Laboratory at NBS for making this calculation on SEAC. The parameter values of this least squares calculation were ($A = 26430.6$), $e_1 = 0.84547$, $e_2 = 0.87946$, $e_3 = 0.29553$. The SEAC code is a multiple purpose code based on the Gram-Schmidt orthogonalization process, and is described in National Bureau of Standards Report No. 3169.

[11] A case in point is the $a\,^1F$ of Ti I which is discussed in reference 25 of A.

theory that must be considered. One major source is configuration interaction, and the effects of this (as well as other less important effects) would have to be estimated in Sc II and Ti III before the errors in Ti II could be regarded as fully significant. The variation of the interaction parameter H_2 between the $3d^2$ and the $3d4s$ configuration is fairly well established,[12] and it can be shown that this configuration effect cannot explain the large errors in $y\,^2D$ and $z\,^2P$. However, the interaction parameters R_d and R_e between $3d4p$ and $4s4p$ cannot be estimated on the basis of previous work,[13] and it is not easy to evaluate the perturbation that would result from interaction between these two configurations. For this reason, the $3d4p$ parameters in calculation (2) of Table II might not indicate true behavior. The good agreement obtained would tend to indicate this is not the case and that configuration interaction can be neglected. If this latter assumption were not true, then the Ti II data would be even more perturbed and a linear theory (which includes this method) would be inapplicable.

With regard to the source of the large errors of $y\,^2D$ and $z\,^2P$ in calculation C it should be noted that $y\,^2D$, $z\,^2P$ and $y\,^2F$ have two pairs of interacting levels separated by 450 K in one pair ($J=2\frac{1}{2}$) and by 370 K in the other ($J=1\frac{1}{2}$), so that breakdown of LS-coupling could be appreciable. If the $J=2\frac{1}{2}$ and $J=1\frac{1}{2}$ term assignments were interchanged in these pairs, then the errors of $y\,^2D$, $z\,^2P$, and $y\,^2F$ would be changed from $+468$, -327, and -75 K, respectively, to $+51$, -80, and $+118$ K so that this procedure would remove all significant discrepancies between theory and experiment; the mean deviation of the revised errors would be ± 123 (a new least squares calculation would reduce this still more).

This interchange is probably not warranted, but an appreciable improvement should result if the actual correction were accurately evaluated and applied. It is likely that the classification of the levels given in Volume I of *Atomic Energy Levels* does specify the dominant component. However, the g-values, which would be the most decisive factor in deciding this, are uncertain. A strong interaction between $y\,^2D_{1\frac{1}{2}}$ and $z\,^2P_{1\frac{1}{2}}$ has been noted by H. N. Russell [Mt. Wilson Contract No. 344 (1927) page 30 (unpublished)]. Except for the $z\,^2P_{1\frac{1}{2}}$ g-value (it is not Landé and was probably not assumed), all g-values given for the levels of $y\,^2D$, $z\,^2P$, and $y\,^2F$ terms of Ti II are assumed Landé values (used to calculate other g-values that are given without colons).

[12] A discussion of this variation and a partial tabulation of values of H_2 is given in Sec. 6 of A. In Sc II and Ti III it is estimated that $H_2=200\pm 20$. The parameters B and C of calculation (2) of Table II were corrected slightly for this effect but no allowance is made for it in calculations A, B, or C of Table I.

[13] The notation for these parameters is that used by N. Rosenzweig [Phys. Rev. 88, 580 (1952)]. G. Racah [Phys. Rev. 62, 523 (1942)] has given an evaluation of these parameters in Sc I ($R_d=-3063$ and $R_e=950$) but his calculation neglects polarization effects which are expected to be large. If his interaction parameters are used in Sc II the value of the $z\,^2P-y\,^2P$ interaction element is very large (-4013 K). Since the observed separation of these terms is 9443 K it would be attributed almost entirely to configuration interaction.

PHYSICAL REVIEW VOLUME 97, NUMBER 3 FEBRUARY 1, 1955

Electromagnetic Spectrum of Am^{241}

PAUL P. DAY
Chemistry Division, Argonne National Laboratory, Lemont, Illinois
(Received October 18, 1954)

The electromagnetic spectrum of Am^{241} has been studied with a ten-inch bent-crystal spectrometer and a sodium iodide scintillation counter. Twelve gamma rays, sixteen Np L x-rays, and eight Am L x-rays have been measured. The gamma rays in Np have energies of 26.363, 33.199, 43.463, 59.568, 103, 113, 130, 159, 210, 270, 328, and 370 kev. The x-ray energies establish the validity of the Mosley extrapolations in this region of the periodic table. Details of the spectrometer operation and calibration are given.

INTRODUCTION

AMERICIUM–241 is a complex alpha emitter which decays with a 470-year half-life[1] to Np^{237}. A transmission type, bent-crystal spectrometer and a 20-channel scintillation counter have been used to analyze the electromagnetic spectrum emitted during the decay of this isotope. The results are reported herein.

The alpha spectrum has been measured by Asaro *et al.*[2] with a magnetic spectrometer. Six alpha groups were reported with energies of 5.546, 5.535, 5.503, 5.476, 5.433, and 5.379 Mev with relative intensities of 0.23 percent, 0.34 percent, 0.21 percent, 84.2 percent, 13.6 percent, and 1.42 percent, respectively. Later,[3] the 5.546-Mev alpha "peak" was ascribed to scattering from one of the baffles in the spectrometer.

[1] B. G. Harvey, Phys. Rev. 85, 482 (1952).

[2] Asaro, Reynolds, and Perlman, Phys. Rev. 87, 277 (1952).

[3] F. Asaro (unpublished data, September, 1953).

Seaborg *et al.*[4] obtained an energy of 62 kev for the prominent gamma ray by absorption methods with an intensity of about 0.4 gamma ray per alpha particle. Martin,[5] using a gamma-ray pulse analyzer, observed two gamma rays, one at 59 kev with an intensity of 0.4 gamma per alpha particle and another at 100 kev with an intensity of about 10^{-4} gamma per alpha particle. Using a bent-crystal spectrometer similar to the one described in this paper, Barton *et al.*[6] measured the energies of the three prominent L x-ray lines due to internal conversion of the gamma rays in neptunium and found them to agree with the Mosley values extrapolated from thorium and uranium. The alpha-gamma coincident measurements of Prohaska[7] gave 0.32 sixty-kev gamma ray per alpha particle. There were three L-electrons for each M-electron and a total electron coincidence rate of 0.49 electron per alpha particle was obtained. O'Kelley[8] ran the conversion spectrum on the Berkeley beta-ray spectrometer and found the L, M, and N conversion lines for a 59.7-kev gamma ray. A value of 0.28 L-electrons per alpha particle was also quoted. Using a proportional counter, Beling *et al.*[9] observed five lines; 59.7, 26.3, 20.9, 17.3, and 13.5 kev with intensities of 1.0, 0.075, 0.177, 0.66, and 0.42, respectively. They attributed the three lowest lines to the Np L x-rays and by coincidence measurements found 0.40 sixty-kev gamma ray per alpha particle. They[10] also derive upper limits for the conversion coefficients for the 59.7- and 26.3-kev gamma rays of 1.5 and 20, respectively. After modifying the Barton spectrometer, Browne[11] ran the Am^{241} spectrum and found eight Np L x-rays which arise from internal conversion of the gamma rays. In addition, he found six other lines which he attributed to gamma rays with energies of 18.83, 22.20, 26.43, 33.36, 38.00, and 59.78 kev. Newton and Rose[12] showed that the 33.36-kev and 38.00-kev lines found by Browne were due to fluoresence of La which was present in the sample. With proportional counters, they set an upper limit of 0.1 percent per sixty-kev gamma ray for the intensity of a 33-kev gamma ray which was predicted by the level scheme. Using a double-focusing beta spectrometer, Passell[13] found conversion electrons for six gamma rays; 26.3, 33.1, 43.4, 56.4, 59.6, and 99.5 kev. Jaffe[14] found two gamma rays with energies of 26.38 and 59.62 kev using the Barton curved-crystal spectrometer and four gamma rays with energies of 102, 128, 168, and 207 kev using a scintillation spectrometer.

The nuclear level structure of Np^{237} may also be obtained by observing the radiations of the 6.7-day beta emitter U^{237}. Wagner *et al.*[15] found ten gamma rays by the use of scintillation spectrometry and a magnetic lens spectrometer; 27, 43, 59, 102, 165, 207, 269, 334, 370, and 430 kev.

APPARATUS

The work described in this paper has been performed on the ten-inch bent-crystal spectrometer located in a shielded underground room at Argonne National Laboratory. The spectrometer is built along the lines of the transmission spectrometer designed and built at Berkeley by Barton.[6] As originally designed, an elastically bent crystal of quartz was used to diffract the radiation which was detected with a proportional counter. Browne[11] made some important changes on this instrument, the two principal ones being the use of topaz instead of quartz and a scintillation counter instead of the proportional counter. Owing to the increased reflectivity of the topaz over the quartz and the high efficiency of a scintillation counter, Browne was able to improve the transmission of the instrument by a factor of 200. The range of the instrument was 10 kev to 130 kev.

The fundamental design and preliminary assembly of the present spectrometer was carried out by G. Barton assisted by C. A. Prohaska. (The construction drawings were brought from The University of California Radiation Laboratory by Barton.) The author undertook the final assembly and calibration with the guidance and help of Melvin S. Freedman. Although a number of improvements were introduced, basically (see Fig. 1) the instrument is the same as the one modified by Browne.[11] The (303) planes of a topaz crystal 0.008 in.×0.75 in.×1.5 in. (which are inclined at an angle of 29° to the crystal face) elastically bent to a radius of ten inches, are used to diffract the radiation (1).[16] The radiation is detected with a scintillation counter which sets inside of a one-inch lead shield (2). The scintillation counter was designed and constructed by R. Swank and J. Moenich and consists of a rectangular NaI(Tl) crystal (3) 0.25 in.×1.5 in.×2.25 in. in an aluminum can, mounted on the end of a DuMont 6292 phototube (4). A window consisting of a disk of 0.020-in. thick Be with a 0.0002-in. Al reflector next to the crystal has a measured transmission of 95 percent at 14 kev. The detector has a resolution (full width at

[4] Seaborg, James, and Morgan, *The Transuranium Elements: Research Papers* (McGraw-Hill Book Company, Inc., New York, 1949), Paper No. 22.1, National Nuclear Energy Series, Vol. 14B, Div. IV.

[5] D. F. Martin (unpublished).

[6] G. W. Barton, University of California Radiation Laboratory Report UCRL-670, May, 1950 (unpublished); Barton, Robinson, and Perlman, Phys. Rev. **81**, 208 (1951).

[7] C. A. Prohaska, University of California Radiation Laboratory Report, UCRL-1395, August, 1951 (unpublished).

[8] G. D. O'Kelley, University of California Radiation Laboratory Report, UCRL-1243, 1951 (unpublished).

[9] Beling, Newton, and Rose, Phys. Rev. **86**, 797 (1952).

[10] Beling, Newton, and Rose, Phys. Rev. **86**, 670 (1952).

[11] C. I. Browne, University of California Radiation Laboratory Report UCRL-1764, June, 1952 (unpublished).

[12] J. O. Newton and B. Rose, Phys. Rev. **89**, 1157 (1953).

[13] T. O. Passell, University of California Radiation Laboratory Report, UCRL-2528, March, 1954 (unpublished).

[14] H. Jaffe, University of California Radiation Laboratory Report, UCRL-2537, April, 1954 (unpublished).

[15] Wagner, Freedman, Engelkemeir, and Huizenga, Phys. Rev. **89**, 502 (1953).

[16] Numerals in parentheses refer to the numbered components in Fig. 1.

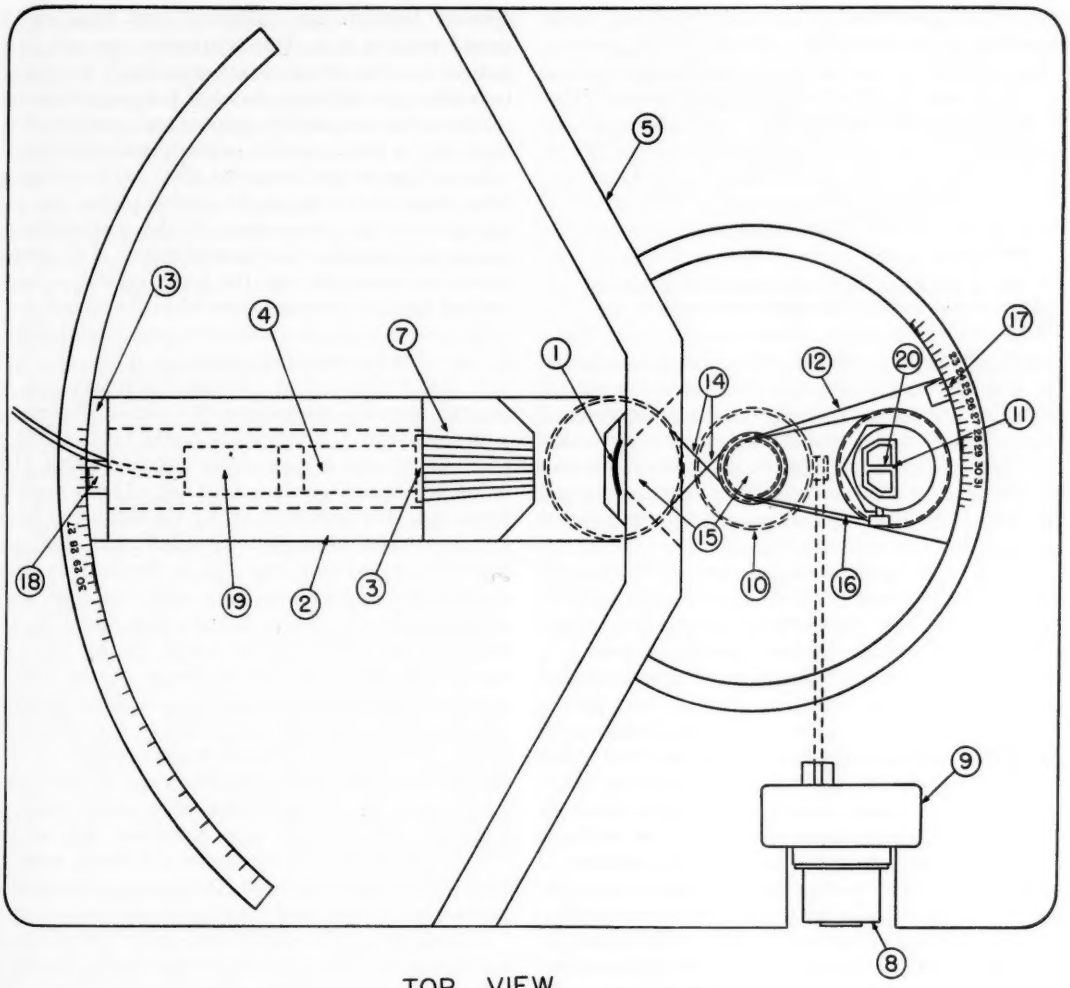

FIG. 1. Schematic diagram of the bent-crystal spectrometer. The source arm (12) and detector arm (13) are shown at 0° Bragg angle for a set of diffracting planes which are perpendicular to the crystal face. e.g., the (310) planes of quartz or the (1000) planes of topaz.

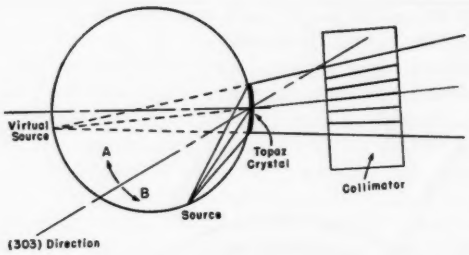

FIG. 2. Schematic diagram illustrating the geometrical optics of the bent-crystal spectrometer.

half-height) of 20 percent at 60 kev and a background (no source in the spectrometer) of about 10 counts/min in the 10-kev region. In order to shield the detector from direct radiation from the source, a stationary 2-in. lead shield (5) is located between the source and the detector. A 1-in. lead shield (6) is placed around the source to keep the radiation level around the spectrometer to a moderate value.

An appreciable gain in transmission over the Browne version was obtained by increasing the topaz crystal dimensions by 30 percent and designing a larger collimator (7) which has an opening sufficient to intercept the entire diffracted beam. The measured transmission of the diffracted beam at 60 kev is 1.7×10^{-6}. The present collimator consist of a truncated pyramidal opening through a 4-in. cube of lead lined with brass plates at the top and bottom in which there are 15 precisely milled grooves, into which fit 0.060-in. thick tungsten sheets. By use of a single collimator with removable baffles it is possible to fulfill the collimation requirements from 8 to ~200 kev.[17] The calculated transmission of the collimator with all 15 tungsten baffles inserted is 44.6 percent in comparison with a measured value of 43.9 percent. Below 30 kev, only 7 baffles are used, to give an increased transmission without a significant increase in the scattered background.

Since the diffracted beam which the collimator intercepts is diverging, the baffles are oriented so that they are parallel to the diverging radiation; thus the collimator will have a "focal point." If the virtual source is located at this "focal point," the diverging rays will pass unhindered through the collimator except for those that are intercepted by the finite thickness of the baffles. It can be seen in Fig. 2 that it is necessary to have the collimator positioned so as to locate its "focal point" at the virtual source. Since the source moves on the circle on which the topaz crystal is mounted, the distance between the source and the topaz crystal varies as much as 4 in., and thus the distance between the collimator and topaz crystal should vary by 4 in. This adjustment was not incorporated into the original design, and thus it is necessary to position the collimator by hand to an approximately correct radial distance for various small portions of the spectrum to obtain precise intensity measurements.

In addition to the divergence effect in the horizontal plane, there is also one in the vertical plane, that is, a variation in the transmission of the instrument for the rays not parallel to the plane of motion of the source. When the source is near the topaz crystal, a larger vertical angle is accepted than when the source is far away. However, if the collimator is positioned properly as defined in the preceding paragraph, it may be shown that this "height effect" almost disappears and for accurate intensity measurements it can be allowed for.

By means of a synchronous motor (Fig. 1) (8), a gear box (9), and a worm drive (10), the source (11), which is mounted on the source arm (12), is made to rotate at a slow uniform rate. By the shifting of levers in the gear box, sweeping rates of 0.3°, 1.5°, 6.0°, and 30.0° Bragg angle per hour can be obtained. In order to have the detector arm (13) make the same angle with the reflecting planes as the source arm (12), the detector arm is linked to the source arm by two steel bands (14) around a pair of drums on the axes of rotation of the respective arms (15). So that the sample will always present the same side to the diffracting crystal, the sample housing is made to rotate in synchronization with the sample arm by the use of another steel band (16). A calibrated scale which reads in arbitrary units of angle plus a vernier (17) on the sample arm permit the reading of the Bragg angle to 0.005°. The scale and vernier (18) by which the detector position is read, are used for aligning the spectrometer.

The pulses from the scintillation counter pass through a preamplifier (19) and a main amplifier before being fed into a pulse height discriminator. Using this differential pulse height analyzer, a small range in pulse amplitude is selected to include the radiation being Bragg reflected. By using a detecting system of this nature, the background is kept down to about 30 counts/min in the 20-kev region (source in the spectrometer, but no peak being Bragg reflected). After discrimination, the pulses are fed into a count-rate meter and a scaler. A Brown chart recorder records the count-rate meter output, while a digital recorder prints the scaler reading at preselected intervals. If the intensity of the line being swept has a counting rate 50 percent higher than the background (defined as the average of the counting rates on the two sides of a peak) or larger, it has usually been found preferable to utilize the chart recorder. This does not reduce the accuracy of the measurements, and it is much less time consuming than taking data from the digital printer. In order to record the angular setting of the spectrometer source arm on the Brown chart at periodic intervals the spectrometer scale is read and the input terminals

[17] The geometry of the spectrometer is such that the diffracted beam and the undiffracted beam (which is about 100 times as intense as the diffracted beam) would both strike the detector for energies higher than 30 kev unless a collimator is placed over it which will discriminate against all radiation except from a preferred direction.

of the Brown chart are momentarily shorted, causing the pen to drop to zero and return very rapidly, thus providing a sharp reference mark. When the counting rate of a line is too low to obtain good statistics by the continuous sweep method, the spectrometer angle is set by hand to 15 or 20 points spanning a peak, and counts are taken at each point. The digital recorder with the continuous sweep method is used primarily to establish the existence of very weak peaks prior to the hand setting method. It has been found that the worm drive is not uniform, and it is necessary to read the sample arm scale every 5 or 10 minutes for precise measurements.

In order to obtain the maximum resolution from a given sample, it is necessary to have the source perpendicular to the plane of the instrument and to have its geometrical center above the center of rotation of the sample housing. A new sample holder has been designed and constructed by F. Hartford which gives the necessary degrees of freedom. The sample, which is contained in a capillary, is taped to a milled groove cut in a Lucite block which is held in a pair of vertical brass ways by a pair of spring clips. Since the groove and ways are made accurately vertical and the groove is located tangentically over the center of rotation of the sample housing, it is necessary to have only two adjustments, one radically along the sample arm and one vertically. It has been found advisable to make the final precise adjustment by sweeping through a strong single diffraction peak, adjusting the sample position (including rotation of the sample capillary) to obtain high resolution and symmetrical diffraction peaks.

Since this instrument is of the Cauchois approximate-focus type,[18] the diffraction peaks will have a width which will be a function of their angular position and thus their energy, because of a geometrical defocusing due to the deviation of the neutral axis of the bent crystal from the focal circle. This aberration is called the Cauchois width[19] and is defined by

$$d\theta = \sin\theta(1-\cos a)/\cos(a+\theta),$$

where θ is the angle the source arm makes with the crystal perpendicular and a is the half-angle the diffracting crystal intercepts from the source when the source arm is perpendicular to the crystal. This broadening effect will have an effective width on the focal circle on side A of the reflecting planes (see Fig. 2) of zero at 10 kev to 0.011 in. at 200 kev and 0.021 in. on side B of the reflecting planes at 18 kev. The experimental data indicate that this broadening is the major source of aberration in the instrument.

In order to mount sources of moderate specific activity (millicuries per milligram) which can utilize the expected resolving power and for considerations of safe mounting of the intense (frequently alpha-emitting) sources required (~1 millicurie), the activity is usually sealed in a fine (preferably 10–15 mil i.d.) glass capillary. With sources of very high specific activity (millicuries per microgram), the source is concentrated into a small quantity of solution and then deposited on a fine strip of filter paper. This filter paper is then clamped between two Lucite jaws and placed in the spectrometer so that the thickness of the paper serves as the source width, and thus a dry source only about 0.005 in. thick is easily prepared. It should be pointed out that intense alpha sources sealed in capillaries with water present will decompose the water and build up sufficient pressure to rupture the capillary. For safety considerations, the Lucite jaws that hold the filter paper are inside of a hollow block of Lucite, and after the source is in place, a piece of thin plastic (0.0005-in. mylar) is fastened to the front of the block. It has been found necessary to place a lead slit (20) about one-half inch in front of the source (11) to cut down the scattering from the Lucite jaws. A pair of lead jaws instead of Lucite jaws was constructed to hold the source, but the fluoresence of the Pb was intense enough to give the Pb x-ray lines with an intensity of about 200 counts/min. With a source mounted in this manner, resolutions of 0.25 percent (full width at half-height) have been obtained in the 15-kev region.

The instrument was originally designed to use the (310) planes of quartz, which are perpendicular to the cleavage plane. Since the (303) planes of topaz are at an angle of 29° to the cleavage plane, it is possible to use a set of (303) planes either to the right or left of the crystal perpendicular. In the preliminary calibration work, it was found that the scale to the left of the perpendicular was not linear, and thus this side of the spectrometer was not used subsequently. Rather than try to establish the orientation of the diffracting planes, a "line" is reflected off one side of the (303) planes and then reflected from the other side of the same set of planes, and the Bragg angle is taken as one-half of the angle between the two reflections. Confirmation that the source is located properly (on the axis of rotation of the sample table) is obtained by comparing the (303) orientation obtained from each pair of lines. Individual center lines usually lie within 0.002° of the average of all of the center lines. Owing to the asymmetry of the (303) orientation, energies down to about only 17 kev are measurable on side B (see Fig. 2) of the reflecting planes. For a line of energy lower than 17 kev, its position is measured on side A of the reflecting planes, and then the average of the center lines obtained from all the higher energy lines is taken as the zero for the Bragg angle.

In running a spectrum, each peak is swept a number of times, and it has been found that the angular positions are reproducible to about 0.002° Bragg angle. To obtain the best accuracy, the spectrum is swept at

[18] Y. Cauchois, Compt. rend. 194, 1479 (1932); 194, 362 (1932); 199, 857 (1943); J. phys. et radium 3, 320 (1932); 4, 61 (1933); Ann. phys. 1, 215 (1934).
[19] J. W. M. DuMond, Rev. Sci. Instr. 18, 626 (1947).

TABLE I. Reflections from selected topaz planes.

Planes	Bragg angle (1)	Intensity Bragg peak (2)	Intensity Diffuse peak (3)
101	1.5°		120
202	2.9°		180
303	4.4°	5000	30
404	5.9°	50	40
505	7.4°		60
606	8.9°	200	···
to			
13013	19.5°	<5	<5
100	1.3°		100
200	2.5°		200
300	3.8°		60
400	5.1°	600	10
500	6.5°		30
600	7.7°	400	5
700	9.0°		30
800	10.3°		···
900	11.6°		5
1000	12.9°	130	···
to			
3000	42.3°	<5	<5

the slowest sweep speed, 0.3° per hour, and thus it takes about 150 hours to make one complete sweep of the spectrum on both sides of the diffracting planes. By using pulse-height discrimination as described above, the background varied from about 70 counts/min at 60 kev (using 15 baffles in the collimator) to about 30 counts/min at 15 kev (using 7 baffles in the collimator) for the Am^{241} source used in these experiments. (This background range depends strongly on the spectrum of the sample.) Background is defined as the average of the intensity on the two sides of a diffraction peak.

The lower energy limit of the instrument is primarily due to the absorption in the topaz crystal, which absorbs 90 percent of the radiation at 8 kev, at which energy the absorption in the air and the self-absorption in the sample also becomes quite large. The upper energy limit is determined by the ability of the collimator to discriminate between the direct and the diffracted beam.[17] The highest-energy line thus far measured has been 120 kev, but from purely geometrical considerations, the upper limit should be about 200 kev. One means of extending the upper limit of the instrument would be to charge the geometry of the collimator by increasing the number of baffles and/or lengthening it. An alternative means would be to use reflections from planes other than the (303) planes with higher dispersion. Table I shows the results of an investigation of the reflectivity of the (*h*0*l*) and the (*h*00) planes with the 60-kev gamma ray of Am^{241}. Column (1) lists the angle at which the 60-kev diffraction peak was observed. Two distinct types of diffraction maxima were observed, the usual Bragg peak which had a full width at half-height of 5.4 minutes (column 2), and a superimposed diffuse maximum with a full width at half-height of 38 minutes (column 3). After removing all possible sources of scattering in the instrument, the intensity and shapes of the peaks were unaltered. The centers of the diffuse maxima lie just where a Bragg reflection would be expected for the various order reflections. It is believed that these diffuse maxima are due to the thermal waves that exist in the crystal lattice.[20] From Table I it may be seen that by using the (1000) planes with a 40-fold loss in intensity, the energy range of the spectrometer could be extended to about 3 times its present limit or 600 kev.

CALIBRATION

In order to establish the reliability and self-consistency of the instrument, a number of known x-ray lines have been measured. The first calibration lines used were the $K\alpha_1$ and $K\beta_1$ lines of zirconium. A 0.010-in. wire of zirconium metal, suspended from its ends in the source holder, was irradiated from above by a tungsten target x-ray tube operating at 25 kev and 300 μa, which readily excited the *K*-radiation of zirconium. The energies of the two x-ray lines due to fluorescence were measured and found to disagree with the Cauchois and Hulubei[21] values. It was found necessary to change the accepted value of the topaz spacing from 1.356 A[22] to 1.3525 A. Although this new choice of lattice constant was made with the measurement of only two lines, it has also given the correct energy values in subsequent calibrations on other elements (Th and La). The final adjusted values obtained for the $K\alpha_1$ and $K\beta_1$ lines of zirconium are 15.772 ± 0.003 kev and 17.671 ± 0.003 kev, respectively, in comparison to the Cauchois and Hulubei[21] values of 15.775 and 17.668 kev, using $E\lambda_e=12372.2$ kev x-units to convert from Siegbahn units to kev as given by DuMond and Cohen.[23] The most recent value for the topaz (303) spacing has been determined by Silfverberg[24] on a double-crystal spectrometer to be 1.352902 A, agreeing to 0.0004 A with the value used in this work.

A sample of thorium in the form of ThO_2 was loaded into a capillary with an internal diameter of 0.012 in. and irradiated with the x-ray tube as described above. The measured values of the $L\alpha_1$ and $L\beta_1$ lines of thorium are 12.964 ± 0.005 kev and 16.207 ± 0.003 kev, respectively; the Cauchois and Hulubei[21] values are 12.968 kev and 16.202 kev.

Since a power supply with sufficient voltage to excite the lanthanum *K* x-rays was not available, a sample of La_2O_3 in a capillary was made to fluoresce with the 60-kev gamma radiation from a sample of Am^{241} in an adjacent capillary. The measured values of

[20] R. W. James, *The Optical Principles of the Diffraction of X-Rays* (G. Bell and Sons, London, 1948), pp. 239–64.

[21] Y. Cauchois and H. Hulubei, *Constantes Selectionnees, Longueurs D'Onde Des Emissions X Et des Discontinuites D'Absorption X* (Hermann and Company, Paris, 1947).

[22] Hermann, Lohrmann, and Philipp, Strukturbericht **2**, 516 (1928–1932).

[23] J. W. M. DuMond and E. R. Cohen, Revs. Modern Phys. **25**, 691 (1953).

[24] L. Silfverberg, Arkiv Mat. Astron. Fysik **B31**, No. 10 (1945).

the $K\alpha_1$ and $K\alpha_2$ energies are 33.440±0.008 kev and 33.031±0.015 kev, respectively; the Cauchois and Hulubei[21] values are 33.442 kev and 33.035 kev.

Since the second-order reflection of the sixty-kev transition (8.9° Bragg angle) of Am^{241} was found to agree with the first-order reflection (4.4° Bragg angle), to within the experimental errors, and calibrations at 33 kev (7.9° Bragg angle), at 16 kev (16.4° Bragg angle), and at 13 kev (20.7° Bragg angle) are in excellent agreement with the Cauchois and Hulubei[21] table values, it is assumed that the entire scale of the spectrometer is linear. It should be noted that the experimental error in the energy varies as

$$dE/E = d\theta/\tan\theta.$$

Thus with a constant angular error of 0.002°, the error in the energy at 30 kev will be 7 ev, while the error at 60 kev will be 28 ev. Thus whenever the second-order reflection is strong enough to obtain good statistics, the energy accuracy can be improved.

Am^{241} SPECTRUM

The sample consisted of 1.5 milligrams of finely powdered AmO_2 loaded into a quartz capillary with an internal diameter of 0.33 mm and a wall thickness of 0.06 mm. The sample filled a 1.7-cm length of the capillary; the calculated bulk density was taken as unity. In the preparation of the sample, specific steps were taken to remove any rare earths, since the K x-rays of these elements lie between 30 and 40 kev, which has proved to be an interesting region in the Am^{241} spectrum (see Introduction). A spectrographic analysis showed that the only rare earth present was La, with a concentration of 0.1 percent. The K-radiation emitted from this quantity of La, which would be excited by the strong 60-kev gamma of the Am^{241} was calculated to be equal to less than one part in ten thousand of the 60-kev radiation. (A 33-kev gamma was found in the Am^{241} spectrum with an intensity of one part in two hundred of the 60-kev radiation.)

With a sample of this diameter, the resolution is still mainly a function of the source width (resolution being defined as the full width of the line at half-maximum). Resolutions of about 0.5 percent and 1.8 percent were obtained in the 17-kev and 60-kev regions, respectively. In other experiments, with sources of higher specific activity, where the source is deposited on a piece of filter paper, the resolution in the 17-kev region has been improved to 0.25 percent. Figure 3 is a picture of a chart record taken with the spectrometer sweeping at 20 times the normal sweep rate and with the pulse height discriminator set to accept all pulses between 10 and 60 kev. From the figure it appears that it would be difficult to establish the existence of any weak gamma rays in the 30- to 50-kev region, but as previously stated (Apparatus), when the pulse height

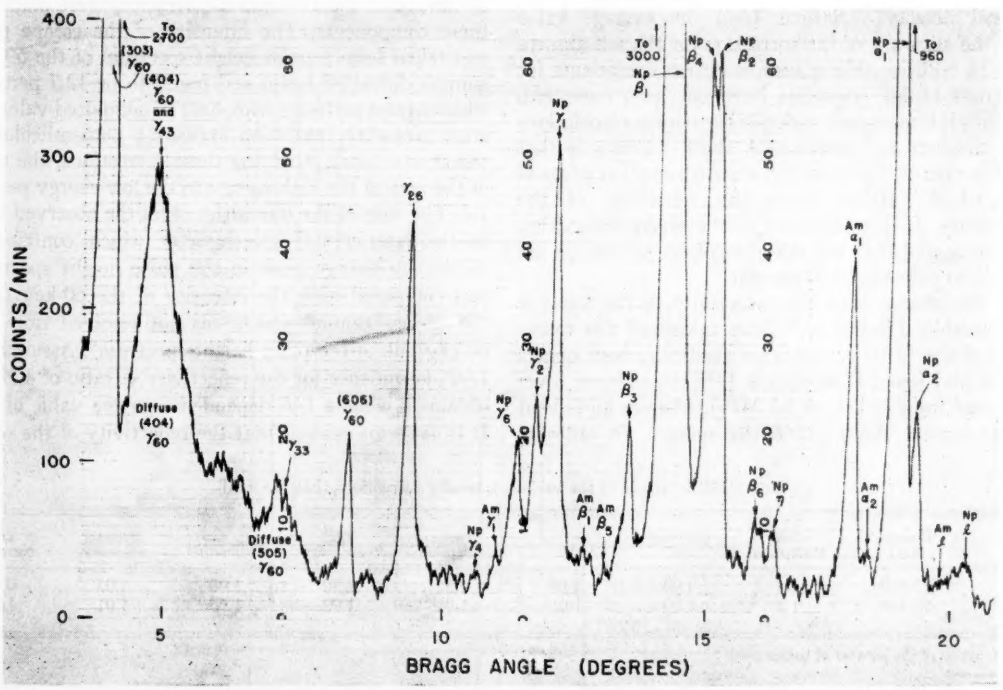

FIG. 3. Chart record of the complete Am^{241} spectrum (pulse height selection not used). Only the more prominent lines have been labeled since the weak lines are indistinguishable from the statistical fluctuations in the background in this plot.

TABLE II. The Am^{241} gamma rays observed on the bent-crystal spectrometer.

Energy (kev)	Background[a] (counts/min)	Observed intensity[b] (counts/min)	Correction[c] factor	Corrected[d] intensity
26.363±0.014	40	520	1.55	8.2
33.199±0.021	39	39	1.32	0.5
43.463±0.085	65	30	2.17	0.6
59.568±0.017	70	5220	1.88	100

[a] Background computed by averaging counting rates on both sides of each peak.
[b] Background subtracted.
[c] Attenuation corrections as explained in text.
[d] Relative to the 60-kev line.

discriminator is set so that any radiation which is being Bragg reflected in orders other than the one under study is rejected, the background in the 30 to 50-kev region is lowered to about 20 counts/min.

Table II lists the energies and the relative intensities of the gamma rays that were observed on the bent-crystal spectrometer. The correction factor (column 3) is made up of the following attenuation factors: self-absorption in the sample, absorption in the capillary wall, absorption in the air, absorption in the topaz crystal, reflectivity of the topaz as a function of energy, absorption in the detector window, and efficiency of the detector. Of these the least certain are the self-absorption and the reflectivity corrections. Table III lists the corrections that were applied to the 17.760-kev $L\beta_1$ x-ray of Np and the 59.568-kev gamma ray.

Local density variations from the average value limit the accuracy of the correction for the self-absorption. In addition, the mass absorption coefficients for the transuranium elements have not been measured, and thus it is necessary to derive them by extrapolations from thorium and uranium. A third difficulty is that the L x-rays of Np lie within the L-absorption edges of Am, which further limits the reliability of the corrections. In consideration of the above difficulties, it is estimated that the self-absorption corrections are reliable to only about 20 percent.

At the present time the reflectivity of the topaz is questionable. Lind *et al.*[25] have measured the reflectivity of the (310) planes of an elastically bent quartz crystal and found it to obey a $1/E^2$ dependence (over the range from 25 kev to 1.3 Mev), whereas an unbent quartz crystal obeys a $1/E$ dependence. In order to roughly check the reflectivity of the (303) planes of topaz, a pulse height spectrum of the bent-crystal spectrometer sample was taken with the same scintillation detector as used in the bent-crystal spectrometer, and the observed intensities were compared to those from the diffracted beam in the bent-crystal spectrometer. In order to cut down the counting rate to a reasonable value, the pulse height curve was taken with the sample several feet from the detector. The same absorption corrections apply to this pulse height experiment as to the bent-crystal spectrometer data except for the air absorption and the topaz crystal absorption corrections. The absorption coefficients of the topaz have been measured at a number of monochromatic energies (13, 17, and 60 kev) in the spectrometer and agree to within 5 percent of the values computed from the known chemical composition $\{[Al(FOH)]_2SiO_4\}$ and the Victoreen[26] absorption tables. The correction for the air absorption in the "pulse height" experiment is considerably more difficult. The pulse height spectrum (Fig. 4) consists of essentially two peaks, the 60-kev peak and a broad peak centering around 18 kev consisting of the L x-rays and a hump on the high-energy side due to the 26-kev gamma and the 60-kev escape peak. To simplify the calculation of the air absorption corrections for each of the components of the low-energy peak, it was assumed to consist of the three prominent components observed in the bent-crystal spectrometer (13, 17, and 26 kev), and the absorption corrections were made for these components. The intensity of the escape peak was taken from a pulse height spectrum of the 60-kev gamma diffracted beam and found to be 12.7 percent, which agrees perfectly with Axel's[27] computed value for good geometry (radiation impinging perpendicular to the crystal face). Applying these corrections, the ratio of the area of the high-energy to the low-energy peak is 1.7. The sum of the intensities of all the observed lines in the bent-crystal spectrometer which contributed to the low-energy peak in the pulse height spectrum was compared with the intensity of the 60-kev (plus the 43-kev gamma which was not resolved from the 60-kev line in the pulse height spectrum). Assuming a $1/E^2$ dependence for the reflectivity, a ratio of 4.2 was obtained, while a $1/E$ dependence gave a value of 1.4. It thus seems evident that the reflectivity of the (303)

TABLE III. Example of the various intensity corrections that are used.

Line	Energy (kev)	Self-absorption	Capillary wall	Air	Topaz absorption	1/E reflectivity	Collimator[a]	Detector efficiency	Total correction
$L\beta_1$	17.760	1.4	1.04	1.08	1.32	0.30	1.00	1.03	0.64
γ_{60}	59.568	1.1	1.00	1.01	1.01	1.00	1.66	1.01	1.88

[a] A function of the number of baffles used.

[25] Lind, West, and DuMond, Phys. Rev. **77**, 475 (1950).
[26] J. A. Victoreen, J. Appl. Phys. **20**, 1141 (1949).
[27] P. Axel, Brookhaven National Laboratory Report BNL-271, September, 1953 (unpublished).

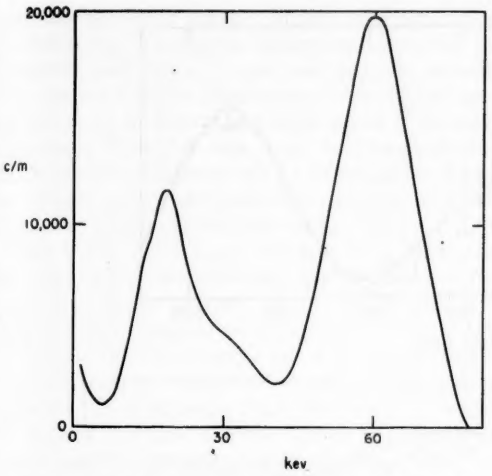

FIG. 4. Pulse height spectrum of the Am^{241} sample used in the bent-crystal spectrometer.

planes of topaz exhibits an approximately $1/E$ dependence rather than $1/E^2$. It is intended to measure this reflectivity dependence more precisely in the near future, but for the present, the $1/E$ dependence will be used.

The gamma-rays listed in Table II fit well into the Np^{237} level scheme proposed by Wagner *et al.*[15] and Asaro *et al.*[2] as shown in Fig. 5. The 33.199-kev gamma ray has not been previously observed. It is to be noted that its intensity of 0.5 percent of the 60-kev gamma is somewhat higher than the upper limit of 0.1 percent set by Newton and Rose[12] on a proportional counter, It is likely that this is a true Am^{241} gamma ray rather than the lanthanum K x-rays, since, as already noted (see Calibration), the $K\alpha$ doublet of La was resolvable into its components, whereas the 33-kev peak in the Am^{241} spectrum is very clearly a single line with the expected width for this energy region. Also as noted above, the maximum La fluorescence from this sample would only be 0.01 percent of the 60-kev gamma intensity. It should also be observed that the sum of the 33-kev and 26-kev gamma-ray energies agrees to within 6 ev with the 60-kev gamma energy.

The 43-kev gamma ray listed in Table II has not previously been observed, but conversion lines due to this energy transition have been observed by Passell[13] and Wagner *et al.*[15] Considerable difficulty was encountered in measuring this line. The diffraction maximum was a composite of two nearly superimposed peaks. It was found that by adjusting the pulse height selector so that practically no 60-kev pulses were passed, the high-energy component disappeared and the low-energy peak was clearly a single one with

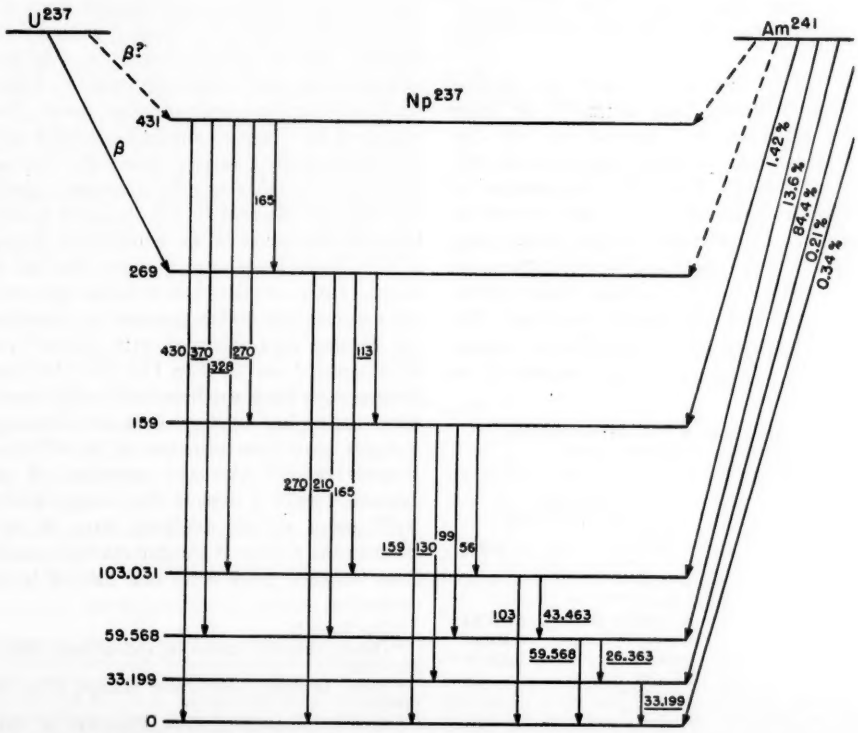

FIG. 5. Energy level scheme of Np^{237} (gamma transitions underlined were observed in this work).

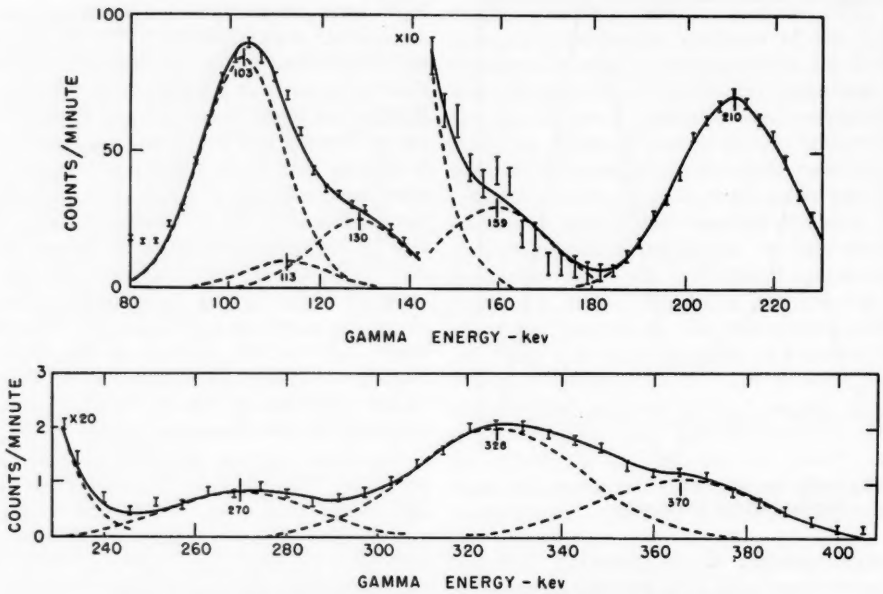

FIG. 6. Pulse height spectrum of Am^{241} taken on the 20-channel scintillation spectrometer through 1.63 g/cm² of Ag.

an energy of 43.463 kev. By setting the pulse height selector so that all the 43-kev pulses were eliminated, the low-energy peak disappeared. The high-energy peak was identified as the (404) reflection of the 60-kev gamma ray.

Gamma rays of 56 kev and 70 kev are possible transitions in the proposed level scheme, but upper intensity limits of about 10^{-4} gamma ray per disintegration may be set for these regions with the bent-crystal spectrometer. Since the transmission of the bent-crystal spectrometer is not high enough to detect the existence of the higher-energy gamma rays reported by Passell[13] and Jaffe,[14] a pulse height spectrum of the sample was taken with a sodium iodide scintillation spectrometer and 20-channel analyzer. The energy scale and linearity of the scintillation counter were established by taking pulse height curves of the 59.6-kev line of Am^{241},[28] the 87-kev line Cd^{109},[29] the 104-kev line of Gd^{153},[30] the 134-kev line of Ce^{144},[31] and the 138-kev, 269-kev, and 405-kev lines of Se^{75}.[32] To prevent the intense low-energy radiation from overloading the detecting system, a 1.63-g/cm² silver absorber was placed over the detector. Figure 6 shows the pulse height spectrum obtained from a 20-microgram sample of Am^{241} using a one-half inch thick sodium iodide crystal at about 1 percent geometry. The pulse height curve was unfolded into the component parts indicated by using the Wagner *et al.*[15] data as a guide, assuming that the resolution of the scintillation detector follows a $1/E^2$ dependence, and a single line has a Gaussian shape. Table IV lists the energies and intensities (if one assumes 0.40 60-kev gamma per disintegration)[9] of the gamma rays observed with Jaffe's[14] values listed in columns 2 and 4. The 113, 270, 328, and 370-kev gamma rays have not been previously observed in the Am^{241} decay, but conversion lines for these gamma-ray energies have been reported in the U^{237} spectrum by Wagner *et al.*[15] with the exception of the 113-kev gamma. Figure 5 depicts the energy level scheme of Np^{237} using all the available data. It is still quite tenuous since some of the gamma rays could be transitions between more than one pair of levels and the

TABLE IV. The Am^{241} gamma rays observed on the 20-channel scintillation spectrometer.

Energy (kev)		Intensity (per/disintegration)	
Observed here	Jaffe[a]	Observed here	Jaffe[a]
103±2	102	4.0×10^{-4}	5.6×10^{-4}
113±5		3.3×10^{-5}	
130±4	128	5.3×10^{-5}	5.6×10^{-5}
159±10	168	4.4×10^{-6}	6.4×10^{-6}
210±5	207	8.4×10^{-6}	7.6×10^{-6}
270±10		1.1×10^{-6}	
328±10		3.0×10^{-6}	
370±10		1.7×10^{-6}	

[a] See reference 14.

[28] See Table II.
[29] Huber, Humbel, Schneiden, and deShalit, Helv, Phys. Acta 25, 3 (1952).
[30] Cork, LeBlanc, Nester, and Stumpf, Phys. Rev. 88, 685 (1952).
[31] F. T. Porter and C. S. Cook, Phys. Rev. 87, 464 (1952).
[32] Jensen, Laslett, Martin, Hughes, and Pratt, Iowa State College Report ISC-252 (unpublished).

higher energy levels are not known very accurately. In attempting to compute reasonable values for the conversion coefficients, it turns out that the intensity of the source and the absolute geometry of the spectrometer must be known to a high degree of accuracy (1 percent). Since this data is not readily obtainable, the conversion coefficients will be tabulated by Freedman *et al.*[33] using their conversion electron data and the relative gamma intensities reported here.

Table V lists the L x-ray lines found due to internal conversion in Np^{237} together with their intensities. The measured energies average about 19 electron volts higher than the extrapolated values in the table of Hill *et al.*[34] Since the latter energy values are not claimed to be reliable to 20 ev, this 19-ev discrepancy is not deemed significant. Upon summing the intensities of the x-rays arising from the three L levels (Table VI), the ratios of the radiative transitions from the three levels are obtained:

$$L_1:L_2:L_3=1.0:4.6:3.6.$$

To determine the relative abundances of initial L_1, L_2, and L_3 vacancies, it is necessary to allow for the Coster-Kronig and Auger transitions. Kinsey[35] has calculated the fluorescence yields from the ratios of the radiation widths to the total widths of the levels, obtaining 0.16, 0.59, and 0.41 for the fluorescence yields of the L_1, L_2, and L_3 levels, respectively, in uranium. Since these values vary only slightly with atomic number, they are applied to neptunium. He also assumes that the Coster-Kronig transitions from the L_1 to L_2 and L_2 to L_3 are negligible compared to the L_1 to L_3 transition. Since the Coster-Kronig effect increases the level width from which it originates, Kinsey computed the probability of this transition by comparing the radiation width of the L_1 level in tantalum, where the effect is small, to the radiation width of the L_1 level in uranium and obtained a value of 0.60. Kinsey expresses the following equations:

$$q_1=u_1f, \tag{1}$$

$$q_2=u_2f_2, \tag{2}$$

$$q_3=f_3(A_{13}u_1+u_3), \tag{3}$$

where q_1, q_2, and q_3 are the number of quanta observed, f_1, f_2, and f_3 are the fluorescent yields, and u_1, u_2, and u_3 are the number of initial vacancies in the L_1, L_2, and L_3 shells, respectively. A_{13} is the probability of the L_1-L_3 Coster-Kronig transition. Using Kinsey's values for A_{13}, f_1, f_2, and f_3, the ratios of initial L vacancies are:

$$L_1:L_2:L_3=1.0:1.3:0.8.$$

[33] Freedman, Porter, and Wagner, to be published in Physical Review.

[34] Hill, Church, and Mihelich, Rev. Sci. Instr. **23**, 523 (1952). Even though the instrument was calibrated by using the Cauchois and Hulubei[21] values, it seems correct to compare the Np x-ray energy values with the Hill *et al.* values since these values are about one or two ev higher than the Cauchois values for Zr and Th and 10 to 15 ev lower for the La.

[35] B. B. Kinsey, Can. J. Research **A26**, 404 (1948).

TABLE V. The Np L x-rays observed on the bent-crystal spectrometer due to internal conversion.

Line	Experimental energy (kev)	Extrapolated energy[a] (kev)	Background (counts/min)	Observed intensity (counts/min)	Correction factor	Corrected relative intensity[b]
l	11.889±0.006	11.87	40	60	2.40	1.3
α_2	13.776±0.003	13.76	60	285	1.09	2.8
α_1	13.961±0.003	13.95	60	2760	1.01	25.2
η	15.876±0.003	15.85	80	150	0.83	1.2
β_6	16.139±0.024	16.11	90	80	0.75	0.5
β_2	16.857±0.006	16.84	130	1020	0.70	6.5
β_4	17.075±0.006	17.05	140	681	0.68	4.2
β_5	17.516±0.009	17.51	120	180	0.62	1.0
β_1	17.764±0.003	17.74	120	6300	0.64	36.4
β_3	18.001±0.005	17.98	200	580	0.63	3.3
γ_5	20.124±0.040	20.09	95	35	0.88	0.3
γ_1	20.796±0.005	20.77	120	1020	0.92	8.5
γ_2	21.108±0.020	21.09	140	110	0.94	0.9
γ_3	21.340±0.017	21.33	120	80	1.47	1.1
γ_6	21.476±0.015	21.49	50	170	1.47	2.2
γ_4	22.200±0.022	22.16	70	80	1.39	1.0

[a] See reference 34, table values.
[b] Relative to 60-kev line = 100.

Some insight as to the correctness of Kinsey's results may be obtained from the relative intensity of the Np $L\beta_2$ satellite[36] that was observed at 86±23 volts higher than the parent line. A satellite of this energy is ascribable to a Coster-Kronig transition as follows: An L_1 vacancy is created due to internal conversion of a gamma-ray, and an L_3 electron falls into the L_1 level, the difference in energy being used to eject an M electron. With the atom in this doubly ionized state, an N electron falls into the L_3 vacancy. The energy of this transition will be emitted as an x-ray of higher energy than if the M vacancy were not present. The energy difference between the normal x-ray line (following an initial L_3 vacancy) and its satellite is

TABLE VI. Designation of the L x-ray line transitions and their relative intensities in Am and Np.

Line	Transition	Intensity[a] Np	Intensity[a] Am
β_4	L_1–M_2	4.2	
β_3	L_1–M_3	3.3	0.4
γ_2	L_1–N_2	0.9	0.3
γ_3	L_1–N_3	1.1	
γ_4	L_1–O_2	1.0	
η	L_2–M_1	1.2	
β_1	L_2–M_4	36.4	2.5
γ_5	L_2–N_1	0.3	
γ_1	L_2–N_4	8.5	1.0
γ_6	L_2–$O_{4,5}$	2.2	
l	L_3–M_1	1.3	0.2
α_2	L_3–M_4	2.8	0.8
α_1	L_3–M_5	25.2	6.4
β_6	L_3–N_1	0.5	
β_2	L_3–N_5	6.5	
β_5	L_3–$O_{4,5}$	1.0	0.4

[a] Relative to 60-kev line = 100.

[36] There is also evidence that there is a satellite on the high-energy side of the $L\beta_5$ line, but since it is close to the intense $L\beta_1$ line, it is not possible to obtain any significant information except that it exists. It would be impossible with the present spectrometer and source to see any $L\alpha$-satellites if they existed, because the energy separation would be less than 10 ev.

TABLE VII. The Am L x-rays observed on the bent-crystal spectrometer due to fluorescence by the gamma rays.

Line	Experimental energy (kev)	Extrapolated energy (kev)	Background (counts/min)	Observed intensity (counts/min)	Correction factor	Corrected relative intensity[a]
l	12.383 ±0.007	12.38	40	15	1.53	0.2
α_2	14.416 ±0.030	14.41	60	90	0.96	0.8
α_1	14.629 ±0.003	14.62	60	760	0.93	6.4
β_6	18.408 ±0.008	18.40	110	65	0.59	0.4
β_3	18.871 ±0.005	18.83	95	300	0.90	2.5
β_4	19.105 ±0.008	19.10	95	40	0.91	0.4
γ_1	22.076 ±0.018	22.04	24	80	1.40	1.0
γ_2	22.359 ±0.025	22.35	80	20	1.43	0.3

[a] Relative to 60-kev line = 100.

given by:

$$dE=[(E_{Mx})_{Z+1}-(E_{Mx})_Z]-[(E_{Ny})_{Z+1}-(E_{Ny})_Z],$$

where $(E_{Mx})_{Z+1}$ is the binding energy of an electron in the M_x subshell of a $Z+1$ atom, and the other symbols have a corresponding meaning. The equation is written on the assumption that when an electron is missing in an inner shell, an electron in an outer shell has the energy of an electron in the corresponding shell of a $(Z+1)$ atom. The energy separations of the satellites due to the absence of an M_3, M_4, or M_5 electron are 89, 89, or 79 ev, respectively, and thus it may be concluded that the prominent component of the satellite was due to one of these vacancies. If it is assumed that the transition probabilities for the various lines do not change when the atom is in the doubly ionized state, then one may use the intensity of the $L\beta_2$ satellite as a measure of the Coster-Kronig transition probability. Using Eq. (3), q_3 (number of observed quanta from L_3) will be equal to the sum of the intensities of $L\beta_2$ and its satellite, and $A_{13}u_1$ (the number of L_3 lines arising from Coster-Kronig transitions from L_1) will be the intensity of the satellite; the data determine a ratio:

$$q_3/A_{13}u_1=3.27.$$

Since q_3 is known and u_1 has been computed from the experimental data, and using Kinsey's value for the L_1 fluorescent yield, one obtains a value of 0.17 for the Coster-Kronig transition probability A_{13}, where Kinsey obtained a value of 0.60. This experimental result is partially substantiated by Jaffe,[14] who set an upper limit of 0.40 on this coefficient in neptunium. If the transition probabilities of the lines change when the atom is in the doubly ionized state, and specifically if the probability for the $L\beta_2$ transition decreases with respect to the other transition probabilities, then the derived value for the Coster-Kronig coefficient would be altered in the direction to agree with Kinsey's calculations. Using the derived value $(A_{13}=0.17)$, the relative excitations of the three levels become:

$$L_1:L_2:L_3=1.0:1.3:1.2.$$

TABLE VIII. Higher-order reflections in the Am^{241} spectrum. Columns (3) and (4) give the ratio of the (303) reflected intensity to the (606) and (404) reflected intensities, respectively.

Line	Energy (kev)	303/606	303/404
$L\beta_1$	17.760	32	
$L\gamma_1$	20.786	25	
γ_{26}	26.356	21	
γ_{60}	59.563	27	104

Table VII lists the energies and the relative intensities of the americium L x-rays observed due to fluorescence from the gamma rays. The measured energies average about 15 ev higher than the values in the Hill *et al.* table,[34] and thus the Mosley extrapolations are verified within about 15 ev.

Four lines in the Am^{241} spectrum were intense enough to be observed in higher-order reflections than the first (Table VIII). The variation in the ratios is not deemed significant since the higher order reflections were quite weak and were not all clearly resolved from other features of the spectrum. The most reliable ratio is the one obtained for the 60-kev gamma ray.

The author wishes to express his indebtness and thanks to Dr. M. S. Freedman for his untiring assistance and advice throughout the work. The author also wishes to thank Mr. J. Malm for the aid in preparing the sample, Dr. D. W. Engelkemeir for his advice on the scintillation detector problems which have arisen, and Dr. S. Siegel for his helpful discussions on the physics of x-ray spectrometry.

Dynamics of Nuclear Deformation

D. R. INGLIS
Argonne National Laboratory, Lemont, Illinois
(Received September 24, 1954)

The droplet model of collective nuclear motions is ordinarily based on the assumption of classical irrotational fluid flow and has been used to obtain both the rotational properties of nuclei associated with a circulating surface wave and the vibrational properties of a surface deformation, though only the rotational results are confirmed experimentally. As a partial justification of the irrotational assumption, the energy of collective rotation of a closed-shell nucleus has been derived from nucleon wave functions in an earlier paper. The vibrational problem is here similarly treated and it is shown that, in contrast to the case of rotation, the vibrational distortion of a closed-shell nucleus is so rapid that the adiabatic treatment used is not valid. The potential energy of distortion calculated with phenomenological nuclear forces is not very different from that calculated by use of the deformed three-dimensional oscillator potential, which verifies that the latter is a fairly good approximation to a "self-consistent field" for a deformed closed-shell nucleus.

INTRODUCTION

THE collective motion of nucleons associated with a change in nuclear shape may be approximated by introducing a nonspherical distortion into the zero-order wave functions of the shell model, as was done for the case of a rotating distortion in a recent paper.[1] There a perturbation procedure equivalent to the adiabatic approximation was used and it was shown that for the low rotational states of moderately heavy and appreciably nonspherical nuclei the rotation is indeed slow compared to the nucleon motions, as required for the validity of the adiabatic treatment. The rotational energy was found to agree with that obtained by assuming irrotational fluid flow in the droplet model, and Aage Bohr has, by defining a local collective velocity associated with a rotating distortion, discussed in general terms the relation between shell-model closed shells and classical irrotational flow.[2] The ad-hoc assumption of irrotational fluid flow introduced into the usual droplet-model treatment is just as essential for the vibration as for the rotation, although no experimental data are as clearly relevant, and it would be desirable to have a similar derivation starting from nucleon wave functions in the vibrational case. Unfortunately, the collective frequencies for vibration are considerably higher than for the rotation and it is here shown that the adiabatic approximation is no longer valid. This treatment is based explicitly on harmonic-oscillator wave functions, but the result leads to the anticipation that more general treatments of collective surface or volume vibration will encounter trouble with density fluctuations. However, it does not preclude the possible existence of states whose properties are determined partly by modes of collective vibration.

In the binding and vibration problem of a diatomic molecule, one calculates the energy of the system, arising principally from the electron behavior, as a function of internuclear distance R considered fixed, and then because of the obviously adiabatic nature of the motion takes this to represent a potential energy curve, of which a term in $(\Delta R)^2$ determines the frequency of vibration. The electrons are so light compared to the two nuclei that one ordinarily does not consider their contribution to the kinetic energy. In the problem of vibration of shape of a nucleus about an equilibrium shape, the mass is contained entirely in the nucleons and their contribution, in the total energy of the system, to a term in the square of the rate of distortion is to be interpreted similarly as the collective kinetic energy.

ADDITIONAL ENERGY ACCOMPANYING ADIABATIC DISTORTION

The method here introduced for calculating the kinetic energy associated with the rate of deformation of a charge distribution which arises from quantization of a particle in a slowly-varying confining field depends on an application of the adiabatic approximation. In solving the slowly time-dependent wave equation $i\hbar\partial\Psi/\partial t=\mathcal{H}(t)\Psi$, we expand $\Psi(x,t)=\sum a_n u_n \exp[-(i/\hbar)\int^t E_n dt']$ in terms of normalized solutions u_n, supposed known at any time, of $[\mathcal{H}(x,t)-E_n(t)]u_n(x,t)=0$. This substitution, followed by multiplying by $\bar{u}_k$ and integrating, yields[3]

$$\dot{a}_k=-\sum I_{kn}a_n \exp\left[-(i/\hbar)\int^t (E_k-E_n)dt'\right], \quad (1)$$

or

$$a_k\approx\sum I_{kn}(a_n/i\omega_{kn})[\exp(-i\omega_{kn}t)-C_k], \quad (2)$$

if in this "adiabatic" integration we consider $(E_n-E_k)=\hbar\omega_{kn}$ and the other factors to vary slowly compared to t. Here

$$I_{kn}=\int_{\text{vol}} \bar{u}_k(\partial u_n/\partial t)d\tau, \quad (3)$$

[1] D. R. Inglis, Phys. Rev. **96**, 1059 (1954).
[2] Aage Bohr, *Rotational States of Atomic Nuclei* (Munksgaards Forlag, Copenhagen, 1954), especially, the appendix. See also A. Bohr, Kgl. Danske Videnskab. Selskab, Mat.-fys. Medd. **26**, No. 14 (1952); A. Bohr and B. R. Mottleson, Kgl. Danske Videnskab. Selskab, Mat.-fys. Medd. **27**, No. 16 (1953).
[3] M. Born and V. Fock, Z. Physik **51**, 165 (1928); L. I. Schiff, *Quantum Mechanics* (McGraw-Hill Book Company, Inc., New York, 1949), p. 209.

an integral which may be further evaluated,[3]

$$I_{kn}=-(k|(\partial\mathcal{H}/\partial t)|n)/\hbar\omega_{kn}, \tag{4}$$

if one wishes to stress the Hamiltonian rather than the wave functions. In this approximation the coefficient a_k experiences no secular increase, since the time-dependent terms in (2) are rapidly oscillatory. Because of these terms, the system cannot remain in one of these states, with $a_n=1$ and all other $a_k=0$ (unless all the I_{kn} vanish), and if this is introduced as an initial condition, as is frequently done with the $C_k=1$, there is inevitably a small temporary occupation of some of the other states k and a corresponding contribution to the average energy of the system. If instead we seek a solution with one a_n large and all other a_k small, we may obtain an energy with no rapid oscillatory time dependence by taking the small a_k from (2) with the initial condition $C_k=0$, neglecting the small terms. Thus we have

$$E=\int\bar{\psi}\mathcal{H}\psi d\tau=E_n+\sum_k(E_k-E_n)\bar{a}_k a_k$$

$$=E_n+\sum_k\hbar I_{kn}{}^2/\omega_{kn}. \tag{5}$$

Since I_{kn} contains linearly the rate of change of a parameter which may describe the size or shape or position of the system, that is, essentially a collective speed, the last term of (5) contains the square of a speed and is equivalent to a kinetic energy in problems involving only the variation of this parameter, as is explicitly exemplified in the Appendix.

KINETIC ENERGY OF AN EXPANDING ONE-DIMENSIONAL OSCILLATOR

The manner in which the adiabatic admixture of other "quasi-stationary" states contributes to the energy of the system is very simply illustrated by considering the problem of a one-dimensional oscillator. In the familiar equations,

$$[(\hbar^2/2M)\partial^2/\partial x^2+E_n-(K/2)x^2]u_n=0 \quad \text{or}$$

$$[\partial^2/\partial\xi^2+\lambda_n-\xi^2]u_n(\xi)=0, \tag{6}$$

we consider $K=K(t)$ as a slowly-varying externally imposed parameter, and as a consequence the scale of length of the wave functions varies, $d=d(t)$, with $d^2=(x/\xi)^2=\hbar/M\omega$, $\omega^2=K/M$, $\lambda=2E_n/\hbar\omega=2n+1$.

The $u_n(x,t)$ normalized in x are then $d^{-\frac{1}{2}}u_n(\xi)=d^{-\frac{1}{2}}H_n(\xi)\exp(-\xi^2/2)$, where the $u_n(\xi)$ are normalized in ξ-space, and obey the recursion relations (10) of reference 1. From these we obtain

$$\partial u_n(x,t)/\partial t=(\dot{d}/2d)[(n+1)^{\frac{1}{2}}(n+2)^{\frac{1}{2}}u_{n+2}(\xi)$$

$$-(n-1)^{\frac{1}{2}}n^{\frac{1}{2}}u_{n-2}(\xi)]. \tag{7}$$

This in (3) gives

$$I_{n+2,\,n}=\int_{-\infty}^{\infty}\bar{u}_{n+2}(\partial u_n/\partial t)dx=(n+1)^{\frac{1}{2}}(n+2)^{\frac{1}{2}}\dot{d}/2d$$

$$I_{n-2,\,n}=-(n-1)^{\frac{1}{2}}n^{\frac{1}{2}}\dot{d}/2d. \tag{8}$$

All the other I_{kn} vanish, so a state consisting mainly of the ground state $n=0$ or the first excited state $n=1$ can have an admixture by this adiabatic process only of the state $k=n+2$, with $\omega_{kn}=2\omega$, and the added energy in (5) arising from the admixture is

$$E-E_n=(\hbar\dot{d}^2/8\omega d^2)(n+1)(n+2)$$

$$=(M/8)\dot{d}^2(n+1)(n+2). \quad n=0,\,1. \tag{9}$$

For a state consisting mainly of a higher state the admixture comes from down as well as up by two units, $\Delta n=\pm2$, and the sum of these two contributions to the average increment of energy is

$$E-E_n=(M/8)\dot{d}^2[(n+1)(n+2)-(n-1)n]$$

$$=(M/2)\dot{d}^2(n+\tfrac{1}{2}). \tag{10}$$

It will be noted that (10) agrees with (9) and thus applies for all n because $(n-1)n$ vanishes for $n=0,1$.

The kinetic energy of the distribution $H_n{}^2(x/d)\exp(-x^2/d^2)$ considered as an expanding classical fluid is likewise $(M/2)\dot{d}^2(n+\frac{1}{2})$. The adiabatic admixture of other states u_k may thus be understood as an adequate wave-packet description of the expanding motion. Although we calculate an average over the admixed quasi-stationary states of their excitation energy $\hbar\omega_{kn}$ which is half kinetic and half potential energy in the varying impressed field, it all appears as kinetic energy associated with the rate of expansion.

In one dimension there is no distinction between irrotational and vortex flow and for this reason the example here given is a somewhat trivial one, but the fact that the kinetic energy calculated in one dimension is equivalent to that of a classical expansion of a density distribution, when taken together with the separability of the contributions from the several dimensions in the calculation below, does lead to the expectation that the three-dimensional flow in this approximation is irrotational, corresponding to a simple expansion in one dimension and contraction in the others.

With more particles in the same varying oscillator potential, each would make its contribution (10) to this "collective" kinetic energy of distortion. Since the Hamiltonian is a sum of single-particle terms, there are no cross-term contributions, and the only effect of antisymmetry of the total wave function is to suppress the contributions of individual-particle states with $n\leq n_{\max}-2$, if the states are filled up to and including $n_{\max}$.

COLLECTIVE VIBRATIONS IN THE DEFORMED OSCILLATOR MODEL

In the central model with a harmonic oscillator potential we substitute for the actual average interaction energy the fictitious zeroth-order potential $V(r)=\frac{1}{2}\,\mathrm{Kr}^2$ so as to have simple oscillator wave functions. If we deform this in such a way that the sphere on which we have $V(r)$ becomes an ellipsoid of semiaxis ar along the z-axis and br along the x- and y-axes, maintaining volume so that $ab^2=1$, then V may be written[4]

$$\begin{aligned}V(xyz)&=\tfrac{1}{2}K[(x^2+y^2)/b^2+z^2/a^2]\\&=\tfrac{1}{2}K[(1-\gamma)^{-\frac{1}{3}}(x^2+y^2)+(1-\gamma)^{\frac{2}{3}}z^2]\\&=\tfrac{1}{2}K[(x^2+y^2)(1+\epsilon)^4+z^2(1+\epsilon)^{-8}]\\&=\tfrac{1}{2}\sum K_i x_i^2. \quad (11)\end{aligned}$$

We shall use the expansion parameter $\epsilon=(a/b)^{1/6}-1$ for a reason that will appear, in preference to $\gamma=1-(b/a)^2$ used by Pfirsh[4] in discussing static deformation. For a nucleon with oscillator quantum numbers n_x, n_y, n_z we have the energy

$$\begin{aligned}E_n&=\hbar\omega[(n_x+n_y+1)(1+\epsilon)^2+(n_z+\tfrac{1}{2})(1+\epsilon)^{-4}]\\&\approx\hbar\omega[n_x+n_y+n_z+\tfrac{3}{2}+2(n_x+n_y-2n_z)\epsilon\\&\quad+(n_x+n_y+10n_z+6)\epsilon^2+\cdots], \quad (12)\end{aligned}$$

with $\omega=(K/M)^{\frac{1}{2}}$. For each particle the oscillator wave function arising from (1) is a product of three factors, one for each dimension,

$$\psi_{ni}(x_i)=H_{ni}(\xi_i)\exp(-\xi_i^2/2), \quad (13)$$

with $\xi_i=\beta_i x_i$ and $\beta_i^2=M\omega_i/\hbar=(MK_i)^{\frac{1}{2}}/\hbar$. In the oscillator representation of O^{16}, for example, each of the following sets of oscillator quantum numbers is characteristic of four nucleons:

n_x	n_y	n_z
0	0	0
0	0	1
0	1	0
1	0	0

(14)

Because of the closed-shell nature of this nucleus, this representation is equivalent to one displaying the nucleon orbital angular momenta l through the relations $P_1^1(\cos\theta)e^{i\phi}\sim x+iy$, etc., or to the (jj) representation obtained by introducing spin and taking further linear combinations, and the total spin-orbit coupling energy for the closed shell is zero. The first set contains the four nucleons of the s-shell, the next three sets the twelve nucleons of the p-shell, and the single-nucleon excitation energy from one shell to the next is $\hbar\omega_i$. The total oscillator energy (12) for the four nucleons of He^4, described by the first row of (14), is

$$E_\alpha=2\hbar\omega[2(1+\epsilon)^2+(1+\epsilon)^{-4}]=6\hbar\omega(1+4\epsilon^2+\cdots), \quad (15)$$

and summing similarly over all of (14) for O^{16}, we obtain $E(O^{16})=6E_\alpha$. The term in ϵ^2 arises equally from kinetic and potential energy of the nucleons, a characteristic property of a harmonic oscillator. If we assume that ϵ varies so slowly that the deformation of the oscillators may be considered adiabatic, we may consider (15) to be the equivalent potential energy of the system as a function of ϵ.

In the oscillator approximation the explicit time dependence of the Hamiltonian lies in the elastic constants $K_i(t)$:

$$\partial\mathcal{H}/\partial t=(1/2)\sum_{\text{nucleons}}\sum_i\dot{K}_i x_i^2 \quad (16)$$

x_i being summed over x, y, and z. One sees from (11) that $K_x=K_y=[1+\epsilon(t)]^4K$ and $K_z(t)=[1+\epsilon(t)]^{-8}K$, so $\dot{K}_x=\dot{K}_y=4K(1+\epsilon)^3\dot{\epsilon}$ and $K_z=-8K(1+\epsilon)^{-9}\dot{\epsilon}$. Since the terms in K_i occur in (11) for the individual oscillators, with no cross terms, there exist matrix elements only between states of the system differing by the excitation of a single oscillator, and these matrix elements are simply the individual-oscillator matrix elements for the x_i^2, which obey the selection rule $\Delta n_i=0,\pm2$. Thus, we have

$$\begin{aligned}(n_i+2|\,\partial\mathcal{H}/\partial t\,|n_i)&=(\dot{K}_i/2)(n_i+2|\,x_i^2\,|n_i)\\&=(\dot{K}_i/4\beta_i^2)[(n_i+1)(n_i+2)]^{\frac{1}{2}}. \quad (17)\end{aligned}$$

There is a state k of the system admixed by the distortion process for an excitation by two units of each oscillator, according to (2) and (4). For He^4, for example, one has eight oscillators of the type n_x (or n_y)$=0$ and four of the type $n_z=0$ and from (5) with $\omega_{km}=2\omega_i$, $\omega_x=\omega_y=(1+\epsilon)^2\omega$, $\omega_z=(1+\epsilon)^{-4}\omega$, one obtains

$$\begin{aligned}E_\alpha(\dot{\epsilon})&=[4(1+\epsilon)^2+2(1+\epsilon)^{-4}](\hbar/\omega)\dot{\epsilon}^2\\&=6(1+4\epsilon^2+\cdots)(\hbar/\omega)\dot{\epsilon}^2. \quad (18)\end{aligned}$$

Similarly for O^{16}, with four times the number of n_i's indicated in (14), we have an effective kinetic energy again just six times as great. The term in the first power of ϵ drops out in this expression because of the choice of the expansion parameter [with the particular powers 4 and -8 in (11)], and we neglect the $\epsilon^2\dot{\epsilon}^2$ term, as is justified for small values of ϵ, in comparison with the leading term in $\dot{\epsilon}^2$. After this explanation of the approximation, the factors $(1+\epsilon)$ may be dropped from the expressions for $\dot{K}_i$ and ω_i in this part of the calculation. If we thus neglect higher powers of ϵ, the sum of (15) and (18) is of the form $(\text{constant}+\frac{1}{2}k\epsilon^2+\frac{1}{2}\mu\dot{\epsilon}^2)$ and in the more general case of any closed-shell nucleus we have

$$\tfrac{1}{2}k=\hbar\omega\sum(n_x+n_y+10n_z+6) \quad (19)$$

$$\tfrac{1}{2}\mu=(\hbar/4\omega)\sum{}'(n_i+1)(n_i+2). \quad (20)$$

[4] D. Pfirsch, Z. Physik **132**, 409 (1952).

The summation in (19) is over all nucleons and the summation $\sum'$ in (20) is over the n_i of the protons in the two outermost proton-filled shells and similarly for the neutrons, that is, over all the n_i which may be excited by two units without making states forbidden by the exclusion principle. Carrying out the summations over the various nucleon states, without multiplying by the number of nucleons per state, up to include the shell with $n_x+n_y+n_z=n$, one finds

$$\sum_{\text{states}} (n_x+n_y+10n_z+6)=\sum_{\text{states}}{}' (n_i+1)(n_i+2)$$
$$=3\sum_{q=0}^{n}(2q+1)(n+2-q)(n+1-q) \quad (21)$$

having the numerical values 6, 36, 120, 300, 630, 1176, and 2016 for $n=0, 1, \cdots 6$, respectively. The noteworthy equality of the first two members of (21) means that the calculated frequency of the deformation vibration, $\Omega/2\pi$, is the same for any "closed-shell" nucleus such as listed in Table I of (I), whether or not it has a neutron excess and independent of A:

$$\Omega=(k/\mu)^{\frac{1}{2}}=2\omega. \quad (22)$$

This result unfortunately denies its own validity, for the adiabatic approximation by which it was derived requires that the frequency of deformation is appreciably less than the frequency of the single-nucleon oscillators, that is, $\Omega \ll \omega$.

DISCUSSION

This unsatisfactory result raises some doubt concerning the possible existence of states of collective deformation of this sort. It probably means more than merely that a convenient method of calculation is not applicable. It suggests that without other physical influences there is not time for the nucleons to define a meaningful vibrating deformed surface in terms of their average positions, and leaves the possibility that some other correlations between nucleon positions, not expressed in terms of the surface, may be more important. In the case of O^{16}, for example, the shell model which seems promising for most of the states of the neighboring nuclei does not explain the first-excited state, a 0^+ state, without two-nucleon excitation and the possibility of accounting for it as a spheroidal surface vibration would be of some interest. There are, on the other hand, special reasons why the correlation in position associated with the stability of the alpha groups of four nucleons should be important in this particular nucleus, and the success of Dennison[5] in accounting for most of its many newly-identified excited states indicates that this type of correlation, leading to a tetrahedral symmetry of the charge distribution, seems here to be dominant. In such a case the effective nuclear surface would also show a distortion with tetrahedral symmetry, but this cannot be included in the simple treatment of the distortion given above, which because it neglects configuration interaction contains the approximations of first-order perturbation theory in addition to the adiabatic approximation.

Correlations invoking the alpha stability through the saturation properties of (phenomenological) nuclear forces would be expected to appear in the second order of a deformed oscillator-model treatment, and might show that the stable shape of a nucleus is a deformation with a favorable symmetry, rather than the spherical shape. This would leave the possibility of small vibrations about the deformed shape analogous in a nebulous way to the molecule-like vibrations of the alpha model, and probably not resembling irrotational flow.

In a nucleus with one shell partly filled with protons and another partly filled with neutrons, there may still be a vibration with a frequency determined mainly by the behavior of the nucleons in unfilled shells. It may be in some sense collective among those nucleons, with a suppressed participation of the closed-shell nucleons given perhaps by the present calculation if the frequency is decreased sufficiently for adiabaticity by such additional complexities as the Gallone-Salvetti "spilling over" discussed in the introduction of reference 1. An extension of this calculation to include the extra nucleons, in order to examine the possible equivalence to irrotational flow, might become rather intricate.

IMPROVED EVALUATION OF THE POTENTIAL

The potential energy responsible for the large value (22) of Ω was calculated from the extreme zeroth-order assumption that the average of the interactions between nucleons may be replaced by the oscillator potential which is unrealistic in having infinitely high boundaries to confine the wave functions. It is perhaps demanding too much of the zeroth-order potential energy to expect it to give the term in ϵ^2 after cancellation of the term in ϵ. We shall show, however, that the first-order potential energy, obtained by integrating over reasonable specific nuclear interactions gives a rather similar result which also fails to justify the adiabatic approximation.

For calculations of this sort, it is customary to admit our ignorance of the detailed nature of nuclear interactions by introducing phenomonological exchange interactions between pairs of nucleons, and the partial success of this procedure in a variety of problems has given rise to the impression that we thereby make a fair approximation to some of the principal dynamical features of the actual interactions which may, for example, be many-particle interactions with the two-particle terms predominant. A convenient form for the assumed interaction is

$$B[\exp(-\alpha r_{ij}^2)]$$
$$\times[(1-g-g_1-g_\sigma)P+gPQ+g_1+g_\sigma Q], \quad (23)$$

where P exchanges space coordinates and Q spin. The

[5] D. M. Dennison, Phys. Rev. **96**, 378 (1954). See also D. R. Inglis, Revs. Modern Phys. **25**, 390 (1953).

parameter $\alpha^{-\frac{1}{2}}$ thus establishes the range of the interaction, assumed Gaussian. We introduce also the parameters σ_i (replacing β_i) to make $\sigma_i^{-\frac{1}{2}}$ give the extension of the wave functions relative to the range of the interaction, the wave function containing a factor $\exp(-\sigma_i\alpha x_i^2/2)$. Thus $\sigma_i=\beta_i^2/\alpha$, $\sigma\alpha=(MK)^{\frac{1}{2}}/\hbar=M\omega/\hbar$, $\sigma_z=\sigma_y=(1+\epsilon)^4$, $\sigma_x=(1+\epsilon)^{-8}\sigma$. The simple integrations encountered in this "Cartesian" representation are conveniently tabulated in an earlier paper.[6] The average of the interaction (23) summed over all pairs of nucleons, calculated with an antisymmetrized product wave function for the ellipsoidally distorted nucleus He^4 is

$$\bar{U}_\alpha=6B(\sigma_x/\tau_x)(\sigma_z/\tau_z)^{\frac{1}{2}}(1-g-g_\sigma)=6B(\sigma/\tau)^{\frac{3}{2}} \times(1-g-g_\sigma)[1-24(\sigma/\tau)(1-\sigma/\tau)\epsilon^2]+\cdots, \quad (24)$$

and for O^{16} it is

$$\bar{U}=24B(\sigma_x/\tau_x)(\sigma_z/\tau_z)^{\frac{1}{2}}\{X+Y(2/\tau_x+1/\tau_z) +Z(8/\tau_x^2+4/\tau_x\tau_z+3/\tau_z^2)\}$$
$$=24B(\sigma/\tau)^{\frac{3}{2}}\{[X+3Y/\tau+15Z/\tau^2] \times[1-24(\sigma/\tau)(1-\sigma/\tau)\epsilon^2+\cdots] -48(\sigma/\tau^2)[Y(1-2\sigma/\tau)+(2Z/\tau)(5-12\sigma/\tau)] \times\epsilon^2+\cdots\}, \quad (24')$$

where $\tau=\sigma+2$, $X=5g_1+2(g_\sigma-g)$, $Y=\frac{2}{3}(1+g-5g_1-3g_\sigma)$, and $Z=\frac{1}{4}(1-g-g_\sigma)$. With $\epsilon=0$ this reduces to the first-order result for the undistorted O^{16} nucleus given by Kroeger.[7] Thus $\bar{U}$ appears in the form of $a+b\epsilon^2$ and it is the coefficient b which contributes to the "stiffness" of the nucleus. Another contribution is made by the kinetic energy of the internal motion of the nucleons, which for He^4 in the oscillator approximation is

$$\bar{T}_\alpha=(9/4)(\hbar^2/M)\sigma\alpha(1+4\epsilon^2+\cdots), \quad (25)$$

and for O^{16} is

$$\bar{T}=(69/4)(\hbar^2/M)\sigma\alpha(1+4\epsilon^2+\cdots)\equiv c+d\epsilon^2. \quad (25')$$

This is essentially half of (15), since a harmonic oscillator has half kinetic and half potential energy, but for He^4 there is a factor $\frac{3}{4}$ and for O^{16} an even more trivial factor 23/24 arising from center-of-mass considerations. The "stiffness" against deformation is then determined by $b+d$, which replaces $k/2$ in (22), to give the frequency of distortional oscillation.

There is considerable arbitrariness in the phenomenological representation of nuclear interactions and it is not immediately clear in a calculation such as this how much the result may depend on this arbitrariness, so we give in Table I the computed numerical result for several fairly reasonable choices of the various parameters involved. The next-to-last row gives the distortional frequency, replacing (22) for He^4, the last row for O^{16}. The first column uses the parameters of reference 7, $\sigma=0.5$ being the result of minimizing the first-order energy of O^{16}. The 1938 range parameter $\alpha\hbar^2/mMc^2=22$ had moved toward shorter ranges from the old long-range value 16 used in 1937, but recent analysis of scattering measurements[8] indicates that the even shorter-range value 26.56 is better. This value, which is used in the rest of Table I, is obtained from the data given in reference 8, pages 56 and 201, and from the unit-of-length conversion factor $\hbar/(mM)^{\frac{1}{2}}c=9.012\times10^{-13}$ cm, thus: $\alpha\hbar^2/mMc^2=(1.4345\times9.012/2.51)^2=26.56$. The values[8] for well depth $-B$ and for $-B(1-g-g_\sigma)$ (that is, "singlet depth"), are then $103.3mc^2$ and $64.5mc^2$, implying $g+g_\sigma=0.1875$. In order to keep the rounded-off value $g+g_\sigma=0.2$, without changing the average of the singlet and triplet depths, we take $B=-105mc^2$. The g's in the second column of Table I are a simplified set which have been used frequently and roughly satisfy the various saturation and other requirements, and the g's in the fifth column correspond[9] to the symmetrical form $\tau_i\cdot\tau_j(0.1+0.23\sigma_i\cdot\sigma_j)$.

Table I. Collective frequency of distortion for various choices of the parameters.

$\alpha\hbar^2/Mmc^2$	22	26.56			26.56			
$-B/mc^2$	92	105			105			
g	0	0			−0.26			
g_1	−0.126	0			−0.13			
g_σ	0.22	0.2			0.46			
σ	0.5	0.7	1.0	1.3	0.7	1.0	1.3	
Ω_α/ω	1.87	2.12	2.37	2.48	2.12	2.37	2.48	
$\Omega(O^{16})/\omega$	2.40	2.32	2.29	2.20	2.31	2.31	2.26	

The choice of nuclear size parameter σ should be made by minimizing the energy. The inadequate available calculations of the total energy serve only to suggest within what range of values it is expected to lie. The first-order energy is given by Eqs. (13) plus (14) with $\epsilon=0$, or by Eq. (8) of reference 7. The g's of column 1 used in reference 7 are less favorable than the others for this purpose. With α and B given by the newer numbers 26.56 and 105, the g's of column 2 give a minimum first-order energy $-50mc^2$ at $\sigma=0.7$, the g's of column 5 give $-89mc^2$ at $\sigma=0.9$, whereas the g's of column 1 give only $-9mc^2$ at $\sigma=0.5$. As an indication of the less pronounced variation with α and B, the latter energy is to be compared with $-19mc^2$ at $\sigma=0.5$ given in reference 7 for the α and B of column 1. The experimental value of the total energy is $-249mc^2$. The improvement available from a more refined calculation is indicated by Kroeger's result[7] that the minimum second-order energy with those parameters is about $-79mc^2$ at the minimizing value $\sigma=0.7$. It is significant that the better calculation not only improves the

[6] D. R. Inglis, Phys. Rev. **51**, 531 (1937).

[7] W. J. Kroeger, Phys. Rev. **54**, 1048 (1938). Erratum: In Eq. (8), the first term in g_σ should have a negative sign.

[8] J. M. Blatt and V. F. Weisskopf, *Theoretical Nuclear Physics* (John Wiley and Sons, Inc., New York, 1952).

[9] L. Rosenfeld, *Nuclear Forces* (North-Holland Publishing Company, New York, 1948).

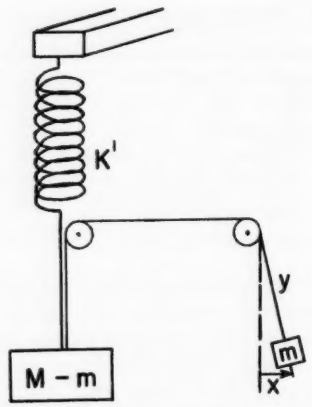

FIG. 1. A simple mechanical system in which the adiabatically varying quantized motion of a small part affects the classical motion of the rest.

calculated energy but also shifts the minimum from $\sigma=0.5$ to 0.7, indicating a more compact nucleus. It is clear from the improved first-order energy that the parameters of column 5 would give a much more satisfactory second-order energy, though probably still considerably higher than the experimental value, and that the minimizing σ would be somewhat greater than 0.9. A good calculation with parameters capable of giving the experimental energy would be expected to give σ considerably greater than unity, perhaps as high as $\sigma=1.3$. Thus the range $\sigma=0.7$ to 1.3 explored in Table I is about sufficient to cover the reasonable possibilities.

The frequency of collective vibration is thus in these simple examples even higher than in (22), and this more careful treatment of the potential energy fails to rescue the validity of the adiabatic approximation. However, the values of Ω/ω in Table I are only slightly larger than the value 2 of (22), which shows that the oscillator potential is a fairly good approximation to a "self consistent" field for a deformed nucleus, and this is relevant to the use[1] of the oscillator approximation as a criterion for the validity of the assumption of irrotational fluid flow in treating rotating surface waves in the droplet model.

Helpful comments of Aage Bohr have been much appreciated.

APPENDIX

In a problem of this sort it is perhaps instructive to illustrate the predominant physical effect in a very simple case. Consider in the harmonic approximation a simple pendulum of mass m tethered by way of small pulleys to a body of large mass $M-m$ suspended on a spring of stiffness K', as in Fig. 1. The potential and kinetic energies are

$$V=\tfrac{1}{2}K'(y-y_0)^2-mgy(1-x^2/2y^2),$$
$$T=\tfrac{1}{2}M\dot{y}^2+\tfrac{1}{2}m\dot{x}^2, \tag{26}$$

where the length of the pendulum, y, describes the motion of the large mass and where x is the horizontal displacement of the pendulum. If y varies slowly compared to x, we may treat the pendulum swing separately, its wave equation being (6) (with $M\rightarrow m$), where $K=mg/y=m\omega^2=\hbar^2/md^4$. The average value of the terms in (26) containing x and $\dot{x}$ is given by E of Eq. (10) and the total energy E_y associated with the y-motion is thus

$$E_y=\tfrac{1}{2}[M+(\hbar/16g^{\frac{1}{2}}y^{\frac{1}{2}})(n+\tfrac{1}{2})]\dot{y}^2$$
$$+\tfrac{1}{2}K'(y-y_0)^2-mgy+(n+\tfrac{1}{2})\hbar(g/y)^{\frac{1}{2}}. \tag{27}$$

This is not in Hamiltonian form, since the momentum conjugate to y has not been defined. With the pendulum excited to the quantum number n, there is an equilibrium position y_n, and in terms of the small coordinate $z=y-y_n$ we may write the total energy:

$$E_y=\tfrac{1}{2}\mu\dot{z}^2+\tfrac{1}{2}\kappa z^2+\text{consts},$$
$$\mu=M+(\hbar/16g^{\frac{1}{2}}y_n^{\frac{1}{2}})(n+\tfrac{1}{2}),$$
$$\kappa=K'+(3\hbar g^{\frac{1}{2}}/4y_n^{5/2})(n+\tfrac{1}{2}). \tag{28}$$

Energy is conserved with a simple solution $z=A\cos\Omega t$ if

$$\Omega=(\kappa/\mu)^{\frac{1}{2}}=\Omega_0\{1+[3-(\Omega_0/2\omega)^2](n+\tfrac{1}{2})\hbar/8K'y_n^2+\cdots\}$$

with $\Omega_0=(K'/M)^{\frac{1}{2}}$ and $\omega=(g/y_n)^{\frac{1}{2}}$. Thus the frequency of the slow classical motion is influenced by the quantization of the small rapid part of the system. The term containing the factor 3 arises from expansion of the quantum energy $(n+\frac{1}{2})\hbar(g/y)^{\frac{1}{2}}$, and may be obtained as well from the constancy of the action variable in the classical adiabatic discussion. The last term arises from the mixing of the quasi-stationary states.

Radiations of 34-Day Xe^{127}†

HIRDAYA B. MATHUR*
Radiation Laboratory and Department of Chemistry, University of California, Berkeley, California
(Received October 18, 1954)

The gamma rays of Xe^{127} have been studied in a sodium iodide scintillation spectrometer and by gamma-gamma coincidence techniques. The results support a decay scheme published previously by Bergström.

XENON-127 exists in two isomeric forms with half-lives of 75 seconds and 34 days, respectively. A recent publication from our laboratory has discussed the 75-second Xe^{127m}.[1]

The 34-day Xe^{127} has been previously studied by several workers, but in great detail by Bergström.[2] Bergström studied the electron spectrum of mass-separated Xe^{127} and reported gamma rays at 56, 145, 170, and 200 kev. His scintillation spectrometric studies did not resolve the gamma rays of energies 145, 170, and 200 kev, but he found an additional gamma ray (at 368 kev), the conversion electrons of which were not detectable in a beta-ray spectrometer. Bergström proposed a tentative decay scheme reproduced in Fig. 3 below.

During the course of some other studies on the isotopes of xenon[1,3] it was convenient to make some measurements of the gamma radiations of Xe^{127} with sodium iodide crystals and gamma-gamma coincidence techniques. The results complement the beta-ray spectrometer studies of Bergström and support his tentative decay scheme.

We prepared Xe^{127} by the (p,n) reaction on I^{127} in the linear accelerator. The iodine was bombarded in the form of potassium iodide. After bombardment, xenon was isolated on 0.1-mil aluminum foil by the glow-discharge method described in previous publications.[1,3]

A sodium iodide-photomultiplier assembly coupled to a 50-channel pulse-height analyzer[1] was used to study the gamma spectrum of Xe^{127}. The results are shown in Fig. 1. Photopeaks at 56, 170, 200, and 368 kev were observed in agreement with Bergström.[2] The small peak at 75 kev is due to lead x-rays produced by the lead castle enclosing the sodium iodide-photomultiplier assembly and the Xe^{127} sample. The peak at 110 kev is due to the backscattered radiation of the most prominent gamma peak (at 200 kev) in the gamma spectrum of Xe^{127}. The gamma ray of 145 kev reported by Bergström was not detectable in the gamma spectrum because of its low intensity, but it was observed in our gamma-gamma coincidence studies (see below). No annihilation radiation was observed, indicating that 34-day Xe^{127} decays entirely by electron capture. Gamma-gamma coincidence measurements were carried out on the equipment mentioned in a previous paper.[1] These studies established that a 56-kev gamma ray was in coincidence with 145- and 170-kev gamma rays and with 28-kev iodine x-rays, as suggested by Bergström[2] because of the fact that the sum of the energies of 145 and 56 kev is 201 kev. In agreement with this, the 200-kev radiation is not in coincidence with the 56- and 145-kev gamma radiations but is in coincidence with the 170-kev gamma ray and the 28-kev iodine x-radiation. Quantitative studies indicate that the 56-kev level should be below the 145-kev level, while the 170-kev radiation should be higher than the 200-kev radiation. For example, in the study of the 170 to 200 kev coincidence, the ratio of coincidence pulses to gate pulses was greatly increased when the gamma ray selected by the

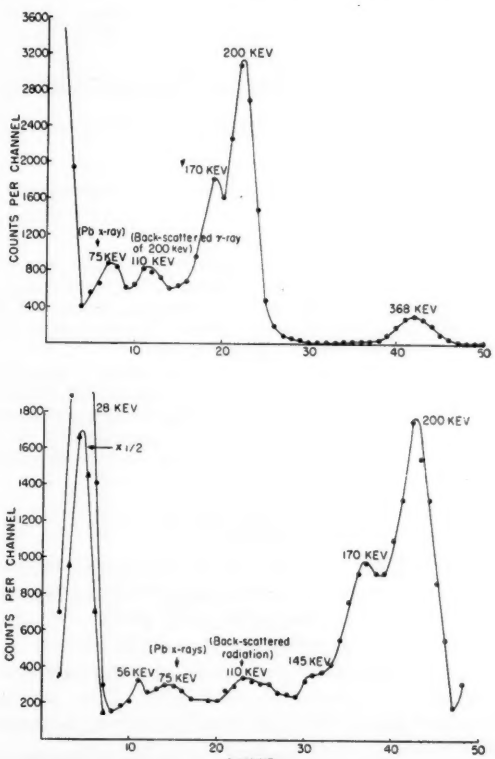

FIG. 1. Gamma spectrum of 34-day Xe^{127}.

* On leave of absence, Department of Chemistry, University of Delhi, Delhi, India. Present address: Institute for Nuclear Studies, University of Chicago, Chicago 38, Illinois.

† This work was performed under the auspices of the U. S. Atomic Energy Commission.

[1] H. B. Mathur and E. K. Hyde, Phys. Rev. **95**, 708 (1954).
[2] I. Bergström, Arkiv Fysik **5**, 191 (1954).
[3] H. B. Mathur and E. K. Hyde, Phys. Rev. **96**, 126 (1954).

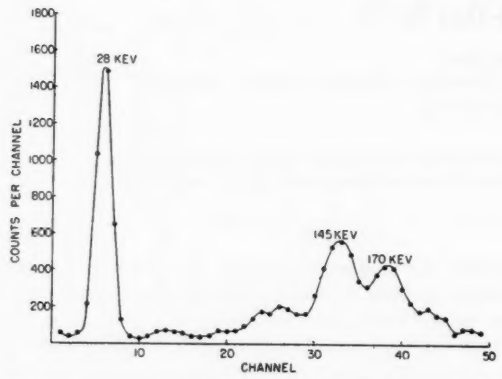

FIG. 2. Gamma spectrum of Xe^{127} showing the gamma rays in coincidence with the 56-kev gamma ray.

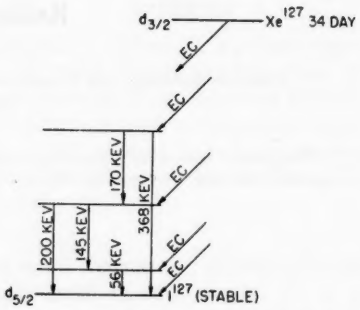

FIG. 3. Proposed decay scheme of Xe^{127}.

gate crystal was changed from 200 to 170 kev. The 368-kev gamma ray was in coincidence with the 28-kev iodine x-rays and with no other gamma rays. Since most of the coincidence measurements were straightforward the curves are not presented. In Fig. 2 the gamma spectrum in coincidence with the 56-kev gamma ray is shown because it indicates that the 145-kev gamma ray is clearly evident. This gamma ray was not resolved in the gamma curves of Fig. 1. All coincidence results are incorporated in the decay scheme of Fig. 3 which agrees with that proposed by Bergström.[2]

ACKNOWLEDGMENTS

I wish to thank Dr. E. K. Hyde for helpful discussion and interest in this work. The assistance of Mr. W. W. Olson, Mr. R. D. Watt, and the linear accelerator crew for the proton bombardment is acknowledged. Thanks are also due to Dr. F. Asaro and Mr. F. S. Stephens for help in the gamma-gamma coincidence studies.

PHYSICAL REVIEW VOLUME 97, NUMBER 3 FEBRUARY 1, 1955

Internal and External Bremsstrahlung in Connection with the Beta Decay of S^{35}

N. STARFELT,* *Radiation Physics Department, University of Lund, Lund, Sweden*

AND

N. L. SVANTESSON,* *Department of Physics, University of Lund, Lund, Sweden*

(Received August 30, 1954)

The *internal* bremsstrahlung, emitted in the β decay of S^{35}, was investigated with a NaI scintillation spectrometer. Neither the shape of the spectral distribution nor the absolute yield was found to agree with theory. At 50 kev the experimental photon yield was 65 percent greater than the theoretical. At 100 kev it was even 180 percent greater. The total photon energy yield per β decay, 2.23×10^{-6} mc^2, was 35 percent greater than the calculated value.

The *external* bremsstrahlung, emitted when the β particles from S^{35} were stopped in matter, was also investigated with the same apparatus. With elements of low atomic number the experimental values agreed with those calculated. In experiments using elements of higher atomic numbers, however, the experimental values differed widely from those calculated, the difference increasing with the atomic number. Thus, for lead at 50 kev the experimental value was 60 percent greater than the theoretical, and at 100 kev it was 170 percent greater.

I. INTRODUCTION

STUDIES are available of the continuous electromagnetic radiation accompanying β decay, i.e., the internal bremsstrahlung (IB), and of the radiation emitted when β particles are stopped in matter, i.e., the external bremsstrahlung (EB), of β emitters with disintegration energies above 1 Mev. Thus at this laboratory[1] IB and EB were investigated in experiments using P^{32} ($E_\beta^{\max}$ 1.70 Mev). The scintillation spectrometer was used because of its good γ-detection efficiency. (Readers interested in a fairly complete list of references of investigations bearing on the problems under consideration are referred to Lidén and Starfelt.[1])

The present paper is concerned with an investigation of a β emitter with low disintegration energy. The investigation, which was carried out with S^{35} ($E_\beta^{\max}=168$ kev) by means of a scintillation spectrometer, included the determination of the spectral distribution and the total radiation energy yield of both the IB and the EB

* Present address: National Bureau of Standards, Washington, D. C.

[1] K. Lidén and N. Starfelt, Phys. Rev. **97**, 419 (1955).

emitted on total absorption of the β particles in C, Al, Cu, Ag, and Pb. A preliminary note on the initial stage of this investigation has been published.[2]

II. EXPERIMENTAL PROCEDURE

A. Arrangements

The scintillation spectrometer used consisted of a NaI(Tl) crystal of diameter 1.8 cm and thickness 0.9 cm, in conjunction with an EMI 5359 photomultiplier, a linear pulse amplifier, and a single-channel pulse-analyzer.[3] The crystal was covered with a thin, 2.3 mg/cm², aluminum reflector. The air in the photomultiplier housing was dried with phosphorus pentoxide to prevent the crystal from being affected by moisture.

Backscattering of photons from that part of the photomultiplier surface not covered by the crystal was prevented by the use of diaphragm D_2 (Fig. 1).

By calculation the radiation scattered in the hole of the diaphragms was found to be negligible.

In order to avoid characteristic x-rays in the energy range under consideration, the lead diaphragms were lined with tin and copper sheeting. The detector was shielded by 8 cm lead.

The β particles from the source were absorbed in a beryllium disk, resting on the diaphragm D_1 and located halfway between the source and the crystal. The diameter of the hole in this diaphragm was the smallest permitting "visibility" of the entire crystal from any point in the source. This kept the EB disturbance below 2 percent of the IB intensity for all energies.

The source was housed in a Perspex container, in which the pressure was kept below 1 mm Hg during measurement. At this pressure the EB disturbance from the air was negligible. At normal pressure and with the geometry used this disturbance exceeded 25 percent of the IB for low energies. Within the entire energy range the calculated EB from the Perspex container was less than 1 percent.

The experimental arrangements for the study of EB were the same as those used for measurement of IB.

B. Sources

Owing to the low intensity of the IB, a strong source would have been preferable, so that the counting rate would far exceed the background counting rate. This was, however, not possible because in thick sources EB is created in the source itself: only when the source is extremely thin and uniform will this disturbance be small in proportion to the IB. The source should be as free as possible from impurities, especially from impurities of high atomic number. The backing film should also be thin and made of material of low atomic number.

In an investigation of the β spectrum of S^{35}, Albert and Wu[4] found the source itself to exert a disturbing effect at low energies when the source thickness exceeded 5 μg/cm², but not otherwise. Albert and Wu mounted their sources on backing films of collodion about 3 μg/cm² thick. In the measurement of the IB a slightly thicker source can be tolerated.

In the present investigation collodion films with a thickness of about 2 μg/cm² were used. These films were fastened to a Perspex ring (Fig. 1). The diameter of the ring was sufficient to prevent EB from the ring from reaching the crystal. The films were made from a solution of roughly 3 percent collodion in amyl acetate. A drop of the solution was allowed to spread over the surface of distilled water containing wetting agent. After evaporation of the solvent, the Perspex ring was placed on the film thus formed. Superfluous parts of the film were removed and the ring with the film attached was taken from the surface of the water. The thickness of the film was assessed both by weighing and by studying the interference colors of superimposed films.

The sources were made from carrier-free S^{35} solution, obtained by neutron irradiation of KCl at AERE, Harwell. However, owing to the presence of sulfate in the potassium chloride, the S^{35} solution used, contained 10–20 μg SO_4 ions per millicurie. Other impurities were mainly B, Na, Cl, and K, together <25 μg/mC. The absolute activity of the S^{35} solution was determined with an accuracy of about ± 5 percent at Harwell by means of a 4π G-M counter.

If the S^{35} solution is placed directly on the film, the latter will be destroyed. The solution was therefore first

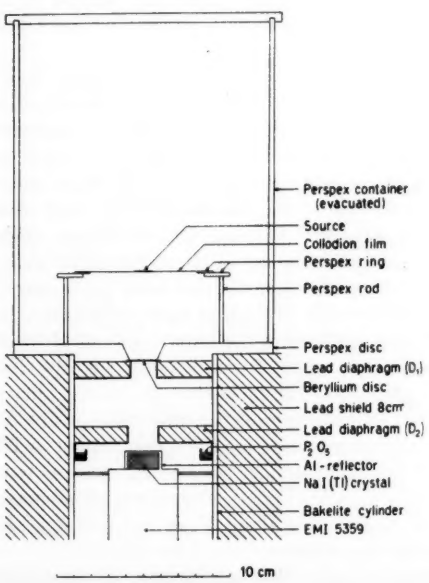

FIG. 1. Experimental arrangement used for the measurement of internal and external bremsstrahlung.

[2] K. Lidén and N. Starfelt, Arkiv Fysik 7, 83 (1954).

[3] W. C. Elmore and M. Sands, *Electronics Experimental Techniques* (McGraw-Hill Book Company, Inc., New York, 1949), first edition, p. 228.

[4] R. D. Albert and C. S. Wu, Phys. Rev. 74, 847 (1948).

evaporated to dryness and the residue then redissolved in distilled water. A suitable amount of this solution was afterwards evaporated with the aid of an infrared lamp on that side of the film which had been in contact with the water. The rest of the film was screened off by means of an asbestos diaphragm. In this way sources thinner than 35 $\mu g/cm^2$ were obtained.

On account of the difficulty to handle the film the absolute activity of an IB source was not determined by weighing but as follows. The IB source was sandwiched between two aluminum radiators. Then the intensity of the IB plus EB from this source was compared with the intensity of the radiation from a similar source, prepared by evaporating a weighed amount of the S^{35} solution directly on one of the two aluminum radiators. The average atomic number of the sources was close to that of aluminum, and therefore any slight variation in the thickness of the source would not appreciably influence the result of this comparison.

Autoradiographs were taken to check any irregularity in thickness of the source. The source was placed on the photographic emulsion, from which it was separated by the backing film only. The variation in activity between different parts of the source with an average thickness less than 7 $\mu g/cm^2$, was found to be less than sevenfold, as measured with a microphotometer. For the thickest source (average thickness <35 $\mu g/cm^2$) used in the measurements of the IB the maximum variation was found to be about tenfold. This infers that the thickest parts of the thin source were less than 35 $\mu g/cm^2$. Calculation of the intensity of the EB emitted when the β particles of S^{35} passed through a layer of this thickness, showed this disturbance to be less than 5 percent of the IB at all energies.

The influence of the EB from the source itself was also investigated by another method. In experiments using sources of different thicknesses, measurements were made of the bremsstrahlung $(N_i+N_e)dE$ in the energy interval between E and $E+dE$ from the source alone, and then of the bremsstrahlung $N_\tau dE$ from the source sandwiched between two aluminum radiators. Here $N_i dE$ is the number of IB photons from the source and $N_e dE$ the EB contribution from the source itself. N_e increases with increasing source thickness, but as the atomic numbers of the impurities and of the radiators are about equal, N_τ varies only slightly with the source thickness. The ratio $B=(N_i+N_e)/N_\tau$ may then be taken as a measure of the uniformity of the source. Of all the sources used for the measurement of IB, the ratio B for those thinner than 35 $\mu g/cm^2$ was found to vary only slightly (Fig. 2). The source with a maximum average thickness of about 17 $\mu g/cm^2$ and $B=0.32$ was distinctly nonuniform.

Figure 2 shows that an increase of the maximum average thickness of the source from 4 to 35 $\mu g/cm^2$ did not cause any demonstrable definite increase of the EB. Judging by Fig. 2, this disturbance was less than 5 percent for all the sources used. This figure was thus in fairly good agreement with that found by the first method.

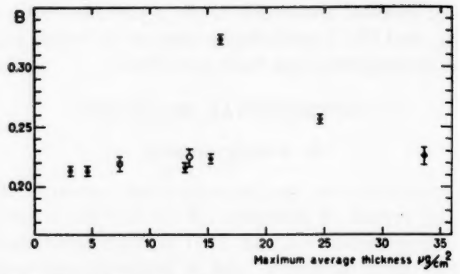

FIG. 2. The influence of the source thickness on the measurement of internal bremsstrahlung as represented by B, the ratio between the counting rate from the source alone and from the source plus aluminum radiators for energies between 20 and 40 kev. Squares and open circles represent the sources used in the measurements of internal bremsstrahlung.

In the measurement of the EB of different elements the radiators used consisted of circular disks (diameter $=13$ mm) thick enough (about 50 mg/cm^2) to stop all the β particles. A weighed amount of the S^{35} solution was evaporated with the aid of an infrared lamp on such a disk and was afterwards covered by another radiator of the same kind. 4π geometry was thereby obtained. Sources of different thicknesses were compared to ensure that no disturbance from the source itself influenced the results.

C. Measurements

The weak sources and the low relative intensity of the radiation, especially at high photon energies, resulted in long observation times. Particular care was therefore necessary to obtain the required accuracy of the energy calibration and of the channel-width. Thus, the electronic apparatus was warmed up for 2–3 hours before any measurements were made, and the temperature of the room was kept constant. Changes in the surface layer of the crystal with consequent variation in energy calibration was minimized by keeping the air in the photomultiplier housing dry. The energy calibration was performed with K x-ray lines[5] from Sn, Pm, Yb, and Pb as well as with the Ce^{141} γ-ray line at 145 kev. The variation of the energy calibration during measurement of a spectrum was less than ± 2 percent. The proportionality between photon energy and pulse height was good within the energy range studied. The channel-width, about 8 kev, was measured with an accuracy of ± 3 percent with a pulse generator.

The IB was measured with three different sources. The EB from aluminum was studied not only with the use of these sources, but also with a source evaporated directly on an aluminum radiator. The spectra of the other elements were investigated with the use of 2–4 different sources in each case.

[5] K. Lidén and N. Starfelt, Arkiv Fysik **7**, 193 (1954).

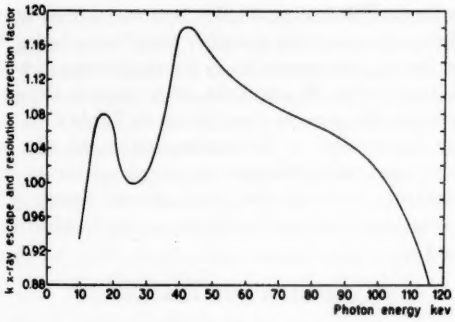

FIG. 3. Correction factor of the pulse-height distribution of the internal bremsstrahlung from S^{35} for K x-ray escape and resolution.

The activity of the sources varied from 70 to 350 microcuries.

D. Corrections

The spectrum of the radiation reaching the crystal was calculated mainly according to Lidén and Starfelt[6] from the measured pulse-height distribution. In the treatment of the experimental results of the EB of silver, only energies not influenced by the peak at about 23 kev were considered. This peak consists of continuous bremsstrahlung as well as of K x-rays caused by bremsstrahlung photons and by β particles. The ratio between these different contributions is known from Lidén and Starfelt.[5] However, their calculation is based on the assumption that the spectral distribution of the EB from elements of higher atomic numbers is the same as that of aluminum, and therefore their results cannot, of course, be used here. No accurate correction for the K x-rays could be made for the lead EB spectrum.

The calculated influence of Compton electrons, of escape electrons as well as of photons backscattered from the photomultiplier, was negligible in the energy range under consideration.

The greatest correction of the measurements is that for the escape of K x-rays from the top and cylindrical surfaces of the crystal. This effect and that of the resolving power were corrected for together.

The scintillation distribution,[7] $N_3(\epsilon_\gamma)$, reaching the photocathode gives rise to a pulse-height distribution, $N_2(\epsilon)$, which differs from $N_3(\epsilon_\gamma)$. The escape of K x-rays causes a discontinuity in $N_3(\epsilon_\gamma)$ at the K absorption edge of iodine. The scintillation distribution, $N_4(\epsilon_\gamma)$, corrected for this effect, was deduced from the experimental pulse distribution $N_2(\epsilon)$ in the following way. $N_3(\epsilon_\gamma)$ was calculated from an estimation of $N_4(\epsilon_\gamma)$ using the K x-ray escape factor $F(\epsilon_\gamma)$ of the crystal. $N_2(\epsilon)$ was then determined with Eq. (27) given in reference 6. Agreement between the calculated and the experimental values of $N_2(\epsilon)$ was obtained by trial and error. As a rule at most only three trials were necessary. At the K-absorption edge of lead, $N_4(\epsilon_\gamma)$ was calculated by a similar method.

Figure 3 shows the correction of the IB pulse distribution for the K x-ray escape and the resolving power. This correction has two maxima, one at about 40 kev and due to the K absorption edge of iodine, the other at about 15 kev and due to the absorption in the Be absorber. The resolving power was determined by measurements of the half-width of the Ce^{141} γ-ray line at 145 kev. It was about 20 percent and varied by less than 5 percent of this value between the different series of observations.

Corrections were made for the γ-detection efficiency of the crystal including the effective photoelectric absorption and the effective solid angle at different energies. This correction was less than 2 percent for energies below 80 kev. The effective photoelectric absorption was calculated according to Maeder *et al.*[8]

Corrections were applied for the absorption in the aluminum reflector and the beryllium absorber. Absorption data from White[9] were used throughout the present study.

The disturbance of the measurement of the IB caused by the EB from the beryllium absorber was calculated by extrapolation of the experimental determinations of the EB for the different elements. At the low energies covered by this investigation, the EB was calculated under the assumption that it was emitted isotropically. The EB disturbance from the beryllium absorber was

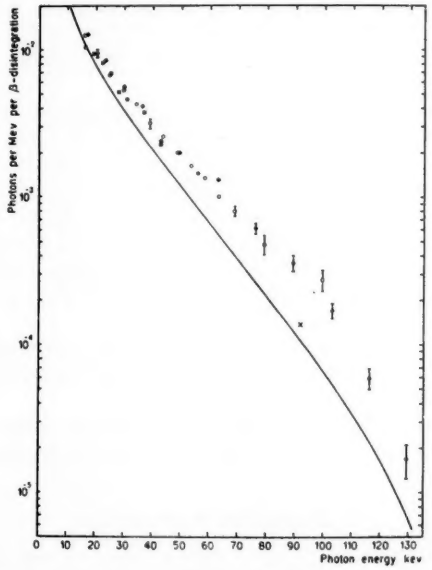

FIG. 4. Internal bremsstrahlung from S^{35}. The curves represent the theory as given by Knipp and Uhlenbeck. × marks the theory according to Nilsson. For explanation of symbols see Fig. 2.

[6] K. Lidén and N. Starfelt, Arkiv Fysik 7, 427 (1954).
[7] The notations are those utilized in reference 6.
[8] Maeder, Müller, and Wintersteiger, Helv. Phys. Acta 27, 3 (1954).
[9] G. R. White, National Bureau of Standards Report 1003, May 13, 1952 (unpublished).

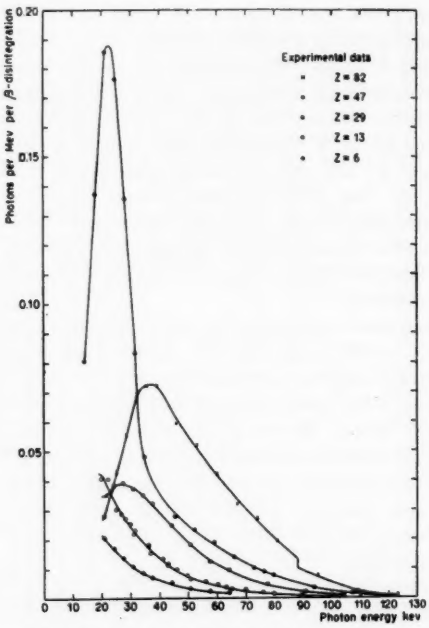

FIG. 5. Experimental total radiation, internal plus external, leaving the radiators (about 50 mg/cm²). The discontinuity at the K-absorption edge of lead is only a rough estimation.

found to be less than 2 percent for all energies. The results of the measurement of the IB are given in Fig. 4.

So far the treatment of the measurements of the IB plus EB is essentially the same as that of the IB. The values of EB plus IB corrected in this way are presented in Fig. 5.

When determining the EB, the absorption in the radiator must also be taken into account. For purposes of calculation it was assumed that all radiation was emitted from the center of the source. The error introduced by this approximation was found to be less than 1 percent for all energies for C and Al, and above 40 kev for Cu, Ag, and Pb. For the smallest energies studied with the three last-mentioned elements it was found to be about 5 percent.

The calculated effect of the Compton scattering of the photons in the radiators on the radiation measured appeared to be about 1 percent.

Finally, the IB was subtracted from the measured radiation, EB plus IB. The EB values found in this way are plotted in Fig. 6.

E. Estimation of the Errors

The errors which are of such an order of magnitude as to effect the result of the investigation of the IB are given in Table I. The errors in the correction for the EB disturbance from the Be absorber presented in Table I are mainly due to the uncertainty caused by the assumption of isotropic distribution of the EB.[10]

[10] G. Sesemann, Ann. Physik **40**, 66 (1941).

As far as EB is concerned, the error caused by the EB from the beryllium absorber must be excluded, but errors due to the absorption in the radiators and by the correction for the IB added. In other respects the errors are mainly the same as those given in Table I.

The inaccuracy in the determination of the total activity does not influence the shape of the spectral distribution, but only the total photon energy yield, and was therefore not included in the total error in Table I.

III. RESULTS AND DISCUSSION

A. Internal Bremsstrahlung

The theory of IB was developed in Born's approximation by Knipp and Uhlenbeck[11] and by Bloch[12] independently.

They arrived at the same expression for the probability per unit time, $S(k)dk$, for the emission of an IB photon with an energy between k and $k+dk$. Knipp and Uhlenbeck rewrote the expression as

$$S(k)=\int_{mc^2+k}^{W_0}\phi(W_e,k)P(W_e,0)dW_e, \qquad (1a)$$

where $P(W_e,0)dW_e$ is the probability per unit time for the emission of a β particle of energy between W_e and W_e+dW_e assuming $Z=0$, and $\phi(W_e,k)dk$ is the conditional probability that an electron emerging from the nucleus with energy W_e will emit a photon of energy between k and $k+dk$. W_0 is the maximum energy of the β spectrum.

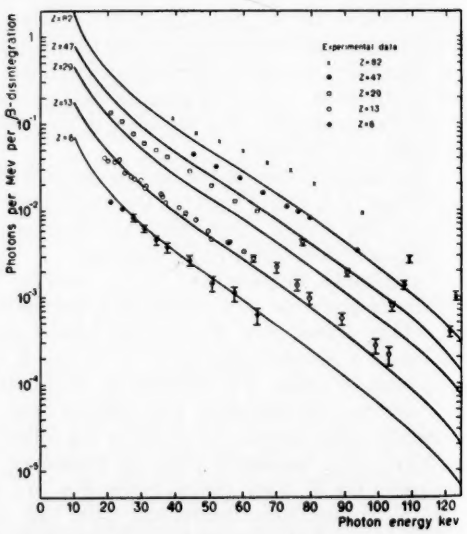

FIG. 6. External bremsstrahlung emitted when S^{35} betas are completely stopped in C, Al, Cu, Ag, and Pb. The curves represent the Sommerfeld-Elwert theory.

[11] J. K. Knipp and G. E. Uhlenbeck, Physica **3**, 425 (1936).
[12] F. Bloch, Phys. Rev. **50**, 272 (1936).

The expression for $S(k)$ was derived for allowed transition and Fermi polar vector interaction. Chang and Falkoff[13] extended the theoretical calculations to forbidden transitions and different types of interactions between the nucleons and the electron-neutrino field, still under the assumption $Z=0$.

When comparing theory with experiment, however, it is necessary to take into account the nuclear charge. As an approximation, Eq. (1a) makes it natural simply to replace $P(W_e,0)$ by the β distribution corrected for the Coulomb effect. Thus

$$S(k)=\int_{mc^2+k}^{W_0}\phi(W_e,k)P(W_e,Z)dW_e \qquad (1b)$$

with $P(W_e,Z)=P(W_e,0)F(Z,W_e)$. [A lower limit of this influence is $F(Z,W_0)=1.7$ for S^{35}.] This is the expression usually employed. It also permits the insertion of the experimental β distribution and thereby avoids the difficulties otherwise encountered in classifying the β decay.

The integrated expression for $S(k)$ evaluated by Bloch does not lend itself readily to a correction for the nuclear charge.

In Fig. 4 and Table II the values calculated from the theoretical expression (1b) are reproduced. For $P(W_e,Z)$ the allowed β spectrum of Fermi is used, with the nonrelativistic Coulomb factor $F(Z,W_e)$ given by Kurie *et al.*[14]

From Fig. 4 and Table II it is also clear that the experimental values were much higher than the theoretical. At low energies the experimental values approach the theoretical curve.

The limits of error in Fig. 4 are those given in Table I. The error in the determination of the absolute activity of the source, about ± 5 percent, is not included. The total yield of IB energy per β decay $2.23\times10^{-5}\ mc^2$ is 35 percent greater than the theoretical value.

In order to ascertain whether the approximation involved in going over from Eq. (1a) to Eq. (1b) might account for the discrepancy, Nilsson[15] calculated $S(k)$ with a more accurate consideration of the Coulomb influence. In the case of S^{35} the correction terms to be added to Eq. (1b) at $k=92$ kev was calculated by Nilsson using the nonrelativistic approximation for the Coulomb factor and was found to be about 28 percent of the value obtained from Eq. (1b). At low energies the expression given by Nilsson approaches the curve in Fig. 4. As is clear from the figure, this improvement is not sufficient to explain the whole discrepancy.

In this calculation Nilsson considered only the influence of the Coulomb field on the creation of the electron in the nucleus. Thus the radiation emitted when the β particle is accelerated in the field of the daughter nucleus was still neglected in the theoretical expression.

When the present paper was being prepared for the press, Boehm and Wu[16] published a similar investigation of the IB.

Boehm and Wu did not mention the disturbance caused by the air round the source. With the geometry used in the present investigation, the EB disturbance from the air was found to be about 25 percent of the IB in the low-energy region. Boehm and Wu used no collimator in their apparatus; therefore the disturbance in their experiment was presumably greater. It might be mentioned that a 5-cm layer of air corresponds to approximately $\frac{1}{5}$ of the total range of a β particle with maximum energy, while an electron with an initial energy of 40 kev is completely absorbed in about 2 cm air. The geometry without collimator used by Boehm and Wu can also give rise to contributions of scattered radiation from various parts of the apparatus.

This makes it possible to explain the discrepancy in the shape of the spectral distribution as found in the two determinations. The difference between the total photon energy yields is about the sum of the limits of error stated.

TABLE I. Estimated errors in the S^{35} internal bremsstrahlung spectrum (in percent). The total error does not include the inaccuracy, about ± 5 percent, of the absolute calibration of the source.

Energy kev	Channel width	Energy calibration	Resolving power $+K$ x-ray escape	Crystal efficiency	External bremsstrahlung from the Be absorber	Counting statistics	Total (rms)
20	3	1	2	1	2	5	7
40	3	3	3	1	1	6	8
70	3	4	1	1	1	6	8
100	3	6	1	1	1	10	12
120	3	10	2	1	1	14	18

TABLE II. The S^{35} internal bremsstrahlung photon spectrum $S(k)_{calc}$ calculated according to the theory of Knipp and Uhlenbeck (on multiplication by 10^{-5} the figures give the number of photons per Mev per disintegration) and $S(k)_{exp}/S(k)_{calc}$, the ratio between the experimental and the calculated values.

Energy kev	15.0	25.6	51.1	76.7	102.2	127.8
$S(k)_{calc}$	1180	506	109	25.9	5.75	0.814
$S(k)_{exp}/S(k)_{calc}$	1.12	1.26	1.65	2.30	2.8	2.9

B. External Bremsstrahlung

Bethe and Heitler[17,18] and Sauter[19] developed the theory of the EB in the Born approximation.

They calculated the probability, $\phi(W_e,k)$, that an electron with the initial energy W_e emits a photon with

[13] C. S. Wang Chang and D. L. Falkoff, Phys. Rev. **76**, 365 (1949).
[14] Kurie, Richardson and Paxton, Phys. Rev. **49**, 368 (1936).
[15] S. B. Nilsson (to be published).
[16] F. Boehm and C. S. Wu, Phys. Rev. **93**, 518 (1954). In this paper there is a drafting error (as confirmed by F. Boehm, private communication): In Fig. 3, for 10^{-6} read 10^{-5} and for 10^{-5} read 10^{-4}.
[17] H. Bethe and W. Heitler, Proc. Roy. Soc. (London) **A146**, 83 (1934).
[18] W. Heitler, *The Quantum Theory of Radiation* (Oxford University Press, London, 1954), third edition, Chap. V, Sec. 25.
[19] F. Sauter, Ann. Physik **20**, 404 (1934).

TABLE III. The S^{35} external bremsstrahlung photon spectra $S(k)_{calc}$ for stopping the β particles in C, Al, Cu, Ag, and Pb, calculated according to the theory of Sommerfeld and Elwert (on multiplication by 10^{-5} the figures give the number of photons per Mev per disintegration) and $R=S(k)_{exp}/S(k)_{calc}$, the ratio between the experimental and the calculated values.

Energy kev	Carbon $S(k)_{calc}$	R	Aluminum $S(k)_{calc}$	R	Copper $S(k)_{calc}$	R	Silver $S(k)_{calc}$	R	Lead $S(k)_{calc}$	R
30.7	666	0.92	1910	1.06	5050	1.19	9030	...	17300	...
51.1	172	0.91	486	1.17	1370	1.33	2480	1.36	4740	1.38
71.5	46.1	0.89	140	1.28	405	1.48	754	1.59	1470	2.13
92.0	11.7	...	34.9	1.34	102	1.78	202	2.0	408	2.7
112.4	2.24	...	7.43	...	24.2	...	48.1	1.9	90.2	2.8

the energy between k and $k+dk$ when it is accelerated in the field of the nucleus.

From Sommerfeld's theory,[20] Elwert[21] deduced a correction factor $f(\xi_0,\xi)$ which makes it possible to use the expression $\phi(W_e,k)$ as given by Bethe and Heitler also in the nonrelativistic case.

$$f(\xi_0,\xi)=\frac{\xi}{\xi_0}\frac{1-e^{-2\pi\xi_0}}{1-e^{-2\pi\xi}}, \tag{2}$$

where $\xi=Ze^2/\hbar v$ and v is the velocity of the electron. The symbols ξ_0 and ξ refer to the electron in the initial and the final state, respectively. When ξ is of the order of unity the expression 2 takes the form $f(\xi_0,\xi)=\xi/\xi_0$.

Numerical calculations by Kirkpatrick and Wiedmann[22] confirmed the result obtained by Elwert.

In the present calculations only the EB from the field of the nucleus was treated. As to the bremsstrahlung originating from the field of the atomic electrons, no calculations are available in the nonrelativistic case. The screening of the Coulomb field by the atomic electrons can be neglected as far as S^{35} betas are concerned.

For the spectral distribution, $n(k,W_e)$, of the EB, emitted when an electron of the energy W_e is stopped in matter, Bethe and Heitler gave the expression

$$n(k,W_e)=\int_{mc^2+k}^{W_e}\frac{N\cdot\phi(k,W)dW}{-(dW/dX)}, \tag{3}$$

where N is the number of atoms per cm^3 and $-dW/dX$ the energy loss per cm, here calculated according to Aron *et al.*[23] The values of the mean excitation potentials were taken from Segrè.[24]

The spectral distribution $S(k)$ of the EB, obtained when the β particles from S^{35} are stopped, is given by

$$S(k)=\int_{mc^2+k}^{W_0}n(k,W_e)P(W_e,Z)dW_e. \tag{4}$$

In Fig. 6 and Table III the values of $S(k)$ for C, Al, Cu, Ag, and Pb are given as number of photons per Mev per β disintegration *vs* energy. The experimental values for the different elements are presented in the same figure. For the experimental points for which no limits of error are given, the limits lie within the symbols.

Good agreement was found between the experimental and the theoretical values for carbon. For aluminum, however, the experimental values at high energies tended to exceed the theoretical curve, but still lay within the limits of error. For copper and silver the experimental values above about 50 kev deviated widely from the theoretical. For lead the experiments gave considerably higher values than did theory. As far as this element is concerned, however, it should be pointed out that no correction was made for the K x-rays.

ACKNOWLEDGMENTS

We wish to express our sincere gratitude to Dr. K. Lidén, not only for proposing the subject, but also for untiring encouragement and guidance throughout the investigation. Thanks are due to Professor S. von Friesen for interest and generous support and to Professor B. Edlén for placing the facilities of the Department of Physics at our disposal. Acknowledgment is due to Dr. S. B. Nilsson for kind assistance with the theoretical aspects of internal bremsstrahlung and for permitting us to use his preliminary results, and to Dr. S. A. E. Johansson for comments on the manuscript.

[20] A. Sommerfeld, *Atombau und Spektrallinien* (Friedr. Vieweg und Sohn, Braunschweig, 1951), second edition, Vol. II, Chap. 7.
[21] G. Elwert, Ann. Physik **34**, 178 (1939).
[22] P. Kirkpatrick and L. Wiedmann, Phys. Rev. **67**, 321 (1945).
[23] Aron, Hoffman, and Williams, Atomic Energy Commission Report AECU-663, May 28, 1951 (unpublished).
[24] E. Segrè, *Experimental Nuclear Physics* (John Wiley and Sons, Inc., New York, 1953), Vol. 1, p. 203.

Energy Levels of Rh^{103} from the Decay of Pd^{103} and Ru^{103}†

BABULAL SARAF*
Bartol Research Foundation of The Franklin Institute, Swarthmore, Pennsylvania
(Received October 26, 1954)

The decay schemes of Pd^{103} and Ru^{103} have been studied with the use of two scintillation spectrometers in coincidence. It has been observed that the electron capture activity of Pd^{103} is accompanied by faint γ radiation having the several quantum energies of 40, 65, 300, 365, and 495 kev with absolute intensities per disintegration of 1×10^{-3}, 4×10^{-5}, 1.2×10^{-4}, 6.6×10^{-4}, and 1×10^{-4}. The gamma rays of energy 65 and 300 kev were found to be in coincidence. The inner bremsstrahlung spectrum associated with the capture transition leading to the 57-minute isomeric level in Rh^{103} is of intensity small in comparison with that of the aforementioned gamma rays. The β decay of Ru^{103} is accompanied by gamma rays of energies 55, 440, 495, 555, and 610 kev with absolute intensities per disintegration of 1×10^{-2}, 5×10^{-3}, 0.90, 5×10^{-3}, and 6×10^{-2}. A β spectrum of end point 110 ± 10 kev is coincident with the 610-kev gamma ray. A level scheme for Rh^{103} with probable orbitals has been proposed.

INTRODUCTION

PREVIOUS investigations[1,2] have indicated that Pd^{103} decays by electron capture only to the isomeric state at 40 kev in Rh^{103}. No unconverted quantum radiations were observed. Recently, in an attempt to study the inner bremsstrahlung of the electron capture process, Rietjens, Van Den Bold, and Endt[3] have reported low-intensity gamma quanta (the absolute intensities per disintegration are indicated parenthetically) of energies 503 kev (1.1×10^{-4}), 367 kev (6.0×10^{-4}), 305 kev (1.1×10^{-4}), and 262 kev ($\sim4\times10^{-5}$). By an argument based upon the calculated intensity of the quantum continuum, they estimated the disintegration energy of the electron capture process to be 494_{-12}^{+27} kev. Since Ru^{103} also decays to Rh^{103}, a comparison of the energy levels excited in Rh^{103} with those excited in decay of Pd^{103} should be possible. The gamma rays of Ru^{103} have been extensively investigated previously,[2,4-7] the various sets of results agreeing poorly. Accordingly, the decay schemes of these two radionuclides having a common residual nucleus have been reinvestigated.

PALLADIUM 103

The natural abundance of Pd^{102} is 0.8 percent. An electromagnetically enriched (34 percent) sample of 200 mg of metallic palladium was obtained from Oak Ridge and exposed for 15 days in the Brookhaven reactor. The irradiated material was chemically purified for removal of any rhodium or silver activities. Finally, palladium was precipitated from an alkaline solution by addition of di-methyl glyoxine. In this manner, a pure source of Pd^{103} of strength nearly five millicuries was obtained.

In order to observe any gamma rays or inner bremsstrahlung of low intensity, it was necessary to absorb before the detector the intense 20-kev x-rays of rhodium which accompany K-capture. The gamma-ray spectrum of Pd^{103} as measured with an intervening absorber of surface density 375 mg/cm² of copper between source and detector, is shown in Fig. 1. The full energy peaks of gamma rays of energies 40, 65, 300, 365, and 495 kev are clearly resolved. In the previously mentioned investigation[3] of this activity, the 65-kev radiation appears to have been heavily attenuated in a 1.7-g/cm² thick brass absorber introduced to suppress the intense K x-radiation, and so is undetected.

The bulk of the low-energy pulses of Fig. 1 below 20 volts could not be accounted for as Compton contributions of the high-energy gamma rays. An analysis

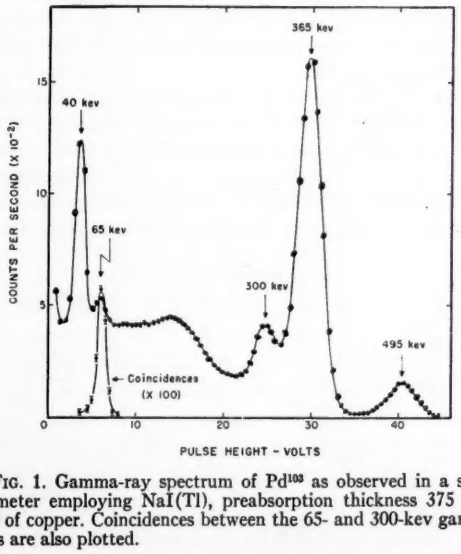

FIG. 1. Gamma-ray spectrum of Pd^{103} as observed in a spectrometer employing NaI(Tl), preabsorption thickness 375 mg/cm² of copper. Coincidences between the 65- and 300-kev gamma rays are also plotted.

† Assisted by the Joint Program of the Office of Naval Research and the U. S. Atomic Energy Commission.
* Research Fellow, Bartol Research Foundation; on leave of absence from Agra College, Agra, India; now at Nobel Institute of Physics, Stockholm, Sweden.
[1] D. E. Matthews and M. L. Pool, Phys. Rev. **72**, 163 (1947).
[2] Mei, Huddleston, and Mitchell, Phys. Rev. **79**, 429 (1950).
[3] Rietjens, Van Den Bold, and Endt, Physica **20**, 107 (1954).
[4] C. E. Mandeville and E. Shapiro, Phys. Rev. **77**, 439 (1950).
[5] E. Kondaiah, Phys. Rev. **79**, 891 (1950); *M. Siegbahn Commemoration Volume*, p. 442 (Uppsala, 1951).
[6] Cork, LeBlanc, Nester, and Stumpf, Phys. Rev. **86**, 575 (1952).
[7] F. K. McGowan, Oak Ridge National Laboratory Report ORNL-952, March, 1951 (unpublished).

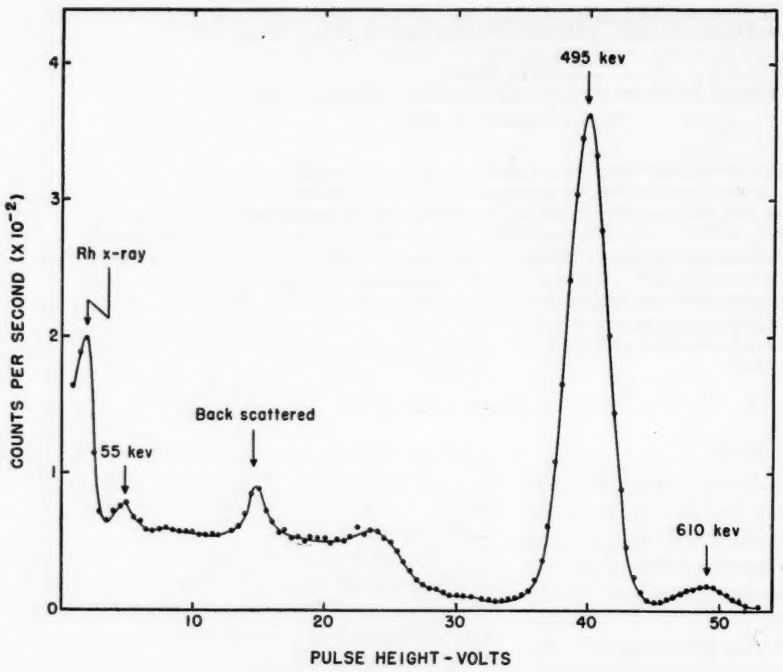

FIG. 2. Gamma-ray spectrum of Ru^{103}.

of the spectrum showed that a gamma-ray continuum of low intensity is partially obscured by the Compton distributions. In addition, the analysis exhibited also the possible presence of a photopeak corresponding to a quantum energy of ~260 kev.[3] This treatment of the data was not so reliable as to yield quantitative information concerning the actual shape of the gamma-ray continuum. However, there was definite indication that the spectral intensity at low energies is considerably greater than that suggested by the early theory of Morrison and Schiff.[8] The spectrum was observed over a period of three months, during which time no significant change in the relative intensities of the various gamma rays was noted.

By a coincidence study, the gamma rays of energies 65 and 300 kev were found to be in cascade. At the lower left of Fig. 1, at a pulse height of 6 volts, a peak corresponding to a gamma-ray energy of 65 kev is present. This photopeak in the coincidence rate was observed by fixing the channel of one spectrometer at 300 kev and scanning the low-energy region with the moving channel of the other spectrometer. No coincidences between any other two gamma rays of the spectrum were detected.

TABLE I. Gamma rays of Pd^{103}.

Probable electron capture transition Energy (kev)	Transition intensity per disintegration	Log *ft*	Associated gamma-ray energy (kev)	Gamma-ray intensity per disintegration
	$(1.0\pm0.2)\times10^{-4}$		495 ± 5	1×10^{-4}
ϵ~185	$(7\pm1)\times10^{-4}$	7.9 ± 0.2	365 ± 5	$(6.6\pm1)\times10^{-4}$
			65 ± 3	$(0.4\pm0.1)\times10^{-4}$
ϵ~250	$\sim0.8\times10^{-4}$	9.2 ± 0.2	300 ± 5	$(1.2\pm0.2)\times10^{-4}$
ϵ~510	0.999	5.7 ± 0.1	40	$\sim1\times10^{-3}$ (unconverted quanta)

The strength of the source of Pd^{103} was measured by counting the total number of x-rays emitted from the source in a solid angle of 3.75×10^{-3} steradian. The following factors were taken into account: (1) Self absorption in the source and absorption in 40 mg/cm² of Al of the crystal assembly; (2) Fluorescence yield of rhodium (0.8); (3) Total conversion coefficient and K/L ratio of the 40-kev radiation. It was further assumed that practically all of the capture transitions terminate at the 57-minute isomeric level in Rh^{103}. The absolute intensities of the gamma rays were estimated from the known thickness of the crystal, the total absorption coefficient for each gamma ray and the ratio for each gamma ray of the area under the full energy peak to the area under the Compton distribution and full energy peak combined. The absolute intensities per disintegration of the various gamma rays are given in Table I along with the associated electron capture transition intensities per disintegration and their respective values of log *ft*.

The experimental value of the half-life of the transition going to the 535-kev level is approximately 1.5×10^{10} seconds and to the isomeric level 1.47×10^{6} sec. According to Marshak's formula,[9] the mean life of an allowed electron capture transition varies inversely as the square of the decay energy. Thus, the

[8] P. Morrison and L. I. Schiff, Phys. Rev. 58, 24 (1940).

[9] R. E. Marshak, Phys. Rev. 61, 431 (1942).

decay energy of an allowed transition leading to the 535-kev level would be about one percent of the energy of the allowed transition to the metastable level. It is probable that the transition to the 535-kev level is indeed allowed. Were it first forbidden, a transition energy of about 100 kev would be necessary to explain the absolute intensity of the 495-kev radiation. Such a transition would in turn lead to an increased energy of the end point of the quantum continuum so that inner bremsstrahlung would be detectable beyond 500 kev, and also the valley between the photopeaks of the 365-kev and 495-kev gamma rays would be less prominent. Hence, in all probability, the electron capture transition to the 535-kev level is allowed.

RUTHENIUM 103

Chemically pure RuO_2 was exposed in the Brookhaven pile to produce the 43-day Ru^{103}. The irradiated material was aged for a month, then further purified for removal of impurities. RuO_4 was distilled from an acid solution in $HClO_4$. The gamma-ray spectrum of Ru^{103} was observed in a cylindrical crystal of NaI(Tl) of diameter 3.5 cm and height 3.5 cm. The data are shown in Fig. 2, where full energy peaks corresponding to quantum energies of 55, 495, and 610 kev are in evidence. A careful comparison in energy was made of the positions of the photopeaks of the 55-kev radiation and the 65-kev gamma rays of Pd^{103}. The difference in energy was found to be 10 ± 2 kev, indicating that two different transitions are involved.

To study beta-gamma coincidences, a thin source of Ru^{103} was placed before an anthracene crystal (dimensions 2.5 cm in diameter, 1 cm thick) which was covered by a reflecting aluminum foil of thickness 1.4 mg/cm² and attached to the photomultiplier tube surface with silicone fluid intervening. The gamma rays were detected in NaI(Tl). Curve *A* of Fig. 3 is a plot of the

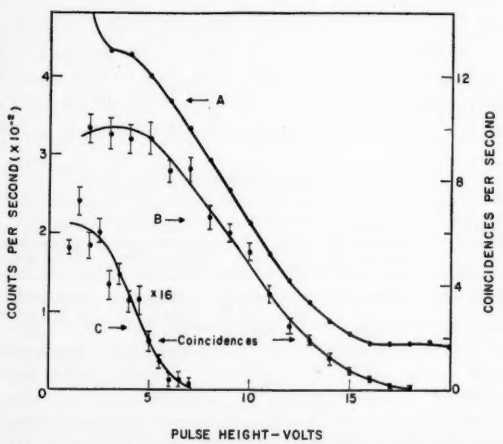

FIG. 3. Curve *A*, pulse-height spectrum in anthracene of an unshielded source of Ru^{103}. Curve *B*, spectrum of beta rays coincident with 495-kev gamma rays. Curve *C*, beta spectrum coincident with 610-kev gamma rays.

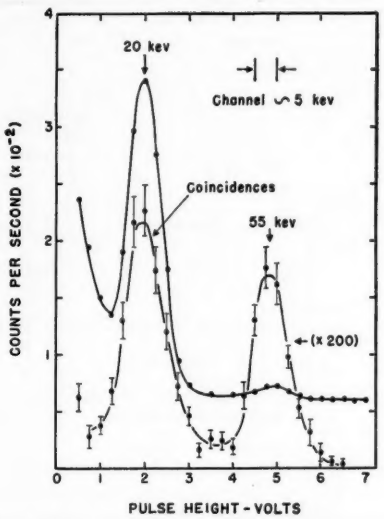

FIG. 4. Spectrum of soft gamma rays coincident with gamma rays of energy greater than 400 kev.

energy distribution of the beta rays of Ru^{103}. Some pulses arising from Compton scattering of the 495- and 610-kev quanta are contained in the spectrum. Beyond a pulse height of twenty volts, the counting rate is undoubtedly composed of both high-energy Compton recoils and hard beta rays from Ru^{103}. Curve *B* of Fig. 3 shows the energy distribution of the beta rays coincident with the 495-kev radiation and curve *C* that of beta rays coincident with the 610-kev gamma rays. Taking the end point of the intense spectrum (Curve *B*) coincident with the 495-kev radiation as 220 kev and taking into account the nonlinear nature of the energy dependence of the pulse heights from anthracene, the end point of the beta spectrum of curve *C* is estimated to be 110 ± 10 kev. This result has also been corrected for energy loss in the covering foil. A search was made for coincidences between the 55-kev radiation and the harder beta rays. From the measurements, it was estimated that at most five percent of the beta rays of the weak hard spectrum might be coincident with any unconverted 55-kev gamma radiation.

In order to determine the nature of the level in de-excitation of which the 55-kev radiation is emitted, gamma-gamma coincidences were studied. In one channel of the coincidence circuit, all pulses corresponding to gamma-ray energies greater than 400 kev were accepted while the channel of the other spectrometer was used to the spectrum at lower energies. A piece of copper, of surface density 1.5 g/cm², was placed before the high-energy detector to absorb any *K*-radiation of iodine which might escape to be detected in the low energy scanning channel and thus give rise to spurious coincidences at 30 kev. The coincidence spectrum obtained in this manner is shown in Fig. 4,

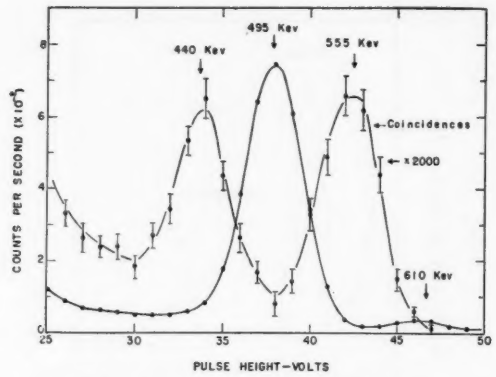

FIG. 5. Spectrum of gamma rays in coincidence with 55-kev radiation.

where a peak of coincidences clearly coincides with a peak at 55 kev in the single counting rate. The peak in the coincidence curve at 20 kev arises from the presence of x-rays of rhodium which result from internal conversion of the 55-kev radiation. A few of the pulses at 20 kev fall in the escape peak of the 55-kev radiation. After correcting for the absorption of the 20 kev and 55-kev radiation in the layer of Al_2O_3 in the crystal assembly and for escape of iodine x-rays[10] in detection of the 55-kev quanta, the K-conversion coefficient of the 55-kev gamma ray was calculated to be 1.2 ± 0.3, indicating a possible $M1$ transition. In similar manner, the coincidence spectrum of Fig. 5 was observed. In this case, pulses corresponding to a gamma-ray energy of 55 kev were accepted in one channel, and the high-energy gamma spectrum was scanned in the other channel. In Fig. 5 are shown coincidence peaks corresponding to gamma-ray energies of 440 and 555 kev. To obtain further assurance that the observed coincidences did indeed correspond to coincidences between the two hard gamma rays and the 55-kev radiation, a molybdenum foil of thickness 550 mg/cm² was placed between the source and the 55-kev detector. The coincidence rates at the peaks of Fig. 5 decreased by more than a factor of 10, as would be expected if the coincidences were actually associated with a 55-kev gamma ray.

Returning to the relative intensities of the gamma rays of Fig. 2, possible branching ratios of the various beta-ray spectra can be estimated, taking the absolute intensity of the 495-kev line as 0.9 per disintegration. The data concerning the β spectra are summarized in Table II.

McGowan[7] has reported gamma rays of energies 312 and 239 kev in Ru^{103}. No unconverted quantum radiations of these energies were detected in the present investigation, suggesting the possibility of presence of impurities in the target material of the earlier studies.[7]

[10] P. Axel, Rev. Sci. Instr. **25**, 391 (1954).

DECAY SCHEMES

The coincidence study of Pd^{103} showed that 65- and 300-kev gamma rays are in cascade. Since the 300-kev quanta are the more intense, it can be concluded that they are preceeded in time by the 65-kev transition. The 365-kev radiation is evidently emitted in the cross-over transition. From all of the previously described measurements, however, it is not possible to ascertain whether the 300 and 365-kev gamma rays terminate at the ground state or the isomeric level at 40 kev. In recent studies of Coulomb excitation of Rh, Heydenburg and Temmer[11] have observed gamma rays of energies 295 and 357 kev. In their measurements, the intensity of the 295-kev radiation is greater than that of the 357-kev line, whereas in the decay of Pd^{103}, the reverse is true. Thus, the two gamma rays cannot originate from the same level, further confirmation of the fact that the 300-kev radiation is preceded by the 65-kev gamma ray. The cross section for Coulomb excitation of the 300-kev gamma ray is such as to suggest that it results from de-excitation of the first rotational level of the ground state. Since the 365-kev radiation is emitted in the cross-over transition of the 65 kev–300 kev cascade, it can be concluded that both the 365-kev and the 300-kev transitions terminate at the ground state of Rh^{103}. A comparison of the energies of the gamma rays from Pd^{103} and from Ru^{103} shows that only the 495-kev gamma ray is emitted in the decay of both radionuclides. The intermediate levels at 300 and 365 kev are not excited in the decay of Ru^{103}.

It has been previously shown[5] that the 495-kev gamma transition of Ru^{103} leads to the 57-minute isomeric level of the residual nucleus so that a level in Rh^{103} is located at 535 kev above the ground state. The energy difference of the end points of the two β spectra, one of which is coincident with the 495-kev radiation and the other with the 610-kev quanta, (see Fig. 3) is 110 ± 10 kev, while the energy difference of the two gamma rays is 115 ± 5 kev, showing that the 610-kev transition must also lead to the isomeric level, originating from a level 650 kev above the ground state of Rh^{103}. From energy considerations, it is con-

TABLE II. Beta spectra and gamma rays of Ru^{103}.

β-ray energy (kev)	Transition intensity per disintegration	Log ft	Associated gamma-ray energy (kev)	Gamma ray intensity per disintegration
110 ± 10	0.07 ± 0.01	5.9 ± 0.2	610 ± 5	0.06 ± 0.01
			555 ± 10	0.005 ± 0.002
220	0.90	5.7 ± 0.1	495 ± 5	0.90
			440 ± 10	0.005 ± 0.002
670	10^{-3}	10.2	55 ± 3	0.005 ± 0.002
715	0.3	9.3	40	···

[11] N. P. Heydenburg and G. M. Temmer, Phys. Rev. **95**, 861 (1954). The author wishes to thank Dr. Heydenburg for supplying helpful information concerning the spin values of the rotational levels of Rh^{103}.

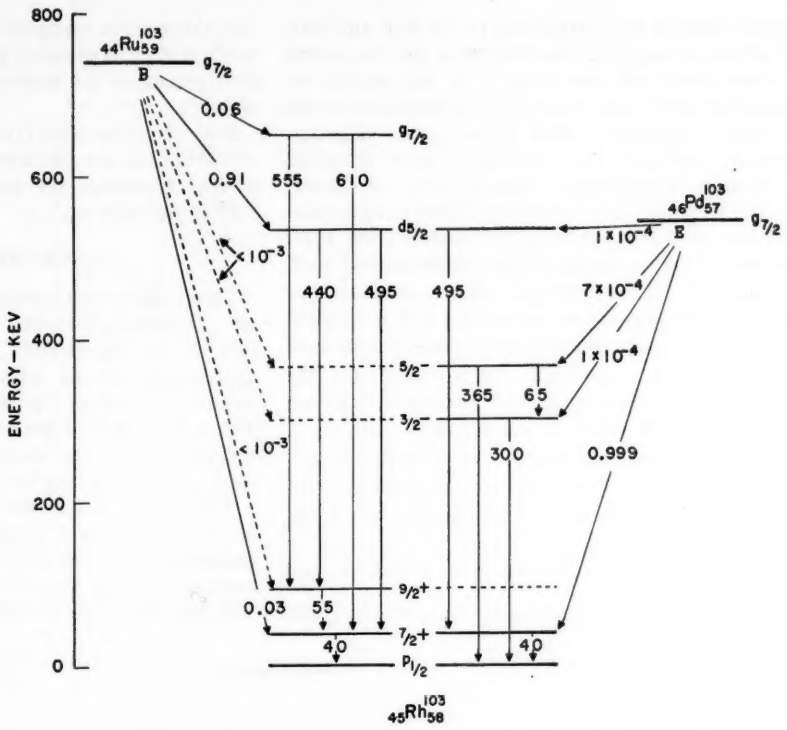

FIG. 6. Energy levels of Rh^{103}

cluded that the aforementioned 495- and 610-kev quanta are emitted in cross-over transitions of the 440 kev −55 kev and 555 kev −55 kev cascades. Thus, a level at 95 kev above the ground state is established.

The spin and magnetic moment of Rh^{103} have been measured.[12] The related orbital was thus determined to be $p_{1/2}$, in agreement with that indicated by the shell model. The 40-kev transition from the 57-minute isomeric level has been classified[13] as $E3$, the level assignment being 7/2+. Since the 55-kev gamma ray is probably emitted in an $M1$ transition; so possible spin values of the level at 95 kev are 5/2+ or 9/2+. The K-shell conversion coefficient of the 495-kev transition is 0.006, the K/L ratio 6.5, and the lifetime less than 2×10^{-9} sec, corresponding to an $M1$ or $E2$ transition[14] ($\Delta I=0, 1, 2$; no!). Thus possible spins for the 535-kev level are 3/2+, 5/2+, 7/2+, 9/2+, or 11/2+. The spin value 3/2+ is not admissible, because there exists no detectable $E1$ transition to the ground state. Since the ground state of Ru^{103} is, according to the shell model, of orbital $d_{5/2}$ or $g_{7/2}$, and since the beta transition between it and the 535 kev level is allowed, the spin of the latter level cannot be 11/2+. A spin of 9/2+ would require that the 7/2+ and 9/2+ configuration states of five $g_{9/2}$ protons have a splitting energy of 495 kev, an improbable condition. The remaining possible spin values for the 535-kev level are 5/2+ or 7/2+. If a purely single particle viewpoint is taken, the level would be characterized by orbitals $d_{5/2}$ or $g_{7/2}$. A similar argument is applicable to the 610-kev gamma transition of the 650-kev level so that its spin assignments could likewise be $d_{5/2}$ or $g_{7/2}$. From a careful consideration of the relative intensities of the 440- and 495-kev gamma rays and the 555- and 610-kev gamma rays, it was concluded that the most probable spin assignments of the 95, 535, and 650 kev levels are 9/2+, $d_{5/2}$, and $g_{7/2}$.

The levels at 300 and 365 kev, which have been interpreted[11] as rotational levels of the collective model of the nucleus, have spin values of 3/2(−) and 5/2(−). If these spin assignments are, indeed, correct, the transition from the 365 kev level to the 57-minute metastable level would be $E1$ and, consequently, prominent, if single particle transition probabilities were to apply. However, no such transition is observed in the present investigations. In the case of Ag, Huus and Lundén[11] have observed a similar $E1$ transition to have only one-fiftieth of the intensity of a competing $E2$ transition. It is further interesting that no observable transitions occur between the single-particle levels at 535 and 610 kev and the supposed rotational levels.

The nucleus of Ru^{103} contains 44 protons and 59 neutrons. According to the shell model, the odd neutron may occupy a $g_{7/2}$ or $d_{5/2}$ state. Either of these orbitals

[12] H. Kuhn and G. K. Woodgate, Proc. Roy. Soc. (London) A64, 1090 (1951).
[13] M. Goldhaber and R. D. Hill, Revs. Modern Phys. 24, 198 (1952).
[14] T. C. Engelder, Phys. Rev. 90, 259 (1953).

suggests allowed beta transitions to the 535- and 650-kev levels as observed. However, with the invocation of conventional selection rules, it is not possible to explain the large value of log *ft* of the transition to the 57-minute metastable level ($\Delta I=1$, no, allowed). Recently, De-Shalit and Goldhaber[15] have discussed the problem of anomalous values of log *ft* for allowed and first forbidden beta transitions. They have emphasized the possible influence of the nuclear core. Their explanation can be applied if the ground state of Ru^{103} is assumed to have orbital $g_{7/2}$. In that event, one or more pairs of neutrons of orbital $d_{5/2}$ will be present in the ground state configuration of Ru^{103}. The most probable configuration would be $g_{7/2}^7\ d_{5/2}^2$. On the other hand, the effect of the $g_{9/2}$ protons of Rh^{103} on the isomeric and 95-kev levels would be such as to make the neutron configuration of those levels $g_{7/2}^8\ d_{5/2}^0$. According to De-Shalit and Goldhaber,[15] the beta transitions would be further slowed by the change of orbitals ($d_{5/2}\rightarrow g_{7/2}$) experienced by one pair of neutrons. From these considerations, it can be said that the neutron configuration of the 535- and 650-kev levels of Rh^{103} is probably $g_{7/2}^6\ d_{5/2}^2$, very similar to the arrangement of the neutron pairs of the ground state of Ru^{103}.

Since the value of log *ft* for the electron capture decay of Pd^{103} to the isomeric level of Rh^{103} corresponds to an allowed transition, the ground state configuration of Pd^{103} is probably $g_{7/2}^7$.

[15] A. De-Shalit and M. Goldhaber, Phys. Rev. **92**, 1211 (1953).

ACKNOWLEDGMENT

The author wishes to acknowledge the kind assistance of C. E. Mandeville both in discussions and in preparation of the manuscript. He wishes also to express appreciation for the continued interest of W. F. G. Swann, Director of the Bartol Research Foundation. The author is also grateful to the Bartol Research Foundation for the award of the fellowship which made possible his stay in the United States.

The author desires also to express his gratitude to N. K. Sethi of Agra College, Agra, India for his kind encouragement. The writer is indebted to the Government of India for award of a travel grant in connection with his visit to the United States.

PHYSICAL REVIEW VOLUME 97, NUMBER 3 FEBRUARY 1, 1955

High-Energy Gamma Rays from the Proton Bombardment of Fluorine*

G. K. Farney,† H. H. Givin,§ B. D. Kern, and T. M. Hahn‡
Department of Physics, University of Kentucky, Lexington, Kentucky

(Received August 19, 1954)

Resonances for emission of gamma rays of energy greater than 8 Mev in the reaction $F^{19}(p,\gamma)Ne^{20}$ have been measured for proton energies from 550 to 1450 kev using a thin target. Resonances were seen at 669, 874, 935, 980, 1090, 1280, 1320, 1355, 1380, and 1430 kev. The effect of false high-energy gamma-ray counts resulting from the nearly simultaneous detection of two 6–7 Mev gamma rays in the reaction $F^{19}(p,\alpha\gamma)O^{16}$ was noted and a method for correcting for this effect was devised. The intensities of gamma rays for the two reactions were compared at each resonance. Also, the angular distribution of the 12-Mev gamma rays emitted at the 669-kev (p,γ) resonance was measured and found to be isotropic to within two percent probable error.

INTRODUCTION

RESONANCES for the emission of 6.1-, 6.9-, and 7.1-Mev gamma rays from the proton bombardment of fluorine in the reaction $F^{19}(p,\alpha\gamma)O^{16}$ are well known.[1] It is also known that at 669-kev proton bombarding energy the compound nucleus Ne^{20*} can decay by alpha-particle emission to O^{16*} and also by gamma-ray emission to the 1.63-Mev level in Ne^{20}. The energy of this gamma ray has been measured to be about 12 Mev.[2,3] It was the purpose of this experiment to look for other resonances for emission of gamma rays of energy greater than 8 Mev, indicating a transition to some lower energy state of Ne^{20}.

The angular distribution with respect to the proton beam of the 12-Mev gamma rays emitted at the 669-kev (p,γ) resonance in fluorine has been measured by using two Geiger counters in an absorption-coincidence measurement.[4] The distribution was found to be isotropic within ten percent. In the present work,

* Sponsored by the Office of Ordnance Research, U. S. Army.
† Now at Bell Telephone Laboratories, Murray Hill, New Jersey.
‡ Now at Virginia Polytechnic Institute, Blacksburg, Virginia.
§ Now at International Business Machines Corporation, Louisville, Kentucky.
[1] F. Ajzenberg and T. Lauritsen, Revs. Modern Phys. **24**, 321 (1952).
[2] Rae, Rutherglen, and Smith, Proc. Phys. Soc. (London) **A63**, 775 (1950).
[3] J. H. Carver and D. H. Wilkinson, Proc. Phys. Soc. (London) **A64**, 199 (1951).
[4] S. Devons and H. G. Hereward, Nature **162**, 331 (1948).

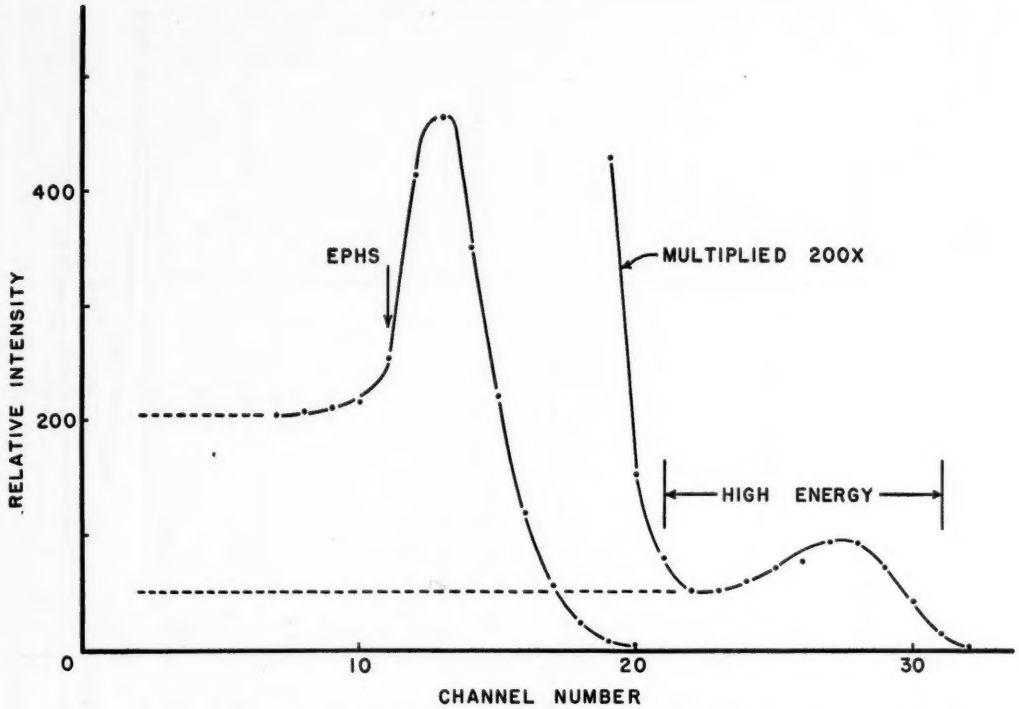

FIG. 1. Spectrum of the gamma rays from proton bombardment of fluorine at the proton energy of 669 kev.

measurements have been made to reduce the uncertainty in the isotropy.

EXPERIMENTAL PROCEDURE

Yield Curves

Protons were accelerated from 550 to 1450 kev using the University of Kentucky electrostatic accelerator. The energy resolution was adjusted to ±0.25 percent for this experiment, and beam currents from 0.5 to 5.0 microamperes were used.

The gamma-ray detector was a scintillation counter composed of a Du Mont 6292 photomultiplier tube and a 1 in.×1½ in. NaI(Tl) crystal enclosed in a thin aluminum casing and surrounded by magnesium oxide. The pulse-height spectrum from the detector was analyzed by a twenty-channel pulse-height analyzer.[5]

When obtaining the yield curves for gamma rays, the voltage on the photomultiplier tube and the gain of the amplifier in the pulse-height analyzer were adjusted so that pulses resulting from the 6–7 Mev gamma rays and from gamma rays of higher energy were simultaneously observed. In this work, 6–7 Mev gamma rays are referred to as low-energy gamma rays, and gamma rays of energy greater than 8 Mev are referred to as high-energy gamma rays. Figure 1 shows a typical pulse-height spectrum obtained with proton bombarding energy of 669 kev. The shape of this spectrum is in agreement with other high-energy gamma-ray measurements and with theoretical predictions.[6] The twenty channels were positioned so that the peak of the pulse-height spectrum from the low-energy gamma rays appeared in the first five channels and the peak from the high-energy gamma rays appeared in the last ten channels. The arrow designated EPHS in Fig. 1 marks the position of channel one.

The ordinate used for plotting the high-energy yield curve was obtained by adding all counts that appeared in the last ten channels; the ordinate used for plotting the low-energy yield curve was obtained from the total count scaler. This included the yield of high-energy gamma rays; but, at most, this never exceeded a two percent addition and in no way appreciably effected the results. It was necessary to do this because the high yield of 6–7-Mev gamma rays caused the mechanical registers in some of the individual-channel "scale of sixteen" scalers to lose counts. The total count scaler is a "scale of 256" circuit and was able to record all pulses.

Figure 2 shows the yield curve obtained for the low- and high-energy gamma rays obtained from a target made by evaporating sodium fluoride upon tantalum backing. The target was twenty kilovolts thick at the 874-kev ($p\alpha\gamma$) resonance in fluorine. The presence of the sodium made the analysis of the fluorine yield

[5] A. B. Van Rennes, Nucleonics **10**, 32 (1952).

[6] J. G. Campbell and A. J. F. Boyle, Australian J. Phys. **6**, 171 (1953).

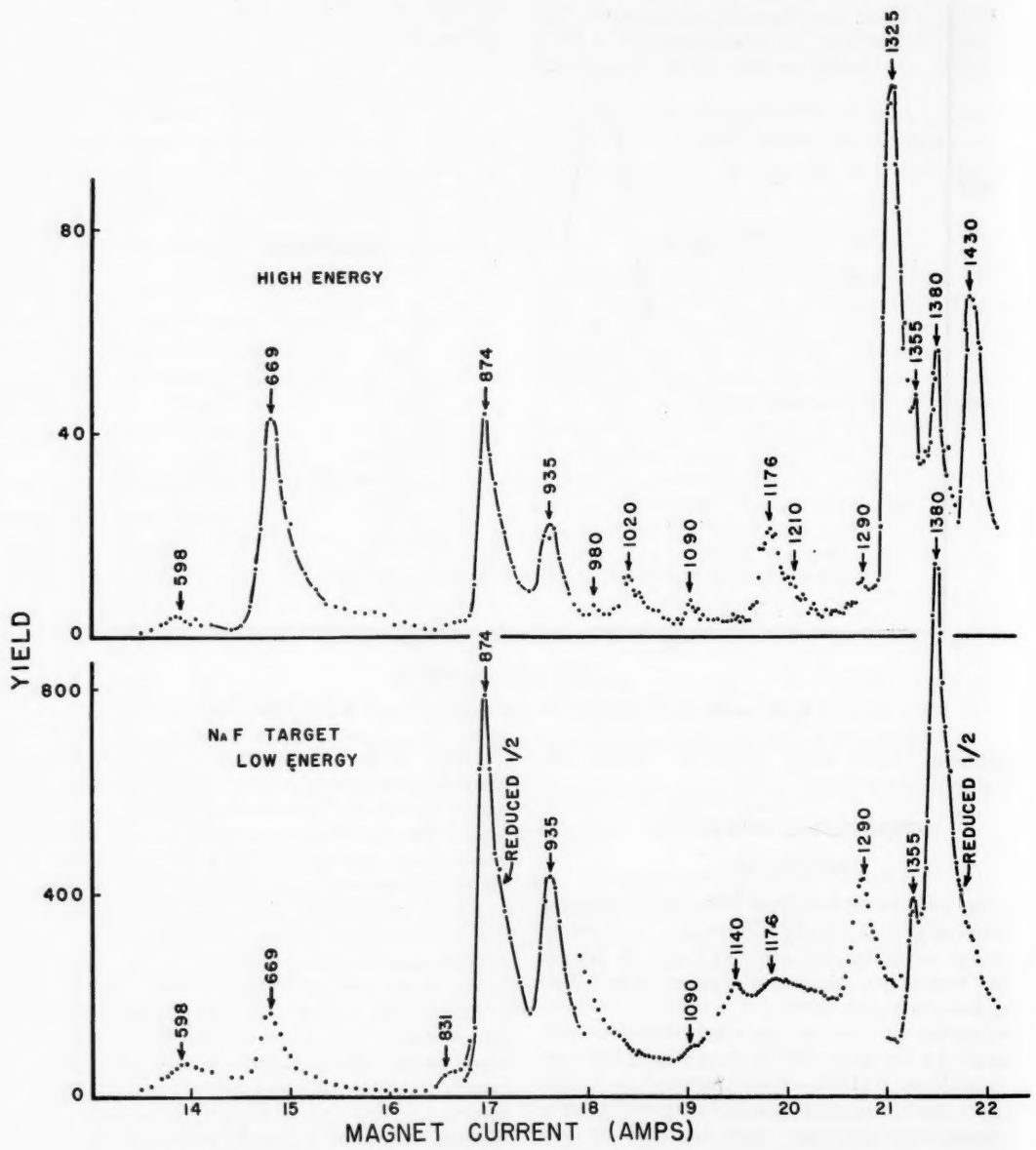

FIG. 2. Gamma-ray yield from proton bombardment of a sodium fluoride target. The high-energy yield has not been corrected for the effect of pile-up. The high-energy ordinate is in units of 16 counts and the low-energy ordinate in units of 256 counts.

difficult, but made possible qualitative confirmation of some of the recently reported work on (p,γ) resonances in sodium.[7]

A second target free of sodium was prepared by etching the surface of a piece of tantalum with hydrofluoric acid. Figure 3 shows the yield curve obtained using this target which was about fifteen kilovolts thick at the 874-kev $(p,\alpha\gamma)$ resonance in fluorine.

While obtaining these yield curves for low- and high-energy gamma rays, it was noted that the number of counts that appeared in the high-energy channels varied with the beam current even though the proton energy remained constant. Closer inspection of this phenomenon showed that the effect was caused by two 6–7 Mev gamma rays causing scintillations in the sodium iodide crystal so close together in time that the two individual output pulses partly overlapped. The resultant output pulse appeared as the sum or

[7] Teener, Seagondollar, and Krone, Phys. Rev. 93, 1035 (1954).

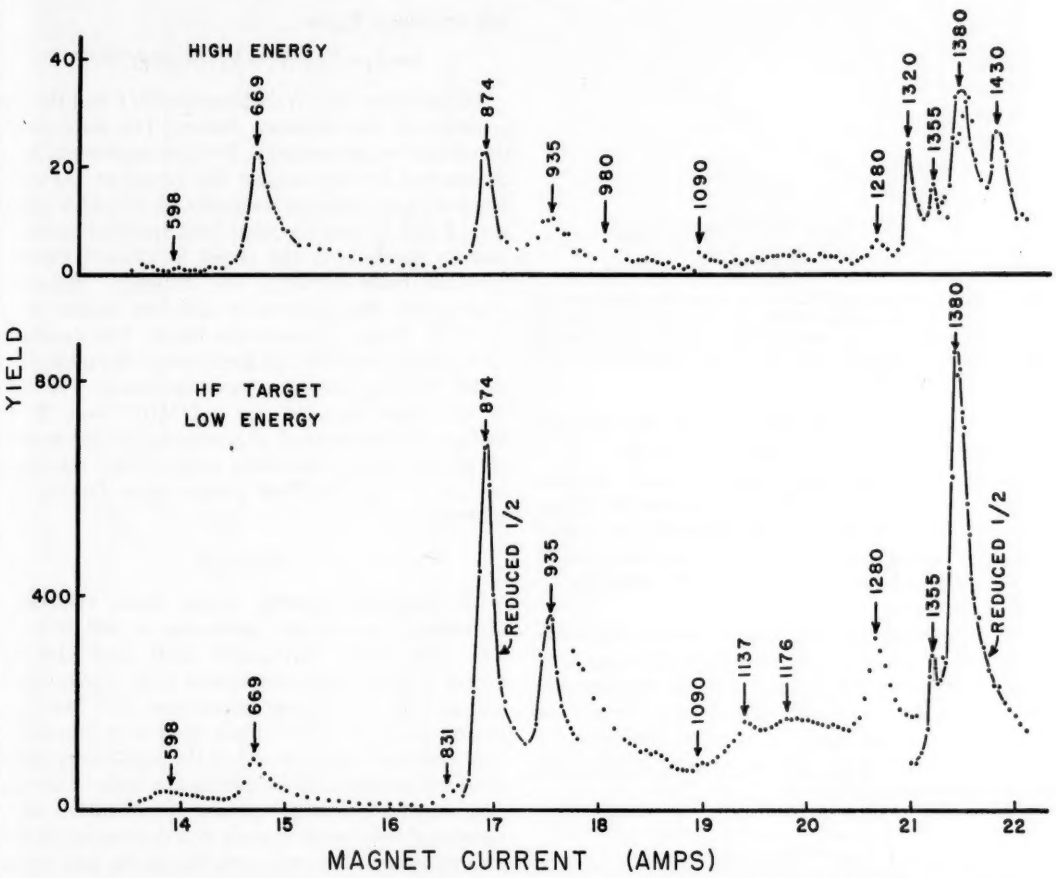

FIG. 3. Gamma-ray yield from proton bombardment of a tantalum fluoride target. The high-energy yield has not yet been corrected for the effect of pile-up. The high-energy ordinate is in units of 16 counts and the low-energy ordinate in units of 256 counts.

partial sum of the two pulses. The analyzer recorded the peak of the resultant pulse and hence a false high-energy count was recorded. This effect is called *pile-up*. A method of correcting for this effect has been devised.

Angular Distribution

The angular distribution of high-energy gamma rays at the 669-kev resonance was obtained by using the previously described scintillation counter, a linear amplifier, and a scaler. The discriminator on the scaler was adjusted to count only pulses from the high-energy gamma rays. No difficulty was experienced here from pile-up.

The detector was placed with the crystal face 7 cm from the target and was rotated in a horizontal plane about an axis through the target and perpendicular to the beam. The yield of gamma rays was measured with the plane of the target making angles of both $+45°$ and $-45°$ with respect to the proton beam. The yield was observed at angles of 0° and 45°, 90° and 135° on either side of the proton beam. This permitted experimental correction for absorption of gamma rays in the 5-mil tantalum target-backing. The angular distribution was found to be isotropic within two percent, after correction for finite solid angle.[8]

PILE-UP CORRECTION

Bateman[9] has shown that for radioactive decay processes the probability that n events will occur in any given time interval t is given by $x^n e^{-x}/n!$. Here x is the average number of events occurring in the time interval considered and is given by at, where a is the average counting rate. From this, then, the probability that no events will occur in a time interval t is e^{-at}. However the probability that an event will occur in a time interval δt is given by $a\delta t$. The probability that an event will not occur for some time interval t but will occur in a time δt immediately following t is given by $e^{-at}a\delta t$. If a total of n_t events are observed, then the

[8] M. E. Rose, Phys. Rev. **91**, 610 (1953).
[9] H. H. Bateman, Phil. Mag. **20**, 704 (1910).

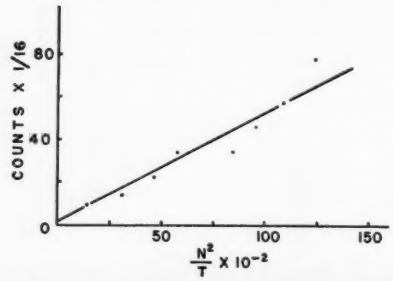

FIG. 4. Pile-up counts *vs* N^2/T for the proton bombardment of fluorine at the proton energy of 874 kev. N is the total yield in units of 256 counts and T is the counting time. The experimental arrangement is the same as that used when obtaining the yield curves of Fig. 2 and Fig. 3.

expected number that will fall within a time between t and $t+\delta t$ after a previous event is $n_t e^{-at} a\delta t$.

This result predicts that small intervals between events are more likely regardless of the counting rate a. This result has been checked experimentally by several authors,[10,11] and it is for this reason that reduction of the beam current did not completely eliminate pile-up in this experiment.

This expression, however, can be used to calculate the number of gamma-ray counts that will occur close enough together in time to cause pile-up. Suppose that scintillations must occur separated by a time t' or less for the leading edges to overlap sufficiently to cause pile-up. The total number of counts that meet this requirement is

$$N_p=\int_0^{t'} n_t e^{-at} a dt = n_t(1-e^{-at'}).$$

The design of the pulse-height analyzer requires that t' be something less than a microsecond. Also the experiment was performed holding a to some value less than 500 counts per second. Hence the above expression may be approximated by

$$N_p=n_t a t'.$$

The value of a will be given very nearly by n_t/T, where n_t is the total number of scintillations occurring in the sodium iodide crystal during the time of observation T. However in this experiment the total number of scintillations n_t was not detected but only some fraction of that total. Since the pulse spectrum has a definite shape, then the total number of scintillations n_t can be obtained from the observed total count N by multiplying by some constant s, or $n_t=sN$. Substituting for a and n_t we have $N_p=s^2N^2t'/T$.

The total number of counts k that appear in the high-energy channels will be composed of the true high-energy counts N_t, background counts N_b, and pile-up counts N_p, or

$$k=N_t+N_b+N_p=N_t+N_b+s^2t'N^2/T.$$

The equation for $k-N_b$ is linear in N^2/T and the slope contains all the unknown factors. The slope can be determined experimentally. For this experiment it was determined by bombarding the target at the strong 874-kev $(p,\alpha\gamma)$ fluorine resonance for 6–7-Mev gamma rays. k and N were recorded for a specified number of protons incident on the target for several values of constant beam current. The resultant high-energy counts were then plotted as ordinates against values of N^2/T. Figure 4 shows the result. The number of background counts in the high-energy channels was so small that no correction was necessary. The value of the slope obtained was 1.24×10^{-6} second. The validity of this method of correcting for the presence of pile-up counts has been satisfactorily established by use of the 0.61-Mev gamma rays from a Cs^{137} source.

RESULTS

The tantalum fluoride target shows evidence of high-energy gamma-ray resonances at 669, 874, 935, 980, 1090, 1280, 1320, 1355, 1380, and 1430 kev. Figure 5 shows these resonances after corrections for pile-up. At the strong resonances for low-energy gamma rays, the effect of pile-up is very pronounced.

A measure of the intensity of the high-energy gamma rays was obtained by comparing the ratio of the peak number of high-energy gamma rays emitted to the number of low-energy gamma rays emitted at the same proton energy. This was done by taking into account the predicted shape of the spectra[6] and the fact that only a portion of it was observed. The results are shown in Table I. At the 874-kev resonance, the value of 0.03 ± 0.01 percent given in the table is in good agreement with an earlier determination[12] of the ratio as having an upper limit of 0.05 percent. The resonances at 1090, 1320, and 1430 kev are in agreement with results published during the course of this experiment.[13]

TABLE I. Intensity ratios. The intensity of the high-energy gamma rays from $F^{19}(p,\gamma)Ne^{20}$ is compared to the intensity of the low-energy gamma rays from $F^{19}(p,\alpha\gamma)O^{16}$ at the corresponding energy.

E_p(kev)	Intensity ratio (percent)
669	1.80 ± 0.36
874	0.03 ± 0.01
935	0.03 ± 0.01
980	0.22 ± 0.04
1090	0.34 ± 0.07
1280	0.06 ± 0.01
1320	0.90 ± 0.18
1355	0.12 ± 0.02
1380	0.08 ± 0.02
1430	0.35 ± 0.07

[10] E. Marsden and T. Barrat, Proc. Roy. Soc. (London) **23**, 367 (1911).
[11] E. Rutherford and H. Geiger, Phil. Mag. **20**, 698 (1910).
[12] D. H. Wilkinson and A. B. Clegg, Phil. Mag. **44**, 1322 (1953).
[13] R. M. Sinclair, Phys. Rev. **93**, 1082 (1954).

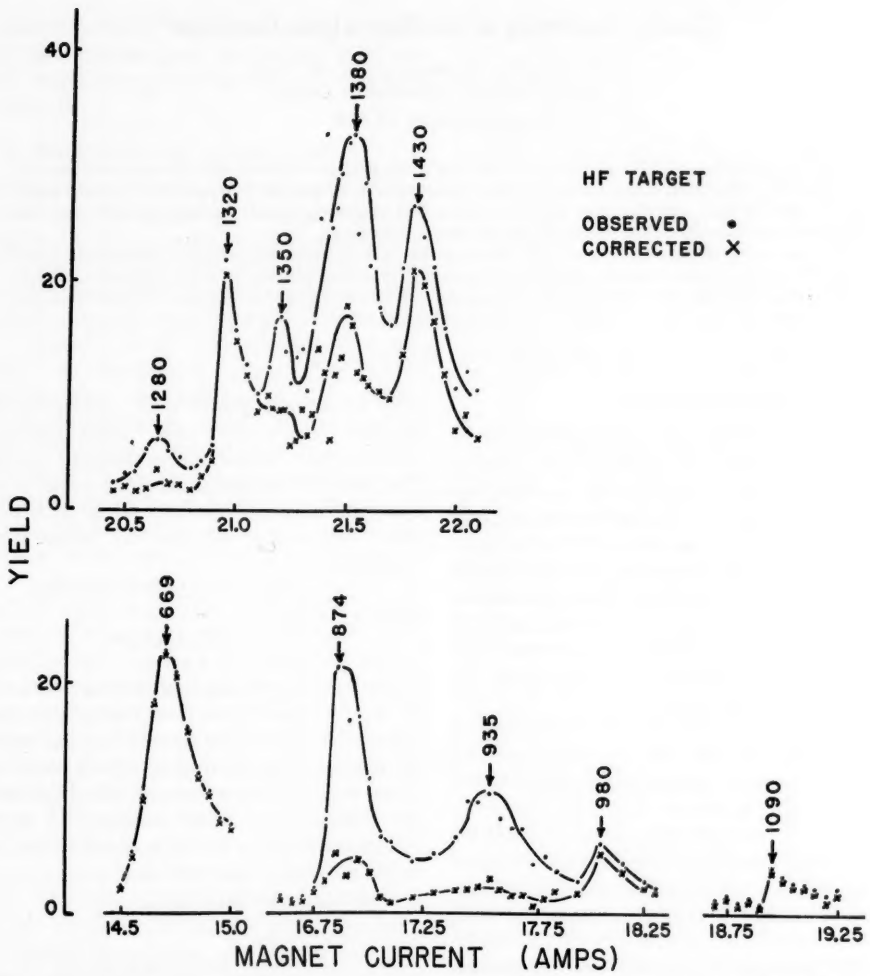

FIG. 5. Yield of high-energy gamma rays from proton bombardment of fluorine, corrected for the effect of pile-up.

The sodium fluoride target shows evidence of high-energy resonances at 598, 669, 874, 935, 980, 1020, 1090, 1176, 1210, 1290, 1325, 1355, 1380, and 1430 kev. The additional resonances may be attributed to (p,γ) resonances in sodium. Other work[7] has shown the existence of resonances in sodium for gamma-ray energies lying between 1.6 and 12 Mev; the present work shows the resonances for gamma-ray energies greater than 8 Mev.

ACKNOWLEDGMENTS

The authors wish to express their gratitude to K. Schneider and K. Ilens for their willing assistance in the construction of apparatus and to Mary E. Farney who assisted greatly in operating equipment and acquiring data.

Note added in proof.—It has been reported that in some scintillation counting arrangements there arise spurious high-energy pulses due to the presence of 5- to 7-Mev gamma rays, in addition to those high-energy pulses due to pile-up. To investigate this effect in the equipment described above, a thick Be^9 target was bombarded at various currents at a fixed proton beam energy. N was maintained constant, on the assumption that the number of spurious counts would be proportional to the number of gamma rays. The curve obtained upon plotting $k-N_b$ *vs* N^2/T is a straight line which extrapolates to the origin. A reasonable upper limit on the number of spurious counts gives an intensity ratio, as defined above, of slightly less than 0.01 percent. It is concluded that the intensity ratios given above are not altered by this effect.

Elastic Scattering of 22-Mev Alpha Particles*

N. S. WALL,† J. R. REES, AND K. W. FORD
Indiana University, Bloomington, Indiana
(Received October 15, 1954)

The elastic scattering of 22-Mev alpha particles from silver, gold, and lead has been measured as a function of angle. The differential cross section has been found to follow Rutherford's equation at forward angles but at some critical angle the cross section deviates, first increasing slightly for lead and gold and then decreasing monotonically. The silver distribution shows no increase.

The lead and gold data have been fitted with a modification of Blair's sharp angular momentum cut-off theory but there is no satisfactory agreement between theory and experiment for the silver data. Using this type of analysis one is able to find a nuclear radius that follows the $R=r_0A^{\frac{1}{3}}$ law with $r_0=1.5\times10^{-13}$ cm only if one assumes a large size, $\sim2.5\times10^{-13}$ cm, for the alpha particle.

I. INTRODUCTION

MANY of the earliest experiments which cast light on nuclear size employed alpha particles emitted from naturally radioactive elements and scattered by thin foils of various elements.[1] The angular distribution of scattered particles was compatible with the assumption of a small nucleus exerting a repulsive Coulomb force on the incident alpha particles. These experiments took place about 40 years ago, and the results were sufficient to establish Rutherford's atomic model and give some quantitative information concerning the nuclear radius and nuclear forces.[2]

Recently, interest has revived in the scattering of alpha particles, because with the cyclotron one can accelerate them to energies sufficient to approach heavy nuclei within the range of nuclear forces. Moreover, we have more intense beams and improved detectors of the scattered particles. Farwell and Wegner[3] have measured the energy dependence of elastic alpha-particle scattering for several elements of high atomic number using the 45-Mev alpha beam of the University of Washington cyclotron. The following experiments are complementary to their work in that we have scattered the same particles from some of the same nuclei and investigated the elastic angular distribution in about the same energy range.

To explain the results of Farwell and Wegner, Blair[4] has made simplifying assumptions concerning the interaction of the alpha particle and the target nucleus. When the apsidal distance of an alpha-particle's classical trajectory is greater than an "interaction radius," he assumes that the particle is elastically scattered with only a Coulomb phase shift, and when the apsidal distance is less than this "interaction radius," he assumes that the particle is absorbed by the nucleus. The coefficient η_l of the outgoing wave,[5,6] under these assumptions, is $e^{2i\sigma_l}$ for $l>l'$, where σ_l is the Coulomb phase shift, and is zero, for $l\leqslant l'$, where l' satisfies the equation,

$$l'(l'+1)=2mR^2\hbar^{-2}(E-E_c), \tag{1}$$

with

$$E_c=Zze^2R^{-1}; \tag{1'}$$

where l' is the orbital angular momentum of a particle of mass m and initial energy E; E_c is the Coulomb potential energy at the classical turning point; and R is the apsidal distance which is here set equal to the sum of the radii of the nucleus and the alpha particle. Ze is the charge of the target nucleus and ze that of the incident particle; both charge distributions are assumed to be spherically symmetrical.

Under these assumptions,

$$\frac{d\sigma}{d\Omega}=\left|\frac{e^{2i\sigma_0}}{2ik}\left\{\frac{-in}{\sin^2(\theta/2)}\exp(-in\ln\sin^2\tfrac{1}{2}\theta)-\sum_{l=0}^{l'}(2l+1)e^{2i(\sigma_l-\sigma_0)}P_l(\cos\theta)\right\}\right|^2. \tag{2}$$

The Coulomb phases are given by

$$e^{2i\sigma_l}=\Gamma(l+1+in)/\Gamma(l+1-in), \tag{3}$$

and

$$n=zZe^2/\hbar v. \tag{4}$$

The first term in this expression represents the scattering due to the Coulomb potential,[6] and the second term represents the interaction of the alpha particles with $l\leqslant l'$ according to Blair.[4] At small angles, $(\sin\frac{1}{2}\theta)^{-4}$ is large and the scattering is predominately Rutherford scattering unless l' is very large. For alpha

* This work was supported in part by a joint program of the U. S. Office of Naval Research and the U. S. Atomic Energy Commission.

† Now at the University of Rochester, Rochester 3, New York.

[1] In addition to the references on the early elastic scattering of alpha particles given in reference 3 there is a summary of this work in Rutherford, Chadwick, and Ellis, *Radiation from Radioactive Substances* (Cambridge University Press, London, 1930).

[2] A very complete series of experiments was conducted and interpreted by W. Riezler, Proc. Roy. Soc. (London) **134**, 154 (1932).

[3] G. W. Farwell and H. E. Wegner, Phys. Rev. **93**, 356 (1954) and Phys. Rev. **95**, 1212 (1954).

[4] J. S. Blair, Phys. Rev. **95**, 1218 (1954).

[5] We use the notation of reference 10 throughout this paper. The Coulomb scattering amplitude however is that given by reference 6.

[6] N. F. Mott and H. S. W. Massey, *The Theory of Atomic Collisions* (Oxford University Press, London, 1949), second edition, Chap. 3.

particles incident on heavy target nuclei with an initial energy of 22 Mev (the energy of the Indiana University alpha beam), n is found to be about 11, and l' should be less than about 10.

II. EXPERIMENTAL TECHNIQUES

The Indiana University cyclotron produces a 22-Mev alpha-particle beam which passes through a focusing magnet and an analyzing magnet and is brought to a focus on a target in the center of a 15-inch inside diameter scattering chamber associated with the 20-inch double focusing magnetic spectrometer.[7-9] A NaI(Tl) scintillation spectrometer for heavy particles has been incorporated into the scattering chamber. The crystal, photomultiplier tube, and preamplifier are mounted within the chamber on an arm which can be rotated in a horizontal plane about an axis passing vertically through the target. A Lucite disk, graduated along its circumference in degrees, is fastened rigidly to the axle of the rotating arm so that the angle of the scintillation counter relative to the beam can be measured with a sensitivity of $\frac{1}{4}$ degree.

In the earliest experiments a Du Mont 6291 multiplier phototube was mounted vertically on the arm with a suitable crystal holder; however, because of the limited dimensions of the scattering chamber and the size of the phototube, the defining aperture of the spectrometer did not move in a plane containing the target. This meant that the angle the spectrometer made with the beam was defined by both a horizontal angle and a vertical angle. We had some difficulty determining the vertical angle, and so, at a sacrifice in resolution, this detector was replaced with one employing a Du Mont type K-1211 miniature photomultiplier situated horizontally in the chamber and rotating in a plane intersecting the target. This counter was aligned vertically with the beam defining slit system by optical means. The resolution of the first detector was 3 percent (full width at half-maximum) for 22-Mev alpha particles elastically scattered from a thin lead target, while that of the second was 8 percent. The lower resolution was attributed to the slightly lower photocathode sensitivity of the K-1211 and to a more compact optical system which resulted in a nonuniform light collection.

The smaller tube made it possible to operate the counter at a smaller minimum angle and thus to show that the small-angle scattering follows the Rutherford formula.

After the installation of the small tube a solid-angle correction as a function of angle was found necessary. A thin thorium alpha-particle source was placed in the target position and the counter was rotated around it. The counting rate varied with the angular position of the counter. Then the source was rotated with the counter fixed and no variation in counting rate was observed. It was concluded that the discrepancy was due to a variation in the solid angle subtended at the source by the counter aperture. Evidently the axis of rotation of the counter did not pass through the center of the target position and the radial distance of the aperture from the source varied with rotation. The effect can be explained if it is assumed that the axis of rotation was displaced 0.1 inch from the center of the target. A plot of the effective solid angle correction as a function of angle is given in Fig. 1. The maximum variation over the range of angles used in these experiments is about 6 percent.

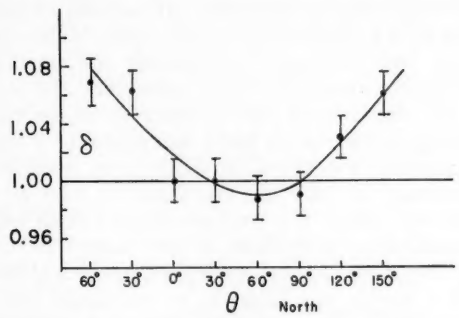

FIG. 1. The correction δ for the effective solid angle as a function of scattering angle.

The graduated Lucite disk was positioned arbitrarily on the axis, so it was necessary to determine, experimentally, what reading on the disk corresponded to an angle of zero degrees with respect to the incident beam. This was done by taking a portion of the angular distribution of elastically scattered particles at about 30 degrees on either side of the beam direction. The angles of equal scattered intensity were determined and from them the zero angle. We feel that this measurement is accurate to $\frac{1}{4}$ degree. Figure 1 shows that the effective solid angle is about 5 percent larger in the region of 30 degrees south than on the opposite side of zero; however, this introduces a systematic error of less than $\frac{1}{2}$ degree in the determination of the zero angle. The over-all accuracy of the angle determination then is well within 1 degree. The counter aperture was approximately 1 degree.

The electronic apparatus associated with the spectrometer consisted of a cathode-follower preamplifier mounted on the arm with the photomultiplier tube, an Atomic Instruments Company Model 204-B linear amplifier, a scaler, and power supplies. The high voltage for the photomultiplier was supplied by the Pittsburgh circuit[10] and was monitored by a potentiometer capable of detecting a change of 0.02 percent. This supply was built by Mr. O. E. Johnson of this laboratory.

[7] Rasmussen, Miller, Carmichael, and Sampson, Phys. Rev. 92, 852(A) (1953).
[8] F. E. Steigert, dissertation, Indiana University, 1953 (unpublished).
[9] B. M. Carmichael, dissertation, Indiana University, 1954 (unpublished).
[10] Progress Report, University of Pittsburgh (unpublished).

The experimental procedure was to count all pulses larger than 85 percent of the pulse height of the elastic group. This was done by adjusting the amplifier's amplitude discriminator to the desired level and counting the discriminator output. Since all of the nuclei investigated were rather heavy and yielded no inelastic groups near the energy of the elastic group, it was found unnecessary to vary the discrimination level as the angle was varied. The level was set at a pulse height corresponding to particles of the energy of those scattered through about 45 degrees, for each element. Such a setting was found to be sufficiently high to discriminate against any elastic alpha particles scattered into back angles by light-weight target contaminants such as carbon or oxygen. At forward angles such particles are only a small fraction of the Coulomb scattered intensity from the heavy nuclei and therefore can be neglected. By displaying the output of the amplifier on an oscilloscope screen and photographing it with a time exposure, the effect of such contaminants in the lead and gold targets was shown to be negligible at back angles. Since the intensity of the alpha-particles scattered by the silver target was quite low, it was difficult to distinguish between silver and contaminant scattering. Thus the silver data presented in Figs. 7 and 8 represent at worst an upper limit.

The cyclotron beam integrator was built and described in detail by Dr. B. M. Carmichael.[9]

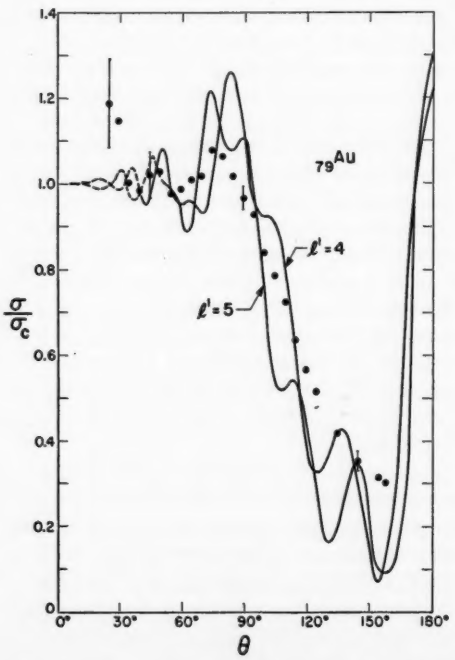

FIG. 2. Scattering of 22-Mev alpha particles by gold. Points are experimental. Curves are theoretical with sharp cut-off model. $n=10.6$.

The gold and silver targets used were commercially available thin foils. The lead target was prepared by evaporation in vacuum onto a thin film of Zapon.

III. RESULTS

The angular distributions of 22-Mev alpha particles elastically scattered from silver, gold, and lead are given in Figs. 2, 3 (Au); Fig. 4 (Pb); and Figs. 7 and 8 (Ag). The curves in these figures are theoretical, and are discussed in the next section. Figure 5(a) shows the lead and gold data alone. The data have been corrected for the variation in solid angle of acceptance mentioned in the preceding section and plotted in Fig. 1. The angular distribution curves have been normalized arbitrarily in the following manner: the product of the counting rate per unit of charge collected by the Faraday cage and $\sin^4(\frac{1}{2}\theta)$, where θ is the angle of deflection from the beam direction, has been set equal to 1.0 at the forward angles from about 30 degrees to 50 degrees.

The errors indicated in the figures are compounded from the statistical counting errors and errors due to an assumed $\frac{1}{2}$ degree error in the angular position of the counter. The over-all errors are thought to be the same as those indicated except at back angles where they may be somewhat higher due to target contaminants. (See Sec. II.) The data show some deviations from Rutherford scattering at forward angles, but they are not consistent from run to run; it is therefore felt that such discrepancies are purely experimental. The beam is collected in a Faraday cup which may leak charge to the counter framework at the most forward angles. Moreover, at the most forward angles the Coulomb differential cross section is so high that the beam intensity must be kept extremely low and the beam integration may not be accurate. The rise for Pb and Au in the vicinity of 90 degrees, however, is thought to be real inasmuch as it appeared, within one standard deviation for all the runs on these two elements.

The experimental data for Au and Pb show very similar behavior. The cross sections rise to about 10 percent above Coulomb at an angle of 80 to 90 degrees, then fall off smoothly, without any indication of a diffraction pattern, to about 30 percent of Coulomb at the largest angles measured.[11] The Ag cross section, which should be influenced by a larger number of partial waves, falls off at a smaller angle, and decreases smoothly to about 1 percent of Coulomb at 135 degrees. For Ag, the experimental errors are too great to detect a 10 percent rise of the cross section before the fall off.

According to Blair's interpretation, the angle corresponding to $\sigma/\sigma_c=\frac{1}{4}$ should give an apsidal distance in agreement with other indications of nuclear size. In these experiments only the silver data drops to $\sigma/\sigma_c=\frac{1}{4}$ and at this angle the interaction distance is calculated to be $(9.1\pm0.3)\times10^{-13}$ cm, in disagreement with

[11] Preliminary data taken at angles back to 167 degrees shows no increase in σ/σ_c for Au.

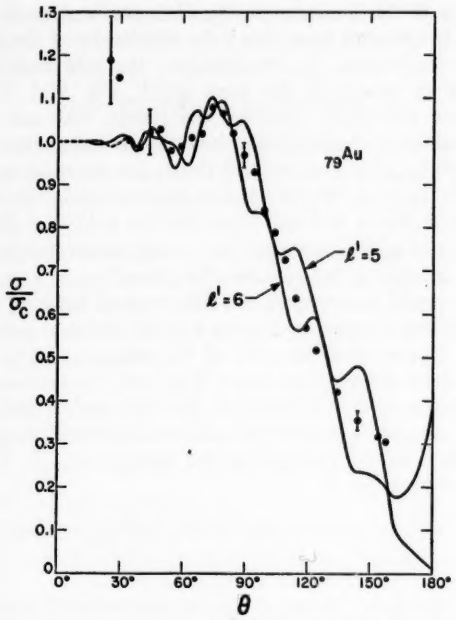

FIG. 3. Scattering of 22-Mev alpha particles by gold. Points are experimental. Curves are theoretical with fuzzy model. $n=10.6$.

Farwell and Wegner's $(8.3\pm0.3)\times10^{-13}$ cm. Further interpretation of the data is given in the next section.

IV. THEORY AND DISCUSSION

The model of Blair, described in Sec. I, has the great merit of simplicity. Because of its rather successful application to the energy dependence of alpha-particle scattering at 60 and 90 degrees, we undertook to use the model to calculate the angular distribution of scattered alpha-particles from gold, lead, and silver, at the fixed energy of this experiment, 22 Mev. A brief discussion of the numerical work is given in an appendix.

(a) Gold

The best fits to the Au data are obtained with $l'=4$ or 5 (Fig. 2), i.e., with partial waves through the fourth or fifth subtracted from the scattered Coulomb wave (for gold, $n=10.6$). The theory reproduces the qualitative features of a rise followed by a sharp fall off of the relative cross section. The rise, however, is to about 20 percent above Coulomb instead of 10 percent, and the theoretical curves show a diffraction pattern, increasing in amplitude with increasing angle. This latter defect of the theory may readily be attributed to the sharp angular momentum cut-off (or, equivalently, radial cut-off) of the Blair model. Most of the ways one might think of to improve the theory, such as the calculation of phase shifts with a complex potential, would increase the difficulties of calculation by orders of magnitude. We therefore altered the theory in the simplest possible way from the sharp cut-off form into what we shall call the fuzzy Blair model. For $l<l'$, the partial waves are still completely absorbed. For $l>l'$, the partial waves are still unaffected by the nucleus. For $l=l'$, we let the scattered wave have the Coulomb phase and an amplitude of 0.5. This smoothes out somewhat the transition from absorption by the nucleus to no effect by the nucleus, not in a realistic way but in a way which may give qualitative understanding of the deficiencies of the sharp cut-off model. In Fig. 3 are shown the same gold data, and the best fits of the fuzzy model ($l'=5$ or 6). The fit to the data is substantially improved. The theoretical maximum relative cross section is now 1.1, in agreement with the experiment, the diffraction pattern is somewhat damped out, and the experimental points between 90 and 150 degrees are followed more closely. From this agreement it seems reasonable to conclude that the first few partial waves are indeed strongly absorbed (from the elastic beam) and that the transition from strong absorption to no absorption occurs over only a few partial waves. The spread in energy of the incident beam of about 0.1 Mev is not sufficient to account for lack of diffraction effects in the experimental results. For Pb and Au, a spread of 0.5 Mev and for Ag a spread of greater than 1 Mev would be required to smooth out the theoretical diffraction effects.

(b) Lead

The remarks above concerning gold apply equally well to lead (for lead, $n=11.0$). For lead also, the fuzzy model gives a substantially improved fit to the data over the sharp cut-off model. In Fig. 4 are shown the

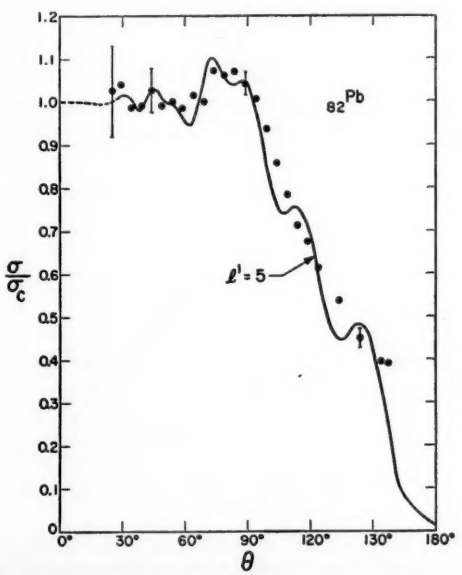

FIG. 4. Scattering of 22-Mev alpha particles by lead. Points are experimental. Curve is theoretical with fuzzy model (and $n=10.6$ instead of 11.0).

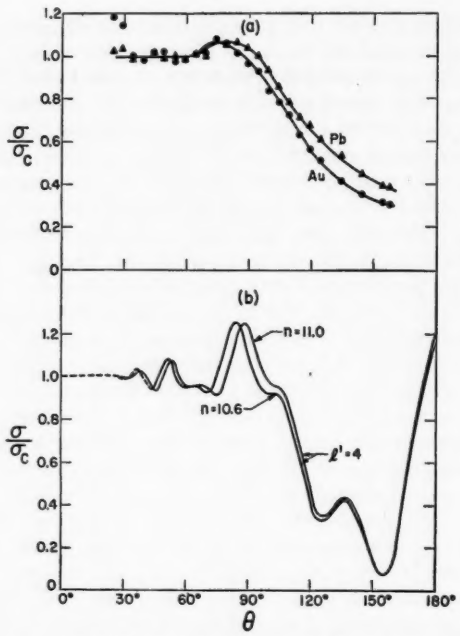

FIG. 5. (a) Gold and lead angular distributions compared. Curves drawn through data are not theoretical. (b) Theoretical cross sections for sharp cut-off model compared at fixed l' for the values of n corresponding to gold and lead.

lead data, together with the best fit—the fuzzy model with $l'=5$, but with $n=10.6$. Because of the small difference in the n-values of Au and Pb, the cross sections for the fuzzy model were calculated for only one of them. [See Fig. 5(b) for the effect of changing n from 10.6 to 11 for a fixed l'.]

(c) Gold *vs* Lead

For both gold and lead separately, values for the "interaction radius" may be obtained [part (e)]. Because of the similarity of the cross sections, however, one can learn in more detail the *relative* size of the gold and lead nuclei. For comparison, the gold and lead data are shown on the same graph, Fig. 5(a). (The curves are drawn through the points, and are not theoretical.) Figure 5(b) gives theoretical curves for $n=10.6$ (gold) and $n=11.0$ (lead) for the same value of l'. These justify the use of $n=10.6$ to fit the lead data in Fig. 4, and also show that the gold-lead difference of Fig. 5(a) is greater than can be accounted for by the different Z (or n) values for given l'.

In order to interpret the difference of the gold and lead cross sections, we turn to a wholly classical picture. We suppose that the ratio of the cross section to the Coulomb cross section depends only on the distance of the point of closest approach from the nuclear surface. Let the alpha particle scattered from element Z_i through angle θ_i have a classical apsidal distance $r_{\min}(i)$. Then our supposition is

$$\sigma_1(\theta_1)/\sigma_c(\theta_1)=\sigma_2(\theta_2)/\sigma_c(\theta_2),$$

if

$$r_{\min}(1)-R_1=r_{\min}(2)-R_2.$$

TABLE I. Determination of difference of radii of Pb and Au nuclei. $\delta R=R_{Pb}-R_{Au}$ in units of 10^{-12} cm. θ_{Au} = angle of scattering from Au nucleus. θ_{Pb} = angle of scattering from Pb nucleus for which the relative cross section is equal to that of Au at θ_{Au}. $\delta\theta=\theta_{Pb}-\theta_{Au}$. All angles in degrees.

		$\delta\theta_{\text{theoretical}}$				
θ_{Au}	$\delta\theta_{exp}$	$\delta R=0$	$\delta R=0.10$	$\delta R=0.15$	$\delta R=0.20$	$\delta R=0.30$
90	6±1	8	6	5	4	3
100	5±1	19	7	6	5	3
110	7±1	13	9	8	6	4
120	10±1	17	12	10	8	4
130	15±1	24	16	13	10	5
140	19±1	···	28	19	14	7

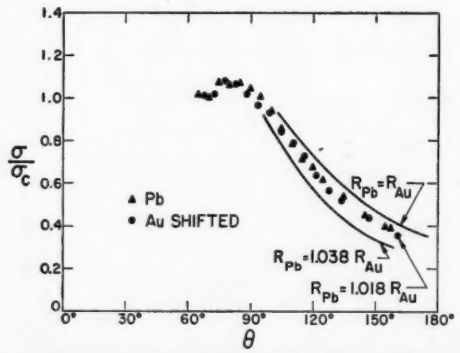

FIG. 6. Determination of relative radii of gold and lead. The gold data are shifted according to the classical arguments of the text into near coincidence with the lead data with $R_{Pb}=1.018\,R_{Au}$. For two other choices of relative radii, the loci of the shifted gold points are shown by solid curves.

This is analogous to Blair's more specific assumption that the relative cross section, σ/σ_c, should be equal to $\frac{1}{4}$ when the classical apsidal distance is equal to the nuclear radius. Our generalization rests on the same physical idea, that for this semiclassical problem ($n\gg1$), one can think of the alpha particle as a rather well-defined wave packet sweeping by the nucleus.

The classical formula for the point of closest approach, $r_{\min}$, is

$$\hbar^{-1}pr_{\min}=n\cot^2\tfrac{1}{2}\theta/(\csc\tfrac{1}{2}\theta-1)\equiv nf(\theta),$$

where p is the incident momentum, and n is defined by (4). Our supposition about relative intensities then leads to

$$n_2f(\theta_2)=n_1f(\theta_1)+\hbar^{-1}p(R_2-R_1), \qquad (5)$$

where θ_1 and θ_2 are the angles for which the cross sections of elements 1 and 2 (relative to Coulomb) are equal. For a given assumption about $R_{Pb}-R_{Au}$, we solve Eq. (5) for θ_{Pb}, the angle where the Pb cross section should be equal to the Au cross section at θ_{Au}. A sum-

mary of these calculations is given in Table I. From the best fit obtained for $\theta_{Pb}-\theta_{Au}$ as a function of θ_{Au}, we conclude

$$R_{Pb}-R_{Au}=(0.15\pm0.05)\times10^{-13}\text{ cm}.$$

This difference is consistent with $R=1.5\times10^{-13}A^{\frac{1}{3}}$ cm; it shows that the radius of Pb exceeds that of gold by a normal amount in spite of the closed shell character of Pb.

A slight variation in this method can be used to obtain a figure for the ratio of the radii of Pb and Au. For classical orbits not far from the nuclear surface, relative cross section for neighboring elements will be nearly equal when

$$r_{\min}(1)/R_1=r_{\min}(2)/R_2.$$

With this assumption, Eq. (5) is replaced by

$$n_2f(\theta_2)=(R_2/R_1)n_1f(\theta_1). \qquad (5)'$$

Now each assumption for the ratio, R_{Pb}/R_{Au}, will lead to a predicted angular shift, $\theta_{Pb}-\theta_{Au}$, between the two cross section curves. In Fig. 6 are shown the lead data,

TABLE II. Nuclear radii. All radii in units 10^{-13} cm. $R+R_\alpha$=interaction radius determined by experiment$=R_0A^{\frac{1}{3}}$. $R=(R+R_\alpha)-2.5\times10^{-13}$ cm$=r_0A^{\frac{1}{3}}$.

Element	l'	$R+R_\alpha$	R_0	R	r_0
Pb	5	11.4	1.92	8.9	1.50
Au	5.5	11.1	1.90	8.6	1.48
Ag	~12	9.9	1.97	7.4	1.5

and the gold data shifted according to this prescription for several assumptions about R_{Pb}/R_{Au}. The best overlap between the lead data and the shifted gold data leads to

$$R_{Pb}/R_{Au}=1.020\pm0.007,$$

which is consistent with an $A^{\frac{1}{3}}$ law of radii and with the result for the difference of radii.

(d) Silver

The silver data, together with the best fit of the sharp cut-off model, are shown in Fig. 7 (for Ag, $n=6.3$). The agreement between theory and experiment is fair below about 70 degrees, and poor above this angle, with only the minima of a very marked diffraction pattern coming close to the experimental points. With a larger number of partial waves being affected by the nucleus, and with a probably more gradual transition from large to small absorption, it is to be expected that the sharp cut-off model will be less satisfactory. The fuzzy model, however, which is fit to the Ag data in Fig. 8, is not very much better. The theoretical curve follows the points reasonably well to about 85 degrees, then diverges sharply into a diffraction pattern which is broadened relative to that of the sharp cut-off model, but not reduced in amplitude. Thus a very considerably refined model will probably be required to fit the large

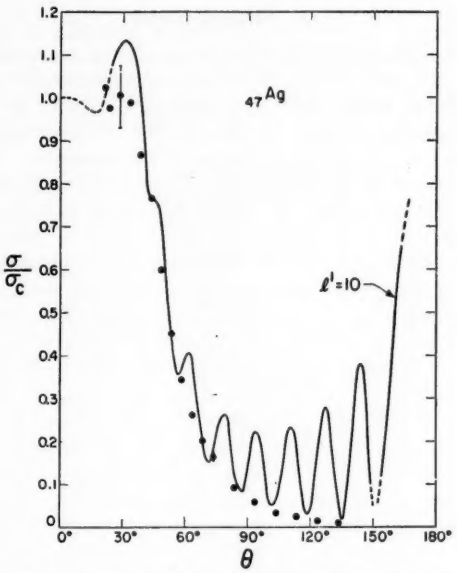

FIG. 7. Scattering of 22-Mev alpha particles by silver. Points are experimental. Curve is theoretical with sharp cut-off model. $n=6.3$.

angle data, which show no evidence at all of a diffraction pattern. A change from an infinite to a finite absorption coefficient of the nucleus may be sufficient to damp out the diffraction pattern, although it seems likely that in addition some account must also be taken of the finite thickness of the nuclear surface in order to explain the complete absence of oscillation in the experimental cross section.

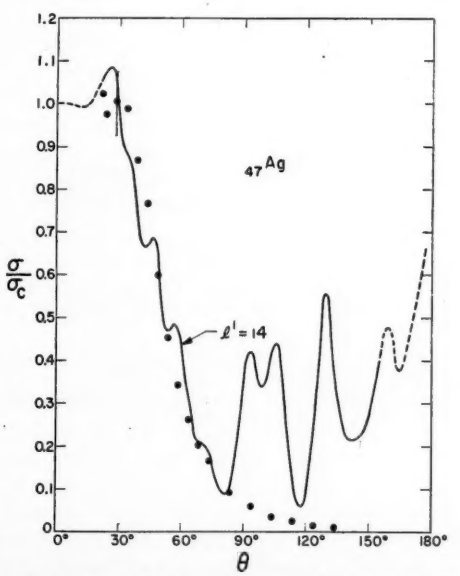

FIG. 8. Scattering of 22-Mev alpha particle by silver. Points are experimental. Curve is theoretical with fuzzy model. $n=6.3$.

(e) Nuclear Radii

The assumption described in Sec. I, and expressed in Eq. (1), that at the critical angular momentum l', the Coulomb barrier plus the centrifugal barrier at the "interaction radius" is equal to the incident energy, allows one to compute values of the interaction radii for the three nuclei studied. These radii, written as $R+R_\alpha$, are given in Table II. Other radial constants given in Table II are defined as follows. $R_0=(R+R_\alpha)/A^{\frac{1}{3}}$. These values are large compared to alpha-decay radii and very large compared to electromagnetic radii. If we make a generous allowance of 2.5×10^{-13} cm for R_α, we obtain the values of nuclear radius R, and of $r_0=R/A^{\frac{1}{3}}$, given in the last two columns of Table II. This correction brings the value of r_0 down to 1.5×10^{-13} cm. These radii of course depend on the model employed to fit the data, but the general conclusion can be drawn that the nuclear interaction radius is very considerably larger than the electromagnetic radius. It should be mentioned that some evidence for a large alpha-particle radius exists, based upon the experiments of Bashkin[12,13] and Adair.[14]

Finally, we remark that Blair's success in fitting the energy dependence of elastic alpha scattering was to some degree dependent on the particular angles used, 60 and 90 degrees. In Fig. 9, we plot, for $n=10.6$, the relative cross section as a function of the number of partial waves absorbed for several angles. The angle 90 degrees (for all n) has the special property of showing no oscillations at large l'. The angle 60 degrees (and other angles less than 90 degrees) shows only a weak oscillation. Angles greater than 90 degrees, here illustrated with 135 degrees, show marked oscillations. It is probable that the model would fail to account for the energy dependence of the scattering at large angles and high energy in the same way that it here fails to account for the angular distribution at larger angles and high l'.

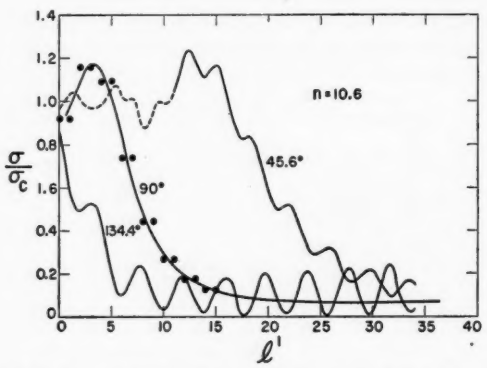

FIG. 9. Relative cross sections *vs* l', the number of partial waves absorbed, according to the sharp cut-off model, for several angles.

[12] J. M. Blatt and V. F. Weisskopf, *Theoretical Nuclear Physics* (John Wiley and Sons, Inc., New York, 1952).
[13] Bashkin, Mooring, and Petree, Phys. Rev. 82, 378 (1951).
[14] R. K. Adair, Phys. Rev. 86, 155 (1952).

The success of this simple model, especially in its fuzzy form, at fitting the gold and lead data suggests that it might be fruitful to analyze in a similar way angular distributions at other energies at and just above the Coulomb barrier.

ACKNOWLEDGMENTS

The authors would like to acknowledge the valuable assistance of Professor D. W. Miller and Professor M. B. Sampson in conducting these experiments; and we would like particularly to thank Professor V. K. Rasmussen for many interesting discussions and for considerable assistance in setting up the instrumentation involved in these experiments, as well as help in the accumulation of the data.

Professor G. S. Blair, Professor G. Farwell, and Dr. H. Wegner were very generous in supplying us with their data and interpretations prior to publication.

We express our appreciation to Dr. Norris Bradbury and Dr. Carson Mark for the opportunity to carry out a part of this work at the Los Alamos Scientific Laboratory.

APPENDIX—NUMERICAL CALCULATIONS

The ratio σ/σ_c was calculated by means of Eq. (2), with a suitable alteration for the fuzzy model. Since the ratio σ/σ_c was calculated directly, it was unnecessary to find the Coulomb phases σ_l, but only the differences, $\sigma_l-\sigma_0$, given by the recursion formula,

$$e^{2i(\sigma_l-\sigma_0)}=[(l+in)/(l-in)]e^{2i(\sigma_{l-1}-\sigma_0)}.$$

For a given value of n (6.3, 10.6, or 11.0) and a given model (sharp or fuzzy), the ratios σ/σ_c were calculated for all l' from 0 to some maximum, variously taken between 15 and 35, and for 40 equally spaced values of $\cos\theta$ between 0.05 and -1.00. The calculations were performed on an IBM 701 computer at the Los Alamos Scientific Laboratory, and were greatly simplified by the use of standard programs developed by Los Alamos Group T-1. The calculation of an angular distribution at given n and l' required several seconds.

Nature of Positron Annihilation in Liquids and Solids

W. R. DIXON* AND L. E. H. TRAINOR
Department of Physics, Queen's University, Kingston, Ontario, Canada
(Received June 15, 1954; revised manuscript received September 27, 1954)

An interpretation of the experimental results on positrons stopping in liquid and solid media is presented in terms of annihilation from excited states of positronium. It is assumed on an empirical basis that the 2*S* states of positronium have sufficient stability in certain materials for direct annihilation.

I. INTRODUCTION

AN experimental study of two-quantum annihilation of positrons in liquid and solid materials has been reported by Bell and Graham.[1] In metals, they observed a single lifetime $\tau_1 \cong 1.5\times10^{-10}$ sec, roughly independent of the particular metal employed. In some insulating materials (usually with crystalline structure), the results were the same as for metals, while in others (usually liquids and amorphous solids) 70 percent of the annihilations occurred with a short lifetime τ_1 and 30 percent occurred with a lifetime τ_2 which was five to ten times longer, depending on the material used. Moreover, the lifetime τ_2 was observed to increase with temperature in some nonmetals. Bell and Graham offered an explanation of the τ_2 component in terms of the conversion rate of triplet to singlet positronium. As they have pointed out, this explanation is not entirely free from objections. The purpose of the present paper is to offer a possible explanation of the τ_2 component in terms of annihilation from excited states of positronium.

There is evidence for the formation of positronium in both metals and nonmetals. This seems to be the most reasonable interpretation of the observation of Madansky and Rasetti[2] that no thermal positrons diffuse from metallic and nonmetallic surfaces surrounding a positron source. Indirect evidence that positronium is formed in metals, as Bell and Graham have pointed out, is the independence of τ_1 on the metal used, and hence the independence of τ_1 on the electron density. In nonmetals, the occurrence of the two components τ_1 and τ_2, is difficult to explain unless some positronium is formed. It should be noted that if positronium has a stable binding in solid media, then its formation is a highly nonequilibrium process. Once the positronium atom is formed it has a high probability of persisting until annihilation takes place, since the ionization energy required to free the positron is not readily available.

The discussion of the Bell and Graham experiment below is based on the assumption that the rate of formation of positronium in condensed matter is considerably faster than the rate of annihilation of free positrons. The conversion interpretation then leads to serious difficulties with the magnitude of the τ_1 lifetime and with the intensity ratio of the two components.

The difficulty with the τ_1 lifetime arises as follows. In nonmetals where the conversion rate has been assumed slow, the observed lifetime τ_1 should correspond to the lifetime $\tau(1^1S)$ for two-quantum annihilation from the singlet state of positronium. However, in metals where the conversion rate has been assumed rapid, τ_1 ought to be *four* times the lifetime $\tau(1^1S)$, as pointed out by Garwin.[3] Since the observed lifetime in metals is $\lesssim 1.5\times10^{-10}$ sec, it follows on this basis that in metals $\tau(1^1S)\lesssim 0.4\times10^{-10}$ sec, in serious disagreement with the theoretical value of 1.25×10^{-10} sec for free positronium[4] and with the observed values of 2.5 to 3.5×10^{-10} sec for those nonmetals exhibiting a τ_2 component. Such a serious disagreement seems unlikely. If one abandons the explanation of the τ_2 component in terms of the conversion rate, one can either suppose that the conversion rate is slow ($\lesssim 10^8$/sec) in all materials, or that it is rapid in all materials ($>10^{10}$/sec). In the former case the disagreement among lifetimes disappears; in the latter case the theoretical lifetime must be modified by a factor of 2 to 3 in all materials.

The other serious difficulty with the conversion interpretation arises when one attempts to account for the observed intensity ratio. An elementary analysis of this problem is given in the Appendix. From Table I it is seen that no choice of the conversion rate gives a satisfactory interpretation both of the two lifetimes and of their relative intensities. More generally, the observed constancy of the intensity ratio I_1/I_2 despite large variations in τ_2 is not consistent with the conversion interpretation. Again this is illustrated by reference to Table I.

These difficulties could be circumvented if the τ_1 component could be largely accounted for by the annihilation of free positrons in flight, although this seems unlikely. The τ_2 component might then be attributed either to triplet-singlet conversion or, as suggested by Garwin,[3] to the annihilation of positrons in collisions between triplet positronium and electrons of appropriate spin on neighboring molecules. One still

* On leave of absence from the National Research Council of Canada, Ottawa, Canada.

[1] R. E. Bell and R. L. Graham, Phys. Rev. **90**, 644 (1953).

[2] L. Madansky and F. Rasetti, Phys. Rev. **79**, 397 (1950).

[3] R. L. Garwin, Phys. Rev. **91**, 1571 (1953).

[4] J. Pirenne, Arch. Sci. phys. et nat. **28**, 273 (1946) and **29**, 121 (1947).

would not seem to have a satisfactory explanation of the temperature effect.

A possible explanation of the Bell and Graham results, in which free positrons do not play a dominant role, is presented in Sec. II.

II. ANNIHILATION FROM EXCITED STATES OF POSITRONIUM

The constancy of the intensity ratio I_1/I_2 despite large variations in τ_2 among nonmetals suggests that in order to explain the τ_2 component, one requires a mechanism of formation (of the state decaying with lifetime τ_2) which is relatively insensitive to environment, even though the lifetime τ_2 itself is sensitive to environment. Such a possibility exists in terms of the annihilation from excited states of the positronium atom, a process which was considered by Ore and Powell[5] for positrons in gaseous media, but which seems to have been ignored or considered unlikely in liquids and solids. It was pointed out by Ore and Powell that the excited $2S$ states normally possess unusual stability against radiative de-excitation. The transition 2^1S-1^1S is absolutely forbidden, and the transitions 2^3S-1^1S and 2^1S-1^3S are extremely slow, since the space wave functions are very nearly orthogonal (in contrast to magnetic dipole absorption of the deuteron, which occurs because the nuclear forces are strongly spin-dependent[6]). It might at first be thought that this stability would be lost for positronium in solid media through collisional de-excitation. In metals such de-excitation will take place rapidly through collisions with conduction electrons. In nonmetals, however, the electrons are firmly bound to their atomic stations so that rapid de-excitation may not be possible. In both cases, coupling with the lattice is very small since the energy transferred in de-excitation must be several electron volts. The possible stability of the 2^1S state then provides a mechanism to explain the occurrence of the τ_2 component in some nonmetals.

It is improbable that states of higher angular momentum will be bound for positronium in solid media. Assuming the effective potential of the electron-positron system is a strongly shielded Coulomb potential, the level sequence is $1S$, $2S$, $2P$, etc. with a relatively large $2S-2P$ separation. For simplicity we will assume here that the $2P$ state is not bound. If it is bound, its role is limited to indirect effects such as influencing the intensity ratio I_1/I_2. This follows from the observation of Ore and Powell[5] that the probability of annihilation from a P state is negligible since the internal wave function vanishes for electron-positron coincidence.

With these assumptions we can now construct the following picture for positrons slowing down in solid and liquid media. In both metals and insulators positrons slow down rapidly, via the usual processes (ionization, Auger effect, etc.), to energies where the probability for the formation of positronium is large. In metals the $2S$ states, if bound, are rapidly de-excited by nonradiative collisions with conduction electrons and a single lifetime τ_1 for two-quantum annihilation is observed. If the 2^1S state is bound in insulators and has sufficient stability, then it decays by two-quantum annihilation directly, so that one observes a second lifetime τ_2. One can even understand in a qualitative way why the τ_1 component has a greater intensity. In insulators, electron pickup from the lattice by the positron is likely to be an endothermic reaction for the formation of the $2S$ states, but even exothermic for the $1S$ states.

The above picture for positrons slowing down in solid media is capable of explaining the following experimental facts:

(i) There exists a short lifetime τ_1 in all materials, and a second lifetime τ_2 in some nonmetals.

(ii) The magnitudes of τ_1 and τ_2 are essentially determined by the lifetimes for two-quantum annihilation, $\tau(1^1S)$ and $\tau(2^1S)$, respectively. Since the probability density for electron-positron coincidence decreases as the cube of the principal quantum number for S states,[5] $\tau_2 \approx 8\times\tau_1 \approx 10^{-9}$ sec.

(iii) The relative constancy of τ_1 compared with the wide variations in τ_2 in different materials follows from the strong binding of the 1^1S state and the weak binding (and hence greater sensitivity to environment) of the 2^1S state.

(iv) The lifetime τ_2 depends rather sensitively upon the small binding energy of the $2S$ state, whereas the intensity ratio I_1/I_2 is determined by the more gross parameters of formation such as the $1S-2S$ binding energy difference. Hence I_1/I_2 is relatively more independent of environment than τ_2.

(v) The long lifetime τ_2 is temperature-dependent. As the temperature is raised, the 2^1S states become less firmly bound so that the wave function for the relative separation of electron and positron "spreads out." The probability density at coincidence then decreases and the lifetime increases contrary to normal expectation.[1] A similar but smaller temperature effect might be anticipated for τ_1.†

The situation in superconductors is uncertain from both experimental and theoretical points of view. A complex decay scheme is indicated by the experimental results.[7] This might be understood by means of arguments similar to those used by Dresden[8] concerning the inability of the electrons to exchange energy with the lattice or with impurities (positronium). Such a

[5] A. Ore and J. L. Powell, Phys. Rev. **75**, 1696 (1949).

[6] See, for example, similar arguments in J. M. Blatt and V. F. Weisskopf, *Theoretical Nuclear Physics* (John Wiley and Sons, Inc., New York, 1952), pp. 603–604.

† *Footnote added in proof.*—One can interpret the results of Graham and Stewart [Can. J. Phys. **32**, 678 (1954)] on the temperature dependence of the three-quantum annihilation rate as evidence for such an effect.

[7] W. E. Millett, Phys. Rev. **94**, 809 (1954); H. Talley and R. Stump, Phys. Rev. **94**, 809 (1954).

[8] M. Dresden, Phys. Rev. **93**, 1413 (1954).

prohibition of collisional de-excitation would imply the stability of the 2^1S state of positronium and lead to a complex decay scheme analogous to that found in some insulators.

The hypothesis that excited states of positronium are responsible for the τ_2 component is not inconsistent with the experimental results of De Benedetti and Siegel.[9] They have found that the three-quantum counting rates are greater in materials exhibiting a τ_2 component, by an amount consistent with the conversion interpretation of τ_2. However, an explanation of these results also follows from the excited-state interpretation of τ_2, provided that the conversion rate is assumed rapid ($\gtrsim 10^{11}$/sec) in metals, and moderately rapid ($\gtrsim 10^{10}$/sec) in nonmetals. This follows from the elementary analysis in the Appendix and from the experimental observation that τ_1 is lengthened in those materials showing a τ_2 component. Thus for fast conversion, the experimental lifetime τ_1 is to be identified with $1/\lambda_2$, and the expected ratio of the three-quantum rate in Teflon to that in aluminum is

$$\frac{\lambda_2(\text{aluminum})}{\lambda_2(\text{Teflon})}=\frac{\tau_1(\text{Teflon})}{\tau_1(\text{aluminum})}\cong 2 \text{ to } 3,$$

in agreement with the measured ratio. (The inclusion of the $2S$ states in the analysis of the Appendix would not materially change this result, of course.) The results of Pond[10] on the ratios of the two-quantum annihilation rates in various pairs of materials are also consistent with the excited-state interpretation.

According to the excited-state hypothesis, if the $2S$ states have sufficient stability against transition to the $1S$ states, one should observe the lifetime of the 2^3S as well as of the 1^3S state in experiments of the kind performed by Deutsch[11] with gases. It might be profitable to look for such an effect, although the longer lifetime and expected smaller intensity of the 2^3S component would make it difficult to observe experimentally.

Finally, let us remark on the question as to whether there is enough room in the solid lattice to accommodate the "orbits" of the $2S$ states of positronium. In this connection it might be noted that the effective atomic size of the positronium atom is likely to be smaller within solid material. Moreover, the validity of the hypothesis actually requires that the $2S$ states be bound only in amorphous solids. Also, positronium need not exist as such in the literal sense; for example, it may appear in the form of a molecular compound. Despite the greater complexity then involved, one might anticipate some of the same general features as discussed above.

The authors wish to thank Dr. B. W. Sargent for having first brought this problem to their attention, and Drs. W. Opechowski and P. R. Wallace for helpful discussion. One of us (L.E.H.T.) is indebted to the Summer Research Institute of the Canadian Mathematical Congress for a Summer Fellowship and the other (W.R.D.) to the National Research Council of Canada for financial assistance.

[9] S. De Benedetti and R. T. Siegel, Phys. Rev. **94**, 955 (1954).
[10] T. A. Pond, Phys. Rev. **93**, 478 (1954).
[11] M. Deutsch, Phys. Rev. **82**, 455 (1951); **83**, 866 (1951).

APPENDIX

The dependence of the observed lifetimes and intensities for two-quantum annihilation of positronium upon the 1^3S-1^1S conversion rate can be illustrated as follows. Let P_S be the probability of finding a positronium atom, once formed, in the 1^1S singlet state, and P_T be the corresponding triplet state probability. Then the rate of change of probability can be expressed by the equations:

$$dP_S/dt=-(3\gamma+\lambda_S)P_S+\gamma P_T,$$
$$dP_T/dt=3\gamma P_S-(\gamma+\lambda_T)P_T,$$

where γ is the rate of conversion between the singlet state and any one of the three triplet states, λ_S is the two-quantum annihilation rate for the singlet state, and λ_T is the three-quantum annihilation rate for the triplet state. Simultaneous solution of these equations yields

$$P_S=C_S\exp(-\lambda_1 t)+D_S\exp(-\lambda_2 t),$$
$$P_T=C_T\exp(-\lambda_1 t)+D_T\exp(-\lambda_2 t),$$

where

$$\lambda_{1,2}=\alpha\pm(\alpha^2-\beta^2)^{\frac{1}{2}},$$
$$2\alpha=4\gamma+\lambda_S+\lambda_T,$$
$$\beta^2=\gamma\lambda_S+3\gamma\lambda_T+\lambda_S\lambda_T.$$

Since $\lambda_S P_S$ is the rate of two-quantum annihilation, one has two lifetimes, a short lifetime $1/\lambda_1$ and a long lifetime $1/\lambda_2$. By integrating from the time of formation to infinity, one gets for the relative intensities of the two components:

$$I_1/I_2=C_S\lambda_2/D_S\lambda_1.$$

The constants C_S and D_S are determined by the initial conditions:

$$P_S(t=0)=\tfrac{1}{4},\quad P_T(t=0)=\tfrac{3}{4}.$$

TABLE I. Lifetimes for two-quantum annihilation and their intensity ratio as a function of the triplet-singlet conversion rate.

3γ (per sec)	$1/\lambda_1$ (sec)	$1/\lambda_2$ (sec)	I_1/I_2
∞	0	5.0×10^{-10}	0
10^{12}	7.5×10^{-13}	5.0×10^{-10}	6.7×10^{-3}
10^{11}	7.2×10^{-12}	5.2×10^{-10}	6.4×10^{-4}
10^{10}	5.0×10^{-11}	7.6×10^{-10}	3.7×10^{-2}
10^{9}	1.1×10^{-10}	3.3×10^{-9}	0.25
10^{8}	1.2×10^{-10}	2.5×10^{-8}	0.39
10^{7}	1.25×10^{-10}	9.6×10^{-8}	1.0
10^{6}	1.25×10^{-10}	1.3×10^{-7}	7.5
0	1.25×10^{-10}	1.4×10^{-7}	∞

It follows that

$$C_S=(\lambda_1-4\gamma-\lambda_T)/4(\lambda_1-\lambda_2),$$
$$D_S=(-\lambda_2+4\gamma+\lambda_T)/4(\lambda_1-\lambda_2).$$

Table I gives the expected lifetimes for two-quantum annihilation and their relative intensity I_1/I_2 for various possible choices of the conversion rate γ, assuming that the triplet three-quantum annihilation rate is $\lambda_T=7.14\times10^6$/sec as given by Ore and Powell[5] and that the singlet two-quantum rate is $\lambda_S=8\times10^9$/sec.[4] As noted in the text, the assumption of rapid conversion would require that these rates be increased by factors of about 2 or 3. For rapid conversion one then obtains $1/\lambda_2\approx2\times10^{-10}$ sec in agreement with the experimental lifetime τ_1.

The dependence of the total rates for two- and three-quantum annihilation on the triplet-singlet conversion rate can be calculated in a similar manner. In the differential equations one replaces the probabilities P_S and P_T by the populations N_S and N_T, respectively, introduces constant rates of formation ($\frac{1}{4}$ for the singlet state and $\frac{3}{4}$ for the triplet state), and finally equates the derivatives to zero. This gives for the total rates:

$$\lambda_S N_S=\lambda_S(4\gamma+\lambda_T)/4\beta^2 \quad \text{(two-quantum)},$$
$$\lambda_T N_T=3\lambda_T(4\gamma+\lambda_S)/4\beta^2 \quad \text{(three-quantum)}.$$

For λ_T small compared to γ and λ_S, one finds

$$\lambda_S N_S\approx1-3\lambda_T/4\lambda_2,$$
$$\lambda_T N_T\approx3\lambda_T/4\lambda_2.$$

For very rapid conversion, $\lambda_2\to\lambda_S/4$, and hence

$$\lambda_T N_T\to3\lambda_T/\lambda_S.$$

PHYSICAL REVIEW VOLUME 97, NUMBER 3 FEBRUARY 1, 1955

Matrix Elements in Superallowed Transitions*

MARK BOLSTERLI† AND EUGENE FEENBERG
Wayman Crow Laboratory, Washington University, St. Louis, Missouri
(Received July 23, 1954)

The nuclear matrix element for superallowed transitions between two states of an isobaric spin multiplet can be expressed in terms of a diagonal matrix element of the spin operator difference $\mathbf{S}_n-\mathbf{S}_p$. Known theoretical results on the nuclear matrix element in image transitions are summarized and the methods which have proved useful in the study of image transitions are extended to superallowed transitions within the lowest $T=1$ isobaric spin multiplet in the $4n$ series.

Experimental results indicate the actual occurrence of such transitions in Na^{20}, Al^{24}, P^{28}, Cl^{32} and Sc^{40}.

1. INTRODUCTION

THE known superallowed transitions now include the following types:

$$\begin{aligned}
&a: \quad \Delta I=0, && T_i=T_f=\tfrac{1}{2} && (A=4n\pm1),\\
&b: \quad \Delta I=\pm1, && T_i=T_f=\tfrac{1}{2} && (A=7),\\
&c: \quad \Delta I_i=\pm1, && \Delta T=\mp1 && (A=4n+2),\\
&d: \quad I_i=I_f=0, && T_i=T_f=1 && (A=4n+2),\\
&e: \quad \Delta I=0, && T_i=T_f=1 && (A=4n).
\end{aligned} \tag{1}$$

Types a to d are well known, but only recently has experimental work on short-lived radioactivities in the $4n$ nuclear series[1–5] indicated the actual occurrence of type e.[6] The list a to e does not exhaust the possible types of superallowed transitions. To see that others may occur, consider the approximation of spin- and charge-independent forces. In the $4n$ series the lowest supermultiplet containing a $T=1$ isobaric spin multiplet has the basic structure shown in Table I. Thus there are seven different final states coupled to the initial ($T_3=-1$) state by nonvanishing Gamow-Teller matrix elements.

Now, by introducing a spin-dependent force, the seven distinct final states are spread out into a spectrum as illustrated in Fig. 1. The Fermi matrix element vanishes in all but the e-type transition. Other transitions with $\Delta T=0$ may occur, but they involve smaller decay energies and smaller decay matrix elements; hence they may be neglected in a preliminary discussion. The remaining three final states (those with $T=0$

TABLE I.

T	S	$I(L\neq0)$
1	1	$L-1, L, L+1$
1	0	L
0	1	$L-1, L, L+1$

* Supported in part by the Office of Naval Research and the U. S. Atomic Energy Commission.
† Shell fellow 1952–1954; now National Science Foundation pre-doctoral fellow.
[1] N. W. Glass and J. R. Richardson, Phys. Rev. **93**, 942 (1954).
[2] Glass, Jensen, and Richardson, Phys. Rev. **90**, 320 (1953).
[3] Brackon, Henrikson, Martin, and Foster, Can. J. Phys. **32**, 223 (1954).
[4] A. C. Birge, Phys. Rev. **85**, 753 (1952).
[5] L. W. Alverez, Phys. Rev. **80**, 519 (1950).
[6] M. Bolsterli and E. Feenberg, Phys. Rev. **95**, 612 (1954).

derived from the lowest $[4^{n-1}31]$ supermultiplet) are not easily fixed on the energy scale. If one or more of these levels falls below the final state involved in the type *e* transition, a complicated decay scheme may occur with two or more strong superallowed components in the beta decay of the $T_3=-1$ isobar.

In this paper we begin with a summary of known theoretical results on the Gamow-Teller and Fermi matrix elements in image transitions (type *a*). The methods which have proved useful in the study of type *a* are then extended to type *e*. Finally the experimental evidence requiring the existence of type *e* transitions is exhibited and compared with theory.

2. GENERAL RELATIONS

The relation

$$ft|M|^2=\text{Constant} \tag{2}$$

and the definitions

$$\begin{aligned}
|M|^2&=r\left|\int 1\right|^2+\left|\int \boldsymbol{\sigma}\right|^2,\\
\left|\int 1\right|^2&=\sum_{mf}|(f|\textstyle\sum Q_k \text{ or } \sum Q_k^*|i)|^2,\\
\left|\int \boldsymbol{\sigma}\right|^2&=\sum_{mf}|(f|\textstyle\sum Q_k\boldsymbol{\sigma}_k \text{ or } \sum Q_k^*\boldsymbol{\sigma}_k|i)|^2,\\
Q&=\tfrac{1}{2}(\tau_1-i\tau_2),\\
Q^*&=\tfrac{1}{2}(\tau_1+i\tau_2),
\end{aligned} \tag{3}$$

give the basic connection between theory and experiment in the analysis of superallowed transitions.

The most recent analysis[7] of image transitions (type *a*) places r on the range 0.75–1.15 in general agreement with earlier studies[8–11] and consistent with the weakly motivated but widespread preference for $r=1$. The theoretical estimates of $|\int\boldsymbol{\sigma}|^2$ are most secure at $A=1$, 3, 13, 15, 17, and 39; the analysis of image transitions in this group favors $r<1$ as does also recent accurate data[12] on the $0\to0$ transition at $A=14$. Fairly good all round agreement obtains for $r\sim0.8$. The values $r=0.8$ and

$$ft|M|^2\sim4700 \tag{4}$$

will be used in analyzing the data on fast transitions in the $4n$ series.

The Fermi matrix element occurring in transitions of types *a*, *d*, and *e* is given by the formula

$$\left|\int 1\right|^2=2T. \tag{5}$$

Deviations from this formula exceeding a few percent are not expected in the mass range covered by known superallowed transitions.[13]

A general formula for Gamow-Teller matrix elements in transitions of types *a*, *b*, and *e* can be derived from the commutation relations[14]

$$\begin{aligned}
[T_1\pm iT_2,\ Y_{1u}\mp iY_{2u}]&=\pm2Y_{3u},\\
[T_3,\ Y_{1u}\mp iY_{2u}]&=\mp(Y_{1u}\mp iY_{2u}),
\end{aligned} \tag{6}$$

in which

$$\begin{aligned}
T_i&=\tfrac{1}{2}\sum_1^A \tau_i^{(k)},\\
Y_{iu}&=\tfrac{1}{2}\sum_1^A \tau_i^{(k)}\sigma_u^{(k)},\quad u=x,y,z.
\end{aligned} \tag{7}$$

If β, T, T_3 and β', T, T_3' represent the initial and final state quantum numbers, Eqs. (6) and (7) yield

$$\begin{aligned}
&(\beta',T,\mp(T-1)|Y_{1u}\pm iY_{2u}|\beta,T,\mp T)\\
&\quad=\mp\left(\frac{2}{T}\right)^{\frac{1}{2}}(\beta',T,\mp T|Y_{3u}|\beta,T,\mp T)\\
&\quad=\mp\left(\frac{2}{T}\right)^{\frac{1}{2}}(\beta',T,\mp T|S_{nu}-S_{pu}|\beta,T,\mp T).
\end{aligned} \tag{8}$$

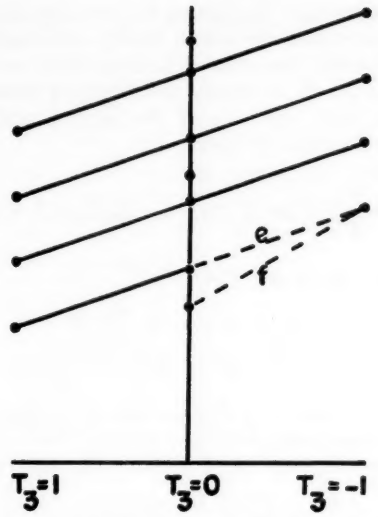

FIG. 1. A possible structure of the first *LS* supermultiplet containing $T=1$ multiplets. *e* denotes the superallowed β transition considered in this paper. *f* is another possible mode of decay.

[7] E. Feenberg, *The Shell Structure of the Nucleus* (Princeton University Press, Princeton, 1954).
[8] G. L. Trigg, Phys. Rev. **86**, 506 (1952).
[9] O. Kofoed-Hansen and A. Winther, Phys. Rev. **86**, 428 (1952).
[10] Wu, Rustad, Perez-Mendez, and Lidofsky, Phys. Rev. **87**, 1140 (1952).
[11] R. Nataf and R. Bouchez, Compt. rend. **234**, 86 (1952); Phys. Rev. **87**, 155 (1952).
[12] J. B. Gerhart, Phys. Rev. **95**, 288 (1954), R. Sherr and J. B. Gerhart, Phys. Rev. **91**, 909 (1953); also J. R. Penning and F. H. Schmidt, Phys. Rev. **94**, 779 (1954).
[13] L. A. Radicati, Proc. Phys. Soc. (London) **A66**, 139 (1953).
[14] E. Feenberg and G. E. Pake, *Notes on the Quantum Theory of Angular Momentum* (Addison-Wesley Press, Inc., Cambridge, 1953).

We observe that T_3 changes by one unit in the beta transition matrix element on the left while on the right $T_3'=T_3=\mp T$ (the value of T_3 in the initial state). The operator $\mathbf{S}_n-\mathbf{S}_p$ is simply the difference between the intrinsic spin operators of the neutron and proton groups. Equation (8) gives

$$\left|\int\sigma\right|^2=\frac{2}{T}\sum_{m'}(I,m',T,\mp T|\mathbf{S}_n-\mathbf{S}_p|I,m,T,\mp T)|^2. \quad (9)$$

In the special case $I'=I$,

$$\left|\int\sigma\right|^2=\frac{2}{T}\frac{|\langle\mathbf{S}_n\cdot\mathbf{I}\rangle-\langle\mathbf{S}_p\cdot\mathbf{I}\rangle|^2}{I(I+1)}. \quad (10)$$

Here $\langle\ \rangle$ denotes a diagonal matrix element of the enclosed operator.

If either $\langle\mathbf{S}_n\cdot\mathbf{I}\rangle$ or $\langle\mathbf{S}_p\cdot\mathbf{I}\rangle$ vanishes, Eq. (10) reduces to

$$\left|\int\sigma\right|^2=\frac{2}{T}\frac{|\langle\mathbf{S}\cdot\mathbf{I}\rangle|^2}{I(I+1)}. \quad (11)$$

3. SUMMARY OF RESULTS ON THE GAMOW-TELLER MATRIX ELEMENT FOR TYPE *a* TRANSITIONS

(i) *LS* Coupling, $S=1/2$

Under the stated condition the ground-state wave functions possess the maximum degree of symmetry in the space coordinates of the nucleons consistent with the exclusion principle. All spins are paired off in the even group of particles; hence either $\langle\mathbf{S}_n\cdot\mathbf{I}\rangle$ or $\langle\mathbf{S}_p\cdot\mathbf{I}\rangle$ vanishes and Eq. (10) can be rewritten in the form

$$\left|\int\sigma\right|^2=4\frac{|\langle\mathbf{S}\cdot\mathbf{I}\rangle|^2}{I(I+1)}$$
$$=(I+1)/I,\quad I=L+\tfrac{1}{2}$$
$$=I/(I+1),\quad I=L-\tfrac{1}{2}. \quad (12)$$

This result was first derived by Wigner.[15] Equation (12) is also valid in jj coupling for doubly magic ±1 configurations ($A=1$, 3, 11, 13, 15, 17, 27, 29, 31, 33, 39, and 41). All spins are paired off in the closed-shell core and only the spin of a single nucleon or hole is involved in the evaluation of $\langle\mathbf{S}\cdot\mathbf{I}\rangle$.

(ii) Linear Combination of *LS* Coupling States, $S=1/2$

The wave function has the form

$$\psi=\alpha\psi_{L=I-\frac{1}{2}}+(1-\alpha^2)^{\frac{1}{2}}\psi_{L=I+\frac{1}{2}}, \quad (13)$$

a linear combination of the two *LS* coupling components possible for given I and $S=\frac{1}{2}$. Now,

$$\langle\mathbf{S}\cdot\mathbf{I}\rangle=\tfrac{1}{2}\{\alpha^2(I+1)-(1-\alpha^2)I\}, \quad (14)$$

and

$$\left|\int\sigma\right|^2=\frac{1}{I(I+1)}[\alpha^2(I+1)-(1-\alpha^2)I]^2. \quad (15)$$

Equation (15), first derived by Trigg,[8] has proved useful in correlating observed values of the Gamow-Teller matrix element with the observed magnetic moment of the daughter nuclide.

Davidson[16] obtains numerical values for α^2 by an interpolation procedure involving the relation of the observed moment μ to theoretical values of the moment derived from the Schmidt single-particle and the Margenau-Wigner uniform models. The corresponding estimates for $|\int\sigma|^2$ generally agree better with experiment than the pure *LS* coupling values.[8] The improvement at $A=29$ and 31 is particularly striking.

(iii) Odd Group Model

A simple explicit formula expressing $|\int\sigma|^2$ in terms of μ can be derived from the assumption that all the angular momentum and magnetic properties are carried by the odd group of particles (odd group model). The moment operator,

$$\boldsymbol{\mu}=g_l\mathbf{L}+g_s\mathbf{S}$$
$$=g_l\mathbf{I}+(g_s-g_l)\mathbf{S}, \quad (16)$$

now yields

$$\mu=g_lI+(g_s-g_l)\langle\mathbf{S}\cdot\mathbf{I}\rangle/(I+1), \quad (17)$$

or

$$\langle\mathbf{S}\cdot\mathbf{I}\rangle=(I+1)(\mu-g_lI)/(g_s-g_l). \quad (18)$$

This relation is consistent with the doublet description of the nuclear state [Eq. (13)], but holds also for an arbitrary linear combination of multiplet components. From Eqs. (11) and (18) we obtain Winther's formula,[17]

$$\left|\int\sigma\right|^2=4\frac{I+1}{I}\left(\frac{\mu-g_lI}{g_s-g_l}\right)^2. \quad (19)$$

Our derivation of Winther's semiempirical formula is at fault in combining a relation [Eqs. (10) and (11)] derived from the assumption that the isobaric spin T is a good quantum number with a consequence [Eq. (18)] of the odd group model (in which the isotopic spin is not, as a rule, a constant of motion). Consequently, in default of a more satisfactory derivation, Eq. (19) must still be interpreted as a more or less useful semiempirical interpolation formula.

(iv) Symmetrical Interpolation Formulas

A more rigorous analysis of image transitions becomes possible when the magnetic moments of both members of mirror pairs are known. This statement follows from the fact that the sum of the moments obeys simpler relations than either moment alone.[18]

[15] E. P. Wigner, Phys. Rev. **56**, 519 (1939).

[16] J. P. Davidson, Phys. Rev. **85**, 432 (1952).

[17] A. Winther, Physica **18**, 1079 (1952).

[18] R. G. Sachs, Phys. Rev. **69**, 611 (1946).

The nucleon moment operator,

$$\mu = g_l^p \sum \mathbf{l}_k \tfrac{1}{2}(1-\tau_3^{(k)}) + g_s^n \sum \mathbf{S}_k \tfrac{1}{2}(1+\tau_3^{(k)}) + g_s^p \sum \mathbf{S}_k \tfrac{1}{2}(1-\tau_3^{(k)}), \quad (20)$$

in the form

$$\mu = \tfrac{1}{2} g_l^p \mathbf{I} + \tfrac{1}{2}(g_s^n + g_s^p - g_l^p)\mathbf{S} + \tfrac{1}{4}(g_s^n - g_s^p)\sum \tau_3^k \boldsymbol{\sigma}_k - \tfrac{1}{2} g_l^p \sum \tau_3^k \mathbf{l}_k, \quad (21)$$

gives immediately the result

$$\langle \mathbf{S}\cdot\mathbf{I}\rangle = (I+1)\frac{\mu(T_3=\tfrac{1}{2}) + \mu(T_3=-\tfrac{1}{2}) - I}{g_s^n + g_s^p - 1}, \quad (22)$$

after setting $g_l^p = 1$.

The introduction of Eq. (22) into Eq. (11) for $|\int \boldsymbol{\sigma}|^2$ is justified only if $\langle \mathbf{S}_n\cdot\mathbf{I}\rangle$ or $\langle \mathbf{S}_p\cdot\mathbf{I}\rangle$ vanishes, and this is physically plausible only under conditions which make the doublet description of Eq. (13) a good approximation. If one assumes the doublet description,[7]

$$\mu(\tfrac{1}{2}) + \mu(-\tfrac{1}{2}) = I + (g_s^n + g_s^p - 1)\frac{\alpha^2(I+1) - (1-\alpha^2)I}{2(I+1)}, \quad (23)$$

$$\left|\int \boldsymbol{\sigma}\right|^2 = 4\frac{I+1}{I}\left[\frac{\mu(\tfrac{1}{2}) + \mu(-\tfrac{1}{2}) - I}{g_s^n + g_s^p - 1}\right]^2. \quad (24)$$

The sum $\mu(\frac{1}{2})+\mu(-\frac{1}{2})$ is expected to depend relatively little on the amount and form of exchange moment operators. When both left- and right-hand members of Eq. (24) are known experimentally deviations from equality of the two members may yield information on the magnitude of quartet components in the ground state wave functions and on relativistic corrections to the moment operators.[19,20]

(v) *jj* Coupling

The magnetic properties of n neutrons and protons in a j shell are described by the moment operator,

$$\mu = g_j^n \sum \mathbf{j}_k(1+\tau_3^k)/2 + g_j^p \sum \mathbf{j}_k(1-\tau_3^k)/2 \quad (25)$$

in which $g_j^n = \mu_j^n/j$ and $g_j^p = \mu_j^p/j$ are the Landé g factors for single nucleons in j orbitals. Equation (25) gives the moment formula:

$$\mu = \frac{1}{2}(\mu_j^n + \mu_j^p)\frac{I}{j} + (\mu_j^n - \mu_j^p)\frac{\langle(\mathbf{I}_n - \mathbf{I}_p)\cdot\mathbf{I}\rangle}{j(I+1)}$$

$$= \frac{1}{2}(\mu_j^n + \mu_j^p)\frac{I}{j} + (-1)^{j-l-\frac{1}{2}}\frac{l+\tfrac{1}{2}}{j}(\mu_j^n - \mu_j^p)\frac{\langle(\mathbf{S}_n - \mathbf{S}_p)\cdot\mathbf{I}\rangle}{I+1}. \quad (26)$$

[19] H. Primakoff, Phys. Rev. **72**, 118 (1947).
[20] G. Breit and R. M. Thaler, Phys. Rev. **89**, 1177 (1953).

Equations (10) and (26) together yield Mayer's formula,[21]

$$\left|\int \boldsymbol{\sigma}\right|^2 = \frac{I+1}{I}\left(\frac{j}{l+\tfrac{1}{2}}\right)^2 \times \left(\frac{2\mu(T_3=\pm\tfrac{1}{2}) - (\mu_j^n + \mu_j^p)I/j}{\mu_j^n - \mu_j^p}\right)^2. \quad (27)$$

Equation (26) also implies

$$\mu(T_3=\tfrac{1}{2}) - \mu(T_3=-\tfrac{1}{2}) = (-1)^{j-l-\frac{1}{2}}\frac{2l+1}{j}(\mu_j^n - \mu_j^p)\frac{\langle(\mathbf{S}_n - \mathbf{S}_p)\cdot\mathbf{I}\rangle}{I+1}, \quad (28)$$

and yields the symmetrical interpolation formula,[7]

$$\left|\int \boldsymbol{\sigma}\right|^2 = \frac{I+1}{I}\left(\frac{j}{l+\tfrac{1}{2}}\right)^2\left(\frac{\mu(\tfrac{1}{2}) - \mu(-\tfrac{1}{2})}{\mu_j^n - \mu_j^p}\right)^2. \quad (29)$$

These relations are particularly useful when the jj coupling configuration provides two or more linearly independent wave functions with $T=\frac{1}{2}$ and the required value of I. In such cases neither $\mu(T_3)$ nor $|\int \boldsymbol{\sigma}|^2$ can be computed independently without information on the correct linear combination of component wave functions in the description of the ground state.

(vi) Special Case: $A=3$

The wave function

$$\psi = \alpha\phi(^2S_{\frac{1}{2}}) + (1-\alpha^2)^{\frac{1}{2}}\phi(^4D_{\frac{1}{2}}) \quad (30)$$

with $\alpha^2 = 0.96$ has been derived from the assumption of strong two particle tensor interactions between pairs of nucleons.[22] In evaluating the D state contribution to the Gamow-Teller matrix element, $\mathbf{S}_n - \mathbf{S}_p$ may be replaced by $\frac{1}{3}\mathbf{S}$. Equation (11) yields[23]

$$\left|\int \boldsymbol{\sigma}\right|^2 = [-\tfrac{3}{4}\alpha^2 - \tfrac{1}{4}(1-\alpha^2)]^2\frac{4}{I(I+1)} = \tfrac{1}{3}(2\alpha^2+1)^2 = 2.88, \quad (31)$$

possibly a little low, but not certainly inconsistent with the experimental requirements. For comparison, Eq. (24), based on the absence of a quartet component, gives only 2.58.

4. TYPE e: $\Delta I = 0$, $T_i = T_f = 1$ ($A = 4n$)

(i) Both Odd Groups of the Parent System Are in Doublet States ($S_n = S_p = 1/2$)

Under these conditions the general wave function

$$\psi = a_0\psi_{L=I,\,S=0} + a_1\psi_{L=I-1,\,S=1} + a_2\psi_{L=I,\,S=1} + a_3\psi_{L=I+1,\,S=1} \quad (32)$$

[21] M. G. Mayer, Indiana Conference on Beta Spectroscopy and Nuclear Structure, 1953 (unpublished).
[22] R. L. Pease and H. Feshbach, Phys. Rev. **88**, 948 (1952).
[23] J. M. Blatt, Phys. Rev. **89**, 86 (1953).

may contain both singlet and triplet components and possibly three different values of L. Equations (9) and (32) give

$$\left|\int\sigma\right|^2=8a_0^2a_2^2\leqq 2. \tag{33}$$

(ii) I_n and I_p Are Good Quantum Numbers; $S_n=S_p=1/2$

The equivalence relations,

$$\mathbf{S}_q\rightarrow\mathbf{I}_q\frac{\langle\mathbf{S}_q\cdot\mathbf{I}_q\rangle}{I_q(I_q+1)},\quad q=n \text{ or } p, \tag{34}$$

make possible the reduction of Eq. (10) to

$$\left|\int\sigma\right|^2=\frac{2}{I(I+1)}\left|\frac{\langle\mathbf{S}_n\cdot\mathbf{I}_n\rangle\langle\mathbf{I}_n\cdot\mathbf{I}\rangle}{I_n(I_n+1)}-\frac{\langle\mathbf{S}_p\cdot\mathbf{I}_p\rangle\langle\mathbf{I}_p\cdot\mathbf{I}\rangle}{I_p(I_p+1)}\right|^2$$
$$=\frac{1}{2I(I+1)}\Bigg|I(I+1)\left\{\frac{\langle\mathbf{S}_n\cdot\mathbf{I}_n\rangle}{I_n(I_n+1)}-\frac{\langle\mathbf{S}_p\cdot\mathbf{I}_p\rangle}{I_p(I_p+1)}\right\}$$
$$+(I_n-I_p)(I_n+I_p+1)$$
$$\times\left\{\frac{\langle\mathbf{S}_n\cdot\mathbf{I}_n\rangle}{I_n(I_n+1)}+\frac{\langle\mathbf{S}_p\cdot\mathbf{I}_p\rangle}{I_p(I_p+1)}\right\}\Bigg|^2. \tag{35}$$

Equation (18) can be used to estimate $\langle\mathbf{S}_n\cdot\mathbf{I}_n\rangle$ and $\langle\mathbf{S}_p\cdot\mathbf{I}_p\rangle$ if the magnetic moments of suitable $4n\pm1$ nuclides are known. These nuclides must have the number of nucleons in the odd group equal to $\frac{1}{2}A-1$ in one and to $\frac{1}{2}A+1$ in the other.

(iii) jj Coupling; One Hole and One Particle

The ground states of $_{15}P_{13}$, $_{17}Cl_{15}$, $_{19}K_{17}$, and $_{21}Sc_{19}$ belong in this category. The preceding relations [Eqs. (34) and (35)] remain valid with the advantage that $\langle\mathbf{S}_n\cdot\mathbf{I}_n\rangle$ and $\langle\mathbf{S}_p\cdot\mathbf{I}_p\rangle$ can be evaluated explicitly. Thus,

$$\begin{aligned}2\langle\mathbf{S}_n\cdot\mathbf{I}_n\rangle&=j_n+1, \quad j_n=l_n+\tfrac{1}{2}\\&=-j_n, \quad j_n=l_n-\tfrac{1}{2}.\end{aligned} \tag{36}$$

Special Cases

For $j_n=l_n+\frac{1}{2}$, $j_p=l_p+\frac{1}{2}$,

$$\left|\int\sigma\right|^2=\frac{(j_n-j_p)^2}{8I(I+1)j_n^2j_p^2}$$
$$\times|I(I+1)-(j_n+j_p)(j_n+j_p+1)|^2. \tag{37}$$

For $j_n=l_n+\frac{1}{2}$, $j_p=l_p-\frac{1}{2}$,

$$\left|\int\sigma\right|^2=\frac{(j_n+j_p+1)^2}{8I(I+1)j_n^2(j_p+1)^2}$$
$$\times|I(I+1)-(j_p-j_n)(j_p-j_n+1)|^2. \tag{38}$$

Interchange of j_n and j_p in Eq. (38) gives $|\int\sigma|^2$ for $j_n=l_n-\frac{1}{2}$, $j_p=l_p+\frac{1}{2}$.

For $j_n=l_n-\frac{1}{2}$, $j_p=l_p-\frac{1}{2}$,

$$\left|\int\sigma\right|^2=\frac{(j_n-j_p)^2}{8I(I+1)(j_n+1)^2(j_p+1)^2}$$
$$\times|I(I+1)-(j_n+j_p+1)(j_n+j_p+2)|^2. \tag{39}$$

(iv) jj Coupling: $j_n=j_p=j$, $l_n=l_p=l$

The ground states of $_{11}Na_9$ and $_{13}Al_{11}$ may be discussed under this heading. Equation (10) yields

$$\left|\int\sigma\right|^2=\frac{2}{I(I+1)(2l+1)^2}|\langle\mathbf{I}_n\cdot\mathbf{I}\rangle-\langle\mathbf{I}_p\cdot\mathbf{I}\rangle|^2$$
$$=\frac{2}{I(I+1)(2l+1)^2}|\langle\mathbf{I}_n^2\rangle-\langle\mathbf{I}_p^2\rangle|^2. \tag{40}$$

In $_{13}Al_{11}$, $I=4$, $l=2$, $\langle\mathbf{I}_p^2\rangle=35/4$, $\langle\mathbf{I}_n^2\rangle\geqq15/4$; hence

$$\left|\int\sigma\right|^2\leqq1/10, \tag{41}$$

if we exclude the unlikely possibility that the accurate description of the odd-neutron group requires a large admixture of component states with $I_n=7/2$ or $9/2$.

Interpolation formulas similar to Eqs. (27) and (29) can be derived immediately from Eqs. (10) and (26):

$$\left|\int\sigma\right|^2=\frac{I+1}{2I}\left(\frac{j}{l+\frac{1}{2}}\right)^2$$
$$\times\left(\frac{2\mu(T_3=\pm1)-(\mu_j{}^n+\mu_j{}^p)I/j}{\mu_j{}^n-\mu_j{}^p}\right)^2, \tag{42}$$

$$\left|\int\alpha\right|^2=\frac{I+1}{2I}\left(\frac{j}{l+\frac{1}{2}}\right)^2\left(\frac{\mu(1)-\mu(-1)}{\mu_j{}^n-\mu_j{}^p}\right)^2. \tag{43}$$

Introducing $I=4$, $j=5/2$, $l=2$, and $\mu(_{11}Na_{13})=1.688$ into Eq. (42), we get

$$\left|\int\sigma\right|^2\sim0.021 \tag{44}$$

for the type e superallowed component in the decay of $_{13}Al_{11}$.

5. EVIDENCE FOR SUPERALLOWED TRANSITIONS IN THE $4n$ SERIES

Recent experimental studies[1–5] indicate the existence of a group of superallowed transitions characterized by $T=1$, $\Delta I=0$, $A=4n$. The transitions probably occur as strong components in the decay of $_{13}Al_{11}$, $_{15}P_{13}$, $_{17}Cl_{15}$, and $_{21}Sc_{19}$. Also a weak superallowed component may produce observable effects in the decay of $_{11}Na_9$.

In principle $_7N_5$ and $_5B_3$ should also decay through superallowed channels, but the theoretical estimates of the branching ratios in these examples places the intensity of the superallowed component below the threshold for observation with present experimental techniques.

The information available for locating the lowest $T=T_3=0$ level (in the level diagram of the stable isobar) may be illustrated by the example at $A=24$. The disintegration energies of $_{11}Na_{13}$ and of $_{12}Mg_{11}$ are known. This information and the approximate relation

$$M(T=1,\ {}_{12}Mg_{12})-M(T=1,\ {}_{11}Na_{13}) \cong M(T=\tfrac{1}{2},\ {}_{12}Mg_{11})-M(T=\tfrac{1}{2},\ {}_{11}Na_{12}) \quad (45)$$

place the lowest $T=1$ state in $_{12}Mg_{12}$ at the excitation energy 9.52 Mev. This value lies above the limit of alpha stability (at 9.33 Mev) in agreement with the observation of delayed α's associated with the decay of $_{13}Al_{11}$. Information on γ transitions in $_{12}Mg_{12}$ may eventually give an independent check on the location of the $T=1$ level. The mass difference $M(_{13}Al_{11})-M(_{12}Mg_{12})$ can also be determined in several ways: (a) from an estimate of the Coulomb energy difference, (b) from the threshold in the pn reaction on $_{12}Mg_{12}$, and (c) from the energy of the most energetic positrons observed in the decay of $_{13}Al_{11}$ (for $_{13}Al_{11}$ this energy has not been reported, but values are given for $_{15}P_{13}$ and $_{17}Cl_{15}$).

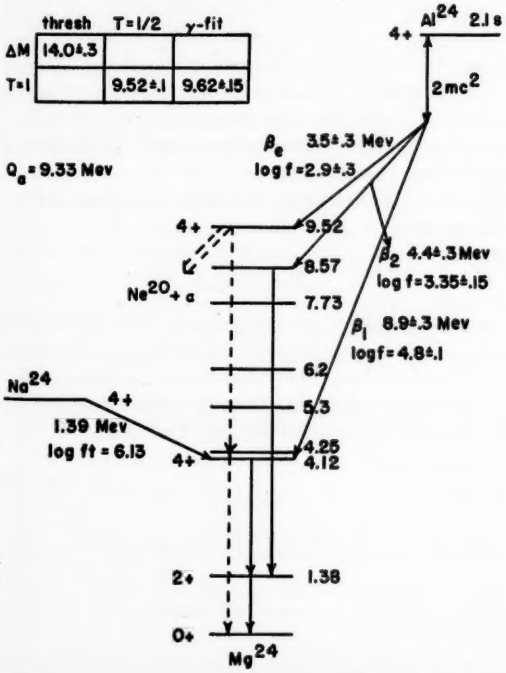

FIG. 2. Tentative decay scheme for Al^{24}. The box in the upper left corner gives values for $\Delta M(Al^{24}-Mg^{24})$ and the height of the $T=1$ level, obtained by the methods which label the columns.

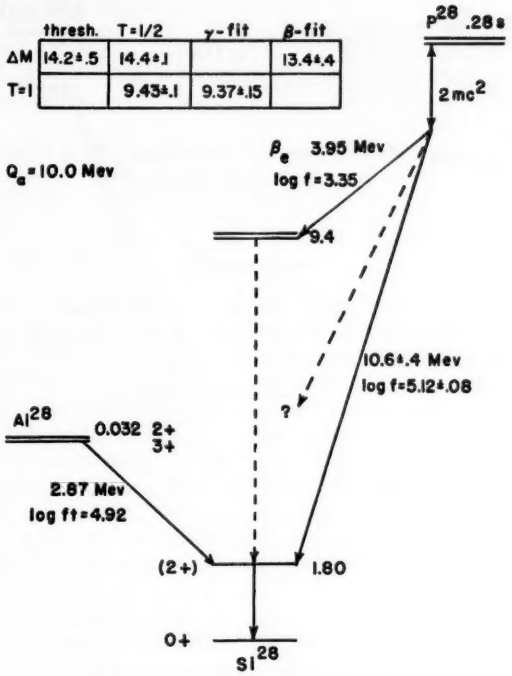

FIG. 3. Partial decay scheme for P^{28}.

$_{13}Al_{11}$, Fig. 2

The diagram shown is supported by all the recent work on $_{11}Na_{13}$, $_{12}Mg_{12}$, $_{13}Al_{11}$, and $_{12}Mg_{11}$. The 4.25-Mev level is probably not fed by β's since it is not observed in the decay of Na^{24}. Turner's work[24] indicates that, except for the $T=1$ level, the only known levels associated with the decay are those at 8.57 Mev and at 4.12 Mev (the latter is reached by the Na^{24} β decay). The $T=1$ level at 9.52 Mev may account for the observation of α's in the decay of Al^{24} (the threshold for the emission of α's by Mg^{24} is 9.33 Mev). The assumption that β^+ and β^- transitions to the 4.12-Mev level have nearly equal transition matrix elements yields a partial half-life $t_{\frac{1}{2}}(_{13}Al_{11}$, 4.12-Mev level$)=18$ to 30 sec, with a branching ratio of approximately 10 percent. If the transition to the 8.57-Mev level is allowed unfavored, it has a minimum partial half-life of about 10 sec and a maximum branching ratio of about 20 percent. If no other important transitions are assumed,

$$\begin{aligned} &70 \text{ percent} \leqq BR(\beta_e) \leqq 90 \text{ percent}, \\ &3 \text{ sec} \geqq t_{\frac{1}{2}}(\beta_e) \geqq 2.34 \text{ sec}, \\ &3.25 \pm 0.3 \leqq \log ft(\beta_e) \leqq 3.4 \pm 0.3. \end{aligned} \quad (46)$$

Equations (41) and (44) give $|M|^2 \sim 1.6-1.7$, close to the minimum possible value. Inserting this into the

[24] O. H. Turner, Australian J. Sci. Research 6, 380 (1953).

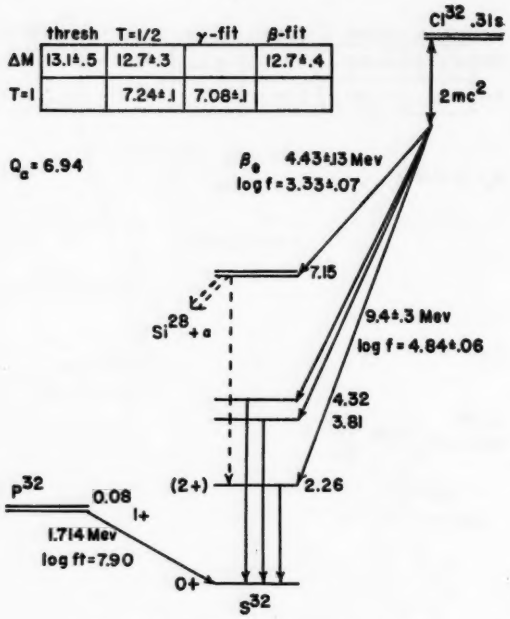

FIG. 4. A possible decay scheme for Cl^{32}.

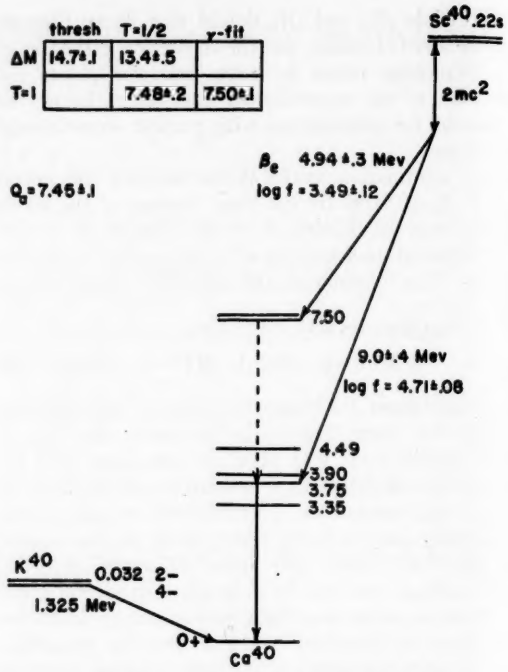

FIG. 5. Tentative decay scheme for Sc^{40}.

preceding inequality, we get

$$3.5\pm0.3 \leqq \log ft|M|^2 \leqq 3.6\pm0.3, \qquad (47)$$

consistent with $ft|M|^2 \sim 4700$, $\log ft|M|^2 = 3.67$.

$_{15}P_{13}$, Fig. 3

In $_{15}P_{13}$, the decay scheme is probably complex. The ground state and the low-lying first excited state in $_{13}Al_{15}$ have spins 3+ and 2+, respectively.[25] The order of these two levels may be reversed in one or both of $_{14}Si_{14}$ and $_{15}P_{13}$; the transition considered here as the superallowed component is that between the ground state of $_{15}P_{13}$ and the corresponding state in $_{14}Si_{14}$.

Since the number of allowed β^+ components in the decay of $_{15}P_{13}$ is unknown, only a minimum estimate of the branching ratio into the type e component can be given. Since $|\int 1|^2 = 2$, we must have $\log ft(\beta_e) \leqq 3.45$; this gives $t_{\frac{1}{2}}(\beta_e) \leqq 1.3$ sec or $BR(\beta_e) \geqq 20$ percent.

[25] Sheline, Johnson, Bell, Davis, and McGowan, Phys. Rev. 94, 1642 (1954).

$_{17}Cl_{15}$, Fig. 4

The close doublet structure exhibited by $_{15}P_{17}$ presumably occurs also in $_{17}Cl_{15}$ and the lowest $T=1$ states of $_{16}S_{16}$. The γ's observed in the decay of $_{17}Cl_{15}$ fit known levels of $_{16}S_{16}$ as shown. Delayed α's observed in the decay of $_{17}Cl_{15}$ may come from the lowest $T=1$ level of $_{16}S_{16}$ since the excitation energy (7.15 Mev) is greater than Q_α (6.94 Mev).

A procedure like that used for $_{15}P_{13}$ gives $BR(\beta_e) \geqq 25$ percent.

$_{21}Sc_{19}$, Fig. 5

A tentative decay scheme is shown. Here a branching ratio ≥ 25 percent is required for the type e component. No delayed α's have been observed in the decay of Sc^{40}, consistent with the assumption that there is no branching to states higher than the first $T=1$ level.

Half-Lives of Mn^{52} and Mn^{54}

E. W. Backofen and R. H. Herber
Department of Chemistry and Laboratory for Nuclear Science, Massachusetts Institute of Technology, Cambridge, Massachusetts
(Received September 15, 1954)

Manganese activities produced by deuteron bombardment of chromium powder and radiochemically purified both by standard chemical techniques and ion-exchange chromatography, have been counted for a period of 2500 hr. The half-life of Mn^{54} is determined to be 291±1 days, while that of Mn^{52} is found to be 5.72±0.02 days.

THE half-life of Mn^{52} has been variously reported as 5.8,[1] 6.0,[2,3] 6.2,[4] and 6.5 days.[5] In a recent study of several $(d,2n)$ reactions, Burgus *et al.*[6] determined the half-life of Mn^{52} as 5.60±0.01 days by following the decay over a period of 30 days.

The half-life of Mn^{54} has been reported[5,7] as 310 days.

In the course of some studies of the separation of transition elements by means of anion exchange techniques, we have had occasion to determine the half-life of the ~6-day and the ~310-day Mn activities over a period of about 2500 hours (18 half-lives of Mn^{52}).

50 mg of Cr powder were bombarded with 6.7 μa-hr of 15.5-Mev deuterons in the Massachusetts Institute of Technology cyclotron. The target was dissolved in 1 cc of 12*N* HCl and 10 mg Mn and 1 mg V carrier added. The solution was fumed down with nitric acid and the residue dissolved in 2 cc of water. The *p*H was adjusted to 7 with NH_4OH if necessary, and MnO_2 precipitated by the addition of $NaBrO_3$. The precipitate was centrifuged, washed with dilute HNO_3, and then redissolved with $NaHSO_3$. V and Cr holdback carriers were again added and the precipitation of MnO_2 repeated two more times. The final precipitate was dissolved in 5 cc of 12*N* HCl and 2 cc of this solution transferred to a counting vial. The remainder of the Mn activity in 12*N* HCl was passed two times through a 12 percent DVB Dowex-1 column, and 2 cc of that portion of the effluent which came through at the position expected for manganese were also transferred to a counting vial.

The samples were counted in a well-type scintillation counter with a AgI(Tl) crystal for a sufficient length of time to reduce the statistical counting error to less than 0.1 percent. The crystal temperature was kept constant at 68°F. A sealed source of Co^{60} in paraffin was counted during each counting period, and the performance of the detector corrected to the counting rate of the standard on the first day of the radio-assay series, corrected for the decay of Co^{60}.

Using a sample of Mn^{54}, the disintegration rate of which was known,[8] the efficiency of the detector for the single 0.85-Mev gamma[9] ray of Mn^{54} was determined to be 18.1 percent at the settings of the scintillation counter used in this study. The Mn^{54} activity of the sample followed for 2500 hr, using our revised value of the Mn^{54} half-life was 6.40 cps at the start of the determination. The yield ratio of Mn^{54}/Mn^{52} is about 0.011.[10] The branching ratio of the Mn^{52} decay is reported[11] to be 0.35; however, both modes of decay lead to a gamma cascade counted by the detector as a single pulse. From these data the counting efficiency for Mn^{52}, which had a zero-time activity of 1891.7 counts/sec, is found to be 60 percent. Using the reported[12] value of 5.27 years for the half-life of Co^{60}, a value of 291±1 days is found for the half-life of Mn^{54} from our data. This value is in good agreement with that (290±10) reported[13] recently from an analysis of the decay data of 20 samples of manganese activity produced by the $Cr^{54}(d,2n)Mn^{54}$ reaction.

Using this value of the Mn^{54} half-life, the half-life of Mn^{52} was calculated from the raw counting data and found to be 5.72±0.02 days. No difference could be found in the half-life of the Mn^{52} determined from the sample subjected only to the MnO_2 precipitation separation, and that determined from the manganese fraction passed two times through the ion exchange bed.

The authors wish to thank Miss Rita J. Goldstein for assistance with counting a portion of the samples in this study.

[1] J. T. Byrne, J. Chem. Phys. **19**, 504 (1951).
[2] Miller, Thompson, and Cunningham, Phys. Rev. **74**, 347 (1948).
[3] T. H. Handley, Oak Ridge National Laboratory ORNL-867 (unpublished).
[4] Haymond, Garrison, and Hamilton, J. Chem. Phys. **19**, 382 (1951).
[5] G. T. Seaborg and J. J. Livingood, Phys. Rev. **54**, 391 (1938).
[6] Burgus, Cowan, Hadley, Hess, Shull, Stevenson, and York, Phys. Rev. **95**, 750 (1954).
[7] *Table of Nuclear Data*, National Bureau of Standards Circular No. 499 (U. S. Government Printing Office, Washington, D. C., 1950).
[8] 2.78×10^3 *d*/sec on April 28, 1954. Furnished by Oak Ridge National Laboratory.
[9] M. Deutsch and L. G. Elliott, Phys. Rev. **65**, 211 (1944).
[10] E. W. Backofen (private communication).
[11] Good, Peaslee, and Deutsch, Phys. Rev. **69**, 313 (1946).
[12] W. K. Sinclair and A. F. Holloway, Nature **167**, 365 (1951); G. L. Brownell and C. J. Maletskos, Phys. Rev. **80**, 1102 (1950).
[13] P. Kafalas, Ph.D. Thesis in Chemistry, Massachusetts Institute of Technology, August 1954 (unpublished).

Short-Period Delayed Neutrons from Fission*

P. J. Bendt and F. R. Scott
Los Alamos Scientific Laboratory, University of California, Los Alamos, New Mexico
(Received October 1, 1954)

A new group of delayed neutrons having a mean-life of 216±60 milliseconds has been observed to follow fission of U^{235}. The apparent yield is 2.7±0.7 percent of the delayed neutrons. The experiment was done using a multiplying assembly of uranium metal bombarded once every 30 seconds by x-rays from a betatron. A discussion is given of the hypothesis that these delayed neutrons follow the decay of Li^9, and that Li^9 is formed as the light fragment in ternary fission.

I. INTRODUCTION

THE five well-established delayed-neutron groups following uranium fission were accurately measured by Hughes, Dabbs, Cahn, and Hall.[1] Hughes *et al.* also reported the possible existence of a group of delayed neutrons having a mean-life (decay time to $1/e$ of initial value) of about 72 milliseconds. de Hoffmann, Feld, and Stein[2] did not observe this period, but did report a 9 millisecond period. Brolley, Cooper, Hall, Livingston, and Schlacks[3] found no gamma, beta, or neutron activities shorter than 0.62 second. Comments on these papers are made in Part VI, Discussion of Results.

The present work is an attempt to resolve the inconsistent results of previous investigators. Further incentive was provided by the availability of a new method of doing the experiment.

II. APPARATUS

The apparatus was arranged so that a burst of x-rays from a betatron produced neutrons in a highly multiplying assembly of U^{235} metal. In the assembly, fission chains sustained by prompt fission-neutrons produced delayed-neutron precursors during a time interval of less than 10 microseconds. A ten-channel time analyzer was used to study neutron leakage from the uranium assembly after the burst.

The betatron was pulsed every 30 seconds by a clock-actuated trigger. The x-ray yield was approximately 0.75 milliroentgen per burst at one meter, and the maximum x-ray energy was about 11 Mev. Length of the x-ray bursts was less than 1 microsecond. Distance from the x-ray source in the betatron to the center of the multiplying assembly was approximately 80 cm.

The multiplying assembly was a uranium sphere highly enriched in U^{235}. The uranium was not surrounded by reflecting material, except for its enclosure in a box of 0.030 inch cadmium. The cadmium box was a precaution against the introduction of a spurious period by the return of room scattered neutrons. Data were taken with the assembly adjusted to give a prompt neutron multiplication $M_p=100$. The mean life of neutron chains at this multiplication is less than 10 microseconds. Because of the hazard involved in operating an assembly at this high multiplication, the assembly was put together by remote control.

The neutron detector consisted of a block of paraffin 8 in.×13 in.×20 in., containing 26 General Electric proportional counters lined with B^{10}. Sensitivity to fission spectrum neutrons intercepted by the detector was about 10 percent; the corresponding sensitivity for counting gamma-ray photons from radium was about 10^{-7}. Because of the modest size of the paraffin moderator, and the large amount of B^{10} present in the counters, the mean life of neutrons in the paraffin block was less than 50 microseconds. The detector assembly was covered with 0.030-inch cadmium, and was located about 25 cm from the multiplying assembly, in a position where it did not intercept the x-ray beam.

Figure 1 is a schematic diagram showing the apparatus in the laboratory on the left, and the equipment in the control room on the right. The time analyzer was triggered by the betatron orbit-shift pulse, and there was a delay of one channel width between the trigger pulse and the opening of the first channel. The channel widths used to study delayed neutrons were 0.001, 0.010, 0.040, 0.100, and 1.000 seconds. All counts from the detector were recorded on a monitor scaler, which counted continuously. In addition, a gated "background" scaler counted for 1 second starting 26 seconds after the betatron was fired.

III. CORRECTIONS TO THE DATA

A background correction was applied to the data to take account of delayed neutron activity from the previous bursts; i.e., bursts preceding the opening of the channels by approximately 30 seconds, 60 seconds, 90 seconds, etc. The data from which the background correction was calculated were obtained from the background scaler. At 0.1 second after a burst, the correction amounted to 10 percent.

At the start and finish of each day, runs were made with 1-second channel widths. Other data taken the same day were normalized to the 1-second data taken

*Work performed under the auspices of the U. S. Atomic Energy Commission.
[1] Hughes, Dabbs, Cahn, and Hall, Phys. Rev. **73**, 111 (1948).
[2] de Hoffmann, Feld, and Stein, Phys. Rev. **74**, 1330 (1948).
[3] Brolley, Cooper, Hall, Livingston, and Schlacks, Phys. Rev. **83**, 990 (1951).

that day by means of the number of monitor counts. This took care of variation in betatron yield during different runs.

Data taken with 0.001-second channel widths were tested to determine the time at which the counting apparatus was fully recovered from saturation during the neutron burst. This was done by setting a strong steady source close to the detector, which by itself gave a counting rate equal to that obtained from the multiplying assembly following a burst. Data were taken with this source in place, and the number of counts the source contributed was subtracted from each channel. It was found that the net counts per channel due to the multiplying assembly were the same within statistics with or without the strong steady source for all channels after 0.003 second. This indicates that the apparatus was fully recovered by the third channel.

One effect of neutron chains in the multiplying assembly is to cause larger fluctuations in the counting than would result from a random source. Analysis of repeated runs shows the points have a probable error about 4.5 times as large as expected from a random source. This is not the result of instability of the apparatus, which was checked with a random neutron source, but is inherent in the use of a multiplying assembly in the experiment. Table I lists the number of counts per point for the data shown in Figs. 2–4, and the "probable error" including the factor 4.5.

TABLE I. Probable error of experimental points.

Channel width (seconds)	Counts per point	"Probable error" of each point[a] (percent)	(units)
1 (lowest points)	60 000	1.2	±0.5
0.1	32 000	1.7	±1.0
0.040	55 000	1.3	±0.8
0.010	4000	4.8	±4
0.001	2000	6.8	±6
Average of 0.001	16 000	2.4	±2

[a] Intercept on the ordinate on Figs. 2–4 is 86 units.

IV. MULTIPLYING ASSEMBLY

The use of a multiplying assembly was necessary in order to increase the yield of the experiment. The phenomena taking place in the assembly may be described as follows: during the x-ray burst from the betatron, prompt neutrons are created in the uranium by γ-n and γ-fission processes. This initial population of neutrons is sustained several microseconds by neutron chains, which create perhaps 200 times as many fissions as were produced by the betatron x-rays. A large number of delayed neutron precursors are formed during this "burst" at zero time. Delayed neutrons emitted after zero time initiate prompt neutron chains which, on the average, are 100 neutrons long, thus increasing the neutron leakage from the assembly by 100. The yield of the experiment is thus 200×100, or 20 000 times as large as would be obtained from a small mass of uranium in a nonmultiplying geometry.

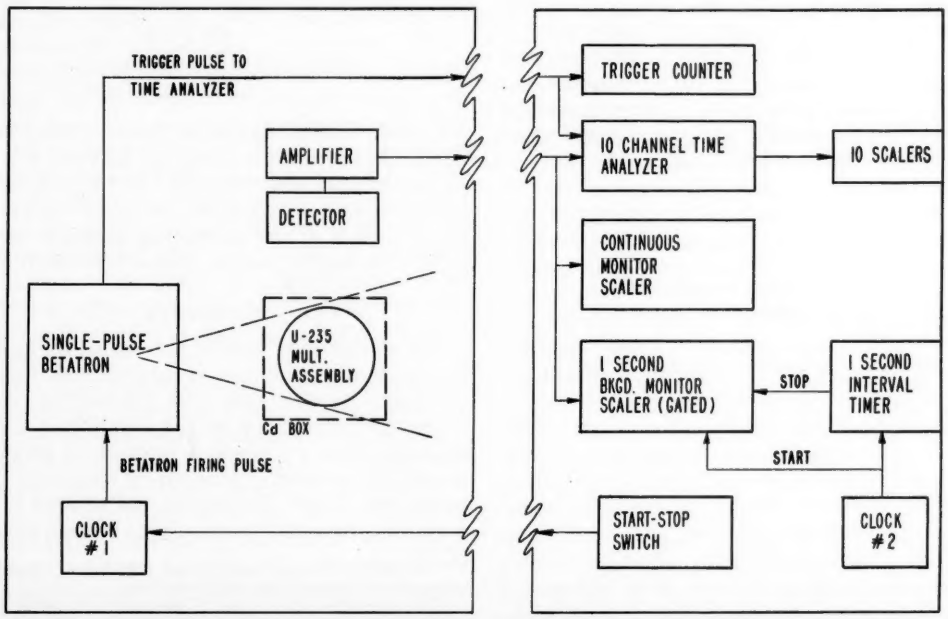

FIG. 1. Schematic diagram of apparatus. Equipment on the left was located in the laboratory, and equipment on the right was located in the control room.

TABLE II. Delayed-neutron groups and corresponding exponentials for a multiplying assembly. The A_j contain an arbitrary normalization factor. τ_i and β_i for the five longest delayed-neutron groups are from Hughes (reference 1).

Delayed-neutron groups		Multiplying-assembly exponentials ($M_p=100$) Five delayed-neutron groups		Six delayed-neutron groups	
τ_i (sec)	$100\beta_i$	T_j (sec)	A_j	T_j (sec)	A_j
80.2	0.025	90.1	0.0141	90.1	0.0141
31.7	0.166	47.6	0.0472	47.6	0.0472
6.51	0.213	9.3	0.1543	9.3	0.1543
2.19	0.241	2.80	0.2098	2.80	0.2104
0.62	0.085	0.668	0.2476	0.669	0.2528
0.216	0.020			0.220	0.1802
Sums=	0.750[a]		0.6730[b]		0.8590[b]

[a] 100 times the apparent yield of delayed neutrons per fission neutron.
[b] These are the intercepts on the ordinate of the curves drawn in Figs. 2–5.

Inasmuch as the delayed neutrons are observed through the neutron chains they initiate, neutrons reaching the detector have the energy spectrum of leakage neutrons from the assembly, and not the energy spectrum of delayed neutrons. The apparent yield of one group of delayed neutrons compared with another group of delayed neutrons thus depends on the relative effectiveness of these groups of neutrons in initiating neutron chains in the uranium assembly. From measurements made with various neutron sources, it is known that the multiplication of the uranium assembly is constant within 5 percent for neutrons with energies from 100 kev up to the mean energy of the fission spectrum. The measured mean energies[1] of the established groups of delayed neutrons fall within this range. The energy spectrum of the new group of delayed neutrons reported here is completely unknown. If it falls generally within the range 100 to 1000 kev, then the apparent yield should not differ from the true yield by more than 5 percent due to energy sensitivity of the multiplying assembly. Energy sensitivity of the detector has no effect on the observed yield.

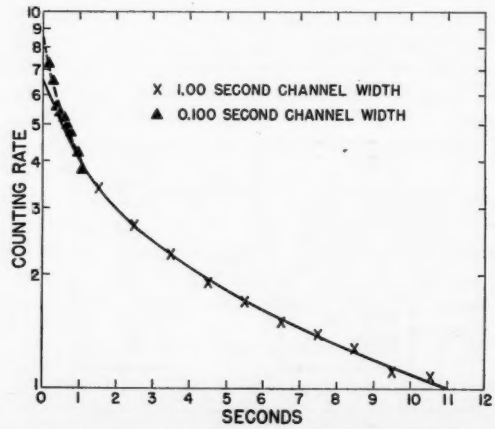

FIG. 2. Neutron leakage from the multiplying assembly followed out to 11 seconds.

Each group of delayed neutron precursors decays exponentially with a characteristic mean life, but the decay of the neutron population in a multiplying assembly is not proportional to the sum of these exponentials. After zero time, fission chains initiated by delayed neutrons create additional precursors. Thus, each delayed neutron period is coupled with all the other periods.

However, the decay of the neutron population in a multiplying assembly is proportional to a sum of exponentials,

$$n(t) \propto \sum_j A_j \exp[-t/T_j], \quad (1)$$

where $n(t)$ is the number of neutrons in the assembly, t is time, T_j are the periods, and A_j are the coefficients of the exponentials. The number of exponentials is the same as the number of delayed-neutron groups.[4] Letting τ_i and β_i represent the mean lives and yields of the delayed neutron precursors, the values of T_j are different from the τ_i, and the values of A_j are different from β_i/τ_i.[5]

The problem of transforming data taken from a multiplying assembly to the delayed neutron mean lives and yields (and *vice versa*) can be solved exactly by use of Laplace transforms.[6] The following equation ("inhour equation"), derived by means of Laplace transforms, was used to determine the values of T_j from assumed values of τ_i and β_i,

$$\sum_i \beta_i\tau_i/(T_j-\tau_i)=\sum_i \beta_i(1-k)/\delta k=0.003155. \quad (2)$$

k is the neutron reproduction constant, and δk is the change in k between delayed and prompt critical. For the coefficients of the exponentials,

$$A_j=2.383\frac{\sum_i \beta_i/(T_j-\tau_i)}{T_j\sum_i \beta_i\tau_i/(T_j-\tau_i)^2} \quad (3)$$

was used. The normalization factor 2.383 was arbitrarily chosen to make the decay curve of the multiplying assembly pass through 0.4 at 1 second when the values reported by Hughes[1] for τ_i and β_i are used. Decay periods of the multiplying assembly are compared with delayed neutron groups in Table II.

V. RESULTS

The experimental results are shown in Figs. 2–4. Where the statistical error is not indicated, the size of the symbol represents the error. The solid line in Fig. 2 is the predicted decay of the multiplying assembly calculated from the τ_i and β_i reported by Hughes[1] for five delayed-neutron groups having mean lives of 0.62 second and longer. The dashed line between zero and 1 second corresponds to six delayed-neutron groups.

[4] The decay of the prompt-neutron population, several orders of magnitude faster, is not considered here.
[5] The convention that τ_i and T_j are positive numbers is used.
[6] G. Goertzel (unpublished); H. Soodak, *The Science and Engineering of Nuclear Power* (Addison-Wesley Press, Inc., Cambridge, 1949), Vol. 2, Chap. 8, p. 93.

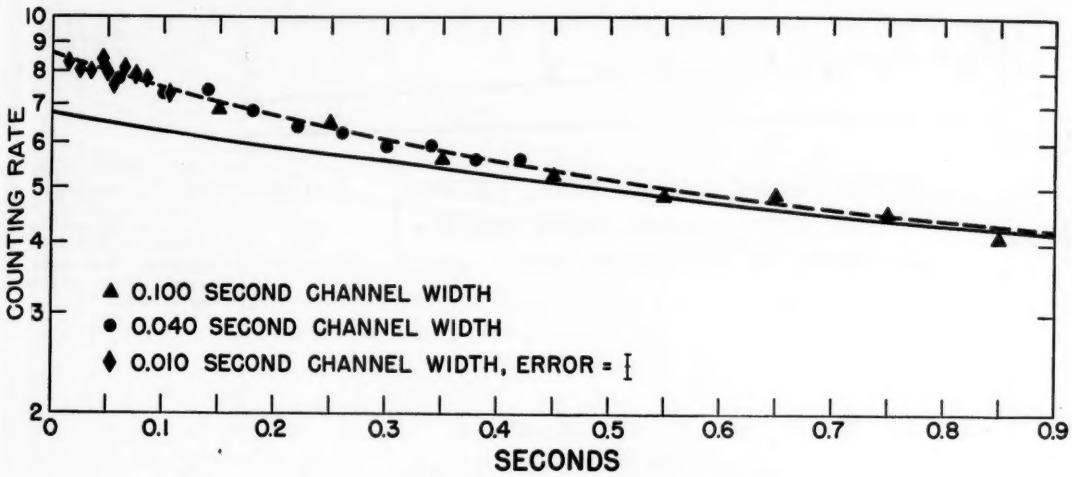

FIG. 3. Neutron leakage from the multiplying assembly.

Hughes measured τ_i and β_i for fission initiated by thermal-reactor neutrons, while the spectrum of neutrons causing fission in our multiplying assembly is approximately equivalent to a fission spectrum. Insufficient knowledge of the fission-product yield curve for fast-neutron induced fission of U^{235}, plus the fact that two of the five delayed-neutron emitters have not been identified, make it impractical to estimate the change (if any) in β_i between thermal-neutron and fission-neutron induced fission. However, the agreement after 1 second between experimental points and the solid line (Fig. 2) indicates the relative values of the five β_i measured by Hughes must be very nearly correct for our experiment.

The solid lines in Figs. 3 and 4 are also the predicted curve based on five groups. For times less than 1 second, the experimental points lie above this line. This indicates the existence of a sixth delayed-neutron group having a shorter mean life. The τ_6 and β_6 of the sixth group were determined by finding a predicted decay curve for the multiplying assembly which best fits the experimental points; this curve is shown by dashed lines on Figs. 2–4. In constructing this predicted curve, the Hughes values of τ_i and β_i for five groups were assumed to be exact, and only τ_6 and β_6 were adjusted to get the best fit.

It should be noted that T_j and A_j for the first five exponentials are somewhat different when calculated from six groups than when calculated from five groups. The sum of five exponential periods in the presence of six groups intercepts the zero time axis 1 percent higher than the solid line drawn in the figures. Therefore, the difference between the dashed line and the solid line is not exactly equal to $A_6 \exp(-t/T_6)$. The best fit to experimental points (Fig. 3) was obtained with $\tau_6 = 216$ milliseconds and $\beta_6 = 2\times10^{-4} = 2.7$ percent of the total delayed neutron yield. Experimental uncertainties assigned to these values are ± 60 milliseconds and ± 0.7 percent. Values of τ_i, β_i, T_j, and A_j are tabulated in Table II.

The data taken with 0.001- and 0.010-second channel widths (Fig. 4) show that no delayed-neutron group was observed having a period between 5 and 50 milliseconds and an apparent yield as large as 0.5 percent of the delayed-neutron yield. The experimental results do not rule out the possibility that the sixth group reported here is actually a composite of two or more delayed-neutron groups having mean lives of approximately 200 milliseconds.

VI. DISCUSSION OF RESULTS

The experimental data reported by Hughes[1] as evidence for a delayed-neutron group having a mean life of 72 milliseconds have been plotted in Fig. 5, along with the same curves shown in Fig. 3. The different experimental procedure used by Hughes requires that the data be modified by four calculations before it can be compared with our results: (1) The Hughes five-period decay curve has been normalized to the same intercept on the zero-time axis as our five-period curve. (2) The Hughes five-period curve has been altered to conform with the decay curve for a multiplying assembly (Table II). (3) The displacement of the (renormalized) Hughes experimental points above the five-period decay curve has been multiplied by 1.504 to correct for decay of the sixth period during the 0.19 second irradiation of their uranium slug. The decay during irradiation was assumed to have a mean life of 216 milliseconds. (4) The Hughes experimental points have been raised (by less than 0.2 percent) because the sixth period in a multiplying assembly would decay at the rate of 220 milliseconds instead of 216 milliseconds. It is seen from Fig. 5 that the Hughes

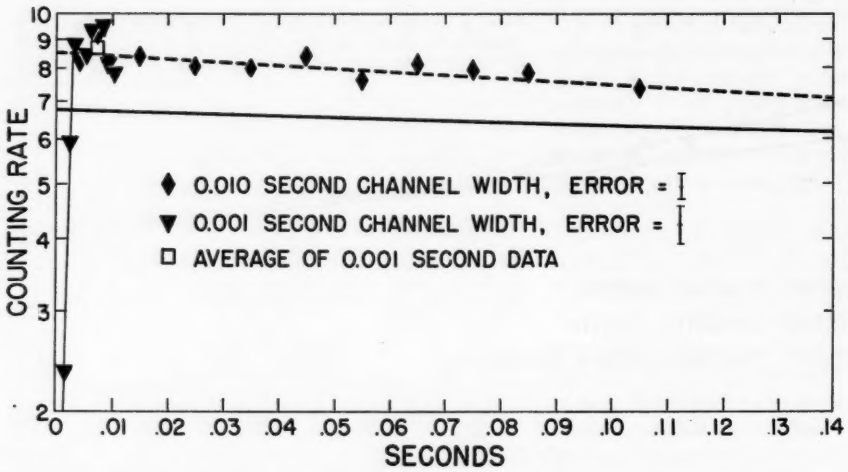

FIG. 4. Neutron leakage from the multiplying assembly. The first two points with 0.001 second channel width were taken before the apparatus was fully recovered from saturation during burst.

data are consistent with our results, except for the first point.

de Hoffmann[2] reported an activity with a mean life of 9 milliseconds and an apparent yield of 2 percent of the delayed neutrons. de Hoffmann states that the initial intensity of the short period after an infinitely short irradiation would be about 10 times that of the other periods together. Our data taken from 0.003 to 0.011 second with 0.001-second channel widths do not show such a period.

Brolley[3] looked for short period gamma- and beta-ray activities following fission, and also delayed neutrons by observing capture gamma rays from cadmium, with negative results. The efficiency of the paraffin block for returning thermalized neutrons to the cadmium converter may well have been too low for Brolley to detect a yield as small as observed here. The failure to observe a 200-millisecond gamma-ray period can be explained by hypothesizing that the delayed neutrons follow the decay of Li^9 (see below), in which case they presumably are not accompanied by the emission of a gamma ray. By using a different technique, Brolley might have observed Li^9 beta particles on those experimental runs in which the decay was followed from zero to 2.7 seconds. However, on these runs a 0.62-inch Al absorber was inserted between the uranium foil and the scintillator. Only a small fraction of Li^9 beta rays could penetrate this absorber.

VII. DECAY OF Li^9 AND TERNARY FISSION

According to beta-decay theory, it is unlikely for an isotope with mass greater than 70, such as products of binary fission, to have a 216-millisecond beta decay followed by neutron emission. The required high energy for so short a beta period would exceed the binding energy of a neutron and lead to emission of a prompt neutron. Neutron emission is more likely to follow short-period beta decay of low-Z isotopes.

It is hypothesized that the short-period delayed neutrons reported here follow the decay of Li^9, and that the Li^9 is formed as the light fragment in ternary fission. Li^9 is the only known delayed-neutron emitter having a mean life in the range 216 ± 60 milliseconds. Its mean life is 242 milliseconds.[7] The decay scheme is assumed to be

$$Li^9 \rightarrow Be^{9*} + \beta, \quad Be^{9*} \rightarrow Be^8 + n, \quad Be^8 \rightarrow 2\alpha.$$

Various schemes by which Li^9 could be formed from boron or other light elements in the counter tubes were considered, and all rejected on the basis that the threshold energies were too high for the reactions to be caused by fission neutrons or gamma rays, or by 11-Mev betatron x-rays. While mass numbers lower than about 70 are not observed for fragments of binary fission, Li^9 could be produced as the light fragment in ternary fission.

It is well established that a 10- to 25-Mev alpha particle is emitted in uranium fission with a frequency of about 1 event per 450 binary fissions.[8] There is some uncertainty regarding the occurrence in ternary fission of a light fragment having a mass and charge greater than an alpha particle. Titterton[8] reports observing three-particle fission in which the light fragment has a range less than 20 microns in photographic emulsion with a frequency of 1 event per 85 ± 10 binary fissions. The most probable value of the range is about 1 cm in air, and work with desensitized emulsions shows the tracks are still observed when the emulsion is no longer recording alpha particles. Allen and Dewan,[9] using counting techniques, report that in 1.3 percent of (slow neutron) fission events in U^{235} short-range charged particles considerably more massive than alpha particles are emitted. They conclude from the initial specific

[7] Gardner, Knable, and Moyer, Phys. Rev. **83**, 1054 (1951); Holt, Thorn, and Waniek, Phys. Rev. **87**, 378 (1952); R. K. Sheline, Phys. Rev. **87**, 557 (1952).
[8] E. W. Titterton, Nature **168**, 590 (1951).
[9] K. W. Allen and J. T. Dewan, Phys. Rev. **82**, 527 (1951).

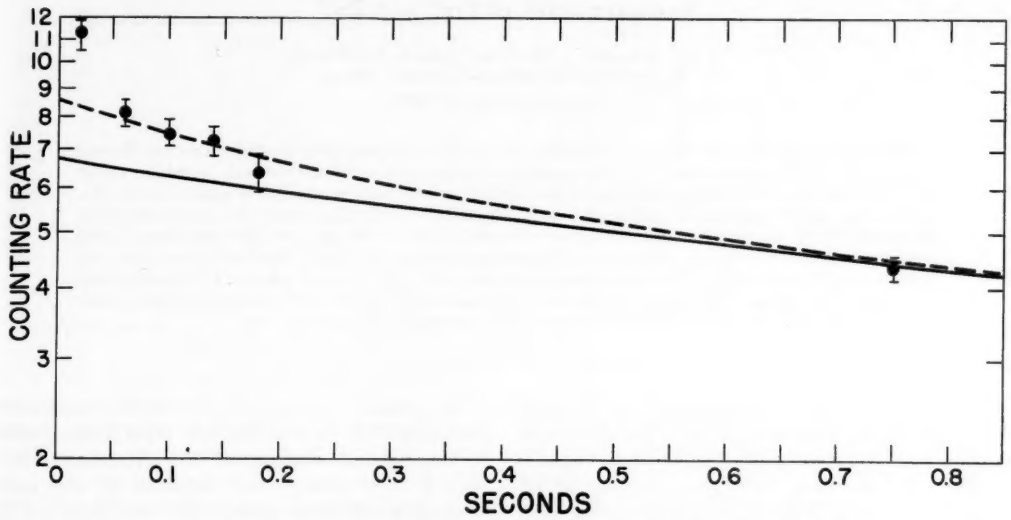

FIG. 5. Plot of the Hughes data (reference 1) with the curves shown in Fig. 3.

ionization of these particles that the mass may be in the range 13 ± 4, but they add that photographic plate evidence is against the existence of particles with mass numbers greater than about 12. Laboulaye, Tzara, and Olkowsky,[10] using a cloud chamber, failed to observe any short-range tracks originating from the vicinity of the fission in excess of the expected nuclear recoils from the two heavy-fission fragments. Marshall[11] and Demers[12] have studied uranium fission extensively in photographic plates and have not reported evidence for this type of fission.

There are 20 known isotopes with masses between 5 and 12, and 24 isotopes in the range 13 ± 4. If the evidence of Allen and Dewan is accepted, an order-of-magnitude estimate of the yield per fission of a particular light isotope such as Li^9 can be made by dividing 0.013 by 24, which gives approximately 5×10^{-4}. If one assumes the total neutron yield per fission is 2.5, this value is consistent with our observed yield of 2×10^{-4} for delayed neutrons with 216-millisecond mean life.

The fact that investigators of fission using photographic plates have not reported ternary fission with a hammer track has been presented as an argument against the formation of Li^9 in fission. The following is a possible explanation for their failure to see such tracks. If Be^{9*} is formed in the lowest excited level at 2.429 Mev,[13] then Be^8 will be formed in the ground state. The kinetic energy of Be^8 would be about 69 kev, since the neutron takes 8/9 of the kinetic energy released in the reaction $Be^{9*}\rightarrow Be^8+n$. The decay of Be^8 releases only 96 kev; the resulting two alpha particles would not make observable tracks in a photographic emulsion. This process for the decay of Li^9 leaves open the possibility that the frequency of observable hammer tracks in photographic emulsion is much lower than the frequency with which Li^9 is formed in ternary fission. A measurement of the energy spectrum of the Li^9 beta particles would help establish the likelihood of the process.

Further experiments looking for a delayed-beta period following fission, or for coincidences between delayed neutrons and beta or alpha particles, are necessary to substantiate or disprove the hypothesis that Li^9 is formed in ternary fission. A measurement of the energy spectrum of the delayed neutrons for comparison with the energy of neutrons from Li^9 decay would give supporting evidence.

[10] Laboulaye, Tzara, and Olkowsky, Compt. rend. **237**, 155 (1953); J. de phys. radium **15**, 470 (1954).
[11] L. Marshall, Phys. Rev. **75**, 1339 (1949).
[12] P. Demers, Can. J. Phys. **31**, 78 (1953).
[13] F. Ajzenberg and T. Lauritsen, Revs. Modern Phys. **24**, 321 (1952).

Radioactivities of Zn^{69} and Zn^{71}

J. M. LeBlanc, J. M. Cork,* and S. B. Burson
Argonne National Laboratory, Lemont, Illinois

(Received October 22, 1954)

The beta and gamma rays emitted in the decay of Zn^{69} and Zn^{71} have been studied with a ten-channel coincidence scintillation spectrometer. The previous assignments of a 435-kev isomeric transition to the 14-hr Zn^{69} activity and a 900-kev beta ray to the 1-hr Zn^{69} activity were confirmed. In addition to the 2.2-min activity of Zn^{71}, a previously unreported 3-hr activity of Zn^{71} was detected. A beta ray with an end-point energy of 2.4±0.2 Mev and gamma rays with energies of 0.12, 0.51, 0.90, and 1.09 Mev were detected and assigned to the 2.2-min activity. A beta ray with an end-point energy of 1.5±0.1 Mev and gamma rays with energies of 0.38, 0.49, and 0.61 Mev were detected and assigned to the 3-hr Zn^{71} activity. It was established that each of the gamma rays in the 3-hr activity is in coincidence with the other two gamma rays as well as the 1.5-Mev beta ray. Decay schemes for the two Zn^{71} activities are proposed.

THE short-lived activities produced by neutron capture in zinc have been previously studied with varying degrees of completeness. The 14-hr and 52-min activities of Zn^{69} had been investigated in some detail, whereas the 2.2-min activity of Zn^{71} had been examined only by absorption and half-life studies. Zn^{69} had been found to have a metastable state which decays with a 14-hr half-life by the emission of a 436-kev[1,2] *M*4 transition[3] to the ground state of Zn^{69}. The ground state then decays with a 52-min half-life[4] to the ground state of Ga^{69}. The beta ray emitted by the 52-min state had been found[3] to have a maximum energy of about 900 kev.

The 2.2-min activity of Zn^{71} was first produced by Hughes *et al.*[5] by neutron capture in normal Zn. By aluminum absorption experiments they determined the maximum energy of the beta rays associated with this activity to be 2.1 Mev. They measured the cross section for thermal neutron capture in Zn^{70} to be about 0.09 barn.

According to the nuclear shell theory, there should exist a metastable state in Zn^{71} similar to the one in Zn^{69}. One should then expect to find a second activity in the Zn^{71} and possibly an isomeric transition between the two states.

ELEMENT	MASS NUMBER							
	64	65	66	67	68	69	70	71
Cu		31%						
Zn	49%	(250D)	28%	4%	18%	(14H, 1H)	0.6%	(2M, 3H)
Ga						60%		40%
Enriched Zn	10%		8%	4%	29%		48%	

FIG. 1. The relative abundance of the Zn isotopes.

The present investigation is concerned mainly with the study of Zn^{71}. A preliminary report[6] was presented at the Detroit meeting of the American Physical Society. The sources were obtained by the neutron irradiation of both normal Zn and enriched Zn^{70}. The relative abundance of the Zn isotopes in both normal Zn and enriched Zn^{70} are illustrated in Fig. 1. Since in the enriched sample, Zn^{70} is enriched by a factor of 80, whereas Zn^{68} is only enriched by a factor of 1.7 and all other isotopes are depleted, one can conclude that any activity which is observed in the enriched samples but not in the normal Zn samples is to be assigned to Zn^{71}.

The sources were examined with a ten-channel scintillation coincidence spectrometer.[7] In all, four activities were found in the enriched Zn^{70} samples. They had half-lives of 2.2 min, 1 hr, 3 hr, and 14 hr.

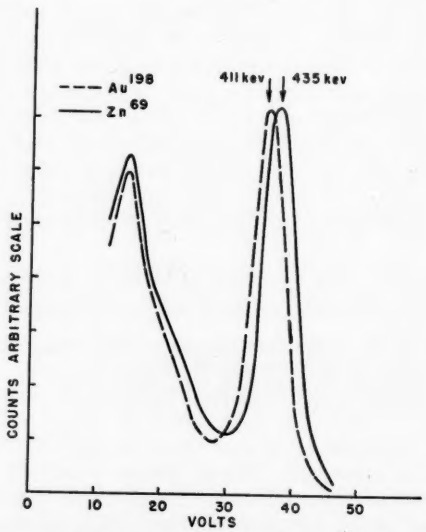

FIG. 2. The NaI(Tl) pulse height distributions of Zn^{69} (14-hr) and the 411-kev gamma-ray of Au^{198}.

* University of Michigan, Ann Arbor, Michigan.

[1] A. Guthrie, Phys. Rev. **60**, 746 (1941).

[2] B. D. Nag-Chowdhury, Proc. Nat. Inst. Sci. India **10**, 317 (1944).

[3] R. B. Duffield and L. M. Langer, Phys. Rev. **89**, 854 (1953).

[4] J. J. Livingood and G. T. Seaborg, Phys. Rev. **55**, 457 (1939).

[5] Hughes, Wallace, Goldfarb, Eggler, Murcock, and Goldstein (unpublished).

[6] LeBlanc, Cork, and Burson, Phys. Rev. **94**, 1436(A) (1954).

[7] S. B. Burson and W. C. Jordan, Phys. Rev. **91**, 498 (1953).

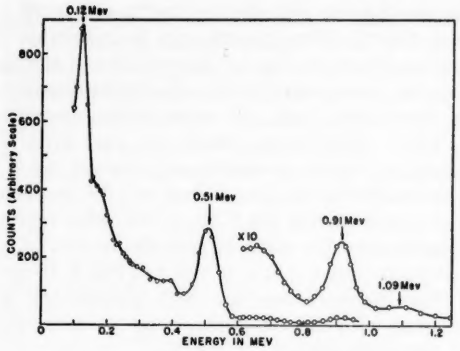

FIG. 3. Zn^{71} (2.2-min) NaI(Tl) pulse-height distribution.

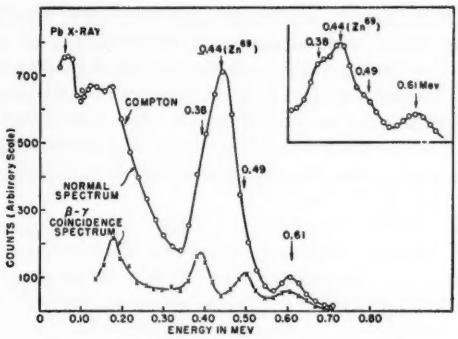

FIG. 4. Zn^{71} (3-hr) NaI(Tl) pulse-height distribution.

Of these, only the 1-hr and 14-hr activities were detected in the normal Zn sources and are thus identified as the previously reported activities of Zn^{69}. The 2.2-min and 3-hr activities must then be due to Zn^{71}. Since the Ga^{71} which is formed by the beta decay of Zn^{71} is stable, the fact that two activities are associated with Zn^{71} implies that one of them must be due to a metastable state in Zn^{71}.

Since the Zn^{69} activities appeared to some extent in all of the samples, it was necessary to examine their photon spectra, coincidence spectra, and beta rays in order that they might be easily identified in the presence of the radiations from Zn^{71}.

1. 14-Hr ACTIVITY OF Zn^{69}

The NaI pulse-height distribution from the gamma rays of the 14-hr decay is shown in Fig. 2. The figure also contains the pulse-height distribution from the 411-kev gamma ray emitted in the decay of Au^{198}. Figure 2 is interpreted to indicate that only one gamma ray is associated with the 14-hr activity and that it has an energy of about 435 kev. In addition, it was established that the 435-kev gamma ray is not in coincidence with beta rays. This confirms the previous assignment of the 14-hr activity to the metastable state.

2. 52-MIN ACTIVITY OF Zn^{69}

There were no gamma rays detected which could be assigned to this activity. Very strong beta rays were observed, and their maximum energy was measured by aluminum absorption experiments to be about 0.85 Mev. This agrees with previous measurements.

3. 2.2-MIN ACTIVITY OF Zn^{71}

Samples of the 2.2-min activity of Zn^{71} were produced by the irradiation of enriched Zn^{70} for periods of about 5 minutes. The half-life of the radioactivity from these samples was measured to be about 2.2 min, in good agreement with previous results. The gamma-ray spectrum was obtained by means of the scintillation spectrometer and is shown in Fig. 3. The photopeaks for four gamma rays are identified and found to decay with the 2.2-min half-life. Their energies are 0.12, 0.51, 0.90, and 1.09 Mev. The 0.51- and 0.12-Mev gamma rays are by far the most intense ones in the spectrum. The results of gamma-gamma coincidence measurements, however, show that the 0.51- and 0.12-Mev transitions are not in coincidence with each other. The 0.90- and 1.09-Mev transitions were too weak for one to be able to obtain reliable gamma-gamma coincidence measurements with them.

It was established that all of the gamma rays are in coincidence with beta rays. The results of aluminum absorption experiments on the beta rays indicate a maximum beta-ray energy of 2.4 ± 0.2 Mev. The slope of the aluminum absorption curve for the beta rays in coincidence with the 0.51-Mev gamma ray is not significantly different from that of the absorption curve for single counts. Because of the rapid decay of the sample, however, statistics of the absorption data are not good enough to allow one to determine if there is any branching to the ground state.

4. 3-Hr ACTIVITY OF Zn^{71}

The 3-hr activity which was detected in this investigation and assigned to Zn^{71} had not been previously observed. Even with enriched isotopes, it was not possible to obtain the 3-hr activity without the presence of strong 1-hr and 14-hr activities of Zn^{69}.

The NaI(Tl) pulse-height distribution obtained from the gamma rays of the 3-hr activity of Zn^{71} is shown as the top curve in Fig. 4. The photopeak of the 0.435-Mev transition of Zn^{69} is the dominant feature of the distribution; however, another photopeak is clearly resolved at 0.61 Mev. In addition, the 0.435-Mev photopeak is distorted on both the low- and high-energy sides, indicating the possibility of more gamma rays being present. This region of the spectrum was examined with better resolution and the results are shown in the inset of Fig. 4. It is clear, from these data, that the peak at about 0.44 Mev is complex. In order to examine this region without the presence of the Zn^{69} gamma ray, the pulse-height distribution of gamma rays which are in coincidence with beta rays

was determined (see bottom curve of Fig. 4). The peaks which occur in this spectrum at 0.38, 0.49, and 0.61 Mev are interpreted as photopeaks of gamma rays of these energies. The peak at about 0.17–0.20 Mev is interpreted as due to Compton electrons and Compton-scattered gamma rays. The rate of decay of each of these peaks was determined and found to correspond to a half-life of about 3 hr.

The source was allowed to decay for one day, and then another normal pulse-height distribution was determined. The only activity which remained was that of the 14-hr Zn^{69}. This pulse-height distribution was then normalized, at the 0.44-Mev peak, to the pulse-height distribution of the previous day and subtracted from it. The resulting distribution was the same as that of the gamma rays in coincidence with beta rays which was obtained the first day. Thus, it is concluded that all of the gamma rays which were found in the 3-hr activity are in coincidence with beta rays.

The maximum energies of the beta rays which are in coincidence with the 0.38, 0.49, and 0.61-Mev gamma rays were determined by measuring the attenuation of the beta rays in aluminum. It was established that each gamma ray is in coincidence with a single beta ray whose maximum energy is 1.5 ± 0.1 Mev in each case. This strongly suggests that the three gamma rays are in cascade.

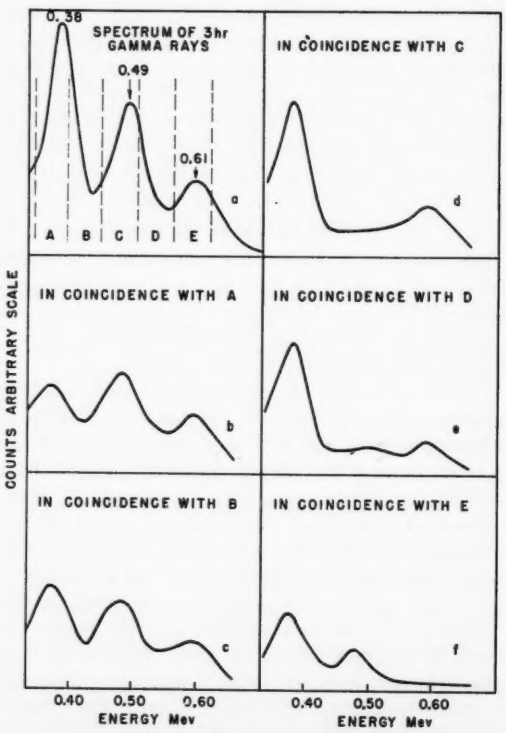

FIG. 5. Zn^{71} (3-hr) gamma-gamma coincidences.

Gamma-gamma coincidence experiments were performed with the three gamma rays in this decay. The results are shown in Fig. 5. The positions of the three gamma-ray photopeaks in the pulse-height distribution were determined from the beta-gamma coincidence pulse-height distribution shown in Fig. 5(a). The single-channel analyzer was then set to cover one of the regions bounded by the dotted lines, and the ten-channel analyzer swept across the 0.30- to 0.65-Mev region of the distribution. The resulting coincidence distributions are shown as curves *b*, *c*, *d*, *e*, and *f* in Fig. 5. It can be seen from these curves that each gamma ray is in coincidence with the other two; thus, the three transitions are in cascade.

5. DECAY SCHEME OF Zn^{71}

The present investigation has confirmed the prediction of the nuclear shell theory that a metastable state should exist in Zn^{71}. It has not been possible, however, to determine from the data which of the two activities is due to the ground state. For this reason the suggested decay schemes of the two activities are shown separately. See Fig. 6. The decay scheme of the 3-hr activity is strongly supported by the beta-gamma and gamma-gamma coincidence measurements. There is no information to indicate in what order the three gamma rays are emitted; the lowest energy transition is arbitrarily placed at the bottom.

The portion of the decay scheme of the 2.2-min state which is indicated by solid lines is confirmed by coincidence measurements. The portion of the level scheme represented by dashed lines is based entirely on the energies of the transitions. The energy of the 1.09-Mev gamma ray does not agree very well with the sum of the 0.12- and 0.91-Mev transitions. This is not considered to be a serious objection since the accuracy of measurement of the energy of the 1.09-Mev transition is rather poor, due to the very low intensity of the peak. There may be additional beta transitions to the 0.12-Mev level and to the ground state.

It is difficult to understand why there are no common states in Ga^{71} in the two decay schemes. One might

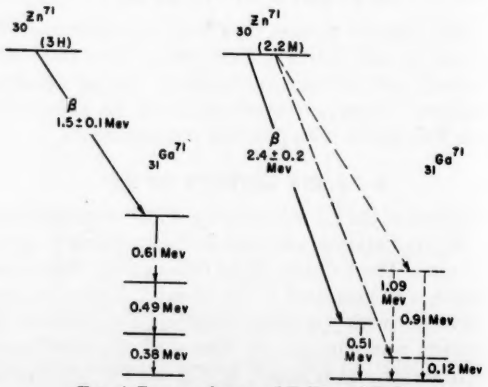

FIG. 6. Decay schemes of Zn^{71m} and Zn^{71}.

suspect that the 0.49-Mev transition which follows the 3-hr beta decay is the same as the 0.51-Mev transition in the 2.2-min decay. In order to check this, the energies of the two transitions were compared without altering the spectrometer settings. It was determined that there were indeed two distinct gamma rays with energies that differed by about 0.03 Mev. The absence of common states in the two decay schemes might be due to some selection rule other than those arising from the conservation of total spin and parity.

The total energy of the Zn^{71} decay is measured to be about 2.9 Mev. This value is in good agreement with that predicted from the beta decay systematics.[8]

[8] K. Way and M. Wood, Phys. Rev. 94, 119 (1954).

PHYSICAL REVIEW VOLUME 97, NUMBER 3 FEBRUARY 1, 1955

Tritium Production from Lithium by Deuteron Bombardment

R. L. Macklin and H. E. Banta
Oak Ridge National Laboratory, Oak Ridge, Tennessee

(Received August 23, 1954; revised manuscript received October 25, 1954)

The tritium production cross section has been measured for Li^6 bombarded by deuterons from 0.4 Mev to 4.0 Mev. The cross section rises fairly rapidly to 190 millibarns near 1 Mev, then more slowly to 290 millibarns near 4 Mev. The cross section for Li^7 rises steeply from the 1.27 Mev threshold to 95 millibarns at 2.4 Mev; then more slowly to about 165 millibarns at 4.1 Mev.

INTRODUCTION

DEUTERON reactions with light nuclei are of considerable theoretical interest, but no detailed study of the reaction with Li^7 seems to have been made. The reactions of deuterons with Li^6 have been studied previously[1] by magnetic analysis at 1 Mev deuteron energy. The reaction $Li^6(d,t)Li^5$, $(p)He^4$ was reported with disintegration energies of $Q=0.9\pm0.1$ Mev and $Q=1.6$ Mev for the two steps. The width of the Li^5 ground state was indicated as 1.5 Mev, and a pronounced forward distribution of the tritons was suggested.[1] We have studied the total triton production by a technique similar to that of Wolfgang and Libby,[2] in which the tritium is recovered and its beta disintegrations counted.

EXPERIMENTAL ARRANGEMENTS

Target Preparation

The target material was lithium fluoride[3] enriched in either isotope. The enriched Li^6 contained 76.31 ± 0.04 atom percent Li^6 as determined mass spectrometrically. The degree of enrichment of the Li^7 was determined by using a Frisch grid chamber in the thermal column of the Oak Ridge National Laboratory (ORNL) Graphite Pile. The yield of the $Li^6(n,t)He^4$ reaction was observed in a comparison with natural lithium fluoride, and the material was found to contain about 55 ppm (parts per million) of Li^6. Thin uniform deposits of this material were vacuum evaporated onto high-purity aluminum disks. The target thickness in terms of deuteron energy loss was chosen as about 80 kev. For the Li^6 cross section no dependence on target thickness was found, with the possible exception of the single thickest target, where a brief deuteron burst of abnormally high intensity apparently caused a few percent volatilization.

In the case of the Li^7 reaction, tritium loss from the lithium fluoride layer was found for a series of thick targets used for the energy range 2.3 to 4.1 Mev.[4] Below 2.5 Mev a modification of the target was employed which avoided such loss. Following a technique described by John Strong,[5] a layer of aluminum thick enough to stop all backward tritons was vacuum-evaporated over the active material of the targets. The thickness of the aluminum overcoat was determined for each target by weight or, preferably, by observing the shift of the $Li^7(d,n)Be^8$ resonance near 1.0 Mev.

Deuteron Bombardment

The D^+ beam of the ORNL 2.5-Mev Van de Graaff was used in the energy range 0.4 to 2.5 Mev while deuterons from 2 to 4 Mev were made available at the ORNL 5.5-Mev Van de Graaff. A correction of $(2\pm\frac{1}{2})$ percent for H_2^+ in the beam was required in the latter case. The beam current falling on the target was integrated[6] to determine the number of deuterons available for reaction. The secondary electrons produced at the collimator (or the target) were driven back to their origin by an electrostatic field. Two $67\frac{1}{2}$-volt batteries connected from ground to the insulated

[1] R. I. Frost and S. S. Hanna, Phys. Rev. 91, 462 (1953), and R. W. Gelinas and S. S. Hanna, Phys. Rev. 86, 253 (1952).
[2] R. L. Wolfgang and W. F. Libby, Phys. Rev. 85, 437 (1952).
[3] Supplied by the Stable Isotope Research and Production Division.
[4] See section on Results, Li^7 Cross Section.
[5] John Strong *et al.*, *Procedures in Experimental Physics* (Prentice Hall, New York, 1943), pp. 178–179.
[6] This integrator, due to F. W. Manning and F. M. Glass, is to be described in a forthcoming paper.

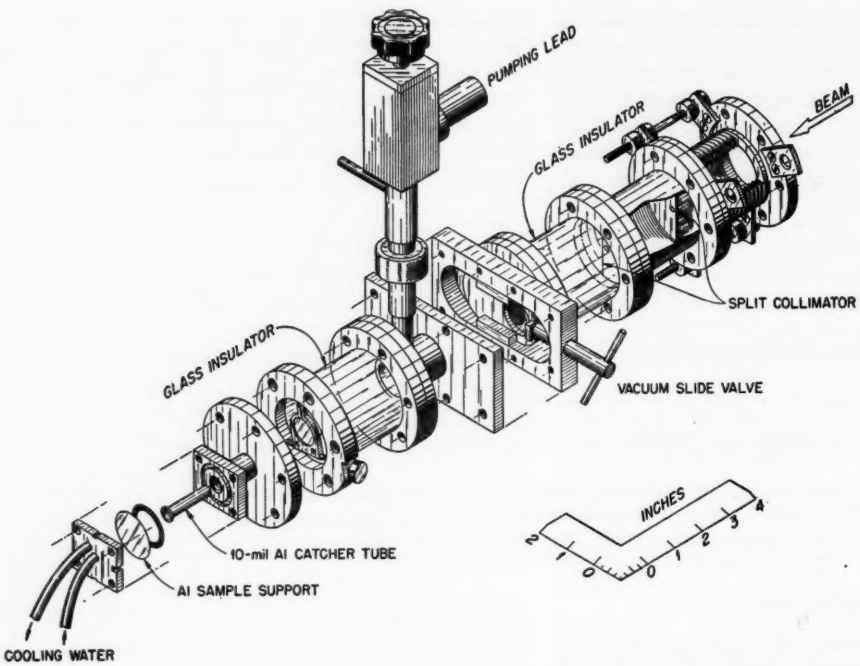

FIG. 1. Deuteron activation apparatus.

vacuum valves between the collimator and target holder (see Fig. 1) sufficed.

To intercept the energetic tritons emerging at back angles from the target, a catcher tube was used (see Fig. 1). This was an aluminum tube $\frac{1}{4}$ inch in diam and $1\frac{1}{4}$ inches long, with a 0.010-inch wall and a rolled lip on which the target pressed. The deuteron beam was carefully aligned, after collimation, so it passed through the catcher tube to the target. The collimator was made of two segments of tantalum disks to allow higher pumping speeds (see Fig. 1). The few bombardments showing deuteron induced beta activities in the catcher tube were discarded. The induced target backing activities decayed to negligible levels in two to three days. The fractional solid angle for triton escape from the target back through the catcher tube is less than 0.2 percent and such loss has been neglected. The target was cooled by a water jet impinging on the back of the aluminum disk (see Fig. 1). Current densities from 5 to 30 microamperes per square centimeter were used successfully. Because of generator characteristics, current densities were lowest at both the lowest and the highest energies.

For the targets with aluminum overcoating, a $\frac{3}{8}$-inch diameter collimator, and a target holder with a $\frac{7}{8}$-inch throat were used.

The beam energy was determined with a nuclear resonance device, which measured the magnetic field necessary to bend the beam through ninety degrees. The nuclear resonance device was in turn calibrated by the $Li^7(p,n)Be^7$ threshold and other reactions. In some cases the beam energy was taken from the generating voltmeter of the Van de Graaff generator, after it had been calibrated by the nuclear resonance device. These were raw energy data, and were corrected by overcoat thickness and target thickness, expressed in energy lost by the beam. The beam energies reported are those midway through the target material.

Tritium Recovery and Analysis

The target area accessible to the charged particle beam was punched out and put into a clean graphite crucible. The aluminum catcher tubes, when used, were put into separate crucibles. The crucible was supported by a $\frac{1}{4}$-inch quartz spacer at the bottom of a quartz "test tube" which in turn was encircled by a two turn radio frequency heating coil.[7]

The tritium was quantitatively recovered by cooking the sample twice at 1100°C in an atmosphere of argon containing 1 percent hydrogen. The gas was transferred to a beta proportional counter tube after cooling to 300°C and argon containing 10 percent methane added for counting.[8] By repeating the entire procedure several times on a high-activity sample, it was possible to evaluate the recovery. With the procedure used this

[7] Many details of the cookout apparatus and procedure were adapted from the work of George Ledicotte and others at the Oak Ridge National Laboratory.

[8] Preliminary results were obtained near the Li^7 threshold using 2 cm alcohol and 14 cm argon with the counter operating in the Geiger region. At higher counting rates, poor reproducibility and excessive deadtime led to the abandonment of this method.

was 98 percent for targets and 96 percent for catcher tubes.

The counting equipment consisted of an *A*1-*A* preamplifier and a modified Nuclear Model 117 alpha counter.[9] The counters were $1\frac{1}{2}$-inch×12-inch stainless steel tubes with a 0.002-inch×$10\frac{15}{16}$-inch W central wire. These counters were designed and constructed by R. K. Abele.[10] A 2-inch shield around the counter gave about 2.5 counts/sec background. Using an external Cs^{137} source near the center of the counter, plateaux of several hundred volts which were essentially flat were obtained. With tritium in the counter a slope of 1.6 percent per hundred volts was typical. This slope has been attributed[11] to improved collection at higher voltages in the vicinity of the central wire end clamps.

In order to investigate the possibility of tritium loss during bombardment, two bombardments of Li^7 were made with about a factor of eight difference in current densities. These two points, at about 1.86-Mev deuteron energy, repeated within 1 percent.

The half-life of the active material resulting from the reaction was investigated. The decay of one sample was followed for a period of one month without demonstrable departure from the decay rate of tritium. Also, some A^{37} was added to a counter containing active material. This, on pulse height analysis, gave a calibration peak at 2.83 kev. Using this calibration, the expected β spectrum of tritium was observed. Less than one percent of the observed pulses exceeded 18 kev, and these may well have been part of the background.

Calibration

The number of tritons produced in a target was first computed from the observed counting rate using the half-life,[12] the recovery efficiency, and the counter efficiency. The counter end effects were measured by scanning with a narrow fan of Cs^{137} gamma rays. An effective volume of 85 percent was found for the proportional counters at 2000 volts. Since the wall losses with tritium are both small and largely compensated by photoelectric emission[13] they have been ignored, and the counter efficiency taken at 85 percent.

A direct calibration of the equipment, including the current measurement, was effected by measuring the charge delivered to an aluminum blank by a 350-kev triton beam from the Cockcroft-Walton accelerator.[14]

A few attempts at calibration by exposing Li^6 to pile neutrons were made. Evaporated targets of natural LiF were made by the same procedure as the enriched Li^6F targets. The scatter of the pile results is quite large so that the most that can be said is that the other two calibrations fall within their range. The reproducibility of the tritium count rate per mg of LiF for the several samples exposed in a group was quite good, however (Table I). These group consistencies give a measure of random errors both in the tritium recovery and counting procedure and in the target preparation and weighing. The LiF weight varied by a factor of 5 among the samples in one of these groups. Yet, the 95 percent confidence interval for the average was only 1.8 percent. The corresponding error to be expected per target, based on both groups, is ±3.6 percent, a value which may be expected to apply also to the targets used for the cross-section measurements.

TABLE I. Tritium samples from $Li^6(n,t)He^4$ in natural LiF.

Pile exposure *A*			Pile exposure *B*		
	100 sec			420 sec	
LiF (μg)	*T* (counts/sec)	Hole 58 counts/sec mg	LiF (μg)	*T* (counts/sec)	Hole *P*2 counts/sec mg
1116	97.6	87.5	876	414	473
1153	99.9	86.6	940	440	468
2105	179.6	85.4	4091	1880	459
1972	174.0	88.3	2174	1045	481
1067	93.9	88.1	2374	1106	466
			1158	536	463
		av 87.2±1.7% L.E.[a]			av 468±1.8% L.E.[a]

Computed statistical deviation per target ±3.61% L.E.[a]

[a] L.E. indicates the 95 percent statistical confidence interval.

The target efficiency calibration gives 6.70×10^8 T/(count/sec) for the proportional counter and the Cockcroft-Walton calibration gives 6.58×10^8 T/(count/sec)±2.7 percent. The difference, 1.8 percent, lies well within the limit of statistical uncertainty. Since the Cockcroft-Walton method was subject to contamination which, though greatly reduced, was probably not entirely eliminated, the former calibration was adopted.

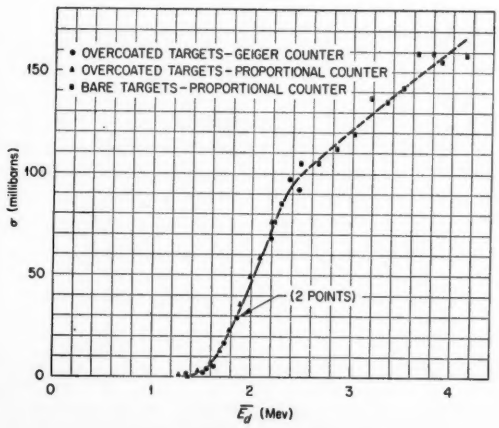

FIG. 2. $Li^7(d,t)Li^6$ cross section.

[9] See ORNL Instrument Information Exchange, p. 97.

[10] ORNL Instrumentation and Controls Division, Counter Laboratory.

[11] C. J. Borkowski, Oak Ridge National Laboratory (private communication).

[12] Values of 12.257 and 12.256 (±0.003) yr have recently been reported from Los Alamos Scientific Laboratory.

[13] A. G. Engelkemeir and W. F. Libby, Rev. Sci. Instr. **21**, 553 (1950).

[14] This method was suggested by W. Kunz of the Oak Ridge National Laboratory.

RESULTS

Li^7 Cross Section

The cross section *vs* energy curve for Li^7 is shown in Fig. 2. The threshold for the reaction was computed from mass data as 1.27 Mev. The results using aluminum overcoated targets on the ORNL 2.5-Mev Van de Graaff are plotted as triangles and circles. As previously mentioned, the point at 1.86 Mev is due to two separate observations which coincide.

It is suggested that the sharp rise exhibited by the cross-section curve above threshold is not entirely due to triton barrier penetrability, but probably involves a resonance in Be^9, as evidenced by similar behavior in the (d,n) and (d,p) cross-section curves.

The lowest point shown as a square (2.23 Mev) was obtained with a thin bare target (50 kev) and very low beam current on the 2.5-Mev ORNL Van de Graaff. It agrees well with the other data using aluminum-overcoated targets. The remaining points shown as squares are from a single series of thick targets on the 5.5-Mev ORNL Van de Graaff and have been corrected empirically for tritium loss from the lithium fluoride layer of the targets. This correction was taken as a constant fraction of the tritons stopping in the fluoride layer. The fraction was normalized to give 85 millibarns at 2.30 Mev and the number of tritons stopping in the fluoride was computed from range curves, assuming isotropy for the reaction. The correction ranged from 25 percent at 2.3 Mev to 17 percent at 4.1 Mev and is considered only approximate. Accordingly an uncertainty of ± 15 percent is attached to the upper end of the cross section curve shown (Fig. 2).

Studies of the yield of the $Li^6(n,t)He^4$ reaction indicated less than 2 percent standard deviation for LiF targets prepared and analyzed as were those used in this study. Also, the calibration for tritium sensitivity by two different methods gave results agreeing within 1.8 percent. The current integrators contain a constant-current source; cross-comparison indicated errors less than 1 percent in current measurement. Energy measurement was based on known nuclear reactions. As corrected, however, these data involve energy loss in the overcoat and target material, and probably are good to ± 2 percent above 1 Mev, 20 kev below. Considering the above factors, it is concluded that cross-section values above 10 mb are correct to ± 5 percent (excepting the values above 2.3 Mev as noted above), and the energy values to ± 2 percent.

Li^6 Cross Section

The cross sections obtained for tritium production by the Li^6 are shown in Fig. 3. Above 1.3 Mev, a correction has been made for the tritium produced from the Li^7 in the targets.[15] This correction increases monotonically above the threshold, reaching 15 percent at 4 Mev. The dashed curve at very low energies was obtained by extrapolation according to the theoretical Gamow penetrability formula, normalized at 0.37 Mev. The errors are estimated at ± 5 percent of the cross section (see discussion in "Results" above).

A study of the separate triton yields in the forward and backward directions as a function of energy has not led to entirely clear cut results. The tritium from each Li^6 target and that from the corresponding catcher tube were extracted separately. Because of the appreciable target thickness, however, some of the tritons emitted at greater than 90° to the beam were retained in the target. Thus, the results cannot be interpreted directly, without correcting for this effect. The correction, in turn, is uncertain since the ground state of Li^5 is broad (1.5 Mev) and there is some contribution from three body breakup.

A calculation has been made assuming the proper average correction to be equal to that for the reaction leaving the Li^5 at the center of the gound state level; i.e., $D+Li^6 \rightarrow T+Li^5+0.9$ Mev. The fraction of the tritium expected in the catcher tube was calculated,

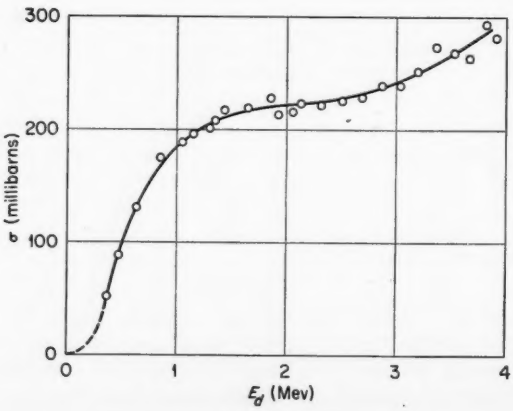

FIG. 3. $Li^6(d,t)Li^5$, $(p)He^4$ cross section.

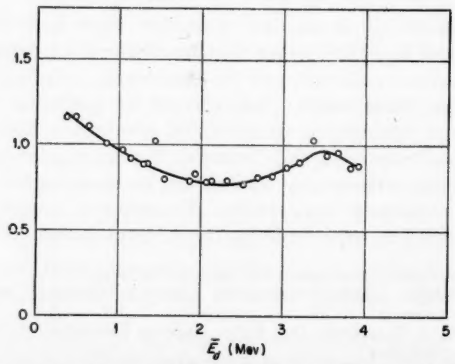

FIG. 4. Ratio of observed to isotropic backward triton yields, assuming $Li^6(d,t)Li^5+0.9$ Mev.

[15] The $Li^6(n,t)$ contribution is readily computed to be less than 0.01 percent of the $Li^6(d,t)$ yield.

assuming isotropy in the center of mass system. A comparison of the observed fractional catcher yield with the calculated one is shown in Fig. 4.

Ratios below 1.0 cannot be considered inconsistent with isotropy if the average triton energy at the back angles is sufficiently lower than corresponds to the two body reaction considered above at each energy. If, on the other hand, the average is higher, an upper limit can be set by considering the reaction $D+Li^6 \rightarrow T+He^4+H+2.51$ Mev to be isotropic for the case where the proton and the alpha particle have no relative motion. Near 0.4 Mev, this assumption barely corresponds to the observed points. This is the limiting case, and it seems likely the average is far from it. The observed effect near 0.4 Mev cannot be explained as due to greater target heating and consequent tritium loss from the targets, as much thinner targets and lower beam currents were used at this energy than above 1 Mev where the assymetry appears reversed.

A more detailed study of the angular distribution should be possible with a modified technique using several tritium catcher foils at various angles to the beam.

SUMMARY

Within the limits of experimental error, the threshold for the $Li^7(d,t)Li^6$ reaction agrees with the computed value, 1.27 Mev. The cross section rises with energy above threshold to about 95 millibarns at 2.4 Mev, and then to about 165 millibarns at 4.1 Mev. The $Li^6(d,t)Li^5$, $(p)He^4$ cross section rises to 190 millibarns near 1 Mev, then to 290 millibarns near 4 Mev. Thanks are due to many of our colleagues at the Oak Ridge National Laboratory who contributed materially to this study.

PHYSICAL REVIEW VOLUME 97, NUMBER 3 FEBRUARY 1, 1955

Recoil Deuterons and Disintegration Protons from the *n-d* Interaction, and *n-p* Scattering at $E_n = 14.1$ Mev*

JOHN D. SEAGRAVE
University of California, Los Alamos Scientific Laboratory, Los Alamos, New Mexico
(Received October 22, 1954)

A counter-telescope consisting of two proportional counters and a NaI scintillator in triple coincidence has been used to study the angular distribution of scattered deuterons and disintegration protons from the interaction of 14.1-Mev neutrons with deuterium. Charged reaction products were identified by simultaneous observation of particle energy and rate of energy loss. Thin radiators of deuterated and normal polyethylene were used, the latter to investigate the incident neutron spectrum and *n-p* scattering at 14.1 Mev.

The absolute differential cross sections observed over the recoil angular range 0 to 55 degrees in the laboratory for elastic *n-d* and *n-p* scattering are in good agreement with the recent nuclear-emulsion results of Allred, Armstrong, and Rosen, and with the theoretical results of Christian and Gammel. The anisotropy of *n-p* scattering was found to be about six percent. Protons from disintegration of deuterium were observed over the angular range of 0 to 80 degrees in the laboratory, and the integrated cross section for the forward hemisphere is larger than has been observed previously. The energy distributions appear more nearly uniform than those estimated by Frank and Gammel, and the angular distribution more strongly peaked forward.

INTRODUCTION

THE study of nucleon-deuteron interactions has been the subject of many theoretical and experimental investigations. A comprehensive survey of the general problem, together with a bibliography to 1953, may be found in a recent review article by Massey.[1] At relatively low energies (below 6 Mev), comparison of *n-d* and *p-d* scattering favors change symmetry (i.e., equivalence of *n-n* and *p-p* nuclear forces) and some type of exchange force, but experimental uncertainties have made detailed comparison difficult. At higher intermediate energies, only two *p-d* experiments have been performed, at 9.66 Mev[2] and at 20.6 Mev.[3] Several *n-d* experiments between 10 and 15 Mev have been reported[4–7] but the results have not been entirely consistent. Since *n-d* elastic scattering is highly anisotropic, it is quite essential for theoretical interpretation that absolute cross section measurements be made. Moreover, neutrons over 3.3 Mev are energetically able to disintegrate the deuteron, and this interaction, which is the simplest case of inelastic scattering and an im-

* Work performed under the auspices of the U. S. Atomic Energy Commission.

[1] H. S. W. Massey, in *Progress in Nuclear Physics*, O. R. Frisch, Editor (Pergamon Press, London, 1953), pp. 235–270.

[2] Allred, Armstrong, Bondelid, and Rosen, Phys. Rev. **88**, 533 (1952).

[3] D. O. Cladwell, University of California at Los Angeles thesis, January 1954 (unpublished).

[4] Ageno, Amaldi, Bocciarelli, and Trabacchi, Phys. Rev. **71**, 20 (1947).

[5] J. H. Coon and R. F. Taschek, Phys. Rev. **76**, 710 (1949).

[6] Griffith, Remley, and Kruger, Phys. Rev. **79**, 443 (1949).

[7] T. C. Griffith, Proc. Phys. Soc. (London) **A66**, 894 (1953).

portant problem by itself, gives rise to protons which must be taken into account and distinguished from deuterons in order to obtain even a relative angular distribution for *n-d* elastic scattering.

The most recent and detailed investigation of the *n-d* interaction was made at Los Alamos by Allred, Armstrong, and Rosen[8] at 14.1 Mev, using the monoenergetic $T(d,n)He^4$ reaction and a multiplate nuclear-emulsion camera, together with a neutron collimator, to insure good angular resolution and low background. These investigators were able to discriminate against the disintegration protons to obtain the absolute elastic differential cross section in detail for cm neutron angles between 46 and 176 degrees, and they found in particular that the differential cross section at the minimum near 120 degrees was only half as large as had been previously reported. Disintegration protons were unequivocally detected between 2 Mev, the lower limit set by track selection criteria, and the allowed maxima, but background and statistical uncertainties were large. A semiquantitative angular distribution for the disintegration protons was obtained which was forward-peaked and extrapolates to about 42 ± 12 mb/sterad for the differential cross section for protons over 2 Mev in the forward direction in the laboratory, with an integral of 53 ± 15 mb.

A new theory[9] of the *n-d* and *p-d* interactions was developed concurrently with the above experiment, which was upsetting to the hope of obtaining information about nuclear forces from analysis of intermediate-energy experiments. Close agreement with experiment was found using a formulation in which the principal physical process is a "pickup" interaction wherein the incident particle interacts with the unlike nucleon to form a "new" deuteron. The triplet even-parity *n-p* force dominates the scattering, which is nearly independent of the *n-n* and *p-p* forces. Moreover, the range, shape, and tensor nature of the *n-p* force do not affect the phase shifts in a sensitive manner. Very good agreement with the most reliable *n-d* and *p-d* scattering experiments was obtained over the energy range of 1 to 14 Mev, and except in the region of the interference minimum, with the *p-d* experiment at 20.6 Mev.[3,10] In view of this result, de Borde and Massey[11] have extended their earlier calculations[12] to include higher order phase shifts using a similar Serber-type exchange force and find reasonably close agreement.

Frank and Gammel[13] have developed a simplified theory of the disintegration process whereby a connection between elastic and inelastic cross sections could be established independent of the properties of two-body forces. Given the elastic distribution, their formulation could be used to make a prediction of both the energy and angular distribution of the disintegration protons from the *n-d* interaction. Comparison with the results of Allred, Armstrong, and Rosen[8] showed qualitative agreement, with the theory predicting somewhat larger values. No comparison energywise was possible. Even quantitatively, the agreement was better than the assumptions of the theory merit, and very much better than the more elaborate calculations of Bransden and Burhop.[14]

We are apparently forced to accept that the *n-n* interaction plays a negligible part in the elastic *n-d* scattering, but it is even more difficult to believe that it does not enter into the disintegration of the deuteron.

The present experiment was designed to investigate the energy and angular distribution of protons from the inelastic interaction of 14-Mev neutrons with deuterons in more detail than was practicable with the nuclear emulsion technique,[8] and to remeasure the *n-p* and *n-d* elastic differential cross sections in an independent manner.

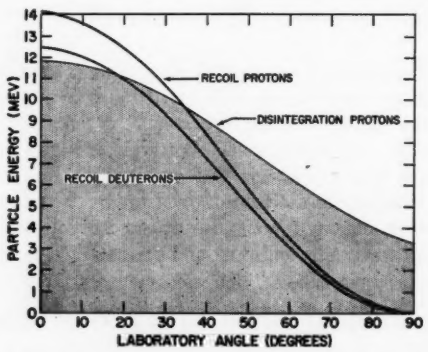

FIG. 1. Energies of charged particles arising in the *n-p* and *n-d* interactions at $E_n = 14.1$ Mev, given as a function of the angle of observation in the laboratory.

METHOD AND APPARATUS

The energies of the different particles to be encountered are shown in Fig. 1, plotted as a function of laboratory angle. For elastically recoiling deuterons and protons, the function is $E_{max}\cos^2\theta$, where E_{max} is 14.1 Mev for protons, and 12.63 Mev for deuterons when struck by 14.1-Mev neutrons. The maximum energy a disintegration proton can have may be calculated by noting that this corresponds to the two neutrons going off together in the cm direction opposite to the proton, so this limit may be treated as a two-body collision. Since the disintegration process which gives rise to the protons is in fact a three-body breakup, protons of all energies up to this maximum may be present. Inspection of Fig. 1 will show that it is difficult to discriminate

[8] Allred, Armstrong, and Rosen, Phys. Rev. **91**, 90 (1953).
[9] R. S. Christian and J. L. Gammel, Phys. Rev. **91**, 100 (1953).
[10] J. L. Gammel (private communication).
[11] A. H. de Borde and H. S. W. Massey (unpublished). See reference 1, Fig. 10.
[12] Buckingham, Hubbard, and Massey, Proc. Roy. Soc. (London) **A211**, 183 (1952).
[13] R. M. Frank and J. L. Gammel, Phys. Rev. **93**, 463 (1954).
[14] B. H. Bransden and E. H. S. Burhop, Proc. Phys. Soc. (London) **A63**, 1337 (1950).

among the different groups on the basis of energy alone, and moreover the finite angular aperture of the detecting system places a limitation on the energy resolution attainable at the larger angles. For the elastic recoils, $E=E_{max}\cos^2\theta$, and $\Delta E/E=2\tan\theta\Delta\theta$. Particularly for the observation of the low-energy portion of the proton spectrum, observation of specific ionization or dE/dx would insure proper identification. Since the use of multiple-coincidence techniques is a practical necessity for the electronic detection of low energy charged particles in the presence of an intense fast neutron flux, a coincidence counter-telescope previously developed for this purpose by Ribe and the author[15] was readily adapted for use in the present investigation. The counter-telescope which consists of two gas proportional counters and a NaI scintillator and photomultiplier in triple coincidence has already been described in detail.[15]

In use, the gas counters were filled with about 0.1 atmos of krypton with 5 percent CO_2, which gave between 25- and 200-kev energy loss by the particles as they traversed each counter, giving a measure of dE/dx in the gas counters simultaneously with a measure of E in the crystal. The counter-telescope was mounted on an indexed stand so that its axis could be rotated in a horizontal plane about a vertical axis lying in the plane of the radiator, and the angle made by the reaction products with respect to the direction of incident neutrons read directly from the index.

The 14-Mev neutrons were obtained from the $T(d,n)He^4$ reaction by bombarding a thick zirconium-tritium target[16] with the 250-kev monatomic deuteron beam from a Cockcroft-Walton accelerator. The radiator was placed at 90 degrees with respect to the deuteron beam. At this position the incident neutrons were almost monoenergetic with an energy of 14.10 $\pm$0.05 Mev. The number of neutrons from the reaction was measured by counting the accompanying alpha particles emitted into a well-defined solid angle. A schematic representation of the counters and the associated electronic circuits is given in Fig. 2. The pulses resulting from the ionization in the two proportional counters and from the scintillation in the NaI crystal are amplified and fed into a triple coincidence circuit, the output of which gates open two multichannel pulse-height analyzers[17] in time to receive the (delayed) pulse-height representations of E and dE/dx, respectively. The Los Alamos Model 301 coincidence circuit[18] provides stable upper and lower discriminator settings whereby a pulse-height group of interest can be selected, and a dynamic rise-time delay together with fixed delays adjustable in steps of 0.1 μsec for each channel whereby the fast proportional counter pulses could be brought into delayed coincidence with the slower NaI scintillation pulses.

[15] F. L. Ribe and J. D. Seagrave, Phys. Rev. **94**, 934 (1954).
[16] Graves, Rodrigues, Goldblatt, and Meyer, Rev. Sci. Instr. **20**, 579 (1949).
[17] C. W. Johnstone, Nucleonics **11**, No. 1, 36 (1953).
[18] Designed by C. W. Johnstone.

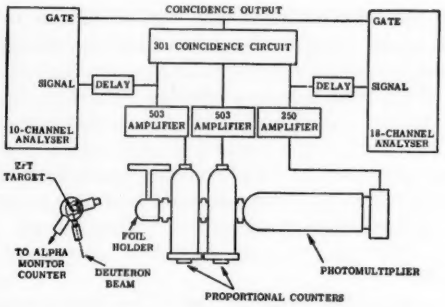

FIG. 2. Schematic block diagram of the apparatus used to study the n-d interaction. Preamplifiers, scalers, and counter details are not shown.

The radiators were thin foils of normal and deuterated polyethylene mounted on platinum and retained in the foil holder by a ring of 20-mil platinum (thick enough to stop 14-Mev proton recoils). On the back side of the foil holder a similar piece of platinum was mounted, so that background counts due to disintegration of the counter lining and filling could be evaluated. The deuterated polyethylene (CD_2) which was prepared by A. R. Ronzio of this laboratory had an isotopic composition of 96.5 atom percent deuterium and 3.5 atom percent hydrogen. The principal impurity was 0.3 percent oxygen (by weight) arising from the catalyst used in polymerization. Small bits of this material, and of normal polyethylene were pressed into foils a few thousandths of an inch thick. After measurement with a sensitive dial gauge, a satisfactorily uniform area of foil was selected and clamped between two cover glasses, so that a circle of known area could be cut out. The chosen radiators were then cleaned in absolute alcohol, dried in vacuum, and weighed in a microbalance. The effective diameter of the radiator was determined by the retaining diaphragm, either $\frac{3}{8}$ or $\frac{7}{8}$ in. in diameter, but the corresponding foil diameters were only slightly oversize, so the uncertainty in the surface density of the area exposed was small. In the $\frac{3}{8}$-in. diameter, CD_2 densities of 4.04, 6.55, and 10.59 mg/cm^2 were used, and in the $\frac{7}{8}$-in. diameter, also 4.04 mg/cm^2. Only one CH_2 radiator was used, $\frac{3}{8}$ in. diameter, of density 10.09 mg/cm^2. The solid-angle defining aperture, which was $\frac{7}{8}$ in. in diameter, was placed directly in front of the NaI crystal, and the solid angle subtended at the radiator by this diaphragm was 1.264×10^{-2} sterad. Three additional diaphragms were placed inside the counter telescope to serve as antiscattering baffles.

Tests of Spectrometer Operation

A mercury-relay precision pulser was used throughout the experiment to establish and check discriminator settings, amplifier gains and linearity, analyzer adjustment, and operation of the coincidence circuit. The coincidence circuit was operated with a resolving time of 0.35 μsec. Unfortunately, the channel delay setting

could not be established with the pulser due to the differing rise times of the pulses from the scintillator and proportional counters, and it was necessary to take data of counting rate as a function of relative channel delay for the elastic recoil group to establish and check the operating point. Under some conditions, the lowest energy protons detectable were not counted when the delays were set for the recoil group, and the precaution was always taken to repeat the observations with several different delays to be sure of counting all the particles.

The individual channel and coincidence counting rates were monitored by scalers (not shown in Fig. 2) so that the accidental counting rate could be calculated; accidental coincidence counts could also be evaluated empirically by inserting an additional 1.5-μsec delay in the scintillator channel so that no true coincidences were recorded. Data was taken under conditions such that both the accidental triple coincidences and double coincidences between analyzer gating and counter singles were negligible.

Several different CD_2 targets (enumerated above) were used, to explore any possible systematic error arising from the targets. At 5° the proton data from targets ranging in thickness from 4.04 to 10.59 mg/cm^2 and in mass exposed from 4.69 to 15.4 mg were in excellent agreement.

The effect of the spectrometer aperture has been discussed previously;[15] the angles given in this paper are the mean angles of observation, and the associated uncertainties indicate the corresponding half-widths of the angular resolution functions. Thus, when the angle between the spectrometer axis and the incident neutrons was zero, the mean angle of observation with the $\frac{3}{8}$-in. diameter radiator was 3.5±2 degrees. The zero-setting of the index was determined by making observations of the sharply-peaked *n-d* angular distribution (see below) in the vicinity of 10 degrees to each side of an arbitrary "zero" until the corresponding measurements agreed, whereupon the true zero-setting could be inferred. The uncertainty in angular position arising from this procedure is less than one degree, which is considerably less than the half-widths of the angular resolution functions.

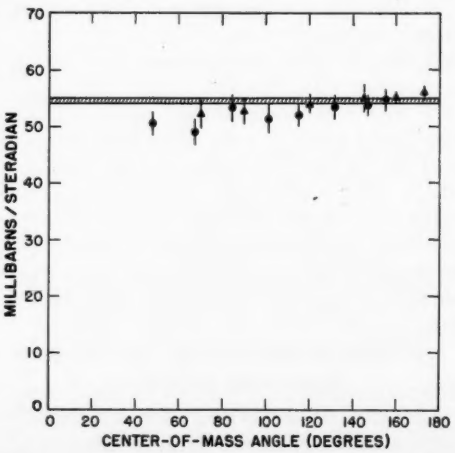

FIG. 3. *n-p* scattering at E_n=14.1 Mev. (▲) This experiment; (●) Allred, Armstrong, and Rosen; shaded region is $\sigma_T/4\pi$ if one uses σ_T=689±5 mb (Poss, Salant, Snow, and Yuan).

In order to establish the energy scale for the disintegration protons from the recoil deuterons observed simultaneously, it is necessary to know the ratio of light emitted in NaI by protons and deuterons of the same energy. Work at the University of Illinois[19] has shown that the light response to NaI to protons and deuterons is linear within a few percent between 1 and 11 Mev, and that protons give about 5 percent more light than deuterons of the same energy. This ratio was determined in the course of this experiment to be L_p/L_d=1.04±0.01 for protons and deuterons between 5 and 14 Mev by mounting CH_2 and CD_2 foils on opposite sides of the foil holder and comparing pulse-height distributions for elastically scattered protons and deuterons at several laboratory angles.

n-p Scattering

A measurement of the *n-p* angular distribution was made with a normal polyethylene radiator in the counter-telescope, to serve three purposes: (1) to check on the calculation of absolute cross sections from counter dimensions and source strengths; (2) to obtain independent data to compare with previous evidence[8,20] of a slight anisotropy in *n-p* scattering at 14 Mev; (3) to observe the spectrum of neutrons incident on the target, in order to make a correction to the *n-d* spectra for deuterons recoiling from degraded neutrons.

The results of the angular distribution measurements are shown in Fig. 3, where they are compared with the results of Allred, Armstrong, and Rosen,[8] and with the assumption of isotropic scattering based on the total cross section 689±5 millibarns measured by transmission.[21] It may be seen that the present results are in good agreement with the results of the very different nuclear plate technique, and the suggestion of anisotropy is confirmed. A least-squares fit to the present results of the form $A+B\cos\theta$ gave a value for $\sigma(\pi)/\sigma(\pi/2)$ =1.047±0.025 while a fit of the form $A+B\cos^2\theta$, which has better theoretical justification, gave the value 1.060±0.023. These values may be compared with the value given by Allred, Armstrong, and Rosen[8] of 1.04 ±0.05 and that given by Barschall and Taschek[20] of 1.06±0.06. The points shown for the present experiment include a correction for the effect of degraded neutrons (see below) which amounts to about twice the statistical uncertainty for the points at 70, 90, and 120

[19] Taylor, Jentschke, Remley, Eby, and Kruger, Phys. Rev. **84**, 1034 (1951).
[20] H. H. Barschall and R. F. Taschek, Phys. Rev. **75**, 1819 (1949).
[21] Poss, Salant, Snow, and Yuan, Phys. Rev. **87**, 11 (1952).

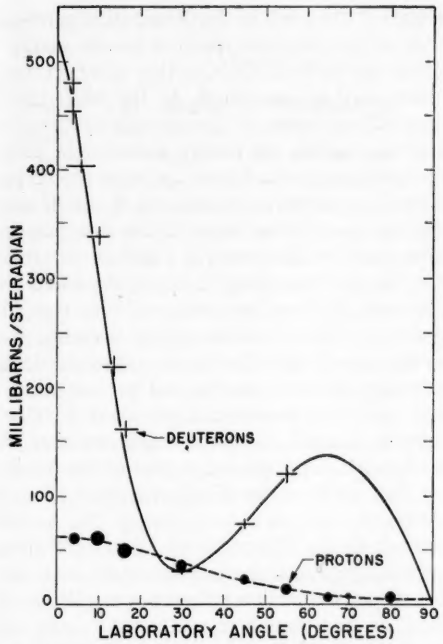

FIG. 4. Angular distribution of protons and deuterons from the n-d interaction at $E_n = 14.1$ Mev. The solid curve is the theoretical result of Christian and Gammel for elastically scattered deuterons; the dashed curve is a least-squares fit through the experimental points (●) for disintegration protons.

degrees. At these points the probable error plotted includes (arbitrarily) half of the amount of the correction; elsewhere the error shown is statistical only. It is not surprising to find anisotropy on the order of 6 percent at 14 Mev, since n-p scattering is markedly anisotropic at higher energies.[22,23] In view of the anisotropy observed, and the possibility of an up-turning of the differential cross section at small neutron angles, no correction was made to force the average value to agree with the total cross section. The disagreement is at worst no more than the uncertainty of 4 percent in the absolute neutron flux.

n-d Interaction

For clarity in the discussion to follow, the angular distributions in the laboratory system for the elastic and inelastic n-d interactions at $E_n = 14.1$ Mev as measured in this experiment are presented in Fig. 4. The distribution of elastically recoiling deuterons is strongly forward, with a sharp minimum in the vicinity of 30 degrees, qualitatively suggestive of a pick-up distribution for $L = 0$. The angular distribution for protons from disintegration of deuterium is also peaked forward, but much less strongly so, and there are more protons than deuterons at 30 degrees.

[22] Brolley, Coon, and Fowler, Phys. Rev. 82, 190 (1951).
[23] Hadley, Kelly, Leith, Segrè, Wiegand, and York, Phys. Rev. 75, 351 (1949).

EXPERIMENTAL PROCEDURE

With a CD_2 foil facing into the spectrometer, bombardments were generally made with an integrated flux at the radiator of 3.09×10^9 neutrons/cm^2, and the E and dE/dx pulse-height distributions recorded for all charged-particle pulses admitted by the particular upper and lower discriminator settings. A bombardment was then made using the same integrated flux of neutrons but with the foil holder rotated so that the platinum bank faced the spectrometer. The background so recorded, principally from disintegration of the gas filling of the first proportional counter, was then subtracted to give the net distributions attributed to the CD_2 radiator.

The principal competing reactions are $C^{12}(n,\alpha)Be^9$ and $C^{12}(n,n)3He^4$, but because of their high specific ionization, all such alphas were excluded by the upper discriminator on the proportional-counter channels. Care was taken that this limit was set below the overload level of the Model 503 amplifiers employed. The $C^{13}(n,\alpha)$ reaction was likewise excluded. The $C^{12}(n,p)B^{12}$ reaction was only 0.5 Mev above its threshold, and such protons (if any) would not have been detected. The $O^{16}(n,\alpha)C^{13}$ alphas were eliminated as above, and the 0.3 percent level of oxygen impurity reduced the contribution of $O^{16}(n,p)$ and (n,d) reactions, for which the cross sections are reported to be 35 and 15 mb, respectively,[24] to a negligible level.

The nature of the data and its treatment will be discussed with reference to Figs. 5 and 6. In Fig. 5 are

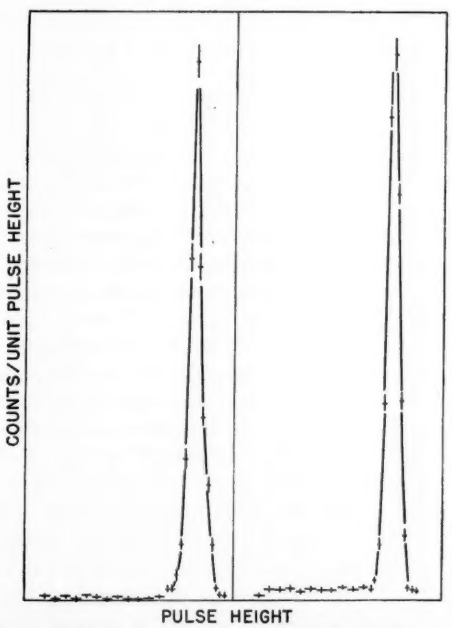

FIG. 5. Typical scintillator pulse-height distributions in the forward direction under bombardment by 14.1-Mev neutrons. On the left, CH_2 radiator; on the right, CD_2 radiator.

[24] A. B. Lillie, Phys. Rev. 87, 716 (1952).

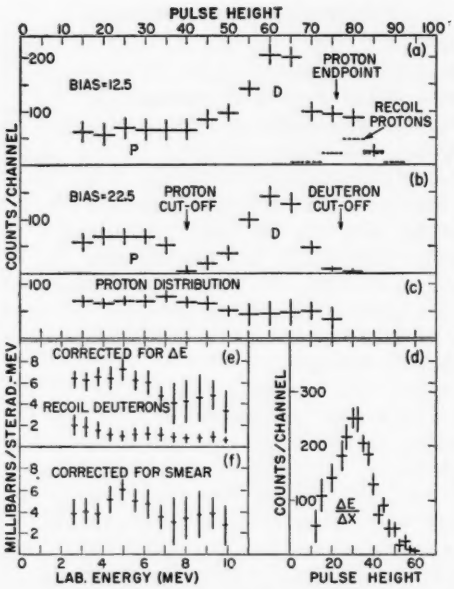

FIG. 6. Typical pulse-height distributions as the laboratory angle of 30 degrees, showing method of analysis. (a) Complete scintillation pulse-height distribution; (b) distribution with dE/dx-bias set to eliminate protons without affecting deuterons; (c) net proton distribution; (d) gas-counter pulse-height distribution; (e) proton distribution in energy, corrected for energy losses. Also shown are deuterons recoiling from degraded neutrons; (f) final proton energy distribution corrected for smearing. See text.

shown typical pulse-height distributions for the forward direction, in a form for comparison of the *n-p* and *n-d* interactions. The resolution of the system was, for 14-Mev protons, 6 percent width at half-maximum when observed with channels 2.5 percent wide. In the *n-p* case, the low-energy pulses correspond to protons recoiling from degraded neutrons present in the incident flux, and in the *n-d* case, the low-energy pulses correspond to disintegration protons, together with a few deuterons recoiling from the degraded neutrons. The manner in which protons and deuterons were disentangled is illustrated in Fig. 6, which shows the steps of analysis in the most difficult case, 30 degrees. In this case the number of protons and deuterons from the *n-d* interaction are nearly equal, and the proton distribution extends completely under the deuteron distribution which has already been broadened by the effect of finite angular aperture mentioned earlier. Moreover, the recoil protons from the hydrogen present in the "CD_2" foil are quite noticeable since the differential cross section for *n-p* scattering is more than five times as large as that for deuteron disintegration, and the recoil protons fall nearly on top of the end point of the disintegration protons. This situation is illustrated in Fig. 6(a). The dE/dx pulse-height distribution [Fig. 6(d)] at this angle cannot be used directly for diagnosis, but the peak of the distribution corresponds to dE/dx of the deuteron group of known energy and establishes the scale of dE/dx, so that other corresponding points may be calculated. As the lower limit for accepting dE/dx pulses in the coincidence circuit was progressively raised, the energy pulse-height distribution changed first by the loss of the recoil proton group, and then by progressive withdrawal of the disintegration proton group from beneath the deuteron group until the condition illustrated in Fig. 6(b) was reached, wherein the deuteron group is essentially unaffected,[25] and the protons have been removed. By comparison of (a) and (b) (and the intermediate steps not shown) the proton pulse-height distribution (c) can be deduced. When energy losses in the foil and gas are taken into account, and the measured light ratio $L_p/L_d=1.04$ (see above) is used, the pulse-height position of the recoil protons can be referred to that of the recoil deuterons. The width of the distribution was taken from the 30-degree data on *n-p* scattering. The amplitude corresponds to the H/D ratio of 3.6 percent given by mass-spectrographic analysis of the deuterated ethylene gas before polymerization. When the amplitude of the recoil-proton distribution was adjusted to give best fit to the data, the H/D ratio was found experimentally to be 4 ± 2 percent. Since this determination is limited statistically by the difficulty of obtaining data at this most sensitive point, the value of 3.6 percent was accepted and used throughout the experiment. The distributions of Fig. 6 (a), (b), and (c) represent the analysis of but one run of several. The average of all such runs was used in plotting Fig. 6(e) which gives the proton *energy* distribution in millibarns per sterad-Mev. Included in this graph is the distribution of recoil deuterons arising from degraded neutrons (discussed below). When these are subtracted, the proton distribution is obtained except for one final correction, the distortion arising from the fact that the energy loss of low-energy particles is larger than that of high-energy particles, so that when the spectrum is observed with channels of constant width, and the counts per channel are replotted at the mean energy of each channel, as in Fig. 6(e), there is a piling-up in lower channels. Or, to say it another way, the lower channels are wider *in energy*, so to get the differential cross section *per* Mev, one must reduce the cross section per channel in proportion to the energy-width of the channel. For a mathematical formulation of this "smearing," let $n(E)=d^2\sigma/d\Omega dE$, the desired distribution of events per unit energy. Since these take place throughout the radiator, particles lose energy according to both their initial energy and their position, so it is necessary to integrate $n(E)$ over the thickness of the foil in units of equal energy loss, as follows. Let E_1 be the emergent energy and $n_1(E_1)$ the corresponding

[25] A small correction for high-energy deuterons lost due to finite dE/dx resolution was applied. See reference 26.

distribution function. Then

$$n_1(E_1)=\frac{1}{X}\int_{E_1}^{E_1+\Delta(E_1)}\frac{n(E)dE}{(dE/dx)},$$

where X is the thickness of the foil and $\Delta(E_1)$ is the energy lost in passing completely through the foil by a particle *emerging* with energy E_1. When $\Delta(E_1)\ll E_1$, as was generally the case in this experiment, the integral may be replaced by a product of averages, so $n_1(E_1)=n(\bar{E})[\Delta(E_1)/\Delta(\bar{E})]$, where $X\langle dE/dx\rangle_{Av}=\Delta(\bar{E})$ and $\bar{E}$ is the mean energy in the foil. The resulting equation may readily be solved for $n(\bar{E})$, which is the desired distribution function. Since the energy loss in the gas was small compared to that lost in the foil, and all the particles passed through all the gas, the correction for smearing in the gas was negligible, and was not applied, although the mean energy loss in passing through the gas was of course taken into account.

In order to make a correction to the disintegration proton spectrum for deuterons recoiling from degraded incident neutrons, one must in principle know the incident flux, both as to energy and angle of incidence, and the highly anisotropic *n-d* differential cross section for all energies. This is a good deal more information than is available. The "tails" of the spectra obtained with a CH_2 radiator are reproduced in Fig. 7, where they are plotted as apparent differential cross sections, or as if they resulted directly from interaction of the target material with the primary 14-Mev neutrons, it being assumed that the degraded flux is proportional to the primary flux. The regions where data are absent are those covered by the primary recoil protons. The last distribution shown in Fig. 7 is the average of applicable data for all five angles, and the shaded region covers this average and an (arbitrary) uncertainty of plus and minus one-half its value. This same shaded region has been replotted over the data for the five angles, and purports to show that in view of the statistical uncertainty of the individual data points, this average is a fair representation of the collective data at the several angles. Were this exactly so, or were the data in better support of this hypothesis, it would mean that the secondary neutron flux was isotropically incident on the radiator. Consider now what could be expected of neutrons proceeding directly from the neutron source, imagined to arise from inelastic scattering in the zirconium, silver, tungsten, and steel of the target assembly. Given a characteristic shape to the recoil spectrum at 0 degrees, the prominent features of the distribution should move down in energy as $\cos^2\theta$ when θ is increased. It is difficult to discern any such effect in the data of Fig. 7. The total amount of degraded flux amounts to about 4 percent of the primary flux. One can account for the order of 1 percent scattering in the target assembly from known cross sections. If there were this much straight from the target it would be

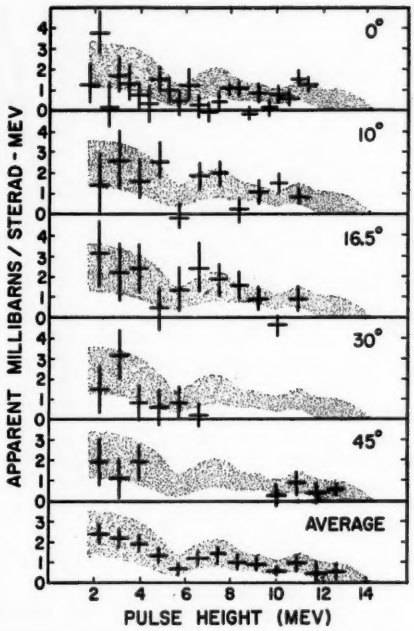

FIG. 7. Distribution of proton recoils from CH_2 radiator arising from degraded neutrons present in the incident flux. The shaded area is a smoothed average over angles with an associated uncertainty of ± half its value. See text.

indistinguishable in the presence of the isotropic 3 percent, but if there were more, it should exhibit dependence on $\cos^2\theta$. A similar problem of course arose in the nuclear-emulsion investigation[8] of the *n-d* interaction, except that there was more evidence to treat the secondary flux as arising primarily from small angle scattering in the aperture of the collimator-shield used; a summary of measurements of *n-d* angular distributions at low energies is presented in that paper. That information was used by the present author to prepare a smoothed logarithmic plot of $d\sigma_{n-d}/d\sigma_{n-p}$ against neutron energy and recoil angle (not shown) as an aid to evaluating a correction for recoil deuterons based on the data for recoil protons. Now if the incident flux were known in detail, or could be unequivocally deduced from the recoil proton distributions, one could proceed to evaluate the recoil deuteron distribution at a given angle of detection by averaging $d\sigma_{n-d}/d\sigma_{n-p}$ over the range of neutron energies which could give rise to the particular choice of angle and recoil energy. For orientation, the correction factor N_d/N_p (E_d,θ) was calculated by averaging in the manner indicated for two assumptions consistent with the data, (1) uniform flux, and (2) one-third direct from the target, two-thirds uniform. In case one, which is in best agreement with the data but hard to accept implicitly, the factor was between 0.7 and 1.0 for all energies and angles. For case two, which is probably more realistic, the factor range from 0.5 to 1.5, being highest for small

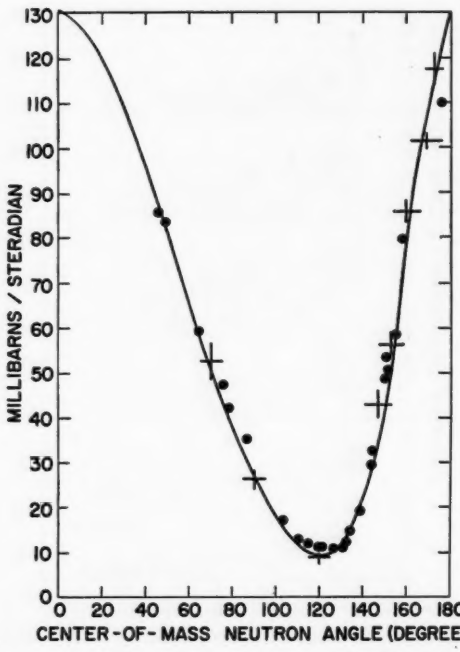

FIG. 8. *n-d* elastic scattering at $E_n = 14.1$ Mev. The solid curve is the prediction of the theory of Christian and Gammel, which is compared with the results of this experiment (+) and the results of Allred, Armstrong, and Rosen (●).

angles and large energies and least for large angles and intermediate energies, and in the vicinity of 1.0 for all angles at the lowest energies detected. These calculations merely indicate that the errors likely to be incurred through ignorance of the neutron flux in complete detail are within reasonable bounds, and are in general comparable with the statistical uncertainty of the data. Accordingly, the correction factor was set equal to 1.0, with an uncertainty of ± 0.5, which was carried along in subsequent estimates of error. A typical distribution obtained in this manner is shown in the lower part of Fig. 6(e). Some confidence that there is no gross error in thus proceeding is to be had from the numerous cases in the original data, one of which is illustrated in Fig. 6(b), where the discriminators for accepting dE/dx pulses were deliberately set so as to exclude protons but not deuterons above a certain pulse height. In no case was the net number of counts above such a point in excess of the correction subsequently applied for deuterons, and in general the correction was less than the statistical uncertainty of the net data. Also, in a number of cases it was possible to compare a set of data corrected in this manner with another in which no correction was made in certain channels because the deuterons were biased out. Good agreement was noted, i.e., the order of magnitude of the correction was correct, and agreement of such sets was within statistical uncertainties only if the correction was made. It may be remarked that deliberate "cutoffs" produced by manipulation of dE/dx limits were rather more sharp than would be inferred from the widths of the combined dE/dx distributions and the theory of energy loss.[26] Experimentally, however, the shape of the cutoff for one kind of particle could generally be inferred from the data for the other type.

TABLE I. Elastic scattering of deuterons by 14.1-Mev neutrons.

Lab. angle θ_d degrees[a]	3.5 ± 2.0	5.5 3.5	10 3	13.5 3	16.5 3	30 2.5	45 2.5	55 2.0
Lab. $d\sigma/d\Omega$ mb/sterad	468 ±14	404 6	339 9	219 10	161 8	30.4 3	75 5	121 9
Cm angle ϕ_n degrees[a]	174 ± 4	169 7	160 6	153 6	147 6	120 5	90 5	70 4
Cm $d\sigma/d\Omega$ mb/sterad	117.5 ± 3.5	101.5 1.5	86 2.3	56.4 2.6	43 3	8.8 0.9	26.5 1.8	52.7 4

[a] Angles given are mean angles of observation, and the associated uncertainties indicate the corresponding half-widths of the angular resolution functions.

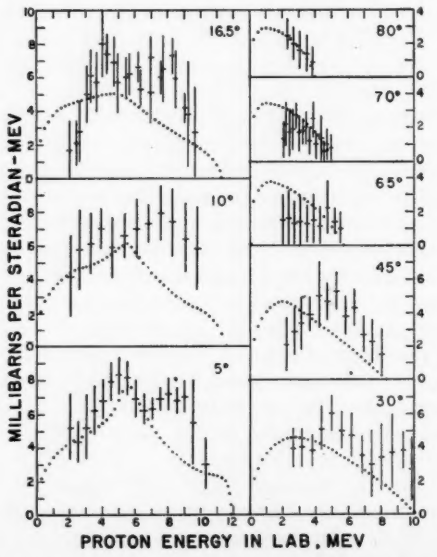

FIG. 9. Distribution in energy of the disintegration protons from the *n-d* interaction at $E_n = 14.1$ Mev. The predictions of the theory of Frank and Gammel are shown as dotted curves.

RESULTS

The differential cross sections for elastic scattering of 14.1-Mev neutrons by deuterium are presented numerically in Table I, and the angular distribution in the center-of-mass system is shown in Fig. 8, where it is compared with the experimental results of Allred, Armstrong, and Rosen,[8] and with the theory of Christian and Gammel.[9] The close agreement between the results of two very different experimental techniques is gratify-

[26] See B. Rossi, *High Energy Particles* (Prentice-Hall, New York, 1952) for a summary of relevant parts of Symon's theory of energy loss by ionization (unpublished).

ing and indeed the small differences can readily be accounted for by the broader angular resolution and statistical uncertainties of the previous experiment. In comparing these two experiments, a possible source of error affecting both experiments equally should be discounted: both experiments were performed with the same neutron source whose absolute strength is uncertain to 4 percent. It is hard to draw a much better curve through the data than that provided by the theory, but it may be noted that most of the data falls slightly above the theoretical curve, and an integral of the present results, granting the extrapolation provided by the theory, is 0.61 ± 0.03 barn. The theoretical value is 0.60 barn.[27]

The distribution in energy of the protons from the disintegration of deuterium by 14.1-Mev neutrons is shown in Fig. 9, where the results of this experiment

TABLE II. Protons from disintegration of deuterons by 14.1-Mev neutrons.

Lab. angle θ_p degrees	5	10	16.5	30	45	55	65	70	80
Lab. $d\sigma/d\Omega$ mb/sterad	60.2 ±4.5	60.8 6.1	49.5 4.6	35.9 4.7	23.2 4.1	15 5	7.5 3.3	8.1 2.6	7.3 5
Deuteron bgnd.[a] percent	12	14	17	20	26	35	47	39	0

[a] See text. The average figure given is the percent correction applied to the data to obtain the proton distribution, although the channel-by-channel correction varied considerably, and in some instances was zero due to the bias setting. At 80 degrees all deuterons were degraded below the threshold of detection.

are compared with the prediction of the theory of Frank and Gammel.[13] Qualitatively it would appear that the experimental distributions lie well above the theoretical curves in the upper third of the energy range, while the theory predicts peaking at from half to one-third of the maximum. More quantitative comparison is probably not warranted since the theory contains a number of convenient assumptions permitting a result in closed form, while on the other hand the experimental probable errors, though believed conservative, are sufficiently large that no smooth curves through the data were drawn.

The data extend over a sufficiently large portion of the allowed range of energy, however, that extrapolation to the end points can be made without appreciably increasing the aggregate probable error of the integral. The distribution must vanish at both end points,[28] so the extrapolation for purposes of integration was made

[27] The value of 0.62 barn quoted on p. 119 of reference 9 is an error.

[28] Reference 13 and J. L. Gammel (private communication).

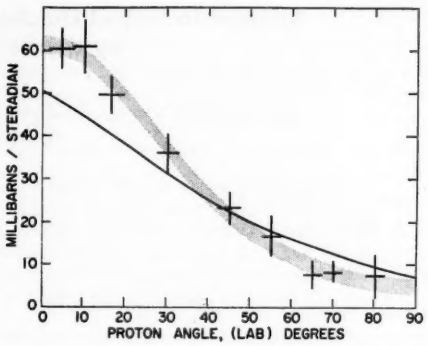

FIG. 10. Comparison of the angular distribution of disintegration protons from the n-d interaction at $E_n=14.1$ Mev as given by this experiment and by the theory of Frank and Gammel.

by drawing straight lines from the last data points to the end points (i.e., constructing triangular areas) and including these areas with probable errors equal to their values in the integral. The resulting differential cross sections are tabulated in Table II, and shown in Fig. 10 in comparison with the theoretical angular distribution. The difference in this case is less marked, with experiment indicating a somewhat more strongly forward-peaked distribution. The integral over the forward hemisphere is slightly greater, namely 117 mb for the theoretical curve than for the experimental curve which gives the value 112 ± 15 mb.

There remains, however, a difference of nearly 200 mb between the total cross section measured by transmission[21] of 803 ± 14 mb and the elastic cross section of 0.61 ± 0.03 barn as determined in this experiment. The cross section for disintegration protons in the rear hemisphere must then be about 90 mb, whereas the theory predicts only 27 mb. It is regrettable that it was not possible to obtain data in the rear hemisphere, since the neglect of the n-n interaction in the theory[13] should have proportionately a larger effect in the rear hemisphere and a direct comparison of distributions would be more enlightening than the grosser comparison just made, namely, that the theory neglecting the n-n interaction accounts for only about one-third of the interactions producing protons in the rear hemisphere.

ACKNOWLEDGMENTS

The author is pleased to acknowledge the helpful interest and advice of Dr. J. H. Coon, Dr. L. Rosen, and Dr. J. L. Gammel throughout this work, and the assistance of R. W. Davis and Miss Joan Newman in the tabulation of data.

Attempt to Detect the Antineutrinos from a Nuclear Reactor by the $Cl^{37}(\bar{\nu},e^-)A^{37}$ Reaction*

RAYMOND DAVIS, JR.
Department of Chemistry, Brookhaven National Laboratory, Upton, Long Island, New York
(Received September 21, 1954)

Tanks containing 200 and 3900 liters of carbon tetrachloride were irradiated outside of the shield of the Brookhaven reactor in an attempt to induce the reaction $Cl^{37}(\bar{\nu},e^-)A^{37}$ with fission product antineutrinos. The experiments serve to place an upper limit on the antineutrino capture cross section for the reaction of 2×10^{-42} cm² per atom. Cosmic-ray-induced A^{37} was observed and the production rate measured at 14 100 feet altitude and sea level. Measurements with the 3900-liter container shielded from cosmic rays with 19 feet of earth permit placing an upper limit on the neutrino flux from the sun.

I. INTRODUCTION

THERE have been a number of experiments performed in the past to detect the neutrino by scattering processes and nuclear interactions.[1] The most sensitive of these experiments serve to place a limit on the scattering cross section for neutrinos on electrons of less than 14×10^{-40} cm²/electron and for nuclear interaction of less than 10^{-30} cm²/atom. Recently Reines and Cowan of the Los Alamos Laboratory performed an experiment with a large hydrocarbon liquid scintillator having a high sensitivity for detecting the interaction $p(\bar{\nu},e^+)n$ within the liquid.[2] Measurements were made with this scintillator located adjacent to the Hanford reactor within a shield designed to absorb other radiations from the reactor to which the scintillator was sensitive. Under these conditions they observed an increase in counting rate of the scintillator of 0.41 ± 0.20 delayed count per minute when the reactor was operating over that observed with the reactor off. This increase in counting rate, if ascribed to the process $p(\bar{\nu},e^+)n$, corresponds to a cross section of $(12\pm6)\times10^{-44}$ cm²/atom.

In 1946 Pontecorvo[3] suggested a radiochemical method of detecting the neutrino by employing the reaction $Cl^{37}(\bar{\nu},e^-)A^{37}$. The experiment involved irradiating a large volume of carbon tetrachloride near a nuclear reactor, removing the A^{37} by physical methods, and counting the electron capture decay of this isotope. Alvarez[4] considered the use of this method of detecting the neutrino in detail, and proposed an extended experiment capable of detecting the theoretically expected cross section for neutrinos of 2×10^{-45} cm²/atom.

The reaction $Cl^{37}(\nu,e^-)A^{37}$ is the inverse process to the 34-day electron capture decay of A^{37}. In this decay a neutrino (ν) is emitted which may be formally distinguished from an antineutrino ($\bar{\nu}$) which accompanies negative beta emission. A nuclear reactor emits antineutrinos which arise from the negative beta decays of fission products. In our experiment an attempt is made to observe an inverse electron capture process which requires neutrinos, using a source emitting antineutrinos. If neutrinos and antineutrinos are identical in their interactions with nucleons one should be able to observe the process upon carrying the experiment to the required sensitivity. However, if neutrinos and antineutrinos differ in their interactions with nucleons one would not expect to induce the reaction $Cl^{37}(\bar{\nu},e^-)A^{37}$. A positive experiment of this type would show that these particles are not to be distinguished in their nuclear reactions. A negative experiment carried to the required sensitivity would indicate that neutrinos and antineutrinos differ in their nuclear reactions, or that the present theory of beta decay is incorrect. The present theory of beta decay and the principle of detailed balancing lead to a reliable calculated cross section for the inverse process. The only evidence concerning the nuclear interactions of neutrinos and antineutrinos comes at present solely from a study of the half-life of the double beta-decay process. These studies have indicated that neutrinos and antineutrinos do differ in their interactions with nucleons.[5]

An experiment has been performed in which a 200-liter (55-gallon) drum of carbon tetrachloride was irradiated outside the shield of the Brookhaven reactor. The argon was removed by sweeping with helium gas and counted. Further measurements were carried out with a 3900-liter (1000-gallon) tank of carbon tetrachloride. As a result of these measurements one can place an upper limit on the cross section for the reaction of 2×10^{-42} cm²/atom for fission product antineutrinos. A background of A^{37} activity was produced in the tank by cosmic-ray interactions and in the present experiment prevented observing lower values of the cross section. The purpose of this paper is to give the results of these measurements.

The present experiment was not sensitive enough to

* Research carried out under the auspices of the U. S. Atomic Energy Commission.

[1] The experiments are reviewed by H. R. Crane, Revs. Modern Phys. **20**, 278 (1948); J. H. Barrett, Phys. Rev. **79**. 907 (1950); Cowan, Reines, and Harrison, Phys. Rev. **96**, 1294 (1954).

[2] F. Reines and C. L. Cowan, Jr., Phys. Rev. **92**, 830 (1953).

[3] B. Pontecorvo, Chalk River Laboratory Report PD-205, 1948 (unpublished).

[4] L. W. Alvarez, University of California Radiation Laboratory Report UCRL 328, 1949 (unpublished).

[5] Reviewed by E. J. Konopinski and L. M. Langer, Ann. Rev. Nuc. Sci. **2**, 261 (1953).

detect the theoretically computed cross section and therefore conclusions could not be drawn concerning the correctness of beta decay theory, or the identity of neutrinos and antineutrinos. The present experiment will be continued in an effort to accomplish this purpose.

II. EXPERIMENTAL

Procedure for Removing Argon-37

Argon-37 produced by nuclear reactions in the carbon tetrachloride can be removed from the liquid by sweeping it with helium gas. The argon can then be removed from the helium by passing the gas through a charcoal trap cooled with liquid nitrogen (−196°C) which adsorbs the argon quantitatively and allows the helium to pass. The carbon tetrachloride was contained in a 200-liter drum and 3900-liter tank. Each was equipped with a stirrer and a valved tube for introducing the helium into the bottom of the container and an exit valve and tube at the top. Helium gas from a cylinder was purified by passing it through a charcoal trap cooled with liquid nitrogen and then passed into the container. Upon leaving the container the gas was passed through condensation traps to remove carbon tetrachloride vapor. Following these the gas passed through two charcoal traps in series. The first was cooled with solid carbon dioxide (−78°C) and served to remove radon and xenon gas which might arise from contaminants in the system. The second charcoal trap was cooled with liquid nitrogen and retained the argon and krypton. Krypton was partially removed by the first charcoal trap at the flow rates and quantities of helium gas used in the sweeping. After completion of the sweeping the second charcoal trap was evacuated to remove the occluded helium, and closed off. The argon contained in this charcoal trap contained some radioactive rare gases that had to be removed before installing the gas in a Geiger-Müller counter. The ones that have been found present are radon, arising from a small amount of radium impurity in the charcoal, and fission product krypton, particularly 9.5-year Kr^{85}, which could be introduced into the connecting tubes on the tanks during the irradiation near the reactor. These were removed by sweeping the gas isolated above with helium through another charcoal trap cooled with solid carbon dioxide into a small charcoal trap cooled with liquid nitrogen. The gas contained in the small trap was evacuated cold to remove the occluded helium, and then desorbed by heating to 200°C. The argon gas was removed from the charcoal trap, heated over Ti metal to 900°C, and installed along with quench gas as the counting gas in a Geiger-Müller counter.

Small amounts of argon could be removed from a 200-liter drum of carbon tetrachloride by sweeping it with approximately 400 liters of helium at a rate of 1 to 2 liters per minute. The 3900-liter tank could be swept out with approximately 4000 liters of helium at a rate of 5 to 7 liters per minute. The efficiency of the sweeping operation was tested in two ways. First, small measured amounts of argon gas (20 to 0.2 cm^3) were introduced into the container, allowed to remain for several days and then removed by the sweeping procedure and the amount recovered was measured. A second method takes advantage of the fact that A^{37} is produced in carbon tetrachloride by cosmic rays. This activity was removed by the sweeping procedure described, and counted. Immediately afterward a second identical sweeping operation was conducted which yielded less than ten percent of the A^{37} activity obtained in the first sweeping. It was also demonstrated that the charcoal trap removes the argon quantitatively. This was shown by sweeping a 320-liter container in which A^{37} was produced in the carbon tetrachloride liquid by irradiation with fast neutrons. Here A^{37} was produced by the reaction $Cl^{37}(p,n)A^{37}$ with protons produced by (n,p) reactions on Cl^{35}. A sweeping operation was carried out by using two charcoal traps in series. The first trap contained 120 counts per minute of A^{37} and the second contained less than 0.1 count per minute.

It was concluded from these experiments that the sweeping procedures used will remove over ninety percent of the A^{37} activity free from other rare-gas radioactive contaminants.

Irradiation at the Brookhaven Reactor

The Brookhaven reactor operates at a power level 20–25 megawatts producing approximately 4×10^{18} antineutrinos per second. The graphite cube is 25 feet on a side and is surrounded by a concrete and iron shield five feet thick. The containers of carbon tetrachloride were placed outside of the shield and irradiated for 36 to 75 days. The 200-liter drum and the 3900-liter tank were located 29 feet from the center of the reactor and received a flux of 3 to 4×10^{11} antineutrinos per cm^2 per second. The 200-liter drum was surrounded by a shield of iron loaded concrete eight inches thick. In addition the drum was shielded from above by two extensive balconies with a combined thickness of 16 inches of concrete. The 3900-liter tank was not shielded. However, both the tank and the drum were effectively shielded on one side by their proximity to the large reactor shield.

Counters

Small Geiger-Müller counters made of stainless steel and cold-rolled steel were used. These were 0.48 cm in diameter and 12 cm long and contained a 0.050-mm tungsten center wire. They were filled with 200 to 400 mm of argon pressure and 25 mm of ethyl acetate quench gas. These counters operated around 1000 volts and had plateaus 100 volts long with a slope of less than five percent per 100 volts. The counter was surrounded by a ring of six anticoincidence counters

TABLE I. Summary of results.

	200-liter container			3900-liter container	
Location during irradiation	Adjacent to reactor	Laboratory	Mt. Evans	Adjacent to reactor	Buried 19 feet underground
Amount of shielding over container, g/cm²	120	None	None	None	970
Duration of irradiation, days	75	77	62	36	41
Average power level of reactor, in megawatts	17	...	...	21	...
Average antineutrino flux/cm²/sec	3.4×10^{11}	...	...	4.4×10^{11}	...
Saturation counting rate, disintegration/min	<0.03	<0.03	3.5±0.5	1.23±0.06	<0.05

2.5 cm in diameter and 30 cm long. The counting was carried out in an iron shield seven inches thick. The background counting rate of the counters may be summarized as follows: outside of shield 15 counts per minute, inside of shield 4.3 counts per minute, and in anticoincidence 0.15 to 0.25 count per minute. A given counter was found to give a reproducible background counting rate upon changing the filling gas. An increase in counting rate of ten percent of the background counting could be detected.

III. RESULTS AND DISCUSSION

Two measurements were made with the 200-liter container of carbon tetrachloride. In one the drum was placed close to the reactor, and in the second it was placed in the laboratory 120 feet from the reactor. The A^{37} activity in both of these drums was below the amount detectable with the counters used (see Table I). From the result an upper limit of 2×10^{-42} cm²/atom can be set for the cross section for the reaction $Cl^{37}(\bar{\nu},e^-)A^{37}$ for fission product antineutrinos. The antineutrino flux from the reactor was computed from the average power level of the reactor and the result of Way and Wigner[6] who showed that on the average 6.1 beta decays follow each fission event. The experiments with these containers showed that it was possible to remove quantitatively small amounts of A^{37} from large quantities of carbon tetrachloride by sweeping with helium and that background effects producing A^{37} activity are below the sensitivity of these experiments. It then appeared possible to continue the experiments with increased sensitivity.

The most serious background effect expected in this experiment arises from the production of A^{37} by energetic protons by the reaction $Cl^{37}(p,n)A^{37}$. The threshold for this reaction is 1.60 Mev. Protons of energy up to 10 Mev are produced in condensed materials at the rate of about two per gram per day at sea level by the nucleonic component of cosmic radiation. These cosmic ray protons may be expected to produce an amount of A^{37} in the drums in the same order of magnitude as the sensitivity of these experiments.

[6] K. Way and E. Wigner, Phys. Rev. 73, 1318 (1948).

In order to measure the cosmic ray background effect a 200 liter drum was exposed for a period of 62 days at the top of Mt. Evans, Colorado (14 150 feet elevation) through the courtesy of the Inter-University High Altitude Laboratory. It was shipped back to the Brookhaven laboratory and processed. The saturation A^{37} activity in this drum was 3.5±0.5 disintegrations per minute and the activity was found to decay with the correct half-life. The corresponding cosmic-ray production rate for A^{37} in carbon tetrachloride was therefore $(1.1\pm0.2)\times10^{-5}$ disintegrations per minute per gram at atmospheric depth of 610 grams per cm². Assuming that the A^{37} observed was produced by the nucleonic component which has an exponential absorption mean free path of 140 grams per cm², the saturation activity expected in a 200 liter drum at sea level should be 0.17 disintegration per minute. The observed activity was less than this by a factor of six. Therefore the cosmic ray component producing A^{37} in the drum has an average absorption mean free path of less than 90 grams per cm².

An experiment was performed with a 3900 liter container located near the Brookhaven reactor as described. The saturation A^{37} activity observed was 1.23±0.06 disintegrations per minute. The decay of this activity was followed and found to have the proper half life of 33±3 days. This corresponds to a cross section of $(2.1\pm0.1)\times10^{-42}$ cm²/atom for the antineutrino capture cross section (see Table I). However, it is probable that this activity was cosmic ray induced; the A^{37} production rate at sea level is $(2.0\pm0.1)\times10^{-7}$ disintegration per minute per gram of carbon tetrachloride uncorrected for shielding effects. The tank was partially shielded by the reactor since the tank stands one foot away from the shield of the reactor and the shield extends about twelve feet higher than the tank. The tank is eleven feet high and four feet in diameter, hence the lower portions of the tank were shielded by the upper portions of the tank. An approximate calculation of the shielding factor leads to a corrected A^{37} production rate of about 6×10^{-7} disintegration per minute per gram at sea level (atmospheric depth of 1035 grams per cm²). The amount of A^{37} observed in the 3900-liter tank near the reactor, corrected for shielding, would correspond to a saturation activity of 0.20 dis-

integration per minute in a 200-liter container. This value is over six times greater than the upper limit of 0.03 disintegration per minute formed with an unshielded 200-liter container irradiated in the laboratory away from the reactor. Further experiments are to be performed to examine this point. At present it is concluded from our experiments that the cross section for the $Cl^{37}(\bar{\nu},e^-)A^{37}$ reaction is less than 2×10^{-42} cm^2/atom for fission product antineutrinos.

An experiment was performed with the 3900-liter tank buried under 19 feet of earth (970 grams/cm^2) to explore the possibility of producing A^{37} in the tank by processes other than those associated with the nucleonic component of cosmic radiation. This amount of earth will reduce the intensity of the nucleonic component by a factor of about one thousand. The amount of A^{37} activity in the buried tank was found to be less than 0.05 disintegration per minute at saturation, a limit set by the sensitivity of the counter used. The limit corresponds to detecting 70 neutrino captures per day in the 3900-liter tank. Since the 3900-liter tank with its associated counters was more sensitive for detecting neutrinos than any previously reported device, it is of interest to consider the possibility of detecting neutrinos from the sun. Two processes are now considered important for energy production in the sun, the proton-proton chain and the carbon-nitrogen cycle.[7] The neutrinos from the proton-proton chain have a maximum energy (0.41 Mev) below the threshold of 0.816 Mev for the $Cl^{37}(\nu,e^-)A^{37}$ reaction and therefore neutrinos from this chain could not be detected by this method. The neutrinos in the carbon-nitrogen cycle arise from the positron decays of N^{13} and O^{15} which have maximum neutrino energies of 1.24 and 1.68 Mev respectively. Based upon this cycle, the flux of neutrinos at the surface of the earth is approximately 6×10^{10} neutrinos/cm^2 sec.[8] The estimated average cross section for these neutrinos is about 3×10^{-46} cm^2 for the reaction. The experiment with the buried 3900-liter tank sets an upper limit on the neutrino flux from the sun of 1×10^{14} neutrinos/cm^2 sec if the energy production of the sun is entirely through the carbon-nitrogen cycle.

ACKNOWLEDGMENT

The author is indebted to Dr. Byron E. Cohn and Dr. Mario Iona of the University of Denver for their generous assistance in the irradiation carried out on the summit of Mt. Evans.

[7] E. E. Salpeter, Ann. Rev. Nuc. Sci. **2**, 41 (1953).
[8] F. G. Houtermans and W. Thirring, Helv. Phys. Acta **27**, 81 (1954).

PHYSICAL REVIEW VOLUME 97, NUMBER 3 FEBRUARY 1, 1955

Interactions of the Heavy Nuclei of the Cosmic Radiation*

J. H. Noon and M. F. Kaplon
University of Rochester, Rochester, New York
(Received August 17, 1954)

Fragmentation probabilities have been obtained for the interactions of heavy nuclei with target nuclei of photographic emulsion and a light element absorber (gelatin and cellulose acetate). The predictions of a simple geometrical model for the fragmentation probabilities in light elements derived from those observed in emulsion are in agreement with experimental observations. Measurements of the interaction mean free paths of heavy nuclei at different latitudes indicate that the interaction cross section is energy insensitive and is smaller than geometric. Curves are presented showing the ratio of the secondary light element (Li, Be, B) flux relative to the medium element ($6\leqslant Z\leqslant 10$) flux as a function of atmospheric depth.

INTRODUCTION

THE heavy primary component of the cosmic radiation consists of nuclei with charges ranging from $Z=3$ to $Z\sim26$.[1] The flux of these nuclei is small in comparison to the proton and α-particle flux (~1 percent of the proton flux) and increased statistics can be obtained by studying the behavior of various charge groups rather than that of individual charged nuclei. In the following discussion three different charge groups will be referred to: (1) L, light nuclei, $3\leqslant Z\leqslant 5$, (2) M, medium nuclei, $6\leqslant Z\leqslant 10$, and (3) H, heavy nuclei, $Z>10$.

In its passage through the atmosphere the heavy primary component changes in character since some particles are lost from the beam because of interaction and ionization loss while others are added to the beam as fragmentation products of interactions of nuclei of higher charge. Since the interaction mean free path of heavy nuclei in atmosphere is quite short (~20 to 40 g/cm^2) direct measurements on the chemical composition must be made at extremely high altitudes. At the balloon altitudes attained on most experiments dealing with the heavy nuclear component of the cosmic radia-

* This research was supported in part by the United States Air Force through the Office of Scientific Research, Air Research and Development Command.

[1] For a review of the situation as of 1951 see the article by B. Peters in *Progress in Cosmic Ray Physics*, edited by J. G. Wilson (North Holland Publishing Company, Amsterdam, 1952), Vol. I. A survey covering results as of the fall of 1953 is given by E. P. Ney in the Report of the Duke Conference on Cosmic Radiation (unpublished).

tion (~10 to 30 g/cm² of residual atmosphere) passage through the residual atmosphere has caused an appreciable adulteration of the incident beam; as a result of these difficulties, *viz.*, a relatively small incident flux and observations under finite amounts of absorber, the true relative flux values at the top of the atmosphere for the three charge groups have not been definitely established. This work was carried out in an attempt to determine more precise values for those parameters involved in the diffusion of the heavy nuclei through atmosphere.

Interactions of heavy nuclei with target nuclei of photographic emulsion have been examined and the fragmentation products from interactions in gelatin and cellulose acetate have also been studied. From this data we have derived the interaction mean free paths and the fragmentation probabilities for the medium and heavy nuclei in atmosphere and calculations have been made to estimate the secondary light element flux at different depths in the atmosphere. By working at two different latitudes, 41° and 55° geomagnetic, information has been gained about the energy dependence of these parameters.

EXPERIMENTAL DETAILS

Three stripped emulsion stacks were used in this experiment. In each case the stripped emulsions (manufactured by Ilford Ltd.) were 4 in.×6 in.×400μ and were mounted on glass after exposure and before processing. The development was by the usual temperature methods, and after completion each plate was cut into four 3 in.×2 in. sections for microscopic observations.

Two of the stacks, the *C* and *SG* stacks, were flown at White Sands, New Mexico ($\Lambda=41.7°$, cutoff energy $=1.5$ Bev/nucleon) and the third stack, the *SM* stack was flown at Minnesota ($\Lambda=55°$, cutoff energy$=0.31$ Bev/nucleon). The *C* stack contained ninety-two 400μ *G*-5 stripped emulsions arranged horizontally with thin tissue paper between successive emulsions. The flight was for ~9 hours at ~92 000 ft. The emulsions in this stack were not aligned. The *SG* stack consisted of 19 triads of *G*-5, *G*-5, *G*-0 (200μ each) combination emulsions, and 400-μ gelatin sheets. All members were in direct contact and the stack was aligned after processing. It was flown with vertical geometry for ~9 hours at an altitude varying from 97 000 ft to 70 000 ft. The *SM* stack consisted of two parts. Part *A* contained 11 triads of *G*-5, *G*-5, *G*-0 combination emulsions, and 400-μ cellulose acetate sheets. Part *B*, in contact with *A*, contained 23 400-μ *G*-5 emulsions. All emulsions were in direct contact and the stack was flown vertically for ~8.2 hours at ~92 000 ft. After processing this stack was aligned for easier tracing.

CHARGE CALIBRATION AND SELECTION CRITERIA

Selection of tracks in scanning in this experiment was done on the basis of δ-ray density. The number of δ rays per unit length $n_\delta(Z)=Z^2F(\beta)$, where $Z=$ the charge of the particle and βc its velocity. At relativistic velocities, $\beta\approx 1$, $F(\beta)$ is constant so that n_δ is directly proportional to Z^2. At 41° geomagnetic latitude almost all particles are at sufficiently relativistic velocities so that in most cases the observed δ-ray density is a direct measure of their charge. However at 55° this does not hold since a large majority of the nuclei are nonrelativistic, and exact charge identification requires a measure of the velocity as well as of δ-ray density. One method of charge determination is to combine measurements of δ-ray density with multiple Coulomb scattering. This, however, imposes severe geometrical limitations on the acceptability of tracks since very long tracks ($\gtrsim 3$ mm/emulsion) are required for scattering measurements, and the number of acceptable tracks is thus severely limited. For this reason this method of charge identification was not used in this experiment (except for a few tracks in the *SM* stack).

The method adopted for charge identification involved the simultaneous measurement of δ-ray density and range, the latter being a measure of velocity. The observed δ-ray density for a track establishes an upper limit for the charge: since $F(\beta<1)>F(1)$, we obtain a maximum estimate for the charge of a given track by assuming that it is relativistic, $Z_{\max}^2=n_\delta$ (observed)$/F(1)$. In addition each track is observed in the stack for some finite range R and since its actual velocity $\beta>\beta(R)$, a minimum estimate for the charge is obtained as $Z_{\min}^2=n_\delta$ (observed)$/F(\beta(R))$. The error in charge determination $\Delta Z=Z_{\max}-Z_{\min}$ obtained in the above manner is a function of the observed range R of the track and varies from $\Delta Z=3$ for $R=10$ g/cm² to $\Delta Z=1$ for $R=30$ g/cm². In practice a better estimate than this can be accomplished by observing the variation of δ-ray density with range. δ-ray counting can be done with sufficient statistical accuracy to detect variations of <10 percent in δ-ray density. For nuclei having an energy per nucleon $\epsilon\geq 0.8$ Bev, the δ-ray density is sufficiently constant and β close enough to 1 so that the observed n_δ is a direct measure of charge. Nuclei which have $\epsilon<0.8$ Bev will change in δ-ray density by >10 percent in a range $R\sim 15$ g/cm². To consider a specific example: a boron nucleus with the same δ-ray density as a relativistic carbon would change its δ-ray density by ~12 percent in 15 g/cm², a beryllium nucleus would change by ~36 percent in the same range and lithium nucleus would have a range of only 7.5 g/cm²; similar results obtain for higher charged nuclei. It is thus possible by observing the variation of δ-ray density with range (for $R\sim 15$ g/cm²) to establish the charge within one unit. For our experimental conditions this situation was realized in most cases. For those cases in which the observed δ-ray density was constant within the statistical accuracy the higher charge ($Z_{\max}$) was assigned, while for the opposite case a charge of $Z_{\max}-1$ was assigned. The variation of δ-ray density with range used in this experiment was derived from the Bristol calibra-

tion[2] which gave δ-ray density as a function of velocity. Verification of this relationship has been recently obtained independently by Tidman *et al.*[3] on both a theoretical and an experimental basis.

Charge calibration was established by studying fast α particles and heavier fragments from interactions of fast heavy nuclei. Some measure of the energy of the incident heavy nucleus can be obtained from the degree of collimation of the fragmentation products. Relativistic α particles are easily distinguished by their grain density and thus measurements can be made on the opening angles of the α particles in the fragmentation products. Kaplon *et al.*[4] have shown that the root-mean-square angle which these shower particles make with the direction of the incident primary in the laboratory system is $\langle\theta^2\rangle^{\frac{1}{2}}=0.056/E$, where $E=$ total energy in Bev of the incident nucleus. As examples, for a nucleus with $\epsilon=1$ Bev and $A=14$ this angle is $\sim 1.8°$ and for a nucleus of $A=31$ the angle is $\sim 1.3°$.

Fast α particles (selected by grain density) from interactions of fast heavy nuclei were δ-ray counted over large distances to obtain satisfactory statistics. This allows one in first order to predict the δ-ray density for fast nuclei of arbitrary charge. This can be checked by studying stripping reactions of heavy nuclei in which charge balance can be obtained between the incoming primary and the outgoing jet of fast fragments. Figure 1 shows an example of a suitable interaction for calibration purposes. In this reaction a fast carbon nucleus interacts to produce as fragmentation products a lithium nucleus, an α particle, and a proton: the charges of all particles involved can be established unambiguously. By studying reactions of this type it was possible to deduce the δ-ray density for a relativistic singly charged particle $n_\delta(1)$ and the background b by using the relation $n_\delta'(Z)=Z^2n_\delta(1)+b$.[5] In our experiments we used a 4-grain convention in δ-ray counting and reduce our observed δ-ray counts to the number observed per 100μ. For the quantities $n_\delta(1)$ and b we found 0.078 and 0.22 for the C stack, 0.106 and 0.06 for the SG stack, and 0.097 and 0.1 for the SM stack. The background contribution b is a function of the length of time between manufacture of the emulsion and subsequent development after exposure. The difference between the value of $n_\delta(1)$ for the C stack and that for the SG and SM stacks is probably due to the geometry. Since the emulsions in the C stack were flown horizontally, the average track length is much shorter than that in the other two stacks which were flown vertically: the difference is thus a reflection of the adoption of different acceptance criteria for δ rays. δ-ray counting, however, could be done consistently in all stacks and calibration

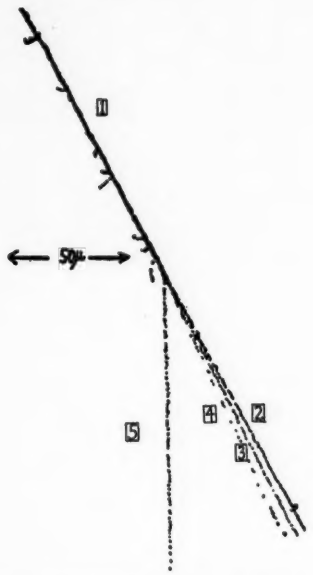

FIG. 1. A carbon nucleus (1) interacts with hydrogen of the emulsion giving a lithium nucleus (2), an α particle (3), and a proton (4). The recoil proton (5) is clearly visible at a wider angle.

tracks in each stack showed variations of less than 5 percent in different emulsions.

The G-0 emulsions in this experiment were used mainly to obtain increased statistics (by grain counting) over that obtained by δ-ray counting for charge determination of α particles and the lighter elements ($Z\leqslant 6$).

The following scanning criteria were adopted. For the vertical emulsions, the SM and SG stacks, all tracks with projected length $>750\mu$ and $n_\delta\geqslant 2$ in the survey plate were accepted. For the horizontal stack, the C stack, all tracks with projected length $>450\mu$ and $n_\delta\geqslant 3$ in the survey plate were accepted. All tracks satisfying the selection criteria were then systematically traced through the stack, either to an exit point or to an interaction. Those slow singly and doubly charged particles which satisfied the acceptance criteria were easily rejected on a range basis. The acceptance criteria for the SM and SG stacks certainly ensured the inclusion of all nuclei with $Z\geqslant 6$, though in the C stack some nuclei of charge 6 may not have been accepted. However, any lack of 100 percent acceptance efficiency in no way affects the results of this experiment with respect to the interaction mean free paths and fragmentation probabilities.

INTERACTIONS IN EMULSION

214 interactions of heavy nuclei in emulsion were analyzed with respect to the fragmentation products, which are collimated in the direction of the incident primary, and the number of star prongs of the target nucleus, N_h, which includes all gray + black tracks. The results are given in Table I. In this table the interactions

[2] Dainton, Fowler, and Kent, Phil. Mag. **43**, 729 (1952).
[3] Tidman, George, and Herz, Proc. Phys. Soc. (London) **A66**, 1019 (1953).
[4] Kaplon, Peters, Reynolds, and Ritson, Phys. Rev. **85**, 295 (1952).
[5] $n_\delta'(Z)$ is the experimentally measured δ-ray density; $n_\delta(Z)$, the true observed δ-ray density, is given by $n_\delta(z)=n_\delta'(z)-b$.

TABLE I. Interactions of the 214 heavy primaries studied are listed according to the charge of the primary. The breakup fragments are also tabulated in the appropriate columns H=heavy ($Z>10$), M=medium ($6\leqslant Z\leqslant 10$), L=light ($3\leqslant Z\leqslant 5$), α—alpha particle, p=proton. The number of black-plus-gray star prongs (N_h) is also listed. The cases where dashes (—) are made are those in which no information could be obtained (see text).

41°	M	L	α	p	N_h
			C		
		Li		3	6
		Be		2	6
		Be	1		5
		B		1	6
			2	2	*H*
			1	4	6
				6	6
			1	4	6
			1	4	12
			1	4	7
			1	4	5
			1	4	9
			1	4	9
				6	5
—	—	—	—	—	6
	Li			3	4
	Li			3	—
	Li		1	1	1
	Be		1		1
			3		—
			3		4
			2	2	0
			1	4	4
			1	4	1
			1	4	1
55°			C		
			2	2	12
			1	4	5
			1	4	7
			1	4	15
				6	8
—	—	—	—	—	6
—	—	—	—	—	9
—	—	—	—	—	11
		3			1
		3			0
		2	2	1	
		2	2	3	

	M	L	α	p	N_h
			N		
		Li	1	2	9
		Be		3	7
			3	1	8
			3	1	14
			3	1	5
			3	1	6
			2	3	5
			1	5	15
			1	5	17
			1	2	9
—	—	—	—	—	11
		Li	2		—
		Li	2		*L*
		Be		3	—
		B		1	0
	C			1	3
—	—	—	—	—	—
			N		
		Li	2		5
		Li	1	2	5
		B	1		10
			2	3	21
			2	3	27
			2	3	5
			1	5	8
			1	5	13
			1	2	5
				7	5
		Li	1	2	—
		Li		4	2
		B	1		1
		B	1	1	1
			3	1	*L*
			3	1	1
			2	3	4
			2	3	3
			1	5	2

	M	L	α	p	N_h
			O		
			2	4	10
			2	4	16
			1	6	19
			1	6	5
				8	10
		Li		5	1
		B		3	1
		B	1	1	1
C			1		—
C				2	*L*
			4		—
			O		
N				1	5
			4		5
			2	4	5
			1	6	9
			1	6	7
			1	6	5
			1	6	5
				8	14
—	—	—	—	—	5
		Li	1	2	1
		Li	2	1	3
		Be	2		3
		Be	2		3
			3	2	3
			3	2	3
			2	4	1
			2	4	4

	M	L	α	p	N_h
			F		
		Li		6	9
O				1	5
			2	5	9
				9	17
		Li	3		4
		Be	1	3	—
		B	1	2	1
C			1	1	2
N				2	*L*
			F		
		Li		1	4	7
N				1		*H*
			2	5	6
—	—		1	7	*H*
		Li, Be	1		1
		B	2		1
N			1		1

	M	L	α	p	N_h
			Ne		
			3	4	20
			2	6	14
			2	6	5
—	—		—	—	13
		Li, Be	1	2	2
		Be	3		3
		B	2	1	0
			2	6	3

	H	M	L	α	p	N_h
			Na			
			Li	3	2	12
			Li	1	6	—
			Be	2	3	6
			Be		7	13
O					3	5
				3	5	12
				2	7	6
			2Li	2	1	—
			Be		7	0
			Be	2	3	4
				3	5	4
				3	5	1
			Na			
			Li	2	4	5
				5	1	5
				3	5	5
				3	5	7
				2	7	14
C				1	3	1
N				1	2	2
O				2		*L*
				1	2	2

	H	M	L	α	p	N_h
			Mg			
			Be		8	8
				5	2	15
			B		7	1
	O			1	2	1
			Al			
	N				6	5
			2Li	2	3	8
	C			3	1	5
				4	5	21
			Si			
	C			3	2	8
	Ne			1	2	11
			Be	3	4	4
Na				1	1	—
			Mg			
			2Li	3		3
			3Li		3	1
	N			1	3	1
	Ne			1		0
Mg						4
				5	2	1
				1	10	—
—	—	—	—	—	—	3
			Al			
			2Li	2	3	8
	C			3	1	5
				4	5	21
				5	3	3
			Si			
Na				1		*H*
				4	6	12
				1	12	10

	H	M	L	α	p	N_h
			P			
			Li, B	3	3	1
P						3
			S			
		Ne			1	4	5
			Cl			
			3Li	3	2	6
Na				1	4	4
			A			
Mg				1	4	—
Mg				1	4	—
			Mg			
			2Li	3		3
			3Li		3	1
				1	3	1
				1		0
						4
	F			1	5	9
				1	10	—
—	—	—	—	—	—	13
			2Li	3	4	4
			Al			
			2Li	2	3	8
Na				1	4	3
				5	7	4
			A			
Na				2	3	7
Na				3	1	*H*
				5	8	15
—	—	—	—	—	—	16

	H	M	L	α	p	N_h
			K			
Na				2	3	1
			Ca			
			2Li, Be	2	6	8
Mg				2	4	6
Ca						*H*
				5	10	23
				5	10	12
				3	14	20
				3	14	10
	C	Be		2	6	1
	N	Be		1	7	1
P				1	3	0
				8	4	4
			Sc			
	N	Li		3	5	7
			Fe			
Fe						10
			Ca			
				6	8	4
				4	12	4
			Ti			
Si	N			1		4
			Cr			
Mg				2	8	18
			Fe			
				4	18	10

and their products are divided according to the latitude of the flight. The primary nucleus is listed and under each primary nucleus is listed the resultant products and the number of star prongs (N_h). In some interactions charge balance was not obtained between the outgoing jet of fragments and the charge of the primary. These involve meson production and will be discussed later; for these cases the number of protons listed in Table I is that number required to give charge balance. Examples of different types of interactions are given in Figs. 1, 2, and 3. Events in which a (—) occurs are ones in which no information could be obtained on the interaction fragments, either because they were indistinguishable from star prongs or because the interaction was geometrically located so that it was impossible to study it in detail and determine the charge of the fragments.

Three separate classes of particles can be seen to result from interactions of heavy nuclei with target nuclei of the photographic emulsion.

(1) Fragmentation products, both singly and multiply charged, arising from the incident nucleus and collimated in the forward direction (the degree of collimation depending on the velocity of the incident primary).

(2) Light and gray shower tracks also emitted in the forward direction but less strongly collimated than the nuclear fragments of (1).

(3) Evaporation prongs and recoil nuclei generally of short range and roughly isotropic in distribution. These three classes of particles can be understood as follows. In an interaction of a fast nucleon with a target nucleus of the photographic emulsion, particles in the second and third classes are observed to be produced. The interaction of a heavy nucleus with a target nucleus of the emulsion can be considered as a superposition of

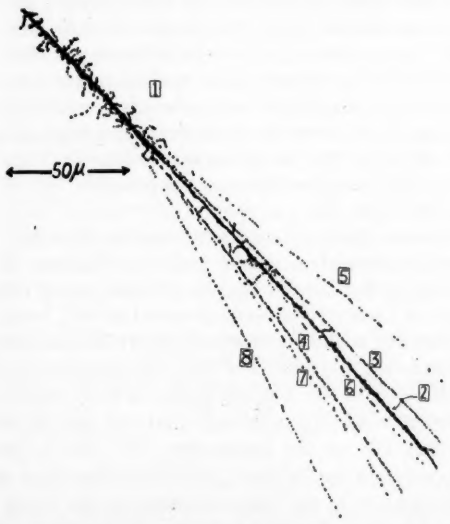

FIG. 2. An argon nucleus (1) interacts with a hydrogen nucleus of the emulsion giving a sodium nucleus (2), two α particles (3) and (4), and three protons (5), (6), and (7). The recoil proton track is track (8).

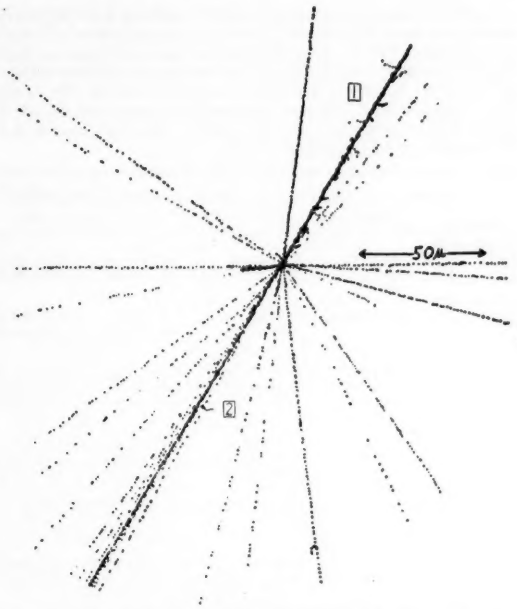

FIG. 3. A fluorine nucleus (1) interacts with a heavy nucleus of the emulsion (probably silver) and produces a lithium nucleus (2), and six protons. The target nucleus gives an evaporation star.

many nucleon-nucleon collisions resulting in the production of particles of the second and third classes. In addition, in the rest system of the incident nucleus, particles of the third class will be produced which will appear in the laboratory system as the jet of fast singly and multiply charged particles collimated in the direction of the incident primary; the relatively small opening angle of the jet is a reflection of the low emission velocity of these particles in the rest system of the incident nucleus.

The photographic emulsion consists of both heavy and light elements; the average atomic weight A of the heavy elements in the emulsion is ~ 84 and that of the light elements (excluding hydrogen) is ~ 14. The ratio of geometric cross-sections for the light and heavy elements indicates that $\sim \frac{1}{3}$ of all the interactions should occur with the light elements. If one distinguishes between light and heavy target nuclei on the basis of N_h, characterizing light target nuclei as $N_h \leqslant 4$ and heavy target nuclei as $N_h > 4$, we find that 0.82 ± 0.11 of all the events are characterized by $N_h \leqslant 4$. This characterization is the same for both medium and heavy incident nuclei. It would appear then that ~ 20 percent of the interactions with heavy target nuclei result in a small number of star prongs and thus simulate collisions with light target nuclei. It is most likely that interactions of this type are due to edge collisions with the heavy target nuclei. Events characterized by $N_h \leqslant 4$ will be referred to as L-type events and those with $N_h > 4$ as H-type events.

In Table II we list the fragmentation probabilities

TABLE II. Fragmentation probabilities derived from the heavy primary interactions studied. P_{IJ} = the average number of J type nuclei produced in the interaction of an incident I-type nucleus. Figures for the 41° and 55° flights are listed separately and divided according to the charge group of the primary nuclei. The heavy group represents $Z>10$ and the medium group $6\leqslant Z\leqslant 10$. H events are those in which $N_h>4$, L events those in which $N_h\leqslant 4$. The errors quoted are statistical only.

(a) *Medium group:* actual ratio of L/H events = 59/72 = 0.82 ± 0.11.

	P_{MM}	P_{ML}	$P_{M\alpha}$	P_{Mp}
H events				
41°	0.03 ± 0.03	0.22 ± 0.08	1.17 ± 0.19	3.75 ± 0.35
55°	0.07 ± 0.05	0.13 ± 0.07	1.0 ± 0.18	4.13 ± 0.38
L events				
41°	0.18 ± 0.08	0.54 ± 0.13	1.0 ± 0.2	1.78 ± 0.25
55°	—	0.52 ± 0.13	1.9 ± 0.26	1.69 ± 0.24
L+H events				
41°	0.09 ± 0.04	0.36 ± 0.07	1.09 ± 0.13	2.89 ± 0.19
55°	0.03 ± 0.02	0.32 ± 0.07	1.44 ± 0.16	2.94 ± 0.22
41°+55°	0.07 ± 0.02	0.34 ± 0.05	1.26 ± 0.1	2.91 ± 0.16
Hydrogen events				
41°	—	0.83 ± 0.37	1.16 ± 0.46	1.0 ± 0.41
55°	—	0.57 ± 0.28	1.71 ± 0.49	1.0 ± 0.37
41°+55°	—	0.69 ± 0.23	1.46 ± 0.33	1.0 ± 0.29

(b) *Heavy group:* actual ratio of L/H events = 40/49 = 0.82 ± 0.12.

	P_{HH}	P_{HM}	P_{HL}	$P_{H\alpha}$	P_{Hp}
H events					
41°	0.15 ± 0.08	0.23 ± 0.09	0.5 ± 0.14	2.04 ± 0.28	5.2 ± 0.4
55°	0.19 ± 0.1	0.14 ± 0.08	0.19 ± 0.1	2.8 ± 0.37	5.58 ± 0.5
L events					
41°	0.3 ± 0.12	0.2 ± 0.1	0.55 ± 0.17	1.8 ± 0.3	3.95 ± 0.44
55°	0.26 ± 0.18	0.37 ± 0.14	0.37 ± 0.14	2.05 ± 0.34	3.05 ± 0.4
L+H events					
41°	0.22 ± 0.05	0.22 ± 0.05	0.52 ± 0.1	1.93 ± 0.21	4.65 ± 0.31
55°	0.23 ± 0.08	0.25 ± 0.08	0.28 ± 0.08	2.45 ± 0.25	4.37 ± 0.33
41°+55°	0.22 ± 0.05	0.24 ± 0.05	0.41 ± 0.07	2.18 ± 0.15	4.52 ± 0.2
Hydrogen events					
41°	0.2 ± 0.2	0.4 ± 0.28	0.8 ± 0.4	1.8 ± 0.6	5.0 ± 1.0
55°	—	1.0 ± 0.71	—	1.0 ± 0.71	3.0 ± 1.2
41°+55°	0.14 ± 0.14	0.57 ± 0.28	0.57 ± 0.28	1.57 ± 0.48	4.4 ± 0.8

obtained for the interaction of medium and heavy nuclei in emulsion. These probabilities represent the average number of particles of a given type produced per event. The probabilities are given for incident medium and heavy nuclei at the two different latitudes for events classified as L- or H-type events according to the value of N_h, for events classified as interactions with hydrogen nuclei of the emulsion and for all events irrespective of classification.

A consistency check on the fragmentation probabilities can be obtained by evaluating $\bar{Z}_G=\sum_I P_{GI}Z_I$, where Z_I = the charge of the Ith type fragment, P_{GI} = the average number of these type fragments produced in interactions of G-type nuclei (either the medium or heavy group) and $\bar{Z}_G$ = an average charge for the group G of heavy nuclei whose interactions are being studied. Evaluation of this sum for $\bar{Z}_M$ and $\bar{Z}_H$ for L, H, and all events independently as a function of latitude gives $\bar{Z}_M=7.3\pm0.3$ and $\bar{Z}_H=15.4\pm0.4$, where the errors encompass the total range of values obtained. In computing these values the *a priori* average Z for the light, medium and heavy nuclei were taken as 4, 7, and 15. These choices were derived from the relative abundances of the different nuclei in each charge group weighted by their interaction cross section. The equality of the *a priori* $\bar{Z}$ for a charge group and the calculated $\bar{Z}$ for that group constitutes the desired consistency check.

The general features exhibited by Tables I and II can be understood qualitatively on the basis of the evaporation model (applied in the rest system of the incident nucleus). The most striking feature is the fact that the fragmentation probabilities, P_{ML} and P_{HL} giving the average number of light nuclei produced per interaction of incident medium and heavy nuclei are distinctly larger for L-type events than for H-type events and are quite high (>0.5) for the hydrogen events. This characteristic strongly suggests that the lighter the target nucleus, the higher the probability of obtaining a light nucleus as a fragmentation product of the incident heavy nucleus.

Gottstein[6] has found some correlation between the charge of fragments and their primaries, *viz.*, that an even-charge primary nucleus tends to give more even- than odd-charge fragments: this correlation was found only for L-type events and for energies >1 Bev/nucleon. No sign of any such correlation has been found in the interactions studied from all three flights or from L-type events in the stacks flown at 41° geomagnetic latitude.

A total of twenty events were observed which were classified as events occurring with a hydrogen nucleus of the emulsion (see Figs. 1 and 2): these are characterized by an interaction in which the incident heavy nucleus is fragmented and one singly charged track (proton) is observed at an angle appreciably wider than that containing the jet of fast breakup fragments: this track is assumed to be the recoil proton. The relative number of these events found (0.09) is in agreement with the number expected on the basis of geometric cross sections ($\sim$0.1). In addition to these cases, three other cases have been observed in which the heavy primary nucleus breaks up with no sign of star prongs or visible recoil of a target nucleus and in which charge balance is obtained between the incoming nucleus and its products: three other events of a similar nature have been observed but because of the geometry of the event it is impossible to state definitely that there are no recoil tracks. These six events (the questionable ones are preceded by a ?) are listed in Table III.

Four events have also been observed in which the target nucleus gives a star while the incident heavy nucleus appears to continue on with no loss of charge. Three of these events were observed at 41°, involving incident P, Ca, and Fe nuclei and one at 55° involving an incident Mg nucleus. For the two heavier incident nuclei, Ca and Fe, it is impossible to δ-ray count with sufficient reliability to be sure that one unit of charge was not lost in the interaction, i.e., that a proton stripped from the incident nucleus was the cause of the disintegration of the target nucleus. In the other two cases, however, there is definitely no loss of charge of the incident nucleus in the interaction.

[6] K. Gottstein, Phil. Mag. 45, 347 (1954).

It seems to us that the two types of events mentioned in the preceding paragraphs i.e., fragmentation without visible recoil, and star production with no loss of charge of the primary, really represent the same physical mechanism, since one can be obtained from the other by a Lorentz transformation. There appear to be two possible explanations for this class of event. The first, and less likely, is to attribute these interactions to Coulomb effects. To estimate this we have considered the decomposition of the Coulomb field into its representative virtual quanta and estimate for our experimental conditions (latitude, flight altitude, charges of nuclei involved, and energy spectrum) the effective mean free path for observing interactions of this type is such that it is very unlikely that more than one of these events could be attributed to this mechanism. The second and more likely assumption is to consider these interactions as initiated by an extended neutron of either the target or incident nucleus. No observable effects in either case would be expected since for those reactions involving interactions with incident nuclei in which no loss of charge occurs, the incident nucleus has long-lived neutron-deficient isotopes (with the exception of Fe) whereas for the other cases (fragmentation with no star prongs) most of the target nuclei of the emulsion have neutron-deficient isotopes that decay by γ emission or by β^+ emission (which could easily be not detected). We believe the latter explanation (extended nuclear structure) represents these events: a situation of this sort is not unexpected in light of recent experiments exploring the nuclear charge distribution.[7]

MESON PRODUCTION

An estimate can be made of the number of fast mesons produced in an interaction where there are collimated light and gray shower tracks in the forward direction. The number of protons among the shower particles is assumed to equal the difference in charge between that of the incident nucleus and the sum of charges in the jet of multiply charged fragments: the remaining light shower tracks are considered to be mesons so that this serves as an upper limit to the number of fast mesons produced (some may be protons from the target nucleus).

In Table IV we list the relative number of events in which meson production occurs and the number of mesons per event. Interactions for the 41° and 55° flights are listed separately and division made according to the charge group of the incident nucleus: L- and H-type events are listed separately. We have estimated the meson production cross section from the data given here on the basis of a geometrical model. We consider each interaction between nuclei to have occurred with the appropriate median impact parameter[8] and assume on the basis of uniform nuclear density that all the nucleons in this region contribute to meson production. We thus estimate a lower limit to the meson production cross section, σ (nucleon-nucleon). The observed cross sections (experimentally averaged over the incident energy spectrum) are ~6.3 millibarns (nucleon-nucleon) at 55° and 19 millibarns (nucleon-nucleon) at 41°, the median energies for these two flights corresponding to 1.1 and 3.3 Bev/nucleon. These figures can be compared with the nucleon-nucleon total cross section observed at Brookhaven National Laboratory[9]: they find a total p-p cross section at 830 Mev of ~49 millibarns, and evidence that the cross section thereafter is approximately constant with energy. For the n-p cross section at ~2 Bev, they find 40 millibarns. At these energies ~$\frac{1}{4}$ of the total cross section is elastic so that the nucleon-nucleon cross section for meson production is ~30 millibarns. Since our estimated cross-sections are lower limits to the nucleon-nucleon cross section, they are not inconsistent with the Brookhaven results.

TABLE III. Fragmentations observed in which no star prongs or recoil nuclei are seen.

C→ 3α
C→ $2\alpha+2p$
N→ B+ α
(?)*Ne→ B+2α+ p
(?)Na→Be +$7p$
(?)Mg→Ne+1α

* Events in which it is impossible to state definitely that there are no recoil tracks are marked (?).

TABLE IV. Relative number of events in which fast mesons are produced and the number of fast mesons per meson-producing event. The data are divided according to the charge group of the incident nuclei and interactions are classified as L events ($N_h \leqslant 4$) and H events ($N_h > 4$).

		Events producing fast mesons	Fast mesons per event
Medium group:			
L events	41°	7/22	5.8 ±0.8
	55°	1/28	2.0 ±1.4
H events	41°	25/37	5.2 ±0.4
	55°	7/28	4.2 ±0.7
Heavy group:			
L events	41°	4/19	8.7 ±1.4
	55°	2/18	5.5 ±1.7
H events	41°	14/23	6.85±0.69
	55°	5/20	3.8 ±0.9

INTERACTION MEAN FREE PATHS

All interactions of heavy nuclei found during the systematic tracing of heavy nuclei were used to measure the interaction mean free path of these particles in emulsion. The observational data and results for the medium and heavy charge groups at the two different

[7] G. Bernardini and E. L. Goldwasser, Phys. Rev. 94, 729 (1954).

[8] See section on "Extrapolation to Atmosphere."

[9] Shapiro, Leavitt, and Chen, Phys. Rev. 95, 663 (1954); Hill, Coor, Hornyak, Smith, and Snow, Phys. Rev. 94, 791 (1954).

TABLE V. Interaction mean free paths observed in emulsion for incident medium ($6 \leqslant Z \leqslant 10$) nuclei and heavy ($Z > 10$) nuclei at 41° and 55° geomagnetic latitude.

41°	
	$\lambda_M = 3559/60 = 59.4 \pm 7.8$ g/cm²
	$\lambda_H = 1270/37 = 34.7 \pm 5.6$ g/cm²
55°	
	$\lambda_M = 2229/37 = 60.4 \pm 10.3$ g/cm²
	$\lambda_H = 876/22 = 45.5 \pm 10$ g/cm²
41°+55°	
	$\lambda_M = 59.6 \pm 6$ g/cm²
	$\lambda_H = 36.5 \pm 4.8$ g/cm²

latitudes of observation are given in Table V.[10] The flux of particles at 55° with energies between 0.31 (cutoff) and 1.5 Bev/nucleon is ~4 times the flux of particles with energies >1.5 Bev/nucleon (cutoff at 41°) so that by comparlng the interaction mean free paths at 55° and 41° one can gain some information on the energy dependence of the mean free path, λ. From the experimental results λ seems substantially independent of energy, for energies at least as high as ~6 Bev/nucleon (30 percent of the nuclei at 41° have $\epsilon > 6$ Bev).

The mean free path can be written as $\lambda = 1/(\sum_i n_i \sigma_i)$, where n_i = the number of atoms/cc of the different emulsion target nuclei and σ_i = the interaction cross section for the ith type nuclei in the emulsion. If one calculates the mean free path λ by using the known emulsion composition and the cross section given by $\sigma_i = \pi(R_i + R_{\text{inc}})^2$, where $R = r_0 A^{\frac{1}{3}}$, ($r_0 = 1.45 \times 10^{-13}$ cm) it is found that the values obtained for λ are much shorter than those observed, or in other words, the observed cross section is smaller than that predicted by a purely geometrical model. The indication is therefore that either nuclei are somewhat transparent, or that the measure of the nuclear radius (r_0) given above is too large.

The experimental data can be fitted in three ways: (1) by using a smaller value for r_0; (2) by requiring some overlap of the nuclear volumes to occur before an interaction can take place[11]; (3) by considering the transparency of nuclear matter. The first two methods will be discussed below. Method (3) has been considered in detail by Eisenberg[12] in a recent paper.

An average Z has to be chosen for both the medium and heavy charge groups of the incoming heavy nuclei. For the medium charge group an average Z, $\bar{Z} = 7$ and for the heavy group $\bar{Z} = 15$, have been obtained by considering the 214 interactions where the primary charges have been established and weighting the relative numbers of incident nuclei by their respective interaction cross-sections. This gives the true relative fluxes of the individual nuclei and allows one to estimate an average charge to represent the medium and heavy groups which were sampled to obtain the interaction mean free paths. If one now tries to fit the experimental data for the interaction mean free path by varying r_0 it is found that a value of $\sim 1.0 \times 10^{-13}$ must be chosen for the medium group and a value of $\sim 1.1 \times 10^{-13}$ for the heavy group. The value of r_0 depends on the value of $\bar{Z}$ chosen but is not sensitive to a change of one in $\bar{Z}$.

The second procedure requires that some overlap (ΔR) of the nuclear radii occur before an interaction takes place, so that the available cross section is reduced. The value of $\Delta R = 0.85 \times 10^{-13}$ cm found by Bradt and Peters[11] for interactions in glass will give good agreement with the observed data for interactions in emulsion. The interaction cross section for the i-th emulsion constituent is given by $\sigma_i = \pi(R_i + R_{\text{inc}} - 2\Delta R)^2$, where the symbols have the same meaning as before, and the same value of r_0 is used. We find $\lambda_M = 56.5$ g/cm² and $\lambda_H = 36.5$ g/cm² to be compared with the experimental values of 59.6 and 36.5, respectively.[13]

This procedure seems preferable since method (1) would predict a nuclear density varying with mass number. We have adopted this procedure [method (2)] to extrapolate our results to atmosphere.

EXTRAPOLATION TO ATMOSPHERE

The interaction mean free paths for the medium and heavy groups were extrapolated to atmosphere by using method (2) and the value of ΔR adopted in the above paragraph. We obtain $\lambda_L = 31.5$ g/cm², $\lambda_M = 26.5$ g/cm² and $\lambda_H = 18.0$ g/cm². These figures are in agreement with those inferred from the measurements in glass by Bradt and Peters.[14] The values measured in glass are not interaction mean free paths but most probably represent a value lying between that of an interaction and an absorption mean free path since interactions occurring in glass involving a loss of one or two units of charge may easily be missed. The value deduced for λ_H in atmosphere is in agreement with the measurement of Freier *et al.*[13] at 30° geomagnetic latitude from observations on the angular distribution. They find a value in air of $\lambda_H = 21 \pm 2$ g/cm²: this is an attenuation mean free path and should therefore be of the order of $\lambda_H/(1 - P_{HH}) = 24$ g/cm².

The various fragmentation probabilities found in emulsion can also be extrapolated to corresponding figures for atmosphere. The experimental data for hydrogen and L-type events show increased fragmentation into light elements and a decrease in the number of protons per interaction. It seems reasonable that in a glancing collision the incoming nucleus will not receive as much excitation as in a more direct collision with a target nucleus. In the latter type of collision one would expect rather complete disintegration, while in a glancing collision there seems a greater probability for

[10] The interaction mean free path for L nuclei (λ_L) was found to be 61.7 ± 19.4 g/cm²; this value was obtained from interactions of L nuclei in a study of a limited number of long tracks in part B of the SM stack.

[11] H. L. Bradt and B. Peters, Phys. Rev. **77**, 54 (1950).

[12] Y. Eisenberg, Phys. Rev. **96**, 1378 (1954).

[13] Freier, Anderson, Naugle, and Ney, Phys. Rev. **84**, 322 (1951).

[14] H. L. Bradt and B. Peters, Phys. Rev. **80**, 943 (1950).

the occurrence of heavier fragments since there will not be as much chance of energy being distributed among the constituent nucleons. This suggests that it is the amount of overlap of the nuclear radii which determines the fragmentation probability in an interaction; the more complete the overlap, the more complete the disintegration of the incoming nucleus.

For collisions between two nuclei, the impact parameter x will have possible values between 0 and D, where D= the maximum distance between the centers of the two nuclei at which an interaction can take place: $D=R_1+R_2-2\Delta R$. Since all collisions are assumed to occur with impact parameters lying between these limits, the probability of an interaction occurring $P=K\int_0^D xdx=1$, where K is the normalization constant. The probability of an interaction with an impact parameter between D and $D-d$ is given by $P_d=K\int_{D-d}^{D} xdx=[D^2-(D-d)^2]/D^2$ (see Fig. 4). For smaller target nuclei, i.e., smaller D, the proportion of collisions with impact parameters between D and $D-d$ increases. For a fixed incoming nucleus (as example we consider an incident heavy nucleus) it is reasonable to assume that collisions with impact parameters between D and $D-d_H$ yield heavy fragments, between $D-d_H$ and $D-d_M$ medium fragments, between $D-d_M$ and $D-d_L$ light fragments, and for smaller impact parameters (greater overlap) mainly α particles and protons occur.

For smaller target nuclei the proportion of interactions which yield heavy, medium, and light fragments will thus be increased and the number which give α particles and protons decreased. And, as suggested by the interactions in emulsion with light elements, and the glancing collision with heavy elements, the number of protons is reduced most.

The expression for a mixture of target nuclei will be

$$P_d=(\sum_i n_iD_i^2-\sum_i n_i(D_i-d)^2)/\sum_i n_iD_i^2,$$

where all symbols have been defined previously in the text. The overlap parameters d_H, d_M, d_L can be determined to fit the observed probabilities P_{HH}, P_{HM}, and P_{HL} (here we specify an incident heavy nucleus) in emulsion: these are then used with the known composition of air to determine the fragmentation probabilities for that medium. The results obtained for atmosphere for both incident medium and heavy nuclei are given in Table VI. The values for the α particle and proton fragmentation probabilities are derived by requiring that $\bar{Z}_I=\sum_{I'} P_{II'}Z_{I'}$ and that $P_{I\alpha}/P_{Ip}$ have the same value as for the L-type events observed in emulsion.

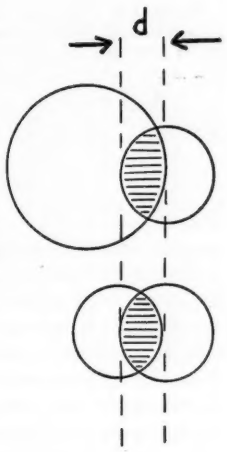

FIG. 4. This figure illustrates collisions between an incident heavy nucleus and target nuclei of different size. Though the overlap d is the same in both cases, for smaller target nuclei proportionately more of the effective cross section is utilized than for larger target nuclei.

TABLE VI. Fragmentation probabilities derived for incident medium- and heavy-nuclei interactions in air. The corresponding fragmentation probabilities observed in emulsions for L type events (averaged for 41° and 55° geomagnetic latitude are listed for comparison).

	Air (derived)	Emulsion (L events)		Air (derived)	Emulsion (L events)
P_{HH}	0.25	0.28			
P_{HM}	0.27	0.24	P_{MM}	0.13	0.18
P_{HL}	0.48	0.45	P_{ML}	0.42	0.53
$P_{H\alpha}$	2.07	1.9	$P_{M\alpha}$	1.42	1.40
P_{Hp}	4.29	3.45	P_{Mp}	1.70	1.73

An experimental check on the fragmentation probabilities listed for atmosphere in Table VI was obtained by studying the fragmentation products emitted in the interactions of heavy primary nuclei with the target nuclei of cellulose acetate and gelatin (each of these consists of only light elements, C, N, O, and H). The sandwich emulsion and absorber stacks only allow one to examine the fast fragments carrying on in the direction of the incident prlmary, not the interaction itself. Since the absorber sheets are approximately equal in thickness to the emulsions used, the geometry is good and it is not likely that fragments at wide angles (see Fig. 2) will be missed (work done with emulsions mounted on glass suffers from the disadvantage that wide-angle fragments could be easily missed in scanning the next emulsion). Since the density of the plastic is low, only a limited number of interactions were found and statistics are not sufficient to give very definite results. We have combined our results for the fragmentation probabilities observed at both latitudes in Table VII. It is seen that these are, within statistics, in agreement with the fragmentation probabilities derived for atmosphere (approximately equivalent in composition with respect to light elements) on the basis of the overlap model. In addition, we note that the fragmentation probabilities derived for air are in agreement with those observed for L-type events in emulsion. In the following discussion we shall use the probabilities and mean free paths in atmosphere calculated on the basis of the overlap model.

SECONDARY FLUX OF HEAVY NUCLEI

Observations made on the flux of heavy nuclei at flight altitude under a finite amount of residual atmosphere must be extrapolated to the top of the atmosphere to obtain true primary flux values. In general corrections

TABLE VII. Observed fragmentation probabilities for interactions in light element absorbers of incident medium and heavy nuclei (the data for both latitudes are combined).

$P_{MM}=0.06\pm0.06$	$P_{HH}=0.16\pm0.16$
$P_{ML}=0.35\pm0.14$	$P_{HM}=0$
$P_{M\alpha}=1.59\pm0.39$	$P_{HL}=0.83\pm0.37$
$P_{Mp}=2.7\ \pm0.66$	$P_{H\alpha}=1.66\pm0.55$
	$P_{Hp}=5.5\ \pm2.2$

must be made for loss by ionization and interaction, and for the proportion of the observed flux which is secondary in origin. The most appropriate way to correct for these effects is to consider the diffusion of the heavy nuclei component in the atmosphere. We assume parallel beams of nuclei travelling through the atmosphere and neglect ionization loss: in addition in interactions of heavy nuclei we assume the fragmentation products maintain the same direction and the same energy per nucleon as the primary. The diffusion equations are:

$$dN_I(x)/dx=-N_I(x)/\lambda_I+\sum_{I'\geqslant I}N_{I'}(x)P_{I'I}/\lambda_{I'},$$
$$I, I'=L, M, H,$$

where $N_I(x)$ is the flux of I-type nuclei after passing through x g/cm² of material, $P_{I'I}$ is the probability (assumed energy-independent) in an interaction of an I' nucleus that an I nucleus will be produced, λ_I is the interaction mean free path of an I-type nucleus, also assumed energy-independent, and $x=h/\cos\theta$, where h is the amount of residual atmosphere in the vertical direction and θ is the zenith angle. These equations are subject to the boundary condition $N_I(0)=N_I{}^0=$ incident primary flux value for I-type nuclei at the top of the atmosphere. The solutions may be written in the following form:

$$N_H(x)=N_H{}^0\exp(-x/\lambda_H'),$$

$$N_M(x)=N_M{}^0\exp(-x/\lambda_M')+(\alpha_{HM}P_{HM}/\lambda_H)\times[N_H{}^0\exp(-x/\lambda_M')-N_H(x)],$$

$$N_L(x)=N_L{}^0\exp(-x/\lambda_L')+(\alpha_{ML}P_{ML}/\lambda_M)\times[N_M{}^0\exp(-x/\lambda_L')-N_M(x)]+(\alpha_{HL}/\lambda_H)(P_{HL}+P_{HM}P_{ML}\alpha_{ML}/\lambda_M)\times[N_H{}^0\exp(-x/\lambda_L')-N_H(x)]'$$

where

$$\alpha_{IJ}=\lambda_I'\lambda_J'/(\lambda_J'-\lambda_I')>0,\quad \lambda_J'>\lambda_I',$$

and

$$\lambda_I'=\lambda_I/(1-P_{II}).$$

In these equations the first term on the right hand side represents the absorption of a given charge group with the absorption mean free path λ' while the additional terms represent contributions to that charge group by interactions of nuclei of higher charge. The attenuation mean free path, which would be the mean free path measured in atmosphere by observations of flux values as a function of depth would be depth dependent and is properly defined by $-dN_I(x)/dx=N_I(x)/\lambda_I{}^{\text{Att}}$.

It is in general difficult to make a calculation which can be applied to all observational cases, since in general the zenith angles accepted and the geometrical acceptance factor depend on the particular experiment. We have thus calculated the observed fluxes (for parallel incident beams) at various depths in the atmosphere assuming different values for the relative incident fluxes. Since the medium element flux is the highest, the light and heavy fluxes are expressed in terms of it. In Fig. 5 we have plotted two different sets of curves relating the light and medium element fluxes. The lower family of curves gives the ratio of secondary light element flux to medium flux $[N_L{}^{\text{sec}}(x)/N_M(x)]$ at a depth x for different values of the fragmentation probabilities and of the ratio of incident medium and heavy fluxes: Curves I and II are calculated with $P_{ML}=0.42$ and $P_{HL}=0.48$ and values of $R_{HM}=N_H{}^0/N_M{}^0$ of 0.5 and 0.33, respectively, while Curve III is calculated with $P_{ML}=P_{HL}=0.23$ (the value used by Bradt and Peters,[14] and

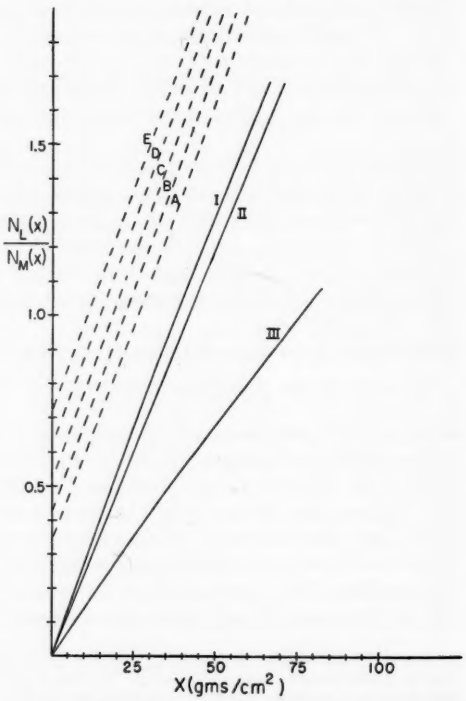

FIG. 5. Curves I, II, III represent the relative secondary light element flux $N_L'(x)/N_M(x)$ *versus* path length in the atmosphere; the following parameters were used.

I:	$P_{ML}=0.42$,	$P_{HL}=0.48$, $R_{HM}=0.5$.
II:	$P_{ML}=0.42$,	$P_{HL}=0.48$, $R_{HM}=0.33$.
III:	$P_{ML}=0.23=P_{HL}$,	$R_{HM}=0.5$.

Curves A, B, C, D, E represent for assumed incident ratios of light to medium elements ($N_L{}^0/N_M{}^0=0.3$ for A in increments of 0.1 up to 0.7 for E) the relative observed light-element flux $N_L(x)/N_M(x)$ *versus* path length in the atmosphere, if one uses the parameters of Curve I.

Dainton *et al.*[2]) and $R_{HM}=0.5$. The upper curves, *A* to *E*, represent the observed ratio of light-element flux to medium-element flux at a depth x if one uses the parameters of Curve I and assumes a ratio of light to medium incident flux, $R_{LM}=N_L^0/N_M^0$, of 0.3, 0.4, 0.5, 0.6, 0.7, respectively for the curves *A* to *E*. Thus from an observed ratio of light to medium flux at a given depth, the ratio at the top of the atmosphere can be read off directly from curves *A* to *E*. These results are not sensitive to variations of ~10 percent in the mean free paths.

The attenuation length for the medium-element group varies from 38 g/cm² at the top of the atmosphere to 30.4 g/cm² at infinite depth. Because of our choice of only three charge groups, the attenuation length for the heavy nuclei is equal to the absorption length (24 g/cm²), which is in agreement with Minnesota results.[13]

RELATIVE ABUNDANCES

The observed number of interactions of the individual charged nuclei within each charge group weighted by their individual interaction cross sections allows one to make an estimate of the ratio of the heavy and medium charge groups observed at a given depth and represents a lower limit to that ratio at the top of the atmosphere since the heavy group is attenuated more strongly than the medium. The figure deduced from the 214 interactions observed[15] is $R_{HM}=0.5$. This figure is in agreement with that of Gottstein[6] who obtained $R_{HM}\sim0.6$ from a study of the interactions of heavy nuclei. From the results of different laboratories[1,11,13,16] of the direct measurement of the heavy-element flux, R_{HM} could lie between 0.33 and 0.5. Application of this same method also allows one to obtain some idea of the abundance of different elements within a given charge group. In an estimation of this type, as well as that made above, some distortion is introduced at high latitudes because of ionization loss in the residual atmosphere. From our results we can make the following qualitative statements. The abundance of nitrogen is greater than that of oxygen while the carbon and nitrogen abundances seem of comparable magnitude. There is no indication that, for particles with Z between 8 and 14 inclusive, nuclei of even charge are 3 times as numerous as those of odd charge as suggested by the Bristol results.[2] For 104 interactions involving incident nuclei in this charge group, the ratio of odd/even nuclei is found to be ~1.0.

[15] We estimate that the loss of carbon nuclei in the *C* stack due to the high δ-ray acceptance criterion, will affect our relative abundances by <10%.

[16] Kaplon, Noon, and Racette, Phys. Rev. 96, 1408 (1954).

CONCLUSIONS

The interaction mean free paths in emulsion have been measured for the medium and heavy charged nuclei at geomagnetic latitudes 41° and 55°. It has been found that the mean free paths are independent of the latitude of measurement and therefore of energy, for energies up to ~6 Bev/nucleon. The cross sections implied by the observed mean free paths in emulsion are smaller than geometric. The data have been fitted by using a simple geometrical model requiring an overlap of the incident and target nuclei before an interaction occurs.

The interactions observed in emulsion show a high probability for the production of light elements in the interactions of medium and heavy nuclei, the probability being greatest for smaller target nuclei. The results observed in emulsion have been extrapolated to atmosphere and fragmentation probabilities derived for incident medium and heavy nuclei. These probabilities are in agreement with experimental observations on interactions occurring in an absorber consisting mainly of C, N, O, and H and with *L*-type events in emulsion. Curves are presented showing the contribution of interactions in the residual atmosphere to the flux of light nuclei as a function of depth.

Information has been obtained about the relative abundances of the heavy primary nuclei. C and N are observed to be of comparable magnitude, while O is less than either of these. The ratio of heavy to medium nuclei at the top of the atmosphere is estimated to be ~0.5. No evidence is obtained for a predominance of nuclei of even charge.

We wish to thank the Aero Medical Field Laboratory of Holloman Air Force Base and the Office of Naval Research for their assistance in obtaining the balloon flights for this experiment. We are indebted to Miss Barbara Hull and Mrs. R. Wargotz for their assistance in scanning and to Miss Phyllis Hull for her assistance both in scanning and with some of the calculations.

Tritium and Neutron Production by 2.2-Bev Protons on Nitrogen and Oxygen*

E. L. FIREMAN† AND F. S. ROWLAND‡
Brookhaven National Laboratory, Upton, New York
(Received October 26, 1954)

The cross sections for tritium production by 2.2-Bev protons on nitrogen and oxygen are measured to be 28±4 and 33±4 mb, respectively. The cross sections for neutron production by 2.2-Bev protons are measured to be 1000±400 mb for nitrogen and 650±250 mb for oxygen. These results indicate that cosmic-ray primaries produce approximately 0.05 tritons/cm² sec and 1–2 neutrons/cm² sec in the first nuclear interaction with the atmosphere.

I. INTRODUCTION AND SUMMARY

NEUTRONS and light elements are produced in the high-energy nuclear interactions of protons on oxygen and nitrogen. The yields of these reactions are of interest both for the study of high-energy reactions and because of their occurrence in the interactions of cosmic radiation with the atmosphere and with meteorites. The cross sections for the (p,T) reactions on nitrogen and oxygen with 2.2-Bev protons accelerated in the Brookhaven cosmotron have been measured to be 28±4 and 33±4 mb, respectively. The cross sections are approximately 10 percent of the geometric cross sections for these elements, indicating triton emission to be a common event in high-energy interactions.

The neutron production cross sections have been measured to be 1000±400 mb for nitrogen and 650±250 mb for oxygen corresponding to about 3 and 2 neutrons per interaction, respectively. The neutron yields are obtained from measurements in the vicinity of 90° to the incident beam and therefore are largely evaporation neutrons.

The primary cosmic radiation is composed of protons and heavier nuclei in proportions varying with latitude, with energies of several Bev/nucleon.[1] The number of primary nucleons[2] is estimated as 0.6/cm² sec over the earth's surface. With the approximation that the tritium production cross section is the same for each primary nucleon, the number of tritons produced in the first interaction with the atmosphere is 0.05/cm² sec.

Additional tritium will be produced by high energy secondaries and by evaporation neutrons. The tritium produced by high-energy secondaries is estimated to be about 0.05/cm² sec on the basis of the attenuation of tritium with depth in area targets and from the attenuation of star-production[3] in the atmosphere. The natural tritium production by evaporation neutrons in the atmosphere has been estimated to be about 0.1/cm² sec.[4] This totals approximately 0.2/cm² sec and may be compared with the value of (0.12±0.04)/cm² sec obtained from the tritium content of natural waters.[5]

II. EXPERIMENTAL DISCUSSION

A. Targets

The target materials for oxygen and nitrogen were water (actually 0.1N HNO_3 for passivity with aluminum) and liquid ammonia. These were contained in aluminum cylinders 4.4 cm in diameter, 6.3 and 10.1 cm in length, and 0.12 cm wall thickness; and were irradiated in the internal beam of the cosmotron. Three cylinders in series (total length 22.7 cm) were used with the water; two (total length 16.4 cm) with the liquid ammonia.

B. Tritium Assay

The water cylinders were opened in an atmosphere of carrier hydrogen, which was then pumped off in such a manner that the hydrogen bubbled through the water. This hydrogen was then purified through a palladium thimble, and counted in a 2.4-liter counter previously described.[4] The counting was done in a low-level counting facility[6] which reduced the background to 30 counts/min. Table I gives the tritium results for this hydrogen. About 10 percent of the tritium produced in the water cylinders was in the molecular hydrogen.

The water from the cylinders was distilled and converted to hydrogen over magnesium at 600°C. The tritium activity was then determined by visual counting of the characteristic tritium tracks in a hydrogen-filled diffusion chamber, as previously described.[7] Table I also gives the results for the tritium produced as water.

The aluminum containers were equipped with pressure fittings and filled with liquid ammonia for the NH_3 run. The irradiated ammonia was expanded directly into the Mg furnace at 600°C where it was converted to Mg_3N_2 and H_2. The exit gas passed

* Work carried out under contract with the U. S. Atomic Energy Commission.
† Physics Department.
‡ Chemistry Department. Permanent address, Department of Chemistry, Princeton University.
[1] *Progress in Cosmic-Ray Physics*, edited J. G. Wilson (North Holland Publishing Company, Amsterdam, 1952).
[2] From the data of Winkler, Stix, Dwight, and Sabin, Phys. Rev. **79**, 656 (1950).
[3] B. Rossi, Revs. Modern Phys. **91**, 922 (1953).
[4] E. L. Fireman, Phys. Rev. **91**, 922 (1953).
[5] S. Kaufman and W. F. Libby, Phys. Rev. **93**, 1337 (1954).
[6] The authors wish to thank Dr. Raymond Davis for the use of his low-level counting facility.
[7] E. L. Fireman and D. Schwarzer, Phys. Rev. **94**, 386 (1954).

TABLE I. Summary of experimental data.

Target cylinder	Analyzed sample	Measured by[a]	Counts/min	$(T/H)\times10^{15}$	$\times(10^{-10})$ Number of tritons	$\times(10^{-13})$ Proton through target	Tritium cross section σ(mb)	Total target contents	Neutrons from contents	Neutron cross section σ(mb)
Front H_2O	330 cc H_2	G.C.	...	158±15	0.28	4.9	31			
75gH_2O	14 g H_2O	D.C.	19.5±0.9	5.6±0.3	2.8					
Middle H_2O	270 cc H_2	G.C.	...	287±15	0.42	4.1	35	250 g H_2O	(1.6±0.6)×10^{12}	650±250
100 g H_2O	14 g H_2O	D.C.	17.9±0.8	5.2±0.2	3.5					
Rear H_2O	310 cc H_2	G.C.	...	138±15	0.23	3.3	32			
75 g H_2O	14 g H_2O	D.C.	13.8±0.7	3.9±0.2	2.0					
Front NH_3	9.0 g NH_3	D.C.	16.8±0.8	4.8±0.2	4.1	6.4	29			
82 g NH_3								133 g NH_3	(2.1±0.8)×10^{12}	1000±400
Rear NH_3	9.0 g NH_3	D.C.	13.3±0.7	3.8±0.2	2.6	5.6	27			
51 g NH_3										
Calibration H_2O	14 g H_2O	D.C.	17.5±0.8	5.0						

[a] G.C. = Geiger Counter; D.C. = Diffusion Chamber.

through a water column and cold trap before going into the diffusion chamber where it was counted. The chemical conversion was shown to be more than 99 percent complete by titrating the water column and by passing a sample of the chamber gas through palladium. The tritium activity is given in Table I.

C. Neutron Detection

The neutrons from the target were detected and measured by the activation of a series of indium foils imbedded in a cadmium-covered paraffin block. The In^{116m} yield as a function of paraffin depth is a measure of the neutron intensity and average energy. The paraffin was 12 in.×12 in.×18 in. with a 12 in.×12 in. side facing the target. The detector was 90° to the beam direction for the water run, and at 60°, 90°, and 120° for the ammonia run. The detector arrangements were calibrated by standard Ra-Be sources at the cosmotron positions and in a large empty room.

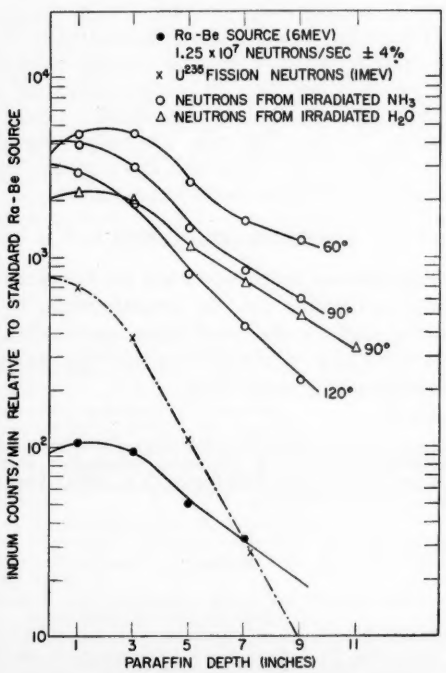

FIG. 1. Indium activation in Cd-covered paraffin.

Figure 1 gives the In activation results for the water, ammonia, a Ra-Be calibration source, and a U^{235} fission neutron calibration source. The In activity falls much more rapidly with depth for the U^{235} neutrons (1 Mev) than for the Ra-Be neutrons (6 Mev). The neutrons at 90° both for the water and ammonia are similar to the Ra-Be neutrons. The neutrons at 60° to the beam direction are of slightly higher average energy and the neutrons at 120° are of slightly lower energy than the Ra-Be neutrons. The NH_3 curves show the neutrons favor the forward direction. The angular distribution is consistent with neutrons being isotropic in a reference frame moving with a velocity of about $\frac{1}{3}$ that of the emitted neutrons.

The detected neutrons are produced not only in the water and liquid ammonia but also in the aluminum containers and by secondary reactions in material in the vicinity of the target. On the basis of an irradiation with empty containers and consideration of geometry and weight, the additional neutrons were estimated to be (35±15) percent of the total. The uncertainty in this correction and in the angular distribution of the neutrons is reflected in the large error assigned to the neutron yields which were (2.1±0.8)×10^{12} for the nitrogen and (1.6±0.6)×10^{12} for the oxygen. The resulting neutron cross sections are 1000±400 mb for nitrogen and 650±250 for oxygen (see Table I).

D. Proton Monitors

The proton flux was measured by Na^{24} production in 0.003-in. aluminum monitor foils inserted between

each cylinder as well as front and back. For the NH_3 run, 0.001-in. gold foils were also used with each aluminum foil. The cylinders were equipped with a $\frac{1}{8}$-in. lip of Lucite projecting $\frac{1}{4}$ in. from the target toward the beam, which intercepted the beam first and scattered it more or less uniformly over the circular cross section of the aluminum containers on the next traversal.

The average number of protons through each cylinder for the NH_3 run was calculated from the average of the gold foil activity at the front and rear of each section. Because the aluminum foils are contaminated to some extent by Na^{24} from the (n,α) reaction, the proton intensity for the water run was calculated by correcting the aluminum foil monitors for contamination. The correction factor, 0.89, was that calculated from the ratio of gold to aluminum activities in the NH_3 run. The average number of protons through each cylinder is given in Table I.

The monitors detect the reactions $Al(p,3pn)Na^{24}$ and $Au(p,15p34n)Tb^{149}$. All cross sections have been calculated on the basis of 9.0 mb for the former reaction with 2.2-Bev protons[8]; the quoted errors do not include the error in this measurement, but represent the error in the cross sections relative to it. The alpha-emitting Tb^{149} is the only activity detected in the gold foil with an alpha-counter after the first two hours. This reaction has a threshold of 0.6 Bev and a cross section of 1.3 mb for 2.2-Bev protons.[9]

E. Secondary Reactions

The use of thick targets, while greatly increasing neutron production and eliminating recoil loss from the target, introduces the possibility of tritium production by secondary reaction. The decrease of tritium activity with target depth parallels the decrease in proton intensity with target depth, and the expected decrease on the basis of geometric cross sections (Table I and Fig. 2), indicating that triton production by high-energy secondaries is negligible, since the secondaries would result in an excess of tritium in the rear cylinder.

The possibility of contamination by low-energy secondaries produced in evaporation processes can be eliminated by comparison of the activities observed on gold and aluminum foil. The most troublesome low-energy secondary reaction for producing tritium is the (n,T) reaction on N^{14}, which has a threshold of

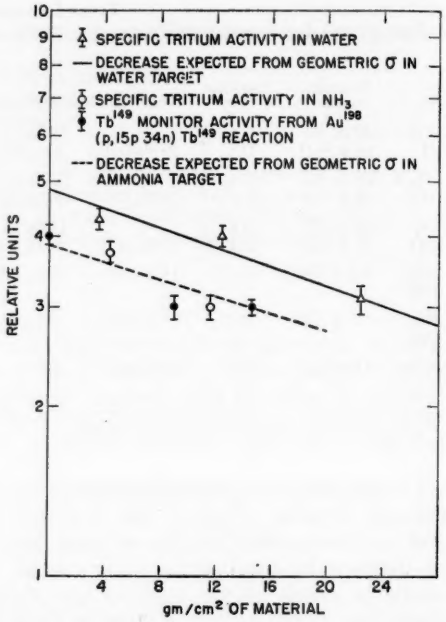

FIG. 2. Tritium and monitor activities *vs* target depth.

4.4 Mev and a cross section of 11 ± 2 mb for fission neutrons above this energy.[4] Since the (n,α) reaction on Al producing Na^{24} has a threshold of 2.7 Mev and a cross section of 110 ± 20 mb for 14-Mev neutrons,[10] it is much more sensitive to neutron secondaries than the $N(n,T)$ reaction. The contamination of the Al foil by this secondary reaction can be calculated from the comparative activities of the gold and aluminum foils, and amounts to less than 20 percent, indicating that secondary neutrons produce only about 1 percent of the tritium in the NH_3 run. The other secondary neutron and proton reactions have much higher thresholds and should be much less significant.

ACKNOWLEDGMENTS

The authors are indebted to Mr. D. Schwarzer for his help in carrying out the measurements, to the cosmotron staff for the irradiations, and to Drs. G. Friedlander and R. Wolfgang for advice and assistance in carrying out the irradiations.

[8] A. Turkevich, Phys. Rev. 94, 775 (1954).
[9] R. B. Duffield and N. Sugarman, Phys. Rev. 94, 776 (1954).
[10] *Neutron Cross Sections*, Atomic Energy Commission Report AECU-2040, Supplement 2 (Technical Information Division, Department of Commerce, Washington, D. C., 1953). Data from Los Alamos and Chalk River.

Proton-Proton Scattering at 437 Mev*

R. B. Sutton, T. H. Fields, J. G. Fox. J. A. Kane, W. E. Mott,† and R. A. Stallwood
Carnegie Institute of Technology, Pittsburgh, Pennsylvania
(Received October 22, 1954)

This paper is a detailed account of measurements, already briefly reported, of the angular distribution of proton-proton scattering at 437 Mev. A description is given of the external proton beam: its collimation, angular spread, energy spectrum, and intensity. The counters, electronics, and targets are described. Two scattering arrangements were used. In one the polyethylene-carbon subtraction method with coincidence detection of the scattered and recoil protons was employed. In the other a counter telescope detected the protons emerging at a given angle from a liquid hydrogen target; at the larger angles but not at the smaller the scattered pairs could also be detected by coincidences between the telescope and another counter. At the smaller angles, when coincidence counting could not be used to insure detection of elastic p-p scattering, precautions were taken to absorb the particles produced in inelastic p-p collisions. The results are that the differential cross section for elastic proton-proton scattering rises smoothly from its value at 90° c.m. to a value about 20 percent higher at 17° c.m. The value at 90° c.m. is 3.49±0.17 mb/sterad.

INTRODUCTION

THIS paper contains details of work, carried out at this laboratory and already briefly reported,[1,2] on measurements of the angular distribution of elastic proton-proton scattering at 437 Mev.

Such measurements have been made by others for protons of energies up to 345 Mev.[3] Descriptions of those for energies in the region 100 Mev to 345 Mev have also been published.[4–10] These experiments indicate that, in this energy range, the nuclear differential scattering cross section in the c.m. system is approximately independent of angle and of energy.

Partial wave analyses of the scattering data for 240 Mev have been carried out recently.[11,12] In these analyses at least S and P states of angular momentum must be included since an S-wave alone can hardly explain the magnitude of the cross section. Furthermore, recent experiments on the scattering of polarized protons by protons indicate that, in the energy region of 320 Mev and above, there are strong interactions in P and F states.[13–15]

It is of interest whether or not the p-p and n-p scattering cross sections are consistent with the hypothesis of charge independence. One of the requirements for this is that

$$\sigma_{p-p}(\theta=90°) \leq 4\sigma_{n-p}(\theta=90°),$$

where θ is the scattering angle in the c.m. system.[16] Recent proton cross section measurements[5,6] indicate that this inequality is satisfied for energies up to 350 Mev.

EXPERIMENTAL METHOD

I. Proton Beam

A. *General Properties*

The source of the high-energy protons was the Carnegie synchrocyclotron. A few percent of the beam is accelerated until it reaches a radius of about 70 inches ($n=1$), where it has sufficient energy to spiral out of the machine. At this radius the energy is about 450 Mev. These protons emerge with apparently equal intensity at all azimuths; their final path is tangent to a radius of about 83 inches. A collimator, appropriately inserted in the concrete shield wall, allows a small fraction of these protons to pass into the experimental region where the intensity is 2×10^6 cm^{-2} sec^{-1}. The collimator restricts the beam to a size of $\frac{1}{2}$ in.$\times\frac{1}{2}$ in. The beam so obtained is quite monoenergetic and free from contamination. Figure 1 shows the cyclotron, the concrete shield wall, and proton collimator.

Figure 2 shows a considerably overexposed (1 min) x-ray film picture of the beam at the exit end of the collimator which is about 30 feet from the cyclotron. The target is normally placed 4 feet from the exit end of the collimator. The beam size at a distance of 20 feet from the collimator is 2.5 inches. This spreading is due

* Supported in part by the U. S. Atomic Energy Commission.
† Now at Gulf Research Laboratory, Harmarville, Pennsylvania.
[1] Mott, Sutton, Fox, and Kane, Phys. Rev. **90**, 712 (1953).
[2] Sutton, Fields, Fox, Kane, Mott, and Stallwood, Phys. Rev. **95**, 663 (1954).
[3] Measurements have also been made at 429 Mev by Marshall, Marshall, and Nedzel [Phys. Rev. **92**, 834 (1953)], but these may have been affected by polarization of the incident beam to an extent which is under investigation [Phys. Rev. **93**, 1431 (1954)]. The value of the differential cross section at 90° c.m. would of course be unaffected by beam polarization.
[4] Chamberlain, Segrè, and Wiegand, Phys. Rev. **83**, 923 (1951).
[5] Marshall, Marshall, and Nedzel, Phys. Rev. **92**, 834 (1953).
[6] Chamberlain, Pettengill, Segrè, and Wiegand, Phys. Rev. **93**, 1424 (1954).
[7] O. A. Towler, Phys. Rev. **85**, 1024 (1952).
[8] C. L. Oxley and R. D. Schamberger, Phys. Rev. **85**, 416 (1952).
[9] Cassels, Pickavance, and Stafford, Proc. Roy. Soc. (London) **214**, 262 (1952).
[10] Kruse, Teem, and Ramsey, Phys. Rev. **94**, 1795 (1954).
[11] A. Garren, Phys. Rev. **92**, 213 (1953).
[12] R. M. Thaler and J. Bengston, Phys. Rev. **93**, 643 (1954), and Thaler, Bengston, and Breit, Phys. Rev. **93**, 644 (1954).
[13] Chamberlain, Segrè, Tripp, Wiegand, and Ypsilantis, Phys. Rev. **93**, 1430 (1954).
[14] de Carvalho, Heiberg, Marshall, and Marshall, Phys. Rev. **94**, 1796 (1954).
[15] Kane, Stallwood, Sutton, Fields, and Fox, Phys. Rev. **95**, 1694 (1954).
[16] D. Feldman, Phys. Rev. **89**, 1159 (1953).

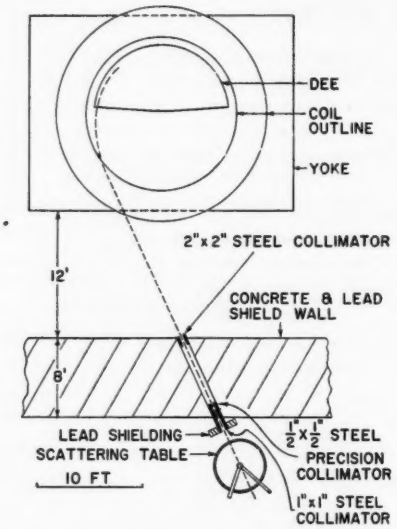

FIG. 1. Schematic diagram of cyclotron, shield wall, and external beam trajectory.

to the nature of the origin of the beam and to multiple scattering by the window on the cyclotron vacuum chamber and by air.

B. *Energy*

The energy and energy spread of the protons have been investigated three ways. The results are that most of the protons at the target have an energy of 437 Mev which may vary by about 3 Mev due to variations in the magnetic field of the cyclotron. The instantaneous energy spread of these protons is probably less than 3 Mev. In addition, about 5 percent of the protons have energies between the maximum energy and 390 Mev. A negligible fraction have energy below 390 Mev. Those with energy lower than that of the main component probably suffered energy degradation in the collimator.

The first method used to investigate this problem was to count the number of coincidences between the scattered and recoil protons, in a p-p scattering experiment, as a function of angle between the two counters. For this experiment two stilbene scintillation counters were used. The stilbene crystals were 1 cm wide and 3.5 cm high in the plane perpendicular to the path of the detected protons and each was at a distance of 66 cm from the scattering target. The two counters were symmetrically placed with respect to the proton beam. The angle between the two counters was checked to about one minute by comparing the counting rates at angles where the slope of counting rate *versus* angle was steep, with and without interchanging the arms which supported the counters. The target was 0.54 g/cm² of CH_2; by replacing the CH_2 with C we were able to obtain the results, shown in Fig. 3, because of hydrogen scattering alone. Nonrelativistically the angle at the target between the two counters for peak intensity should of course be 90°. Relativistically this angle, 2θ, for symmetrically-placed counters, is given by

$$\tan 2\theta = \left(\frac{2m_0c^2}{E_0}+1\right)\tan\theta + \frac{2m_0c^2}{E_0}\cot\theta,$$

where E_0 is laboratory kinetic energy. For 437 Mev this angle is 84°. Thus from the counting rates at angles between 84° and 90° we could obtain an indication of the number of low-energy protons in the beam. An energy scale is included in Fig. 3. From the curve we were able to conclude that the peak lay at the correct angle within a maximum error of 10 minutes, that to an accuracy of 1 percent there were no protons with energies between 150 Mev and 350 Mev, and from consideration of the area and shape of the curve and the resolution of the equipment, that there may have been between 5 percent and 15 percent with energy above 350 Mev but below 437 Mev. This method, though it did not have very high dispersion, was used to obtain a semiquantitative result quickly and before we had set up better equipment for the purpose.

Higher dispersion was obtained by a method involving the observation of Čerenkov radiation. Plate glass of ½-inch thickness was placed in the proton beam. Čerenkov radiation from the glass passed through a lens and slit system and was detected by a 1P21 photomultiplier. The experimental arrangement is shown in Fig. 4. The intensity of the radiation was

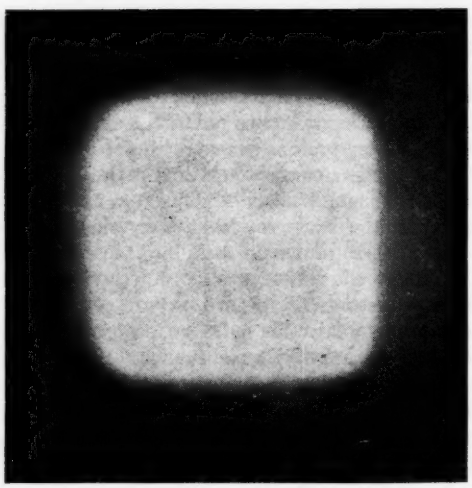

FIG. 2. A positive print from an x-ray film picture showing the cross section of the proton beam emerging from the collimator. The bright area was formed by the beam after emerging from the end of the ½ inch by ½ inch precision collimator which was 24 inches from the film. The sharp outer edges are the shadow of the 1-inch by 1-inch end-section of the collimator which shielded the counters from the spray of protons scattered by the walls of the precision collimator. The picture indicates the degree of alignment usually achieved.

measured as a function of its angle, θ, with the proton beam. The angle θ inside the glass is related to the $\beta(=v/c)$ of the protons by the relation $\cos\theta=1/n\beta$, where n is the index of refraction of the glass. Hence, the radiation at a particular angle originates from protons of a particular β. The glass was rotated with the optical system so that the light detected always emerged perpendicular to the glass surface. Figure 5 shows the measured intensity of the radiation as a function of the angle θ; an energy scale is also shown. The constant background appeared to be arising from fluorescence of the glass since it remained when the velocity of the protons was reduced by absorption in copper to a value at which Čerenkov radiation could not be emitted. A rough analysis of this curve indicated that about 5 percent—8 percent of the protons had energies between 390 Mev and the peak energy. The number of protons having energies between 300 Mev and 390 Mev was zero to an accuracy of 1 percent.

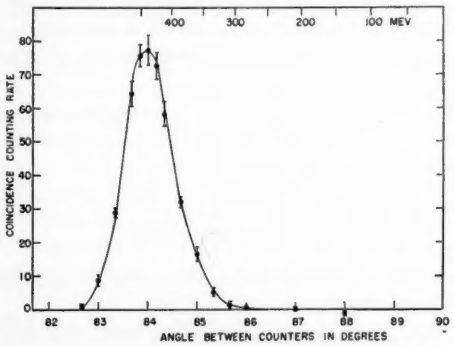

FIG. 3. p-p coincidence rate *versus* the angular separation between two counters which form equal angles with the incident beam. The width of the peak is largely due to the finite sizes of the counters. The energy scale shows the expected position of the peak for various incident proton energies.

Finally, having set up for other purposes a coincidence-anticoincidence counting telescope we have obtained differential range curves in copper for the protons. The telescope consisted of four scintillation counters as shown in Fig. 6; they are numbered 1, 2, 3, 4 in the order in which the beam traversed them. 1 and 2 are coupled in coincidence and used as a monitor; 1, 2, and 3 are in coincidence with 4 in anticoincidence. Thus, a count from 1+2+3−4 arises from a particle traversing 1, 2, and 3, but not entering 4. The ratio of 1+2+3−4 to 1+2 as a function of copper thickness between 2 and 3 is shown in Fig. 7. The energies of protons at particular copper ranges are also shown. Because of nuclear absorption in the copper, there is a small counting rate of 1+2+3−4. This rate varies slowly with thickness of copper, particularly in the first few centimeters because of the finite range of the fragments produced in nuclear events. At the end of the range of the protons the expected peak in counting rate is seen.

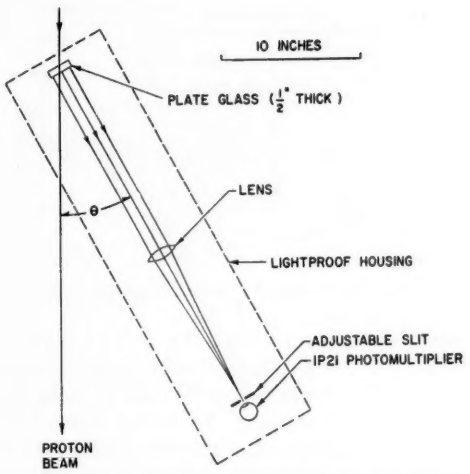

FIG. 4. Apparatus used to observe Čerenkov radiation.

Also shown for comparison is a differential range curve taken after the beam had passed through a magnet. The similarity of these curves at copper thickness below 1 inch indicates the absence of low-energy contamination even for energies below 150 Mev, a region not reached by the other methods described.

It would seem that the existing low-energy contamination should have little effect on the results of this experiment. The rate of loss of energy in argon is only 5 percent higher for 400 Mev than for 450-Mev protons. Hence, the effect on the chamber sensitivity is negligible. Since the scattering of protons is relatively insensitive to energy the cross sections should not be affected measurably.

C. *Polarization*

Since this beam spirals out of the cyclotron without being scattered there is no reason to expect it to be polarized. However, we have checked this point by

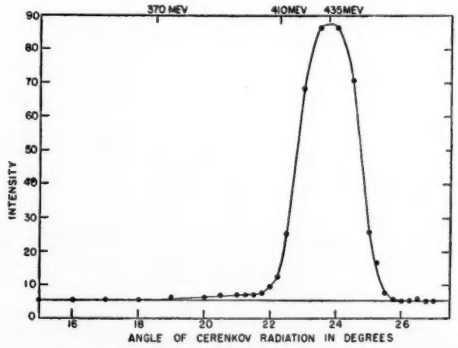

FIG. 5. Intensity of Čerenkov radiation produced by proton beam traversing glass as a function of the angle of emission. The beam direction was not measured accurately so that only relative angles are significant. The energy scale was computed so as to agree with the known energy of the beam.

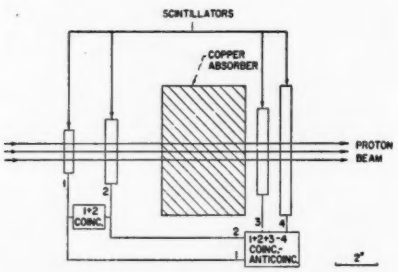

FIG. 6. Counter telescope used to obtain differential range curves.

scattering it from a carbon target and measuring the asymmetry of the scattered protons. Under conditions at which a 45 percent polarized beam gave an asymmetry of about 25 percent,[15] the normal external beam gave (0.4±0.7) percent. Furthermore, the *p-p* scattering data reported in this paper were taken on both sides of the beam. We thus conclude that these results are not subject to error on account of beam polarization.

D. *Intensity Measurement*

The method used to monitor the beam intensity was essentially that used by Chamberlain *et al.*[4] The protons passed through an argon-filled ionization chamber which was very similar to the one used at Berkeley for the same purpose. A condenser of 0.181-μf capacity was charged by the current from the chamber. The resulting condenser voltage was measured by a dc amplifier. The leakage resistance of the system was high enough to make loss of charge negligible during the charging time.

The ionization-chamber calibration is dependent upon a knowledge of the energy loss of protons in argon and the average energy loss per ion pair. These we have obtained from Aron *et al.*[17] and Chamberlain *et al.*[4,6]

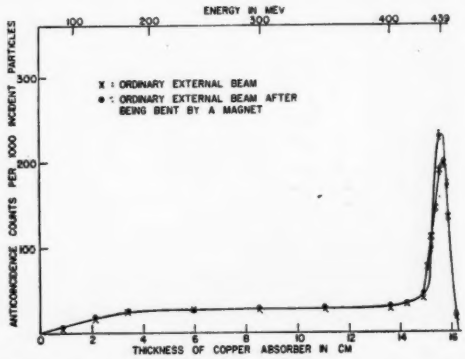

FIG. 7. Differential range curves. The copper absorber thickness and the energy scale have been corrected to allow for counter thicknesses.

[17] Aron, Hoffman, and Williams, Atomic Energy Commission Report AECU-663, 1949 (unpublished) and W. Aron, University of California Radiation Laboratory Report UCRL-1325, 1951 (unpublished).

respectively. In the case of the energy loss per ion pair, we thus include the assumption that this quantity does not vary significantly from 345 Mev to 440 Mev.

II. Counters and Electronics

Scintillation counters were used to detect the scattered protons. They consisted of stilbene crystals or plastic scintillators viewed through short plastic light pipes by RCA-5819 photomultiplier tubes. The tubes were well shielded against stray magnetic fields. Signals were developed at the multiplier anodes across 100-ohm resistors. These signals were transmitted through about 100 feet of 100-ohm coaxial cable, RG7U, directly into a crystal diode coincidence circuit.[18] The pulses were clipped to a duration of 2×10^{-9} sec by shorted cables of about 25 cm length connected at the coincidence input. The coincidence resolving time of the circuit was thus about 4×10^{-9} sec. The output pulses from the coincidence circuit were amplified by an Atomic 204-C linear amplifier. The pulses from the output of the amplifier discriminator were fed to a standard scaler. Coincidence counting rates were always sufficiently low that no dead time corrections were necessary. In order to obtain a pulse height spectrum of the coincidence pulses, the amplifier output was fed into a 24-channel pulse-height analyzer which was gated by the discriminator pulse.

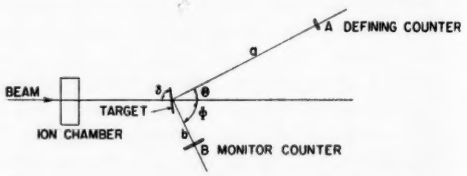

FIG. 8. The scattering arrangement used with CH_2 targets.

III. Experiments Using a CH_2 Target

The experimental arrangement is shown in Fig. 8. Two counters *A* and *B* were so located and of such sizes that if counter *A* detected a proton scattered by hydrogen, *B* would detect the recoil proton. Counter *A*, which thus defined the solid angle, and which normally counted the high-energy proton, presented to the scattered protons an area of linear dimensions of the order of 2 to 3 cm. It was placed at a distance of about 1 meter from the target. Counter *B* was larger than *A* and nearer the target, its size and distance being determined by the requirements of geometry with allowance made for multiple scattering in the target. (*B* was sufficiently large that it would count the recoil even though either proton suffered a deviation in any direction of twice the root mean square multiple scattering angle calculated for complete traversal of the target.) In most cases the adequacy of the geometry

[18] S. DeBenedetti and H. Richings, Rev. Sci. Inst. **23**, 37 (1952).

was checked by comparing results with B at two different distances.

Coincidence counts will arise from: (a) proton-proton scattering events from hydrogen, (b) quasi proton-proton scatterings from carbon in which an incident proton and a proton in the carbon nucleus are involved, (c) real coincidences which do not originate at the target, (d) accidental coincidences. In order to obtain the number of events (a), it is necessary to make a determination of (b), (c), and (d). At each angle it therefore becomes necessary to measure the coincidences, for a given number of incident protons, with a CH_2 target, a C target, and with no target, and to measure for each of these the accidental counts. Accidental counts were measured by increasing the length of cable connecting one counter to the coincidence circuit. The extra length was such that the time for transmission of a pulse along it was equal to the period of the radio-frequency voltage of the cyclotron. Thus the intensity of single counts was the same as when coincidence counting, but no true coincidences could be counted.

The carbon targets were chosen to have stopping power approximately equal to that of the corresponding CH_2 target. Thus, there were more carbon atoms per cm^2 of target surface than for the CH_2 targets. The reason for this choice was to have similar conditions for the CH_2 and C targets for emergence of very low-energy recoil protons from carbon.

If we use a CH_2 target with a surface density of carbon atoms equal to R times the surface density of the atoms in the carbon target, then the number of coincidences from hydrogen is given by

$$H=(CH_2-CH_{2a})-(B-B_a)-R[(C-C_a)-(B-B_a)].$$

Here CH_2 is the number of coincidences with the CH_2 target, CH_{2a} is the number of accidental coincidences with the CH_2 target, B and B_a, C and C_a are the corresponding quantities for no target and for the carbon target. Each of these quantities is measured for the same number of protons traversing the target.

In order to be certain that the discriminator was set low enough to trigger on all hydrogen coincidences, pulse height analyses of the coincidence pulses were made as described in Sec. II. A typical example of such a pulse height analysis is shown in Fig. 9, where the data using a carbon target and no target have been appropriately subtracted from the CH_2 data. These data were taken simultaneously with the recording of the coincidence counts. We concluded from curves such as this that the equipment was missing a negligible number of the proton-proton events.

It would be possible when making measurements at small scattering angles to count as true proton-proton scatterings the meson in counter B and the proton in counter A from the reaction

$$p+p\rightarrow\pi^++p+n.$$

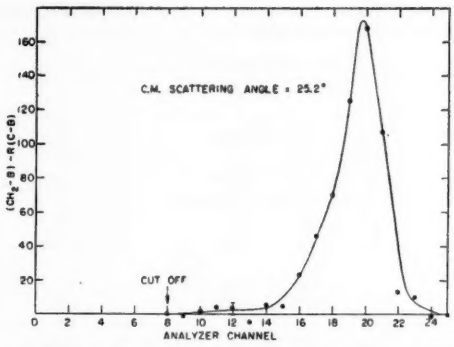

FIG. 9. Pulse height distribution of p-p coincidence pulses in a typical run. The discriminator level was set at channel 8 as shown. The symbols C, R, B, and CH_2 are defined in the text.

The contribution of such events depends on the cross section for this reaction and on the angular correlation of the meson and proton. Because the range of the recoil proton when it appears at a large angle is very small compared to that of the meson in question, the coincidence-counting rate with 0.13 cm of copper in front of counter B should be due only to meson-proton coincidences. Such an experiment was carried out for the 25° center-of-mass measurement. It was found that the contribution to the measured scattering cross section from the meson production reaction was (0.5 ± 3) percent. It should also be noted that the counter geometry was always such that no events of the type $p+p\rightarrow\pi^++d$ could be counted.

IV. Experiments Using a Liquid Hydrogen Target

This method was used so that scattering at a smaller angle could be investigated (at center-of-mass angles less than 25° the lower energy proton of the pair has

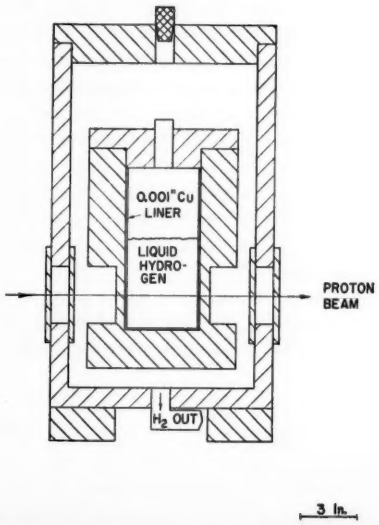

FIG. 10. Cross section of Styrofoam container for liquid hydrogen.

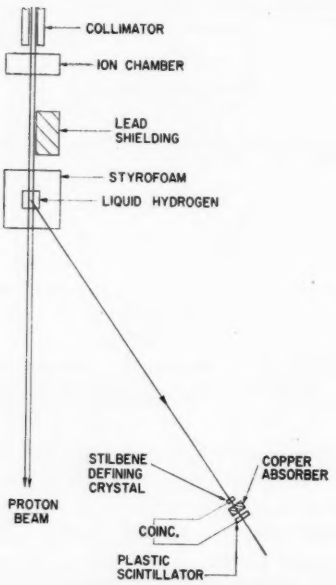

FIG. 11. The scattering arrangement used with liquid hydrogen. For the measurements at 90° c.m. and 50° c.m., an additional counter detected the other proton of the scattered pair in coincidence with the front telescope counter.

too low an energy to be counted with certainty) and also to provide a check on the work with CH_2 targets.

The target is shown in Fig. 10. It consisted of a double walled container made of Styrofoam. The liquid hydrogen was held in an inner container constructed of one-mil copper. This copper liner was used to prevent the hydrogen from coming in direct contact with the Styrofoam, and so producing thermal strains and, hence, possible cracking of the container; also, should a crack appear in a Styrofoam joint, the liner retains the hydrogen. The target was approximately 10 cm long in the beam direction. The hydrogen surface density was about twice that of the container. Warping of the copper while the container was being filled resulted in an uncertainty of about 5 percent in the surface density of the hydrogen. As a result the absolute cross sections obtained using liquid hydrogen have considerably greater errors than those from the CH_2 measurements. Thus, only relative cross sections are given for the liquid hydrogen data. The absolute value given is obtained only from CH_2.

Three methods were used to count protons scattered by the hydrogen: (1) At 90° and 50° c.m. scattering angle, both scattered protons were detected, as with

FIG. 12. Arrangement used for measuring the efficiency of the counter telescope as a function of the energy of the detected proton.

CH_2. Here a counter with a 10×15 cm plastic scintillator was used as counter *B*. (2) For all angles at which measurements were taken, a two-counter telescope was also used (Fig. 11) which detected only the high-energy proton of the pair. The front-telescope counter, which defined the solid angle, was a stilbene crystal and the back counter was of plastic and larger than the front one. At 90° and 50°, this telescope was used with no absorber between the two counters. (3) At 50 degrees 7.5 cm of copper, and at smaller angles 8.8 cm of copper, was inserted between the two counters of the above telescope. This copper stopped all particles accompanying meson production.

The measurements with no copper between the counters required a correction to be made for the mesons produced in some of the proton-proton collisions. These corrections were made on the basis of published cross sections[19,20] for the reactions $p+p\rightarrow\pi^++d$ and

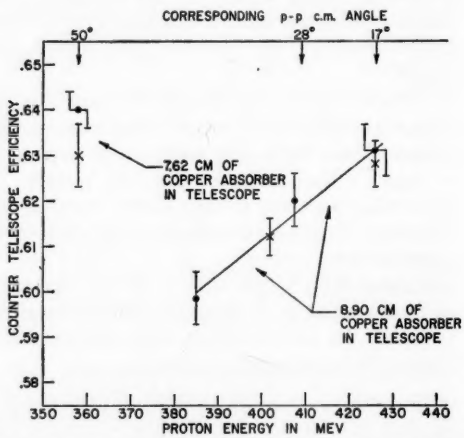

FIG. 13. Counter telescope efficiencies. The points marked with crosses were taken on a different day from those marked with circles, as described in the text. The various proton energies were obtained with various thicknesses of the copper degrader shown in Fig. 12.

$p+p\rightarrow\pi^++p+n$, and were about 5 percent of the measured scattering cross sections.

For the interpretation of the data taken with copper between the counters, it was necessary to calibrate the efficiency of the telescope for protons of the energy appropriate to each scattering angle. To determine the efficiency, the telescope was put in the direct proton beam at reduced intensity. Figure 12 shows the experimental arrangement. The required proton energy was obtained by degrading the beam with absorber. The efficiency of the telescope with copper between the counters was taken as the ratio of the telescope counts with copper to the counts with no copper for the same number of protons incident on the telescope. In order to monitor the protons incident on the telescope, a large

[19] Fields, Fox, Kane, Stallwood, and Sutton, Phys. Rev. 95, 638 (1954).
[20] A. H. Rosenfeld, Phys. Rev. 95, 638 (1954).

TABLE I. Data obtained with CH_2 targets.

C.m. angle (deg)	$d\sigma/d\Omega$ (mb/sterad)	Standard deviation (mb/sterad)	Target thickness[b] (g/cm²)	Target angle, δ (deg)	Counter sizes[c] A	B	Counter distances (cm) A	B	Counts per 10^9 incident protons CH_2	C	B	Time in sec for 10^9 incident protons
90	3.33	0.16	α	57.3	a	b	85	20	1303	193	0	3000
90	3.38	0.15	β	55.3	c	b	65	15	446	142	13	2100
90	3.58	0.17	β	55.0	a	b	65	15	706	212	33	2500
90	3.41	0.10	α	57.3	a	b	75	20	1736	284	30	3000
90[a]	3.53	0.10	γ	70.0	d	e	80	30	156	24	6	180
90	3.49	0.18	γ	70.0	d	e	80	30	153	24	2	270
90	3.64	0.11	γ	70.0	d	e	80	20	172	41	8	170
65[d]	3.62	0.15	β	45.3	c	b	75	20	265	52	5	2600
65[d]	3.65	0.09	α	45.3	a	b	75	20	1590	287	24	1200
65[d]	3.77	0.18	β	45.3	a	b	75	20	455	118	40	1000
65[d]	3.42	0.13	α	41.5	a	b	100	20	926	189	29	1700
65[d]	3.63	0.11	α	46.4	a	b	75	20	1520	232	11	2800
36[d]	4.23	0.22	β	31.6	a	b	65	20	635	263	192	1000
36	4.02	0.15	γ	60.0	c	b	85	7	303	84	14	1300
36[d]	4.22	0.17	β	33.9	a	b	65	20	432	75	19	2500
36[a]	4.02	0.18	γ	47.0	d	e	130	12	139	33	6	250
36	4.06	0.14	γ	47.0	d	e	130	12	131	20	5	240
36	3.92	0.15	γ	47.0	d	e	130	18	122	13	5	160
30[a]	3.96	0.14	γ	50.0	d	e	130	15	124	16	5	340
30[a]	4.07	0.19	β	54.5	d	e	130	7.7	209	67	11	170
30	4.00	0.09	γ	54.5	d	e	130	15	115	12	2	130
30	4.10	0.13	γ	54.5	d	e	130	12	122	17	5	130
25	4.48	0.25	γ	60.0	c	b	85	5	384	139	29	1000
25[a]	4.27	0.13	γ	50.0	d	b	130	10	138	20	5	170
25[a]	4.36	0.18	γ	50.0	d	b	130	7.7	142	26	7	130

[a] For these results accidental coincidences have been measured and included.
[b] The symbols in this column have the following meaning: α—0.643 g/cm² CH_2, 0.781 g/cm² C; β—0.164 g/cm² CH_2, 0.223 g/cm² C; γ—0.110 g/cm² CH_2, 0.127 g/cm² C.
[c] The symbols in this column have the following meaning: a—3.57 cm×3.60 cm; b—3.50 cm×3.52 cm; c—2.59 cm×3.28 cm; d—2.06 cm×3.97 cm; e—4.00 cm×6.00 cm.
[d] For these runs the defining counter detected the lower-energy proton.

third counter was placed next to the degrading absorber. Incident protons were measured by counting coincidences between this third counter and the front telescope counter. It was found that the distance between the telescope and the absorber used to degrade the beam energy, was large enough to have had no measurable effect on the efficiency measurement. Thus the efficiency was sufficiently independent of angular spread of the beam, and there was an egligible effect because of secondaries produced in the degrader. A check on the efficiency measurement was given by the comparison of the results at 50° obtained by the telescope method with those obtained by counting both protons.

Figure 13 shows the efficiency of the telescope as a function of proton energy. These data were taken immediately before the hydrogen runs. The two sets were taken with different counters, one set with sizes 2.5×3.5 cm and 10×10 cm, the other with sizes 3.5×3.5 cm and 7.5 cm diameter. The close agreement between these indicates that counter size relative to beam spread is unimportant when the second counter is large enough.

RESULTS

The results of the CH_2 experiments are given in Table I. Errors quoted are the standard deviations obtained from the numbers of counts. For all angles except 25°, the correction due to the inclusion of the accidentals was one-half of one percent or less. At 25° the correction was less than 2 percent. Runs for which the times are over 1000 sec for 10^9 incident protons are those for which the first results were published.[1]

The results of the data obtained using the liquid hydrogen target are shown in Table II. Absolute values are not given because of the uncertainty in absolute length

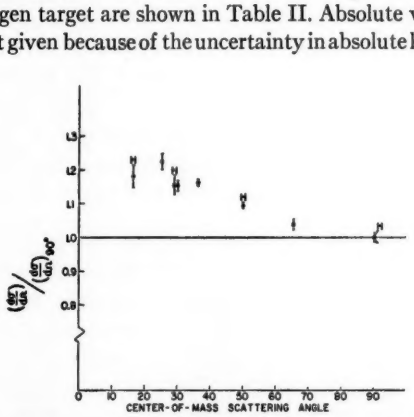

FIG. 14. The angular distribution of p-p scattering at 437 Mev. The points marked H were measured using a liquid hydrogen target; the other points were measured using a CH_2 target. The errors are standard deviations from counting statistics.

TABLE II. Data obtained with liquid hydrogen target.*

C.m. angle (deg)	Method	$\frac{\sigma(\theta)}{\sigma(90°)}$	Error	Telescope absorber (cm of copper)	Telescope efficiency	Dimensions of defining crystal	Distance of defining crystal (cm)	Ratio of H to empty target counting rate
90	Recoil	0.98	0.03	...	...	*f*	283	27
90	Telescope	1.04	0.04	0	1.00	*f*	283	1.5
90	Recoil	1.00	0.04	...	...	*b*	300	52
90	Telescope	1.00	0.05	0	1.00	*b*	300	3
50	Recoil	1.09	0.02	...	...	*f*	283	28
50	Telescope	1.11	0.03	7.62	0.63	*f*	283	5
50	Telescope	1.08	0.04	0	1.00	*f*	283	1.2
50	Recoil	1.11	0.02	...	...	*b*	300	50
50	Telescope	1.05	0.03	7.62	0.64	*b*	300	6.9
28	Telescope	1.17	0.05	8.90	0.62	*f*	283	2.7
28	Telescope	1.14	0.04	8.90	0.62	*b*	300	3.3
17	Telescope	1.19	0.05	8.90	0.63	*f*	283	0.75
17	Telescope	1.17	0.05	8.90	0.63	*b*	300	0.87

* The methods in the second column are described in the text. The errors in the fourth column are standard deviations from counting statistics, including efficiency measurements. In the seventh column *f* denotes 2.50 cm ×3.47 cm; *b* denotes 3.50 cm ×3.52 cm.

of the target. The accidental counts here were completely negligible. The several runs at 90° and 50° show satisfactory agreement among the various methods used. The background became excessive at c.m. angles smaller than about 17° (7.5° lab angle).

The ratios of the average cross sections at the various angles relative to the average cross section at 90° for both the CH_2 and the liquid hydrogen data are given in Table III and Fig. 14. The agreement between the two sets of values is satisfactory.

A weighted average for the absolute cross section at 90° was obtained from the data in Table I. It is 3.49 mb/sterad with a standard deviation of 0.05 mb/sterad from counting statistics. We estimate a value of 5 percent for what might be termed the standard deviation of this cross section. It was obtained from an rms combination of the error from counting statistics and the estimated errors arising from multiple scattering, effective counter area and distance, target composition, angle, and thickness, properties of the dc-amplifier system which integrated the ion-chamber current, and background ionization in the chamber; also included was an estimated uncertainty of 2 percent in the value of the multiplication factor of the ionization chamber as given by the work at Berkeley.[4,6,17]

TABLE III. Final average cross sections.

C.m. angle (deg)	$\frac{d\sigma/d\Omega}{d\sigma/d\Omega(90°)}$	Statistical standard deviations
17	1.182	0.035
25	1.223	0.023
28	1.156	0.031
30	1.152	0.015
36	1.160	0.010
50	1.094	0.015
65	1.037	0.017
90	1.000	0.014

From the above angular distribution and absolute cross section at 90°, we calculate the total cross section for elastic nuclear *p-p* scattering at this energy to be 23.8±1.2 mb.

DISCUSSION

As mentioned earlier, one of the main features of the angular distribution of proton-proton scattering in the range 150–345 Mev is its isotropy from 15° to 90° in the c.m. system within the experimental errors.[21] The present results provide definite indications of a deviation from isotropy at 437 Mev in the form of a 20 percent rise in cross section at small angles. Hartzler and Siegel[22] found similar behavior at energies in the neighborhood of 430 Mev; at 400 Mev and below their measurements were consistent with isotropy.

Our value of 3.49±0.17 mb/sterad for the absolute cross section at 90° is related to the Berkeley values through the ionization-chamber calibration. Since our value is equal, within the errors, to theirs it appears that the cross section is quite constant from 120 Mev to 437 Mev. This conclusion is also supported by the results of Marshall, Marshall, and Nedzel.[5] It is also of interest that their value for the 90° cross section of 3.42±0.13 mb/sterad, which was obtained by direct counting of the incident flux, agrees excellently with our value.

A value of 1.5 mb/sterad for the *n-p* scattering cross section at 90° c.m. and a neutron energy of 400 Mev has been obtained by Hartzler and Siegel.[23] This value together with the present results indicates that the inequality

$$\sigma_{p-p}(\theta=90°) \leq 4\sigma_{n-p}(\theta=90°),$$

[21] Kruse, Teem, and Ramsey (reference 10) have recently reported a 6 percent rise in $\sigma(\theta)$ from 90° c.m. to 40° c.m. at 97 Mev.

[22] A. J. Hartzler and R. T. Siegel, Phys. Rev. 95, 185 (1954).

[23] Hartzler, Siegel, and Opitz, Phys. Rev. 95, 591 (1954).

discussed in the introduction, is satisfied in the 400-Mev region.

ACKNOWLEDGMENTS

It is a pleasure to thank Professor L. Wolfenstein for numerous valuable discussions on many aspects of this problem. The help of Dr. S. A. Friedberg and other members of the Low Temperature Laboratory in providing liquid hydrogen is appreciated. The cooperation of the personnel of the Carnegie Institute of Technology Nuclear Research Center was an important contribution to the successful completion of this work.

PHYSICAL REVIEW VOLUME 97, NUMBER 3 FEBRUARY 1, 1955

Scattering of 151-Mev Positive Pions by Protons*

RAYMOND A. GRANDEY† AND ARNOLD F. CLARK‡
Carnegie Institute of Technology, Pittsburgh, Pennsylvania
(Received October 4, 1954)

Nuclear emulsions have been exposed to the external positive pion beam of the Carnegie synchrocyclotron and have been scanned for elastic π-p scatterings. Seventy events have been found while scanning plates exposed to a final energy of 151±7 Mev, which, combined with results obtained at Columbia and the recent accurate determinations of the total cross section in this region by the Carnegie Group, yield a value for the differential cross section of $d\sigma/d\Omega=(7.7\pm2.1)-(3.1\pm2.4)\cos\theta+(17.3\pm7.2)\cos^2\theta$ mb/sterad. The best Fermi type phase shifts calculated from the above are: $\alpha_3=-26°$, $\alpha_{33}=50°$, and $\alpha_{31}=0°$.

Recent data on pion-proton scattering at various energies are discussed, and it is found that the present data can be fitted with just three phase shifts which can be treated on semi-empirical models.

I. INTRODUCTION

THE elastic scattering of both positive and negative pions from hydrogen has been studied over a considerable range of energies. Counter techniques have been applied at Chicago, Columbia, and Rochester to obtain angular distributions for negative pion-proton scattering from 40 to 217 Mev.[1-6]

Unfortunately, the very low positive-pion fluxes obtained externally from the present synchrocyclotrons have made it impractical to extend counter techniques in studying angular distributions for positive pion-proton scattering much above the 135-Mev point obtained by the Chicago group.[1] Nuclear emulsion techniques can be well applied in this high-energy positive-pion region. By using the hydrogen content of the emulsion as a scatterer, data can be collected with a minimum of cyclotron running time, and since the entire solid angle is available, this leads to the additional advantage of sampling scattering into all angles.

II. EXPERIMENTAL PROCEDURE

A magnetically analyzed 160-Mev external positive-pion beam is available from the Carnegie cyclotron with a flux at the focus of the analyzing magnet of from 2 to 7 mesons per cm² per sec.[7] This flux is so small that it causes serious experimental difficulties in a counter angular distribution experiment. The small flux requires exposures for plates on the order of one hour for intensities in the emulsion of 10^4 mesons/cm².

The beam is formed by allowing the main internal proton beam to strike a Cu target placed at a cyclotron radius just inside the $n=0.2$ resonance. Positive pions produced in the backward direction are deflected out of the cyclotron by the fringing field and are focused at the same time.

The beam passes through a channel cut in the 8-ft thick magnetite concrete shield wall separating the cyclotron room from the experimental area and is further analyzed upon emergence by passing through a double-focusing 45° sector magnet. The energy and muon contamination of the beam were measured by taking range curves in Cu with counters. Three scintillation counters were placed before the absorber and one large counter behind. The ratio of quadruple to triple coincidences was counted as a function of absorber thickness. The equipment and geometry of the counter group[7] was used. Figure 1 shows the range curve.

The relatively long exposure required together with

* This paper is a condensation of a thesis submitted by R. Grandey in partial fulfillment of the requirements for the degree of Doctor of Philosophy in Physics at Carnegie Institute of Technology. The research was partially supported by the U. S. Atomic Energy Commission. Preliminary results were reported in Phys. Rev. 94, 766 (1954).

† U. S. Atomic Energy Commission Predoctoral Fellow.

‡ Now at the Radiation Laboratory, University of California, Livermore, California.

[1] Anderson, Fermi, Martin, and Nagle, Phys. Rev. 91, 155 (1953).

[2] Fermi, Glicksman, Martin, and Nagle, Phys. Rev. 92, 161 (1953).

[3] M. Glicksman, Phys. Rev. 94, 1335 (1954).

[4] M. Glicksman, Phys. Rev. 95, 1045 (1954).

[5] Bodansky, Sachs, and Steinberger, Phys. Rev. 93, 1367 (1954).

[6] A. Roberts and J. Tinlot, Phys. Rev. 94, 766 (1954).

[7] Ashkin, Blaser, Feiner, Gorman, and Stern, Phys. Rev. 96, (1954).

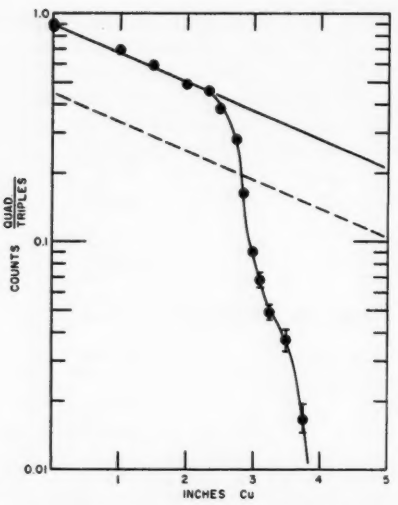

FIG. 1. Range curve for 151-Mev positive pions range=2.83 inches with 1 inch plexiglass in front of the first counter. Contamination=(8±3) percent.

the high general radiation background level caused by neutrons escaping through the shield wall made it necessary to shield the plates during exposure. This was effected by building an 8 ft ×8 ft blockhouse of magnetite concrete about the plates with an inner core of two cubic feet of Pb. In addition, a large mass of Pb was placed on the coil can of the cyclotron in the median plane in an effort to reduce the general background in the experimental area. Ilford G-5 600 3 in. ×3 in. plates were used with the beam incident perpendicular to the 3-in. edge but in the plane of the emulsion.

III. SCANNING

The low intensity of the meson beam together with the high background made it impossible to reduce the background-to-meson ratio in the plates sufficiently to permit area scanning. Reliable results in area scanning are obtained only if the plates are very clean. It was therefore necessary to scan along the tracks. The procedure is essentially that described by Homa, Goldhaber, and Lederman,[8] hereinafter referred to as HGL. Their plates were obtained by internal exposures and had a great deal of background. Our plates are much cleaner, and we believe that we are operating close to 100 percent efficiency in the angular region under consideration. Our total cross section agrees within statistical errors with the counter transmission cross section. We have normalized our angular distribution to the counter total cross section which is statistically much better, so that the efficiency is important only if it varies appreciably with the type of elastic event. The efficiency at small and large meson angles is discussed in Sec. V. It is possible that efficiency is lower for large azimuthal angles, the azimuthal angle being the angle made by the plane of the event with the plane of the emulsion, since events are often difficult to measure in these regions. The azimuthal distribution of our 70 events is plotted in Fig. 2. The concentration of events with azimuthal angles less than 15° is regarded as a purely statistical fluctuation, since we are quite sure that our efficiency could not fall off until well over 45°. Such a possible inefficiency should not be a function of the meson angle.

[8] Homa, Goldhaber, and Lederman, Phys. Rev. 93, 554 (1954), henceforth referred to as HGL.

IV. IDENTIFICATION OF EVENTS

Elastic pion-proton scattering events were identified by applying the usual criteria of coplanarity and angular correlation.[8] When the scattered proton stopped in the emulsion, its range was measured and energy determined as an additional check. In general, the outgoing meson was not grain-counted if the density looked normal unless there was some additional reason to suspect the event, for instance a possible third outgoing particle or a borderline satisfaction of the two criteria. One event which was quite coplanar and within one-half degree of angular correlation was rejected because of obviously high-grain density. This event was already suspect because of the presence of an electron track originating with the event. This additional criterion of "cleanliness" appears to be very good. All quasi-elastic pion-proton scatterings had either an electron track or a very short (less than 5μ) stub originating with the event. All elastic scatterings appeared clean at the origin except in a few cases where an electron could be discerned. In all of these later cases, the electron does not appear to originate with the event but is probably a chance coincidence with one of the numerous background electrons.

$\Theta/\Delta\theta$, the deviation from angular correlation measured in units of the rms errors in measurement,

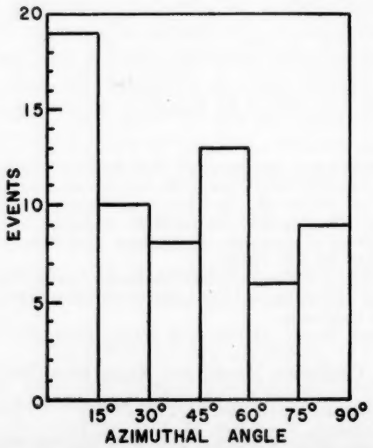

FIG. 2. Azimuthal distribution of elastic scattering events.

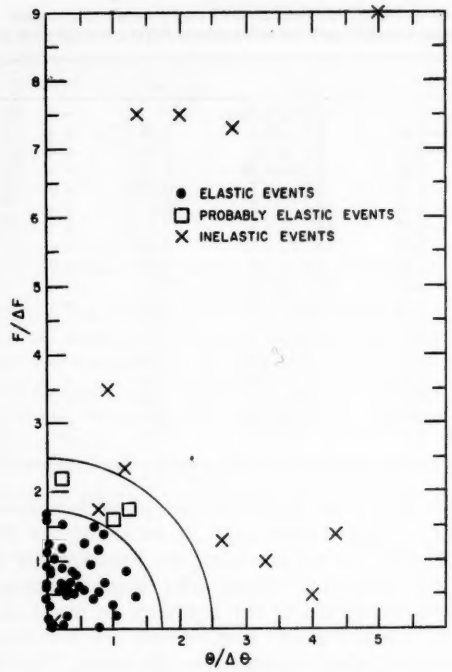

FIG. 3. Coplanarity—Angular correlation plot.

is plotted against $F/\Delta F$, the corresponding measure of deviation from coplanarity in Fig. 3 for all events which were at all close to satisfying the two criteria. F is defined by HGL. It is the volume of the pyramid formed by going out unit distance along each of the three tracks and connecting the end points. It equals zero for coplanarity. The elastic events cluster about the origin. We have applied the same criterion for acceptance as HGL. We find, as they did, that, assuming a fairly broad distribution of quasi-elastic events, statistically one event might be expected to fall in the region of acceptance. As noted, one such event was found and ruled out because of grain density and an electron track. We have made no further correction for this effect.

V. ANALYSIS OF DATA

One of the energies investigated by HGL was 151±7 Mev. This energy is fortuitously the same energy that we have in our plates after correcting the energy obtained from the range curve for the energy loss in the plates and in the absorber used to eliminate protons passing through the analyzing magnet. This made it feasible to get significant data by pooling the results. HGL had no good method of determining directly muon-electron contamination in their beam. They estimated it as (10+10) percent. From this estimate they calculated their track length scanned as 8500±850 cm at this energy. In the process of scanning, we found 453 stars in 14430±450 cm of pion track. This gives us a mean free path for star formation of 31.8±1.9 cm. This value is sufficiently accurate to permit a better determination of the HGL track length from the 260 stars observed by them. Their track length is 8220±700 cm HGL have observed 41 events and we have found 63 which can be counted in the total cross section. These are events found while scanning along track which enters in the total track length. A few additional events are available from a small amount of area scanning done by us, a few found beyond the limits of track measurement and some found while area scanning to relocate events. These additional events are included in the angular distribution. Care was taken to accept only events which would not have been missed regardless of the difficulty of seeing an event in order to prevent biasing the angular distribution.

Since the range of the recoil proton vanishes at a 0° scattering angle for the meson and is less than 5μ at 5°, a lower angle cutoff was taken at this point. Also small angle scatterings from hydrogen can be easily confused with elastic scattering from heavier nuclei if they are noticed at all. A large angle cutoff was taken at 175°, since events beyond this angle could be confused with a chance crossing of tracks, especially if they occurred near another intersection of tracks. These two cutoffs include 0.8 percent of the solid angle. In addition, HGL assume (94±6) percent scanning efficiency. These two corrections amount to 4 percent. The mean free path for elastic scattering of 151-Mev positive pions by protons is thus 0.96(22650±800 cm)/(104±10 events)=209±22 cm. The total cross section is 151±19 millibarns.

The counter value for the total cross section at this energy is 168±4 mb.[7] This value is far beyond our accuracy. Our result is in agreement, although on the low side.

Angular Distribution

There are 56 events from HGL and 70 from our group available for investigation of the angular distribution. The center-of-mass (c.m.) angle has been calculated for each event. The data have been analyzed

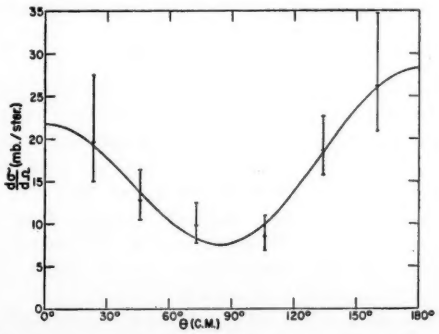

FIG. 4. Angular distribution (c.m.) for 151-Mev positive pions.

TABLE I. Angular distribution of pion-proton scattering: $\pi^{+(-)}+p\rightarrow\pi^{+(-),0}+p(p,n)$. $d\sigma/d\Omega=a+b\cos\theta+c\cos^2\theta$ mb/sterad. a_c, b_c, and c_c are calculated from treatments of α_1, α_3, and α_{33}, under the assumption that the other phase shifts are negligibly small.

E(Mev)	η	a	a_c	b	b_c	c	c_c	Proc.	Ref.
65	0.88	0.89±0.13		−1.38±0.09		0.21±0.36		−0	5
78	0.98	1.9 ±0.3	1.50	−1.7 ±0.4	−2.46	1.6 ±0.9	3.29	++	1
110	1.18	3.6 ±0.7	3.52	−4.8 ±0.8	−4.13	7.5 ±1.9	8.74	++	1
120	1.24	0.49±0.11	0.44	0.34±0.16	0.30	1.16±0.34	1.26	−−	1
120	1.24	0.6 ±0.4	1.20	−1.9 ±0.5	−1.73	3.2 ±1.7	2.53	−0	1
135	1.33	3.9 ±2.3	6.11	−7.1 ±2.8	−4.10	18.0 ±6.8	16.1	++	1
140	1.35	7.5 ±1.8	6.43	−3.7 ±2.3	−3.87	15.1 ±5.5	17.0	++	17
144	1.37	0.82±0.16	0.68	0.73±0.24	0.34	1.52±0.50	2.08	−−	1
144	1.37	1.05±0.5	1.70	−1.9 ±0.5	−1.55	3.9 ±2.0	4.17	−0	1
151	1.41	7.7 ±1.9	7.3	−3.3 ±2.4	−2.96	17.3 ±7.0	19.5	++	
169	1.51	0.64±0.19	0.83	0.47±0.29	0.24	3.04±0.62	2.43	−−	2
169	1.51	1.82±0.72	1.98	−0.61±0.63	−0.61	4.25±2.27	4.87	−0	2
187	1.60	0.81±0.13	0.87	0.35±0.20	0.53	3.08±0.38	2.62	−−	4
187	1.60	1.46±0.24	2.02	−0.16±0.30	0.27	5.63±0.88	5.24	−0	4
194	1.64	1.12±0.24	0.85	0.65±0.62	0.56	2.87±0.80	2.42	−−	2
194	1.64	1.73±0.80	2.42	−0.09±0.74	0.19	5.89±2.61	4.84	−0	2
217	1.76	0.85±0.15	0.71	0.75±0.22	0.65	2.36±0.44	2.06	−−	3
217	1.76	1.36±0.22	1.68	1.23±0.26	1.14	4.82±0.76	4.11	−0	3

by dividing the angular region into six thirty-degree regions. The average differential cross section in each region is calculated on the assumption that the total cross section is 168 mb. A least squares best fit is then made to the assumed angular dependence $d\sigma/d\Omega=(a+b\cos\theta+c\cos^2\theta)$ mb/sterad, where θ is the meson scattering angle in the c.m. system. The results are corrected for the fact that the average value of $d\sigma/d\Omega$ over an interval does not necessarily fall in the center of the interval. The distribution is: $d\sigma/d\Omega=(7.7\pm2.1)-(3.1\pm2.4)\cos\theta+(17.3\pm7.2)\cos^2\theta$ millibarns/steradian. The errors are least-squares errors. The experimental points and the above curve are plotted in Fig. 4. The errors on the experimental points are asymmetric because of the small number of events. A measure of how well the curve fits the points can be obtained by calculating $M=\Sigma_i(\Delta i/\epsilon_i)^2$, where Δi is the deviation of point i from the curve and ϵ_i is the associated standard deviation of the point. A value of $m-n$ is expected when fitting m points with n parameters, i.e., $6-3=3$. The calculated value is $M=0.98$ which is very low. It is seen from this that the curve can be changed considerably and maintain a reasonable agreement with the data. It is obvious that it is not necessary to use another form for the cross section. For example, no D-wave contributions are required.

Phase Shift Analysis

Ashkin and Vosko have devised a graphical method for the analysis of both positive and negative pion-proton scattering differential cross sections assuming only S- and P-wave scattering and charge independence.[9] We have analyzed our data using an algebraic computation derived directly from this method. If we use Fermi's notation, the least-squares solution for the Fermi-type phase shifts gives: $\alpha_3=-26°$, $\alpha_{33}=50°$, and $\alpha_{31}=0°$.

It is very difficult to determine the errors involved in the above phase shifts. An attempt has been made to obtain a least-squares type of error for the above phase shifts by writing down the equations for a, b, and c in terms of the phase shifts. Error equations are derived by expanding the equations in terms of the errors (assumed small) keeping only the first powers. This yields linear equations in the errors. The treatment led to the following errors, which are of doubtful meaning: $\delta\alpha_{33}=9°$, $\delta\alpha_{31}=9°$, $\delta\alpha_2=20°$. These errors are overestimates since the restrictions imposed by the total cross section were not utilized in determining the errors.

There are, of course, Coulomb effects in direct scatterings. Ashkin and Smith[10] and Van Hove[11] have obtained expressions for the differential cross sections including Coulomb effects. The interference term depends strongly on the nuclear phase shifts. The difference in the integrated cross section above 5.5°, the experimental cutoff point in the c.m., system between constructive and destructive interference is about 0.5 percent, which means that several hundred events would be required to detect the effect.

VI. DISCUSSION OF AVAILABLE DATA

Total cross sections for π^+-p scattering have now been measured from energies of 33 to 197 Mev[1,7,12] with accuracies of from 4 to 10 percent. Preliminary data are available up to over 700 Mev.[13,14] Angular distributions for π^+-p scattering extend from 40 Mev to the 151 Mev reported here with an additional rough point at 188 Mev[1,5,8,15–17] and for both direct and exchange

[9] J. Ashkin and S. H. Vosko, Phys. Rev. 91, 1248 (1953).

[10] Ashkin and Smith, O.O.R. Technical Report No. 1, Carnegie Institute of Technology, Februrary 2, 1953 (unpublished).

[11] L. Van Hove, Phys. Rev. 88, 1358 (1952).

[12] S. L. Leonard and D. H. Stork, Phys. Rev. 93, 568 (1954).

[13] S. J. Lindenbaum and L. C. L. Yuan, Phys. Rev. 92, 1578 (1953).

[14] Cool, Madansky, and Piccioni, Phys. Rev. 93, 637 (1954).

[15] J. P. Perry and C. E. Angell, Phys. Rev. 91, 1289 (1954).

[16] Orear, Lord, and Weaver, Phys. Rev. 93, 575 (1954).

[17] Orear, Tsao, Lord, and Weaver, Phys. Rev. 95, 624(A) (1954).

TABLE II. Fermi-type phase shifts taken from the references listed.

Energy (Mev)	α_3	α_{33}	α_1	α_{31}	α_{11}	α_{13}	Ref.
40	−1.75±0.75	+5 ±1	+10±1	0	0	0	6,18
45	−5.7 ±1.2	+4.4±1.1		+2.4±1.8			16
65	−6.2	+9.1	+10.9	−1.9	+0.4	−2.6	5
78	−6	+13		−3			1
120	−15	+30	+9	+4	−3	+2	1
135	−14	+38	+10	+5	−5	+2	1
140	−18	+47		−4			17
151	−26	+50		0			
217	−26	+100	−3	0	0	0	3

π^--p scattering from 40 to 217 Mev.[1-6] Table I lists the published values of the angular distributions measured to date and analyzed on the assumption of only S- and P-wave scattering. The various total π^+-p cross sections have been correlated and plotted as a function of energy in Fig. 5.

The Fermi-type phase shift analyses of the above data are summarized in Table II. These analyses have

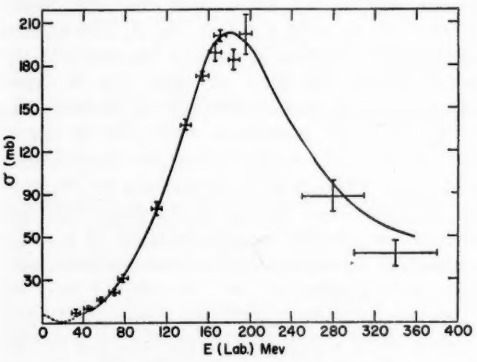

FIG. 5. Total cross section $\pi^+ + p - \pi^+ + p$.

been made by the respective investigators. It is seen that three of the phase shifts, α_{11}, α_{13}, and α_{21}, are all much less than the other three at all energies. The phase shifts α_3, α_1, and α_{23} appear to be the only ones of significance in their effect on the cross sections. The S-wave phase shifts are plotted as a function of η in Fig. 6, and α_{33} is plotted in Fig. 7. η is the relative momentum in the c.m. system in units of $\mu_0 c$, where μ_0 is the reduced mass of the system. Noyes and Woodruff[18] have recently discussed the behavior of the S-wave phase shifts. The very small value of α_3 at 40 Mev and the recent results of Bernardini *et al.*[19] on photoproduction near threshold have led them to predict that α_3 passes through zero in the vicinity of 25–30 Mev and becomes positive at lower energies, a behavior which follows from a Jastrow-type potential. Noyes and Woodruff have assumed simple potential models for the S-state interactions to try to fit the data. The isotopic spin $\frac{3}{2}$ state interaction is represented by an attractive exponential with a hard repulsive core (Jastrow potential) and the $\frac{1}{2}$ state by a simple attractive exponential. Proper choice of well depths and ranges allows a reasonable fit to the observed S-wave phase shifts. The results of this phenomenological treatment by Noyes and Woodruff are plotted in Fig. 6.

Glicksman[3] has recently analyzed his 217-Mev negative-pion data under the assumption that the three small phase shifts are negligible and found that the best fit is obtained by taking α_1 slightly negative. A value of α_1 less than 4 or 5 degrees is consistent with his data. This can be done on a potential model and still retain good agreement with the low-energy data.

An effective range treatment of α_1 has been made from the available data, by assuming that three terms are required in the expansion of $k \cot\alpha_1$, where k is the meson momentum divided by $\hbar$. One may write: $k \cot\alpha_1 = 1/a + \frac{1}{2} r_0 k^2 + P r_0^3 k^4$. The result of the treatment is: $\eta \cot\alpha_1 = 3.0 + 1.2\eta^2 + 1.2\eta^4$. The phase shifts are plotted as curve IV in Fig. 6. The values of the effective range, scattering length and shape dependent parameter are $r_0 = 4.2 \times 10^{-13}$ cm, $a = 0.47 \times 10^{-13}$ cm,

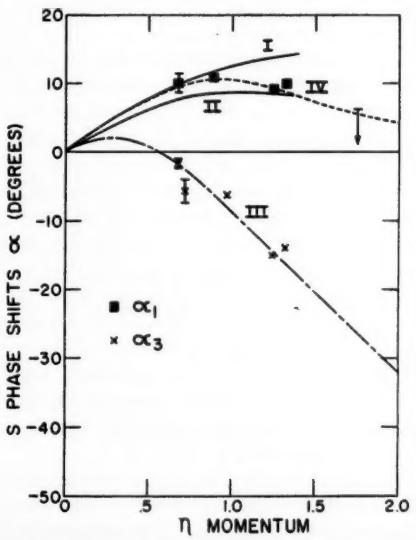

FIG. 6. Phenomenological and empirical treatment of pion-nucleon S-wave phase shifts. I and II. Noyes and Woodruff (reference 18) α_1. III. Noyes and Woodruff (reference 18) α_3. IV. Effective range fit α_1.

[18] H. P. Noyes and A. E. Woodruff, Phys. Rev. 94, 1401 (1954).
[19] G. Bernardini, Phys. Rev. 93, 930 (1954).

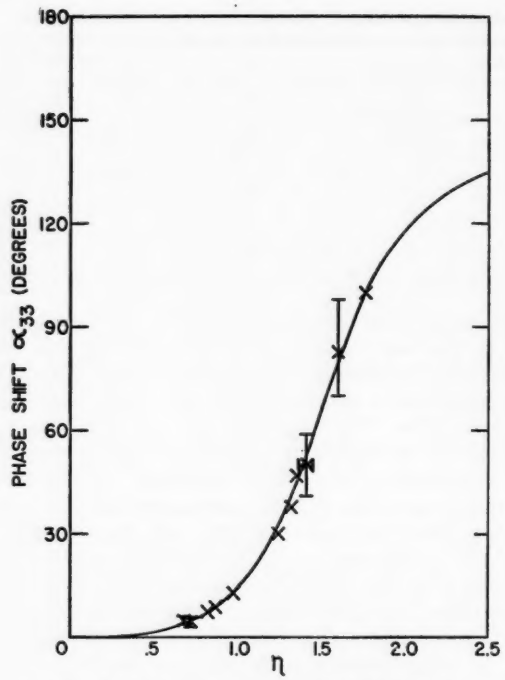

FIG. 7. Calculated values of the $\frac{3}{2}-\frac{3}{2}$ phase shift.

and $P=0.04$. The large value of r_0 and the corresponding large values of the coefficients in the expansion indicate a slow convergence of the series, i.e., the data should be fitted with several more terms. Further terms would have the effect of reducing the effective range and causing α_1 to fall off more rapidly at high energies. This should be kept in mind when better data on α_1 become available.

Brueckner has pointed out that the α_{33} phase shifts can also be subjected to an effective range treatment.[20] Such a treatment for P waves leads to coefficients which are somewhat similar to those defined for S waves. The expansion for $k^3\cot\alpha_{33}$ correct to three terms is written as $k^3\cot\alpha_{33}=a^{-3}-k^2/r_0+Pr_0k^4$. The effective range is again a measure of the range of the potential giving rise to the interaction. The coefficient P is not merely shape-dependent in the case of P-state interactions. It has an inherent energy dependence as a result of the rather sharp spatial dependence of a P-state wave function in the vicinity of the potential. Brueckner has written out an expression for P. The result is that P may be rather large and negative if r_0 is somewhat larger than the scattering length a, since the ratio r_0/a has a critical effect on P.

The α_{33} data presently available have been analyzed on the assumption that three terms are sufficient in the effective-range expansion. The values obtained by Orear, Lord, and Weaver[16] at 45 Mev, the results of Bodansky, Sachs, and Steinberger[5] at 65 Mev, the results of the Chicago group[1-4] from 78 to 217 Mev, and our result at 151 Mev have been subjected to a least-squares analysis. The resultant solution can be expressed as $\eta^3\cot\alpha_{33}=5.0-0.55\eta^2-0.44\eta^4$. The phase shifts calculated from this are plotted in Fig. 7. The results of the Rochester group at 40 Mev are plotted although the analysis was made before obtaining their data. The scattering length, effective range, and correction coefficient are $a=0.82\times10^{-13}$ cm, $r_0=2.55\times10^{-13}$ cm, and $P=-0.24$. The effective range is again somewhat larger than a Compton wavelength, and the convergence is also bad. Again, more terms are probably required, which would possibly lead to a smaller effective range.

Positive-pion cross sections are now available with very good (better than 5 percent) accuracy in the energy range from 40 Mev to 197 Mev as a result of the recent work of Ashkin *et al.*[7] in the energy range above 135 Mev. The total cross section as a function of energy has been calculated from the previously discussed expressions for α_3 and α_{33}. The result is expressed by the solid curve in Fig. 5. The agreement with the cross section is seen to be excellent up to energies above 200 Mev although this is expected since the fit to the phase shifts is good. It does indicate that α_{31} does not contribute noticeably to the total cross section. At the higher energies investigated at Brookhaven,[13,14] there is a tendency for the curve to be high. This can easily be due to the omission of higher terms in the effective range treatment of α_{33} as well as errors in extrapolating the S-wave treatment of Noyes and Woodruff.

As a more severe test of the above treatments of the phase shifts as well as of the legitimacy of neglecting the three "small" phase shifts, the differential cross sections for the various processes have been calculated at all energies above 70 Mev where they have been measured. The columns in Table I to the right of the experimental values of a, b, and c; i.e., a_c, b_c, and c_c are coefficients calculated from the three treatments of the "large" phase shifts, and the assumption that the other three are zero. The data below 70 Mev were not compared in this manner because of the Coulomb effects. The above treatments are calculated from the low energy data so it is to be expected that the agreement would be good in this region. In all, 17 cross sections involving a total of $3\times17=51$ experimental points are involved. Each phase shift introduces three parameters. We are thus fitting 51 points with 9 parameters and expect an M value for the fit of $51-9=42$, where M is as defined previously in discussion of our 151-Mev data. M has been calculated and equals 43.2. It is apparent that the agreement is good.

Concluding Remarks

We arrive at the conclusion that the presently available pion-proton scattering data can be represented well by using only three of the six phase shifts.

[20] K. Brueckner, Phys. Rev. 87, 1026 (1952).

The energy dependence of the phase shifts can be "explained" in terms of simple static potentials. There definitely appears to be a resonance in the state of isotopic and ordinary spin both $\frac{3}{2}$, and the resonant energy occurs near $\eta=1.67$, corresponding to an energy of 200 Mev. No states of higher angular momenta are required up to and including data at 217 Mev, if the Fermi solutions are assumed to be correct.

The low-energy behavior of the S-wave phase shifts may be completely different than described. The low-energy data are still too poor to permit us to say definitely that α_3 changes sign. It is seen in Fig. 5 that the given models predict a dip in the total positive pion-proton cross section in the region from 10 to 30 Mev. It would be difficult to distinguish this from an energy dependence for α_3 in which α_3 remains negative but levels off. However, such a dependence would not give a rise below 10 Mev, and very low-energy total cross sections would be valuable in determining the low-energy behavior of α_3.

At this point it is appropriate to express our indebtedness to the members of the meson scattering group for their assistance and the use of their electronics equipment.

We wish to thank Dr. Jay Orear, Dr. Lederman, Dr. Homa, and Dr. Noyes for sending reprints and for very helpful communications. Professor Gregory Breit contributed a valuable discussion of effective-range theory.

We wish to thank Mrs. R. Cutosky, Mrs. F. Feiner, Mr. J. Morrison, Mr. R. Klein, Mr. G. Stranahan, and Miss J. Kugell for their efficient scanning.

PHYSICAL REVIEW VOLUME 97, NUMBER 3 FEBRUARY 1, 1955

π^--p Interactions at 1.4 Bev*

L. M. Eisberg, W. B. Fowler, R. M. Lea,† W. D. Shephard,‡ R. P. Shutt, A. M. Thorndike, and W. L. Whittemore
Brookhaven National Laboratory, Upton, New York

(Received October 6, 1954)

π^--p interactions have been observed in the hydrogen filling of diffusion cloud chambers exposed to a π^- beam of average energy 1.37 Bev at the Brookhaven Cosmotron. If 9 interactions leading to heavy unstable particles are omitted, there remain 147 interactions observed with magnetic field and 323 interactions without field. The total cross section is estimated to be 34.6±2.7 millibarns. The elastic scattering cross section is 10.0±0.8 millibarns. The elastic scattering angles are mostly less than 60° in the center-of-mass system and are accordingly interpreted as mainly due to diffraction scattering. The observations are consistent with diffraction by a sphere with radius $(1.18\pm0.10)\times10^{-13}$ cm and transparency 0.61±0.10. However, the 20 percent of elastic scattering observed through angles >60° may indicate a region of very strong interaction with radius $\sim0.5\times10^{-13}$ cm surrounded by a region of much weaker interaction. Of the inelastic events only the 95 observed in the magnet cloud chamber can be analyzed further. Of these 71 to 81 are considered to involve the production of one secondary pion and 14 to 24 two pions, depending on the assignment of unidentified inelastic cases. This indicates a slightly greater multiplicity than predicted by Fermi's statistical theory. Angle and momentum distributions of emitted pions are discussed in terms of possible pion-pion interactions and excited nucleon states, but conclusions on these questions are uncertain.

THIS paper reports some results concerning the nature of π^--p collisions at an energy of about 1.4 Bev. It is the second dealing with a preliminary cloud chamber survey of nucleon-nucleon and pion-nucleon interactions at the Cosmotron, the previous one having been concerned with n-p collisions at about 1.7 Bev.[1] The paper on n-p collisions will be referred to as I.

A considerable number of investigations of pion-nucleon interactions have been made at energies up to about 250 Mev,[2] but higher energy experiments have until recently been possible only with cosmic rays, and there are few cases where pions could be identified and their behavior studied.[3] A number of measurements of π-p total cross sections have been made using pion beams at the Cosmotron,[4] and π-p interactions have been studied in nuclear emulsions exposed to a 1.5-Bev π^- beam.[5]

In this experiment π-p interactions are observed in the hydrogen gas filling of diffusion cloud chambers, which are operated in a negative pion beam with average energy 1.37 Bev. (The experimental procedure is described in Sec. II.) Consequently, there is little ambiguity concerning the nature of the interacting particles. The situation is more definite than was the

* Work performed under the auspices of the U. S. Atomic Energy Commission.

† Now at Yale University, New Haven, Connecticut.

‡ Now at University of Wisconsin, Madison, Wisconsin.

[1] Fowler, Shutt, Thorndike, and Whittemore, Phys. Rev. 95, 1026 (1954), henceforth referred to as I.

[2] For summary see Henley, Ruderman, and Steinberger, Ann. Rev. Nuc. Sci. 3, 1 (1953).

[3] See, for example: Camerini, Fowler, Lock, and Muirhead, Phil. Mag. 41, 413 (1950); R. L. Cool and O. Piccioni, Phys. Rev. 87, 531 (1952).

[4] Shapiro, Leavitt, and Chen, Phys. Rev. 92, 1073 (1953); S. J. Lindenbaum and L. C. L. Yuan, Phys. Rev. 92, 1578 (1953); Cool, Madansky, and Piccioni, Phys. Rev. 93, 249 (1954); 93, 637 (1954).

[5] Crussard, Walker, and Koshiba, Phys. Rev. 94, 736 (1954); Walker, Crussard, and Koshiba, Phys. Rev. 95, 852 (1954).

case in I because the π^- beam has a more definite energy than the neutron beam, and the tracks of incident particles are seen. Elastic π^--p scatterings are easily found, while elastic n-p scatterings were not often recorded and were, therefore, ignored in I. One might expect that the theoretical interpretation of π-p interactions would be somewhat simpler than that of n-p interactions, since only one nucleon is present.

I. OBJECTIVES OF THE EXPERIMENT

The experiment described here was intended to give a qualitative picture of the nature of π^--p interactions and, if possible, to provide information on the following specific questions:

1. Production of "new unstable particles." Cosmic ray observations had suggested that many instances of production of heavy unstable particles were due to pions, and it was of interest to attempt to confirm this observation. A few examples of production of such particles in π^--p collisions have been reported in detail.[6] Several more will be discussed in a later paper. This paper will discuss the other π^--p interactions observed.

2. Multiplicity of pion production. As in I, it is of interest to determine the number of cases in which 0, 1, 2, · · · secondary pions are produced in addition to the incoming pion. It was shown in I that two pions are frequently produced in n-p collisions, but there was some indication that one pion may have been emitted from each nucleon involved in the collision. In π^--p collisions only one nucleon is present, so that a comparison of the two results should provide information concerning the mechanism of pion production.

3. Angular distribution of elastic scattering. It should be of interest to compare the angular distribution with that observed at lower energies. In particular, the existence of inelastic interactions should lead to elastic diffraction scattering which would have a characteristic forward angular distribution. Such an effect could, in principle, yield information concerning the size and opacity of a proton.

4. Energy, angle, and charge of emitted particles. In addition to pion multiplicity such detailed information is of interest for comparison with theories of pion production.

5. Angular correlations between emitted particles. Such angular correlations may give evidence of meson-nucleon or meson-meson forces acting between emitted particles. If the forces are strong enough to produce definite intermediate states (as, for example, an excited nucleon with spin and isotopic spin $=\frac{3}{2}$) this condition should be recognized.

II. EXPERIMENTAL PROCEDURE

The observations were made with two diffusion cloud chambers filled with hydrogen at a pressure of about 20 atmospheres, with methyl alcohol as condensable vapor. One group of photographs was taken in a 16-inch diameter chamber provided with a magnetic field of about 10 500 gauss, and a second group was taken in a chamber 6 feet long and 11 inches wide with no magnetic field. The procedure is similar to that followed in I. Details of the cloud chambers have been described.[7]

The π^- beam was selected by a channel about $2\frac{1}{2}$ inches high and 10 inches wide in the Cosmotron shield, placed so that negative pions emitted in a forward direction from the target in the straight section were deflected through the channel by the magnetic field in the following quadrant of the Cosmotron. The channel was one similar to that used by Cool, Madansky, and Piccioni[4] except that the width was greater. 2.2-Bev circulating protons struck a carbon target at a radius of 350 inches. After emerging from the Cosmotron shield the beam was bent through about 16° by an analyzing magnet and allowed to pass through a channel in the 3-foot wall of a concrete block house around the cloud chamber.

Under these conditions the beam has an average momentum of 1.50 Bev/c (kinetic energy 1.37 Bev) as determined by measurements of the momentum of a group of beam tracks in the magnet cloud chamber. These measurements were made by projecting through a prism following Blackett's procedure.[8] The system was calibrated with photographs of ruled curves of known curvature. The momentum spectrum is shown in Fig. 1. The width of the main group is partly due to errors in measurement. Pion trajectories were plotted to determine the expected beam momentum, with results entirely consistent with the cloud chamber

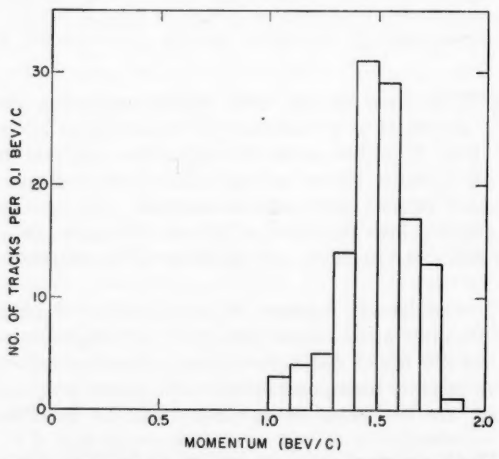

FIG. 1. Momentum spectrum of π^- beam determined from momentum measurements on 117 beam tracks in the magnet cloud chamber.

[6] Fowler, Shutt, Thorndike, and Whittemore, Phys. Rev. **91**, 1287 (1953); **93**, 861 (1954).

[7] Fowler, Shutt, Thorndike, and Whittemore, Rev. Sci. Instr. **25**, 996 (1954).

[8] P. M. S. Blackett, Proc. Roy. Soc. (London) **A159**, 1 (1937).

TABLE I. Types of π^--p interactions considered in this article.

Type	Charge state[a]	Number of secondary pions	Number of prongs	Number of neutral particles
Elastic	$(p-)$	0	2	0
Inelastic (recorded)	$(p-0)$	1	2	1
	$(n+-)$	1	2	1
	$(p-00)$	2	2	2
	$(n+-0)$	2	2	2
	$(p-+-)$	2	4	0
Charge exchange and inelastic (not recorded)	$(n0)$	0	0	2
	$(n00)$	1	0	3
	$(n000)$	2	0	4

[a] For example, $(n+-)$ means that neutron, π^+, and π^- result from the collision.

value, when energy loss in passing through the Cosmotron wall was taken into account. Since the channel is fairly wide, the plotted trajectories also indicate a momentum spread of about ± 0.1 Bev/c. The low-energy tail presumably results from pions that scatter from the channel walls or have unusually large energy loss in passing through the wall of the Cosmotron vacuum chamber. The *average* momentum of 1.50 Bev/c has an uncertainty of about ± 0.05 Bev/c. The "beam" contains tracks within an angular spread of ± 5 degrees for the magnet chamber, and $\pm 4°$ for the long chamber. Tracks outside this range were omitted in all instances.

About 28 000 Cosmotron pulses were photographed with the magnet chamber and about 14 000 with the 6-foot chamber. The pictures were scanned for deflections or interactions of beam tracks. Disappearances-in-flight were occasionally noted, but no attempt was made to scan for them, since in scanning it was difficult to distinguish them from tracks leaving the sensitive region or entering gaps, and since their interpretation would be ambiguous in any case (see Table I). Angles were measured in space relative to the incoming pion direction, using projectors that reproduced the geometry of the cameras. Curvatures were measured with a micrometer stage microscope. Momenta are corrected, when appropriate, for optical distortion, magnification, and for velocity parallel to the magnetic field, but the measurements are not accurate enough to justify detailed corrections for conical projection.

If one assumes that the frequency of events with the production of three or more secondary mesons is negligible, the events to be expected are as listed in Table I. Events resulting in heavy unstable particles are omitted.

The $(p-+-)$ events are easily recognizable because they are the only type with four emerging prongs. The elastic events can be identified by the fact that emergent tracks are coplanar, and angles and momenta have the values required to conserve energy and momentum.

The identification of the inelastic $(p-0)$, $(n+-)$, $(p-00)$, and $(n+-0)$ events is more difficult, however, since they all involve two prongs whose energy and momentum fail to balance because of the presence of one or more neutral particles. There is no practical means of distinguishing between these possibilities unless there is a magnetic field so that momenta can be measured. In principle measurement of the momentum and density of ionization of the positive tracks would determine which were protons and which pions, while conservation of momentum and energy would determine unambiguously whether one or more neutral particles were involved. In practice our measurements are not usually accurate enough to do so, and some element of uncertainty is present as to the classification of the events. The details of the procedure used in classifying them are given in Sec. V.

III. TOTAL CROSS SECTION

This experiment provides a direct measurement of the total cross section from the number of scattering events observed and the pion path length. The best way to determine the total pion path length is by counting π-μ decays, as was done at lower energies.[9] The largest possible deflection resulting from π-μ decay for a 1.4-Bev π meson is 1.54°. This angle is too small to be discovered with any degree of certainty in the magnet chamber photographs. The photographs of the long cloud chamber, however, were scanned with a distorted projected image which magnified small angles by a factor of about five, and π-μ decays could be observed easily. Consequently the path length for data taken with the long chamber could be determined by the π-μ count, while it was necessary to count beam tracks in the magnet chamber photographs. The two estimates are, therefore, discussed separately.

With the magnet chamber corrections are necessary for beam contamination, inefficiency in scanning, and interactions having all neutral prongs, which were not recorded. To obtain an accurate total cross section, it is necessary to determine the corrections for these effects carefully. We have only made rough estimates of these corrections, so that the resulting value for the total cross section is correspondingly approximate.

The length of beam tracks in the magnet chamber pictures was measured in every 50th picture in every other 100-foot roll of film, counting all tracks that had entry angle within $\pm 5°$ of the average beam direction, and momentum that was not obviously incompatible with 1.50 Bev/c. From the average track length per picture and total number of pictures taken, the total track length was estimated to be 17 000 g/cm^2 of H_2. The muon contamination is probably higher than the 5.4 percent determined by Cool, Madansky, and Piccioni[4] because of the wider channel, and a few low energy tracks probably were included. An estimate of (15 ± 10) percent seems reasonable for the beam contamination as the beam was defined here.

[9] Fowler, Fowler, Shutt, Thorndike, and Whittemore, Phys. Rev. 91, 135 (1953).

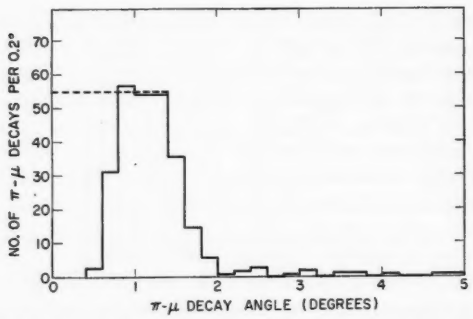

FIG. 2. Distribution of projected angles of π-μ decay deflections. A cut-off angle of 1.54° corresponds to a pion energy of 1.4 Bev. The dashed line represents an extrapolation to zero angle.

The actual number of interactions observed was 151, (including 4 events resulting in heavy unstable particles which must be included in the total cross section). The number of unrecorded zero prong events (resulting in neutral particles only) was estimated as 22, as described in Sec. IV, leading to a total of 173 interactions. The scanning procedure was certainly not 100 percent efficient. In fact, a "fast scanning" procedure was used for most of the magnet chamber pictures, which involved only area scanning and no repeated scanning. Consequently, there was no experimental determination of the efficiency. On the basis of previous experience it seems appropriate to assume an efficiency of (80±10) percent under these circumstances. With all these corrections taken into account, the cross section obtained is 25±6 millibarns.

A more reliable value is found with the long chamber. Here it has been possible to determine the intensity of the incident pions directly by counting the number of π-μ decays observed.[9] In this manner the effect of beam contamination is eliminated. Also the scanning efficiency is of little importance since it has been determined that in general the chances for missing π-μ decays and scattering events are about equal.

A total of 532 π-μ events were observed. Their distorted *projected* angles were converted to actual values. The distribution of projected π-μ decay deflections is shown in Fig. 2. Ideally this distribution should be constant and be cut off sharply at the largest possible π-μ decay angle. Actually the distribution appears to be flat only between 0.8° and 1.4°. Above 1.4° it falls off fairly rapidly to a negligibly small value at 1.8°. Cut-off angles between 1.4° and 1.8° correspond to a pion momentum spectrum between 1.7 and 1.3 Bev/c, respectively, in agreement with the magnetically measured spectrum given in Fig. 1. Deflections below 0.8° were often missed as seen in Fig. 2. A correction is made by extending the distribution to zero angle as indicated by the dashed line in Fig. 2. The integral under the distribution represents the total number of π-μ decays that should have occurred inside the chamber and gives a value of 903±50 cases. As previously[9] the lifetime of the pions is taken to be 2.55×10^{-8} sec.

The absolute hydrogen pressure was 21.3 atmos, and the average temperature −40°C. A total of 323 π^--p collisions with two or four emitted prongs were found in the hydrogen. From the given data a cross section of 32.4±2.3 millibarns would follow. However, closer inspection of the ratio of the number of interactions to the number of π-μ decays in different locations in the chamber shows that near the ends of the chamber too few π-μ decays were found since there either the incident π or the outgoing μ track became so short that the relatively small deflections could not be observed reliably. Omitting all events occurring in the regions near the ends, one is left with 452 π-μ decays and 250 interactions. These values lead to a more reliable cross section of 29.7±2.4 millibarns. Adding 5 events showing production of heavy unstable particles not yet included results in a cross section of 30.3±2.5 millibarns. To obtain the total cross section we have again the estimated correction, amounting to 14.6 percent, for the zero-prong events which were not recorded. (See Sec. IV). The final value for the total π^--p cross section at 1.4 Bev is 34.6±2.7 millibarns, in good agreement with the value of 34±3 millibarns obtained by counter methods.[4] We feel that the magnet chamber result of 25±6 millibarns involves no real discrepancy in view of the uncertainties in the correction factors. (Actually the counter value was obtained at a slightly higher pion energy than that of our beam, but probably the π^--p cross section varies very slowly in this energy region.)

Conversely, one might conclude that the difference between the counter value of 34±3 mb and our value of 30.3±2.5 mb is due to the reactions resulting in neutral particles only, such as charge exchange, (n0), and the inelastic reactions (n00) and (n000). The cross section for these reactions is then 3.7±3.7 mb, which is quite small compared to the value of 30.3 mb for reactions resulting in charged prongs. This is quite different from the observations on π^--p collisions at lower energies (<200 Mev) where up to twice as much charge exchange scattering as ordinary scattering has been observed.

IV. ELASTIC EVENTS

It is often difficult to be sure to which one of the inelastic classes a particular event belongs, even when observed in the magnet chamber, but the criteria described in Sec. II usually make it fairly clear whether an event is elastic or inelastic. Any event for which the observations were consistent, within errors, with the specifications of an elastic event was classified as "elastic."[10] The remainder were considered to be inelastic. They are discussed in Sec. V.

[10] In many cases, of course, the errors of measurement were great enough that one could also devise an inelastic event that would fit them. It seems unlikely, however, that inelastic events

With this procedure 52 events were classed as elastic and 95 as inelastic in the magnet chamber, or 35.4 percent were elastic. The distribution of the angles through which pions were scattered in the elastic events is given in Table II, columns 1 and 2. Here ΔN is the number of angles observed in the angular interval $\Delta\theta$ in the laboratory system. The majority of the elastic scatterings are at angles less than 30°, which implies that the differential cross section is very strongly peaked in the forward direction.

In the long chamber 110 events were classed as elastic and 213 as inelastic. Thus 34.0 percent were elastic, in agreement with the magnet chamber data. The distribution of the scattering angles from the 110 elastic events is given in Table II, columns 3 and 4. Comparison of columns 2 and 4 shows that the distributions for the two chambers agree within the statistical uncertainties. We shall, therefore, lump the data together for the further discussion of the elastic events.

Both distributions lack events with scattering angles $<5°$. Few are expected because of the small available solid angle. A reasonable distribution should result in ≥ 9 percent scattering into angles $\leq 5°$. Instead we find zero percent for the magnet chamber, and 4 ± 2 percent with the long chamber. An interference effect due to Coulomb scattering is not an explanation for the discrepancy since at the present high energies Coulomb scattering becomes important only at scattering angles $<1°$. The discrepancy might be entirely due to statistical fluctuations. In addition, in the magnet chamber, where "area scanning" only was employed, a small deflection might be missed even though a heavily ionized recoil proton should emerge at the point of deflection, since a short proton track might not make itself too apparent among heavily ionized background tracks. In the long chamber a few small angle scatterings may have been counted as π-μ decays.

TABLE II. Distribution ($\Delta N/\Delta\theta$) of elastic scattering angles in the laboratory system.

$\Delta\theta$ (Degrees)	(1) Magnet chamber ΔN	(2) Magnet chamber %	(3) Long chamber ΔN	(4) Long chamber %
0–5	0	0	4	4±2
5–10	12	23±7	32	29±5
10–15	15	29±7	25	23±5
15–20	8	15±5	15	14±4
20–25	6	11±5	6	5±2
25–30	2	4±3	3	3±2
30–60	4	8±4	7	6±2
60–90	3	6±3	7	6±2
90–120	2	4±3	8	7±2
120–150	0	0	2	2±2
150–180	0	0	1	1±1
Total	52	100	110	100

would often disguise themselves as elastic ones in view of all the other possibilities at their disposal. Thus any event which could be elastic is considered actually to be elastic, so that one obtains an upper limit for the number of elastic scatterings, but this upper limit is probably close to the true number.

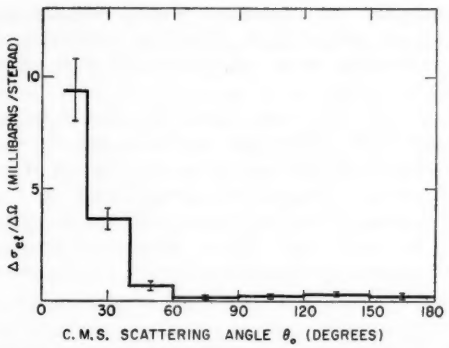

FIG. 3. Center-of-mass angular distribution of all elastic scattering events from magnet and long chambers. Data from the interval $\theta_0 = 0 - 10°$ are omitted.

We shall make use only of the data for angles $\geq 5°$ in the laboratory system. The combined elastic scattering distribution $\Delta\sigma_{el}/\Delta\cos\theta_0$ in the c.m. system is given in Fig. 3.

Since there are a large number of inelastic events and the elastic scatterings are largely confined to forward angles, it seems natural to conclude that the elastic scattering is largely a diffraction scattering effect, which is a consequence of the inelastic scattering. Such diffraction scattering is a necessary consequence of the inelastic interactions.[11] If there is a "reaction" cross section for an incoming wave of certain angular momentum, then a partial cross section for diffraction scattering for that angular momentum follows from quantum mechanics.

The role of diffraction scattering is clear if one considers pion-nucleon collisions to occur in a way similar to that involved in Fermi's statistical theory of meson production. There is assumed to be a region of strong interaction about the nucleon with radius of about 10^{-13} cm. Since $\lambda\!\!\!^{-}_0$ (in c.m. system) for the pion is about 2.7×10^{-14} cm, we may consider it either to hit this region and interact or miss it and fail to do so. If it hits, the region may then emit two or more pions, in which case the process is obviously a "reaction," or it may re-emit one pion as an elastic scattering. In the latter case the event should be counted as a "reaction" if the emitted pion is considered to arise from a truly "thermal" process so that its phase is random with respect to the incoming pion and cannot interfere with it (incoherent elastic scattering). In this case any pion which hits the strongly interacting region undergoes a "reaction" and there should be an equal number of elastic diffraction scatterings.

If, however, the events in which a single elastic pion is emitted from the region of interaction are considered to arise from "potential scattering," they should not be counted as "reactions," but one should

[11] See, for example, J. M. Blatt and V. F. Weisskopf, *Theoretical Nuclear Physics* (John Wiley and Sons, Inc., New York, 1952), Chap. VIII.

then consider the interference of such outgoing waves with those arising from diffraction scattering. The picture becomes more complicated for such coherent elastic scattering.

It is clear that some distinction should be made between elastic diffraction scattering and the elastic scatterings predicted in the statistical theory. It seems reasonable to interpret the forward peak of Fig. 3 as diffraction scattering (up to $\sim 60°$ in c.m. system), while the large angle elastic events are thought to arise through the statistical process. One interesting qualitative observation can now be made: that the number of elastic cases is considerably less than the number of inelastic ones, and therefore, the region in which the interaction is so strong as to establish thermal equilibrium is rather transparent to the incident pions, a situation which seems inconsistent.

To make the situation more specific we will develop a phenomenological picture of a proton as a partially transparent sphere using the methods commonly applied to nuclei.[12] If we assume that the sphere is a purely absorbing one (resulting in incoherent reactions only), we can determine the size of the sphere from the reaction cross section σ_a, and diffraction cross section σ_d, using Bethe and Wilson's curve for $k_1\lambda=0$. (Here k_1 depends on the size of the potential, if one is present, and λ is the mean free path in nuclear matter, assumed to be zero in the "thermal" picture.)

We have observed a total of 33 scatterings through c.m. system angles greater than 60° which should be counted toward σ_a following the "thermal" model. Since in the purely statistical model the angular distribution for incoherent scattering is assumed to be isotropic, a statement with which Fig. 3 is not inconsistent, we will add 11 more events from the $\theta_0=0$ to 60° interval, giving 44 incoherent scatterings. (Solid angle for $\theta_0=0$ to 60° is $\frac{1}{4}$ of solid angle for $\theta_0=0$ to 180°.) There were also the 9 events resulting in production of heavy unstable particles.[6] In addition, an allowance must be made for unrecorded events ($n0$), ($n00$), and ($n000$). An estimate was made using statistical weights calculated by Fermi[13] and the observed numbers of inelastic events resulting in charged particles from Part V, leading to 70 unobserved events.[14] The total number of diffraction scatterings is then $162-44=118\pm15$, and the total number of reactions is $308+44+9+70=431\pm20$. If we now divide the total cross section of 34 millibarns in this proportion, we obtain $\sigma_a=26.7\pm1.3$ millibarns, $\sigma_d=7.3\pm1.0$ millibarns. These values are consistent[12] with a radius, $R=(1.18\pm0.10)\times10^{-13}$ cm, and transparency $=\sigma_a/\pi R^2=0.61\pm0.10$. One can make a rough estimate of the angular distribution expected by using the Bessel function formula[12] applicable to an opaque sphere. Taking $R=1.18\times10^{-13}$, one obtains the expected distribution given by the curve in Fig. 4. A better estimate might be obtained by treating the proton as a transparent sphere, in which a pion mean free path of $\lambda=1.5\times10^{-13}$ cm corresponds to the observed transparency. Using the methods of Fernbach, Serber, and Taylor[12] one obtains a distribution that differs very little from that for the opaque sphere. The observed diffraction scattering distribution also given in Fig. 4 seems to be somewhat weighted toward larger angles, but the discrepancy hardly seems significant.

Perhaps the most important experimental deviation from the "thermal" model, postulating a sphere of radius R with very strong interaction, lies in the fact that the amount of diffraction scattering is less than $\frac{1}{3}$ the amount of incoherent interaction. An alternate treatment might be to interpret *all* of the observed elastic scattering as due to coherent scattering from

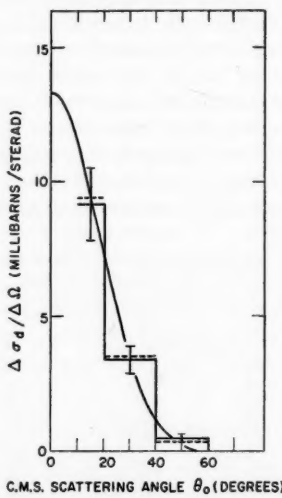

FIG. 4. Center-of-mass distribution of elastic scattering events considered to be due to diffraction scattering. Here all large-angle scattering events have been treated as incoherent. The dashed lines give the average values of the theoretical curve, corresponding to the intervals used for plotting the experimental data. The derived radius of interaction of $R=1.18\times10^{-13}$ cm was used.

[12] Fernbach, Serber, and Taylor, Phys. Rev. **75**, 1352 (1949); H. A. Bethe and R. R. Wilson, Phys. Rev. **83**, 690 (1951).

[13] E. Fermi (private communication).

[14] These weights were calculated making use of the hypothesis of charge independence. Within each state of multiplicity the probabilities for the different reactions are then given. (See Table I.) A π^--p collision can proceed through the isotropic spin $T=\frac{1}{2}$ or $\frac{3}{2}$ state. In Fermi's statistical calculation the results from these two states were mixed in the ratio 2:1, respectively. If only elastic and charge exchange scattering occurred, the correction for ($n0$) would depend very strongly on whether or not the reaction really proceeds according to this ratio, since for $T=\frac{1}{2}$ twice as much elastic as charge exchange scattering is expected while this ratio is reversed for $T=\frac{3}{2}$. Since, however, mostly single meson production is observed (Sec. V), the correction should mostly take into account the reaction ($n00$), which amounts to 17 percent of all single meson production for $T=\frac{1}{2}$, to 13 percent for $T=\frac{3}{2}$, and to 16 percent for the mixture used by Fermi. Thus the correction of 70 for the unobserved events should not depend much on the initial isotopic spin state. That a correction of this magnitude really applies has also been shown in Sec. IV, where its application brought about agreement between cloud chamber and counter values. (The excited nucleon model also leads to corrections of the given magnitude.)

a sphere within which the interaction varies from very strong near the center to rather weak at the outside. The observed scattering through large angles ($\theta_0 = 60°$ to 180°) would then be due to interactions occurring near the center (s- and perhaps p-waves, $L=0, 1$), while most of the observed forward scattering would come from the outer regions ($L=2, 3, 4$). For instance, a calculation shows that making the mean free path in nuclear matter $\lambda \approx 0$ for $L=0, 1$, and $\lambda \approx 5\times10^{-13}$ cm for $L=2, 3, 4$ (up to a radius $R=1.4\times10^{-13}$ cm) would result in the observed cross section $\sigma_{el}=10$ millibarns, $\sigma_{inel}(=34-\sigma_{el})=24$ millibarns, and would also give a large angle tail similar to the observed one. Of course, instead of a step function for λ, some continuous function can also be used to give a similar result. Such a function might, for instance, be similar to the Yukawa potential which indeed gives an average interaction ~20 times stronger in the region $L=0, 1$ than in the region $L=2, 3, 4$. If "potential scattering" were admitted we would have to use complex phase shifts instead of the purely imaginary ones used so far, and other possibilities exist to fit the observed data. One such possibility is to assume $\lambda \approx 4\times10^{-13}$ cm = constant in a sphere with radius $R=1.4\times10^{-13}$ cm and to have a potential well with depth ~500 Mev in the region $L=0, 1$.[15] Very probably, however, such an elementary picture is much oversimplified, particularly in the light of the known difficulties at relativistic energies. Nevertheless, the fact remains that all of the experimental data can be accounted for by the assumption of a very strongly interacting region with average radius $\sim5\times10^{-14}$ cm and a surrounding much more weakly interacting region up to $R\approx1.4\times10^{-13}$ cm.

V. PION MULTIPLICITIES AND CHARGE STATES

Of the charge states listed in Table I, the $(p-)$ and $(p-+-)$ are definitely identified as described in Sec. II. With the long chamber no further distinction can be made. With the magnet chamber pictures one can classify inelastic events as $(p-0)$ or $(n+-)$, $(p-00)$ or $(n+-0)$, but the problem is more difficult, and it is necessary to follow a procedure somewhat like that used in I for the classification of n-p interactions. In the π^- case, however, the incident energy is known, which makes the analysis of cases with one outgoing neutral particle somewhat more definite, and makes it possible to try to determine whether two outgoing neutral particles are involved. The following discussion refers only to magnet chamber events, except where noted explicitly.

In analyzing the events the first problem is to try to identify the positive track as a π^+ or proton. All events were analyzed on this basis, without considering identification as a K^+ a possibility, since there should be few K^+ particles. In some cases the positive track could be identified by density of ionization and momentum. In some additional cases tracks at angles greater than 75° could be identified as π^+ since protons cannot be emitted at such large angles from inelastic events.[16] In addition, a proton emitted at an angle close to the maximum must be denser than minimum, so the limiting angle can be made a few degrees smaller for minimum tracks.

If the positive track is identified as a proton and both momenta are measured, then the mass of a single neutral particle can be calculated, in principle, by:

$$M_4=(E_4^2-p_4^2)^{\frac{1}{2}}, \tag{1}$$

$$E_4=E_1+M-E_2-E_3, \tag{2}$$

$$\mathbf{p}_4=\mathbf{p}_1-\mathbf{p}_2-\mathbf{p}_3. \tag{3}$$

Here E_1, p_1 are total energy and momentum of the incident π^-, E_2, p_2; E_3, p_3 are total energy and momentum of the two outgoing tracks; E_4, p_4 are those of the neutral particle. M is mass of struck proton. If one obtains $M_4=0.14$ Bev, or can obtain such a result by adjusting p_2, p_3, and the angles of these tracks within their experimental errors, the event is classed as $(p-0)$. If, however, one cannot select values within the experimental errors that give $M_4=0.14$, but only higher values of M_4, the event must be classed as $(p-00)$. (The two π^0's carry off more total energy than corresponds to their resultant momentum, and so, in general, would be expected to appear like a single particle of higher mass.) If either $M_4=0.14$ or $M_4=0.28$ was possible within the errors of measurement on 2 and 3, the event was classed as $(p-0)$ because it is unlikely that there would really be two π^0's going with the same velocity in so nearly the same direction that their total energy and momentum would closely resemble a single π^0. If, however, either p_2 or p_3 is measured poorly, it may not be possible to determine whether the event is $(p-0)$ or $(p-00)$. Each event must be considered as an individual case.

If the positive track is identified as a proton, and only one outgoing momentum measured, say p_2, then various choices of p_3 are tried. In each case p_4 is then determined by Eq. (3), and assuming the event is $(p-0)$, $E_4=(p_4^2+0.14^2)^{\frac{1}{2}}$. If this value of E_4 satisfies Eq. (2) within ±0.05 Bev, that value of p_3 is considered to give a satisfactory solution as a $(p-0)$ event. If $E_1+M>E_2+E_3+E_4$, an additional π^0 is required. In most cases values of p_3 could be chosen appropriate to either $(p-0)$ or $(p-00)$ classifications.

If the positive track is identified as a π^+, the corresponding calculations are made to test whether the event should be classified as $(n+-)$ or $(n+-0)$.

If the positive track is not identified, and one or

[15] There are several theoretical mechanisms to produce such large forces of very short range. Short-range forces have been treated by R. Jastrow [Phys. Rev. 81. 165 (1951)] and related to pion field theory by M. M. Lévy [Phys. Rev. 88, 725 (1952)] and S. D. Drell and E. M. Henley [Phys. Rev. 88, 1053 (1952)]. Other suggestions involve heavy particles, such as K-mesons, etc.

[16] R. M. Sternheimer, Phys. Rev. 93, 642 (1954).

TABLE III. Classification of inelastic events.

$(p-0)$	16
$(p-00)$	1
$(p-0)$ or $(p-00)$	6
$(n+-)$	8
$(n+-0)$	6
$(n+-)$ or $(n+-0)$	23
$(p-+-)$	4
"unidentified inelastic"	31
Total	95

both momenta are measured, all four possibilities must be considered and an attempt made to see whether any of them is more or less consistent with the observations than the others.

If the positive track is not identified and neither momentum measured, the event is simply classed as "unidentified inelastic" and no calculations made.

Table III shows a breakdown of inelastic events. The "unidentified inelastic" category includes all those which could be classified in either of two or more classes except for the possibilities "$(p-0)$ or $(p-00)$" and "$(n+-)$ or $(n+-0)$" which are tabulated explicitly. For example, an event which could be $(p-0)$ or $(n+-)$ or $(n+-0)$ would simply be tabulated as "unidentified inelastic."

There are certainly some cases in which two secondary pions are produced, a total of 11 being listed. The number classified as single secondary pion cases is 24, the number that are uncertain is 60. Under these conditions one cannot say much concerning the frequency of double pion production.[17] If one simply apportions the uncertain cases in the same ratio as the classified ones, i.e., $24/7=[(p-0)+(n+-)]/[(p-00)+(n+-0)]$, one obtains totals of 71 single pion cases and 24 double pions. On the other hand the most reliable double pion cases are the $(p-+-)$, which are rare. If one makes the $(p-+-):(p-00):(n+-0)$ ratio fit the Fermi statistical weights[18] of 1.4:1:2.3 one would infer that since only $4(p-+-)$ were observed, there should be about $3(p-00)$ and $7(n+-0)$, with the remaining 81 cases all single pion production.[18]

These numbers should be compared with the frequency of zero pion production cases, leaving out those due to diffraction scattering, that is, to the large-angle elastic scatterings, of which there were 9 with $\theta_0>60°$, or 12, correcting for those with $\theta_0<60°$, assuming isotropic distribution. This is done in Table IV, for the usual nucleon radius of $R=1.4\times10^{-13}$ cm and also for the $R=1.18\times10^{-13}$ cm derived in Sec. IV, which is more consistent with this experiment. The figures given for the statistical theory are based on an approximation in which pions are taken to be extremely relativistic, and it is probable that more exact calculations such as those of Yang and Christian[19] would favor lower multiplicities. The discrepancy between observation and statistical theory does not seem to be as striking as in I, however.

TABLE IV. Number of cases with different pion multiplicities.

No. of pions	Uncertain inelastic divided proportionately	Division based on No. of $(p-+-)$	Statistical theory $R=1.4\times10^{-13}$ cm	Statistical theory $R=1.18\times10^{-13}$ cm
0[a]	12	12	22	34
1	71	81	65	61
2	24	14	20	12

[a] Omitting diffraction scattering cases.

The division between $(p-0)$ and $(n+-)$ events is also of interest. Using the Fermi statistical weights the ratio $(p-0)/(n+-)$ is 17/21, but if it is assumed that the reaction goes through an intermediate excited state with $T=\frac{3}{2}$ the ratio is decreased to 37/76. Using the estimate of 3 $(p-00)$ and 7 $(n+-0)$ one gets correspondingly 20 $(p-0)$ and 30 $(n+-)$, with ratio 0.67, which could be consistent with either predicted ratio, so no decision is possible. The predicted ratio $(p-+-):(p-00):(n+-0)$ for the reaction going

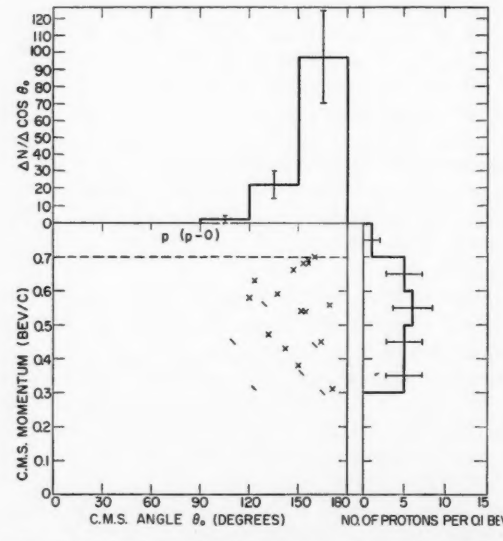

FIG. 5. Center-of-mass scatter diagram of the protons from the reaction $(p-0)$. At the top the differential angular distribution of the protons is plotted, and at the right their momentum distribution. The dashed line in the scatter diagram shows the maximum c.m. system momentum for protons. Events identified as probable $(p-0)$ are plotted as oblique crosses (×). Events identified as $(p-0)$ or $(p-00)$ are plotted as oblique lines (\), using angles and momenta that fit the $(p-0)$ possibility.

[17] The reason why it is harder to determine the double to single ratio here than in I is that in the events studied in I the single pion cases had no neutral particles emerging, the double pion cases one neutral. Here one must distinguish between one neutral and two neutrals, which is much harder.

[18] In the long chamber 6 $(p-+-)$ events were observed in the total of 323 events. This would correspond to ~3 events in the present 147 obtained with the magnet chamber, in agreement with the four actually found.

[19] C. N. Yang and R. S. Christian, Brookhaven internal report (unpublished).

through an intermediate $T=\frac{3}{2}$ state is 78:55:115 which is not appreciably different from that based on Fermi's statistical weights, so the double meson production cases could not be used to decide this question.

VI. DISTRIBUTIONS OF ANGLES AND MOMENTA OF INELASTIC EVENTS

The angular distribution of elastic scatterings has been discussed in Sec. IV. We now consider the angles and momenta of the particles emitted in inelastic events. Unfortunately, there are not very many events which provide useful information, since momentum measurements on the "unidentified inelastic" are incomplete or nonexistent. Furthermore, whenever there are two neutral particles, as in $(p-00)$ or $(n+-0)$, the angles and momenta of the neutral particles cannot be

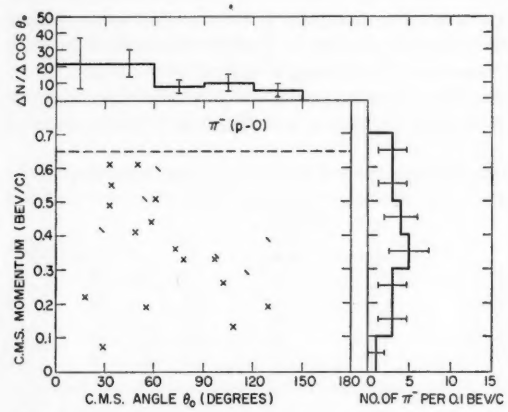

FIG. 6. Center-of-mass scatter diagram of the π^- from the reaction $(p-0)$. At the top the differential angular distribution of the π^- is plotted, and at the right their momentum distribution. The dashed line in the scatter diagram shows the maximum c.m. system momentum for π^-. Events identified as probable $(p-0)$ are plotted as oblique crosses (×). Events identified as $(p-0)$ or $(p-00)$ are plotted as oblique lines (\), using angles and momenta that fit the $(p-0)$ possibility.

determined unambiguously from energy and momentum balance. As a result it does not seem worth while to analyze distributions of angles and momenta except for $(p-0)$ and $(n+-)$ events.

There is still an element of uncertainty in the events classed as "$(p-0)$ or $(p-00)$" and "$(n+-)$ or $(n+-0)$" in Table III. According to the discussion presented in Sec. V it is probably most reasonable to think that most of these events are $(p-0)$ or $(n+-)$ respectively, since the number of $(p-+-)$ events is small. We have included all "$(p-0)$ or $(p-00)$" events as $(p-0)$ in the angle and momentum distributions, and all "$(n+-)$ or $(n+-0)$" as $(n+-)$, since it is not possible to tell which of them should be excluded. The same procedure was followed by Crussard, Walker, and Koshiba in analyzing events found in emulsions.[5] One should remember, however, that a few cases of mistaken identity are, no doubt, included.

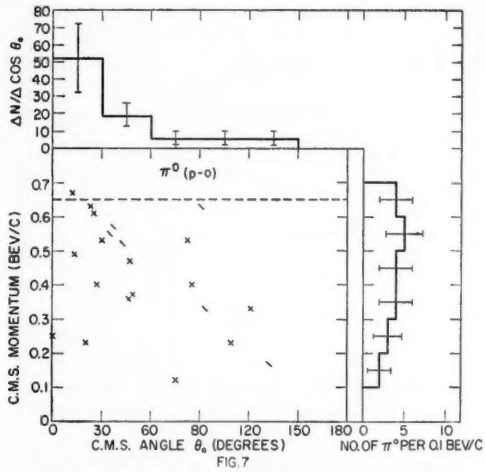

FIG. 7. Center-of-mass scatter diagram of the π^0 from the reaction $(p-0)$. At the top the differential angular distribution of the π^0 is plotted, and at the right their momentum distribution. The dashed line in the scatter diagram shows the maximum c.m. system momentum for π^0. Events identified as probable $(p-0)$ are plotted as oblique crosses (×). Events identified as $(p-0)$ or $(p-00)$ are plotted as oblique lines (\), using angles and momenta that fit the $(p-0)$ possibility.

The data are summarized by the scatter diagrams shown in Figs. 5–10 which plot momentum *vs* angle in the center-of-mass system. In analyzing these data one must note that the selection of events has introduced a bias in favor of events in which the positive particle goes backwards in the center-of-mass system. If the positive particle (p or π^+) goes forward in the c.m.

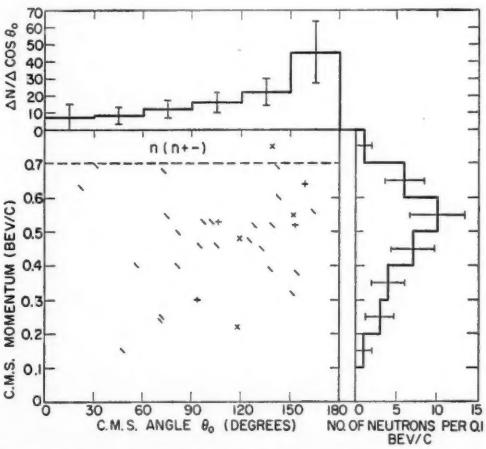

FIG. 8. Center-of-mass scatter diagram of the neutrons from the reaction $(n+-)$. At the top the differential angular distribution of the neutrons is plotted, and at the right their momentum distribution. The dashed line in the scatter diagram shows the maximum c.m. system momentum for the neutrons. Events identified as definite $(n+-)$ are plotted as vertical crosses (+), those identified as probable $(n+-)$ as oblique crosses (×). Events identified as $(n+-)$ or $(n+-0)$ are plotted as oblique lines (\), using angles and momenta that fit the $(n+-)$ possibility.

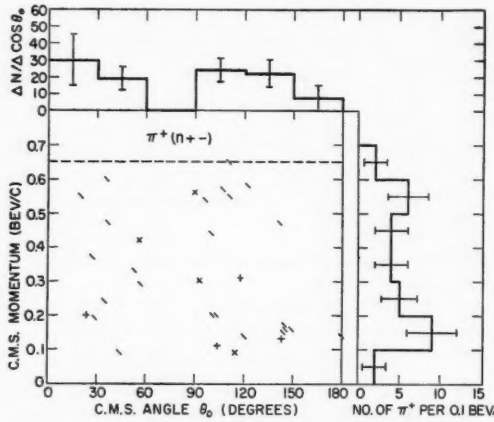

FIG. 9. Center-of-mass scatter diagram of the π^+ from the reaction $(n+-)$. At the top the differential angular distribution of the π^+ is plotted, and at the right their momentum distribution. The dashed line in the scatter diagram shows the maximum c.m. system momentum for the π^+. Events identified as definite $(n+-)$ are plotted as vertical crosses (+), those identified as probable $(n+-)$ as oblique crosses (×). Events identified as $(n+-)$ or $(n+-0)$ are plotted as oblique lines (\) using angles and momenta that fit the $(n+-)$ possibility.

system, its laboratory momentum is usually so high that it is not possible to tell whether it is p or π^+. Such events are classed as "unidentified inelastic" and not included. This bias probably accounts for the backwards preference of the $\pi^+(n+-)$[20] and to some extent for the sharp backwards peak for $p(p-0)$.

Even allowing for this bias, however, it seems that the angular distributions show a backward preference

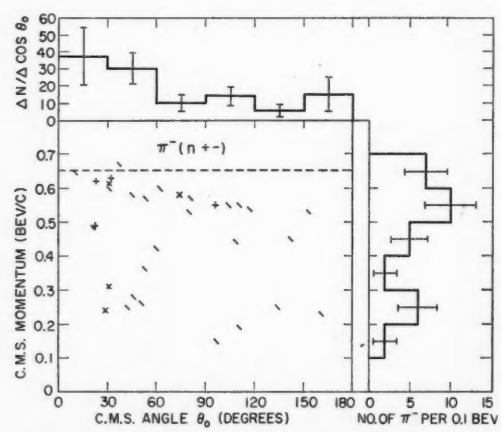

FIG. 10. Center-of-mass scatter diagram of the π^- from the reaction $(n+-)$. At the top the differential angular distribution of the π^- is plotted, and at the right their momentum distribution. The dashed line in the scatter diagram shows the maximum c.m. system momentum for the π^-. Events identified as definite $(n+-)$ are plotted as vertical crosses (+), those identified as probable $(n+-)$ as oblique crosses (×). Events identified as $(n+-)$ or $(n+-0)$ are plotted as oblique lines (\) using angles and momenta that fit the $(n+-)$ possibility.

[20] The symbol $\pi^+(n+-)$ means π^+ mesons from $(n+-)$ events, and similarly for $n(n+-)$, etc.

for the nucleons and a forward preference for the pions, as shown in Fig. 11. The momentum distribution of the nucleons is peaked at high momenta, while that for the pions is much broader, as shown in Fig. 12.

These results can be discussed from two points of view, which are not necessarily mutually exclusive. From the diffraction scattering interpretation of the elastic events one concludes that the region in which the incident pion interacts has a radius of about 1×10^{-13} cm. This region contains the nucleon and virtual pions making up its pion field in some strongly interacting association. The forward angular preference of the pions and backward preference of the nucleons would be expected if the incoming pion collides with a virtual pion in some cases, rather than with the nucleon itself, so that momentum transfer to the nucleon would be small. On the other hand the pion momentum spectrum resembles what would be expected if the low momentum pions were emitted by a $T=J=\frac{3}{2}$ state with excitation $\sim$160 Mev as was already suggested by the results in I.

A simple way to check whether the data are consistent with the idea of π-π collisions is to calculate the angle between the two outgoing pions. For a collision between an incoming pion of 1.37 Bev and a stationary pion this angle varies from 45° to 90° in the laboratory system. Of course, the virtual pion would be expected often to have a momentum of at least $\mu c=0.14$ Bev/c which would modify the angles considerably. Kovacs has calculated the distribution of the angle between the two pions using scalar theory and obtained a curve peaked strongly at 0° for strong pion-pion interaction.[21] The experimental results are given in Table V. There is indeed a preference for angles of 45°–90°. The forward peak is not marked, but there is a greater preference for forward angles than indicated by Kovacs' curve for strong pion-nucleon interaction. Of course calculations based on scalar theory may not be a reliable guide to the interpretation of the experimental results, but the results are not inconsistent with the possibility that meson-meson interactions play a significant role.

If, on the other hand, one expects the interaction to lead to an excited state of the nucleon which then decays to emit the pion with lower c.m. system momentum, this fact should show up most clearly in the momentum spectrum. In addition one should be able to calculate Q values for the excited state. If we take

TABLE V. Angle between emitted mesons in laboratory system.

Angle θ_{12}	Number of cases (+−) from (n+−)	Number of cases (−0) from (p−0)	Total	Kovacs prediction π-π	Kovacs prediction π-p
0–60	7	11	18	35	19
60–90	16	9	25	15	14
90–120	8	2	10	3	11
120–150	1	0	1	1	10

[21] J. S. Kovacs, Phys. Rev. 93, 252 (1954).

0.16 Bev for the excitation energy, the c.m. system momentum of the scattered pion is 0.55 Bev/c, while that for the pion emitted from the excited nucleon is spread about a most probable value of about 0.3 Bev/c. The pion momentum distribution in Fig. 12 fits this prediction very well. The low-momentum hump on this curve is probably to some extent due to the bias favoring low-energy π^+, however, so this agreement may be fortuitous.

The best evidence for an excited state might be obtained by calculating Q values for nucleon-pion pairs. In particular, the pair $(n-)$ which involves a pure $T=\frac{3}{2}$ state should give Q values near 0.16 Bev. The distribution of Q values is given in Table VI. One would expect low Q values for the pion emitted from the excited state, high apparent Q values (to conserve energy and momentum) for the scattered pion. There is some indication of such a grouping in the $(n+-)$ events, but since the $(n+)$ pair has the most definite low Q value group it may well be a spurious effect due to the bias favoring low energy positive particles. While the data certainly do not prove the existence of an excited state, they are not in disagreement with such a picture either.

TABLE VI. Q values for different pion-nucleon pairs.

Q value Bev	Number of cases From $(p-0)$ $(p-)$	$(p0)$	From $(n+-)$ $(n+)$	$(n-)$
0–0.1	3	2	9	3
0.1–0.2	3	3	8	5
0.2–0.3	5	3	2	1
0.3–0.4	2	3	1	5
0.4–0.5	3	3	1	3
0.5–0.6	5	3	9	7
0.6–0.7	1	5	1	6
>0.7	0	0	0	1

It may seem confusing that the results at the same time show some properties of strong pion-pion interactions and of strong pion-nucleon interactions, but this probably involves no real inconsistency. One can imagine that the incoming pion transfers momentum to the pion field, but that the interactions between that field and the nucleon are such as to enhance emission of pions in the "resonant" state. The implied separation into pion-nucleon and pion-pion interactions is, of course, somewhat artificial, since the two should be considered as different aspects of the same phenomenon in a consistent theory.

VII. COMPARISON WITH OTHER EXPERIMENTS

As mentioned in Sec. III, our best estimate for the total $\pi^- - p$ cross section at our energy agrees well with the counter determination of 34±3 millibarns.[4] Counter measurements had given an indication that small-angle scatterings were frequent, which is well confirmed by our angular distribution for diffraction scattering.

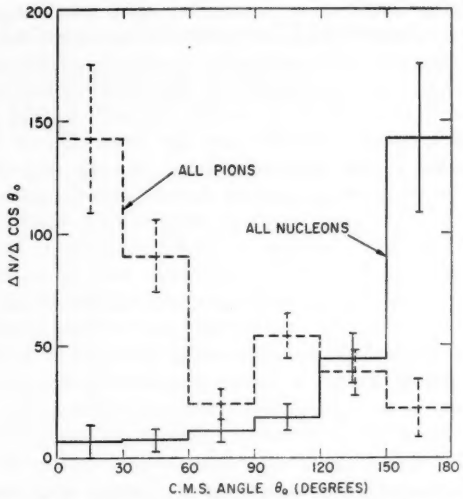

FIG. 11. Center-of-mass differential angular distributions for all pions and nucleons from $(p-0)$ and $(n+-)$ events, based on same events as Figs. 5–10.

Emulsion results have also shown that most elastic scatterings occur at small angles.[5]

In making a detailed comparison of our results with the emulsion data of Crussard, Walker, and Koshiba,[5] it is important to note that about half of the emulsion events were considered to involve interactions with protons bound in nuclei. Such interactions would not be expected to be exactly the same as those of free protons. Emulsions provide better information on density of ionization than our diffusion chambers. On the other hand, no information on the sign of electric charge can be obtained. Information on outgoing pion energies is more often available in the cloud chamber data so that our analysis includes an attempt to identify events

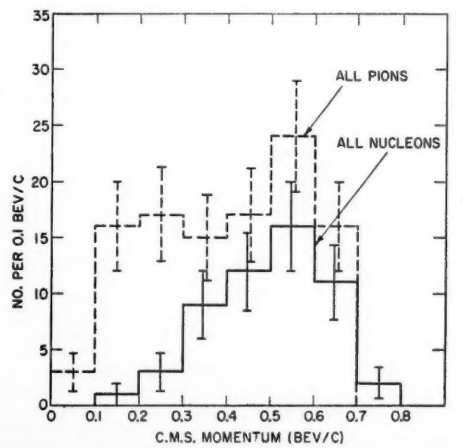

FIG. 12. Center-of-mass momentum distributions for all pions and nucleons from $(p-0)$ and $(n+-)$ events, based on same events as Figs. 5–10.

involving double pion production while this process was assumed to be negligible in the emulsion experiment.

The results are in good general agreement, considering the differences in procedure. Our data show a somewhat higher fraction of elastic events, 162/470 instead of 16/68, probably because they are more difficult to recognize in the emulsion events. In each case the number of $(p-+-)$ is small. In each case the ratio of $(p-0)$ to $(n+-)$ is about unity within statistics: 20/30 for cloud chamber, 31/20 for emulsion. In both experiments the inelastic scatterings show a marked tendency for the nucleons to be emitted backwards in c.m. system. The conclusions concerning angular distribution of pions are somewhat different in that the emulsion data seem to show a very definite low energy backwards group and high energy forwards group in c.m. system, which were interpreted as being pions emitted from an excited nucleon and scattered incident pions, respectively. In the cloud chamber data most pions tend to go forwards, and the apparent backwards group of π^+ is probably due to a selection bias. Attempts to calculate Q values for the hypothetical excited nucleon were inconclusive in both cases.

VIII. CONCLUSIONS

The results show that inelastic collisions in which secondary pions are produced are common at an energy of 1.37 Bev (65 percent of all interactions resulting in charged particles). There are some cases in which two secondary pions are produced (an estimated 15 percent of the inelastic collisions resulting in charged particles). The frequencies of events with different pion multiplicities are not well determined because of the difficulty of analyzing cases with poor momentum measurements, but seem to be very roughly consistent with the predictions of the Fermi statistical theory (Table IV). Elastic scatterings (35 percent of all interactions) occur mainly at angles $<30°$ in the laboratory system, and are mainly a shadow scattering phenomenon. This indicates that the region in which the incoming pion interacts has a radius of about 1.2×10^{-13} cm and is somewhat transparent, a conclusion which is inconsistent with the statistical model's basic assumption of very strong interaction. An alternate interpretation fitting the observed cross sections $\sigma_{el}=10$ mb and $\sigma_{inel}=24$ mb, and the observed large angle elastic scattering, would indicate the existence of a region near the center where the interaction is very strong ($\lambda\approx0$) and an outside region where the interactions becomes quite weak ($\lambda\approx5\times10^{-13}$ cm).

Angular correlations of pions suggest that pion-pion interactions may play a role in the interactions studied. The momentum spectra of the pions seem to show low and high groups which may be due to the $T=J=\frac{3}{2}$ "resonant" state. No definite conclusions are possible on these last points, and they are presented mainly as questions to be answered by future experiments.

We are indebted to the Cosmotron staff for providing us with very reliable operation of the machine, and to the other members of the cloud chamber group for their effective help in operating the cloud chamber equipment. M. R. Burns and F. S. Keene have aided us considerably by scanning most of the photographs.

Search for Electromagnetic Interactions Between μ Mesons and Electrons*

L. S. Osborne, W. D. Rankin, P. C. Stein, A. Wattenberg, and A. Winston
Laboratory for Nuclear Science, Massachusetts Institute of Technology, Cambridge, Massachusetts

(Received October 8, 1954)

An attempt was made to observe the reaction $\gamma \rightarrow \mu^{\pm} + e^{\mp}$ up to 23 Mev above threshold. It was found that the cross section for this reaction is less than 10^{-31} cm² per proton. We have also looked for the decay $\mu^{\pm} \rightarrow e^{\pm} + \gamma$, and we find that its lifetime is longer than 10^{-3} second.

A SEARCH for electromagnetic transitions between electrons and μ mesons was undertaken at the Massachusetts Institute of Technology synchrotron by attempting to observe the reactions (A) $\gamma \rightarrow \mu^{\pm} + e^{\mp}$ and (B) $\mu^{\pm} \rightarrow e^{\pm} + \gamma$.

(A) The reaction $\gamma \rightarrow \mu^{\pm} + e^{\mp}$ might have been observed in previous attempts to detect the direct production of μ mesons. The cross section for the direct production of μ mesons was found by Peterson *et al.*[1] to be less than 2 percent of the cross section for π-meson production. We have undertaken to set a new upper limit for the direct production of μ mesons by photons with energies below the π-meson production threshold. The maximum bremsstrahlung energy was kept 23 Mev above the threshold for $\gamma \rightarrow \mu^{\pm} + e^{\mp}$ (i.e., at 136 Mev).

In these measurements, the apparatus of Osborne and Winston[2] was used (see electron detector of Fig. 1). This apparatus detects μ mesons by observing the delayed emission of their decay electrons after a short (approximately 2 μsec) synchrotron pulse. A sufficiently large polyethylene target was employed so that most of the mesons with energies less than 23 Mev would have stopped and decayed in the target.

In a 24-hour run below π-meson threshold 2 events were recorded. The computed number of accidental counts for this run was 0.2 count. With this low a counting rate, we cannot rule out the possibility that these two events arose from electronic failures or fluctuations (e.g., fluctuations that permitted the energy of the synchrotron to rise with the accompanying production of π^+ mesons).

π^+ mesons were used to calibrate the apparatus and geometry by raising the maximum energy of the bremsstrahlung beam to 23 Mev above the π-meson threshold. From the number of π^+ mesons observed, it is calculated that the direct production of μ mesons is less than 3×10^{-3} of the cross section for π^+ meson production. From the cross section for π^+ production determined by Janes and Kraushaar,[3] the mean cross section for direct μ-meson production is less than 1×10^{-31} cm² in the range from 0 to 23 Mev above threshold. This upper limit is about 1/7 of that previously given by Peterson *et al.*[1]

(B) In regard to the transition $\mu^{\pm} \rightarrow e^{\pm} + \gamma$, previous published experiments have shown that the probability for this transition to occur is less than 5 percent of the probability for all other modes of decay of μ mesons.[4]

A search for the decay $\mu^+ \rightarrow e^+ + \gamma$ was made, using the $\pi^+ \rightarrow \mu^+ + \nu$ as a source of μ mesons. The apparatus employed is shown in Fig. 1. The γ ray and electron detectors are on opposite sides of the target in which most of the μ mesons decay. The γ-ray detector was biased to exclude γ rays with energies below 25 Mev. The efficiency of the γ-ray detector was checked with 70-Mev γ rays from π^0 mesons and was found to be 36 percent. The electron detector was estimated to be capable of counting 53 percent of the $\mu^+ \rightarrow e^+ + 2\nu$ electron spectrum.[5] The solid angle was effectively determined by the electron detector.

Two events were recorded in the $\gamma + e$ coincidence circuits in a long run in which 10 000 electron events were observed ($\mu^+ \rightarrow e^+ + 2\nu$ decay). As we cannot be certain that these two events were real, we can only set an upper limit on the process $\mu^+ \rightarrow e^+ + \gamma$. From the

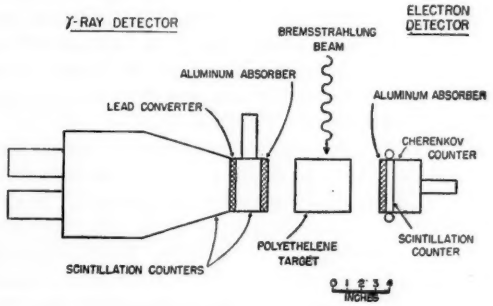

GAMMA-RAY AND DELAYED ELECTRON COINCIDENCE COUNTER

FIG. 1. Top view of apparatus used in search for electromagnetic transitions. The electron detector consists of a scintillation counter in front of a Čerenkov counter. The γ-ray detector consists of a thin anticoincidence scintillation counter, a ¼-in. lead converter, and a large scintillation counter. The electron detector was used alone in the search for direct production of μ mesons. The electron and γ-ray detectors were used in coincidence for the process $\mu^+ \rightarrow e^+ + \gamma$.

* This work was supported in part by the joint program of the U. S. Office of Naval Research and the U. S. Atomic Energy Commission.

[1] Peterson, Gilbert, and White, Phys. Rev. 81, 1003 (1951).

[2] A. Winston, Ph.D. thesis, Massachusetts Institute of Technology, 1954 (unpublished).

[3] G. S. Janes and W. Kraushaar, Phys. Rev. 93, 900 (1954).

[4] E. P. Hinks and B. Pontecorvo, Can. J. Research A28, 29 (1950); R. D. Sard and E. S. Althaus, Phys. Rev. 73, 1251 (1948); Phys. Rev. 74, 1364 (1948).

[5] J. H. Vilain and R. W. Williams, Phys. Rev. 94, 1011 (1954).

above data we estimate that $\mu^+ \to e^+ + \gamma$ occurs less than 6×10^{-4} as frequently as the process $\mu^+ \to e^+ + 2\nu$. This means that the decay $\mu^+ \to e^+ + \gamma$ has a lifetime longer than 10^{-8} second. This value of the lifetime is about 100 times longer than the lower limits previously given in the literature.[4,6]

It might be mentioned that if the same strength of interaction were responsible for both reactions (A) and (B) that the result obtained on reaction (B) is more significant than the result on reaction (A) by many orders of magnitude in setting a limit on the strength of the interaction.

[6] Since these measurements were performed, we have been informed by J. Steinberger that he and S. Lokanathan have found that the lifetime for the decay $\mu \to e + \gamma$ is appreciably longer than the value we obtained. S. Lokanathan and J. Steinberger, Abstract for the Chicago, Illinois meeting of the American Physical Society, November, 1954 [Bull. Am. Phys. Soc. 29, No. 7, 25 (1954)].

PHYSICAL REVIEW VOLUME 97, NUMBER 3 FEBRUARY 1, 1955

Biquadratic Spinor Identities

K. M. Case
Randall Laboratory of Physics, University of Michigan, Ann Arbor, Michigan
(Received June 2, 1954)

The representation-independent biquadratic identities which Pauli has proved to hold between a Dirac wave function and its adjoint are shown to be generalizable in several ways. To obtain these generalizations it is first shown how the symmetrical Kronecker product of two spinor representations of the orthogonal group in n dimensions decomposes. Then a method is given to express the tensors formed in a particular way from two covariant and two contravariant spinors in terms of those formed in any other way. These results are applied to write explicitly all biquadratic scalar and pseudoscalar identities in 2ν dimensions and all scalar identities in $2\nu+1$ dimensions. The way to obtain more general tensor identities is indicated.

BIQUADRATIC SPINOR IDENTITIES

SOON after the discovery of the Dirac equation it was noted by Fock and Darwin[1] that there are some quadratic identities which hold between the scalars obtained from the five covariants which can be formed with a Dirac wave function and its adjoint. The proof consisted of writing down these scalars with a particular choice of the matrices and comparing terms. Additional identities involving the pseudoscalars, vectors, and pseudovectors which can be formed from the square of a wave function and the square of its adjoint were given by Uhlenbeck and Laporte.[2] Again a special representation was used.

In 1936 Pauli[3] gave a representation-independent proof of the scalar and pseudoscalar identities. A proof from a different point of view was given by Harish-Chandra,[4] who also proved some of the other identities given in reference 2. In addition Harish-Chandra obtained some relations which hold between tensors formed with two arbitrary wave functions and their adjoints. To a certain extent these relations are similar to results of Fierz.[5] Fierz was interested in expressing the scalars occurring in beta decay interaction terms formed from one arrangement of wave functions in terms of those with another arrangement.

In the following a systematic method is described which gives directly all identities of the desired type. It is hoped that the general mathematical structure of these relations will become particularly clear. The origin of the identities can be stated, group theoretically, quite succinctly. Certain of the irreducible representations of the orthogonal group which occur in the direct product of the spinor representation with itself do not occur in the symmetrized product.

The theory of spinors in n dimensions has been shown by Brauer and Weyl[6] to be extremely similar to the Dirac (four-dimensional) case. Since the essence of the argument to be used is independent of the number of dimensions and since it is desired to shed light on the mathematical basis, we show how to obtain directly all the biquadratic identities existing between n-dimensional spinors. As an essential step, the decomposition of the symmetrical Kronecker square of the spin representation of the orthogonal group is obtained.

Briefly, the method is the following. First we show that certain of the covariants formed with two covariant (or with two contravariant) spinors vanish when the spinors are identical. Second, the work of Fierz is generalized. The biquadratic covariants, formed with two covariant and two contravariant spinors by combining the first and second sets separately into tensors and then combining the two sets of resulting tensors, are expressed in terms of the covariants obtained by first combining a covariant with a contravariant spinor in the more usual manner. Using these two groups of results the desired identities are obtained. It will be

[1] V. Fock, Z. Physik 57, 261 (1929); C. G. Darwin, Proc. Roy. Soc. (London) 120, 621 (1928).
[2] G. E. Uhlenbeck and O. Laporte, Phys. Rev. 37, 1552 (1931).
[3] W. Pauli, Ann. inst. Henri Poincaré 6, 109, (1936).
[4] Harish-Chandra, Proc. Indian Acad. Sci. 22, 30 (1945).
[5] M. Fierz, Z. Physik 104, 553 (1937).
[6] R. Brauer and H. Weyl, Am. J. Math. 57, 425 (1935).

readily apparent that *all* identities of any given type are found and that all the identities given are independent.

In Sec. II a short summary of the relevant results of Brauer and Weyl[6] are given in a form similar to that used by Pauli.[3] The representation of the matrices is not specified. Section III discusses the connection between covariant and contravariant spinors by means of a generalization of an argument of Pauli and Haantjes.[3] The results of III are applied in IV to obtain the decomposition of the symmetrical product of two spin representations. The differences between even and odd dimensions require separate discussions for the identities. These are given in V and VI. Some physical applications, primarily to beta decay, are indicated. Most computational details are relegated to Appendices, as are some of the arguments which differ in only minor ways from those given in the major part of the text.

II. SUMMARY OF SPINOR PROPERTIES

For brevity we confine the discussion to the spin representations of the complex orthogonal group. No essential modifications are necessary for the groups obtained on restriction to real variables except that the definitions of some tensors formed with the spinors might be more conveniently given by prefixing various factors of i.

By following Brauer and Weyl,[6] it is simplest to discuss the cases of even and odd dimensions separately.

$n=2\nu$

We consider a set of 2ν quantities $\Gamma(i)$ satisfying

$$\Gamma(i)\Gamma(j)+\Gamma(j)\Gamma(i)=2\delta_{ij}. \tag{1}$$

These quantities together with a unit element (1) and its negative generate a group with elements:

$$\begin{array}{ll} 1 & -1 \\ \Gamma^{(1)} & -\Gamma^{(1)} \\ \Gamma^{(2)} & -\Gamma^{(2)} \\ \cdots & \cdots \\ \Gamma^{(2\nu)} & -\Gamma^{(2\nu)}, \end{array} \tag{2}$$

where $\Gamma^{(f)}$ is the set of $\binom{2\nu}{f}$ quantities[7]:

$$\Gamma^{(f)}(i_1 i_2\cdots i_f)=i^{[f/2]}\Gamma(i_1)\Gamma(i_2)\cdots\Gamma(i_f), \qquad i_1<i_2<\cdots<i_f. \tag{3}$$

The power of i in (3) is chosen so that for any element Γ_A of the form

$$\Gamma_A=\Gamma^{(f)}(i_1 i_2\cdots i_f),$$

we have

$$(\Gamma_A)^2=1. \tag{4}$$

[7] $[a]$ denotes the largest integer contained in a.

The group (2) has one faithful irreducible representation. From now on the symbols Γ will denote the matrices of this representation. Their degree is 2^ν. Since, for any element of (2) which is not (1) or (-1), both Γ_A and $-\Gamma_A$ are members of the same class, we have

$$\mathrm{tr}\Gamma_A=-\mathrm{tr}\Gamma_A=0. \tag{5}$$

As a consequence the $2^{2\nu}$ matrices,

$$1,\ \Gamma^{(1)}(i_1)\cdots,\ \Gamma^{(2)}(i_1 i_2)\cdots,\ \Gamma^{(2\nu)}(i_1\cdots i_{2\nu}), \tag{6}$$

are linearly independent.

Proof

Let

$$a^{(f)}\cdot b^{(f)}=\sum_{i_1<i_2<\cdots<i_f} a^{(f)}(i_1 i_2\cdots i_f)b^{(f)}(i_1 i_2\cdots i_f). \tag{7}$$

If the quantities (6) are not linearly independent there exists a nontrivial relation of the form

$$\sum_{f=0}^{2\nu} a^{(f)}\cdot\Gamma^{(f)}=0. \tag{8}$$

Multiplying (8) by $\Gamma^{(f')}(j_1 j_2\cdots j_{f'})$, noting that

$$\Gamma_A\Gamma_B\neq 1 \quad (A\neq B), \tag{9}$$

and taking the trace yields

$$a^{(f')}(j_1 j_2\cdots j_{f'})=0 \quad (\text{all } a^{(f')}). \tag{10}$$

Hence there is no relation of the form (8).

It may be remarked that since the group (2) is finite we can (and always will) take the matrices Γ_A to be unitary. Since the square of any Γ_A is 1 the matrices will also be Hermitian.

The matrices Γ_A of (6), being linearly independent and $2^{2\nu}$ in number, provide a basis by means of which all $2^\nu\times 2^\nu$ matrices can be linearly expressed.

The spin representation of the orthogonal group is obtained by noting that corresponding to an orthogonal transformation,

$$x_i'=\theta_{ik}x_k, \tag{11}$$

we can find a new set of matrices $\Gamma'(i)$,

$$\Gamma'(i)=\theta_{ki}\Gamma(k), \tag{12}$$

which also satisfy (1). These new matrices then give another representation of the group (2). By Schur's lemma the two representations are equivalent and

$$\Gamma'(i)=S(\theta)\Gamma(i)S^{-1}(\theta) \quad (\text{all } i). \tag{13}$$

A set of 2^ν quantities which transform as

$$\psi_A'=\textstyle\sum_B S_{AB}(\theta)\psi_B(\theta) \tag{14a}$$

or

$$\psi'=S(\theta)\psi \tag{14b}$$

are called covariant spinors. Quantities which transform as[8]

$$\psi^{t\prime}=S^{t-1}\psi^{t}=\psi^{t}S^{-1} \tag{15}$$

are contravariant spinors.

The connection between covariant and contravariant spinors is obtained by noting that if the $\Gamma(i)$ are a fixed set of matrices giving a representation of (2), the matrices $\Gamma^{t}(i)$ also satisfy (1). Hence these matrices give an equivalent representation and

$$\Gamma^{t}(i)=C\Gamma(i)C^{-1}, \tag{16}$$

with some nonsingular matrix C. The matrices $S(\theta)$ are defined by (13) only up to a multiplicative constant. In reference 6 it is shown that this constant can be chosen so that

$$(S^{t})^{-1}(\theta)=CS(\theta)C^{-1}. \tag{17}$$

Using this matrix C we can associate a contravariant spinor ψ with a covariant spinor ψ by means of the relation

$$\psi^{\dagger}=C\psi. \tag{18}$$

Further properties of C are discussed below.

$n+2\nu+1$

Again we consider quantities $\Gamma(i)$ $(i=1, 2, \cdots, 2\nu+1)$, $2\nu+1$ in number, satisfying (1). Forming the quantities

$$\begin{array}{cc} 1 & -1 \\ \Gamma^{(1)} & -\Gamma^{(1)} \\ \cdots & \cdots \\ \Gamma^{(2\nu)} & -\Gamma^{(2\nu)} \\ U=i^{\nu}\Gamma(1)\Gamma(2)\cdots\Gamma(2\nu+1) & -U, \end{array} \tag{19}$$

we obtain a group of $2^{2\nu+2}$ elements. The only irreducible representations of dimension greater than one are two inequivalent 2^{ν} dimensional representations. Since U commutes with all the elements, we obtain by Schur's lemma:

$$U=b1. \tag{20}$$

But

$$U^{2}=1, \tag{21}$$

and thus

$$b=\pm 1. \tag{22}$$

The two inequivalent representations can then be characterized by

$$U=1 \quad \text{or} \quad U=-1. \tag{23}$$

That these representations are inequivalent is readily seen by noting that the character of U is 2^{ν} or -2^{ν}, respectively.

The argument given previously shows that all traces except those of $1, -1, U, -U$ are zero. Applying the same method as gave (1) shows that the even rank quantities $(\Gamma^{(0)}\equiv 1, \Gamma^{(2)}, \Gamma^{(4)}, \cdots)$ are linearly independent. In number they are

$$N=\sum_{i=0}^{\nu}\binom{2\nu+1}{2i}=2^{2\nu}, \tag{24}$$

i.e., the even-rank quantities are just sufficient to provide a basis for all $2^{\nu}\times 2^{\nu}$ matrices.

The connection with the orthogonal group proceeds as for even dimensions. We restrict ourselves to the pure rotation group. (Representations of the full orthogonal group can be obtained from the one below by adding the commuting operation of reflection.) Let

$$\Gamma(i) \quad i=1, 2, \cdots, 2\nu \tag{25}$$

be the matrices of the irreducible representation for the case $n=2\nu$. Choosing

$$\Gamma(2\nu+1)=i^{\nu}\Gamma(1)\Gamma(2)\cdots\Gamma(2\nu) \tag{26}$$

gives a representation of (19) with $U=1$.

Associated with a rotation,

$$x_{i}'=\theta_{ik}x_{k}, \tag{27}$$

we have a new set of matrices $\Gamma'(i)$,

$$\Gamma'(i)=\theta_{ki}\Gamma(k), \tag{28}$$

which also satisfy (1) and thus give a 2^{ν} dimensional representation of (19). Since

$$U'=(\det\theta)U=U=1, \tag{29}$$

we see this new representation is equivalent to the original representation. Hence there is a nonsingular $S(\theta)$ such that

$$\Gamma'(i)=S(\theta)\Gamma(i)S^{-1}(\theta). \tag{30}$$

The covariant-contravariant connection is also similar to that for $n=2\nu$. Consider the matrices $\Gamma(i)$ $(i=1, 2, \cdots, 2\nu+1)$, given by (25) and (26). The matrices $\Gamma^{t}(i)$ satisfy the same relations except, perhaps, for the condition $U=1$. Direct use of the relations (1) yield

$$i^{\nu}\Gamma^{t}(1)\Gamma^{(t)}(2)\cdots\Gamma^{t}(2\nu+1)=(-1)^{\nu}, \tag{31a}$$

or

$$U'=(-1)^{\nu}. \tag{31b}$$

Hence if ν is even, the matrices $\Gamma^{t}(i)$ give an equivalent representation and thus

$$\Gamma^{t}(i)=C\Gamma(i)C^{-1}. \tag{32a}$$

Indeed, if C_{e} be the matrix occurring in (16) for the case $n=2\nu$, we see we can take $C=C_{e}$, or

$$\Gamma^{(t)}(i)=C_{e}\Gamma(i)C_{e}^{-1}. \tag{32b}$$

If ν be odd, consider the quantities $-\Gamma(i)$ $(i=1, 2, \cdots, 2\nu+1)$. These also satisfy the relations (1) and give

$$\begin{aligned}\tilde{U}&=i^{\nu}[-\Gamma(1)][-\Gamma(2)]\cdots[-\Gamma(2\nu+1)]\\ &=(-1)^{2\nu+1}U=-1.\end{aligned} \tag{33}$$

[8] t denotes transposed, $*$ complex conjugate, $\dagger$ Hermitian conjugate.

Hence, the matrices $-\Gamma(i)$ give the other, inequivalent, representation. For ν odd, the representation by means of $\Gamma^t(i)$ give a representation equivalent to this and so there is a C such that

$$C\Gamma(i)C^{-1}=-\Gamma^t(i). \tag{34}$$

A matrix satisfying this is

$$C=C_\nu\Gamma(2\nu+1). \tag{35}$$

The equivalence of covariant and contravariant representations is then seen, since in either case we can write

$$C\Gamma(i)C^{-1}=(-1)^\nu\Gamma^t(i), \tag{36}$$

which implies that

$$[S^t]^{-1}=CS(\theta)C^{-1}. \tag{37}$$

III. PROPERTIES OF THE MATRICES C

$n=2\nu$

C can be chosen unitary.

Proof

$$\Gamma^t(i)=C\Gamma(i)C^{-1}. \tag{16}$$

Take the Hermitian conjugate,

$$\Gamma^t(i)^\dagger=C^{-1\dagger}\Gamma^\dagger(i)C^\dagger, \tag{38}$$

or, since we are taking the $\Gamma(i)$ to be Hermitian,

$$\Gamma^t(i)=C^{-1\dagger}\Gamma(i)C^\dagger. \tag{39}$$

Then, inserting (16) in (39), we obtain

$$C^\dagger C\Gamma(i)=\Gamma(i)C^\dagger C. \tag{40}$$

By Schur's lemma,

$$C^\dagger C=\epsilon 1, \tag{41}$$

or

$$\epsilon=\sum_j C^\dagger_{ij}C_{ji}=\sum_j|C_{ij}|^2. \tag{42}$$

Thus ϵ is real and positive. Dividing C by $\epsilon^{1/2}$ we obtain

$$C^{-1}=C^\dagger; \tag{43}$$

i.e., C is unitary.

We can obtain the symmetry properties of C in a similar manner. From (16),

$$\Gamma^{tt}(i)=\Gamma(i)=[C^t]^{-1}\Gamma^{(t)}(i)C^t=[C^t]^{-1}C\Gamma(i)C^{-1}C^t, \tag{44}$$

or

$$[C^t]^{-1}C\Gamma(i)=\Gamma(i)[C^t]^{-1}C. \tag{45}$$

Hence

$$[C^t]^{-1}C=a1, \tag{46}$$

and

$$C=aC^t. \tag{47}$$

Thus

$$C^t=aC=C/a, \tag{48}$$

or

$$a^2=1, \quad a=\pm1; \tag{49}$$

i.e., C is either symmetric or antisymmetric. The determination of which proceeds by an argument of Pauli and Haantjes. Fortunately, this also yields much useful additional information.

Let us suppose first that $a=+1$. Then $C=C^t$. By repeated use of (16) and (1), we find:

$$C\Gamma^{(f)}C^{-1}=(-1)^{[f/2]}[\Gamma^{(f)}]^t, \tag{50}$$

or

$$C\Gamma^{(f)}=(-1)^{[f/2]}[C\Gamma^{(f)}]^t. \tag{51}$$

Hence

$$\begin{aligned} &C\Gamma^{(f)} \text{ is symmetric,} && f=0,\ 1 \pmod 4,\\ &C\Gamma^{(f)} \text{ is antisymmetric,} && f=2,\ 3 \pmod 4. \end{aligned} \tag{52}$$

We now ask how many matrices (N_1) there are of the form

$$C\Gamma^{(f)}, \quad f=0,\ 1 \pmod 4,$$

$$N_1=\binom{2\nu}{0}+\binom{2\nu}{1}+\binom{2\nu}{4}+\binom{2\nu}{5}+\cdots. \tag{53}$$

It is readily shown that

$$N_1=(2^{2\nu}+2^\nu)/2, \quad \nu=0,\ 1 \pmod 4, \tag{54a}$$

$$N_1=(2^{2\nu}-2^\nu)/2, \quad \nu=2,\ 3 \pmod 4. \tag{54b}$$

The number of matrices (N_2) of form

$$C\Gamma^{(f)} \quad f=2,\ 3 \pmod 4$$

is

$$N_2=2^{2\nu}-N_1$$

$$=(2^{2\nu}-2^\nu)/2, \quad \nu=0,\ 1 \pmod 4 \tag{55a}$$

$$N_2=(2^{2\nu}+2^\nu)/2, \quad \nu=2,\ 3 \pmod 4. \tag{55b}$$

These matrices $C\Gamma^{(f)}$ are all linearly independent since the $\Gamma^{(f)}$ are all linearly independent and C is unitary.

The number of linearly independent symmetric (N_s) or antisymmetric matrices (N_{as}) of degree 2^ν are:

$$N_s=[2^\nu(2^\nu-1)/2]+2^\nu=(2^{2\nu}+2^\nu)/2, \tag{56a}$$

$$N_{as}=2^\nu(2^\nu-1)/2=(2^{2\nu}-2^\nu)/2. \tag{56b}$$

Comparing (54a) with (56a) we see the assumption $a=+1$ is correct for $\nu=0,\ 1 \pmod 4$ but incorrect for $\nu=2,\ 3 \pmod 4$. In the latter case we must have $a=-1$. Indeed from (52), (54), and (56) we can conclude further that:

If $\nu=0,\ 1 \pmod 4$,

$$C\Gamma^{(f)} \text{ is symmetric,} \quad f=0,\ 1 \pmod 4; \tag{57a}$$

$$C\Gamma^{(f)} \text{ is antisymmetric,} \quad f=2,\ 3 \pmod 4. \tag{57b}$$

If $\nu=2,\ 3 \pmod 4$,

$$C\Gamma^{(f)} \text{ is antisymmetric,} \quad f=0,\ 1 \pmod 4; \tag{58a}$$

$$C\Gamma^{(f)} \text{ is symmetric,} \quad f=2,\ 3 \pmod 4. \tag{58b}$$

TABLE I. Symmetry properties of $C\Gamma^{(f)}$ for $n=2\nu+1$.

ν (mod 4)	$C\Gamma^{(f)}$ symmetric	$C\Gamma^{(f)}$ antisymmetric
0	$f=0, 1$ (mod 4)	$f=2, 3$ (mod 4)
1	$f=0, 3$ (mod 4)	$f=1, 2$ (mod 4)
2	$f=2, 3$ (mod 4)	$f=0, 1$ (mod 4)
3	$f=0, 3$ (mod 4)	$f=1, 2$ (mod 4)

$n=2\nu+1$

The unitarity of the matrix C occurring in (36) follows directly from (43). For ν even, $C=C_e$ (32b), which is unitary. For ν odd:

$$\begin{aligned} &C=C_e\Gamma(2\nu+1),\\ &C^\dagger=\Gamma^\dagger(2\nu+1)C_e^\dagger=\Gamma^{-1}(2\nu+1)C_e^{-1} \qquad (35)\\ &\quad=C_e\Gamma^{-1}(2\nu+1)=C^{-1}. \end{aligned}$$

The symmetry properties of C (and $C\Gamma^{(f)}$) follow directly from those for C_e. The results are given in Table I.

IV. DECOMPOSITION OF THE SYMMETRICAL DIRECT PRODUCT

$n=2\nu$

Consider two covariant spinors ϕ, ψ. The $2^{2\nu}$ products $\phi_A\psi_B$ form a $2^\nu\times 2^\nu$ matrix which from the results of II can be expanded in terms of the matrices,

$$\Gamma^{(f)}(i_1i_2\cdots i_f)\equiv\Gamma^{(f)}(f_i). \qquad (59)$$

Alternately, since C is unitary we can expand using the quantities $\Gamma^{(f)}(f_i)C^{-1}$ as a basis. Thus:

$$\phi_A\psi_B=\sum_f a^{(f)}\cdot(\Gamma^{(f)}C^{-1})_{BA}. \qquad (60)$$

To determine the coefficients $a^{(f)}(f_i)$, we multiply by

$$[C\Gamma^{(f')}(f'_i)]_{AB}, \qquad (61)$$

and sum over A and B:

$$\begin{aligned} (\phi,C\Gamma^{(f')}(f'_i)\psi)&=\sum_f a^{(f)}\cdot\sum_{AB}C\Gamma^{(f')}(f'_i)\Gamma^{(f)}C^{-1}\\ &=\sum_f a^{(f)}\cdot\mathrm{tr}C\Gamma^{(f')}(f'_i)\Gamma^{(f)}C^{-1}. \qquad (62) \end{aligned}$$

From (9) and (5) we find:

$$\mathrm{tr}C\Gamma^{(f')}(f'_i)\Gamma^{(f)}C^{-1}=2^\nu\delta(i_1,i'_1)\delta(i_2,i'_2)\cdots. \qquad (63)$$

Hence,

$$a^{(f)}=(\phi,C\Gamma^{(f)}\psi)/2^\nu, \qquad (64)$$

or

$$\phi_A\psi_B=\sum_{f=0}^{2\nu}\frac{(\phi,C\Gamma^{(f)}\psi)\cdot(\Gamma^{(f)}C^{-1})_{BA}}{2^\nu}. \qquad (65a)$$

The results of (57) and (58) for C can be summarized as

$$C^t=(-1)^{[\nu/2]}C. \qquad (66)$$

Thus (65a) can also be written:

$$\phi_A\psi_B=\sum_{f=0}^{2\nu}\frac{(-1)^{[\nu/2]}(C\phi,\Gamma^{(f)}\psi)\cdot(\Gamma^{(f)}C^{-1})_{BA}}{2^\nu}. \qquad (65b)$$

Under an orthogonal transformation the spinors transform [(14b), (18), (15)] as:

$$\psi'=S(\theta)\psi,\quad \phi'=S(\theta)\phi,\quad C\phi'=(C\phi)S^{-1}(\theta).$$

Then (65b) becomes:

$$\phi_A'\psi_B'=\sum_{f=0}^{2\nu}\frac{(-1)^{[\nu/2]}(C\phi,S^{-1}\Gamma^{(f)}S\psi)\cdot(\Gamma^{(f)}C^{-1})_{BA}}{2^\nu}. \qquad (67)$$

From (12) and (13) we then obtain the well-known result that the direct product $(S\times S)$ decomposes into the representations

$$S\times S\sim\sum_{f=0}^{2\nu}\{1^f\}, \qquad (68)$$

where $\{1^f\}$ denotes the representation whose basis are the antisymmetric tensors of rank f.

Returning to (65a), we obtain on identifying ϕ with ψ:

$$\psi_A\psi_B=\sum_{f=0}^{2\nu}\frac{(\psi,C\Gamma^{(f)}\psi)\cdot(\Gamma^{(f)}C^{-1})_{BA}}{2^\nu}. \qquad (69)$$

From (57) and (58) we know that if $\nu=0, 1\ (=2, 3)$ mod 4 then $C\Gamma^{(f)}$ is antisymmetric for $f=2, 3\ (=0, 1)$ mod 4. These terms in (69) must then vanish. Thus corresponding to the decomposition (68) we obtain for the decomposition of the symmetrical direct product $(S^{[2]})$:

$$S^{[2]}\sim\sum_{f=0}^{2\nu}{}'\{1^f\}, \qquad (70)$$

$$\begin{aligned} f&\neq 2, 3 \quad \text{for} \quad \nu=0, 1 \pmod 4\\ f&\neq 0, 1 \quad \text{for} \quad \nu=2, 3 \pmod 4. \end{aligned}$$

As examples we have the familiar results:

$n=2\ (\nu=1)$

$$\begin{aligned} &S\times S\sim\text{scalar}+\text{vector}+\text{pseudoscalar},\\ &S^{[2]}\sim\text{scalar}+\text{vector}; \end{aligned} \qquad (71)$$

$n=4\ (\nu=2)$

$$\begin{aligned} &S\times S\sim\text{scalar}+\text{vector}+\text{second rank tensor}\\ &\qquad+\text{pseudovector}+\text{pseudoscalar},\\ &S^{[2]}\sim\text{second rank tensor}+\text{pseudovector}; \end{aligned} \qquad (72)$$

$n=6\ (\nu=3)$

$$\begin{aligned} &S\times S\sim\text{scalar}+\text{vector}+\text{second rank tensor}\\ &\qquad+\text{third rank tensor}+\text{fourth rank tensor}\\ &\qquad+\text{pseudovector}+\text{pseudoscalar},\\ &S^{[2]}\sim\text{second rank tensor}+\text{third rank tensor}\\ &\qquad+\text{pseudoscalar}. \end{aligned} \qquad (73)$$

$n=2\nu+1$

The procedure is as above with the exception that now only the even rank quantities $\Gamma^{(2\lambda)}C^{-1}$ are used as a basis. For the product of two spinors we obtain:

$$\phi_A\psi_B=\sum_{\lambda=0}^{\nu}\frac{(\phi,C\Gamma^{(2\lambda)}\psi)\cdot(\Gamma^{(2\lambda)}C^{-1})_{BA}}{2^\nu}. \tag{74a}$$

From Table I

$$C^t=(-1)^{\alpha_\nu}C, \tag{75}$$

where

$$\begin{aligned}\alpha_\nu&=0, \quad \nu=0,\,1,\,3 \pmod 4\\ &=1, \quad \nu=2 \pmod 4.\end{aligned} \tag{76}$$

Hence (74a) can also be written:

$$\phi_A\psi_B=\sum_{\lambda=0}^{\nu}\frac{(-1)^{\alpha_\nu}(C\phi,\Gamma^{(2\lambda)}\psi)\cdot(\Gamma^{(2\lambda)}C^{-1})_{BA}}{2^\nu}. \tag{74b}$$

The same argument as leads to (68) gives the well known result:

$$S\times S\sim\sum_{\lambda=0}^{\nu}\{1^{2\lambda}\}. \tag{77}$$

Since the terms with $C\Gamma^{(2\lambda)}$ antisymmetric in (74a) vanish when ϕ and ψ are identified we obtain from Table I the decomposition of the symmetrical product:

$$S^{[2]}\sim\sum_{\lambda=0}^{\nu}{}'\{1^{2\lambda}\}, \tag{78}$$

where the sum is over

$$\begin{aligned}&\lambda \text{ even}, \quad \nu=0,\,1,\,3 \pmod 4\\ &\lambda \text{ odd}, \quad \nu=2 \pmod 4.\end{aligned}$$

Examples are:

$n=3$ $(\nu=1)$:

$$\begin{aligned}&S\times S\sim\text{scalar}+\text{pseudovector},\\ &S^{[2]}\sim\text{scalar};\end{aligned} \tag{79}$$

$n=5$ $(\nu=2)$

$$\begin{aligned}&S\times S\sim\text{scalar}+\text{second rank tensor}+\text{pseudovector},\\ &S^{[2]}\sim\text{second rank tensor}.\end{aligned} \tag{80}$$

V. IDENTITIES FOR $n=2\nu$

As a preliminary to obtaining the desired identities it is convenient to consider the relations between covariant quantities formed from two covariant and two contravariant spinors by combining the spinors in various arrangements. First we prove the following:

Theorem

Let ψ, $\phi(\psi^\dagger,\phi^\dagger)$ be two covariant (contravariant) spinors. (No relation is assumed between the two sets.) Then, if θ, θ' are two arbitrary 2^ν dimensional matrices,

$$(\psi^\dagger,\theta\phi)(\phi^\dagger,\theta'\psi)=\sum_{f=0}^{2\nu}\frac{(\psi^\dagger,\Gamma^{(f)}\psi)\cdot(\phi^\dagger,\theta'\Gamma^{(f)}\theta\phi)}{2^\nu}. \tag{81}$$

Proof

We can expand the matrix $\psi^\dagger{}_A\psi_B$ as:

$$\psi^\dagger{}_A\psi_B=\sum_{f'=0}^{2\nu}a^{(f')}\cdot(\Gamma^{(f')})_{BA}. \tag{82}$$

As was previously done we determine the coefficients $a^{(f)}$ by multiplying with $(\Gamma^{(f)})_{AB}$ and summing over A and B. This gives

$$(\psi^\dagger,\Gamma^{(f)}(f_i)\psi)=\sum_{f'=0}^{2\nu}a^{(f')}\cdot\mathrm{tr}\Gamma^{(f)}(f_i)\Gamma^{(f')}=a^{(f)}(f_i)2^\nu, \tag{83}$$

and hence:

$$\psi^\dagger{}_A\psi_B=\sum_{f=0}^{2\nu}\frac{(\psi^\dagger,\Gamma^{(f)}\psi)\cdot(\Gamma^{(f)})_{BA}}{2^\nu}. \tag{84}$$

Multiplying (84) by $\theta_{AC}\phi_C\phi_D{}^\dagger\theta'_{DB}$ and summing over $ABCD$ gives (81).

To illustrate the utility of this result we consider the problem of expressing the scalars formed by first combining ϕ and $\psi^\dagger$, ψ and $\phi^\dagger$ into tensors and then contracting in terms of the scalars formed by first combining $\psi^\dagger$ and ψ, $\phi^\dagger$ and ϕ. From (68) it is clear that with two covariant and two contravariant spinors we can form $2\nu+1$ scalars. As a basis for all such scalars we can use the $2\nu+1$ scalars:

$$S^{(0)}{}_f(\psi^\dagger,\psi;\phi^\dagger,\phi)\equiv(\psi^\dagger,\Gamma^{(f)}\psi)\cdot(\phi^\dagger,\Gamma^{(f)}\phi). \tag{85}$$

That these are linearly independent is proved by assuming the converse. Then there exists a nontrivial relation of the form

$$\sum_{f=0}^{2\nu}A_f(\psi^\dagger,\Gamma^{(f)}\psi)\cdot(\phi^\dagger,\Gamma^{(f)}\phi)=0, \tag{86}$$

for all $\phi^\dagger$, ϕ. But this implies

$$\sum_{f=0}^{2\nu}A_f(\psi^\dagger,\Gamma^{(f)}\psi)\cdot(\Gamma^{(f)})_{BA}=0, \quad \text{all } A,\,B, \tag{87}$$

i.e., the $\Gamma^{(f)}$ would not be linearly independent, contrary to a theorem proved previously. Hence, there exists a $2\nu+1$ dimensional matrix $(a_{\lambda f})$ by means of which the scalars obtained by grouping $\psi^\dagger$, ϕ and $\phi^\dagger$, ψ in (85) can be linearly expressed in terms of the $S^{(0)}{}_f$. Thus if we define

$$S^{(0)'}{}_\lambda\equiv S_\lambda{}^{(0)}(\psi^\dagger,\phi;\phi^\dagger,\psi)\equiv(\psi^\dagger,\Gamma^{(\lambda)}\phi)\cdot(\phi^\dagger,\Gamma^{(\lambda)}\psi), \tag{88}$$

we have

$$S^{(0')}{}_\lambda=a_{\lambda f}S_f{}^{(0)}. \tag{89}$$

Substitution of

$$\theta=\theta'=\Gamma^{(\lambda)}(i_1 i_2\cdots i_\lambda)\equiv\Gamma^{(\lambda)}(\lambda_i) \tag{90}$$

in Eq. (81) and summing over all components of $\Gamma^{(\lambda)}$ gives:

$$(\psi^\dagger,\Gamma^{(\lambda)}\phi)\cdot(\phi^\dagger,\Gamma^{(\lambda)}\psi)$$
$$=\sum_{f=0}^{2\nu}\frac{(\psi^\dagger,\Gamma^{(f)}\psi)}{2^\nu}\cdot\sum_{\lambda_i}(\phi^\dagger,\Gamma^{(\lambda)}(\lambda_i)\Gamma^{(f)}\Gamma^{(\lambda)}(\lambda_i)\phi). \tag{91}$$

Now all $\Gamma^{(\lambda)}(\lambda_i)$ and $\Gamma^{(f)}(f_j)$ either commute or anticommute. Moreover,

$$[\Gamma^{(\lambda)}(\lambda_i)]^2=1.$$

Hence

$$\sum_{\lambda_i}\Gamma^{(\lambda)}(\lambda_i)\Gamma^{(f)}(f_j)\Gamma^{(\lambda)}(\lambda_i)=(\text{constant})\Gamma^{(f)}(f_j). \tag{92}$$

Since we are summing over all components of $\Gamma^{(\lambda)}$ it is apparent that the constant is independent of which component of $\Gamma^{(f)}$ is involved. Thus, with a suitable normalization, we have

$$\sum_{\lambda_i}\Gamma^{(\lambda)}(\lambda_i)\Gamma^{(f)}\Gamma^{(\lambda)}(\lambda_i)=\binom{2\nu}{\lambda}d_{\lambda f}\Gamma^{(f)}. \tag{93}$$

Comparing (93), (91) and (89) we have:

$$a_{\lambda f}=\binom{2\nu}{\lambda}d_{\lambda f}/2^\nu, \tag{94}$$

where

$$\binom{2\nu}{\lambda}d_{\lambda f}\Gamma^{(f)}=\sum_{\lambda_i}\Gamma^{(\lambda)}(\lambda_i)\Gamma^{(f)}\Gamma^{(\lambda)}(\lambda_i). \tag{95a}$$

Multiplying the f_j component of this equation by $\Gamma^{(f)}(f_j)$ and summing over f_j gives:

$$d_{\lambda f}\binom{2\nu}{f}\binom{2\nu}{\lambda}1$$
$$=\sum_{\lambda_i f_j}\Gamma^{(\lambda)}(\lambda_i)\Gamma^{(f)}(f_j)\Gamma^{(\lambda)}(\lambda_i)\Gamma^{(f)}(f_j). \tag{95b}$$

Taking the trace and dividing by factors on the left yields the very convenient expression

$$d_{\lambda f}=\frac{1}{\binom{2\nu}{f}\binom{2\nu}{\lambda}2^\nu}$$
$$\times\operatorname{tr}\sum_{\lambda_i f_j}\Gamma^{(\lambda)}(\lambda_i)\Gamma^{(f)}(f_j)\Gamma^{(\lambda)}(\lambda_i)\Gamma^{(f)}(f_j). \tag{95c}$$

Properties of $d_{\lambda f}$ and special values are given in Appendix (A). The most generally useful form of the results obtained are:

$$d_{\lambda f}=\frac{1}{\binom{2\nu}{\lambda}}(-1)^{f\lambda}$$
$$\times\{\text{coefficient of } x^\lambda \text{ in } (1+x)^{2\nu-f}(1-x)^f\}. \tag{95d}$$

Hence,

$$a_{\lambda f}=(-1)^{f\lambda}$$
$$\times\{\text{coefficient of } x^\lambda \text{ in } (1+x)^{2\nu-f}(1-x)^f\}. \tag{96}$$

As a well-known illustration we consider the β-decay interaction. Here we have the four spinors $\Psi_n^\dagger$, Ψ_p, $\phi_\nu^\dagger$, ϕ_e representing neutron, proton, neutrino, and electron wave functions, respectively. The scalars formed by grouping neutron-electron, neutrino-proton are then expressed in terms of the usual grouping neutron-proton, neutrino-electron as:

$$S_\lambda^{(0)\prime}\equiv S_\lambda^{(0)}(\Psi_n^\dagger,\phi_e;\ \phi_\nu^\dagger,\Psi_p)$$
$$=a_{\lambda f}S_f^{(0)}(\Psi_n^\dagger,\Psi_p;\ \phi_\nu^\dagger,\phi_e). \tag{97}$$

From the results of Appendix A it follows trivially that

$$(a_{\lambda f})=\begin{bmatrix}\frac14 & \frac14 & \frac14 & \frac14 & \frac14\\ 1 & -\frac12 & 0 & \frac12 & -1\\ \frac32 & 0 & -\frac12 & 0 & \frac32\\ 1 & \frac12 & 0 & -\frac12 & -1\\ \frac14 & -\frac14 & \frac14 & -\frac14 & \frac14\end{bmatrix}. \tag{98}$$

Hence[9]:

$$\begin{aligned}
S_0'&=\tfrac14\{S_0+S_1+S_2+S_3+S_4\},\\
S_1'&=S_0-\tfrac12 S_1+\tfrac12 S_3-S_4,\\
S_2'&=\tfrac32 S_0-\tfrac12 S_2+\tfrac32 S_4,\\
S_3'&=S_0+\tfrac12 S_1-\tfrac12 S_3-S_4,\\
S_4'&=\tfrac14\{S_0-S_1+S_2-S_3+S_4\}.
\end{aligned} \tag{99}$$

The inversion of the relation (89) is particularly easy. Since the prime merely denotes the interchange $\phi\rightleftarrows\psi$, a double prime brings the expression back to its original form:

$$S_\lambda^{(0)\prime\prime}=S_\lambda^{(0)}=a_{\lambda f}S_f^{(0)\prime}=(a^2)_{\lambda f}S_f^{(0)}, \tag{100}$$

i.e.,

$$a^2=1, \tag{101a}$$

or

$$a^{-1}=a. \tag{101b}$$

A direct proof of this using the formula (96) is given in Appendix B.

Similar considerations are obviously applicable to the other tensors formed with four spinors. A particularly simple case is that of the pseudoscalars.

While it is intuitively clear that there are $2\nu+1$ independent pseudoscalars it may be worth while to give a simple proof. Restricting ourselves (temporarily)

[9] This is essentially Eq. (1.4) of reference 5.

to the real orthogonal group will not change this number and permits the use of group integration. Let h denote the volume of the pure rotations, dS denote the volume element for pure rotations, dU for rotation-reflections, and dT a general volume element. Then if χ be the character of the spinor representation, χ^4 is the character of the representation given by four spinors. The number (N_s) of scalars contained in this representation is:

$$N_s=(1/2h)\int\chi^4 dT$$

$$=(1/2h)\left\{\int\chi^4 dS+\int\chi^4 dU\right\}, \qquad (102a)$$

while the number of pseudoscalars (N_{ps}) is:

$$N_{ps}=(1/2h)\left\{\int\chi^4 dS-\int\chi^4 dU\right\}. \qquad (102b)$$

Since χ vanishes for reflections:

$$N_{ps}=N_s=2\nu+1. \qquad (103)$$

For our independent pseudoscalars we may choose those obtained by inserting a factor $\Gamma^{(2\nu)}$ in one of the two factors in our scalars. Thus a basis is formed by:

$$S_f^{(2\nu)}\equiv S_f^{(2\nu)}(\psi^\dagger,\psi;\phi^\dagger,\phi)$$
$$=(\psi^\dagger,\Gamma^{(f)}\psi)\cdot(\phi^\dagger,\Gamma^{(2\nu)}\Gamma^{(f)}\phi). \qquad (104)$$

The quantities $S_\lambda^{(2\nu)\prime}$ obtained by interchanging ψ and ϕ may be expressed in terms of these as:

$$S_\lambda^{(2\nu)\prime}=a_{\lambda f}^{(2\nu)}S_f^{(2\nu)}. \qquad (105)$$

Inserting

$$\theta=\Gamma^{(\lambda)}(\lambda_i),\quad \theta'=\Gamma^{(2\nu)}\Gamma^{(\lambda)}(\lambda_i),$$

in (81) and summing over λ_i gives:

$$(\psi^\dagger,\Gamma^{(\lambda)}\phi)\cdot(\phi^\dagger,\Gamma^{(2\nu)}\Gamma^{(\lambda)}\psi)=\sum_{f=0}^{2\nu}(1/2^\nu)(\psi^\dagger,\Gamma^{(f)}\psi)$$
$$\cdot\sum_{\lambda_i}(\phi^\dagger,\Gamma^{(2\nu)}\Gamma^{(\lambda)}(\lambda_i)\Gamma^{(f)}\Gamma^{(\lambda)}(\lambda_i)\phi). \qquad (106)$$

But we have seen that

$$(1/2^\nu)\sum_{\lambda_i}\Gamma^{(\lambda)}(\lambda_i)\Gamma^{(f)}\Gamma^{(\lambda)}(\lambda_i)=a_{\lambda f}\Gamma^{(f)}. \qquad (107)$$

Comparing (107), (106), and (105) gives:

$$a_{\lambda f}^{(2\nu)}=a_{\lambda f}. \qquad (108)$$

Of paramount importance for the identities is the problem of expressing the covariants formed by combining the two covariant and the two contravariant spinors together first in terms of the combinations as in (85). For this the relevant starting point is obtained from (84) by multiplying by

$$(\theta C^{-1})_{AC}\phi_C^\dagger\phi_D(C^t\theta')_{DB}$$

and summing over A, B, C, and D. This gives:

$$(\psi^\dagger,\theta C^{-1}\phi^\dagger)(\phi C^t\theta'\psi)$$
$$=\sum_f(1/2^\nu)(\psi^\dagger,\Gamma^{(f)}\psi)\cdot(\phi,C^t\theta'\Gamma^{(f)}\theta C^{-1}\phi^\dagger). \qquad (109)$$

From (109) we obtain the scalars,

$$T_\lambda^{(0)}=(\psi^\dagger,\Gamma^{(\lambda)}C^{-1}\phi^\dagger)\cdot(\phi,C^t\Gamma^{(\lambda)}\psi), \qquad (110)$$

in terms of the $S_f^{(0)}$ of (85) by substituting

$$\theta=\theta'=\Gamma^{(\lambda)}(\lambda_i)$$

and summing over the components λ_i. Remembering

$$\Gamma^t(i)=C\Gamma(i)C^{-1},\quad [C^t]^{-1}=(-1)^{[\nu/2]}C^{-1}, \qquad (111)$$

and (107) gives:

$$T_\lambda^{(0)}=g_{\lambda f}S_f^{(0)}, \qquad (112)$$

where

$$g_{\lambda f}=(-1)^{([\nu/2]+[f/2])}a_{\lambda f}. \qquad (113)$$

Since it has been seen that $(a)^2=1$ the inverse of (g) is obviously:

$$(g^{-1})_{\lambda f}=(-1)^{([\nu/2]+[\lambda/2])}a_{\lambda f}. \qquad (114)$$

The application of (112) to β decay is of some importance. From (113) and (98) we obtain

$$(g)=\begin{pmatrix}-\frac14 & -\frac14 & \frac14 & \frac14 & -\frac14\\ -1 & \frac12 & 0 & \frac12 & 1\\ -\frac32 & 0 & -\frac12 & 0 & -\frac32\\ -1 & -\frac12 & 0 & -\frac12 & 1\\ -\frac14 & \frac14 & \frac14 & -\frac14 & -\frac14\end{pmatrix}, \qquad (115)$$

giving (on omitting superscripts for convenience)

$$\begin{aligned}T_0&=\tfrac14\{-S_0-S_1+S_2+S_3-S_4\}\\ T_1&=\tfrac12\{-2S_0+S_1+S_3+2S_4\},\\ T_2&=\tfrac12\{-3S_0+S_2-3S_4\},\\ T_3&=\tfrac12\{-2S_0-S_1-S_3+2S_4\},\\ T_4&=\tfrac14\{-S_0+S_1+S_2-S_3-S_4\}.\end{aligned} \qquad (116)$$

To obtain the scalar biquadratic identities we need only combine (112) with (57) and (58). Thus if we identify $\psi=\phi$, $\psi^\dagger=\phi^\dagger$ those $T_\lambda^{(0)}$ will vanish for which $C\Gamma^{(\lambda)}$ is antisymmetric. This gives as the scalar identities:

(a) If $\nu=0,1 \pmod 4$

$$0=g_{\lambda f}S_f^{(0)}(\psi^\dagger,\psi;\psi^\dagger,\psi)\quad \lambda=2,3 \pmod 4. \qquad (117)$$

Hence there are ν scalar identities in this case.

(b) If $\nu=2,3 \pmod 4$

$$0=g_{\lambda f}S_f^{(0)}(\psi^\dagger,\psi;\psi^\dagger,\psi)\quad \lambda=0,1 \pmod 4. \qquad (118)$$

These are $\nu+1$ identities.

Since $(g_{\lambda f})$ is nonsingular (113), we see that these identities are all independent. Moreover, since only one of the two factors of $T_\lambda^{(0)}$ need vanish, (117) and (118) are correct provided only $\psi^\dagger=\phi^\dagger$ *or* $\psi=\phi$.

For $n=2$ ($\nu=1$), (117) yields the single identity:

$$g_{2f}S_f^{(0)}=0. \tag{119}$$

Since the matrix (g) is readily found to be

$$(g)=\begin{bmatrix} \frac{1}{2} & \frac{1}{2} & -\frac{1}{2} \\ 1 & 0 & 1 \\ \frac{1}{2} & -\frac{1}{2} & -\frac{1}{2} \end{bmatrix}, \tag{120}$$

we obtain

$$S_0-S_1-S_2=0; \tag{121a}$$

or, expressing Γ's as Pauli matrices:

$$(\psi^*,\psi)^2=\sum_{i=1}^{3}(\psi^*,\sigma_i\psi)^2. \tag{121b}$$

For $n=4$ ($\nu=2$) we have, using (118) and (115), the three identities:

$$0=\tfrac{1}{4}\{-S_0-S_1+S_2+S_3-S_4\}, \tag{122a}$$

$$0=\tfrac{1}{2}\{-2S_0+S_1+S_3+2S_4\}, \tag{122b}$$

$$0=\tfrac{1}{4}\{-S_0+S_1+S_2-S_3-S_4\}. \tag{122c}$$

Adding (a) and (c) gives

$$S_0+S_4-S_2=0. \tag{123a}$$

Subtracting (c) from (a) gives

$$S_1=S_3. \tag{124}$$

Substituting this in (122b) gives

$$S_0-S_4-S_1=0, \tag{123b}$$

and

$$S_0-S_4-S_3=0. \tag{123c}$$

Identities (123b, a, c) are just Pauli's[3] Eqs. (34, 1, 2, 3).

Pseudoscalar identities may be obtained in a similar manner. Thus by an argument paralleling that leading from (81) to (112) we obtain

$$T_\lambda^{(2\nu)}(\psi^\dagger,\phi^\dagger;\ \phi,\psi)=h_{\lambda f}S_f^{(2\nu)}(\psi^\dagger,\psi;\ \phi^\dagger,\phi), \tag{125}$$

where

$$T_\lambda^{(2\nu)}(\psi^\dagger,\phi^\dagger;\ \phi,\psi)=(\psi^\dagger,\Gamma^{(\lambda)}C^{-1}\phi^\dagger)\cdot(\phi C^{-1}\Gamma^{(2\nu)}\Gamma^{(\lambda)}\psi), \tag{126}$$

and

$$h_{\lambda f}=(-1)^{([\nu/2]+[f/2]+\nu+f)}a_{\lambda f}. \tag{127}$$

(h) has the inverse

$$(h^{-1})_{\lambda f}=(-1)^{([\nu/2]+[\lambda/2]+\nu+\lambda)}a_{\lambda f}. \tag{128}$$

From (57b) and (58b) we have:

If $\nu=0, 1 \pmod 4$,

$$(\psi^\dagger,\Gamma^{(\lambda)}C^{-1}\psi^\dagger)=0, \quad \lambda=2, 3 \pmod 4. \tag{129}$$

If $\nu=2, 3 \pmod 4$,

$$(\psi^\dagger,\Gamma^{(\lambda)}C^{-1}\psi^\dagger)=0, \quad \lambda=0, 1 \pmod 4. \tag{130}$$

Thus, irrespective of the relation between ϕ and ψ, we have for $\phi^\dagger=\psi^\dagger$ the identities,

$$0=h_{\lambda f}S_f^{(2\nu)}, \tag{131}$$

for the values of λ in (129) and (130) corresponding to the respective values of ν.

Similarly, from (57b), (58b), and (1) it can be shown that (all equations for ν and λ holding mod 4):

$$(\psi,C^{\dagger}\Gamma^{(2\nu)}\Gamma^{(\lambda)}\psi)=0 \begin{cases} \text{if } \nu=0, \text{ for } \lambda=1, 2 & \text{(132a)} \\ \text{if } \nu=1, \text{ for } \lambda=0, 3 & \text{(132b)} \\ \text{if } \nu=2, \text{ for } \lambda=0, 3 & \text{(132c)} \\ \text{if } \nu=3, \text{ for } \lambda=1, 2. & \text{(132d)} \end{cases}$$

Hence, for arbitrary $\phi^\dagger$ and $\psi^\dagger$, we obtain for $\phi=\psi$ the identities (131) holding for the λ corresponding to the ν of (132).

The most interesting identities are those in which we have simultaneously $\psi^\dagger=\phi^\dagger$, $\psi=\phi$. Combining the two sets of identities given shows that

$$h_{\lambda f}S_f^{(2\nu)}(\psi^\dagger,\psi;\ \psi^\dagger,\psi)=0, \quad \lambda\neq\nu \pmod 4. \tag{133}$$

While (133) gives *all* the pseudoscalar identities it is unnecessarily complicated for calculation since some of the identities contained therein are rather trivial and better obtained by other methods. This is seen by two examples.

For $\nu=1$, we have

$$(h)=\begin{bmatrix} -\frac{1}{2} & \frac{1}{2} & \frac{1}{2} \\ -1 & 0 & -1 \\ -\frac{1}{2} & -\frac{1}{2} & \frac{1}{2} \end{bmatrix}, \tag{134}$$

and the identities:

$$\sum_{f=0}^{2}h_{\lambda f}S_f^{(2)}=0, \quad \lambda=0, 2; \tag{135}$$

i.e.,

$$0=\tfrac{1}{2}\{-S_0^{(2)}+S_1^{(2)}+S_2^{(2)}\}, \tag{136a}$$

$$0=\tfrac{1}{2}\{-S_0^{(2)}-S_1^{(2)}+S_2^{(2)}\}. \tag{136b}$$

Adding, we get the identity:

$$S_0^{(2)}=S_2^{(2)}, \tag{137a}$$

which, on expressing the $S_\lambda^{(2)}$ in terms of Pauli matrices and wave functions, is seen to be the trivial statement that

$$(\psi^\dagger,\psi)(\psi^*,\sigma_3\psi)=(\psi^*,\sigma_3\psi)(\psi^*,\psi). \tag{137b}$$

For obvious reasons this will be called a "relabeling identity."

Inserting (137a) in (136) gives as the other identity,

$$S_1^{(2)}=0. \tag{138a}$$

In terms of the Pauli matrices this is the trivial result;

$$\begin{aligned}&(\psi^*,\sigma_1\psi)(\psi^*,\sigma_3\sigma_1\psi)+(\psi^*,\sigma_2\psi)(\psi^*,\sigma_3\sigma_2\psi)\\ &\quad=i(\psi^*,\sigma_1\psi)(\psi^*,\sigma_2\psi)-i(\psi^*,\sigma_2\psi)(\psi^*,\sigma_1\psi)=0,\end{aligned} \tag{138b}$$

which we will also call a "relabeling identity."

For $\nu=2$ we have:

$$(h)=\begin{bmatrix} -\frac{1}{4} & \frac{1}{4} & \frac{1}{4} & -\frac{1}{4} & -\frac{1}{4} \\ -1 & -\frac{1}{2} & 0 & -\frac{1}{2} & 1 \\ -\frac{3}{2} & 0 & -\frac{1}{2} & 0 & -\frac{3}{2} \\ -1 & \frac{1}{2} & 0 & \frac{1}{2} & 1 \\ -\frac{1}{4} & -\frac{1}{4} & \frac{1}{4} & \frac{1}{4} & -\frac{1}{4} \end{bmatrix},$$

and the identities:

$$h_{\lambda f}S_f^{(4)}=0, \quad \lambda=0, 1, 3, 4. \tag{139}$$

Explicitly these are (omitting the superscript 4)

$$0=-S_0+S_1+S_2-S_3-S_4, \tag{140a}$$

$$0=-S_0-S_1/2-S_3/2+S_4, \tag{140b}$$

$$0=-S_0+S_1/2+S_3/2+S_4, \tag{140c}$$

$$0=-S_0-S_1+S_2+S_3-S_4. \tag{140d}$$

Subtracting (d) from (a) and adding (b) to (c) gives the two trivial relabelling identities:

$$S_1=S_3, \tag{141a}$$

$$S_0=S_4. \tag{141b}$$

Inserting (141) in (140a) and (140b) gives the two nontrivial identities:

$$S_2=2S_0, \tag{142a}$$

$$S_1=0. \tag{142b}$$

These are Pauli's[3] Eqs. (34_4) and (34_5), respectively.

The nature of the "relabeling identities" is shown from the result of Appendix C that

$$S_{\nu+i}^{(2\nu)}=(-1)^{\nu+i}S_{\nu-i}^{(2\nu)}. \tag{143}$$

This gives an identity for each of the ν possibilities $i=1, 2, \cdots, \nu$. Moreover if ν is odd Eq. (143) for $i=0$ shows that

$$S_\nu^{(2\nu)}=0. \tag{144}$$

Thus for even ν, we have ν of these trivial statements, while for odd ν we have $\nu+1$ relabeling identities. Table II shows the number of pseudoscalar identities (N_{ps}) given by (133), the number of trivial relabeling identities (N_t), and the remaining number of nontrivial identities N_n.

From (139) and (143) explicit forms for the nontrivial identities can be obtained. However, in practice it is just as convenient to use (139) as it stands merely remembering (143).

VI. IDENTITIES FOR $n=2\nu+1$

All calculations proceed the same as for even dimensions except that now we need only use the even quantities $\Gamma^{(2\lambda)}$ as a basis for expansion of $2^\nu\times 2^\nu$ matrices and we use the properties of Table I. For brevity we will give only the results for scalars formed with 2 covariant and 2 contravariant spinors. The proof of the statements is outlined in Appendix D

TABLE II. The number of pseudoscalar identities N_{ps}, trivial relabeling identities N_t, and nontrivial identities N_n.

	Pseudoscalar identities		
ν (mod 4)	N_{ps}	N_t	N_n
0	$\frac{3}{2}\nu$	ν	$\nu/2$
1	$\frac{3}{2}\nu+\frac{1}{2}$	$\nu+1$	$\nu/2-\frac{1}{2}$
2	$\frac{3}{2}\nu+1$	ν	$\nu/2+1$
3	$\frac{3}{2}\nu+\frac{3}{2}$	$\nu+1$	$\nu/2+\frac{3}{2}$

where we also give various properties of the matrices introduced.

The $\nu+1$ scalars obtained by first combining the spinors as $\psi^\dagger$ with ϕ, $\phi^\dagger$ with ψ are expressed in terms of those with the grouping $\psi^\dagger$ with ψ, $\phi^\dagger$ with ϕ as:

$$S_{2\lambda}'(\psi^\dagger,\phi;\,\phi^\dagger,\psi)=\sum_{f=0}^{\nu}\alpha_{\lambda f}S_{2f}(\psi^\dagger,\psi;\,\phi^\dagger,\phi),$$

$$\lambda=0, 1, \cdots, \nu, \tag{145}$$

where

$$S_{2\lambda}'(\psi^\dagger,\phi;\,\phi^\dagger,\psi)=(\psi^\dagger,\Gamma^{(2\lambda)}\phi)\cdot(\phi^\dagger,\Gamma^{(2\lambda)}\psi), \tag{146}$$

$$S_{2f}(\psi^\dagger,\psi;\,\phi^\dagger,\phi)=(\psi^\dagger,\Gamma^{(2\lambda)}\psi)\cdot(\phi^\dagger,\Gamma^{(2\lambda)}\phi), \tag{147}$$

$$\alpha_{\lambda f}=(1/2^\nu)\{\text{coefficient of } x^{2\lambda} \text{ in } (1+x)^{2\nu+1-2f}(1-x)^{2f}\}. \tag{148}$$

As examples we have:

For $n=3$ $(\nu=1)$ $(\lambda,f=0,1)$

$$S_0'=\tfrac{1}{2}(S_0+S_2), \tag{149a}$$

$$S_2'=\tfrac{1}{2}(3S_0-S_2). \tag{149b}$$

For $n=5$ $(\nu=2)$ $(\lambda,f=0,2,4)$

$$S_0'=\tfrac{1}{4}\{S_0+S_2+S_4\}, \tag{150a}$$

$$S_2'=\tfrac{1}{2}\{5S_0-S_2+S_4\}, \tag{150b}$$

$$S_4'=\tfrac{1}{4}\{5S_0+S_2-3S_4\}. \tag{150c}$$

The scalars formed by combining first covariant with covariant, contravariant with contravariant spinors can be expressed in terms of the S_{2f} of (147) as

$$T_{2\lambda}(\psi^\dagger,\phi^\dagger;\,\psi,\phi)=\sum_{f=0}^{\nu}\gamma_{\lambda f}S_{2f} \quad (\lambda=0, 1, \cdots \nu), \tag{151}$$

where

$$T_{2\lambda}(\psi^\dagger,\phi^\dagger;\,\psi,\phi)=(\psi^\dagger,\Gamma^{(2\lambda)}C^{-1}\phi^\dagger)\cdot(\phi,C^t\Gamma^{(2\lambda)}\psi), \tag{152}$$

$$\gamma_{\lambda f}=(-1)^{(f+\nu+[\nu/2])}\alpha_{\lambda f}. \tag{153}$$

For example we have, for $\nu=1$,

$$T_0=\tfrac{1}{2}(-S_0+S_2), \tag{154a}$$

$$T_2=\tfrac{1}{2}(-3S_0-S_2); \tag{154b}$$

while, for $\nu=2$,

$$T_0=\tfrac{1}{4}(-S_0+S_2-S_4), \tag{155a}$$

$$T_2=-\tfrac{1}{2}(5S_0+S_2+S_4), \tag{155b}$$

$$T_3=-\tfrac{1}{4}(-5S_0+S_2+3S_4). \tag{155c}$$

As in Sec. V, we obtain nontrivial identities between the S_{2f} for $\psi^\dagger=\phi^\dagger$ and (or) $\phi=\psi$ for those values of λ in (151) for which these assumptions make $T_{2\lambda}$ vanish. That is, we obtain identities for those λ such that $C\Gamma^{(2\lambda)}$ is antisymmetric. Thus from Table I we obtain the identities:

$$\sum_{f=0}^{r}\gamma_{\lambda f}S_{2f}=0\begin{cases}\lambda \text{ odd}, & \nu=0 \pmod 4\\ \lambda \text{ even}, & \nu=1 \pmod 4\\ \lambda \text{ even}, & \nu=2 \pmod 4\\ \lambda \text{ odd}, & \nu=3 \pmod 4.\end{cases} \tag{156}$$

For $n=3$ ($\nu=1$) we have only the equation for $\lambda=0$:

$$\gamma_{0f}S_{2f}=0, \tag{157a}$$

or

$$S_0=S_2. \tag{157b}$$

It may be noted that (157b) is just the identity (121b) obtained for $n=2$.

For $n=5$ ($\nu=2$), we obtain identities (156) for $\lambda=0, 2$. These are

$$-S_0+S_2-S_4=0, \tag{158a}$$

$$-5S_0+S_2+3S_4=0, \tag{158b}$$

or

$$S_0=S_4, \tag{159a}$$

$$S_2=2S_0. \tag{159b}$$

In Table III we give the number (N_I) of scalar identities given by (156). Since there are $\nu+1$ scalars formed from two arbitrary covariant and two arbitrary contravariant spinors, the number (N_s) of independent scalars when spinors are identified is:

$$N_s=\nu+1-N_I \tag{160}$$

which is also given in Table III.

VII. CONCLUSION

The decomposition of the representation of the orthogonal group in n dimensions given by the symmetrical product of two covariant or two contravariant spinors has been obtained. It has been shown that using the decomposition all identities holding between covariants formed with four such spinors when some of them are identical are readily found. Explicit formulas for the scalar and pseudoscalar identities in $n=2\nu$ dimensions and for the scalar identities in $n=2\nu+1$ dimensions are given.

TABLE III. Numbers N_s of scalars formed from 2 sets of identical spinors. $n=2\nu+1$. N_I is the number of scalar identities.

ν (mod 4)	N_I	N_s
0	$\nu/2$	$(\nu/2)+1$
1	$(\nu/2)+\frac{1}{2}$	$(\nu/2)+\frac{1}{2}$
2	$(\nu/2)+1$	$\nu/2$
3	$(\nu/2)+\frac{1}{2}$	$(\nu/2)+\frac{1}{2}$

APPENDIX A. PROPERTIES OF THE MATRIX $a_{\lambda f}$

In the text we obtained the result

$$a_{\lambda f}=\binom{2\nu}{\lambda}d_{\lambda f}/2^\nu, \tag{A1}$$

where

$$d_{\lambda f}=\left\{\binom{2\nu}{\lambda}\binom{2\nu}{f}2^\nu\right\}^{-1}$$

$$\times\mathrm{tr}\sum_{\substack{i_1<i_2<\cdots i_\lambda\\ j_1<j_2<\cdots j_f}}[\Gamma^{(\lambda)}(i_1i_2\cdots i_\lambda)\Gamma^{(f)}(j_1j_2\cdots j_f)]^2. \tag{A2}$$

Since (A2) is symmetrical in λ and f, we have

$$d_{\lambda f}=d_{f\lambda}. \tag{A3}$$

To calculate $d_{\lambda f}$ we will assume $\lambda\leq f$. (From (A3) we see this is no significant restriction.) Since it is clear that each term in the sum over $j_1, j_2, \cdots j_f$ gives the same contribution we can restrict ourselves to the single term $\Gamma^{(f)}(12\cdots f)$ on multiplying by $\binom{2\nu}{f}$. Thus

$$d_{\lambda f}=\left\{\binom{2\nu}{\lambda}2^\nu\right\}^{-1}\mathrm{tr}\sum_{i_1<i_2<\cdots<i_\lambda}\Gamma^{(\lambda)}(i_1i_2\cdots i_\lambda)$$

$$\times\Gamma^{(f)}(12\cdots f)\Gamma^{(\lambda)}(i_1i_2\cdots i_\lambda)\Gamma^{(f)}(12\cdots f). \tag{A4}$$

Consider a fixed term in the sum. Since $\Gamma^{(\lambda)}(i_1i_2\cdots)$ either commutes or anticommutes with $\Gamma^{(f)}(12\cdots f)$ and the squares of both are unity we have:

$$(2^\nu)^{-1}\mathrm{tr}\Gamma^{(\lambda)}(i_1i_2\cdots i_\lambda)\Gamma^{(f)}(12\cdots f)$$

$$\times\Gamma^{(\lambda)}(i_1i_2\cdots i_\lambda)\Gamma^{(f)}(12\cdots f)=\pm1. \tag{A5}$$

If k of the indices $i_1, i_2, \cdots i_\lambda$ are greater than f, the sign is

$$[(-1)^{f-1}]^{\lambda-k}[(-1)^f]^k. \tag{A6}$$

This occurs in the sum over $i_1, \cdots, i_\lambda$ a number of times equal to

$$\binom{f}{\lambda-k}\binom{2\nu-f}{k}.$$

Hence

$$d_{\lambda f}=\left[\binom{2\nu}{\lambda}\right]^{-1}(-1)^{f\lambda}$$

$$\times\sum_{k=0}^{\lambda}(-1)^{\lambda-k}\binom{f}{\lambda-k}\binom{2\nu-f}{k}. \tag{A7}$$

Comparing with the power series expansion,

$$(1+x)^m(1-x)^n=\sum_{i=0}^{m}\sum_{j=0}^{n}\binom{m}{i}\binom{n}{j}(-1)^jx^{i+j}, \tag{A8}$$

we see that

$$d_{\lambda f}=\left[\binom{2\nu}{\lambda}\right]^{-1}(-1)^{f\lambda}$$

$$\times\{\text{coefficient of } x^{\lambda} \text{ in } (1+x)^{2\nu-f}(1-x)^{f}\}. \quad \text{(A9)}$$

Using (A1), we obtain the result (96).

A further symmetry property is obtained by changing the sign of x in (A9). Thus

$$d_{\lambda f}=\left[\binom{2\nu}{\lambda}\right]^{-1}(-1)^{f\lambda}(-1)^{\lambda}$$

$$\times\{\text{coefficient of } x^{\lambda} \text{ in } (1-x)^{2\nu-f}(1+x)^{f}\}. \quad \text{(A10)}$$

However, (A9) also says that

$$d_{\lambda,\,2\nu-f}=\left[\binom{2\nu}{\lambda}\right]^{-1}(-1)^{f\lambda}$$

$$\times\{\text{coefficient of } x^{\lambda} \text{ in } (1+x)^{f}(1-x)^{2\nu-f}\}. \quad \text{(A11)}$$

Comparing, we see

$$d_{\lambda,\,2\nu-f}=(-1)^{\lambda}d_{\lambda f}. \quad \text{(A12)}$$

From the symmetry properties (A3) and (A12), we need the coefficients $d_{\lambda f}$ only for $\lambda\leq f\leq\nu$. This is only $(\nu+1)(\nu+2)/2$ coefficients.

For λ small, Eq. (A7) is particularly easy to use. Thus, by direct calculation we readily obtain:

$$d_{0f}=1, \quad \text{(A13)}$$

$$d_{1f}=(-1)^{f}(\nu-f)/\nu, \quad \text{(A14)}$$

$$d_{2f}=[2(\nu-f)^{2}-\nu]/\nu(2\nu-1). \quad \text{(A15)}$$

A particularly simple result when one of the indices is ν is obtained from (A10).

$$d_{\nu f}=d_{f\nu}=\left[\binom{2\nu}{f}\right]^{-1}(-1)^{\nu f}$$

$$\times\{\text{coefficient of } x^{f} \text{ in } (1+x)^{\nu}(1-x)^{\nu}\}. \quad \text{(A16)}$$

But

$$(1+x)^{\nu}(1-x)^{\nu}=(1-x^{2})^{\nu}=\sum_{i=0}^{\nu}(-1)^{i}\binom{\nu}{i}x^{2i}. \quad \text{(A17)}$$

Thus:

$$d_{2i+1,\,\nu}=0, \quad \text{(A18)}$$

$$d_{2i,\,\nu}=\left[\binom{2\nu}{2i}\right]^{-1}(-1)^{i}\binom{\nu}{i}. \quad \text{(A19)}$$

The simple formulas (A13–19) give all coefficients of the matrices (d), (a), (g), (h) for ν up to and including $3(n=6)$.

APPENDIX B. PROOF THAT $a^2=1$

A direct proof is obtained using the generating function of (96). This relation may be rewritten

$$a_{\mu\sigma}=2^{-\nu}(-1)^{\mu\sigma}(2\pi i)^{-1}$$

$$\times\oint_{C}(1+x)^{2\nu-\sigma}(1-x)^{\sigma}dx/x^{\mu+1}, \quad \text{(B1)}$$

where the contour C encloses the origin. Similarly, using the generating function (A16) for (d), the symmetry property (A3) and the relation (A1) between (a) and (d) we obtain:

$$a_{\sigma\gamma}=2^{-\nu}(-1)^{\gamma\sigma}\binom{2\nu}{\sigma}\binom{2\nu}{\gamma}^{-1}(2\pi i)^{-1}$$

$$\times\oint(1+y)^{2\nu-\sigma}(1-y)^{\sigma}dy/y^{\gamma+1}. \quad \text{(B2)}$$

Hence:

$$\sum_{\sigma=0}^{2\nu}a_{\mu\sigma}a_{\sigma\gamma}=2^{-2\nu}\binom{2\nu}{\gamma}^{-1}(2\pi i)^{-2}$$

$$\times\oint\oint dxdy\{\ \}/x^{\mu+1}y^{\gamma+1}, \quad \text{(B3)}$$

where

$$\{\ \}=\sum_{\sigma=0}^{2\nu}\binom{2\nu}{\sigma}[(-1)^{\mu+\gamma}]^{\sigma}$$

$$\times[(1-x)(1-y)]^{\sigma}[(1+x)(1+y)]^{2\nu-\sigma}$$

$$=\{(-1)^{\mu+\gamma}(1-x)(1-y)+(1+x)(1+y)\}^{2\nu}. \quad \text{(B4)}$$

It is convenient to divide the discussion into two cases.

Case 1. $\mu+\gamma$ Even

$$\{\ \}=2^{2\nu}(1+xy)^{2\nu}. \quad \text{(B5)}$$

Inserting this in (B3), expanding by the binomial theorem and evaluating by residues gives:

$$\sum_{\sigma=0}^{2\nu}a_{\mu\sigma}a_{\sigma\gamma}$$

$$=\binom{2\nu}{\gamma}^{-1}(2\pi i)^{-2}\oint\oint dxdy(1+xy)^{2\nu}/x^{\mu+1}y^{\gamma+1}$$

$$=\binom{2\nu}{\gamma}^{-1}(2\pi i)^{-2}\oint\oint dxdy(x^{\mu+1}y^{\gamma+1})^{-1}\sum_{i=0}^{2\nu}\binom{2\nu}{i}x^{i}y^{i}$$

$$=(2\pi i)^{-1}\oint x^{\gamma}dx/x^{\mu+1}=\begin{cases}0, & \gamma\neq\mu\\ 1, & \gamma=\mu.\end{cases} \quad \text{(B6)}$$

Case 2. $\mu+\gamma$ Odd

$$\{\ \}=2^{2\nu}(x+y)^{2\nu}$$

$$\sum_{\sigma=0}^{2\nu} a_{\mu\sigma}a_{\sigma\gamma}$$

$$=\binom{2\nu}{\gamma}^{-1}(2\pi i)^{-2}\oint\oint\frac{dxdy}{x^{\mu+1}y^{\gamma+1}}\sum_{i=0}^{2\nu}\binom{2\nu}{i}x^i y^{2\nu-i}$$

$$=\binom{2\nu}{\mu}\left[\binom{2\nu}{\gamma}\right]^{-1}(2\pi i)^{-1}\oint y^{2\nu-\mu}dy/y^{\gamma+1}$$

$$=0 \quad \text{unless} \quad 2\nu-\mu=\gamma. \tag{B7}$$

Thus in Case 2 we get zero unless

$$\mu+\gamma=2\nu, \tag{B8}$$

which was treated under Case 1. Hence:

$$\sum_{\sigma=0}^{2\nu} a_{\mu\sigma}a_{\sigma\gamma}=0, \quad \mu\neq\gamma,$$
$$=1, \quad \mu=\gamma, \tag{B9}$$

or

$$a^2=1. \tag{B10}$$

APPENDIX C. THE RELABELING IDENTITIES

From the definition

$$S_\lambda{}^{(2\nu)}(\psi^\dagger,\psi;\psi^\dagger,\psi)=(\psi^\dagger,\Gamma^{(\lambda)}\psi)\cdot(\psi^\dagger,\Gamma^{(2\nu)}\Gamma^{(\lambda)}\psi)$$
$$=\sum_{i_1<i_2\cdots<i_\lambda}(\psi^\dagger,\Gamma^{(\lambda)}(i_1i_2\cdots i_\lambda)\psi)$$
$$\times(\psi^\dagger,\Gamma^{(2\nu)}\Gamma^{(\lambda)}(i_1i_2\cdots i_\lambda)\psi), \tag{C1}$$

it is clear that

$$S_\lambda{}^{(2\nu)}=\mathfrak{a}S_{2\nu-\lambda}{}^{(2\nu)}, \tag{C2}$$

with some constant $\mathfrak{a}$. To determine $\mathfrak{a}$ we need only find the relationship between a fixed term on the left and the corresponding term on the right. For simplicity we consider the term in which $i_1\cdots i_\lambda$ is the sequence $1, 2, \cdots\lambda$. This term is

$$(\psi^\dagger,i^{[\lambda]}\Gamma(1)\Gamma(2)\cdots\Gamma(\lambda)\psi)i^\nu(\psi^\dagger,\Gamma(1)\cdots$$
$$\times\Gamma(2\nu)i^{[\lambda]}\Gamma(1)\Gamma(2)\cdots\Gamma(\lambda)\psi)$$
$$=(-1)^\lambda(\psi^\dagger,\Gamma(1)\cdots\Gamma(\lambda)\psi)$$
$$\times i^\nu(\psi^\dagger,\Gamma(\lambda+1)\cdots\Gamma(2\nu)\psi). \tag{C3}$$

The corresponding term of $S_{2\nu-f}{}^{(2\nu)}$ is

$$(\psi^\dagger,i^{[2\nu-\lambda]}\Gamma(\lambda+1)\cdots\Gamma(2\nu)\psi)i^\nu(\psi^\dagger,\Gamma(1)\Gamma(2)\cdots$$
$$\times\Gamma(2\nu)i^{[2\nu-\lambda]}\Gamma(\lambda+1)\cdots\Gamma(2\nu)\psi)$$
$$=(\psi^\dagger,\Gamma(1)\cdots\Gamma(\lambda)\psi)i^\nu(\psi^\dagger,\Gamma(\lambda+1)\cdots\Gamma(2\nu)\psi). \tag{C4}$$

Comparing (C3) and (C4) we see that

$$\mathfrak{a}=(-1)^\lambda, \tag{C5}$$

and hence

$$S_\lambda{}^{(2\nu)}=(-1)^\lambda S_{2f-\lambda}{}^{(2\nu)}, \tag{C6}$$

or, more symmetrically,

$$S_{\nu+i}{}^{(2\nu)}=(-1)^{\nu+i}S_{\nu-i}{}^{(2\nu)}. \tag{C7}$$

APPENDIX D. DETAILS IN CASE $n=2\nu+1$

To express the covariants obtained by interchanging ϕ and ψ, we expand

$$\psi^\dagger{}_A\psi_B=\sum_{f=0}^{\nu}A^{(2f)}\cdot(\Gamma^{(2f)})_{BA}. \tag{D1}$$

Taking traces:

$$A^{(2f)}=2^{-\nu}(\psi^\dagger,\Gamma^{(2f)}\psi), \tag{D2}$$

or

$$\psi^\dagger{}_A\psi_B=\sum_{f=0}^{\nu}2^{-\nu}(\psi^\dagger,\Gamma^{(2f)}\psi)\cdot(\Gamma^{(2f)})_{BA}. \tag{D3}$$

Multiplying by $\theta_{AC}\phi_C\phi^\dagger{}_D\theta'{}_{DB}$ and summing gives

$$(\psi^\dagger,\theta\phi)(\phi^\dagger,\theta'\psi)=\sum_{f=0}^{\nu}2^{-\nu}(\psi^\dagger,\Gamma^{(2f)}\psi)(\phi^\dagger,\theta'\Gamma^{(2f)}\theta\phi). \tag{D4}$$

In particular this gives for the scalars:

$$(\psi^\dagger,\Gamma^{(2\lambda)}\phi)\cdot(\phi^\dagger,\Gamma^{(2\lambda)}\psi)$$
$$=\sum_{f=0}^{\nu}2^{-\nu}(\psi^\dagger,\Gamma^{(2f)}\psi)\cdot\sum_{\lambda_i}(\phi^\dagger,\Gamma^{(2\lambda)}(\lambda_i)\Gamma^{(2f)}\Gamma^{(2\lambda)}(\lambda_i)\phi)$$
$$\text{for} \quad \lambda=0, 1, \cdots, \nu. \tag{D5}$$

Now

$$2^{-\nu}\sum_{\lambda_i}\Gamma^{(2\lambda)}(\lambda_i)\Gamma^{(2f)}\Gamma^{(2\lambda)}(\lambda_i)=\alpha_{\lambda f}\Gamma^{(2f)}. \tag{D6}$$

Using the same arguments as in the even-dimensional case, we have:

$$\alpha_{\lambda f}=\binom{2\nu+1}{2\lambda}\epsilon_{\lambda f}/2^\nu, \tag{D7}$$

$$\epsilon_{\lambda f}=\left[2^\nu\binom{2\nu+1}{2\lambda}\binom{2\nu+1}{2f}\right]^{-1}\operatorname{tr}\sum_{\lambda_i f_j}[\Gamma^{(2\lambda)}(\lambda_i)\Gamma^{(2f)}(f_j)]^2$$
$$=\epsilon_{f\lambda}. \tag{D8}$$

Performing the sum as in Appendix A, we obtain

$$\epsilon_{\lambda f}=\binom{2\nu+1}{2\lambda}^{-1}\sum_{i=0}^{2\lambda}[(-1)^{2f-1}]^{2\lambda-i}$$
$$\times[(-1)^{2f}]^i\binom{2f}{2\lambda-i}\binom{2\nu+1-2f}{2i}$$
$$=\binom{2\nu+1}{2\lambda}^{-1}\sum_{i=0}^{2\lambda}(-1)^{2\lambda-i}$$
$$\times\binom{2f}{2\lambda-i}\binom{2\nu+1-2f}{i}, \tag{D9}$$

or

$$\epsilon_{\lambda f}=\binom{2\nu+1}{2\lambda}^{-1}\{\text{coefficient of } x^{2\lambda} \text{ in}$$
$$(1+x)^{2\nu+1-2f}(1-x)^{2f}\}. \tag{D10}$$

On changing the sign of x in (D10) we see

$$\epsilon_{\lambda f}=\epsilon_{\lambda,\frac{1}{2}(2\nu+1-f)}. \tag{D11}$$

Some special values are

$$\epsilon_{0f}=1, \tag{D12}$$

$$\epsilon_{\lambda\nu}=\binom{2\nu+1}{2\lambda}^{-1}\left\{\binom{2\nu}{2\lambda}-\binom{2\nu}{2\lambda-1}\right\}. \tag{D13}$$

To obtain the linear combinations formed by combining similar type spinors, we multiply (D3) by $(\theta C^{-1})_{AC}\phi^{\dagger}{}_{C}\phi_{D}(C^{t}\theta')_{DB}$ and sum:

$$(\psi^{\dagger},\theta C^{-1}\phi^{\dagger})(\phi,C^{t}\theta'\psi)$$

$$=\sum_{f=0}^{\nu}2^{-\nu}(\psi^{\dagger},\Gamma^{(2f)}\psi)\cdot(\phi^{\dagger},C^{t-1}\theta^{t}\Gamma^{t(2f)}\theta^{t\prime}C\phi). \tag{D14}$$

Putting $\theta=\theta'=\Gamma^{(2\lambda)}(\lambda_i)$ and summing over components gives:

$$T_{2\lambda}=\sum_{f}2^{-\nu}(\psi^{\dagger},\Gamma^{(2f)}\psi)\cdot\sum_{\lambda_i}(\phi^{\dagger},C^{t-1}\Gamma^{t(2\lambda)}(\lambda_i)\Gamma^{t(2f)}\Gamma^{t(2\lambda)}(\lambda_i)C\phi). \tag{D15}$$

Using the symmetry properties of C, which can be summarized as

$$C^{t}=(-1)^{(\nu+[\nu/2])}C, \tag{D16}$$

and Eqs. (1), (36), and (D6) gives:

$$T_{2\lambda}=\sum_{f=0}^{\nu}(\psi^{\dagger},\Gamma^{(2f)}\psi)\cdot(-1)^{(f+\nu+[\nu/2])}\alpha_{\lambda f}(\phi^{\dagger},\Gamma^{(2f)}\phi), \tag{D17}$$

or

$$T_{2\lambda}=\gamma_{\lambda f}S_{2f}, \tag{D18}$$

where

$$\gamma_{\lambda f}=(-1)^{(f+\nu+[\nu/2])}\alpha_{\lambda f}. \tag{D19}$$

PHYSICAL REVIEW VOLUME 97, NUMBER 3 FEBRUARY 1, 1955

Renormalization of a Covariant Approximation Scheme in Field Theory*

R. ARNOWITT† AND S. GASIOROWICZ
Radiation Laboratory, Department of Physics, University of California, Berkeley, California
(Received October 18, 1954)

An approximation scheme for the one-nucleon Green's functions previously put forward by the authors is renormalized. The experimental mass and the constants Z_1 and Z_2 are rigorously expressed as free-particle limits of integrals over the kernels appearing in the scheme. The mass and wave-function renormalization are carried out rigorously; the vertex renormalization is performed by a slight redefinition of the approximation scheme, without greatly altering the physical assumptions peculiar to each approximation. General prescriptions for renormalization are written down, and the first three approximations are explicitly shown to be finite.

1. INTRODUCTION

RECENTLY the authors[1] have proposed a covariant approximation scheme for the treatment of the coupled Green's functions equations of meson-nucleon systems. The procedure led to the replacement of the infinite set of coupled equations for the rigorous kernels by a finite set of approximate equations, involving Green's functions which describe processes with no more than a fixed number of external meson lines.

In (I) the question of renormalization was ignored. It is of course not known whether the usual infinities of pseudoscalar meson theory with pseudoscalar coupling are due to the use of the perturbation expansions in which they appear; however, whether the theory is finite or not, a renormalization has to be carried out. In the approximation scheme, whose validity may only be motivated in the low-energy region, it is expected that such high-frequency phenomena as the self-energy, etc., will not be described correctly, and the existence of infinities are a not unexpected feature. Nevertheless the lack of a correct description in the high-energy domain does not prevent one from performing a renormalization. For example, when a subset of perturbation graphs is summed rigorously,[2] the radical difference in the high-energy behavior of the sum and the individual terms of the series does not prevent the renormalization of the latter by perturbation methods.

In this paper a nonperturbation renormalization of the approximation scheme is carried out, i.e., equations involving the renormalized Green's functions, with finite masses and coupling constants, are derived. Although it is of course necessary to solve the resulting

* This work was performed under the auspices of the U. S. Atomic Energy Commission.
† Now at the Institute for Advanced Study, Princeton, New Jersey.
[1] R. Arnowitt and S. Gasiorowicz, Phys. Rev. **95**, 538 (1954), to be referred to as (I).
[2] S. F. Edwards, Phys. Rev. **90**, 284 (1953).

equations to see whether the solutions are finite, it will be shown that these equations generate the renormalized perturbation series, when expanded in powers of the coupling constant.

As already suggested in (I), it is hoped that neglecting vacuum polarization will not strongly affect the low-energy results. Thus the meson propagation function $\Delta_+(\xi-\xi')$ will be assumed to be a given function (namely the free particle kernel) of the experimental meson mass μ.

In the following section the conditions to be satisfied by the finite equations are stated. In subsequent sections rigorous expressions for the renormalization constants Z_1, Z_2, and m' are derived, the role of the overlapping divergences is discussed, and the approximation scheme for the renormalized equations is set up. In Sec. 5 the second approximation is renormalized in detail, and in 6, the procedure for renormalizing the third approximation is outlined. While the general case is not discussed, the work of these two sections makes the extrapolation reasonably clear.

2. PRELIMINARY DISCUSSION

In (I) a rigorous set of equations coupling Green's functions involving one nucleon and an arbitrary number of mesons was derived. The approximation made there, which involves a decomposition of the last Green's function (appearing in a finite subset of equations) into a sum of products of lower Green's functions, was labeled by the number of "thick lines" in a particular time ordering. While this labeling was adequate in the unrenormalized equations, it was found to be ambiguous in dealing with the problem of renormalization, owing to the necessity of successively substituting the kernels back into earlier equations. These equations require an integration over some of the "thick line" variables, thus destroying the particular time ordering chosen. An equivalent convention, which we will adopt here, is to count the number of "strong interactions" between the meson and nucleon. Thus, for example, in the first approximation, writing $G(\xi\xi')\simeq G\Delta_+(\xi-\xi')$ involves no strong interactions, while the second approximation, $G(\xi\xi'\xi'')\simeq G(\xi)\Delta_+(\xi'-\xi'')+\cdots$ involves one strong meson interaction, namely the one appearing in $G(\xi)$. In general the nth approximation will allow $(n-1)$ strong interactions.

Introducing the Fourier transform of the Green's functions,

$$G(xx';\xi_1\cdots\xi_m)=(2\pi)^{-4(1+[m/2])}\int e^{ip(x-x')}\prod_{i=1}^{m}e^{ik_i(\xi_i-x)}\times G(p,k_1\cdots k_m)d^4p\,d^4k_1\cdots d^4k_m, \quad (2.1)$$

where $[m/2]$ is the integral part of $m/2$, the rigorous Eqs. (I 2.7), (I 2.8), and (I 2.9) become

$$[\gamma p+m]G(p)=1-g\int\gamma G(p,k)dk, \quad (2.2)$$

$$[\gamma(p-k)+m]G(p,k)=ig(2\pi)^{-4}\int\gamma G(p,kk')dk', \quad (2.3)$$

$$[\gamma(p-k-k')+m]G(p,kk')=\Delta(k)\delta(k+k')-g\int\gamma G(p,kk'k'')dk''. \quad (2.4)$$

The particular choice of transform variables in (2.1) corresponds diagrammatically to a nucleon of momentum p emitting (in any order whatever) m mesons with momenta $k_1, k_2, \cdots, k_m$.

To exhibit some of the conditions which we wish to impose on the renormalization procedure, and to illustrate some of the difficulties which arise in a non-perturbation renormalization, let us briefly consider the renormalization of the equations in the first approximation.

Decomposing

$$G(p,kk')\simeq G(p)\Delta(k)\delta(k+k') \quad (2.5)$$

in Eq. (2.3) and substituting into Eq. (2.2), we obtain the equation for the one-nucleon Green's function,

$$\left[\gamma p+m+ig^2(2\pi)^{-4}\int\gamma G_0(p-k)\gamma\Delta(k)dk\right]\times G(p)=1. \quad (2.6)$$

As is well known, the integral appearing in Eq. (2.6) may be renormalized by subtracting from it the first two terms in a Taylor expansion about $\gamma p+m=0$. Thus Eq. (2.6) becomes

$$\left[(\gamma p+m')\left(1+\int_1'\right)-\delta m\int_1'+R(p)\right]G(p)=1, \quad (2.7)$$

where

$$m'=m+\delta m=m+ig^2(2\pi)^{-4}\times\left(\int\gamma G_0(p-k)\gamma\Delta(k)dk\right)_{\gamma p+m=0}\equiv m+\int_0', \quad (2.8)$$

$$\int_1'=ig^2(2\pi)^{-4}\left(\frac{\partial}{\partial\gamma p}\int\gamma G_0(p-k)\gamma\Delta(k)dk\right)_{\gamma p+m=0}, \quad (2.9)$$

and

$$R(p)=ig^2(2\pi)^{-4}\int\gamma G_0(p-k)\gamma\Delta(k)dk-\int_0'-(\gamma p+m)\int_1'. \quad (2.10)$$

While $R(p)$ is indeed finite, it is only true to order g^2 that $\delta m \int_1'$ may be neglected and the factor $(1+\int_1')$ utilized to renormalize the Green's function. Furthermore, $R(p)$ is a function of m rather than the renormalized mass m'. Thus if perturbation theory is not made use of, Eq. (2.7) is effectively still unrenormalized.

For a satisfactory program, only the renormalized masses, coupling constants, and Green's functions should appear in the final equations, without any use being made of perturbation theory, though of course the limitations of the approximation to a given number of "strong interactions" must be imposed upon the infinite constants. A necessary condition for a successful renormalization is that the renormalized equations, upon solution in powers of the coupling constant, yield a series of renormalized graphs.

3. RENORMALIZATION CONSTANTS

The renormalization procedure to be described below makes no use of perturbation theory. That multiplicative renormalization can be carried out will be explicitly assumed. Thus, in the notation of Matthews and Salam[3] we define the infinite constants Z_1 and Z_2 by

$$\psi(x)=Z_2^{\frac{1}{2}}\psi_1(x), \tag{3.1}$$

$$g=(Z_1/Z_2)g_1, \tag{3.2}$$

where $\psi(x)$ represents the second-quantized nucleon operator and the subscript "1" will denote the renormalized (finite) quantities. From Eq. (3.1) it follows that

$$G(p,k_1\cdots k_m)=Z_2G_1(p,k_1\cdots k_m). \tag{3.3}$$

In terms of the renormalized quantities, Eqs. (2.2) to (2.4) take the form

$$[\gamma p+m]Z_2G_1(p)=1-g_1Z_1\int\gamma G_1(p,k)dk, \tag{3.4}$$

$$[\gamma(p-k)+m]Z_2G_1(p,k)=ig_1(2\pi)^{-4}Z_1\int\gamma G_1(p,kk')dk', \tag{3.5}$$

$$[\gamma(p-k-k')+m]Z_2G_1(p,kk')=\Delta(k)\delta(k+k')-g_1Z_1\int\gamma G_1(p,kk'k'')dk''. \tag{3.6}$$

Defining $\bar{G}_1(p,k_1\cdots k_m)$ by

$$\bar{G}_1(p,k_1\cdots k_m)\equiv G_1(p,k_1\cdots k_m)G_1^{-1}(p), \tag{3.7}$$

Eq. (3.4) may be written as

$$\left[\gamma p+m+g_1(Z_1/Z_2)\int\gamma\bar{G}_1(p,k)dk\right]Z_2G_1(p)=1. \tag{3.8}$$

Invoking the usual boundary condition on $G_1(p)$, that in the free particle limit

$$G_1(p)\rightarrow(\gamma p+m')^{-1}, \tag{3.9}$$

where m' is the renormalized mass, Eq. (3.8) may easily be recast into the form

$$\left[\gamma p+m'+g_1Z_1\int_R\gamma\bar{G}_1(p,k)dk\right]G_1(p)=1, \tag{3.10}$$

where

$$m'=m+g_1(Z_1/Z_2)\left(\int\gamma\bar{G}_1(p,k)dk\right)_{\gamma p+m'=0}=m+g_1(Z_1/Z_2)\int_0, \tag{3.11}$$

$$Z_2=1-g_1Z_1\left(\frac{\partial}{\partial\gamma p}\int\gamma\bar{G}_1(pk)dk\right)_{\gamma p+m'=0}=1-g_1Z_1\int_1, \tag{3.12}$$

and

$$\int_R=\int-\int_0-(\gamma p+m')\int_1. \tag{3.13}$$

Although Eq. (3.10) appears to be infinite, owing to the explicit presence of Z_1, this constant is needed to renormalize the additional overlapping vertex infinities arising from the k-integration. This will be discussed below. Z_1 of course renormalizes the vertex operator, as may easily be seen from its definition,

$$\Gamma(\xi)=[\delta/\delta g\phi(\xi)]G^{-1}=Z_1^{-1}[\delta/\delta g_1\phi(\xi)]G_1^{-1}=Z_1^{-1}\Gamma_1(\xi). \tag{3.14}$$

To perform the mass and Green's function renormalizations in the higher equations, we break up $G_1(p,k_1\cdots k_m)$:

$$G_1(p,k_1\cdots k_m)=G_{1r}(p,k_1\cdots k_m)+\eta\bar{G}_1(p-k_1-\cdots-k_{m-1},k_m)G_1(p,k_1\cdots k_{m-1}), \tag{3.15}$$

where $\eta=1$ for $m=$odd; $\eta=i(2\pi)^4$ for $m=$even, and define a generalized $\int_R$ when more than one meson variable is present:

$$\int_R\gamma G_1(p,k_1\cdots k_m)dk_m=\int\gamma G_{1r}(p,k_1\cdots k_m)dk_m+\eta\left(\int_R\gamma\bar{G}_1(p-k_1-\cdots-k_{m-1},k_m)dk_m\right)\times G_1(p,k_1\cdots k_{m-1}). \tag{3.16}$$

The second term on the right-hand side of Eq. (3.15) is that part of the Green's function in which the k_m meson is emitted last and its vertex is not coupled to any of the other vertices. Using Eq. (3.16), and the definitions Eqs. (3.11) to (3.13), Eqs. (3.5) and (3.6)

[3] P. T. Matthews and A. Salam, Revs. Modern Phys. **23**, 311 (1951).

take the form

$$[\gamma(p-k)+m']G_1(p,k) = ig_1(2\pi)^{-4}Z_1\int_R \gamma G_1(p,kk')dk', \quad (3.17)$$

$$[\gamma(p-k-k')+m']G_1(p,kk') = \Delta(k)\delta(k+k') - g_1Z_1\int_R \gamma G_1(p,kk'k'')dk''. \quad (3.18)$$

We next turn to the rigorous definition of Z_1. Comparing the mass operator in Eq. (3.10) with the usual expression for that quantity,[4] one sees that

$$\bar{G}_1(p,k) = ig_1(2\pi)^{-4}G_1(p-k)\Gamma_1(p-k,p)\Delta(k). \quad (3.19)$$

An expression for Z_1 may now be obtained by invoking the boundary conditions on $\Gamma_1(p-k,p)$ in the free particle limit, namely[5]

$$\lim_{k^2+\mu^2\to 0} \bar{\psi}_1{}^0(p-k)\Gamma_1(p-k,p)\psi_1{}^0(p) = \bar{\psi}_1{}^0(p-k)\gamma_5\psi_1{}^0(p), \quad (3.20)$$

where $\psi_1{}^0(p)$ is the renormalized plane wave spinor, a function of m'. Comparing with Eq. (3.19), the free particle limit of $\bar{G}_1{}^*(p,k)\equiv\bar{G}_1(p,k)\Delta^{-1}(k)$ is

$$\bar{G}_1{}^*(p,k) \to ig_1(2\pi)^{-4}[\gamma(p-k)+m']^{-1}\gamma_5. \quad (3.21)$$

Introducing the "reaction matrix,"

$$R_1(p,kk')\equiv G_1(p,kk') - G_1(p)\Delta(k)\delta(k+k'). \quad (3.22)$$

Equation (3.17) in the free particle limit becomes, after slight rearrangement,

$$Z_1\gamma = \gamma - \left(\int_R Z_1\gamma\bar{R}_1{}^*(p,kk')dk'\right)_0, \quad (3.23)$$

where $(\ )_0$ denotes the free particle limit defined in Eq. (3.20).

Before we proceed to a more detailed discussion of Z_1 it might pay to re-examine the renormalization of the first approximation, in which $Z_1=1$, since

$$\int_R \gamma R_1(p,kk')dk' = 0$$

there. Using the decomposition of the integral on the right-hand side of Eq. (3.17), one finds that

$$G_1(p,k) = G_1{}^{(0)}(p-k)(ig_1(2\pi)^{-4}\gamma)\gamma\Delta(k)G_1(p), \quad (3.24)$$

where $G_1{}^{(0)}(p)\equiv(\gamma p+m')^{-1}$, which when substituted into Eq. (3.10) yields the finite equation

$$\left[\gamma p+m'+ig_1{}^2(2\pi)^{-4}\int_R \gamma G_1{}^{(0)}(p-k)\gamma\Delta(k)dk\right] \times G_1(p)=1, \quad (3.25)$$

in which only renormalized quantities enter.[6]

4. VERTEX RENORMALIZATION

The rigorous Eqs. (3.10), (3.17), (3.18)$\cdots$ appear to be asymmetric in that the meson line corresponding to the integrated variable on the right-hand side always goes to the top of the diagram with a lowest-order vertex connection. This asymmetry is only apparent, as the rigorous equations contain all possible perturbation graphs. It is in fact possible to derive from the adjoint equation of motion,

$$\bar{\psi}[-\gamma\overleftarrow{p}+m+g\gamma\phi]=0, \quad (4.1)$$

an "adjoint"[7] set of equations, in which the integrated meson line ends at the bottom of the diagram, *viz.*:

$$G_1{}^\dagger(p)[\gamma p+m'] = 1-g_1\int_R G_1{}^\dagger(p+k,k)\gamma Z_1{}^\dagger dk, \quad (4.2)$$

$$G_1{}^\dagger(p+k,k)[\gamma(p+k)+m'] = ig_1(2\pi)^{-4}\int_R G_1{}^\dagger(p+k+k',kk')\gamma Z_1{}^\dagger dk' \quad (4.3)$$

$$G_1{}^\dagger(p+k+k',kk')[\gamma(p+k+k')+m'] = \delta(k+k')\Delta(k) - g_1\int_R G_1{}^\dagger(p+k+k'+k'',kk'k'')\gamma Z_1{}^\dagger dk'' \quad (4.4)$$

where $G_1{}^\dagger(p,k_1\cdots k_m)=G_1(p,k_1\cdots k_m)$.[8] Proceeding as in Sec. 3, one may write down rigorous expressions for $Z_2{}^\dagger(\equiv Z_2)$ and $Z_1{}^\dagger(\equiv Z_1)$, in terms of integrals over the $G_1{}^\dagger$'s.

Owing to this equivalence between the adjoint and the "normal" (nonadjoint) quantities, one may generate an infinite variety of equivalent sets of rigorous equations by replacing any of the G_1's and Z_1's by their adjoints. However, once one cuts off the set of equations by means of the breakup approximation, the apparent differences between the various sets of equations become real and each approximate set, though still

[4] J. Schwinger, Proc. Nat. Acad. Sci. U. S. **37**, 452, 455 (1951).

[5] An alternate definition would be to impose Eq. (3.20) in the limit of $k_\mu\to 0$. This was adopted by N. Kroll and M. Ruderman, Phys. Rev. **93**, 194 (1954). It is purely a matter of convention whether one wants to treat the meson field as the static electromagnetic field or as the nucleon field. For the purposes of this paper, the choice of definition makes no difference.

[6] The correct Eq. (3.25) could of course be obtained in a trivial fashion from Eq. (2.7) by simply dropping the undesired terms. However, in the higher approximations, it is not clear which terms are to be dropped.

[7] Any "adjoint" quantity will henceforth be denoted by †. This is not to be confused with the Hermitian adjoint which does not appear in this paper.

[8] These two sets of equations are precisely related to the two ways of writing the mass operator:

$$T\rho\gamma G\Gamma\Delta \equiv T\rho\Delta\Gamma G\gamma.$$

having the same general physical validity, generates a somewhat different set of graphs. One is thus presented with an infinite number of approximation schemes. The requirement of renormalizability narrows down the possibilities. The particular set chosen here is closely related to the normal set and is defined by replacing Z_1 by $Z_1^\dagger$ in Eqs. (3.10), (3.17), (3.18)$\cdots$ in those parts of the right-hand-side integrals in which the integrated meson line is connected to the nucleon line (a similar change being made in the adjoint set). For example, if one uses Eq. (3.22),

$$Z_1\int\gamma G_1(p,kk')dk'\rightarrow Z_1\int\gamma G_1(p)\Delta(k)\delta(k+k')dk' +Z_1^\dagger\int\gamma R_1(p,kk')dk'. \quad (4.5)$$

This convention has the consequence of symmetrizing the free particle limits of the two vertex points in the mass operator,[8] since now the adjoint quantities will generate graphs that are the mirror images of the "normal" graphs. While it appears that the introduction of the adjoint quantities (albeit only in their free-particle limit) into the normal equations couples the two sets, it turns out in practice that since the $Z_1^\dagger$ necessary in the normal set can always be obtained directly from Z_1 via the mirror property mentioned above without solving the adjoint set, the apparent coupling does not exist.

We now consider the equations in a given approximation with the Z_1's and their adjoints appropriately inserted. Since Z_1 is the free-particle part of a Green's function appearing in the scheme, its presence in an equation implies that a *rigorous* factorization, in addition to the decomposition peculiar to the approximation, has already taken place. Thus the $Z_1\gamma$ which appears in the right-hand integrals of the rigorous equations acts as a free-particle limit of a strong interaction (at that vertex). Since we are restricted, in any approximation, to a fixed number of strong interactions, we must extract the relevant parts of Z_1 to fit in with this limitation. Thus, in the last equation, in which the largest kernel on the right-hand side is decomposed, the Green's function appearing in the factored form already contains the largest number of interactions allowed (by definition), and therefore the $Z_1\gamma$ appearing in this equation must represent a zero interaction vertex, i.e., $Z_1\gamma\cong\gamma$. When the resultant expression is substituted back into the next equation, one obtains an integral equation for the Green's function with the largest number of interactions allowed. In this case one simply counts the number of strong interactions in each term, and supplies the Z_1 necessary to yield the maximum number. Thus in this equation Z_1's defined by *lower* approximations (and hence containing fewer interactions) will appear. In determining the relevant parts of Z_1 for the earlier equations, complication appears in that fewer than the maximum number of interactions allowed appears on the left. Thus a question arises as to how to count the interactions appearing in the right-hand integrals. It turns out that the Z_1 needed here is the one that is obtained by counting one interaction more than the maximum, the meson line integration again being taken not to affect the interaction weight of a particular Green's function.[9,10] Using these conventions, we will show in the succeeding sections that the equations in the second and third approximation are renormalized. The extension to higher approximations seems in principle straightforward, but an explicit proof of convergence would involve tedious algebraic manipulation.

5. RENORMALIZATION OF THE SECOND APPROXIMATION

The equations of the second approximation are obtained by substituting the decomposition,

$$G_1(p,kk'k'')\cong G_1(p,k)\Delta(k')\delta(k'+k'') +G_1(p,k')\Delta(k'')\delta(k''+k) +G_1(p,k'')\Delta(k)\delta(k+k'), \quad (5.1)$$

into Eqs. (3.10), (3.17), and (3.18). Following the conventions discussed in the previous section, Eq. (3.18) becomes

$$G_1(p,kk')=\Delta(k)\delta(k+k')G_1(p) -g_1G_1^{(0)}(p-k-k')\gamma G_1(p,k)\Delta(k') -g_1G_1^{(0)}(p-k-k')\gamma G_1(p,k')\Delta(k), \quad (5.2)$$

where, in obtaining the first term on the right, use was made of Eq. (3.10). Substituting this result into Eq. (3.17), one obtains

$$[\gamma(p-k)+m']G_1(p,k)=ig_1(2\pi)^{-4}Z_1^{(2)}\gamma\Delta(k)G_1(p) -ig_1^2(2\pi)^{-4}\left(\int_R\gamma G_1^{(0)}(p-k-k')\gamma\Delta(k')dk'\right)G_1(p,k) -ig_1^2(2\pi)^{-4}\int\gamma G_1^{(0)}(p-k-k')\gamma\Delta(k)G_1(p,k')dk'. \quad (5.3)$$

The subscript "R" does not appear on the second integral, as this term corresponds to the G_{1r} in Eq. (3.16) for this approximation. The first integral is just the correctly renormalized mass operator of the first

[9] This convention also holds for terms that are identifiable with the right-hand-side integrals of "earlier" equations, when these appear in the last equation, in which the decomposition is made.

[10] This prescription appears to admit an extra interaction in the renormalization constant in the earlier equations. A similar phenomenon of the inclusion of a higher approximation structure to renormalize one of lower order occurs in the conversion of a subtractive renormalization into a multiplicative one in perturbation theory. Thus for the second-order vertex operator one has

$$\Gamma=\gamma+e^2\Gamma_1=\gamma+e^2\gamma A+e^2\Gamma_c\cong(1+e^2A)(\gamma+e^2\Gamma_c),$$

where A is the infinite constant and Γ_c the convergent part of Γ_1.

approximation. No Z_1 appears in the integrals, as $G_1(p,k)$ and $G_1(p,k')$ already contain one strong interaction. The first term, on the other hand, contains the rigorous $Z_1(\equiv Z_1^{(2)})$ of this approximation, defined by Eqs. (3.23) and (5.2):

$$Z_1^{(2)}\gamma=\gamma+g_1\left(\int_R \gamma G_1^{(0)}(p-k-k')\gamma\bar{G}_1(p,k')dk'\right)_0 \quad (5.4)$$

[again on the right-hand-side Z_1 of Eq. (3.23) is set equal to unity by our convention]. Equation (5.3) may be rewritten in the form

$$\bar{G}_1(p,k)=ig_1(2\pi)^{-4}G_1^{(1)}(p-k)\gamma\Delta(k)$$

$$-ig_1^2(2\pi)^{-4}G_1^{(1)}(p-k)\left[\int \gamma G_1^{(0)}(p-k-k')\gamma\bar{G}_1(p,k')dk'\right.$$

$$\left.-\left(\int_R \gamma G_1^{(0)}(p-k-k')\gamma\bar{G}_1(p,k')\right)_0\right]\Delta(k), \quad (5.5)$$

where $G_1^{(1)}(p)$ is the one-nucleon propagator of the first approximation. Equation (3.10) becomes

$$[\gamma p+m']G_1(p)$$

$$=1-g_1\left(\int_R Z_1^{(2)\dagger}\gamma\bar{G}_1(p,k)dk\right)G_1(p). \quad (5.6)$$

Here the rigorous $Z_1^{(2)\dagger}$ appears, since we wish to include an extra interaction as discussed in the previous section. Writing

$$\bar{G}_1(p,k)=ig_1(2\pi)^{-4}G_1^{(1)}(p-k)\Gamma_1^{(2)}(p-k,p)\Delta(k), \quad (5.7)$$

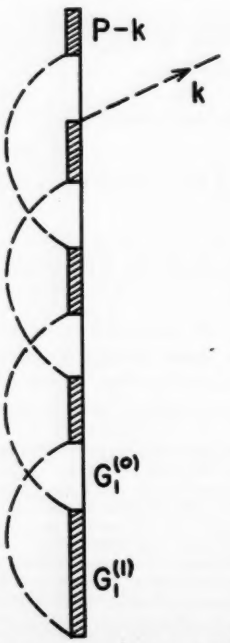

FIG. 1. Graphs generated by $G_1^{(2)}(p,k)$.

Eq. (5.5) becomes an integral equation for the vertex operator $\Gamma_1^{(2)}(p,k)$. A straightforward perturbation expansion shows that Eq. (5.5) yields the graphs of Fig. 1 correctly renormalized.[11] The proof of the finiteness of Eq. (5.6) involves showing that the mass operator $g_1\int_R Z_1^{(2)\dagger}\gamma\bar{G}_1(p,k)dk$ is finite. This can be done directly by examining the perturbation solution of the equations, and indeed it is found that Eq. (5.6) is divergence free. However a simpler proof, depending only on the symmetry[12] of the mass operator, is available, and it has the advantage of greatly simplifying the proof in higher approximations.

Consider the rigorous mass operator $g^2\int_R\gamma G\Gamma\Delta = g_1^2Z_1^2\int_R\gamma G_1\Gamma_1Z_1^{-1}\Delta$. As is well known, the $\int_R$ in the above expressions $\sim Z_1^{-2}$, since the above expression is finite. One of the Z_1^{-1} comes from Γ, the other one results from the overlapping divergences caused by the integration.[13] This can be seen more explicitly by considering the alternate form for the mass operator, $g_1^2Z_1^2\int_R\Gamma_1Z_1^{-1}G_1\gamma\Delta$, which shows that in the rigorous case the upper interaction point has all the structure of the complete vertex operator. In any approximation scheme, the mass operator will still be of the form $\int_R\gamma G^a\Gamma^a\Delta$, which will explicitly go as $(Z_1^a)^{-1}$ (this factor coming from Γ^a). Furthermore, one can always find quantities $\Gamma^{a'}$, $G^{a'}$ such that $\int_R\Gamma^{a'}G^{a'}\gamma\Delta$ generates the same set of diagrams, so that the approximate $\int_R$ also goes as $(Z_1^{a'})^{-1}$. Consequently $\int_R$ must be proportional to $(Z_1^aZ_1^{a'})^{-1}$. If the mass operator is symmetric,[12] it is clear that $G^{a'}=G^a$ and $\Gamma^{a'}=\Gamma^{a\dagger}$, and therefore the dependence of $\int_R$ on Z_1 is $(Z_1^aZ_1^{a\dagger})^{-1}$. Hence in this case the overlapping divergences produced by the integration in $\int_R\gamma\bar{G}_1(p,k)dk$ yields a proportionality factor $(Z_1^{a\dagger})^{-1}$. Thus $g_1Z_1^{a\dagger}\int\gamma\bar{G}_1(p,k)dk$ is finite. As can be seen from Fig. 1, the mass operator (obtained by joining the external meson line to the top of the diagram) is indeed symmetric,[14] and hence the factor $Z_1^{(2)\dagger}$ renormalizes Eq. (5.6).[15]

6. RENORMALIZATION OF THE THIRD APPROXIMATION

In this approximation, the highest Green's function appearing on the right-hand side of

$$[\gamma(p-k-k'-k'')+m']G_1(p,kk'k'')$$

$$=ig_1(2\pi)^{-4}\int Z_1\gamma G_1(p,kk'k''k''')dk''' \quad (6.1)$$

[11] Aside from the presence of $G_1^{(1)}(p)$, Eq. (5.5) is identical with that obtained by B. P. Nigam, *Proceedings of the Rochester Conference on High-Energy Physics* (University of Rochester Press, Rochester, 1954).

[12] By symmetry we mean that the same diagrams are present when all the graphs are turned upside down.

[13] A. Salam, Phys. Rev. **84**, 217 (1951).

[14] The symmetry of the mass operator seems to be a general feature of the approximation scheme.

[15] The mass operator in Eq. (5.6), though convergent, appears as the product of two infinite quantities. Presumably, however, a treatment via the Feynman cutoff method would yield a unique finite limit as the cutoff approached infinity.

is decomposed in accordance with our general scheme [See (I), Eq. (2.20)], to yield

$$G_1(p,kk'k'')=ig_1(2\pi)^{-4}G_1^{(0)}(p-k-k'-k'')$$
$$\times\gamma[R_1(p,kk')\Delta(k'')+R_1(p,k'k'')\Delta(k)$$
$$+R_1(p,k''k)\Delta(k')]+\Delta(k)\delta(k+k')G_1(p,k'')$$
$$+\Delta(k')\delta(k'+k'')G_1(p,k)$$
$$+\Delta(k'')\delta(k''+k)G_1(p,k'). \quad (6.2)$$

Use was made of Eq. (3.17) to reduce some of the structures to yield the $G_1(p,k)$ terms. Substituting this into Eq. (3.18) we obtain the integral equation for the unknown quantity $R_1(p,kk')$:

$$R_1(p,kk')=-g_1G_1^{(0)}(p-k-k')$$
$$\times[Z_1^{(2)}\gamma G_1(p,k)\Delta(k')+Z_1^{(2)}\gamma G_1(p,k')\Delta(k)]$$
$$-ig_1^2(2\pi)^{-4}G_1^{(0)}(p-k-k')\int\gamma G_1^{(0)}(p-k-k'-k'')$$
$$\times\gamma\{R_1(p,kk')\Delta(k'')+R_1(p,k'k'')\Delta(k)$$
$$+R_1(p,k''k)\Delta(k')\}dk'', \quad (6.3)$$

the Z_1's being chosen in accordance with our convention of Sec. 4. The reaction matrix, $R_1(pkk')$, represents a two-meson emission process, and may be divided into four disjoint parts:

$$R_1(p,kk')=(2\pi)^4i\bar{Q}_1(p-k',k)G_1(p,k')$$
$$+T_1(p,kk')+(2\pi)^4i\bar{Q}_1(p-k,k')G_1(p,k)$$
$$+S_1(p,kk'). \quad (6.4)$$

The first two terms correspond to the emission of k' *followed* by the emission of k from two uncoupled vertices and from a compound vertex respectively. The second two terms interchange k and k'. Substituting this into Eq. (6.3) and separating the four disjoint processes, one obtains the following integral equations for $\bar{Q}_1$ and S_1:

$$\bar{Q}_1(p-k',k)=ig_1G_1^{(1)}(p-k-k')Z_1^{(2)}\gamma\Delta(k)$$
$$-ig_1^2(2\pi)^{-4}G_1^{(1)}(p-k-k')\int\gamma G_1^{(0)}(p-k-k'-k'')$$
$$\times\gamma\bar{Q}_1(p-k',k'')\Delta(k) \quad (6.5)$$

$$S_1(p,kk')=-ig_1^2(2\pi)^4G_1^{(1)}(p-k-k')$$
$$\times\int\gamma G_1^{(0)}(p-k-k'-k'')\gamma\Delta(k')$$
$$\times\{(2\pi)^4i\bar{Q}_1(p-k'',k)G_1(p,k'')$$
$$+T_1(p,kk'')+S_1(p,kk'')\} \quad (6.6)$$

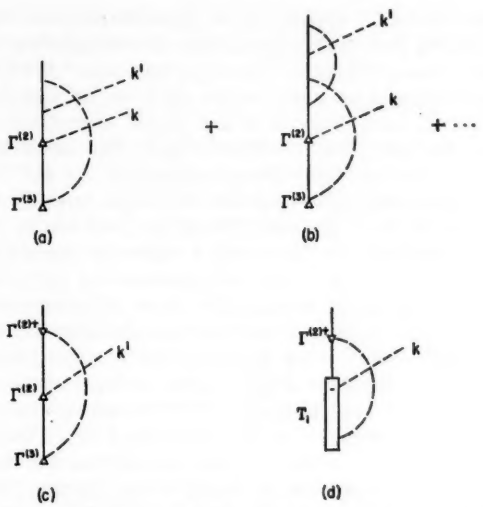

FIG. 2(a), (b). Some of the graphs of $S_1(p,k,k')$. (c), (d). A graphical representation of the first three integrals on the right-hand side of Eq. (6.8).

and a similar equation for T_1. Comparing Eq. (6.5) with Eq. (5.3), we see that

$$\bar{Q}_1(p,k)=\bar{G}_1^{(2)}(p,k), \quad (6.7)$$

and hence $Z_1^{(2)}$ in Eq. (6.5) correctly renormalizes that equation. In Eq. (6.6) it is clear that since S_1 (and T_1) contain only coupled vertices, the integrated meson line k'' goes past at least two vertex points, and thus all graphs generated are of the "finite self-energy" type. Thus Eq. (6.6) is also finite.

In terms of the quantities appearing in Eq. (6.4), Eq. (3.17) has the form

$$[\gamma(p-k)+m']\bar{G}_1^*(p,k)=ig_1(2\pi)^{-4}Z_1^{(3)}\gamma$$
$$+ig_1(2\pi)^{-4}\Big[(2\pi)^4i\int Z_1^{(2)\dagger}\gamma\bar{G}_1^{(2)}(p-k',k)$$
$$\times\bar{G}_1^*(p,k')dk'+\int Z_1^{(2)\dagger}\gamma\bar{T}_1^*(p,kk')dk'$$
$$+\int Z_1^{(2)\dagger}\gamma\bar{S}_1^*(p,kk')dk'+(2\pi)^4i$$
$$\times\Big(\int Z_1^{(2)\dagger}\gamma\bar{G}_1^{(2)}(p-k,k')dk'\Big)\bar{G}_1^*(p,k)\Big], \quad (6.8)$$

where $Z_1^{(3)}$ is the rigorous vertex renormalization constant of this approximation:

$$Z_1^{(3)}\gamma=\gamma-\Big(\int Z_1^{(2)\dagger}\gamma[(2\pi)^4i\bar{G}_1^{(2)}(p-k',k)\bar{G}_1^*(p,k')$$
$$+\bar{T}_1^*(p,kk')+\bar{S}_1^*(p,kk')]dk'\Big)_0. \quad (6.9)$$

Again the $Z_1^{(2)\dagger}$ appears on the right-hand side of Eqs. (6.8) and (6.9) in accordance with the rule allowing one extra strong interaction in earlier equations.[16] We first note that the last term on the right can be identified with the mass operator of the second approximation [see Eq. (5.6)] multiplied by $\bar{G}_1^*(p,k)$. This was shown in Sec. 5 to be finite. We next show that the $Z_1^{(2)\dagger}$ in the remaining right-hand-side structures correctly renormalize the overlapping divergences produced by the k' integration. In Eq. (6.6), a series of generalized graphs for $S_1(p,kk')$ may be generated by using the term proportional to $G_1(p,k'')$ as an inhomogeneous term and iterating (ignoring the presence of the $T_1(pkk'')$ term). These graphs [Figs. 2(a), (b)], when substituted into the $S_1(pkk')$ term in Eq. (6.8), combine with the first integral to yield the unrenormalized vertex structure $\Gamma^{(2)\dagger}$ at the top [Fig. 2(c)]. Thus to renormalize the overlaps of this combination, it is clear that a $Z_1^{(2)\dagger}$ is required at the top of the diagram. Similarly the remaining diagrams of S_1 can be obtained by using the T_1 structure in Eq. (6.6) as an inhomogeneous term. When the k' integration in Eq. (6.8) is carried out for these graphs, and they are combined with the second term on the right-hand side of that equation, the vertex $\Gamma^{(2)\dagger}$ is again obtained at the top [Fig. 2(d)], and the $Z_1^{(2)\dagger}$ therefore renormalizes this structure. When $Z_1^{(3)}\gamma$ is replaced by its definition Eq. (6.9), Eq. (6.8) reduces to the term $ig_1(2\pi)^{-4}\gamma$ together with the terms representing Figs. 2(c) and 2(d), with their free-particle limits subtracted off. Since all vertices had previously been renormalized, this final subtraction renders the graphs of Figs. 2(c) and 2(d) finite.

Finally, to show that the mass operator is symmetric, and therefore that Eq. (3.10) is finite [Sec. 5], we note that all terms on the right of Eq. (6.8) have a $G_1(p,k)$ structure at the bottom of the graph,[17] and thus a straightforward iteration of the type leading to Fig. 2 shows that $\int\gamma\bar{G}_1^{(3)}(p,k)dk$ is symmetric, and hence that $Z_1^{(3)\dagger}\int\gamma\bar{G}_1^{(3)}(p,k)dk$ is finite.

7. CONCLUSION

In the preceding sections a method has been given for the renormalization of an approximation scheme for the meson-nucleon interaction problem. Starting with the assumption that the renormalization is multiplicative, we carry out the mass and amplitude renormalizations (Z_2) independently of the approximation. The vertex renormalization presented a more complicated problem, owing to the existence of overlapping divergences. The definition of the renormalization constant in terms of integrals over Green's functions was derived by imposing, upon the vertex, a boundary condition analogous to the one usually applied in quantum electrodynamics, rather than that of Deser, Goldberger, and Thirring.[18] In order to carry out the vertex renormalization it was necessary to consider the equations order by order. By redefining the approximation scheme to include the necessary diagrams forming Z_1, an unambiguous prescription for carrying out the renormalization was found. Actually this seems to confirm the fact that any covariant approximation scheme, which (order by order) approaches the rigorous solution, (i.e., eventually includes all Feynman graphs), can, by a suitable adjunction to what is included in an approximation, be renormalized in a consistent fashion, provided that the renormalized perturbation series can be rearranged and summed in any sequence. In this paper a redefinition of the approximation was made without significantly changing the physical content of each approximation. Such an approach would appear go be applicable to the renormalization of the Tamm-Dancoff method.

[16] Note that in this approximation, the equation defining $Z_1^{(3)}$ is the free-particle limit of an "earlier" equation, which requires the use of an extra interaction on the right. The second approximation was anomalous in that the $Z_1^{(2)}$ equation was the free-particle limit of the integral equation of that approximation, and therefore this convention did not apply there.

[17] That S_1 and T_1 have this property is evident from iterating Eq. (6.6) and the corresponding equation for T_1 (which we have not written down).

[18] Deser, Goldberger, and Thirring, Phys. Rev. 94, 711 (1954).

Letters to the Editor

PUBLICATION of brief reports of important discoveries in physics may be secured by addressing them to this department. The closing date for this department is five weeks prior to the date of issue. No proof will be sent to the authors. The Board of Editors does not hold itself responsible for the opinions expressed by the correspondents. Communications should not exceed 600 words in length and should be submitted in duplicate.

Possibility of the Observation of Exchange Resonance Near a Ferrimagnetic Compensation Point*

ROALD K. WANGSNESS
U. S. Naval Ordnance Laboratory, White Oak, Maryland
(Received December 16, 1954)

THE theory of ferrimagnetic resonance for a system containing two sublattices[1] shows that there are two branches to the frequency curve. The lower branch corresponds to the ordinary ferromagnetic resonances which have been studied and it can be conveniently characterized by the effective gyromagnetic ratio when one is sufficiently far from a compensation point.[2] The upper branch is ordinarily dominated by the molecular field, and, when the molecular field is very large compared to the applied and anisotropy fields, the frequency of this branch becomes simply the "exchange" frequency given by[1]

$$\omega_e=\lambda(\gamma_2 M_1+\gamma_1 M_2), \qquad (1)$$

where λ is the molecular field coefficient, and γ_i and M_i are sublattice gyromagnetic ratios and magnetizations, respectively. Resonance corresponding to this branch has not heretofore been observed since for the usual ferrimagnetics, Eq. (1) predicts resonance for radiation whose wavelength is of the order of a tenth of a millimeter. However, we can put (1) into a more desirable form: thus, if we factor out the product $\gamma_1\gamma_2$ we get

$$\omega_e=\lambda\gamma_1\gamma_2 S, \qquad (2)$$

where $S=(M_1/\gamma_1)+(M_2/\gamma_2)$ is the net angular momentum of the system. Equation (2) suggests at once that the possibility of the observation of the upper branch resonance will be greatly enhanced by working near a compensation point for angular momentum ($S=0$) since then, in spite of the large value of λ, ω_e can be brought down to a value within the range of available apparatus.

Although (2) would predict the resonance caused by this branch to occur at zero applied field, the actual situation near $S=0$ is, of course, more complicated. Exact calculations[2] have shown that the frequencies of the two branches still depend on H and nearly coincide at $S=0$. In fact, it is easily shown that the results given by Eqs. (18) and (19) of reference 2 for the frequencies of the two branches at $S=0$ can be put into the form

$$\omega_-^2=-\lambda\gamma_1\gamma_2 M H_x' \quad \text{and} \quad \omega_+^2=-\lambda\gamma_1\gamma_2 M H_y', \qquad (3)$$

where H_x' and H_y' are the effective fields appearing in the usual ferromagnetic resonance formula, i.e., $\omega_f^2=\gamma_{\text{eff}}^2 H_x' H_y'$. We see from (3), therefore, that the frequencies of the two branches will be equal if the sample is a sphere and if the x and y components of the anisotropy fields are equal.

Qualitatively, then, in a small range about the angular momentum compensation point we could expect to observe the following: as this point is approached the normal resonance peak would move down to lower fields (higher g values); at the same time, a new peak should appear at still lower fields, and move into near coincidence with the first at $S=0$; after $S=0$ has been passed through, the new peak should recede toward the origin and disappear, while the original peak would move back to the more usual high field values. Since the resonance conditions involve the applied field, the positions of the peaks could still be described in terms of observed apparent g values and the g-value curve would also have two branches which would meet or nearly meet at $S=0$.

* A brief report of this work was given at the Naval Ordnance Laboratory Conference on Ferrimagnetism on October 12, 1954.

[1] R. K. Wangsness, Phys. Rev. **91**, 1085 (1953). See also: J. Kaplan and C. Kittel, J. Chem. Phys. **21**, 760 (1953); F. Brown and D. Park, Phys. Rev. **93**, 381 (1954).

[2] R. K. Wangsness, Phys. Rev. **93**, 68 (1954).

Observation of Exchange Resonance Near a Ferrimagnetic Compensation Point*

THOMAS R. MCGUIRE
U. S. Naval Ordnance Laboratory, White Oak, Maryland
(Received December 16, 1954)

MEASUREMENTS have been made under the conditions described by Wangsness[1] in order to see if a ferrimagnetic resonance would be observed which could be ascribed to the exchange frequency branch. The sample used was a small sphere, 0.076 inch in diameter, of lithium chromium ferrite ($Li_{0.5}Cr_{1.25}Fe_{1.25}O_4$) whose composition was believed to be very near that for which van Wieringen[2] found a compensation temperature for angular momentum at about 60°C.

The microwave bridge apparatus employed has been described previously.[3] A frequency of 22 500 Mc/sec was used so that the usual resonance would occur at a field high enough to enable the upper branch resonance to be distinguishable. The absorption as a function of applied field was measured at about one-degree intervals in a range of approximately fifteen degrees centered between 55 and 60°C. Typical results obtained from these

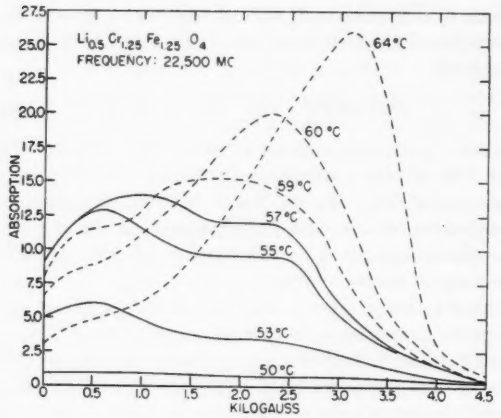

FIG. 1. Resonance absorption curves at various temperatures.

records are shown in Fig. 1. It is clear from the figure that a new peak at lower fields appears and vanishes as the temperature is increased. One is faced with a difficulty that the peaks overlap to some extent, but for purposes of further analysis the separate peaks were outlined as well as possible. Apparent g values were then calculated for each peak by the formula $h\nu=g\beta H$, where H is the magnitude of the applied field at the position of maximum absorption. The two sets of g values obtained in this way are shown as a function of temperature by the solid lines in Fig. 2. One set has extremely high values, while the other set, although high, never becomes larger than the value of 7 or 8 which can reasonably be expected for the lower branch near $S=0$.

The peak height of the lower branch resonance is shown by the open circles in Fig. 2; it is steadily increasing as the net magnetization is increasing again from the value $M=0$ which occurs at about 40°C. On the other hand, the peak height assigned to the upper branch resonance, which is shown by the open triangles, increases to a maximum and vanishes again in the range

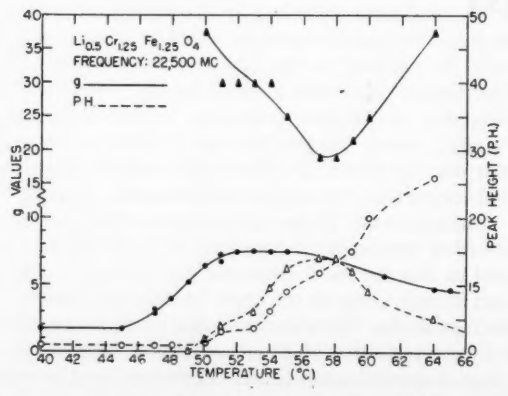

FIG. 2. g values and peak heights as a function of temperature.

of temperature shown. From these measurements the angular momentum compensation point is placed at 57 to 58°C.

The fact that the low-field resonance peak remains distinct over a wide temperature interval lends support to its identification as exchange resonance. If the specimen were porous, or contained a considerable number of local inhomogeneities in the chemical composition, it would show unduly broad resonance curves. The effect of such broadening would give poorer resolution and might conceivably merge the two peaks shown in Fig. 1 into one. It seems clear, therefore, that the material was sufficiently good to show exchange resonance in the region of a ferrimagnetic compensation point for angular momentum.

* A brief mention of these results was made at the Naval Ordnance Laboratory Conference on Ferrimagnetism on October 12, 1954.

[1] R. K. Wangsness, preceding letter [Phys. Rev. **97**, 831 (1955)].
[2] J. S. van Wieringen, Phys. Rev. **90**, 488 (1953).
[3] L. R. Maxwell and T. R. McGuire, Revs. Modern Phys. **25**, 279 (1953).

X-Ray Measurements of Pile-Irradiated LiF†

D. T. KEATING*
Massachusetts Institute of Technology, Cambridge, Massachusetts
(Received October 25, 1954)

X-RAY measurements have been made upon two LiF single crystals cleaved upon the (001) face and exposed to slow-neutron flux in the Argonne pile. The exposures were approximately 2.1×10^{17} and and 7.5×10^{17} nvt. Li^6 is 7.5 percent abundant in natural lithium, and slow neutrons react with this iostope according to $Li^6+n^1\rightarrow H^3+He^4+4.8$ Mev with a cross section of 950 barns. The tritium receives 2.74 Mev, and the α particle 2.06 Mev of kinetic energy. The major radiation effects are presumed to be caused by this reaction with slow pile neutrons. A Seitz calculation for the exposure 7.5×10^{17} nvt gave 4300 displacements per million atoms.[1]

Five orders, (002), (004), (006), (008), and (0010) were examined with x-rays. Table I gives the integrated reflections for three samples. Each reflection for the unirradiated sample is set equal to 100 percent. Irradia-

TABLE I. Integrated reflections of irradiated LiF relative to unirradiated LiF (expressed in percent).

Reflection	Unirradiated	Irradiated 2.1×10^{17} nvt	Irradiated 7.5×10^{17} nvt
002	100	216	206
004	100	90	95
006	100	83	86
008	100	105	93
0010	100	89	100

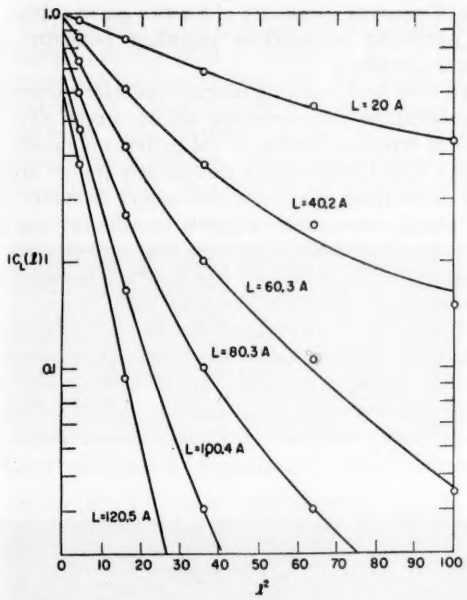

FIG. 1. Semi-log plot of $|C_L(l)|$ *versus* l^2 for the first five orders of (00*l*), measured on a single crystal of LiF irradiated 7.5×10^{17} nvt.

tion produced a twofold increase in the integrated reflection of (002). This increase for (002) is presumably by a reduction in extinction upon irradiation. Reflections (004), (006), (008), and (0010) do not show any definite correlation between integrated intensity and exposure or intensity and order.

The line shapes of the five orders were analyzed in terms of Fourier coefficients, corrected for instrumental broadening by the Stokes' method.[2] The breadth from the unirradiated crystal was assumed to be entirely instrumental. From the plots of the Fourier coefficients for the five orders, semilog polts of $|C_L(l)|$ *versus* the square of the order, l, were made. For small values of l the curves approach a straight line, and the intercept gives the particle size coefficient.[3] The plot for the crystal with exposure 7.5×10^{17} nvt is given in Fig. 1. The intercepts gave values of the particle size coefficients corresponding to a particle size of 500 A or more for both irradiated crystals.

The integral breadths, B, of the reflections expressed in terms of $\sin\theta/\lambda$ were closely proportional to the order of the reflection. The integral breadths corrected for instrumental broadening are tabulated in Table II. When properly corrected, the peak positions as measured by their centers of gravity gave an expansion of about 0.012 percent for both irradiated samples, but the shifts were so small that the value is scarcely outside of experimental error. The integral breadths were larger than the shifts in peak position by a factor of nearly 100. The predominant effect of the pile irradiation was to broaden the reflections rather than shift their positions.

TABLE II. The integral breadths for five orders of LiF, corrected for instrumental broadening.

Reflection	2.1×10^{17} nvt B	2.1×10^{17} nvt B/l	7.5×10^{17} nvt B	7.5×10^{17} nvt B/l
002	0.00170	0.000853	0.00219	0.001093
004	0.00349	0.000873	0.00427	0.001067
006	0.00530	0.000882	0.00653	0.001089
008	0.00718	0.000897	0.00872	0.001090
0010	0.00853	0.000853	0.01114	0.001112

In terms of a length, L, perpendicular to the (00*l*) planes the strain $\epsilon=\Delta L/L$ is defined for the change in L due to the damage. Distribution functions, $P_L(\epsilon)$, were synthesized from the Fourier coefficients of the reflections for the distances $L=40.2$ A, 80.3 A, and 120.5 A.[4] It was found that the strain distribution functions $P_L(\epsilon)$ were independent of the distance L up to 120 A, the largest distance considered. When allowance is made for the small expansion of 0.012 percent, the distributions were symmetrical corresponding to equal probabilities of expansion or compression. They could be fitted by $P_L(\epsilon)=(\frac{1}{2}\sigma)[\cosh\pi(\epsilon-\bar{\epsilon})/2\sigma]^{-1}$, where $\bar{\epsilon}$ is the average strain of 0.012 percent, and $\sigma=\langle\epsilon^2\rangle^{\frac{1}{2}}$ is the root mean square strain. $\sigma=0.00350$ and 0.00438 for the samples irradiated 2.1×10^{17} and 7.5×10^{17} nvt, respectively. Figure 2 gives points from the synthesized distributions for the sample 7.5×10^{17} nvt. The solid curve was fitted by using the analytical expression with $\bar{\epsilon}=0.00012$ and $\sigma=0.00438$.

The important features of the damage produced in LiF single crystals by pile irradiation are pronounced broadening of the x-ray reflections and no marked change in the integrated reflections. There are small shifts in the positions of the reflections corresponding to expansions which are scarcely outside of experimental error. The broadening is due primarily to strains rather than to small particle size. The constant values of the strain over such large distances indicate that rather

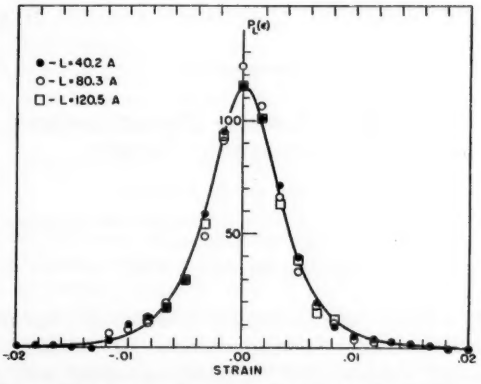

FIG. 2. Points from the synthesized strain distributions for $L=40.2$ A, 80.3 A, and 120.5 A in a single crystal of LiF irradiated 7.5×10^{17} nvt, and the function $P_L(\epsilon)=(\frac{1}{2}\sigma)[\cosh\pi(\epsilon-\bar{\epsilon})/2\sigma]^{-1}$ with $\bar{\epsilon}=0.00012$ and $\sigma=0.00438$.

large regions of the crystal must be in uniform compression or expansion. This suggests that the distortion cannot be due to isolated vacancies or interstitials. These results suggest that the imperfections collect in patches along certain (00*l*) planes, spreading these planes apart over areas whose diameters may be several hundred angstroms, and which are separated vertically by distances of 500 A or more. The regions directly above and below such imperfections would be in uniform vertical compression while regions near the periphery of such a collection of imperfections would be in vertical tension. For ionic crystals such as rock salt, the ratio of the breaking strength to Young's modulus, S/E, varies between a theoretical value of 0.1 and measured values as low as 2×10^{-4}. The measured root mean square strains fall in this range. The migration of imperfections would be a way of partially relieving strains and might be expected to proceed to such an extent that strains are kept down to values corresponding to S/E. From this picture it is not surprising that strains for the crystal irradiated 7.5×10^{17} nvt are only slightly greater than those irradiated 2.1×10^{17} nvt.

Since compressions and extensions normal to the cleavage planes have been postulated, additional measurements on samples cut parallel to (110) and (111) should be made before definite conclusions as to the nature of radiation damage in LiF can be drawn. It is conceivable that the effects in powdered LiF might differ from those in single crystals.

The author is indebted to Professor B. E. Warren for his suggestion of this research and for his counsel through the course of this work, and to Dr. Gerhart Hennig of the Argonne National Laboratory for the irradiated samples of LiF.

† Work done under contract with the U. S. Atomic Energy Commission.

* Now at the Brookhaven National Laboratory, Upton, New York.

[1] F. Seitz, Discussions Faraday Society **5**, 271 (1949).
[2] A. R. Stokes, Proc. Phys. Soc. (London) **61**, 382 (1948).
[3] B. E. Warren and B. L. Averbach, J. Appl. Phys. **23**, 497 (1952).
[4] B. E. Warren and B. L. Averbach, J. Appl. Phys. **21**, 595 (1950).

Domains of Reverse Magnetization in Ferromagnetic Metals

T. G. Nilan and W. S. Paxton

United States Steel Corporation, Applied Research Laboratory, Pittsburgh, Pennsylvania

(Received December 2, 1954)

In a recent communication, Goodenough[1] has calculated the nucleation energies for domains of reversed magnetization at grain boundaries and at crystal surfaces. He concludes that the probability for creation of such nuclei is largest at grain boundaries and depends on the relative angles of orientation of the axes of magnetic symmetry of the two grains subject to his particular assumptions regarding geometry and crystal symmetry.

We have been studying magnetic powder patterns in polycrystalline grain-oriented silicon steels. On the basis of extensive studies of the patterns obtained, we believe that Goodenough's calculations are not applicable to the types of material and sample geometry that one usually encounters in power transformer applications, i.e., laminated $3\frac{1}{4}$ percent silicon steel, with laminations of the order of 0.014 in. thick having grain sizes in the neighborhood of 5×10^{-3} cm^2.

A typical set of patterns we obtained on well oriented material is shown in Fig. 1. The patterns were obtained by the technique employed by Williams *et al.*[2] The orientation of each of the grains included in the figure was separately obtained by means of an optical goniometer using the etch pit technique.[3] It is evident from Fig.

Fig. 1. Domains of reverse magnetization on well-oriented material, showing that in the demagnetized state these domains are not influenced by the orientation of the adjacent grains.

1 that the spikes which form along the lower boundary of grain A are characteristic of the absolute orientation of the grain itself and are not related to the orientation of the neighboring grain. It has been ascertained that these spikes are nuclei of reversed magnetization. In fact, on the basis of an intensive investigation of the orientation and magnetic domain texture of more than 200 grains on like materials, it is possible to establish that the pattern of observed closure and reversed magnetization domains corresponds very closely to the orientation of the grain relative to the plane of the sheet and the direction of rolling.

The type of pattern observed on demagnetized material is found to depend exclusively on the angle of tilt out of the plane of the direction of easy magnetization ([100] direction) nearest the rolling plane. This angle we call ϕ. Typical patterns obtained on demagnetized material for various values of ϕ are shown in

Fig. 2. It has been found that one can estimate *a priori* the orientation of a grain to within 2° for $\phi<10°$ by observing the domain pattern and the details of its symmetry. As one traverses hysteresis loops, the symmetry of these patterns appears as the field is decreased from saturation. Grain orientation measurements coupled with the study of the powder patterns

FIG. 2. Typical domain patterns found on demagnetized material, showing the effect of orientation on the type of pattern observed. ϕ is the angle of tilt of the [100] direction out of the plane of the sample.

show that it is the direction of tilt of the [100] direction which determines both the geometry of the spikes and the boundaries at which they nucleate. It appears evident, therefore, that at least for this case the grain boundary energy is not the dominant term in the nucleation energy for domains of reverse magnetization. A more detailed description of our work including dynamic studies of domain patterns in impressed fields will be published elsewhere.

The authors are grateful to Professor J. E. Goldman of Carnegie Institute of Technology for helpful discussion and suggestions.

[1] J. B. Goodenough, Phys. Rev. **95**, 917, (1954).
[2] Williams, Bozorth, and Shockley, Phys. Rev. **75**, 155, (1949).
[3] C. S. Barrett, *Structure of Metals* (McGraw-Hill Book Company, Inc., New York, 1943), pp. 174–177.

Treatment of Liquid He^3 Based on the "Cell" Model

H. N. V. TEMPERLEY
National Bureau of Standards, Washington 25, D. C.
(Received December 17, 1954)

MANY properties of liquid He^3 are described semi-quantitatively by applying van der Waals corrections to the "Fermi gas" model.[1] The consideration of some other simple liquid models showed that the assignment to a typical *pair* of neighboring atoms of the scheme of discrete energy levels shown in Fig. 1, together with a continuous spectrum of Debye type, gives surprisingly accurate representation of the vapor pressure, entropy, specific heat, and magnetic susceptibility of the liquid. The following expression for the Gibbs free energy was finally chosen:

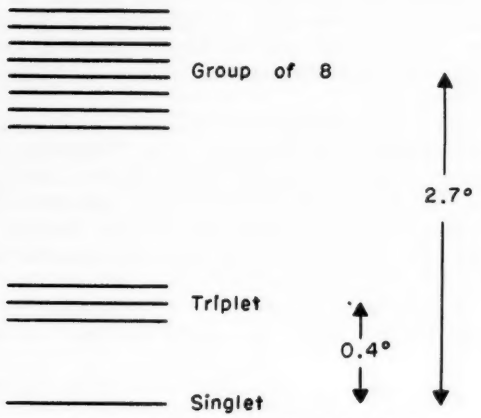

FIG. 1. Scheme of proposed energy levels.

$$g_{\text{liq}}=-L_0-\tfrac{1}{2}NkT\ln(1+3e^{-0.4/T}+8e^{-2.7/T})-0.0108NkT^4+Pv. \quad (1)$$

By differentiating with respect to temperature we get the entropy and specific heat. By equating it to Chen and London's expression[2] for the Gibbs free energy of the slightly imperfect vapor,

$$g_{\text{vap}}=NkT[\ln(P_{\text{mm}}/T^{5/2})-5.325]+BP-(BP)^2/2NkT, \quad (2)$$

we obtain a vapor pressure equation. If L_0 is taken as 5.16 calories/mole, the predictions of the new equation are practically identical with those of the empirical equation of Chen and London,[2] but every term of the new equation can be given a precise physical interpretation. Finally, by using a general formula found by Price,[3] we arrive at the following simple expression for the "low temperature" behavior of the magnetic susceptibility:

$$kT\chi/N\mu^2=4/(3+e^{0.4/T}). \quad (3)$$

TABLE I. Calculated values of $\log_{10}(P_{mm}/T^{5/2})$.[a]

Temperature (°K)	0.3	0.6	1.0	1.2	1.5	2.0	2.5
New equation	$\bar{2}.4553$	+0.2367	0.9272	1.0971	1.2620	1.4280	1.5176
Abraham *et al.*	$\bar{2}.6494$	0.2828	0.9363	1.0999	1.2636	1.4284	1.5280
Chen and London	$\bar{2}.3849$	0.2317	0.9379				

[a] The two empirical equations are already known (see reference 2) to agree between 1° and 2.5°. Above 2.5° higher virial coefficients of the vapor become important.

In the foregoing equations, B is the second virial coefficient of the vapor, L_0 the "latent heat at absolute zero," P_{mm} the vapor pressure in millimeters of mercury. the other symbols having their usual meanings.

Some calculated vapor pressures are given in Table I. Between 1° and 2.5° the comparison is with the equation of Abraham *et al.*[4] which represents a satisfactory smoothing of their data. Below 1°, comparison is also made with the equation of Chen and London.[2] In the latter range preliminary measurements by Sydoriak and Roberts[5] agree with the latter equation to within 2 percent. These workers give a value of 5.30 calories/mole for L_0.

In Fig. 2 the calculated specific heat is compared with measurements by Abraham *et al.*,[6] Sydoriak and Roberts[7] and de Vries and Daunt.[8] (Only a few representative values have been taken from the rather large number of points reported by the last workers.) In Table II, calculated susceptibilities are compared with the data of Fairbank *et al.*[9]

A Gibbs' function like (1) can be plausibly derived from the cell model of a liquid developed on lines

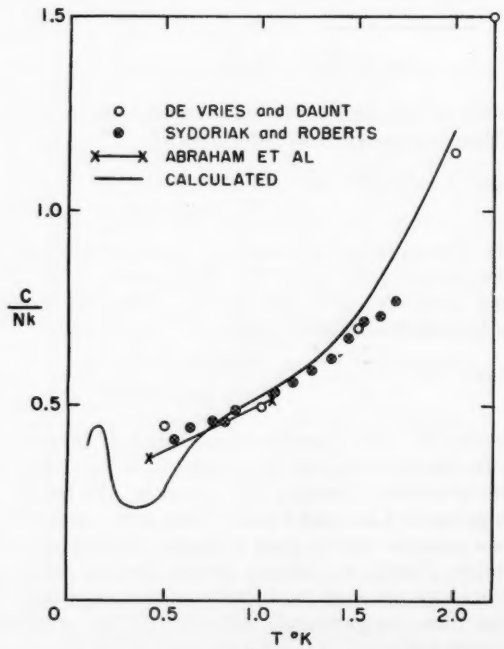

FIG. 2. Calculated and observed specific heats.

TABLE II. Calculated and observed values of $kT\chi/N\mu^2$.

Temperature (°K)	0.2	0.3	0.5	0.6	0.8	1.0	1.2	1.5
Calculated	0.385	0.661	0.776	0.808	0.861	0.891	0.910	0.929
Observed	0.50	0.63	0.82	0.85	0.90	0.93	0.94	0.95

suggested by the "pairwise" approximation of Heitler-London type. A detailed derivation will be published shortly, together with a critical comparison with the Fermi gas model. It turns out that an acceptable level scheme cannot depart greatly from that shown in Fig. 1.

The present equations predict a transition at about 0.1–0.2°K to an antiferromagnetic state, via a Schottky type anomaly (Fig. 2). A Curie type anomaly is predicted if the theory is developed on lines suggested by the theory of ferromagnetism, but it may be difficult to establish its existence experimentally. Either way, it is very likely that the specific heat will start to rise again at about 0.2°K–0.3°K.

[1] H. N. V. Temperley, Proc. Phys. Soc. (London) **A67**, 495 (1954).
[2] T. C. Chen and F. London, Phys. Rev. **89**, 1038 (1953).
[3] P. J. Price (unpublished).
[4] Abraham, Weinstock, and Osborne, Phys. Rev. **80**, 366 (1950).
[5] S. G. Sydoriak and T. R. Roberts in Proceedings of the Low Temperature Conference at Rice Institute, *Abstracts of Papers* (Rice Institute, Houston, 1953).
[6] Abraham, Weinstock, and Osborne, Phys. Rev. **94**, 202 (1954).
[7] S. G. Sydoriak and T. R. Roberts, Phys. Rev. **93**, 1418 (1954).
[8] G. de Vries and J. G. Daunt, Phys. Rev. **93**, 631 (1954).
[9] Fairbank, Ard, and Walters, Phys. Rev. **95**, 567 (1954).

Mechanism of Intermetallic Diffusion*

L. SLIFKIN† AND C. T. TOMIZUKA

Department of Physics and Electrical Engineering Research Laboratory, University of Illinois, Urbana, Illinois

(Received December 6, 1954)

THREE mechanisms for intermetallic diffusion have been extensively discussed: (1) interchange, (2) vacancy, and (3) interstitial. The interchange mechanism cannot result in a net atomic flow and hence is presumably not of major importance in those cases in which a Kirkendall effect is exhibited. It is proposed that a distinction may be made between the other two possibilities by studying self-diffusion in ordered crystals.

Consider a binary alloy which is ordered such that each atom is surrounded only by unlike atoms. If vacancies move by jumping to nearest-neighbor sites then the motion of a vacancy through the lattice would produce equal amounts of diffusion of both constituents. The interstitial mechanism, on the other hand, would allow the two types of atoms to move independently and, if they are quite dissimilar, would be expected to lead to different diffusion coefficients. The existence of an appreciable difference in diffusion coefficients alone, however, does not necessarily imply the interstitial

mechanism, since it is still conceivably possible for two independent processes of vacancy diffusion to take place within the sublattices which are each made up solely of one of the constituents of the alloy. Thus, a comparison of the diffusion of tracers of both components should allow, to a limited extent, a choice to be made between the two mechanisms.

Tracer experiments on β brass which should give such information are now being performed by Kuper and Tomizuka[1] of this laboratory.

Measurements of the diffusion of In and Sb in InSb are underway by Millea and Tomizuka. Preliminary data on this experiment by Slifkin and Tomizuka indicate an appreciably faster diffusion rate of In than of Sb.

The authors wish to thank Dr. Frederick Seitz for many helpful discussions.

* Supported in part by the U. S. Atomic Energy Commission and the U. S. Office of Naval Research.

† Present address, Physics Department, University of Minnesota, Minneapolis, Minnesota.

[1] A. B. Kuper and C. T. Tomizuka, Bull. Am. Phys. Soc. **29**, No. 7, 29 (1954).

Decay of Co^{57}†

L. Madansky and F. Rasetti

Johns Hopkins University, Baltimore, Maryland

(Received December 3, 1954)

Livingood and Seaborg[1] attributed a 270-day positron activity to Co^{57} and deduced a maximum positron energy of 0.26 Mev from absorption measurements. Plesset[2] assigned to the same isotope gamma rays of 117 and 130 kev determined by a magnetic analysis of the conversion spectrum. Deutsch and Wright[3] reported a 14-kev transition with a mean life of 0.1 microsecond. Cheng, Dick, and Kurbatov[4] analyzed the positron spectrum of a mixed source of Co^{57} and Co^{58}, attributing to Co^{57} a component with 0.32-Mev maximum energy. They also observed conversion electrons from gamma-ray lines at 119 and 133 kev. Alburger and Grace[5] studied the gamma-ray spectrum using proportional counters and reported gamma-ray energies of 123 and 137 kev with relative intensities in emission about 20:1. In the conversion spectrum, however, the lines appeared with equal intensities. Crasemann and Manley[6] reported energies of 119 and 133 kev, an intensity ratio of 30:1, and a K/positron ratio of the order of 10^3.

A source of Co^{57}, prepared by proton bombardment of nickel, was supplied by the Oak Ridge National Laboratory. Examination of the radiation with a scintillation spectrometer showed almost total absence of annihilation radiation, indicating that the main decay process could not be positron emission. The radiations of this source were studied by means of scintillation spectrometers with various crystal thicknesses (sometimes used in coincidence with resolving time of 1.5 microseconds) and Geiger counters. Chemical separation from added Fe and Ni showed that the activity was due to cobalt.

Gamma-ray lines of approximately 14 and 120 kev were observed, in addition to strong x-rays at 6.4 kev (K radiation of Fe). The reported line (crossover transition) at 134 kev was not found; however, in view of its low reported intensity it is doubtful whether it could be resolved from the wing of the 120-kev line. Cohen, Charpie, Handley, and Olson[7] state that in the spectrum of Mn^{57} the 117- and 134-kev lines have approximately equal intensities; this is certainly not true in our case. Extremely weak annihilation radiation (about 8×10^{-3} quanta for each quantum of 120 kev) was detected by means of thick NaI crystals. However, the annihilation photons did not appear to coincide with the 120-kev line, indicating either that they belong to an impurity, or that positron decay, if any, leads mainly to the ground state of Fe^{57}.

Within the accuracy of the measurements, every gamma ray of 14 kev and every x-ray coincide with the 120-kev gamma ray. The 14-kev gamma ray, however, does not coincide with the x-ray. A low coincidence rate observed with one spectrometer covering the x-ray region and the other scanning the 14-kev region appeared to be due to Compton scattering of the 120-kev line in one of the crystals and other spurious effects. This conclusion was also confirmed by preparing a NaI(Tl) crystal containing the activity. Pulses of 14 kev were observed in this crystal, instead of pulses of 21 kev as expected in the case of prompt coincidence of the gamma transition with K excitation.

Intensity measurements showed that the numbers of x-rays and 120-kev gamma rays are about equal, indicating one 120-kev transition per disintegration. The intensity of the 14-kev gamma ray is about 0.1 quantum per decay. Within the accuracy of the measurements its intensity did not appear higher when the source was embedded in the crystal, showing that the conversion coefficient is low. We also measured the number of high-energy conversion electrons in a Geiger counter with a 2-mg/cm^2 mica window. An absorption curve taken with additional mica foils was used to correct for absorption in the window. The ratio of conversion electrons to 120-kev photons was found to be 0.10.

These observations show that: (1) Co^{57} decays mainly if not exclusively, by orbital electron capture. (2) The 14-kev and 120-kev transitions are in cascade. (3) The 14-kev transition precedes the other, has a lifetime at least an order of magnitude longer than a microsecond, and is not highly converted. (4) The 120-kev transition has a short lifetime and a conversion coefficient lower than 0.1. (5) The crossover transition is weak. (6) Most of the disintegrations lead to the 120-kev excited state, about 10 percent to the 134-kev state, and none or few to the ground state. The decay scheme is repre-

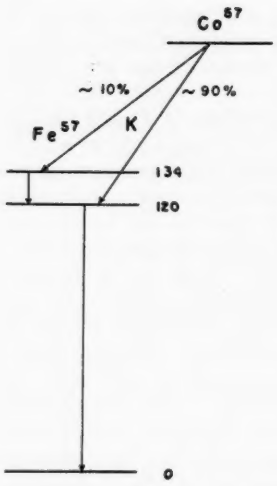

FIG. 1. Decay scheme of Co^{57}.

sented in Fig. 1. It differs from the one presented by Goldhaber and Hill[8] in that positron emission has been suppressed and the order of the two gamma rays reversed.

Experiments are in progress to determine the lifetime of the 120-kev state and the angular correlation of the two gamma rays.

We wish to thank Dr. W. S. Koski for performing chemical separations.

† Work supported by the U. S. Atomic Energy Commission.

[1] J. J. Livingood and G. T. Seaborg, Phys. Rev. **60**, 913 (1941).
[2] E. H. Plesset, Phys. Rev. **62**, 181 (1942).
[3] M. Deutsch and W. E. Wright, Phys. Rev. **77**, 139 (1950).
[4] Cheng, Dick, and Kurbatov, Phys. Rev. **88**, 887 (1952).
[5] D. E. Alburger and M. A. Grace, Proc. Phys. Soc. (London) **67**, 280 (1954).
[6] B. Crasemann and D. L. Manley, Bull. Am. Phys. Soc. **29**, No. 8, 31 (1954).
[7] Cohen, Charpie, Handley, and Olson, Phys. Rev. **94**, 953 (1954).
[8] M. Goldhaber and R. D. Hill, Revs. Modern Phys. **24**, 179 (1952).

Nuclear Electric Quadrupole Moment of Na^{23}†

M. L. PERL, I. I. RABI, AND B. SENITZKY
Columbia University, New York, New York
(Received December 7, 1954)

THE hyperfine interaction constants of the $3\,^2P_{\frac{3}{2}}$ and $3\,^2P_{\frac{1}{2}}$ excited states of Na^{23} have been measured by the atomic beam resonance method proposed by Rabi.[1] In this method, the Na^{23} beam is excited by resonance radiation from a sodium discharge lamp, while a radio-frequency magnetic field is simultaneously applied. The rf changes the magnitude of the refocused beam when the rf corresponds to the separation of two hyperfine levels in the excited state. Since this change is small, high rf power and an intense light source are necessary. For the light source both Philips SO 60 W and General Electric NA-1 sodium lamps were used. From 10 to 20 percent of the atoms in the beam were excited, depending on the way the lamps were operated. Two continuously tunable triode oscillators were used to cover the rf range of 6 to 240 Mc/sec.

The small excited state rf effect also required a more elaborate detection system than is used in the usual atomic beam experiment. The rf field is square-wave modulated at 34 cps so that the refocused beam contains modulated excited state signal and unmodulated background. The atoms are ionized on the usual hot, oxidized, tungsten ribbon and deflected through a simple mass spectrometer onto the first dynode of an Allen type electron multiplier. The modulated portion of the output signal of the Allen tube is then amplified in a narrow band tuned amplifier. The signal is then rectified in a lock-in circuit, averaged in a long time constant *RC* circuit, and put on a recorder.

A typical set of experimental points for the $3\,^2P_{\frac{3}{2}}$ state at near-zero magnetic field is shown in Fig. 1. The narrow lines of the typical atomic beam resonance experiment are absent in this experiment. This is because the fundamental line width is here determined by the natural lifetime of the excited state, rather than by the atom in the rf field. The experimental points are fitted by means of two overlapping resonance curves of the form

$$\frac{h_{\mathrm{I}}}{(f-f_{\mathrm{I}})^2+g^2}+\frac{h_{\mathrm{II}}}{(f-f_{\mathrm{II}})^2+g^2},$$

where h_{I} and h_{II} are the heights of the individual resonances, f_{I} and f_{II} are the centers of the individual resonances, and g is their width. These five constants are determined by trial for a best fit. The results obtained in a series of five runs are given in Table I. The widths are in agreement with the results of Stephenson.[2] In addition, the $F=2$ to $F=1$ hyperfine separation in the

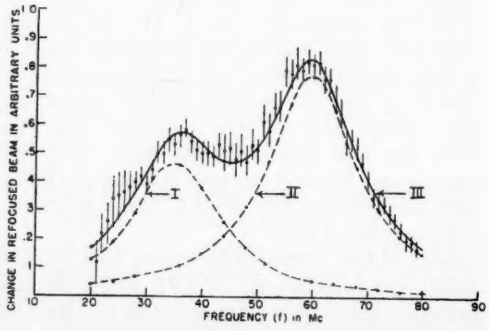

FIG. 1. Typical resonance curve for $3\,^2P_{\frac{3}{2}}$ state of Na^{23}, taken at 1.84-gauss static field. The dots with vertical probable error lines are the experimental points. Curves I and II are the individual resonance curves and curve III is their sum. The parameters of the curves are selected to give a best fit of curve III to the experimental points.

TABLE I. Constants obtained from the resonance curves of five different runs.

f_I, center of lower peak (Mc/sec)	f_{II}, center of upper peak (Mc/sec)	g, line width (Mc/sec)
35.0	58.5	9.75
35.5	59.8	9.80
35.4	59.8	9.80
36.0	60.2	9.75
35.8	60.5	9.90

$3\,^2P_{\frac{1}{2}}$ state was measured at near-zero magnetic field. This measurement gives a magnetic hyperfine interaction constant in the $3\,^2P_{\frac{1}{2}}$ state of $a_{\frac{1}{2}}=94.4\pm0.5$ Mc/sec.

In the $3\,^2P_{\frac{1}{2}}$ state, the three hyperfine level separations are given by

$$(3a_{\frac{1}{2}}+b) \quad \text{for} \quad F=3 \quad \text{to} \quad F=2,$$
$$(2a_{\frac{1}{2}}-b) \quad \text{for} \quad F=2 \quad \text{to} \quad F=1,$$
$$(a_{\frac{1}{2}}-b) \quad \text{for} \quad F=1 \quad \text{to} \quad F=0,$$

where $a_{\frac{1}{2}}$ and b are the magnetic dipole and electric quadrupole hyperfine interaction constants for the $3\,^2P_{\frac{1}{2}}$ state. Since the theoretical ratio of $(a_{\frac{1}{2}})/(a_{\frac{3}{2}})$ is 5 we can uniquely assign the two observed overlapping resonances to the 3–2 and 2–1 transitions. The weak 1–0 transition was not observed, so that there are two possible values of b, each giving a different value for the nuclear electric quadrupole moment, Q. It is difficult to assign a probable error to the values of b which one gets from the kind of curve-fitting one is compelled to use in evaluating this experiment. The average value of the two possible coefficients are $b=+2.58\pm0.18$ Mc/sec and $b=-21.6\pm0.5$ Mc/sec, where the error is taken to be the extreme of the deviation from the average. However if the peak positions of I and II from different runs are taken the limits become much wider. For this reason we do not trust the resultant values of b to better than about 10 percent. The corresponding values of Q are $Q=+0.11\times10^{-24}$ cm^2 and $Q=-0.91\times10^{-24}$ cm^2, without corrections of the Sternheimer type.

In conventional optical spectroscopy, further assignment can be made by the ratio of the intensities of lines. In our case a comparison of the experimental ratio with a simplified theoretical calculation of the ratio favors the assignment of the upper transition to the 3–2 transition. This gives a Q of $+0.11\times10^{-24}$ cm^2. However we do not feel that the experimental conditions of either the light source or the application of the rf are sufficiently definite to make this assignment with full confidence. These remarks apply equally to the results of Sagalyn[3] obtained by the double-resonance optical method. Current nuclear theory would find it very difficult to accept the value $Q=-0.91\times10^{-24}$ cm^2.

Full details will be published in an extended paper in this journal. We are now in the course of making similar measurements on rubidium. We wish to acknowledge the important contributions of Dr. Charles A. Lee and Dr. G. K. Woodgate who participated in the construction and operation of the early form of the apparatus.

† This work was supported in part by the U. S. Office of Naval Research.

[1] I. I. Rabi, Phys. Rev. **87**, 379 (1952).
[2] G. Stephenson, Proc. Phys. Soc. (London) **A64**, 463 (1951).
[3] P. L. Sagalyn, Phys. Rev. **94**, 885 (1954).

CONTENTS—Continued

Observation of Exchange Resonance Near a Ferrimagnetic Compensation . . . Roald K. Wangsness 831

Exchange Resonance Near a Ferrimagnetic Compensation Point . . . . . Thomas R. McGuire 831

Measurements on Pile-Irradiated LiF . . . . . D. T. Keating 832

Saturation Magnetization in Ferromagnetic Metals . T. G. Nilan and W. S. Paxton 834

Based on the "Cell" Model . . . . . H. N. V. Temperley 835

Diffusion . . . . . L. Slifkin and C. T. Tomizuka 836

. . . . . L. Madansky and F. Rasetti 837

Quadrupole Moment of Na^{23} . . . . M. L. Perl, I. I. Rabi, and B. Senitzky 838

CONTENTS

THE PHYSICAL REVIEW SECOND SERIES, VOLUME 97, NUMBER 2 JANUARY 15, 1955

Thermodynamic Properties of He^3 and He^4 Solutions . . . . . V. S. Mo
Compressibilities of Some Solidified Gases at Low Temperatures . . . . . John W. Stew
Enhancement of Fluorescence in Sulphides Under High-Energy Irradiation . . . . . Milton Kallmann and Bermuth Kall
Energy Levels of a Disordered Alloy . . . . . R. H. Parm
Irradiation Effects in Cu, Ag, and Au Near 10°K . . . . . H. G. Cooper, J. S. Koehler, and J. W. Mar
Measurements of Electrical Conductivity and Magnetoresistance of Gold Wir . . . . . A. C. E. Quint
Gold as an Acceptor in Germanium . . . . . C. Dunlap
Molecular Field in the Spherical Model . . . . . Marshall
Effective Carrier Mobility in Surface-Space Charge Layers . . . . . J. R. Schrieffer
Band Model for Hall Effect, Magnetization, and Resistivity of Magnetic Metals . . . . . Emerson M. Pugh and Norman Rostoker
Elastic Spectrum of Copper from Temperature-Diffuse Scattering of X-Rays . . . . . E. H. Jacobsen
Slow Electrons in a Polar Crystal . . . . . R. P. Feynman, R. W. Hellwarth, C. K. Iddings, and P. M. Platzman
Resistance and Thermoelectric Measurements of Cold-Worked Copper and the Resistance Minimum at Low Temperatures . . . . . W. B. Pearson
Properties of Germanium Doped with Cobalt . . . . . W. W. Tyler, R. Newman, and H. H. Woodbury
Vibrational Anharmonicity and Lattice Thermal Properties. II . . . . . D. K. C. MacDonald and S. K. Roberts
Physical Defects in Silver Halides . . . . . Chester R. Berry
Millimeter Wave Spectra of SbH_3 and SbD_3 . . . Albert W. Jache, Gilbert S. Blevins, and Walter Gordy
Millimeter Wave Spectra of AsH_3 and AsD_3 . . . Gilbert S. Blevins, Albert W. Jache, and Walter Gordy
Polarization Energy for 3*d* and 4*p* Electrons . . . . . R. E. Watson
Electromagnetic Spectrum of Am^{241} . . . . . Paul F. Gast
Dynamics of Nuclear Deformation . . . . . D. R. Inglis
Radiations of 34-Day Xe^{135} . . . . . Jnanadaya B. Mukerji
Internal and External Bremsstrahlung in Connection with the Beta Decay of P^{32} . . . . . N. Svartholm and N. L. Swanberg
Energy Levels of Rh^{105} from the Decay of Pd^{105} and Ru^{105} . . . . . Babulal Sarkar
High-Energy Gamma Rays from the Proton Bombardment of Fluorine . . . . . G. K. Farney, H. H. Givin, B. D. Kern, and T. M. Hahn
Elastic Scattering of 22-Mev Alpha Particles . . . . . N. S. Wall, J. R. Risser, and K. W. Ford
Nature of Positron Annihilation in Liquids and Solids . . . . . W. R. Dixon and L. E. H. Trainor
Matrix Elements in Superallowed Transitions . . . . . Mark Bolsterli and Eugene Feenberg
Half-Lives of Mn^{53} and Mn^{54} . . . . . E. W. Bertram and R. H. Hildebrand
Short-Period Delayed Neutrons from Fission . . . . . P. A. Benedetti and F. R. Bennett
Radioactivities of Zn^{69} and Zn^{71} . . . . . J. M. LeBlanc, J. M. Reid, and S. B. Burson
Tritium Production from *Lithium* by Deuteron Bombardment . . . . . R. L. Macklin and H. E. Banta
Recoil Deuterons and Disintegration Protons from the *n-d* Interaction, and *n-p* Scattering at $E_n = 16.1$ Mev . . . . . John D. Seagrave
Attempt to Detect the Antineutrinos from a Nuclear Reactor by the $Cl^{37}(\bar{\nu},e^-)A^{37}$ Reaction . . . . . Raymond Davis, Jr.
Interactions of the Heavy Nuclei of the Cosmic Radiation . . . . . J. H. Noon and M. F. Kaplon
Tritium and Neutron Production by 2.2-Bev Protons on Nitrogen and Oxygen . . . . . E. L. Fireman and F. S. Rowland
Proton-Proton Scattering at 437 Mev . . . . . R. B. Sutton, T. H. Fields, J. G. Fox, J. A. Kane, W. E. Mott, and R. A. Stallwood
Scattering of 151-Mev Positive Pions by Protons . . . . . Raymond A. Cutkosky and Arnold F. Clark
π^--p Interactions at 1.4 Bev . . . . . E. M. Eisenstein, W. B. Fowler, R. M. Lea, W. D. Shephard, R. P. Shutt, A. M. Thorndike, and W. L. Whittemore
Search for Electromagnetic Interactions Between μ Mesons and Electrons . . . . . L. S. Osborne, W. D. Rankin, F. C. Senn, A. Silverberg, and A. Wattenberg
Biquadratic Spinor Identities . . . . . K. M. Case
Renormalization of a Covariant Approximation Scheme in Field Theory . . . . . R. Arnowitt and S. Gasiorowicz

(*continued on cover page three*)

PRINTED IN U.S.A.